

**NASA TECHNICAL  
MEMORANDUM**

NASA TM X-64726

**LARGE SPACE TELESCOPE  
PHASE A FINAL REPORT**

**Volume III – Optical Telescope Assembly**

By Program Development  
(This volume prepared by Itek Corporation)

December 15, 1972

**CASE FILE  
COPY**

**NASA**

*George C. Marshall Space Flight Center  
Marshall Space Flight Center, Alabama*

## DOCUMENT CONTENTS

### Volume I – Executive Summary

- Chapter I – Introduction
- Chapter II – Mission Analysis
- Chapter III – LST Configuration and Systems Design
- Chapter IV – Maintenance Analysis
- Chapter V – Conclusions and Recommendations

### Volume II – Mission Description and System Design Characteristics

- Chapter I – Scientific Uses of the LST
- Chapter II – Phase A Study Approach
- Chapter III – Mission Analysis
- Chapter IV – LST Configuration and System Design
- Chapter V – Configurations and System Alternatives
- Chapter VI – Interfaces
- Chapter VII – Low Cost Considerations
- Chapter VIII – Program Implementation
- Chapter IX – Conclusions and Recommendations
- Appendix A – Alternate LST Structural Design Employing Graphite/Epoxy Shells
- Appendix B – Solar System Observations
- Appendix C – LST Configuration Concept Comparison

### Volume III – Optical Telescope Assembly

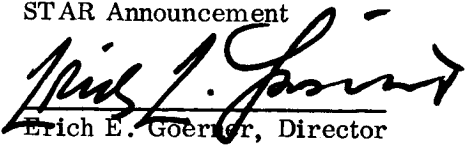
- Section A – Introduction
- Section B – System Considerations
- Section C – System Design

### Volume IV – Scientific Instrument Package

- Section 1 – Introduction
- Section 2 – General Scientific Objectives
- Section 3 – SIP System Analysis
- Section 4 – Scientific Instrumentation
- Section 5 – Ancillary Subsystems
- Section 6 – Imaging Photoelectric Sensors
- Section 7 – Environmental Considerations of the Scientific Instrumentation Design
- Section 8 – Scientific Instrument Package Physical Description
- Section 9 – Interface Considerations
- Section 10 – Reliability and Maintainability
- Section 11 – Program Planning
- Appendix A – Resolvable Element Size vs Pointing Parametric Analysis
- Appendix B – Signal-to-Noise Ratio

### Volume V – Support Systems Module

- Chapter I – Configuration and System Design
- Chapter II – Structures
- Chapter III – Thermal Control System
- Chapter IV – Electrical System
- Chapter V – Communication and Data Handling
- Chapter VI – Attitude Control System
- Chapter VII – Maintainability Analyses
- Chapter VIII – Reliability Analysis
- Chapter IX – Conclusions
- Appendix A – LST Contamination Control
- Appendix B – Scientific Data Gathering Efficiency
- Appendix C – Derivation of Optimum Readout Bandwidth for Preamplifier of SEC Vidicon

1. REPORT NO. TM X- 64726	2. GOVERNMENT ACCESSION NO.	3. RECIPIENT'S CATALOG NO.	
4. TITLE AND SUBTITLE Large Space Telescope Phase A Final Report Volume III - Optical Telescope Assembly		5. REPORT DATE December 15, 1972	6. PERFORMING ORGANIZATION CODE
		8. PERFORMING ORGANIZATION REPORT #	
7. AUTHOR(S) By Program Development*		10. WORK UNIT NO.	
9. PERFORMING ORGANIZATION NAME AND ADDRESS  George C. Marshall Space Flight Center Marshall Space Flight Center, Alabama 35812		11. CONTRACT OR GRANT NO.	
		13. TYPE OF REPORT & PERIOD COVERED  Technical Memorandum	
12. SPONSORING AGENCY NAME AND ADDRESS  National Aeronautics and Space Administration Washington, D.C. 20546		14. SPONSORING AGENCY CODE	
15. SUPPLEMENTARY NOTES  Prepared by Program Development  *This volume prepared by Itek Corporation			
16. ABSTRACT <p>This document is a report of the Phase A study of the Large Space Telescope (LST). The study defines an LST concept based on the broad mission guidelines provided by the Office of Space Science (OSS), the scientific requirements developed by OSS with the scientific community, and an understanding of long range NASA planning current at the time the study was performed.</p> <p>The LST is an unmanned astronomical observatory facility, consisting of an optical telescope assembly (OTA), scientific instrument package (SIP), and a support systems module (SSM). The report consists of five volumes: Volume I is an executive summary, Volume II is a summary of the entire report, and Volumes III, IV, and V contain the analyses and conceptual designs of the OTA, SIP, and SSM, respectively. The report describes the constraints and trade off analyses that were performed to arrive at a reference design for each system and for the overall LST configuration.</p> <p>The LST will be launched into low earth orbit by the Space Shuttle and operated for 10 to 15 years. The Shuttle will also be used to maintain the LST and to update the scientific instrument complement. Several maintenance modes have been investigated, including on-orbit pressurization of the SSM to provide a shirtsleeve environment for maintenance, and earth return of the LST.</p> <p>The LST will provide the scientific community with several fundamentally unique capabilities which will permit the acquisition of new and important observational data. Its location in space permits observations over the entire spectrum from about 100 nm to the far infrared.</p> <p>A low cost design approach was followed in the Phase A study. This resulted in the use of standard spacecraft hardware, the provision for maintenance at the black box level, growth potential in systems designs, and the sharing of Shuttle maintenance flights with other payloads.</p>			
17. KEY WORDS Large Space Telescope Scientific Satellite Astronomy Payload High Resolution Astronomy Faint Object Detection Conceptual Satellite Design <del>Shuttle Maintenance Spacecraft</del>		18. DISTRIBUTION STATEMENT STAR Announcement  Erich E. Goerner, Director Preliminary Design Office	
19. SECURITY CLASSIF. (of this report) Unclassified	20. SECURITY CLASSIF. (of this page) Unclassified	21. NO. OF PAGES 537	22. PRICE NTIS

## LIST OF ACRONYMS

A/D	analog to digital
ACN	Ascension Island (tracking station)
ACS	attitude control system
AFO	Announcement for Flight Opportunity
AGC	automatic gain control
AGO	Santiago, Chili (tracking station)
ALU	arithmetic logic unit
AM	airlock module
AOS	acquisition of signal
APP	antenna position programmer
ASCS	attitude sensing and control system
ASR	automatic send/receive
ASTAM	automated system test and monitor
ATM	Apollo Telescope Mount
ATS	Applications Technology Satellite
AVE	Mojave, California (tracking station)
BDA	Bermuda (tracking station)
BECO	Teledyne-Brown Engineering Company
BER	bit error rate
BITE	built-in test equipment
BOL	beginning of life
BOM	basic operating module
BUR	Johannesburg, South Africa (tracking station)
C&DH	communications and data handling

## LIST OF ACRONYMS (Continued)

C&DHS	communications and data handling system
C&W	caution and warning
CAM	computer address matrix
CCD	charge couple device
CCS	contamination control system
CDR	critical design review
CG, C.G.	center of gravity
CMG	control moment gyro
CMOS	complementary metal oxide semiconductor
CPU	central processor unit
CRO	Carnarvon (tracking station)
CSS	coarse sun sensor
CTU	command and telemetry unit
CYI	Canary Islands (tracking station)
D/A	digital to analog
DAU	data acquisition unit
DDT&E	design, development, test, and engineering
DEA	drive electronics assembly
DG	double gimbal
DGCMG	double gimbal CMG
DOD	depth of discharge
DPA	digital processor assembly
DSIF	Deep Space Instrumentation Facility
DTPL	domain tip propagation logic

## LIST OF ACRONYMS (Continued)

DTU	data transmission unit
ECA	electrical control assembly
EC/LSS	environmental control/life support system
EDS	electrical distribution subsystem
EDU	electrical distribution unit
EIRP	effective isotropic radiated power
EM, em	electromagnet; engineering model
EMC	electromagnetic control
EMI	electromagnetic interference
EOL	end of life
EOM	end of mission
EPS	electrical power subsystem
ERTS	Earth Resources Technology Satellite
ESE	electrical support equipment
ETC	Engineering Training Center, Greenbelt, Maryland
EVA	extravehicular activity
EVLSS	extravehicular life support system
FGS	fine guidance system
FHST	fixed-head star tracker
FM	frequency modulated
FMEA	failure mode effects analysis
FOV	field of view
FRUSA	flexible, rollup solar array
FST	fixed star tracker

## LIST OF ACRONYMS (Continued)

GAC	Grumman Aerospace Corporation
GDN	ground data network
GDSX	Goldstone (tracking station)
GESE	ground electrical support equipment
ghu	gyro hang-up
GMT	Greenwich mean time
GRARR	Goddard range and range rate
GSE	ground support equipment
GSFC	Goddard Space Flight Center
GST	gimbaled star tracker
GWM	Guam (tracking station)
HAW	Hawaii (tracking station)
HEAO	High Energy Astronomy Observatory
HEPA	high efficiency particulate air
HPI	high performance insulation
HSK	Honeysuckle Creek, Australia (tracking station)
I/O	input/output
I. D.	inside diameter
IESE	in-space electrical support equipment
IOCC	integrated operations control console
IOP	in the orbit plane
ISA	interstage adapter; interface systems adapter
IVA	intravehicular activity
LCP	left circular polarized
LOHARR	Lockheed heat rate program
LOS	line of sight

## LIST OF ACRONYMS (Continued)

LSI	large scale integration
LST	Large Space Telescope
MAC	maximum allowable concentration
MAD	Madrid, Spain (tracking station)
MCC	mission control center
MCF	Mating/Checkout Facility
MIB	minimum impulse bit
MIL	Merritt Island, Florida (tracking station)
MMS	micrometeoroid shell
MNOS	metal nitride oxide silicon
MOJAVE	tracking station at Barstow
MOS/LSI	metal oxide semiconductor/large-scale integrated
MSFC	Marshall Space Flight Center
MSFN	Manned Space Flight Network
MSS	magnetometer sensing system
MT	magnetic torquer
MTBF	mean time between failures
MTE	magnetic torquer electronics
MTF	modulation transfer function
MTS	magnetic torquing system
MTU	magnetic tape unit
NASCOM	National Aeronautics and Space Administration Communications Network
NASO	National Astronomical Space Observatory
NDRO	nondestructive readout
NEA	noise equivalent angle



## LIST OF ACRONYMS (Continued)

NFL	St. John's, Newfoundland (tracking station)
OAAR	other activities as required
OAO	Orbiting Astronomical Observatory
OAS	Orbit Adjust Stage
OMS	orbit maneuvering system
OOC	observatory operation center
ORRX	Orroral Valley (tracking station)
OSR	optical solar reflector
OTA	optical telescope assembly
OWS	Orbital Workshop
PCM	phase change material; pulse code modulator
PCS	peripheral communication system
PCU	power converter unit
PDR	preliminary design review
PEP	perpendicular to the ecliptic plane
PGA	pressure garment assembly
PM	pulse modulated
POP	perpendicular to the orbit plane
PRR	preliminary requirements review
PSD	power spectral density
PSK	phase shift keyed
PSU	power switch unit
QUI	Quito, Equador (tracking station)
R&D	research and development
RAM	research applications module (studies); reference alignment mode

## LIST OF ACRONYMS (Continued)

RBV	return beam vidicon
RCD	remote command decoder
RCP	right circular polarized
RCS	reaction control system
REC	recurring costs
RF	radio frequency
RFI	radio frequency interference
RGA	reference gyro assembly
ROM	read-only-memory
ROS, ROSMAN	tracking station at Rosman, North Carolina
RSDP	remote site data processor
RTV	room temperature vulcanizing
RW	reaction wheel
SAA	South Atlantic anomaly
SBU	sensor buffer unit
SCAMA	switching, conferencing, and monitoring arrangement
SEC	secondary electron conduction
SFP	solicitation for proposal
SG	single gimbal
SGCMG	single gimbal CMG
SI	science instrument
SIP	scientific instrument package
SIT	silicon intensified target
SMS	secondary mirror sensor
SPD	solar power distributor

## LIST OF ACRONYMS (Continued)

SPEH	special purpose equipment handler
SPF	single-point failure
SPG	single-point ground
SSM	support systems module
SSP	Space Station prototype
STADAN	Space Tracking and Data Acquisition Network
STDN	Spaceflight Tracking and Data Network
2-SPEED	two scissored pair ensemble explicit distribution
TA	transfer assembly
TACS	thrust attitude control system
TAN	Tananarive, Malagasy Republic (tracking station)
TBC	The Boeing Company
TCS	thermal control system
TDRS	tracking and data relay satellite (network)
TEX	Corpus Christi, Texas (tracking station)
TMR	triple modular redundancy
TOOMBA	tracking station at Cooby Creek
TRW	TRW Systems, Incorporated
TTY	teletypewriter
TWT	traveling wave tube
ULA	Fairbanks, Alaska (tracking station)
UPD	update buffer
USB	unified S-band
USBE	unified S-band equipment
VAB	Vertical Assembly Building
VGP	vehicle ground point

## LIST OF ACRONYMS (Concluded)

VPM	variable permanent magnet
W-R	Wolf-Rayet
WASS	wide angle sun sensor
WFE	wavefront error
WNK	Winkfield, United Kingdom (tracking station)
XPDR	transponder

## CONTENTS

A. Introduction . . . . .	A.1-1
B. System Considerations . . . . .	B.1-1
B.1 Review of Mission-Related Parameters . . . . .	B.1-1
B.2 Selection of Optical Parameters . . . . .	B.2-1
B.3 Error Budgets . . . . .	B.3-1
C. System Design . . . . .	C.1-1
C.1 Summary Description of System Arrangement and Family Tree . . . . .	C.1-1
C.2 Structural Design and Analysis . . . . .	C.2-1
C.3 Optical System Design . . . . .	C.3-1
C.4 Thermal Design . . . . .	C.4-1
C.5 Stabilization and Control Design . . . . .	C.5-1
C.6 Alignment, Focus, and Figure Control Design . . . . .	C.6-1
C.7 Electronic Systems Design . . . . .	C.7-1
C.8 Scientific Instrument Design . . . . .	C.8-1
C.9 Interface and Support Requirements . . . . .	C.9-1
C.10 Reliability . . . . .	C.10-1
C.11 Mass Properties . . . . .	C.11-1

FIGURES

A.1-1	LST/SIP Configuration . . . . .	A.1-5
B.2-1	Comparison of Aplanatic Gregorians and Baseline Cassegrain . . . . .	B.2-2
B.2-2	Effect of Focal Ratios on Obscuration and Telescope Length. . . . .	B.2-4
B.2-3	Calculated Point Spread Function at $\lambda = 315$ and $633$ Nanometers for the Perfect Unobscured Case and the Fully Toleranced LST. These Curves are All Normalized to the On-Axis, Unobscured, Untoleranced Case. . . . .	B.2-6
B.2-4	Calculated Encircled Energy for $\lambda = 316$ . . . . .	B.2-7
B.2-5	Development of Baseline LST Modulation Transfer Function. . . . .	B.2-8
B.2-6	Distortion in $f/12$ Image Versus Field Height. . . . .	B.2-9
B.3-1	Error Budget Tree . . . . .	B.3-3
B.3-2	System Wavefront Error Budget; $\lambda = 633$ Nanometers . . . . .	B.3-4
B.3-3	Image Stabilization Error Budget. . . . .	B.3-8
B.3-4	Top Level Absolute Pointing Error Budget. Note That Use of Slit Jaw Guidance for Spectroscopy Considerably Relaxes This Budget Requirement . . . . .	B.3-11
C.1-1	OTA Family Tree . . . . .	C.1-3
C.1-2	OTA System Block Diagram . . . . .	C.1-4
C.1-3	Matrix of Relationship of System Family Tree and Design Discussion Topics in Subsequent Report Sections . . . . .	C.1-5
C.1-4	Structural Support Assembly . . . . .	C.1-6
C.1-5	OTA Structural Interface . . . . .	C.1-7
C.1-6	OTA Main Optics System . . . . .	C.1-11
C.1-7	OTA Thermal Control System . . . . .	C.1-14
C.1-8	OTA Pointing Control System . . . . .	C.1-17
C.1-9	Performance Control System . . . . .	C.1-21
C.1-10	Telescope Protection/Diagnostic System . . . . .	C.1-24
C.1-11	Sun Shield Assembly . . . . .	C.1-27
C.1-12	Aperture Door Assembly. . . . .	C.1-31
C.1-13	Pressure Bulkhead Assembly . . . . .	C.1-33
C.1-14	Data Management System . . . . .	C.1-34
C.1-15	Power Distribution System . . . . .	C.1-37
C.2-1	Metering Structural Concepts . . . . .	C.2-3
C.2-2	Primary to Secondary Despace Versus Change in Temperature; Based on Length of 5.5 Meters . . . . .	C.2-4
C.2-3	Primary to Secondary Despace Versus Change in Temperature With Thermal Soak Loading Versus Change in Temperature; Based on Length of 5.5 Meters . . . . .	C.2-5
C.2-4	Secondary Metering Structure Natural Frequency Versus Primary Mirror $f$ /Number for Shell and Truss Configurations and Various Primary Mirror Apertures . . . . .	C.2-7
C.2-5	Active and Passive Mirror Configurations. . . . .	C.2-9
C.2-6	Primary Mirror Configuration for Structural Mathematical Model. . . . .	C.2-13
C.2-7	Viking Shroud Payload Envelope . . . . .	C.2-15
C.2-8a	Optical and Nonoptical Structural System . . . . .	C.2-16
C.2-8b	OTA Structural Interface and Configuration . . . . .	C.2-17
C.2-9	LST Dynamic Model . . . . .	C.2-21
C.2-10	LST Dynamic Model (All-Metal Structure). . . . .	C.2-22
C.2-11	Thermal Structural Response . . . . .	C.2-24
C.2-12	Mirror Analytical Flow Diagram . . . . .	C.2-28

C.2-13	3-Meter Monolithic Mirror . . . . .	C.2-29
C.2-14	Mirror Mounts . . . . .	C.2-31
C.2-15	Point Mount Types. . . . .	C.2-32
C.2-16	Axial-Leaf, Cantilevered, 3-Meter Mirror Radial Mount Force Versus Stiffness/Expansivity Constant for a 3-Meter Mirror Subjected to Various Temperatures . . . . .	C.2-35
C.2-17	RMS Surface Error of a 3-Meter Monolithic Mirror for Radial Loads at Three Points . . . . .	C.2-36
C.2-18	Mirror-Mount Attachment Concepts . . . . .	C.2-37
C.2-19	Computer Drawing of Eight-Point Invar-Titanium Truss . . . . .	C.2-40
C.2-20	OTA Secondary Metering Structure . . . . .	C.2-42
C.2-21	Modulus of Elasticity and Longitudinal Coefficient of Expansion Versus Laminar Orientation of Eight-Point Graphite-Epoxy Truss . . . . .	C.2-45
C.2-22	Orbital Thermal Condition Response. . . . .	C.2-47
C.2-23	Early SIP Structural Configuration . . . . .	C.2-49
C.2-24	Athermalized Radial Bay, Cantilevered Axial Bay SIP Structure . . . . .	C.2-50
C.2-25	Athermalized Radial Bay, Trussed Axial Bay SIP Structure . . . . .	C.2-51
C.2-26	Graphite-Epoxy Truss Configuration. . . . .	C.2-52
C.2-27	Plot of SIP Structural Mathematical Model. . . . .	C.2-55
C.2-28	SIP Temperature Distribution—Constant Q System . . . . .	C.2-56
C.2-29	Thermal Response of Structures, Constant Q . . . . .	C.2-60
C.2-30	Meteoroid Shield, Extended Configuration . . . . .	C.2-61
C.2-31	Main Baffle Assembly . . . . .	C.2-67
C.2-32	Forward Sunshade Support in Retracted Position . . . . .	C.2-69
C.2-33	Baffle Attachment to Meteoroid Shield . . . . .	C.2-71
C.2-34	Pressure Bulkhead Door and Mechanism . . . . .	C.2-73
C.2-35	Shuttle Support Points . . . . .	C.2-75
C.2-36	Manufacturing and Assembly Sequence for Composite Metering and SIP Truss Structure . . . . .	C.2-77
C.3-1	LST Telescope Design . . . . .	C.3-2
C.3-2	Effect of Central Obscuration Diameter on Modulation Transfer Function of High Resolution Camera. . . . .	C.3-6
C.3-3	Strehl Definition as Function of RMS Wavefront Error and Central Obscuration Diameter Ratio. . . . .	C.3-7
C.3-4	Telescope Field Curvature . . . . .	C.3-9
C.3-5	Fractional Distortion at f/12 Focus . . . . .	C.3-10
C.3-6	Distortion at f/12 Focus. . . . .	C.3-11
C.3-7	Null Lens Interferometer . . . . .	C.3-13
C.3-8	Tests Showing Surface Ripple on Parabolic Mirrors . . . . .	C.3-15
C.3-9	Fold Optics Layout . . . . .	C.3-17
C.3-10	Former Focal Plane Layout . . . . .	C.3-19
C.3-11	f/12 Image Plane Format . . . . .	C.3-20
C.3-12	Local Field Correction, Using Spherical Fold Mirrors 90 Centimeters in Front of Focus . . . . .	C.3-23
C.3-13	Focal Plane Layout . . . . .	C.3-24
C.3-14	Irradiance in LST Image Plane as a Function of Visual Magnitude of a Stray Light Source at Edge of Data Field . . . . .	C.3-30
C.3-15	Stray Light From Baffled Edges . . . . .	C.3-32
C.3-16	Percentage of Degradation in Equivalent Number of Monolayers . . . . .	C.3-35
C.3-17	Measured Reflectance of $Al + Al_2O_3$ as a Function of Wavelength. . . . .	C.3-36
C.3-18	Reflectance Changes of a $MgF_2/Al$ -Coated Cer-Vit Mirror . . . . .	C.3-37
C.3-19	Returning Flux Versus Altitude . . . . .	C.3-38
C.3-41	Spectral Performance of $MgF_2$ and $LiF$ Overcoated Aluminum . . . . .	C.3-41
C.4-1	LST Telescope Thermal Model . . . . .	C.4-7
C.4-2	Nodal Model of Primary Mirror . . . . .	C.4-10
C.4-3	Nodal Network for Truss Structure . . . . .	C.4-11
C.4-4	Nodal Model for Secondary Mirror . . . . .	C.4-12
C.4-5	Orbit and Orientation. . . . .	C.4-14
C.4-6	Temperature History of Primary Mirror Face . . . . .	C.4-15

C.4-7	Temperature History of Truss Structure . . . . .	C.4-17
C.4-8	Time/Temperature History of Primary Mirror in Perpendicular Operation . . . . .	C.4-22
C.4-9	Time/Temperature History of Primary Mirror in Perpendicular Operation . . . . .	C.4-23
C.4-10	Time/Temperature History of Primary Mirror in Perpendicular Operation . . . . .	C.4-24
C.4-11	Time/Temperature History of Secondary Mirror in Perpendicular Operation . . . . .	C.4-25
C.4-12	Time/Temperature History of Primary Mirror in Parallel Operation . . . . .	C.4-27
C.4-13	Time/Temperature History of Primary Mirror in Parallel Operation . . . . .	C.4-28
C.4-14	Time/Temperature History of Primary Mirror in Parallel Operation . . . . .	C.4-29
C.4-15	Time/Temperature History of Secondary Mirror in Parallel Operation . . . . .	C.4-30
C.4-16	Time/Temperature History of Truss Structure in Perpendicular Operation; Circumferential Distribution . . . . .	C.4-31
C.4-17	Time/Temperature History of Truss Structure in Perpendicular Operation; Circumferential Distribution . . . . .	C.4-32
C.4-18	Time/Temperature History of Secondary Spider in Perpendicular Operation; Axial Distribution . . . . .	C.4-33
C.4-19	Time/Temperature History of Secondary Spider in Perpendicular Operation . . . . .	C.4-34
C.4-20	Time/Temperature History of Meteoroid Shell in Perpendicular Operation . . . . .	C.4-35
C.4-21	Time/Temperature History of Truss Structure in Parallel Operation; Circumferential Distribution . . . . .	C.4-36
C.4-22	Time/Temperature History of Truss Structure in Parallel Operation; Circumferential Distribution . . . . .	C.4-37
C.4-23	Time/Temperature History of Truss Structure in Parallel Operation; Axial Distribution . . . . .	C.4-38
C.4-24	Time/Temperature History of Secondary Spider in Parallel Operation . . . . .	C.4-39
C.4-25	Time/Temperature History of Meteoroid Shell in Parallel Operation . . . . .	C.4-40
C.4-26	Response Time of Secondary Spiders . . . . .	C.4-41
C.4-27	Response Time of Forward Truss Elements . . . . .	C.4-43
C.4-28	Response Time of Truss Elements Near Main Support Ring . . . . .	C.4-45
C.4-29	Orbital Thermal Condition Response . . . . .	C.4-47
C.4-30	Outer Thermal Control Surface—Nodal Network . . . . .	C.4-51
C.4-31	Pressure Cylinder Wall—Nodal Network . . . . .	C.4-52
C.4-32	Radial Truss—Nodal Network . . . . .	C.4-53
C.4-33	Axial Truss—Nodal Network . . . . .	C.4-54
C.4-34	Fine Guidance Housing—Nodal Network . . . . .	C.4-55
C.4-35	SIP Temperature Distribution — Constant Q System . . . . .	C.4-57
C.4-36	SIP Temperature Distribution — Constant T System . . . . .	C.4-58
C.4-37	SIP Temperature Distribution — Insulated Structure . . . . .	C.4-60
C.5-1	OTA Pointing Control System . . . . .	C.5-2
C.5-2	Cascaded Representation of Vehicle and Secondary Mirror Control Loops . . . . .	C.5-6
C.5-3	Accommodation Ranges for Various Components of the Pointing and Stabilization System . . . . .	C.5-6
C.5-4	Pointing Control System . . . . .	C.5-7
C.5-5	Proposed Location of Electromagnets . . . . .	C.5-8
C.5-6	Astigmatism-Compensating Prismatic Grating . . . . .	C.5-11
C.5-7	Use of Reticle Plate in Generating Attitude Control Signals . . . . .	C.5-12
C.5-8	Fold Optics Layout . . . . .	C.5-13
C.5-9	Photoelectron Noise Limit to Fine Guiding, at Several Bandwidths . . . . .	C.5-15
C.5-10	Cumulative Star Density as a Function of Visual Stellar Magnitude . . . . .	C.5-16
C.5-11	Relative Location of Two Guide Stars in Guide Field . . . . .	C.5-18
C.5-12	Poisson Statistics for Guide Stars . . . . .	C.5-20
C.5-13	Sensor Noise Distribution for a Given Guide Field Area, Galactic Pole Viewing . . . . .	C.5-21
C.5-14	Sensor Noise Contribution to Line Of Sight Error for Minimum Area Configurations . . . . .	C.5-22
C.5-15	Image Plane Format, in Object Space Coordinates . . . . .	C.5-23
C.5-16	Guide Signal Noise of Fine Guidance System Relative to Noise From One Sensor . . . . .	C.5-24
C.5-17	Guide Signal Noise From Two-Sensor System, 4-Hertz Bandwidth, 4-Channel Image Dissector . . . . .	C.5-25
C.5-18	Beam Splitter With Two Image Dissectors . . . . .	C.5-28
C.5-19	Single Image Dissector With Dual Field of View . . . . .	C.5-29
C.5-20	Field-Variable Focal Length Relay . . . . .	C.5-31



C.5-21	Star Tracker Schematic . . . . .	C.5-32
C.5-22	Fine Guidance Mode Schematic . . . . .	C.5-33
C.5-23	Format on Image Dissector. . . . .	C.5-34
C.5-24	LST Fine Guidance Sensor Assembly . . . . .	C.5-37
C.5-25	Error Transfer Characteristics for Single Stars and Double Stars. . . . .	C.5-39
C.5-26	Image Dissector Tracker . . . . .	C.5-44
C.5-27	Line Spread Function and Signal Transfer Function for Astigmatic Images at LST Focal Plane (3.5 Milliradians Off Axis, $\lambda = 633$ Nanometers). . . . .	C.5-48
C.5-28	Image Dissector Tracker—Method of Signal Modulation . . . . .	C.5-49
C.5-29	Photoelectron Noise Limit to Tracking Accuracy, Refractive Reticle Mode . . . . .	C.5-54
C.5-30	Photoelectron Noise Limit to Tracking Accuracy, Image Dissector Mode . . . . .	C.5-55
C.5-31	Dark Field Optical Photomicrograph of Prismatic Grating (92 $\times$ ) . . . . .	C.5-56
C.5-32	Scanning Electron Microscope Photograph of Prismatic Grating (83 $\times$ ) . . . . .	C.5-56
C.5-33	Scanning Electron Microscope Photograph of Edge Pointed Out in Fig. C.5-32 (1,000 $\times$ ). . . . .	C.5-57
C.5-34	Scanning Electron Microscope Photograph of Surface Defects of Master Grating Occlusions Replicated in Prismatic Grating (1,600 $\times$ ) . . . . .	C.5-57
C.5-35	Maximum Value of Differential Aberration Versus Orbital Altitude for Several Separations of Two Stars . . . . .	C.5-59
C.5-36	Effect of Lateral Color Smear on Guide Signal Transfer Function . . . . .	C.5-62
C.5-37	Functional Diagram of Reticle Star Tracker . . . . .	C.5-63
C.5-38	Reticle Star Tracker, Coarse Positioning: Initial Acquisition . . . . .	C.5-65
C.5-39	Reticle Star Tracker, Coarse Positioning: Linear Servo Tracking. . . . .	C.5-66
C.5-40	Reticle Star Tracker, Fine Positioning . . . . .	C.5-67
C.5-41	Flow Chart of Tracker Head Acquisition/Lock-On Sequence . . . . .	C.5-68
C.5-42	Fine Stabilization Control System (Concept) . . . . .	C.5-73
C.5-43	Dynamic Force Isolation Actuation System for LST Secondary Mirror . . . . .	C.5-76
C.5-44	Secondary Mirror Actuator Configuration . . . . .	C.5-77
C.5-45	Piezoelectric Transducers . . . . .	C.5-79
C.5-46	Approximate Open Loop and Closed Loop Responses of Force Isolation Loop . . . . .	C.5-80
C.5-47	Frequency Response Relating to Mirror Angular Acceleration to the Corresponding Reaction Torque, $T_{gt}$ , Exerted on the Telescope Structure . . . . .	C.5-81
C.5-48	Signal Diagram of Secondary Mirror Actuation System. . . . .	C.5-82
C.5-49	Force Isolation Feedback Amplifier . . . . .	C.5-83
C.5-50	Guide Error Signal Coordinate Transformation Process . . . . .	C.5-86
C.5-51	Signal Processing for Fine and Coarse Tracking. . . . .	C.5-87
C.5-52	Signal Processing to Measure Slope of Guide Star Tracking Error Detector . . . . .	C.5-89
C.5-53	Vehicle Control Loop for Coarse Tracking . . . . .	C.5-90
C.5-54	Fine Tracking Control System for LST . . . . .	C.5-92
C.5-55	Asymptotic Plots of Secondary and Vehicle Loop Gains . . . . .	C.5-94
C.5-56	Transfer Function of Fine Tracking Loop . . . . .	C.5-95
C.5-57	General Torque Disturbance . . . . .	C.5-98
C.5-58	Limits on Allowable Torque Disturbances for $J = 10.85 \times 10^4$ Meter-Newton Second <sup>2</sup> and Peak Tracking Error of 0.0155 Microradians . . . . .	C.5-100
C.5-59	LST Stabilization Simulation Without Force Actuation Isolation System for Secondary Mirror . . . . .	C.5-102
C.5-60	Force Isolation Actuation System of Secondary Mirror Control System . . . . .	C.5-103
C.5-61	Bode Plot for Secondary Mirror Control Loop (Structural Dynamics Ignored) . . . . .	C.5-107
C.5-62	Bode Plot for Vehicle Control (Structural Dynamics Ignored) . . . . .	C.5-108
C.5-63	LST Tracking Responses to Line-of-Sight Step . . . . .	C.5-110
C.5-64	LST Tracking Responses to Line-of-Sight Step . . . . .	C.5-111
C.5-65	LST Tracking Responses for Line of Sight Step of 10 Microradians . . . . .	C.5-112
C.5-66	LST Tracking Responses . . . . .	C.5-113
C.5-67	Nonlinear Transfer Characteristic of Guide Star Tracking Error Sensor. . . . .	C.5-115
C.6-1	Performance Control System Components . . . . .	C.6-2
C.6-2	A-Frame Secondary Mirror Actuation System . . . . .	C.6-5
C.6-3	Alignment Sensors Used to Measure Tip of Secondary Mirror . . . . .	C.6-9
C.6-4	Alignment Sensors Used to Measure Decenter at Neutral Point . . . . .	C.6-10
C.6-5	Lateral Separation Focus Sensor Used in LST . . . . .	C.6-11

C.6-6	Basic Detector Used in Tilt and Decenter Sensors . . . . .	C.6-14
C.6-7	Electro-Optical Schematic Diagram of Two-Axis High Stability, Automatic Tilt Sensor . . . . .	C.6-15
C.6-8	Electro-Optical Schematic Diagram of High Stability, Two-Axis Automatic Decenter Sensor . . . . .	C.6-16
C.6-9	Engineering Model of Alignment Sensor. . . . .	C.6-17
C.6-10	Alignment Sensor Layout . . . . .	C.6-19
C.6-11	Focus Sensor Layout . . . . .	C.6-21
C.6-12	Optical Arrangement and Signal Characteristics . . . . .	C.6-23
C.6-13	Slit Image Diffraction Characteristics . . . . .	C.6-24
C.6-25	Cer-Vit Air Path Retroreflective Penta Set . . . . .	C.6-25
C.6-15	LSFS Functional Diagram . . . . .	C.6-28
C.6-16	Focal Plane Figure Sensor Using Image Dissector . . . . .	C.6-29
C.6-17	Diffraction Grating Shearing Interferometer . . . . .	C.6-31
C.6-18	Principles of White Light Grating Shearing Interferometer . . . . .	C.6-32
C.6-19	Breadboard Grating Shearing Interferometer . . . . .	C.6-33
C.6-20	Focal Plane Figure Sensor Block Diagram. . . . .	C.6-35
C.6-21	Shearing Interferometer Measuring Grid (36 Points, 56 Measurements) . . . . .	C.6-37
C.6-22	A-Frame Secondary Mirror Actuation Concept . . . . .	C.6-41
C.6-23	Secondary Mirror Actuator System . . . . .	C.6-42
C.6-24	Secondary Mirror Alignment Actuator System Design . . . . .	C.6-45
C.6-25	Secondary Mirror Alignment Actuator Layout . . . . .	C.6-47
C.6-26	Minimum Actuator Configurations for Controlling Astigmatism . . . . .	C.6-51
C.6-27	Figure Correction in a Thick, Lightweight, Monolithic Mirror . . . . .	C.6-52
C.6-28	Primary Mirror Force Actuator Layout . . . . .	C.6-54
C.7-1	LST/OTA Block Diagram . . . . .	C.7-3
C.7-2	Maximum Sustained Power Expected Versus Orbit Time . . . . .	C.7-5
C.7-3	Thermal Control System—Overall Power Control . . . . .	C.7-6
C.7-4	Typical Thermal Controller . . . . .	C.7-7
C.7-5	Siemens Three-Wire Connection . . . . .	C.7-8
C.7-6	Pointing Control System . . . . .	C.7-9
C.7-7	Guide Star Coordinates . . . . .	C.7-10
C.7-8	Typical Theta Servo . . . . .	C.7-11
C.7-9	Alignment Matrix Electronics . . . . .	C.7-12
C.7-10	Matrix Electronics . . . . .	C.7-14
C.7-11	Secondary Alignment Actuators . . . . .	C.7-15
C.7-12	Alignment Actuator Electronics . . . . .	C.7-17
C.7-13	Typical Force Actuator—Servo Subsystem . . . . .	C.7-18
C.7-14	Sun Shield Master Control . . . . .	C.7-20
C.7-15	Aperture Door Control . . . . .	C.7-21
C.7-16	Pressure Bulkhead Door Controls . . . . .	C.7-22
C.7-17	Temperature Sensor Controls . . . . .	C.7-23
C.7-18	Typical Temperature Sensor . . . . .	C.7-24
C.7-19	Typical Strain Sensor. . . . .	C.7-26
C.7-20	Vibration Sensor Controls . . . . .	C.7-27
C.7-21	Command Decoder Interface . . . . .	C.7-29
C.7-22	Typical Data Acquisition Unit Interface. . . . .	C.7-30
C.7-23	Power Distribution System . . . . .	C.7-31
C.7-24	Typical Power Conditioner and Control Unit . . . . .	C.7-32
C.8-1	Former Focal Plane Layout From NASA GSFC X-670-70-480 . . . . .	C.8-3
C.8-2	f/12 Image Plane Format . . . . .	C.8-4
C.8-3	Reference Focal Plane Layout. . . . .	C.8-5
C.8-4	LST/OTA Reflectance in Far-Ultraviolet . . . . .	C.8-6
C.8-5	LST/OTA Encircled Energy at 300 Nanometers . . . . .	C.8-7
C.9-1	Location of f/12 Image Plane . . . . .	C.9-2
C.9-2	f/12 Image Plane (in Object Space Coordinates) . . . . .	C.9-3
C.9-3	Instrument Locations in SIP Forward Truss . . . . .	C.9-6
C.9-4	OTA/SIP Coordinate System . . . . .	C.9-7
C.9-5	OTA/SSM Pointing Control Interfaces . . . . .	C.9-10

C.9-6	OTA/SSM Data Management Interface . . . . .	C.9-12
C.10-1	OTA/SIP Critical Paths . . . . .	C.10-2
C.10-2	OTA Reliability Prediction . . . . .	C.10-4
C.11-1	Mass Properties System Configuration and Math Model . . . . .	C.11-6
C.11-2	System Coordinates and Reference Data . . . . .	C.11-7

TABLES

B.3-1	Reduction of the Effect of Manufacturing Tolerances by Figuring of the Secondary Mirror Autocollimation . . . . .	B.3-5
B.3-2	Alignment Error Budget (Decenter and Tip) . . . . .	B.3-5
B.3-3	Focus Maintenance Budget . . . . .	B.3-7
B.3-4	Thermal Optical Design Requirements . . . . .	B.3-9
B.3-5	Mirror Mounts . . . . .	B.3-9
B.3-6	Fine Guidance System Error Sources for Star Observation . . . . .	B.3-10
B.3-7	Dimensional Stability Errors for f/96 Imagery . . . . .	B.3-10
C.1-1	OTA Command Requirements . . . . .	C.1-35
C.1-2	OTA Diagnostic Data Summary . . . . .	C.1-36
C.1-3	Power Conditioning and Control Subsystem Power Handling Requirements . . . . .	C.1-38
C.1-4	Power Conditioning and Control Subsystem Physical Characteristics . . . . .	C.1-39
C.2-1	Selected Data From System Structural Model Analysis . . . . .	C.2-25
C.2-2	Triangular-Element Model for 3-Meter (118-Inch) Primary Mirror . . . . .	C.2-27
C.2-3	Launch-Induced Mirror Stresses . . . . .	C.2-30
C.2-4	Comparative Truss Characteristics . . . . .	C.2-43
C.2-5	Comparative Truss Characteristics . . . . .	C.2-44
C.2-6	SIP Structure Material Properties Used . . . . .	C.2-53
C.2-7	Thermal Operating Environment . . . . .	C.2-57
C.2-8	Applied Weight Breakdown for Radial and Axial Bays . . . . .	C.2-58
C.2-9	Comparison of Actual and Allowable Motions Due to Thermal Loads . . . . .	C.2-59
C.2-10	OTA and SIP Structure Thermal Response Summary . . . . .	C.2-78
C.2-11	Recommended System . . . . .	C.2-79
C.3-1	LST Optical Parameters . . . . .	C.3-4
C.3-2	Design Specifications, Baseline 3-Meter LST . . . . .	C.3-5
C.3-3	Astigmatic Correction Values for Various Local Field Radii . . . . .	C.3-22
C.3-4	Material Comparison . . . . .	C.3-26
C.4-1	Thermal-Optical Design Requirements Primary and Secondary Mirror Budget: $0.026\lambda$ . . . . .	C.4-2
C.4-2	Thermal Nodal Information . . . . .	C.4-9
C.4-3	System Equilibrium Time . . . . .	C.4-19
C.4-4	Mirror Temperature Effects, °C . . . . .	C.4-20
C.4-5	Heater Power in Watts to Maintain $21 \pm 0.3$ °C ( $70 \pm 0.5$ °F) . . . . .	C.4-21
C.4-6	Transient Camera and Instrument Temperature Distribution—Insulated Truss Concept . . . . .	C.4-61
C.4-7	Thermal Control Power . . . . .	C.4-63
C.5-1	OTA Pointing and Stabilization Requirements . . . . .	C.5-3
C.5-2	Image Stabilization Error Budget . . . . .	C.5-5
C.5-3	Star Tracking Sensors . . . . .	C.5-27
C.5-4	Absolute Pointing Budget for Image Dissector Tracking . . . . .	C.5-43
C.5-5	Planetary Motions To Be Accommodated by Optical Micrometer, Microradians . . . . .	C.5-60
C.5-6	Fine Stabilization Options in Descending Order of Effectiveness . . . . .	C.5-70
C.5-7	Alternate Fine Stabilization Approaches Within OTA . . . . .	C.5-72
C.5-8	Parameters of Fine Tracking Control System . . . . .	C.5-97
C.5-9	Limits on Allowable Torque Disturbances . . . . .	C.5-99
C.5-10	Basic Dynamic Parameters for Control Loops . . . . .	C.5-106
C.5-11	Other Dynamic Parameters for Simulation . . . . .	C.5-109
C.5-12	Definition of Response Curves in Figs. C.5-63 Through C.5-66 . . . . .	C.5-116
C.5-13	Comparison of Rise Time Values of Transient Responses . . . . .	C.5-117

C.5-14	Parameters of Response Curves in Figs. C.5-63 and C.5-65 . . . . .	C.5-119
C.5-15	Fine Guidance System Error Sources for Star Observation . . . . .	C.5-121
C.5-16	Dimensional Stability Errors for f/96 Imagery . . . . .	C.5-121
C.6-1	Comparative Sensitivities to Optical Element Motions . . . . .	C.6-3
C.6-2	Modified A-Frame System Influence Matrix . . . . .	C.6-6
C.6-3	Minimum Cross-Coupled System 5-Degree-of-Freedom Influence Matrix . . . . .	C.6-6
C.6-4	Desirable Actuator Features . . . . .	C.6-6
C.6-5	Reconstructed Wavefront Errors for 0.01 $\lambda$ RMS Shear Measurement Error . . . . .	C.6-38
C.6-6	Interferometer Measurement Time in Starlight . . . . .	C.6-40
C.6-7	$ \Delta ^{-1}$ for Baseline System at Neutral Point . . . . .	C.6-48
C.6-8	Alignment Errors From Actuator Error . . . . .	C.6-49
C.6-9	Performance Control Subsystem Interface Summary . . . . .	C.6-55
C.6-10	Alignment Sensitivities for f/2.2-f/12 System . . . . .	C.6-55
C.6-11	Alignment Error Budget . . . . .	C.6-57
C.6-12	Focus Maintenance Budget . . . . .	C.6-57
C.7-1	Relative Direction of Actuators for Positive Misalignment Direction, Five Degrees of Freedom . . . . .	C.7-16
C.8-1	LST/OTA Pointing Requirements Based on Telescope WFE = 0.05 $\lambda$ at $\lambda = 633$ Nanometers . . . . .	C.8-8
C.10-1	Preliminary Reliability and Maintainability Analysis Summary . . . . .	C.10-5
C.10-2	OTA Failure Rate Tabulation and Reliability Prediction . . . . .	C.10-12

## FOREWORD

The final report of the study to generate for the Large Space Telescope (LST) a conceptual design that is compatible with a Shuttle (Titan backup) launch vehicle in late 1980 is contained in three volumes:

- I: Project Planning Data
- II: Cost Estimates
- \*III: Design Analysis and Trade Studies

Preliminary design analysis has demonstrated the feasibility of the selected concept and a supporting research and technology program (SR&T) has been identified to ensure that the schedule and cost objectives of the program will be satisfied. The configuration that has been developed is compatible with the scientific instrument configuration [developed by Kollsman Instrument Corporation under contract number NAS5-23068 to the Goddard Space Flight Center (GSFC)]. In addition, the study has interfaced with the on-going system support module (SSM) studies at the Marshall Space Flight Center (MSFC) to assist in the evolution of an overall LST payload configuration.

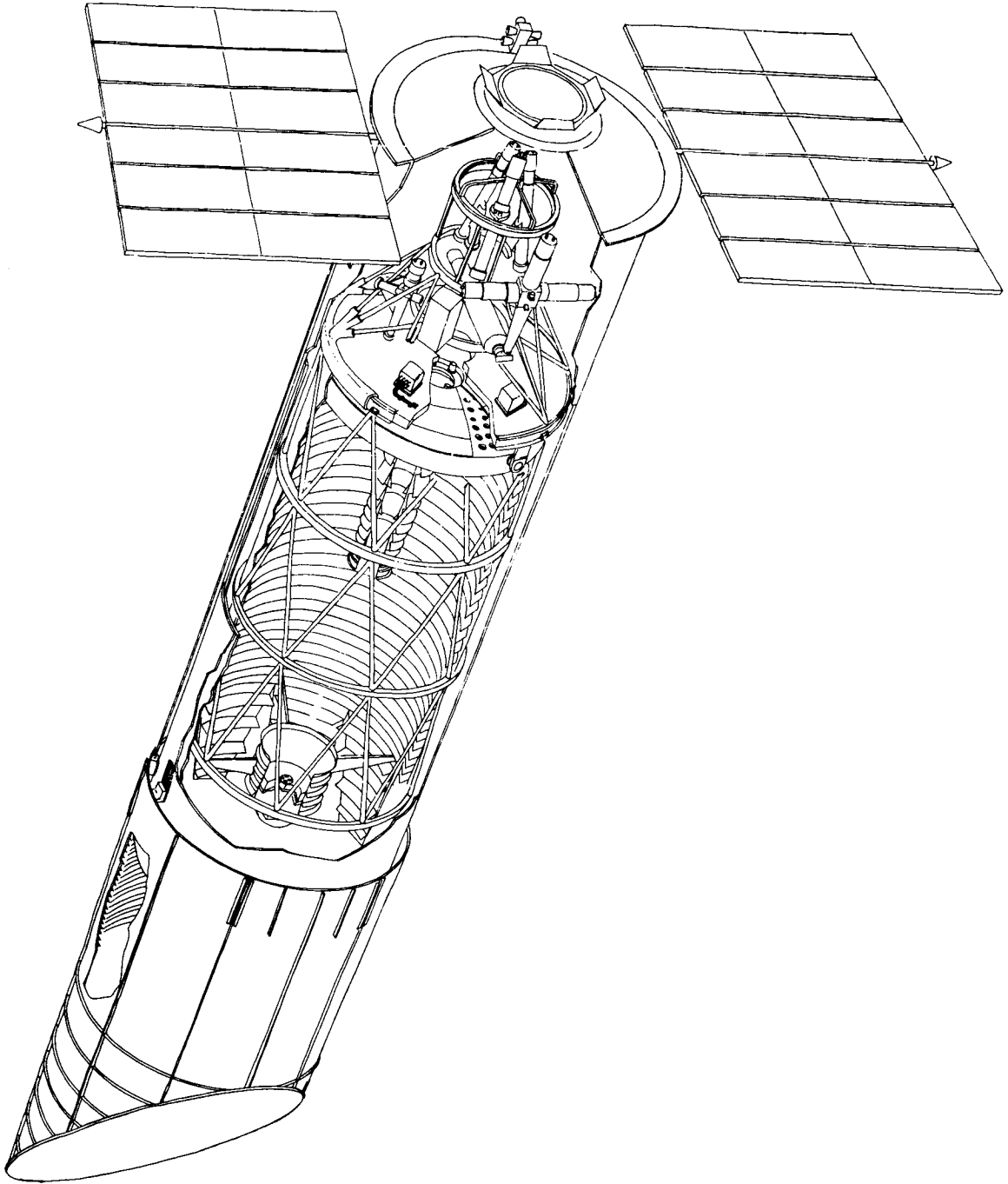
This volume, prepared in accordance with the requirements of contract number NAS8-27948 for the Marshall Space Flight Center, presents the preliminary design of the reference optical telescope assembly (OTA) configuration. The tradeoff studies and supporting design analyses for the various telescope system concepts that were studied are also included in this volume.

Comments or requests for additional information should be directed to either Garvin Emanuel/PD-MP-A, LST Phase A Definition Study, Contracting Officer's Representative, George C. Marshall Space Flight Center, Alabama 35812, or to Edmund J. Galat, LST Phase A Definition Study, Itek Corporation, 10 Maguire Road, Lexington, Massachusetts 02173.

---

\*This volume.

OTA—ARTIST'S CONCEPT



## A. INTRODUCTION

### REFERENCE OPTICAL TELESCOPE ASSEMBLY

The purpose of the phase A Definition Study conducted by Itek was to design conceptually an LST optical telescope assembly (OTA) that would be compatible with the Titan IIIE and Shuttle launch modes. The OTA reference design was established by tradeoffs and analysis of feasible candidate configurations. A supporting research and technology program was defined to accomplish the orderly execution of a telescope hardware definition program. Cost and schedule data were also developed, and the overall program content was defined in broad terms.

The phase A study program evolved in two distinct phases. Initially, a pre-phase A study was directed at evolving a baseline configuration compatible with a set of preliminary requirements defined for the program. As a result of extensive configuration optimization studies, during which the performance and physical characteristics of various payload configurations were investigated, the configuration that evolved was a Ritchey-Chretien Cassegrain optical system with a primary mirror focal ratio of  $f/2.2$  and a system focal ratio of  $f/12$ . The 3-meter aperture of this telescope was compatible with the launch capabilities of both the Titan III and the Space Shuttle. It was estimated that this telescope could be launched in 1978, with the phase C/D program starting in 1973. In the second phase of the phase A study program, the design studies of the reference configuration were continued, with specific emphasis on the focal plane design, the metering and instrument structure material selection, and the optimization of the fine pointing system error sensing and error correction subsystems.

The telescope focal plane configuration presented in this report is compatible with the instrument configuration developed by Kollsman Instrument Corporation under contract to GSFC. The system support module (SSM) studies at MSFC provided spacecraft SSM interface data to the OTA design studies. At the completion of the design effort, the programmatic were updated for the phase C/D program for concurrence with the latest MSFC program schedules.

### ASTRONOMY COMMITTEE REVIEW

As the study progressed, the results were presented to the Astronomy Steering Committee, chaired by Dr. Nancy Roman. The selection of primary mirror focal ratio and the system focal ratio was tentatively accepted contingent upon further review in phase B. The present approach to fine guidance, which encompasses artificial stars to maintain alignment and uncorrected astigmatic images in the error detectors, was suggested by Dr. Lyman Spitzer and Dr. Robert Danielson, of Princeton. The Astronomy Committee also recommended that a provision be made for observing the position of the spectrograph slits with respect to the target object and that a capability be included for the introduction of offset motions between the target object and the offset guide stars so that the target object can be optimally placed with respect to the entrance slits of the spectrographs.

### OTA PERFORMANCE REQUIREMENTS

Optical performance must be significantly superior to that obtained from earth-based telescopes. In space, this is obtainable because of the absence of an atmosphere and gravity effects. The NASA Blue Book has translated these requirements into a specification that is achievable with the application of the best existing technology. Therefore, diffraction-limited resolution (0.25 microradian at 300 nanometers) with image motion less than 0.025 microradian rms over a spectrum ranging from 110 nanometers to more than 2,000 nanometers will be provided.

### OTA ENVIRONMENTAL REQUIREMENTS

Structural load requirements for this study were supplied by MSFC and are consistent with the worst-case combination of Titan IIIE and Space Shuttle boost and return environments. To ensure optical quality on orbit, it is necessary that the telescope be manufactured at a temperature convenient for handling and testing and that this



temperature be later maintained during the orbital phase of the operation. This requirement is conditioned by the dispersion of thermal expansion coefficient in critical telescope optical and structural components. A second environmental requirement peculiar to optical systems is that scrupulous cleanliness must be maintained during all handling and mission operations. This has been tentatively set as maintaining class 10,000 clean room conditions during system construction and integration. The system is designed to be man-maintained in a shirtsleeve environment inside the spacecraft.

## OPTICAL TELESCOPE INTERFACE REQUIREMENTS

The Titan IIIE/OAS launch vehicle envelope determines the maximum outer dimensions of the OTA as well as its weight. This envelope is the principal determinant of the primary optical parameters of the OTA – aperture, primary  $f$ /number, system  $f$ /number, and weight – which are discussed later. In addition,  $g$ -loadings and acoustic environments characteristic of this vehicle determine the working stress levels in the OTA, where more stringent requirements are not imposed for optical reasons.

The requirements of the Space Shuttle are not so confining as the Titan IIIE/OAS with respect to weight and space. However, structural loads are higher and were used in sizing system elements where relevant.

The SSM is the principal interface of the OTA, i.e., power, structural support (excepting Shuttle cradle), command multiplexers, and the operational interfaces. The OTA now influences the thermal and structural design approach behind the pressure bulkhead ring to prevent loads from being transmitted into the surface figure of the primary mirror. The OTA also provides part of the pressure structure that will maintain the integrity of the SSM for manned operations.

The OTA provides structural support for the scientific instruments. The optical interface is at the  $f/12$  focal plane, which is controlled so that the telescope image is stationary with respect to a reticle fiducial in that plane regardless of thermal drift of the system structure. Instruments that are sensitive to this drift because of large dimensions or high resolution must contain the means to sense the fiducial position and correct the effects of this drift internally to the instrument. The ability to mount one end of the instrument directly to the reticle plate focal plane structure will be allowed for in the OTA design. The OTA provides structural mounting interfaces for each scientific instrument.

## KEY SYSTEM TRADEOFFS

The key tradeoff performed in the phase A study was the determination of the primary mirror focal ratio. A variational analysis showed that a balance could be achieved between the effects of central obstruction reduction on one hand and of alignment sensitivity, vibration sensitivity, and difficulty of manufacture on the other hand. It was possible to show a weak optimum near  $f/2.2$ . However, it must remain clear that the variation in performance was very small, of the order of a few percent in terms of Strehl ratio. The strongest driving factor was the length of the system and the boost capability of the Titan IIIE/OAS, which leads to the choice of the shortest, lightest system; i.e., it was reasonable to pick a system near the optimum in spite of its weak relationship to performance.

Considerations of system length also apply to the choice of system  $f$ /number. If the  $f$ /number gets large, the tracking field gets large and it becomes difficult to ensure the geometric integrity of the focal plane area. A clear cut advantage would accrue if the system  $f$ /number were to be of the order of  $f/30$  to  $f/100$ , since it would be possible to place directly in the telescope focal plane image sensors whose modulation transfer function (MTF) would not degrade the system angular resolution and would maximize system transmission and minimize geometric thermal disturbances. Unfortunately, such large  $f$ /numbers imply an excessively large guide field (and central obstruction and reduction of MTF) as well as demand extreme compromises in spacecraft design arrangement, since the focal plane would have to be placed at the rear end of the spacecraft. Therefore, if these slow  $f$ /numbers are not possible, an intermediate optical system is required to match the telescope MTF to the sensor. Consequently, there is no advantage to using a slow  $f$ /number of the order of  $f/24$ , for instance, if the instrument complements and guidance

can be accommodated by a faster system without vignetting. Therefore,  $f/12$ , which was chosen in the GSFC instrument studies, was adopted for the reference configuration.

Structural systems considered for the LST include athermalized trusses of aluminum and titanium, titanium and Invar, graphite-epoxy composites and Invar, and composite semimonocoque shells. To damp the response of the structure to orbital isolation so that thermal drifts do not affect image blur, it is necessary to wrap the metering structural systems with thermal insulating blankets. The meteor protection, the baffles, and the sunshield are noncritical and can be made of aluminum semimonocoque. The graphite-epoxy composite metering truss that was selected was least sensitive to thermal loads and was the lightest. This material was also selected for the instrument support structure.

The fine guidance approach selected from the initial trade studies depended on static structural stability for the control of image blur at  $f/96$  with respect to the telescope  $f/12$  focal plane. The Astronomy Committee objected to this approach, since it depended on very tight thermal tolerances provable only by analysis; they recommended an active closed loop approach. Based on Dr. Lyman Spitzer's suggestion, a guidance arrangement was devised where fiducial marks are actively tracked by sensors in the  $f/96$  focal plane. The drift corrections in the  $f/12$  focal plane can then be applied to the magnetic lens of the image intensifier section of the sensor or as an offset to the optical micrometer device in the guide heads.

Two materials are suitable for the OTA primary and secondary mirrors Cer-Vit (Owens-Illinois) and ultra low expansion (ULE) glass (Corning). The technical differences between these two materials are not sufficient to justify selection of one over the other, at least until a very rigorous set of measurements is made on the dispersion of expansion coefficients of the two materials. Presently, there is a 2:1 cost difference for the primary mirror blanks, and on this basis Cer-Vit is the material recommended.

The various instrument support approaches investigated on this program and previous programs contain radial and axial instrument orientations. It is necessary to make the instrument support structure of a material having as low an expansion coefficient as is available to maintain thermally induced image blur to a tolerable level. Furthermore, it has been shown that, to minimize instrument sensitivity to thermal growth, the  $f/12$  focal plane components should be configured so that they move as a rigid body with respect to each other and to the fine guidance error sensor. These two approaches have lowered the thermal sensitivity of the instrument support structure by about an order of magnitude, simplifying the detailed structural design requirements. Image tubes located in the instrument bay are cooled by direct radiation to the SSM walls. Peltier devices are used for those sensors requiring low temperature operation. The definition of the image tube complement and the image tube thermal analysis was done by Itek under subcontract to Kollsman Instrument Corporation.

#### REFERENCE OTA DESIGN CONCEPT

The reference concept that resulted from this study is a Ritchey-Chretien telescope, 3 meters in aperture, which is depicted in Fig. A.1-1. The primary mirror is a Cer-Vit monolith and is supported at three points with Invar leaf springs attached to a titanium supporting bulkhead. A metering truss, manufactured from graphite-epoxy, supports the four-point secondary mirror spider and support ring to which is attached the secondary mirror, its alignment system, and the fine guidance actuation and drive.

The telescope assembly is enclosed in an aluminum semimonocoque meteoroid shell to which is attached the extendible truncated light baffle, designed in a related contract by The University of Arizona. The inner light baffles are attached to the meteoroid shell by standoffs, and the metering truss is fully insulated from these inner and outer shell assemblies. Aperture doors at the forward end of the telescope are provided to prevent inadvertent illumination of the primary optics by the sun, as well as to seal off the telescope aperture during maintenance visits by the Shuttle. A pressure bulkhead door is provided directly behind the primary mirror to seal the pressure compartment during shuttle revisits. The telescope system is maintained in alignment by means of tip, tilt, and decenter sensors mounted in the primary mirror that sense the alignment of the primary and secondary mirrors and activate position

control mechanisms located in the secondary mirror assembly; these correct for misalignments due to gravity release and the orbital and thermal environment. The focus sensor is mounted to the fine guidance assembly and corrects focus by axial displacements of the secondary mirror.

The telescope wavefront error can be periodically measured by observing reference stars brighter than 6th magnitude with a shearing interferometer whose output is relayed to the ground for analysis. Subsequent figure control commands developed from these interferograms are transmitted to the satellite and converted into actuation forces to restore the surface of the primary mirror to the desired figure.

The thermal control concept developed for the LST includes active thermal control for the optical elements and passive thermal control for the supporting structure. The primary mirror and the secondary mirror are actively controlled at  $21 \pm 3^\circ\text{C}$  by means of multizoned heaters. Furthermore, these items are thermally isolated from their surroundings by multilayered insulating blankets to reduce thermal power consumption. Passive thermal control of the metering structure and the instrument structure is accomplished with multilayered insulating blankets that insulate the trusses from the structural shell and/or heat-generating components.

The fine guidance system includes a reticle plate error detecting system that develops fine guidance error signals for the suppression of high frequency errors by the introduction of compensatory motions with the secondary mirror. Misalignment signals from the secondary mirror then provide error signals to the vehicle for coarse pointing of the telescope line of sight. Acquisition, which is initiated from star trackers attached to the instrument truss, provides initial pointing to approximately 30 arc-seconds. At this point, two of the three guide star trackers available, located in the reticle tracker assembly, acquire the guide stars and initiate development of intermediate and fine error control signals.

The telescope electrical system internally effects fine guidance operations, thermal controls, and telescope realignments and calibration. Activation commands and power are supplied from the SSM to the OTA.

The telescope concept described above is based on applying currently available technology to the required design, development, and fabrication program. Scientific research and technology requirements have been identified so that no schedule slips and their attendant cost overruns need occur as a result of the application of this technology to the LST. A study program is now under way to verify that the current optical surface technology is compatible with the LST goals. This program is scheduled for completion in June 1973 and should provide the confidence necessary for full acceptance of the  $f/2.2$  aspheric primary mirror selected as the reference configuration for the OTA.

## COST SENSITIVITY

The present study has produced a reference design and initial cost figures. In forthcoming work, it will be necessary to perform an analysis of cost sensitivity to performance for the largest cost centers and to identify cost thresholds as a function of design configuration so that management decisions can proceed on a completely objective basis. Of particular importance is the balance between image blur and optical wavefront error. The present system is specified at a point that is a compromise arrived at in previous studies. In future studies, the present error allocations should be frequently reviewed for a cost-effective balance of all error sources.

Typically, if it can be shown that the entire pointing function can be fulfilled by means of telescope star sensors commanding SSM attitude actuators, significant savings are likely in the resultant simplification of the OTA secondary mirror design. However, backup design work on the secondary drive should continue until a high confidence level can be achieved by the SSM attitude control system performance.

At the completion of the present design cycle, it has become evident that a somewhat slower primary mirror could be fitted within the SSM and the Titan IIIE/OAS. The advantages to accrue from such a reduction should be explored in cost and performance terms. The impact of Shuttle-only operation should also be analyzed.



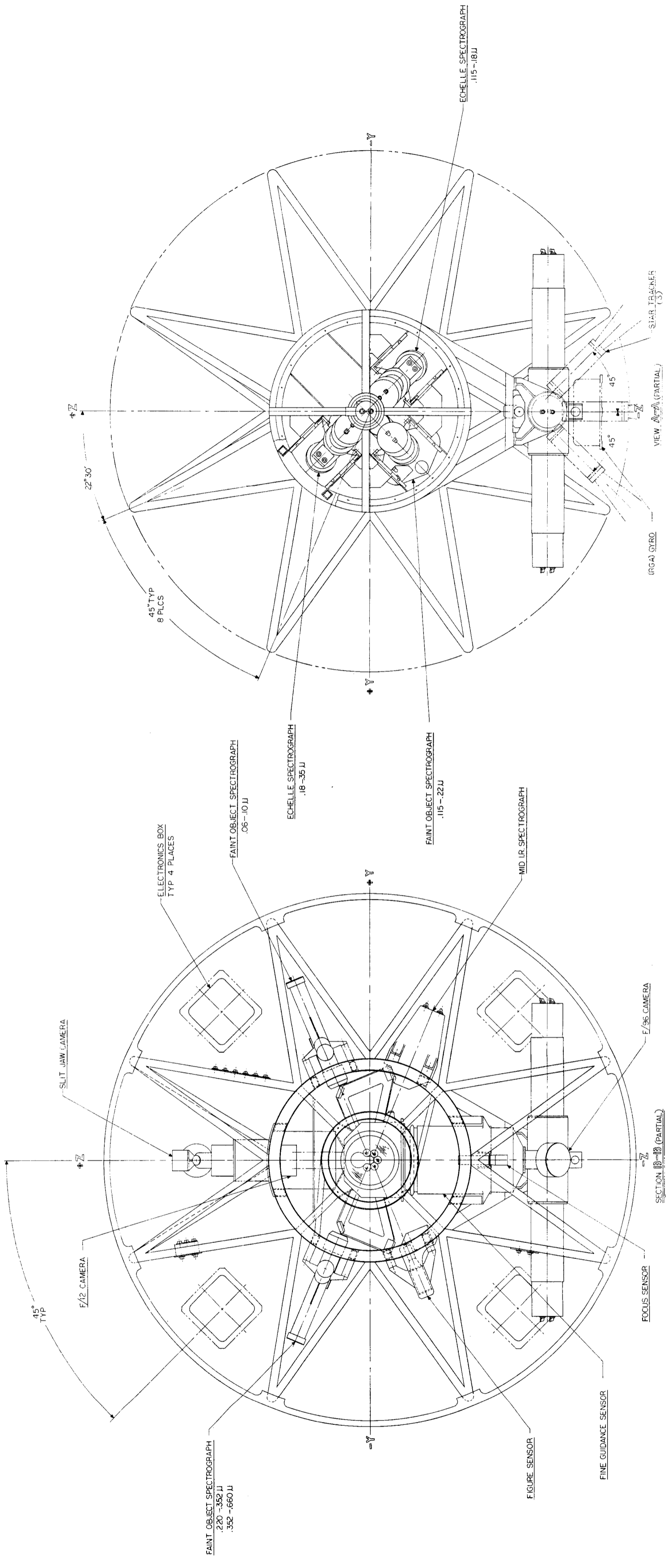


Fig. A.1-1 — LST/SIP configuration (dwg. no. 185510, sheet 2) (Cont.)

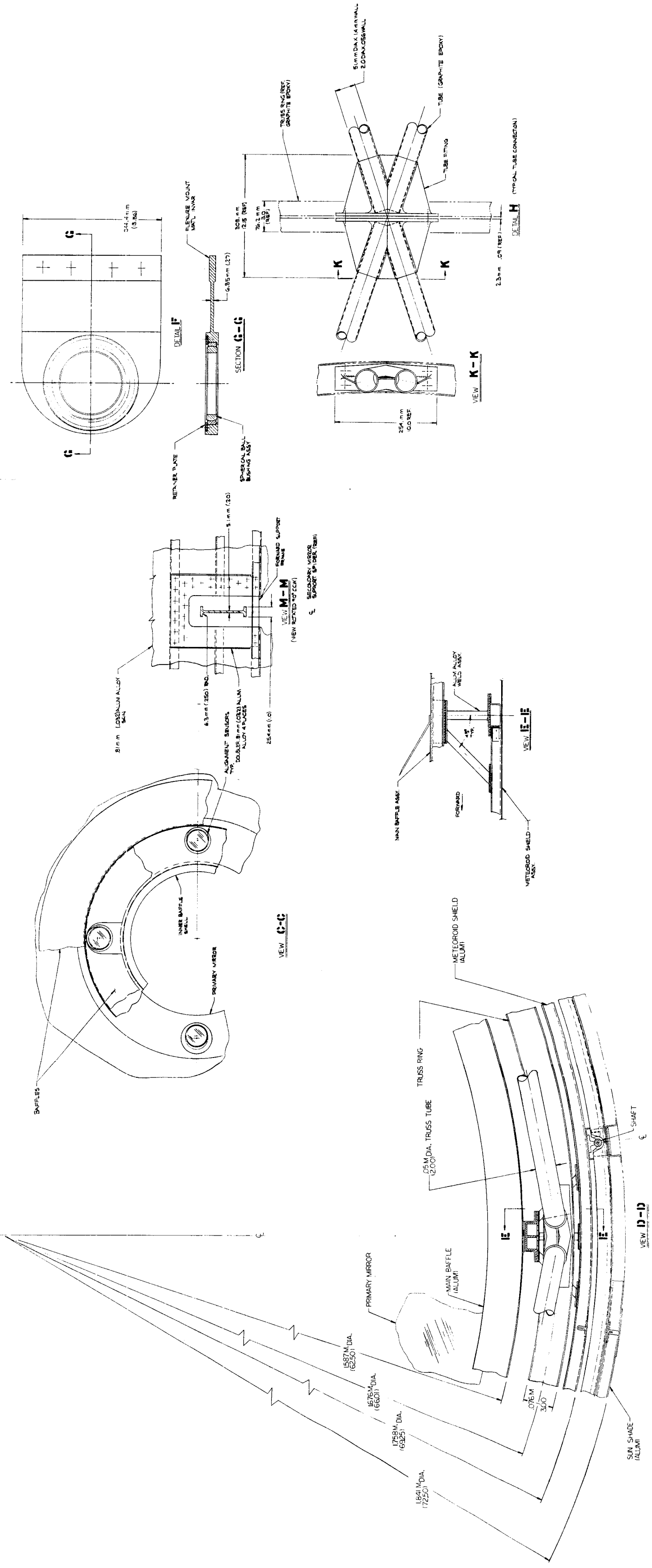


Fig. A.1-1 — LST/SIP configuration (dwg. no. 185510, sheet 3) (Cont.)

One of the larger cost centers is in test facilities and test operations, as well as the extra telescope models associated with verifying system performance. The need to perform full optical tests that account for gravity release should be reviewed. Furthermore, the role of the force actuator system during ground testing should be analyzed. The Space Shuttle may make an orbit figure verification a viable cost saving technique.

Simple independent interface designs offer great cost savings in the engineering administration of a job, since the interface elements are manned by nearly identical engineering teams by the contractor and subcontractor and the Government. These teams seldom contribute to the design of line item hardware tasks because of the complex nature of interface management. Therefore, isolation of interfaces into clean, minimally interdependent elements is a desirable system design objective.

## B. SYSTEM CONSIDERATIONS

### B.1 REVIEW OF MISSION-RELATED PARAMETERS

This review of mission-related parameters, performed by Martin-Marietta Corporation under subcontract to Itek, appears in Volume II of this report.



## B.2 SELECTION OF OPTICAL PARAMETERS

### B.2.a Introduction

An important part of the activity of the phase A study program has been to establish the basic optical parameters most appropriate to the LST. These parameters are compatible with the specified boost vehicles and will enable the LST to perform the widest possible scientific mission. These parameters were reviewed by the NASA Headquarters Astronomy Steering Committee. The June 12-13, 1972, meeting of the committee agreed tentatively, pending further study in later program phases, to the baseline parameters described in this report. There was some reservation about the relatively fast primary mirror and an insistence upon a method of fine guidance that actively accounted for the thermal deformations of the instrument structure that contribute to image blur.

The speed of the primary mirror was governed by the necessity of matching the length of the telescope to that of available boost vehicles (Titan IIIE/OAS) and by weight considerations. The chosen  $f/2.2$  speed yielded the lightest and shortest payload. The upper boundary for an acceptable primary  $f$ /number appeared to be about  $f/3$ . It was shown\* that a performance optimum exists at  $f/1.7$  and  $f/2.3$  but that the depth of the optimum is very shallow and, hence, should not be regarded as an overriding consideration in choosing the system geometry. Indeed, the largest optical effect is obtained from the variation of the central obstruction with general system parameters; during the progress of the study, substantial reductions in this factor were obtained by reducing the size of the annular field used for offset guidance. The improvement in performance due to this reduction in the obscuration by the tracking field is much larger than the entire variation obtained by varying the  $f$ /numbers over ranges of 2.0 to 4.0 and 8 to 24, respectively. An additional benefit to be obtained from the reduced guide field is that the complex five-element refracting corrector is not needed.

### B.2.b Aperture Selection

The scientific usefulness of a space-based telescope is most importantly related to the improvement in angular resolution that may be obtained by removal of atmospheric degradation and the consequent improvement in ability to detect dim objects. As the aperture of the space telescope decreases, its performance becomes comparable to earth-based instruments and the primary justification for the instrument is the wider spectral response, free from atmospheric effects. To justify an LST, it is necessary that its performance be maximum. Therefore, the maximum aperture that can be fabricated to the required quality and be launched must be chosen. Since the largest available launch vehicle is the Titan IIIE/OAS, the outside diameter of the telescope is limited to 3.7 meters (145 inches). The Space Shuttle has a larger aperture capacity, but would place the launch date too far into the future for the current LST program concept. When allowance has been made for sunshade, meteoroid shield, metering structure, and baffles, the largest feasible aperture is 3 meters (118 inches).

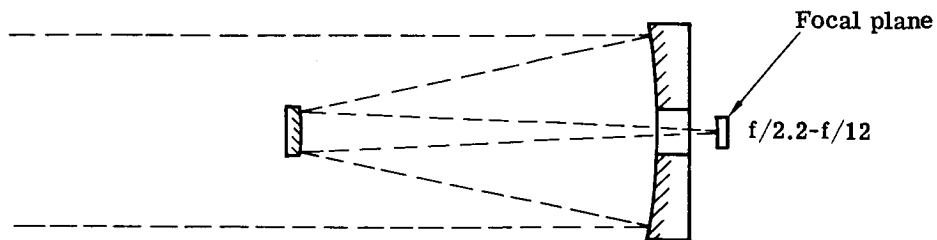
### B.2.c Choice of Telescope Type

The work carried out under contract NASw-1925 involved tradeoffs defining the suitability of the Ritchey-Chretien telescope design for the LST. Work done on study NAS5-21540 showed that a Gregorian type of telescope should be considered on the basis of optical performance alone. During the beginning of the present phase A study, a more detailed comparison of the Gregorian and Ritchey-Chretien telescopes was carried out under the added constraint of a length-limited Titan III vehicle.

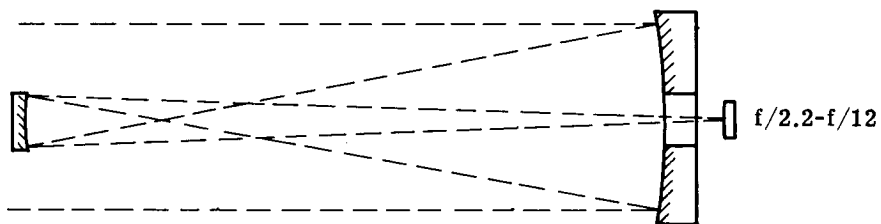
The length constraints imposed by the Titan IIIE on the selection of the telescope configuration quickly limited the selection to Cassegrain and Gregorian telescopes of equal length. A faster primary was required for the Gregorian  $f/1.5$  versus  $f/2.2$  for the Cassegrain, as shown in Fig. B.2-1. The departure from a spherical surface for the faster primary will be much greater; hence its manufacture will be much more difficult. The alignment tolerances are also tighter for the faster primary, further complicating the thermo-structural design of the primary-secondary metering truss and requiring far more precise decenter measurement. The backward curving focal plane would be an advantage with some imaging tubes, although present efforts at Princeton University are directed toward the development of flat surface, magnetic focused image tubes for the LST, and these are equally compatible with either system.

---

\*Itek 72-8209-1.

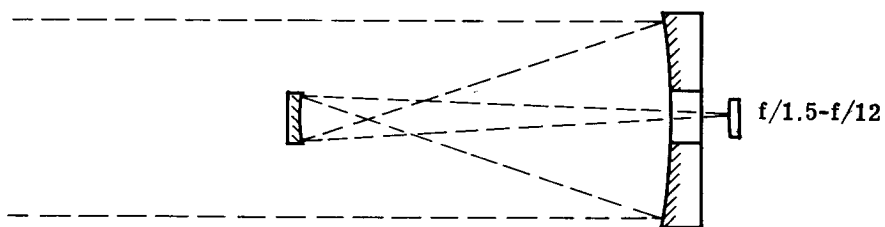


(a) Baseline Cassegrain



(b) Gregorian with equal f/numbers

45% longer  
 ~2% greater wavefront error  
 per unit decenter  
 10% larger high quality field  
 30% less field curvature,  
 backward



(c) Gregorian with equal length

3.4% greater wavefront error  
 per unit decenter  
 2% greater image motion per  
 unit decenter  
 Possibly 10% less obscuration  
 20% smaller high quality field  
 70% more field curvature,  
 backward

Fig. B.2-1 — Comparison of aplanatic Gregorians and baseline Cassegrain

#### B.2.d Selection of Primary Mirror f/Number

As mentioned above, the primary mirror f/number has been set by the compromise in length between the spacecraft (SSM) and telescope (OTA) portions of the LST. The optical factors relating to this choice are (1) manufacturing ease versus quality, (2) the ability to maintain alignment, (3) sensitivity to vibration, and (4) central obstruction. A previous detailed study showed that the above factors balanced in such a way that variation in optical quality was insignificant over the range of relevant values. An important exception to this statement occurs when one considers the surface quality aspects of fast mirrors which, because of the generation process, tend to have annular zones of differing curvature. This important problem is being addressed by an experimental study program (NAS-28993) for NASA MSFC in which a 183-centimeter (72-inch), f/2.2 parabolic mirror is being made and tested to a goal of  $\lambda/50$  rms surface quality. Fig. B.2-2 shows how telescope length varies as a function of primary mirror f/number. The baseline primary mirror f/number is placed near the weak optimum arrived at in the earlier phase of this study and is compatible with current spacecraft concepts.

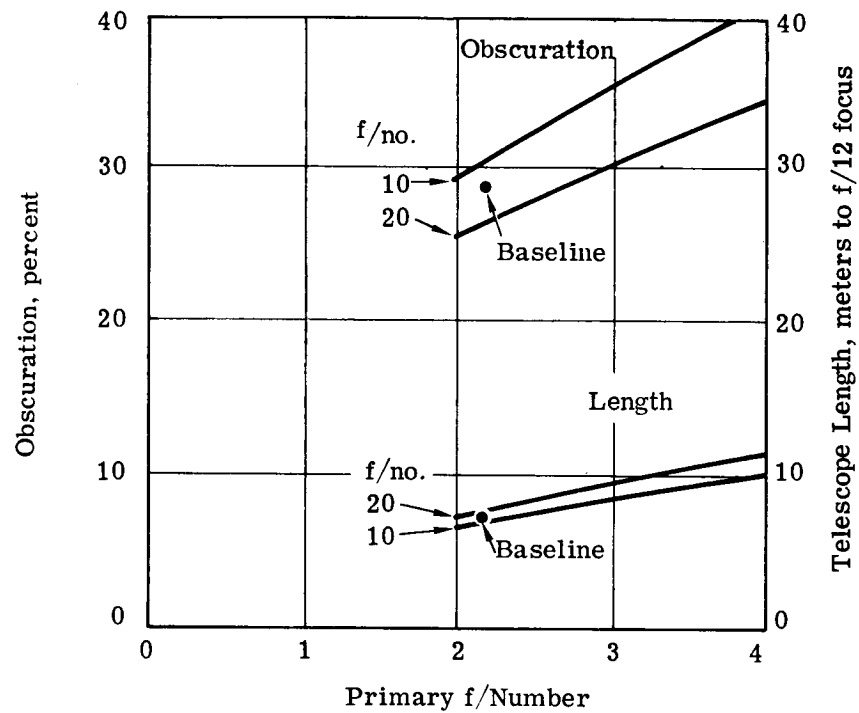
#### B.2.e Selection of System f/Number

When the overall system f/number is faster than about f/15, greater care must be exercised in the design of such instrument accessories as the fine guidance or spectrograph slits, because the size of the diffraction limited star image becomes small (i.e., has point spread functions of the order of 7 to 14 micrometers) as compared to easily fabricated components. Furthermore, the small image scale makes it difficult to package several instruments in close proximity. A faster system provides a larger field of view with a given image tube, which is usually limited by the ability to span distances with thin flimsy elements within the tube or by the pixel throughput of the electron beam readout. A slower system decreases obscuration up to a point, beyond which it increases again. The most important potential of a slow system is the possibility of placing the image sensor surface directly into the first real image plane of the telescope. The state of the art of image tubes is presently such that spatial resolution of the order of 20 lines per millimeter is obtained at 50 percent modulation. If the tube resolution is not to significantly degrade the telescope optical resolution, a system f/number of the order of f/100 is required. Clearly, it is not feasible to build a telescope at f/100 without gravely compromising the fine guidance system, and there is the difficulty of staying within the vehicle length without an excessive number of folding mirrors. An intermediate alternative was pointed out in which a stage of electronic magnification of the order of 2 to 3 x is introduced into the tube. This method would require an optical focal plane of about f/30 to f/50. Such systems were investigated in the study, and it was found that the system length required for this configuration was excessive for the Titan III vehicle. By drastically altering the spacecraft configuration and using a side-mounted docking adapter, it was found to be conceptually possible to accommodate an f/30 system, but the drastic nature of the required alterations made this alternative unacceptable to MSFC since a possible incompatibility with the shuttle and space tug programs was introduced. If the emphasis of the scientific community on far-ultraviolet observations were to be considerably increased, one might reconsider imaging in the first real image plane of the telescope because of the greatly increased optical system transmission below 110 nanometers.

The present choice of system f/number (f/12) has been made for reasons of system compactness and because we have been able to show that existing sensing elements are compatible with the small scale images in the focal plane (see Section C.5). Fig. B.2-2 shows the effect of system f/number on central diametral obstruction.

#### B.2.f Telescope Performance

Of the several criteria by which the LST image quality may be judged, each is meaningful to certain types of astronomical observations. The point spread function (PSF) is used to provide the Strehl ratio (which in many cases impacts limiting magnitude), encircled energy,  $E_c$ , which is useful in assessing performance of photomultiplier photometers or polarimeters, and enslitted energy,  $E_s$ , used in assessing spectrographs with narrow entrance slits. All of these parameters are used primarily when considering how well the LST performs against such point objects as stars. For nebulae and other continuous tone objects the modulation transfer function (MTF) is used. The MTF and PSF are mathematically related. An aberration affecting the low angular frequencies in the MTF will take energy from the center of the PSF and distribute it in the outer rings. Conversely, any change in the higher frequencies of the MTF is accompanied by extra energy in the first rings of the PSF.



D = 3 meters aperture  
 B = 2.1 meters focus behind primary mirror vertex  
 $\theta_T = 6.96$  mrad (24 arc-min tracking field diameter)

Fig. B.2-2 — Effect of focal ratios on obscuration and telescope length

Point spread function, modulation transfer function, and encircled and enslitted energies are used as appropriate in this report. They are generally specified at one of two wavelengths: 316 or 633 nanometers. Since optics are generally tested with a He-Ne laser, 633 nanometers will probably be the wavelength for LST component specification. On the other hand, the scientific observations will be made between 100 and 1,000 nanometers, 316 nanometers being the geometric mean of these wavelengths.

The three principal causes of image degradation are central obscuration of the aperture,  $\epsilon$ , wavefront error,  $\omega$ , and image motion,  $\sigma$ . We will discuss these in turn and show how the adopted values of each affects the MTF, PSF, and  $E_c$ . Since the slitted and encircled energy curves vary similarly, with these parameters only  $E_c$  is considered here.

Obscuration is well determined when the  $f$ /numbers of the primary mirror and system are chosen and the field of view is set. These parameters dictate the number and configuration of the stray light baffles, these being the primary sources of obscuration. With the  $f/2.2$ - $f/12$  LST and a fully baffled guide field diameter of 7 milliradians (24 arc-minutes), the obscuration  $\epsilon$  will be 30 percent with baffles. The effect of this obscuration on PSF,  $E_c$ , and MTF is shown in Figs. B.2-3, B.2-4, and B.2-5, where the curves labeled A represent a perfect system.

Wavefront error results from limitations of the optical design, fabrication and test errors, and misalignment or defocus of the assembled optics. Misalignment and defocus can result from initial assembly (static errors) or from such dynamic errors as thermal changes, material instabilities, stresses, etc. The error budget for the LST must consider all the many sources of wavefront error, and must balance the individual items to provide least error at minimum cost. The resulting budget for the baseline LST sums to  $0.05\lambda$  rms at 633 nanometers or  $0.1\lambda$  rms at 316 nanometers, producing the effects on PST,  $E_c$ , and MTF shown by the curves labeled C in Figs. B.2-3, B.2-4, and B.2-5.

Image motion results from noise in the guide system, vibrations, and thermally induced movement of optical components. The image motion budget constructed for the baseline LST lists all motion sources and sums to 0.024 microradian (0.005 arc-second) rms, a value producing the PSF,  $E_c$ , and MTF relations shown in the curves labeled D in Figs. B.2-3, B.2-4, and B.2-5. This image motion specification is probably unnecessarily tight insofar as PSF and  $E_c$  are concerned, but it does influence the high frequency end of the MTF curve.

#### B.2.g Off-Axis Imagery of OTA

The above discussion concerned image quality on the optical axis of the telescope. The scientific instruments that require best imagery (the  $f/96$  field camera and the spectrographs) are placed near the optical axis to benefit from the high image quality.

The  $f/12$  field camera, with approximately 1.45-milliradian (5-arc-minute) field of view, is centered 1.6 milliradians (5.5 arc-minutes) off the optical axis. The large wavefront errors at the edge of the field can be tolerated because at  $f/12$  the system is limited more by the detector (50 percent response at 20 line pairs per millimeter) than by optics. The area-weighted loss in resolution is only 10 percent compared to what the on-axis performance would be. Because other instruments are not detection-limited, the on-axis tolerance should be kept very stringent.

The distortion of the telescope is a function of field height. Fig. B.2-6 shows distortion for a flat focal plane. It is totally negligible in an  $f/96$  camera 16-microradian (36-arc-second) field. Distortion is less than 0.05 microradian (0.01 arc-second) in the  $f/12$  camera.

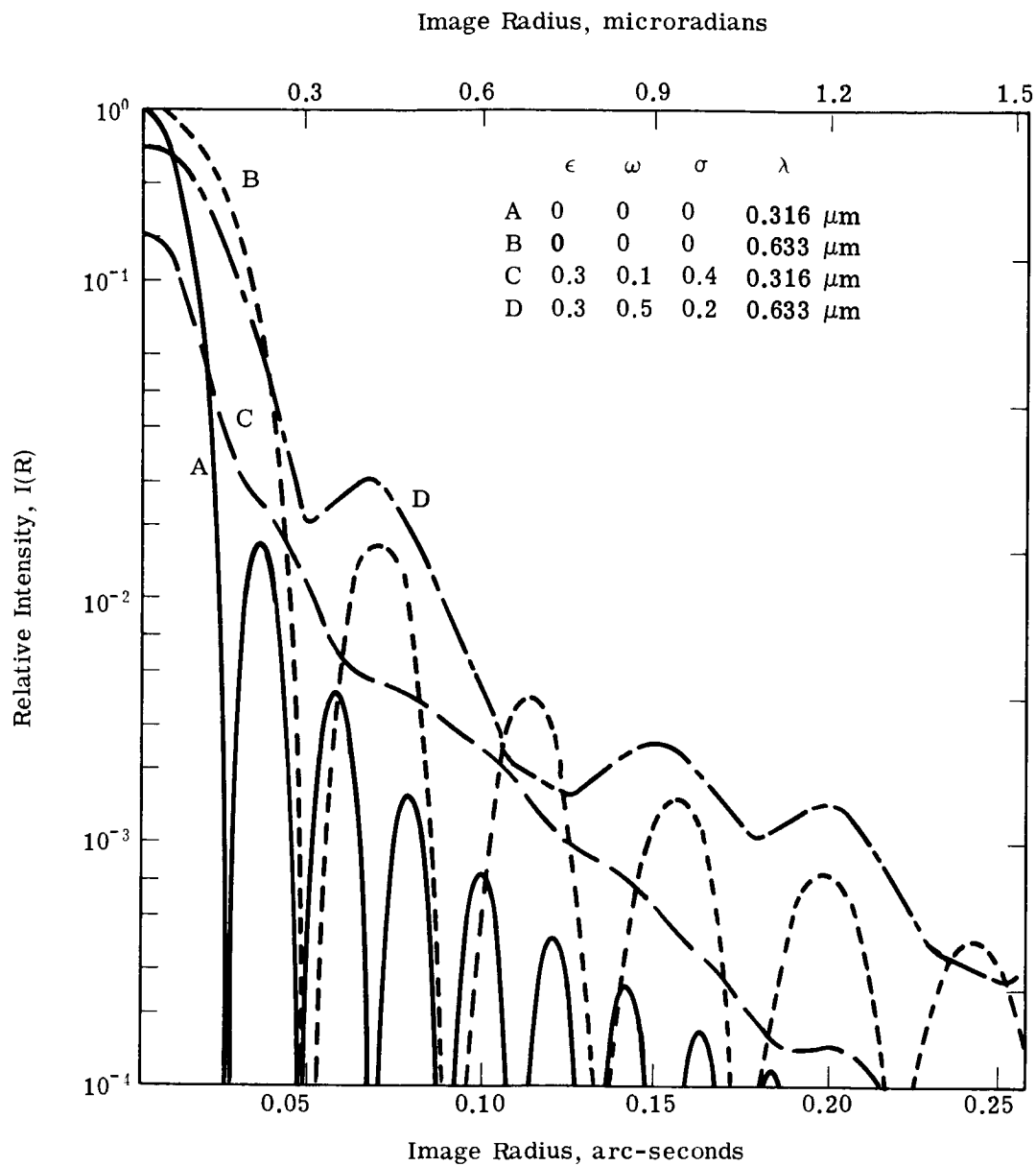


Fig. B.2-3 — Calculated point spread function at  $\lambda = 315$  and  $633$  nanometers for the perfect unobscured case and the fully tolerated LST. These curves are all normalized to the on-axis, unobscured, untoleranced case.

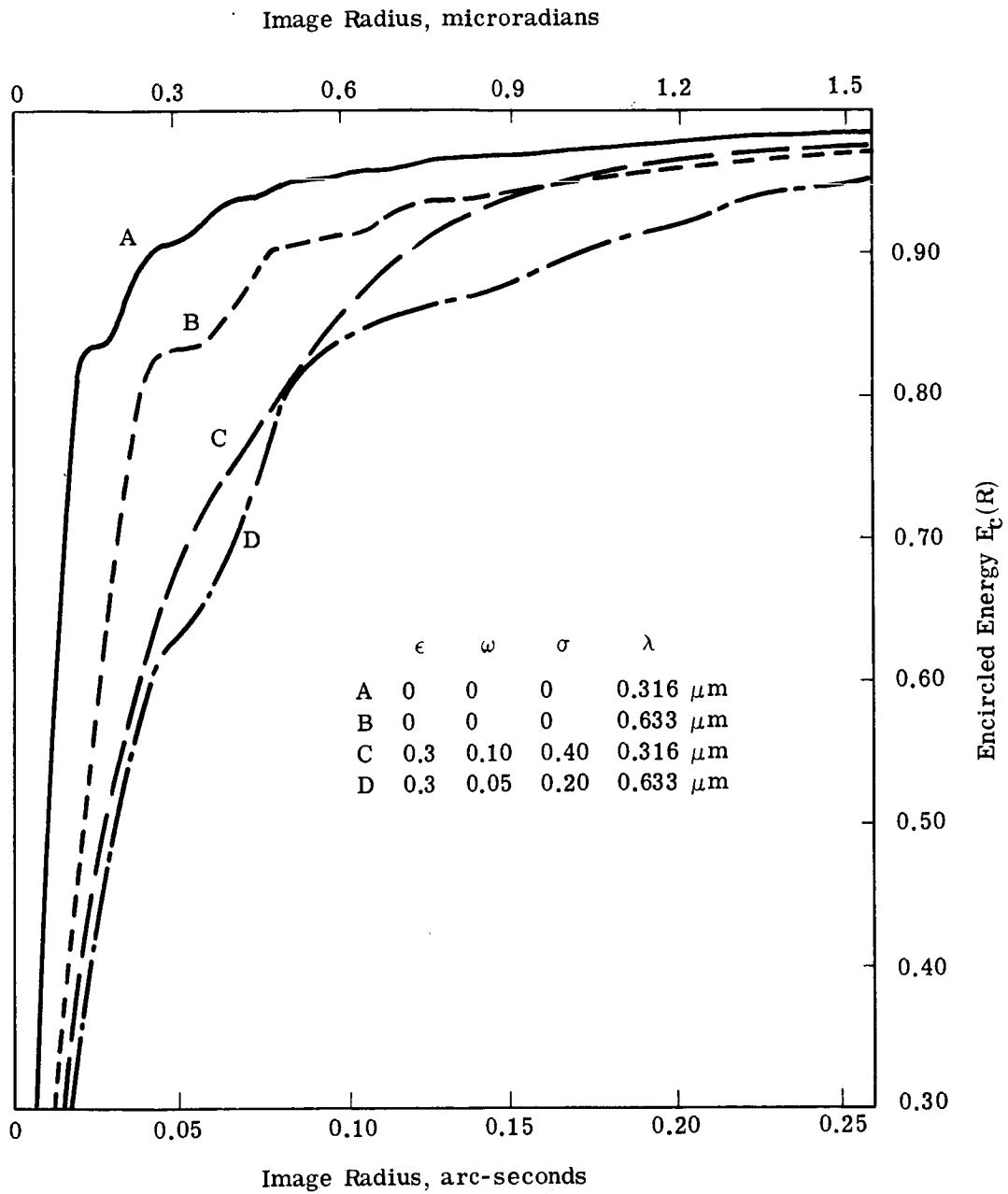
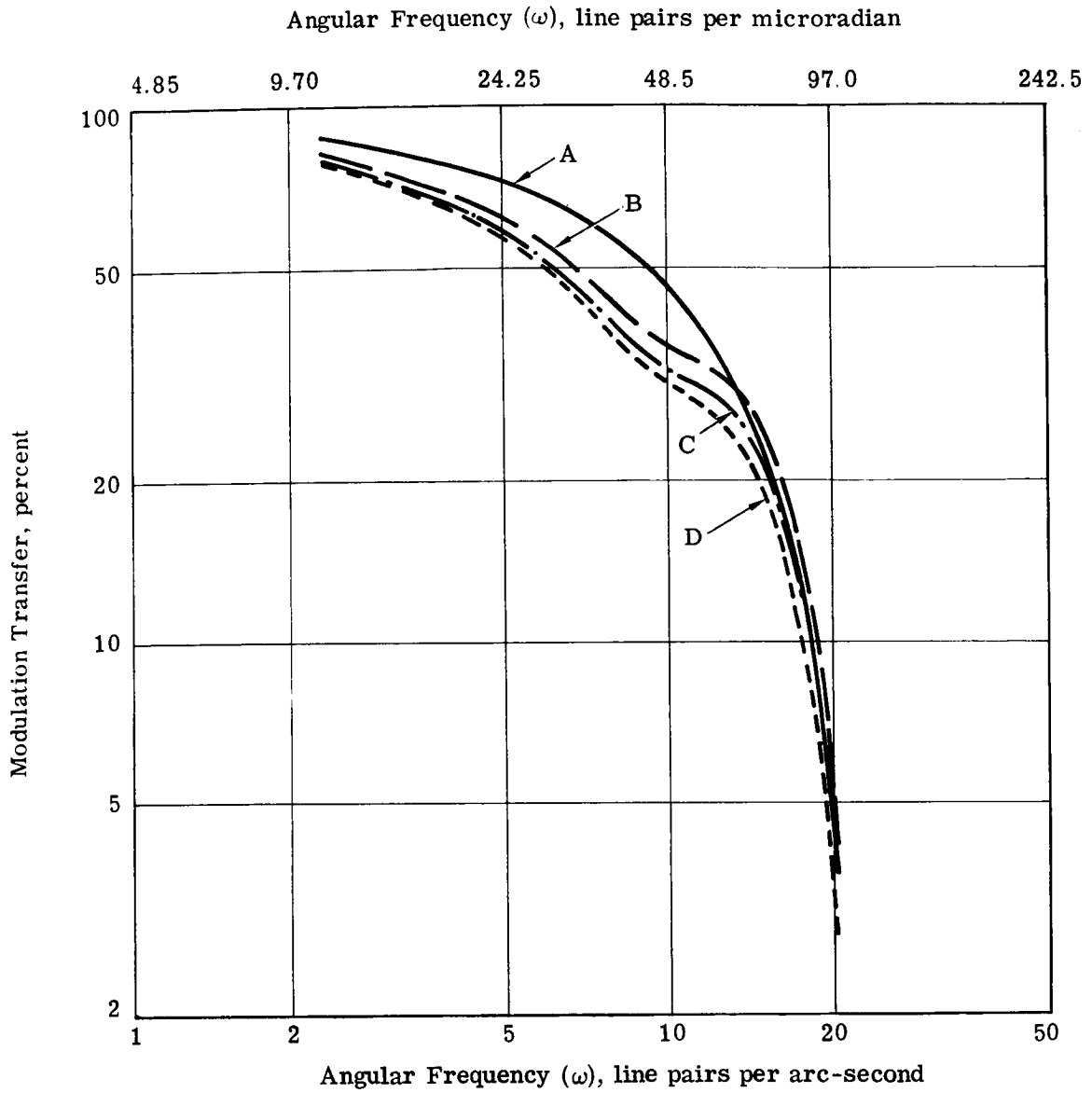


Fig. B.2-4 — Calculated encircled energy for  $\lambda = 316$



	$\epsilon, \%$	$\omega, \lambda_{rms}$ $\lambda = 633 \text{ nm}$	$\sigma, \text{arc-}$ $\text{sec rms}$
A —————	0	0	0
B —————	30	0	0
C - - - - -	30	0.05	0
D - · - · -	30	0.05	0.005

Fig. B.2-5 — Development of baseline LST modulation transfer function



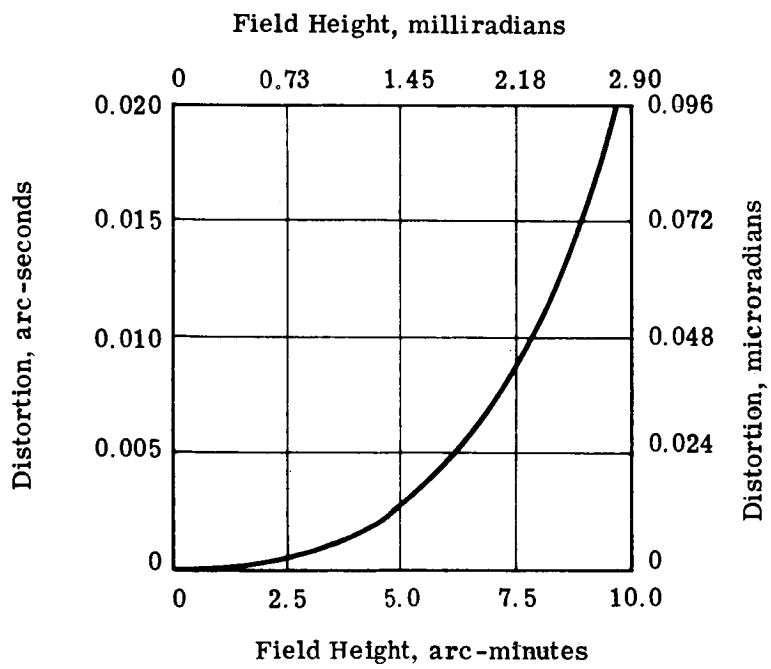


Fig. B.2-6 — Distortion in f/12 image versus field height

## B.3 ERROR BUDGETS

### B.3.a Introduction

Because the LST is primarily an imaging system, the error budgets affecting its performance are most properly presented in terms of wavefront error (WFE). We have therefore developed an error budget wherein most sources of error are expressed by their effect on the wavefront quality of the system. However, even if the imaging system is operating perfectly, any drift in the pointing of the telescope from the desired direction will also result in performance degradation. Consequently, we consider these two effects (wavefront error and guide error) on the LST's imagery and build our error budgets within their terms. Fig. B.3-1 shows how these errors are related in the LST system.

It can be shown rigorously that if the factors degrading optical performance are small so that the optical performance is still essentially diffraction limited, a degrading factor can be described sufficiently and evaluated in terms of its rms value without regard to its actual form.\* This applies to wavefront errors (e.g., defocus, astigmatism, spherical aberration, higher order aberrations) and to motion of the image during an observation (e.g., Gaussian motion, linear motion, sinusoidal motion).

Most of the errors can be viewed as uncorrelated with each other. Wavefront errors from different causes are uncorrelated in terms of the exact function across the pupil or the time at which they occur or the amount in which they occur. Motion from different sources is different in its time profile. Since there are many ways in which these errors can be different from each other during an observation and over the life of the telescope, they have been treated (except for some of the thermal errors) as completely uncorrelated. The rms value for all the wavefront errors has been determined by finding the root-sum-square value of the individual error rms values.

It is not possible in this phase of the LST program to state a probability level to be associated with each error. To do that would require a better definition of the mission, precise definition of the mission goals, and evaluation of each error source in terms of the actual mission profile. Nevertheless, it is safe to say that the error budgets are generally drawn to a high probability level ( $2\sigma$  to  $3\sigma$ ).

Most of the error budget allocations are treated in the design as worst case specifications, so that the system will operate within the budgeted values almost all of the time. Consider, for example, the star sensor noise in the fine guidance system. The noise equation gives the rms value to be expected in guiding from a star of a given brightness. This is sufficient to describe the error, as was mentioned before. If the observation time were very short relative to the control system response time, the rms noise error would represent a  $1\sigma$  probability level, since this is Gaussian random noise. Since the observation time is generally much longer than the control system response time, the rms noise level describes the motion with virtual certainty, indicating that the probability indicated by that noise level is very high, e.g.,  $> 3\sigma$ . In addition, the noise is dependent on star brightness. The guide field is sized so that the budgeted noise level can be met by having bright enough guide stars available for 90 percent of the targets in the galactic polar regions, or in excess of 90 percent for targets in the whole celestial sphere. From this point of view, then, the noise figure represents perhaps  $2\sigma$  probability.

In the following section we present the wavefront and guide error budgets. It is our belief that these goals can indeed be achieved in practice. The budgets show, however, that extreme care must be taken at every step, since almost all items are at the limits of physical achievement. The boundary conditions for these budgets (i.e., assumptions, models, etc.) and some of the backup data are either given here or reference is made to the section in which the budget items are detailed.

All budget items are to be taken as rms values at 633 nanometers.

#### System Error Budget

In Section C.6.f we examine the effects of wavefront error (WFE) and guide error (GE) on the LST's imagery. By point spread function (PSF) and modulation transfer function (MTF) analysis, we show that image degradation can be kept "small" (e.g., 10 percent loss due to each cause) by limiting the WFE to  $0.05\lambda$  rms and GE to 25 nanoradians (0.005 arc-second) rms. The degree to which these goals are met in large part determines the scientific

\*Large Space Telescope Image Quality Analysis, Itek Final Report 72-9486-1, NASA contract NASw-2313 (Dec 1972), p. 3-28 ff.

success of the LST. All the structural, dynamic, thermal, and electrical analyses which are reported in succeeding sections are oriented toward achieving  $0.05\lambda$  rms WFE and 25 nanoradians (0.005 arc-second) rms GE.

On the basis of PSF diameter, it seems appropriate to set absolute pointing error at 0.5 microradians (0.1 arc-second) rms, because some scientific instruments (e.g., spectrographs and photometers) have very small entrance apertures. A large error could lead to wrong measurements of radiation and/or to longer exposures than would otherwise be necessary. If low frequency tracking error signals are derived from the slit, it is possible to eliminate this requirement.

### B.3.b Wavefront Error Budgets

Sources of WFE have been grouped into several categories in Fig. B.3-1. In the concept of the LST presented here, this budget applies to the two mirrors of the system as launched into orbit and maintained by the automatic alignment equipment and the thermal control system. If figure changes in the mirrors and drift of the alignment systems are significant, the system can be maintained in a somewhat degraded state through the use of the interferometric diagnostic sensor, as is explained in Section C.6. Absolute focusing of the telescope is best performed on-orbit, and the most direct focusing technique is to make a through-focus run on a bright star for each focus-sensitive instrument, and then to use the closed loop focus control to maintain focus over an observation cycle. Such a technique is limited by the instrument being used, but in any case the error added by improper focusing is limited to that just detectable by the instrument in question. As is indicated in Section C.6 the diagnostic interferometer or special absolute focus sensors might be used in an indirect determination of focus, and, if desirable, an allowance for such a focus error can be made in the overall wavefront budget, as is shown in Fig. B.3-2. It is noted that the WFE budget presented here is for the center of the Cassegrain focus, corresponding to the  $f/96$  data field. The WFE due to the design, fabrication, and placement of the 8:1 relay is not considered here, since it is regarded as belonging to the SIP.

#### B.3.b(1) Design

The high resolution imagery is expected to occupy a maximum field of about 175 microradians (0.6 arc-minute). Data\* indicate that the inherent error of the telescope design is on the order of  $0.001\lambda$  rms, area weighted average over the  $f/96$  field of view in the center of the telescope field.

#### B.3.b(2) Manufacturing

The quality of the manufactured optics, and hence the upper limit of wavefront quality that they can produce, will be enhanced by a process of final hand figuring of the secondary mirror to compensate for errors in the primary as measured in an autocollimation test of the system. This process is detailed in Section C.3, where we also consider the sources of errors inherent in the manufacturing of the system. We also consider the manufacture of the secondary prior to final figuring in this section. In Section C.3, the production of the primary is addressed. Because some of the errors in the primary will be corrected by hand figuring the secondary to it, this budget is given for the two-mirror system and not for the individual mirrors. The manufacturing error budget is given in Table B.3-1. Most of the terms in the budget are directly dependent on the accuracy with which the wavefront can be measured. The budget is made assuming a  $0.01\lambda$  rms measurement accuracy, a level which is currently becoming operational in optical shops.

#### B.3.b(3) Alignment

The alignment concept is described in Section C.6. The WFE budget is given in Table B.3-2. The alignment error budget (decenter and tip, focus, and figure sensor) is treated in detail in Section C.6.e; only a review of the numbers is given here. The initial alignment of the secondary mirror relative to the primary is made interferometrically, and the associated error falls within the autocollimation test error in the manufacturing budget. Maintenance of alignment is dependent primarily upon the accuracy of the decenter sensors and the thermomechanical stability of the metering structure during an observation, when the alignment mechanism is inactive. Thermally induced decentering motion is conservatively estimated at 5 times the defocus motion described below.

---

\*Large Space Telescope, Continuation of a Technology Study, Itek Final Report 71-9463-2 (3 Sept 1971), also Itek Report 70-9443-1.

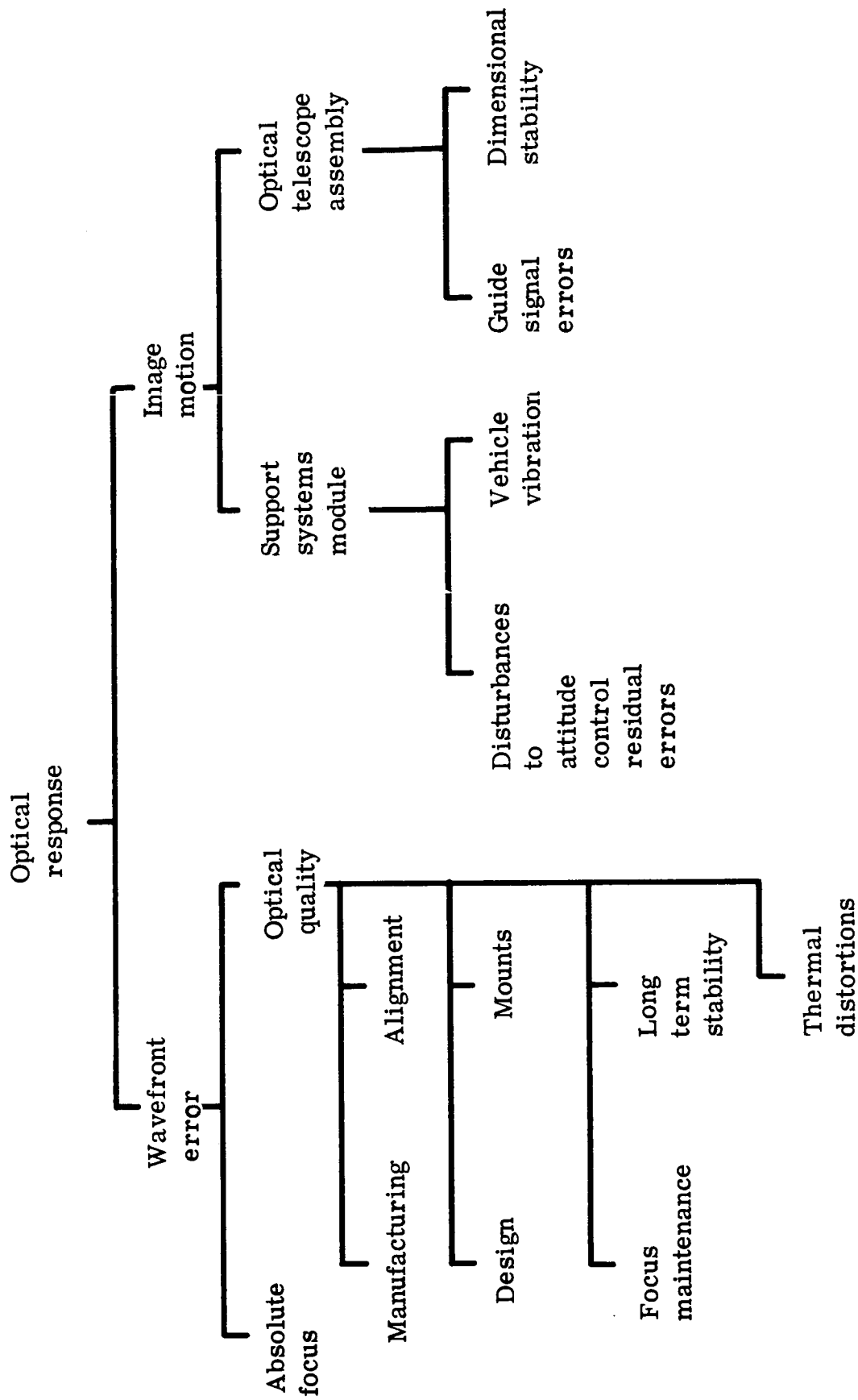


Fig. B.3-1 — Error budget tree

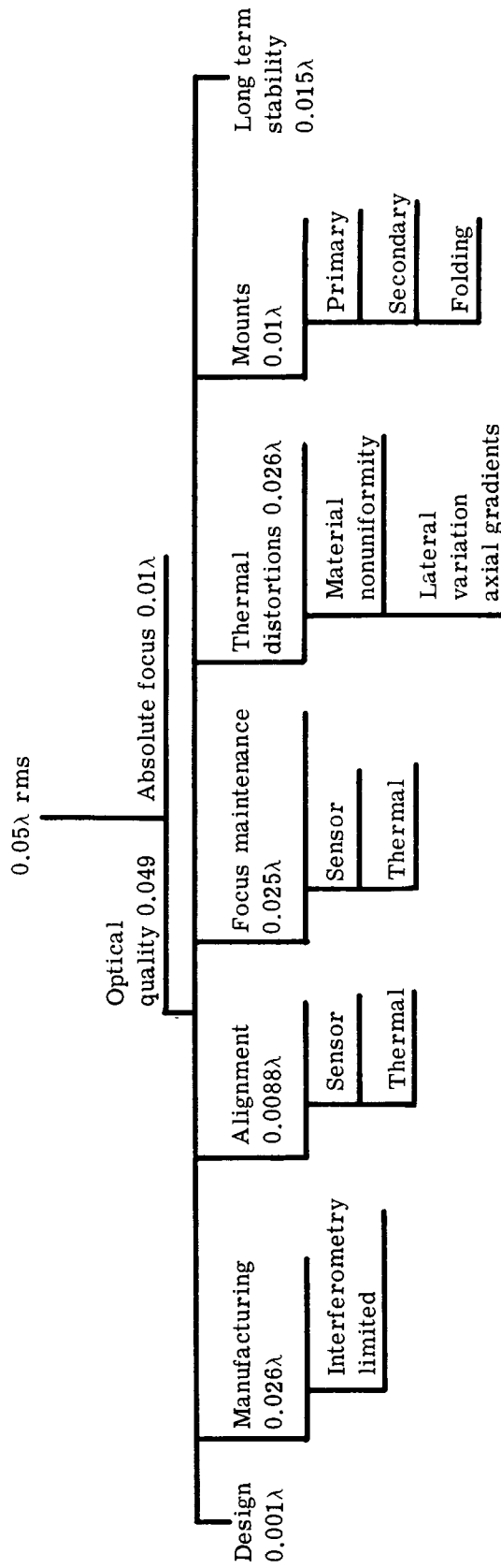


Fig. B.3-2 — System wavefront error budget;  $\lambda = 633$  nanometers

Table B.3-1 – Reduction of the Effect of Manufacturing Tolerances by Figuring of the Secondary Mirror in Autocollimation

	Tolerance, wavelengths rms	Resulting Wavefront Error wavelengths rms ( $\lambda = 633$ nanometers)
Interferometry – limited factors		
Calibration of reference flat and diverger	0.01	0.01
Autocollimation test (three orientations of flat, includes aligning and focusing)	0.017	0.0085
Secondary figuring (against primary polish/measure)	1:1	0.0085
Residual flat error (seven measurements in Ritchey test, reduce by 2 for detectable astigmatism)	0.038	0.014
Off-axis errors (30 percent primary error)	0.007	0.004
Tilt alignment error (off axis)	--	0.007
Other		
Calibration sphere	0.01	0.005
Primary zero-gravity simulation	0.005	0.005
Secondary zero-gravity simulation	0.005	0.005
Secondary coating	0.005	0.005
Off-axis points (30 percent primary error)	–	0.009
Thermal stability in test	$\pm 1^\circ\text{C}$	<u>0.005</u>
RSS system manufacturing error		0.026

Table B.3-2 – Alignment Error Budget (Decenter and Tip)

	Wavefront Error, wavelengths rms ( $\lambda = 633$ nanometers)
Initial alignment	
Sensor, 1 microradian at 6.6 meters	0.0036
Alignment maintenance	
Sensor, 1 microradian at 6.6 meters	0.0036
Thermal drift during observation	0.0055
10 micrometers (decenter) 5 microradians (tip)	0.0016
Tilt of secondary for 1-arc-second line of sight correction	0.0040
Adjustment mechanism, 3.5 micrometers	<u>0.0019</u>
RSS error	0.0088

#### B.3.b(4) Focus Maintenance

The concept for maintaining focus is also detailed in Section C.6; we present the focus maintenance budget in Table B.3-3. The autocollimating focus sensor to be used can detect very small changes in focus; the most critical item in the budget is maintaining the thermomechanical stability of the metering structure during an observation while the focus adjustment mechanism is inactive. Analysis of the thermal control system, as described in Section C.4, indicates that during a 20-minute observation, the average temperature of the metering structure will not vary by more than  $0.2^{\circ}\text{C}$  (worst case), which in a graphite-epoxy truss will produce a mirror spacing change of no more than 2 micrometers. Preliminary review of graphite-epoxy materials indicates that larger temperature excursions can be tolerated if the overall properties of this material prove satisfactory for the metering structure.

#### B.3.b(5) Thermal Effects in Mirrors

Thermal degradation of the mirror figures is treated in detail in Section C.1 with the resulting budget given in Table B.3-4. The thermal requirements are also presented; these served as the baseline for both the systematic and random errors shown. The most significant distortions can be expected in the primary mirror from the nonuniformity of the coefficient of expansion of the mirror material (Cer-Vit) and from lateral variations in the axial temperature gradient to which the mirror is subjected as part of the thermal control system. The WFE budget for the primary and secondary mirrors sums to the  $0.026\lambda$ , and this value is presented in Fig. B.3-2.

#### B.3.b(6) Mirror Mounts

The mirror mount design is described in detail in Section C.2, and the WFE attributed to the mount are shown in the budget in Table B.3-5. The boundary conditions and the WFE derivations are also covered in Section C.2. Changes in the soak temperature cause thermal differential expansion, and distortions are introduced into the mirror figure through the mounts. The distortion introduced at the time the mounts are attached is less severe. Mounting of the primary mirror is considerably more critical than mounting of the secondary.

#### B.3.b(7) Long Term Mirror Distortion

We have budgeted 0.0152 rms to allow for long term instabilities in the mirror blanks.

#### B.3.b(8) Guide Error Budgets

Independent of the WFE budget just outlined, we have a guide error budget as noted at the beginning of this section.

#### B.3.c Image Stabilization

The 0.025-microradian (0.005-arc-second) rms stabilization error is broken into four error classes, each pair of which is allotted equal portions between the SSM and OTA in the image stabilization error budget presented in Fig. B.3-3. Although true error syntheses of the different classes have not been made pending further definition of the actual system in the next study phase, feasibility of meeting the allocations has been demonstrated in the current concept definition. Disturbances to guiding, guide signal errors (Table B.3-6), vibration, and thermal displacements in the OTA (Table B.3-7) have been shown to be tractable within the above allocations.

#### Absolute Pointing Error Budget

The budget in Fig. B.3-4 shows how the absolute pointing error of 0.5 microradian (0.1 arc-second) rms may be achieved. Some of the numbers are based on actual experience; some are estimates. The individual items are discussed below. Use of slit guide error sensors permit enlarging or eliminating this requirement.

The astronomer will be expected to select two guide stars brighter than 14th magnitude, having offset angles from the data star between 8 and 12 arc-minutes. The angle between these stars as seen from the data star must exceed 90 degrees. He will also be expected to measure the offset angles with 0.05-microradian (0.01-arc-second) accuracy, which is within the capability of modern astrographic cameras. If the data star is too faint to be seen, then

the 0.5-microradian (0.1-arc-second) rms pointing requirement will be relaxed, since a larger scientific instrument aperture will be used.

The buildup of the guide head error is primarily a function of the reticle plate, which is inherently very stable and can be made with great accuracy. An additional factor is the optical micrometer used in interpolation between the reticle lines.

B.3.d System Calibration for Reducing Error Effects

In practice it may be possible to calibrate out some of these budget items by on-orbit procedures. In particular it may be that the location of the scientific instrument (0.21 microradian) (0.045 arc-second) rms could be made more accurate by introducing incremental pointing changes and observing how the signal changes through a small aperture.

The decenter sensors and the focus change sensor can be calibrated by means of the diagnostic figure sensor. The scale constant of the guide system detection loop can be calibrated by movement of the secondary mirror or by movement of the optical micrometer. Calibration of the structural response to changes in the thermal loading might enable the focus and centering of the secondary to be preset to such a position that the defocus and decentering between corrections is minimized. Finally, perhaps thermal, mount, gravity-release, and creep-induced changes in the mirror figure can be measured by means of the figure sensor and corrected to some extent by use of the mirror actuators, even though the errors do not exceed the design goals.

The system is not designed to depend upon this calibration, but the availability of calibration provides a safety factor in the design or the possibility of very fine tuning of the system.

Table B.3-3 -- Focus Maintenance Budget

	Wavefront Error, wavelengths rms ( $\lambda = 633$ nanometers)
Calibration of relative focus sensor	0.009
Internal dimension knowledge, 5 micrometers	0.0018
Relative focus sensor threshold	0.009
Mechanism error, 0.47 micrometer	0.005
Thermal drift, 2 micrometers	<u>0.021</u>
RSS error	0.025



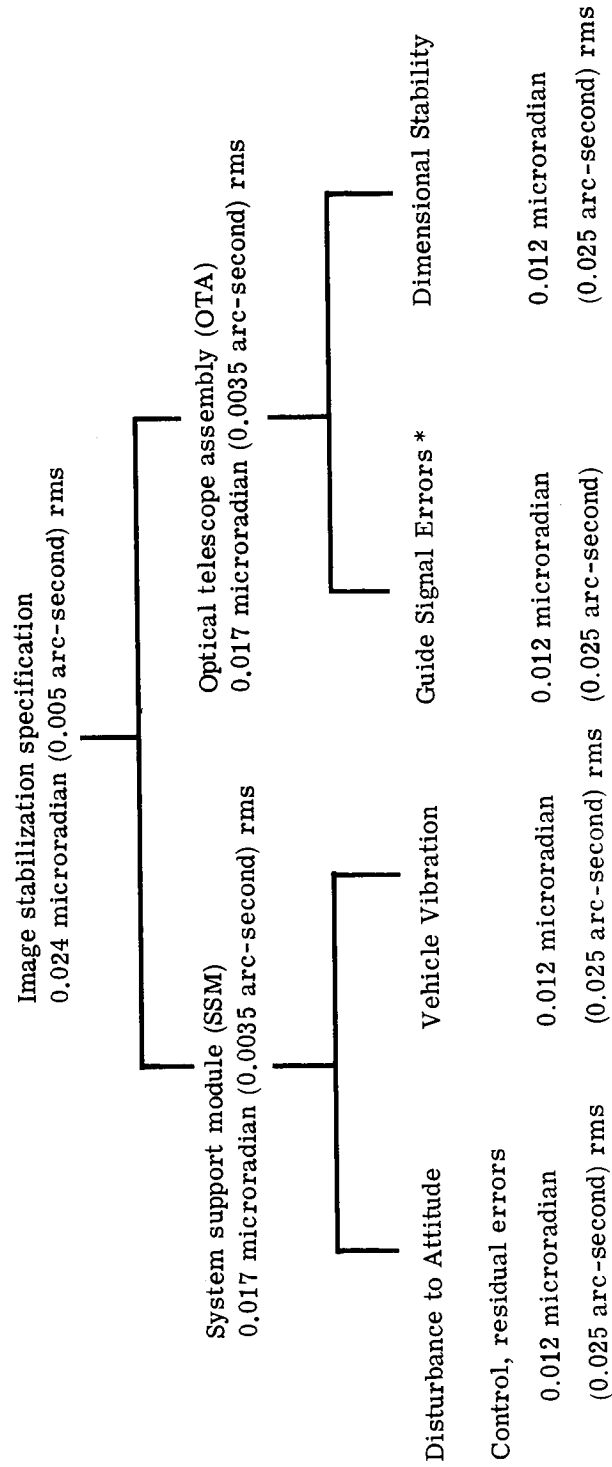


Fig. B.3-3 — Image stabilization error budget

Table B.3-4 -- Thermal Optical Design Requirements\*

Element	Optical Degradation, wavelengths rms ( $\lambda = 633$ nanometers)		Thermal Requirement °C
	Systematic	Random	
Primary mirror			
Axial gradient	0.00157	—	9
Radial gradient	0.00433	—	3.25
Secondary mirror			
Axial gradient	0.00015	—	4.5
Radial gradient	0.001	—	3.3
Primary mirror			
$\alpha$ variation, soak	—	$\pm 0.0105$	$\pm 4.4$
Axial gradient variation	—	$\pm 0.0155$	$\pm 1.2$
Secondary mirror			
$\alpha$ variation, soak	—	$\pm 0.0004$	$\pm 0.5$
Axial gradient variation	—	$\pm 0.0006$	$\pm 0.25$

Systematic = 0.00705, random = 0.01875

Total (systematic + random) = 0.026

\*Primary and secondary mirror optical budget:  $0.026\lambda$

Table B.3-5 -- Mirror Mounts

		wavelengths rms ( $\lambda = 633$ nanometers)
Primary		0.009
Thermal soak	0.008	
Assembly	0.004	
Secondary		0.0045
Thermal soak	0.004	
Assembly	0.002	
RSS		0.01

Table B.3-6 – Fine Guidance System Error Sources for Star Observation

Source	RMS Error ( $\lambda = 633$ nanometers)	
	Microradians	Arc-Seconds
Guide sensor noise (90% of targets, maximum optical micrometer offset)	0.0053	0.0011
Optical micrometer lateral color	0.0009	0.0002
Optical micrometer tracking for differential velocity aberration compensation and grid interpolation	0.005	0.001
Mirror actuator error, noise and hysteresis (0.1% of 5 microradians)	0.005	0.001
Granularity in control system (5 microradians divided into 11 bits)	0.0024	0.0005
Roll error coordinate transformation (10% calibration of loop gain)	0.00170	0.00035
	<hr/>	<hr/>
RSS	0.0092	0.0019
Allocation	0.0120	0.0025

Table B.3-7 – Dimensional Stability Errors for f/96 Imagery

Source	RMS Error ( $\lambda = 633$ nanometers)	
	Microradians	Arc-Seconds
Reticle plate dimensional change (fused silica, $\pm 1^\circ\text{C}$ )	0.002	0.0004
Primary-secondary spacing (2 micrometers)	0.0019	0.00038
Primary – SIP spacing (10 micrometers)	0.0038	0.00078
Primary mirror focal length (5 micrometers)	0.0045	0.00092
Secondary mirror focal length (2 micrometers)	0.0041	0.00085
Artificial star sensor noise and calibration to 1% of one star image diameter	0.005	0.001
	<hr/>	<hr/>
RSS	0.0092	0.0019
Allocation	0.0120	0.0025

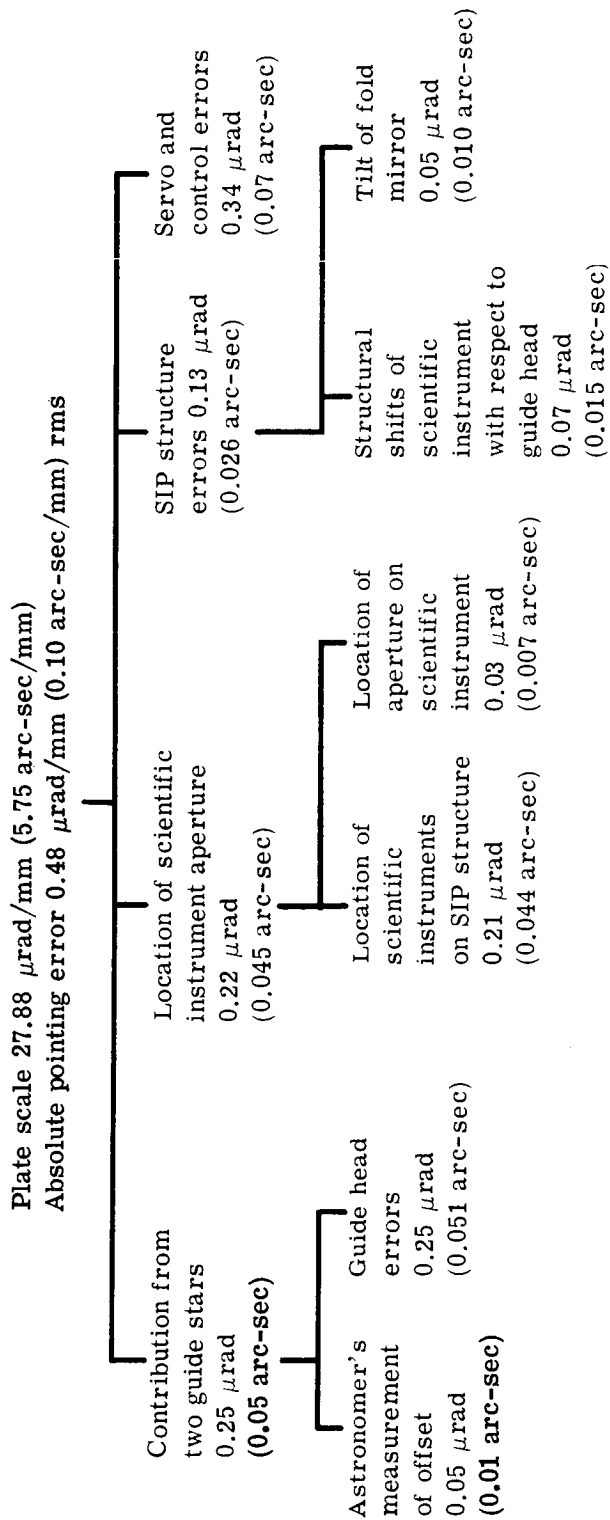


Fig. B.3-4 — Top level absolute pointing error budget. Note that use of slit jaw guidance for spectroscopy considerably relaxes this budget requirement

## C. SYSTEM DESIGN

### C.1 SUMMARY DESCRIPTION OF SYSTEM ARRANGEMENT AND FAMILY TREE

The optical telescope assembly (OTA), its design, the arrangement of its components, and some of the requirements that govern this design are discussed in this section. The family tree shown in Fig. C.1-1 contains a subassembly breakdown of the OTA and corresponds to the block diagram shown in Fig. C.1-2. The OTA comprises eight systems, each of which is portrayed in an isometric view showing the approximate physical arrangement of the system in the telescope. In order to show the relationship of all electrical systems and subsystems, a more detailed overall block diagram is shown in Fig. C.7-1. The listing of requirements under each system is not meant to be comprehensive; however, it does contain most of the more important features of each system and describes them in a relatively brief manner, and can be used as a guide for future specification activities. Much more detailed information on each design discipline is given in succeeding sections. It should be pointed out that the information given is organized in two different ways, each of which is one side of a matrix that describes the telescope system. The aforementioned family tree describes the system by functional elements that may cut across various disciplines, while the design text is organized by disciplines and cuts across various systems. The former is needed for a functional understanding of the telescope, while the latter provides an efficient review of the material of interest to each area of overall interest or discipline (see Fig. C.1-3).

#### C.1.a Structural Support Assembly

The LST structural support assembly (Fig. C.1-4) comprises three distinct systems: the OTA metering truss configuration, the scientific instrumentation package (SIP) truss structure, and an assembly of semimonocoque components that contains the optics for orbital flight. The OTA metering truss is manufactured from graphite-epoxy and is mounted to a very stiff titanium support bulkhead. The telescope instrument support structure is also manufactured from graphite-epoxy material and is supported by the same titanium bulkhead. The primary mirror is supported by leaf spring Invar flexure mounts located at three equidistant points on its circumference. The secondary mirror is supported by a four-strut spider support ring located on the forwardmost ring of the OTA metering truss.

The assembly of aluminum semimonocoque components is isolated from both optical assemblies, and comprises the meteoroid shield, the main light baffle, and the inner light baffles. The meteoroid shield serves to support all other aluminum assembly components and itself is supported on the SSM structure.

#### C.1.a(1) Interface Definition

##### OTA Structural Interface

The OTA structure consists of a metering truss assembly, primary and secondary mirrors, and a honeycomb bulkhead that supports the primary mirror. The OTA interfaces with the system support module (SSM) pressurized cylinder by attachment of the stiffened outer edge of the pressure bulkhead to the cylinder flange. The structural interface is shown in Fig. C.1-5.

##### Secondary Mirror

The structural interface of the secondary mirror is through a four-strut secondary mirror support ring, which is secured to the forward metering truss ring.

##### OTA Protective System

The meteoroid shield serves to support all aluminum assembly components and itself is supported by the SSM pressurized cylinder located approximately 1.5 meters (59 inches) beyond the aft side of the edge of the pressure bulkhead. The aluminum components supported by the meteoroid shield include the main light baffle and elements of the protective system, the aperture doors, and the extendible light shield. The main light baffle is attached to the meteoroid shield by 12 standoffs (three to a row) spaced 1.57 radians (90 degrees) apart at each axial location.

### Instrument Interface

The telescope instrument support structure is attached to the aft side of the OTA pressure bulkhead at its reinforced edge. The instruments are attached to the truss members and rings of the telescope instrument support structure.

### Vehicle Interface

The OTA/SIP structural configuration interfaces with the vehicle by attachment of the SSM pressurized cylinder at a point approximately 5 meters (197 inches) beyond the aft side of the pressure bulkhead. The shuttle support interface will be on fittings provided on the primary ring at the pressure bulkhead.

### C.1.a(2) Characteristics

#### Performance Requirements

The OTA is expected to have an operating lifetime of 10 years. There will be a 2.5-year no-maintenance interval. In the sizing of the structural elements of the telescope, the major forces are a result of the booster launch, shuttle reentry, and pressurization loads. The design launch acceleration loads are  $\pm 6$  g in the longitudinal direction combined with 1.5 g in a lateral direction. The reentry loads are tentatively  $-3$  g longitudinal, combined with lateral loads of 2.7 g (pitch) and 1.5 g (yaw). Landing loads are not considered to be critical and are therefore not stated here. A factor of 1.4 applied to the above limit loads is used to obtain ultimate loads. The pressurizable portion of the structure will see  $10^2 \times 10^3$  newtons/meter<sup>2</sup> (14.7 psia) with a factor of 2 applied to the pressure loading to obtain ultimate loads.

#### Mirror Mounts

The primary mirror mount is a universal three-point system that satisfies both the launch and operational environments. In the design of the primary mirror support system provisions are made in the performance control system for a series of force actuators to be located behind the primary mirror. The actuators act as a contingency against unpredictable long term changes of the mirror surface.

The secondary mirror mount system is mounted at nine points to allow testing in a 1-g environment, as well as by three tangent bars. Alignment control is provided by the performance control system. The secondary mirror assembly is a four-strut, thermally insensitive structure.

The primary and secondary mirror mounts are as free as possible from ferromagnetic materials. As a design goal, the structural dynamics of the mounting systems will be kept in excess of 30 hz both in tilting and translation. The surface error induced by the mounts to the mirrors from the thermal environment is to be limited to  $0.0045\lambda$  rms for the primary and secondary mirrors.

The maximum stress levels in the mounts are kept substantially below the microyield stress of the mount materials, while the stresses induced locally in the mirrors by the mounts are limited to  $6.9 \times 10^6$  newtons/m<sup>2</sup> (1,000 psi).

#### Optical Metering Structure

The primary function of the optical metering structure is to fix the spatial relationship between the primary and secondary mirrors. The degree of accuracy to which this spatial relationship is maintained affects the overall performance of the optical system. The structural design criteria to be met by the metering structure to ensure acceptable optical performance between active alignment corrections are:

Despace of secondary mirror*	$\pm 2$ micrometers ( $0.02\lambda$ rms)†
Decenter of secondary mirror*	$\pm 10$ micrometers ( $0.0055\lambda$ rms)
Tilt of secondary mirror*	4.9 microradians ( $0.004\lambda$ rms)

\*With respect to primary mirror.

†  $\lambda = 633$  nanometers.

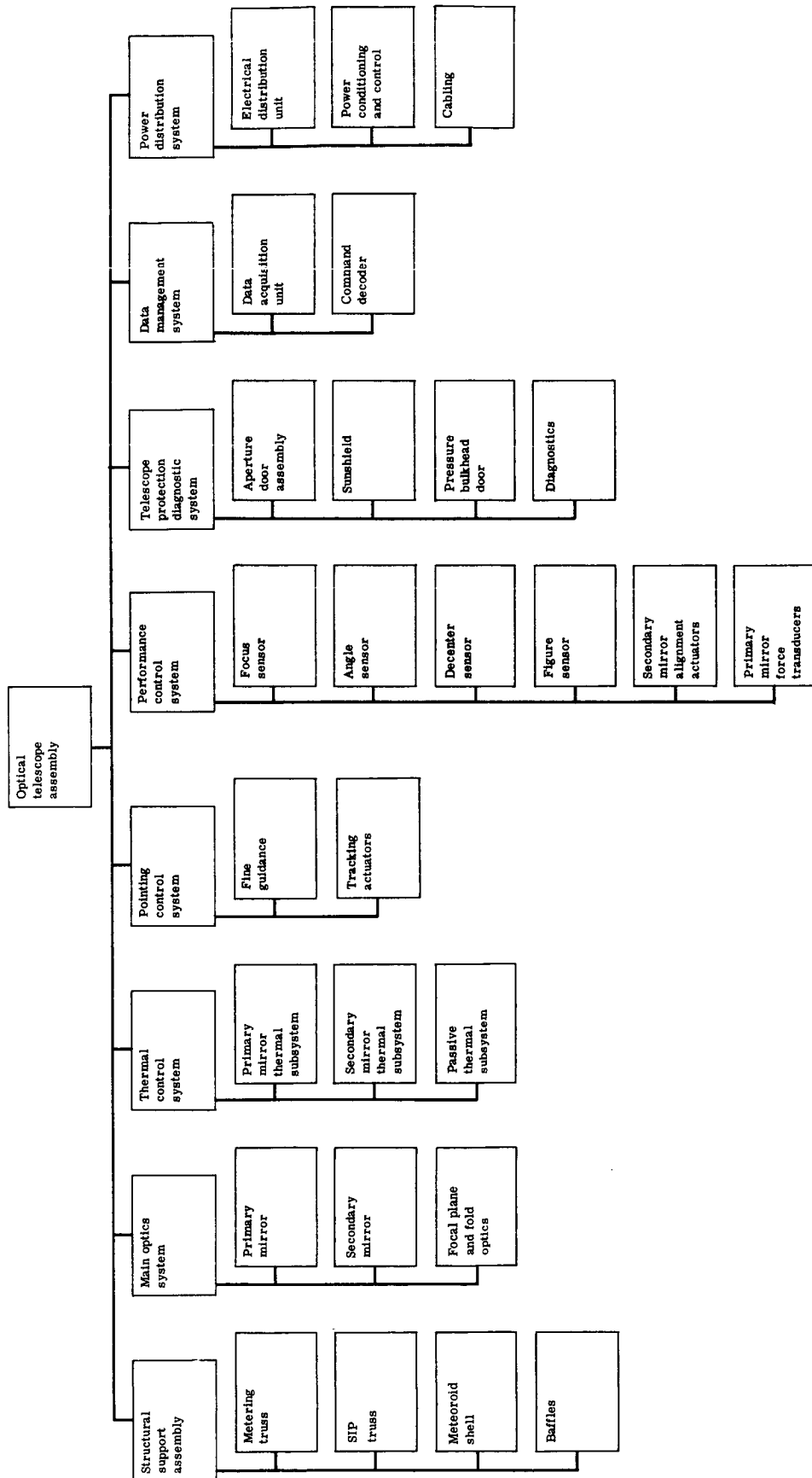


Fig. C.1-1 — OTA family tree

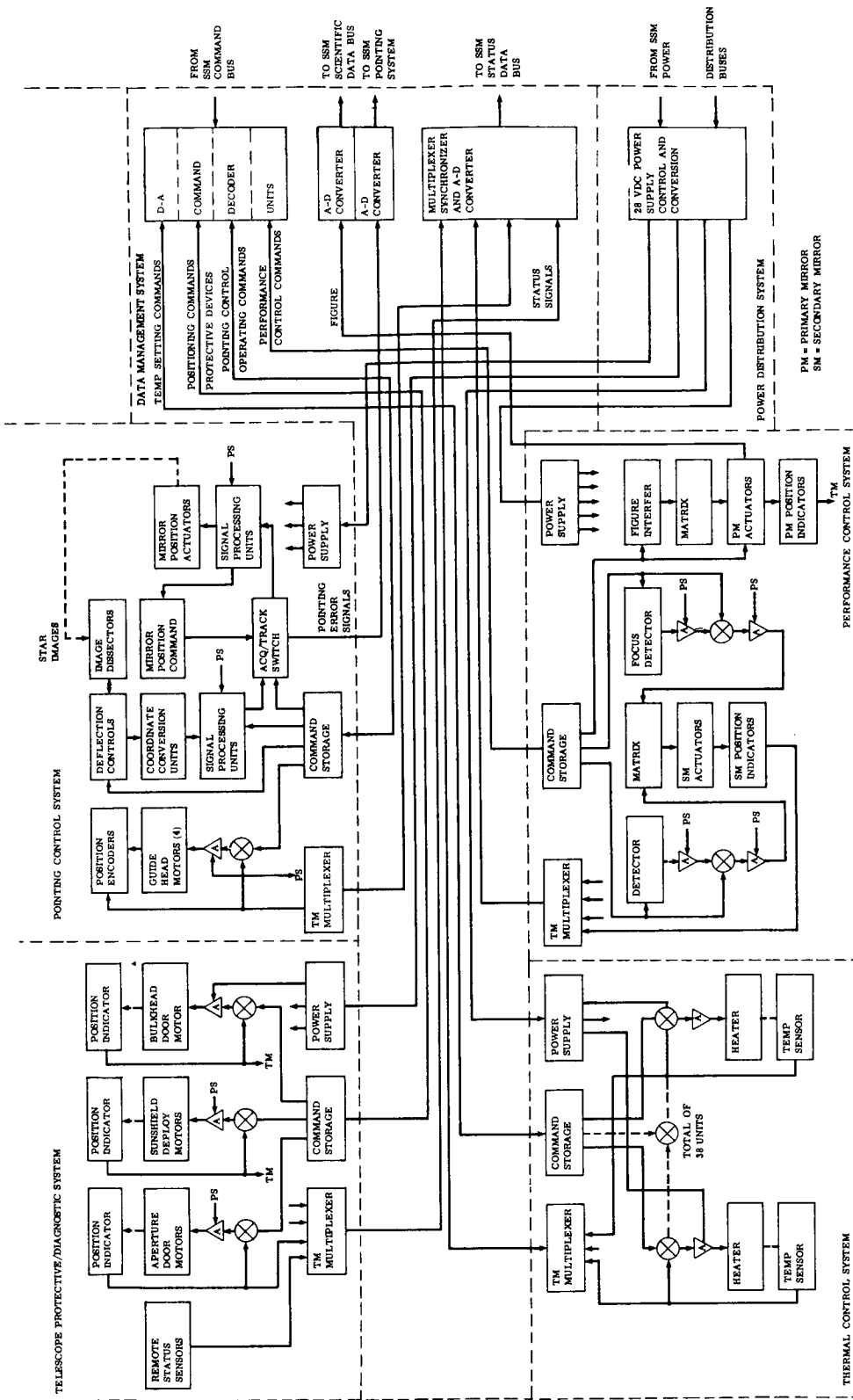


Fig. C.1-2 — OTA system block diagram

PM = PRIMARY MIRROR  
SM = SECONDARY MIRROR



Design Discussion Topic	Structural Support Assembly	Main Optics System	Thermal Control System	Pointing Control System	Performance Control System	Telescope Protective Diagnostic System	Data Management System	Power Distribution System	Report Section
Structural design	X	X		X	X	X			C.2
Optical design	X	X	X	X	X	X			C.3
Thermal design		X	X		X			X	C.4
Stabilization and control design	X	X		X			X	X	C.5
Alignment and focus control design		X	X		X		X	X	C.6
Electronic systems design			X	X	X	X	X	X	C.7
Scientific instrument design	X	X	X	X					C.8
Interfaces	X	X	X	X	X	X	X	X	C.9
Reliability	X	X	X	X	X	X	X	X	C.10
Mass properties	X	X	X	X	X	X	X	X	C.11

Fig. C.1-3 — Matrix of relationship of system family tree and design discussion topics in subsequent report sections

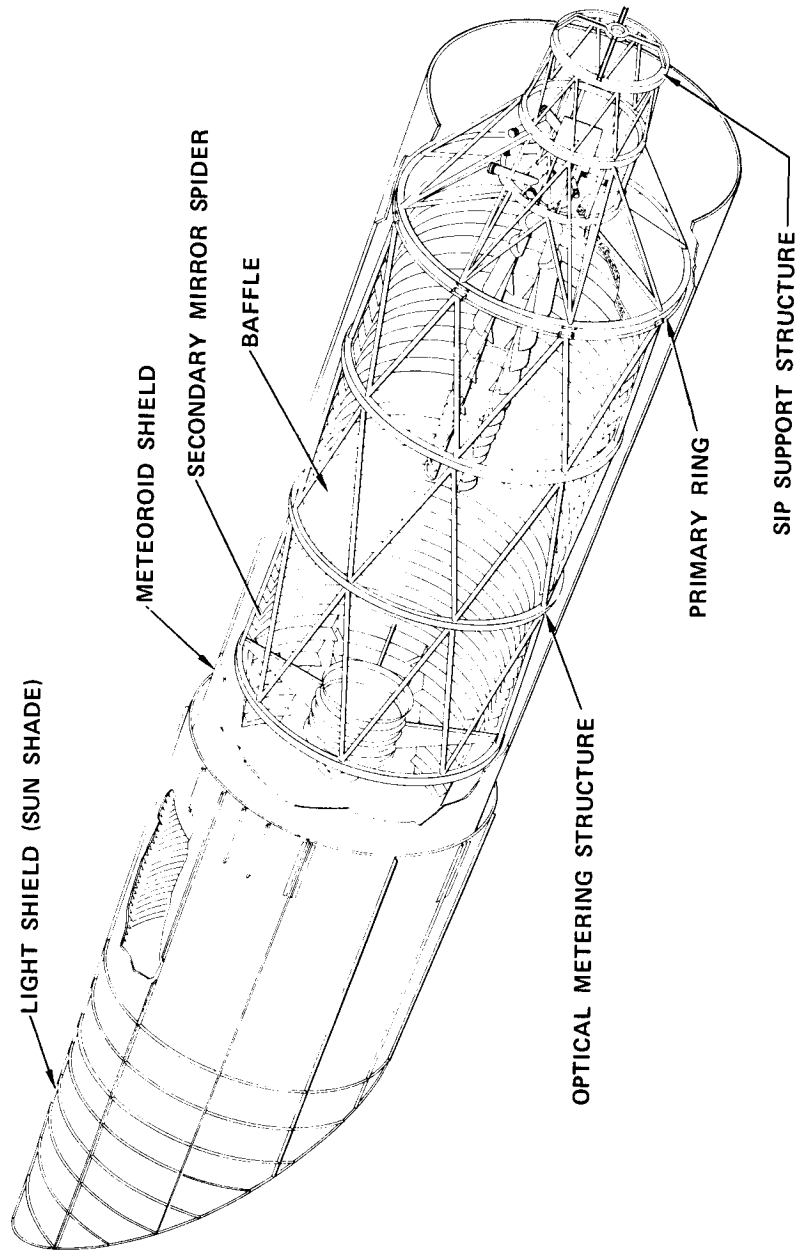
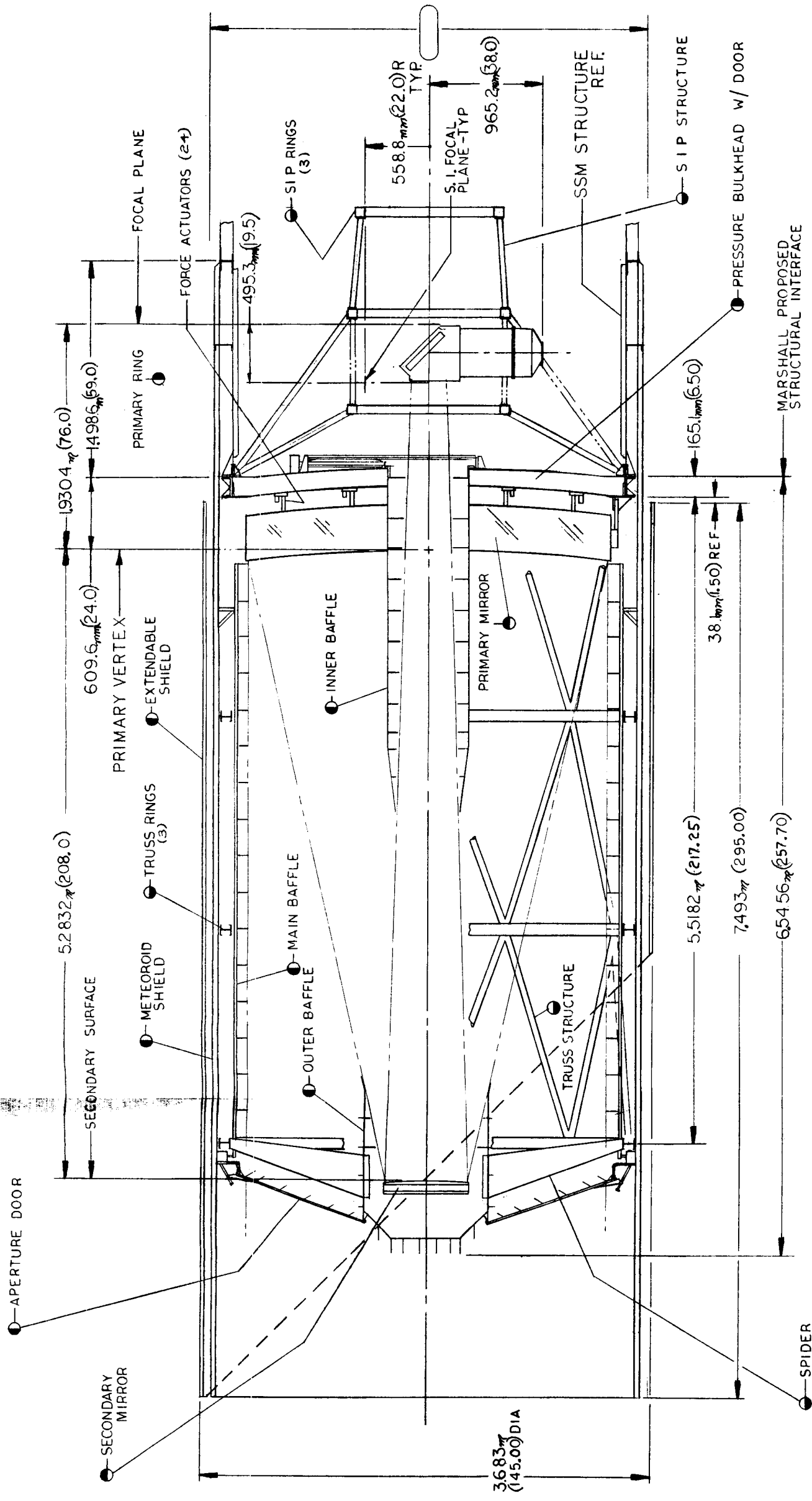


Fig. C.1-4 — Structural support assembly



MATERIAL LEGEND	
SYMBOL	DESCRIPTION
●	ALUMINUM
●	GRAPHITE-EPOXY
●	TITANIUM
●	CER-VIT

NOTE: DIMENSIONS SHOWN IN PARENTHESES ARE ENGLISH EQUIV

Fig. C.1-5 — OTA structural interface (drawing no. 185505)

The metering structure is designed to be structurally independent and environmentally isolated from the rest of the OTA. This is necessary so that all the forces on the metering system (i.e., launch, orbiting, reentry) are not influenced by forces acting on other parts of the OTA and so that the environment (i.e., thermal, meteoroid, radiation) will have little or no effect on the metering truss. A thermally insensitive structure which is also stable is very important, especially during an observation period. The metering truss is a lightweight design with minimum ferromagnetic materials. The stiffness design goal is fixed base natural frequency greater than 15 hz, while the forces in the metering truss are such that the resulting stresses are well below the microyield stress.

#### Scientific Instrument Package (SIP) Support Structure

The structural design of the SIP support structure is governed by the same requirements as those of the metering truss structure. The structure is lightweight, is thermally insensitive, has a fixed base, fundamental natural frequency above 25 hz, and is capable of withstanding the launch and reentry forces without any significant detrimental effects.

Environmental coupling to the SIP truss, as seen at the fine guidance sensor, will conform to the following during the active observation interval and will allow for action of the performance control system:

Axial despace to primary mirror	10 micrometers
Lateral position with respect to primary mirror	18 micrometers
Tip with respect to primary mirror	TBD microradians

The nature of the SIP support structure provides ease of accessibility and maintainability. Provision for future growth to incorporate additional instruments has also been considered in the design.

#### Nonoptical Structure

The structure that contains the optical system comprises the meteoroid shield, the main light baffles, and the inner light baffles. The design philosophy is to provide independent structural and thermal load paths so as not to influence the optical elements of the telescope assembly.

This structure is lightweight and capable of withstanding the launch and reentry forces. The stiffness of the structure is such that the fundamental, fixed base natural frequency is above 40 hz and the dynamic displacements remain small so as not to affect the optics. Thermally induced displacements are also kept small to ensure against interference with the optical structure.

The meteoroid shield is designed for a 0.95 probability against penetration for 5 years. A series of light baffles located to eliminate stray light is included as part of the containment system.

#### Pressurizable Structure

The pressurizable portion of the OTA structure includes the pressure bulkhead and the SSM pressurized cylinder. Design of this area is governed by the pressure forces. Deflections on the bulkhead are kept small so as not to cause unacceptable stresses on the primary mirror and mounts. Since the pressure bulkhead supports the primary mirror, metering structure, and SIP structure, the displacements in the bulkhead from the pressure and acceleration forces must be minimal so as to keep the stresses in the optical structure well below the microyield stresses.

### C.1.a(3) Physical Characteristics

#### Size

The maximum length of the system is 10.95 meters (430 inches) with the extendible shield retracted. The maximum diameter of the system is 3.67 meters (145 inches).

#### Weight

The maximum weight of the structural support system is 1,536 kilograms (3,388 pounds), including electronic box structure.

## Maintainability

As a design goal there will be no requirements for maintainability to the structural support assembly. Any maintenance to the structural support assembly in space will require the system to be de-orbited.

### C.1.b Optical Design

The main optics system (Fig. C.1-6) consists of three major sections: the primary mirror, the secondary mirror, (both of which comprise a Ritchey-Chretien telescope), and the focal plane and folding optics that direct the  $f/12$  images to telescope subsystems and scientific experiments. The primary mirror has an aperture of 3 meters and the secondary mirror has an aperture of 0.65 meter. The primary mirror is fixed relative to the LST, while the secondary mirror design allows the mirror to be movable on an intermittent basis for the alignment function of the performance control system.

In addition, a dynamic tracking mode can be operated continuously for guidance by the pointing control system. The focal plane and fold mirrors are mounted in a rigid, athermalized assembly at the  $f/12$  focal plane to which the pointing control devices, the DVA drives, and the image dissector sensors are rigidly attached. This structure, in addition, provides a mounting interface for the  $f/12$  camera and filter wheel, the spectrograph slit assembly, and an array of mirrors in front of the focal plane (large and small). The small mirrors in front of the focal plane can be spherically figured to remove astigmatism for instruments such as the faint object spectrographs and the infrared spectrograph. Small flat mirrors can be used, if appropriate, for other purposes such as figure or focus sensing. A large folding flat is used to direct the 7- by 4.7-milliradian (24- by 16-arc-minute) inner diameter tracking field below the telescope optical axis, as well as the on-axis  $f/96$  data field. A smaller fold mirror directs a portion of the data field to the  $f/12$  camera.

#### C.1.b(1) Mirror Material

The material selected for the optical mirrors must fulfill a number of requirements. It must have a low and uniform coefficient of thermal expansion to limit thermally induced optical wavefront errors. It must also possess high thermal conductivity and diffusivity to minimize temperature gradients. Good long term stability and a high microyield limit are also requirements (which will be quantified later). A material with a high stiffness to weight ratio is also desirable in order to keep deflections and weight down. The design requirements of the mirror are for a lightweight configuration with errors in the faceplate upon gravity release to be below  $\lambda/200$  rms ( $\lambda = 633$  nanometers). The design goal is to keep the stress levels of the silicate materials below  $6.0 \times 10^6$  newtons/m<sup>2</sup> (1,000 psi). Both Cer-Vit and ULE satisfy the technical requirements; Cer-Vit is specified because of lower cost.

#### C.1.b(2) Interface Definition

##### Structural—Primary Mirror

The structural interface of the primary mirror is through three Invar flexures secured to the primary structure ring/pressure bulkhead.

##### Structural—Secondary Mirror

The structural interface of the secondary mirror is through a nine-point tangent bar mount, supported by the performance control and pointing and guiding systems, which are attached to a four-strut spider secured to the forward metering truss ring.

##### Structural—Folding Optics

The folding optics assembly is secured to the instrument support truss by means of low conductance joints. The folding optics assembly provides interface mounting for:

1. Fine guidance (image dissectors and DVA drives)  
to  $f/96$  cameras
2.  $f/12$  camera and filter wheel
3. Spectrograph slits and slit camera
4. Folding mirrors to:
  - a. Faint object spectrographs (2)
  - b. Infrared spectrometer
  - c. Figure sensor
  - d. Focus sensor.

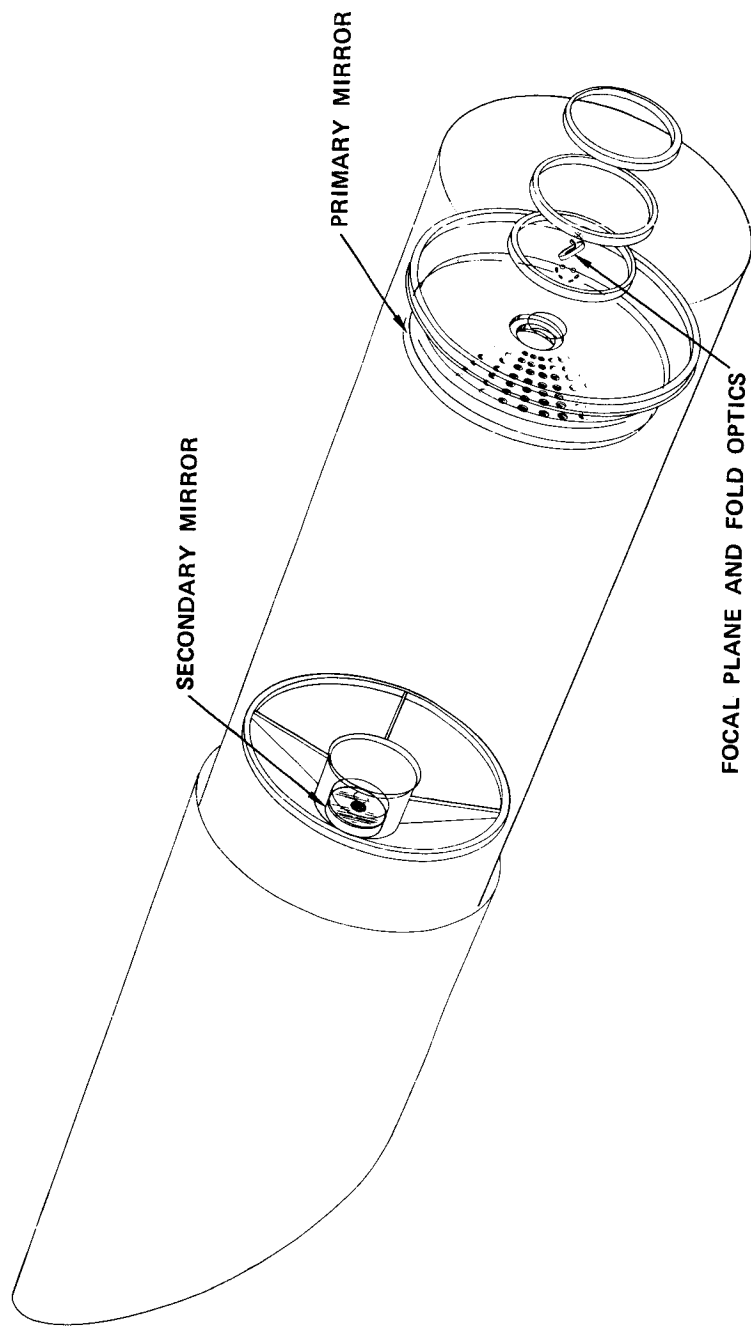


Fig. C.1-6 -- OTA main optics system

### Thermal Control—Primary Mirror

The primary mirror requires active thermal control, and employs the use of multizone heaters, temperature sensors, and insulation blankets to achieve the following temperature requirements:

Temperature level	21 ±4.4°C
Axial gradient	9.0°C
Axial gradient variation	1.2°C
Radial gradient	3.25°C

### Thermal Control—Secondary Mirror

A similar thermal interface for the secondary mirror achieves the following temperature requirements:

Temperature level	21 ± 0.5°C
Axial gradient	4.5°C
Axial gradient variation	0.25°C
Radial gradient	3.3°C

### Thermal—Focal Plane and Fold Optics

The conductance of the mounting joints is as low as is consistent with structural stability requirements. The allowable temperature variation as measured on the fine guidance housing and the set point will be determined by analysis in the next program phase.

### Interface—Performance Control System

#### Figure Sensor

The figure sensor provides wavefront error information between the main optics system and the performance control system. Force actuators mounted to the pressure bulkhead load the primary mirror from ground control command for figure control. The figure sensor uses a fold mirror forward of the focal plane and is mounted on the instrument structure.

#### Alignment and Focus Interface

All alignment and measuring instruments are operable via ground command and data link via the SSM. The tilt and decenter sensors are integrally mounted directly to the primary mirror blank. The targets for the tilt and decenter sensors are mounted to the secondary mirror in such a way as to decouple the interaction between tilt and decenter measurements. A pentaprism and penta roof prism are mounted to the secondary mirror spider in order to provide targets for the focus change sensor. The focus change sensor is integrally mounted to the fine guidance housing.

### Interface—Pointing Control System

The secondary mirror is mounted by means of a nine-point tangent bar mount to minimize gravity release effects on figure. The nine-point mount is attached to the tracking actuators of the pointing control system. The tracking actuators in turn are mounted to the secondary mirror alignment actuators of the performance control system. When actuated by the tracking actuators, the mirror rotates about its center of gravity.

### Optical Beam Interfaces

The OTA main optics system delivers a near-diffraction-limited image to the principal focal plane ( $f/12$ ) with at least a 1.5-milliradian (5-arc-minute) diameter. The main optics system delivers the image at a location within the SSM at a distance of 1.93 meters behind the vertex of the primary mirror. The image plane format is described in Section C.9.

#### C.1.b(3) Performance

### Wavefront Error of Main Optics System

The total wavefront error for the main optics system is a maximum of  $0.05\lambda$  rms, when measured at the

standard test wavelength of 633 nanometers at the principal focus, area weighted average over the scientific data field exclusive of the folding optics and not including image motion effects.

#### Surface Quality

The surface quality of the primary and secondary mirrors is compatible with the system wavefront error specification. Proprietary Itek techniques for measurement, control, and production of low scatter optical surfaces are used to maximize performance at short wavelengths.

#### Mirror Reflectance

The minimum normal incidence reflectance of each mirror common to all optical paths is 85 percent or greater to all wavelengths between 0.20 micrometer and the maximum useful infrared wavelength, nominally 2.0 micrometers. Below 0.2 micrometer, the normal incidence reflectance is as high as possible down to 0.11 micrometer. This requirement may be deviated from for optical paths used for a restricted spectral region only, if such deviation results in an increased reflectance for that spectral region.

#### Mirror Alignment

The primary mirror and mount is provided with alignment reference surfaces.

#### Folding Optics Vignetting

The folding optics subsystem is sized to introduce zero vignetting in the tracking field (design goal) or the scientific data field (requirement).

#### Folding Optics Failure Modes

Single failure modes of mechanisms within the focal plane optical system do not result in loss of all scientific instrument measurement capabilities.

#### Central Obstruction

The main optical system is designed with a diametral central obstruction which does not exceed 30 percent of the primary mirror aperture.

### C.1.b(4) Physical Characteristics

#### Weight

The maximum weights of the main optics system are as follows:

Primary mirror assembly	2001 kilograms	(4,412 pounds)
Secondary mirror assembly	40 kilograms	(88 pounds)
Focal plane and fold optics	40 kilograms	(88 pounds)

#### Shape and Size

The optical system layout and the configuration of the optical elements are shown in Fig. C.1-5.

### C.1.c Thermal Design

The OTA thermal control system (TCS) is shown in Fig. C.1-7.

#### C.1.c(1) Active Elements

The active elements of the TCS consist of electrical heating elements, temperature sensors, and the associated electrical controls for these elements.

#### C.1.c(2) Passive Elements

The passive elements of the TCS consist of external thermal control finishes and thermal insulation.



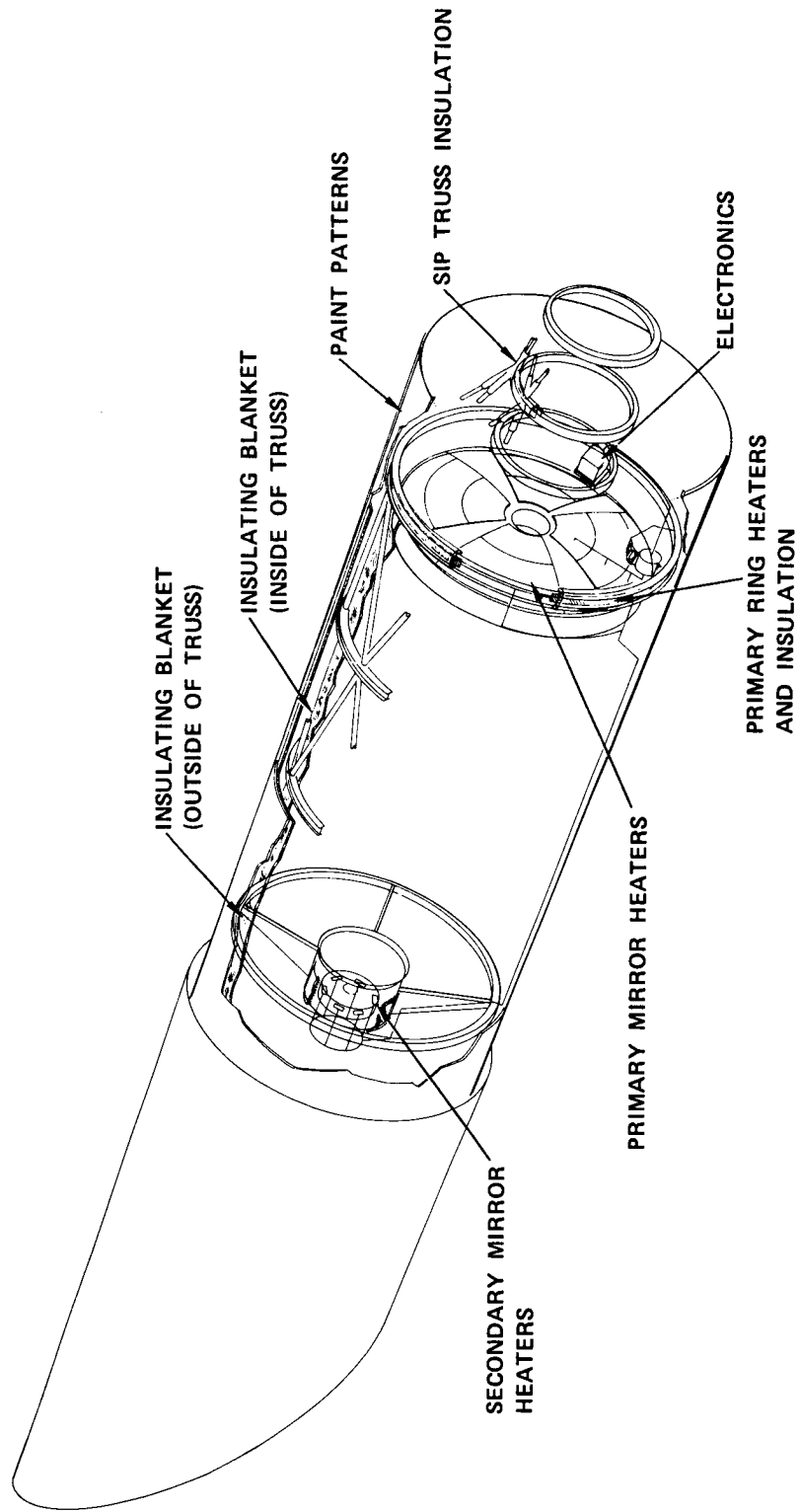


Fig. C.1-7 — OTA thermal control system

### C.1.c(3) Interface Definition

#### OTA-SIP Interface

This interface refers to the thermal relationship and control of individual scientific instruments at their attachment points to the instrument truss of the OTA, as well as the means needed to control radiative transfer from the instruments to the truss.

#### OTA-SSM Interface

The thermal design of this interface is conditioned by the requirement for shirtsleeve manned maintenance of the SSM and by the rejection of all waste heat from the OTA/SI compartment, which sets the sink temperature of the SSM at approximately 15°C (MSFC data), as seen by those OTA components that interface directly with the SSM. The OTA interface is placed at the main ring/pressure bulkhead, the instrument truss, with design control over the placement of paint patterns, heat loads, and insulation on the first 1.5 meters (59 inches) of the SSM behind the ring/pressure bulkhead.

### C.1.c(4) Performance

#### Life

The TCS is designed for a useful operational life of 10 years with manned orbital maintenance.

#### Active TCS

##### Primary Mirror

The primary mirror requires active thermal control and employs multizone heaters, temperature sensors, and insulation blankets to achieve the temperature requirements stated under optical systems interface, thermal.

##### Secondary Mirror

A similar thermal interface is designed for the secondary mirror.

##### Primary Ring

#### Power

The power requirement for the TCS is 500-watt capacity.

Primary mirror thermal subsystem	400 watts peak, 306 watts sustaining
Secondary mirror thermal subsystem	52 watts peak, 40 watts sustaining

#### Passive TCS

The passive TCS is capable of reducing overall thermal control power for the active system and attenuating thermal gradients resulting from orbital orientation variations and normal orbital thermal variations. In no case does the passive TCS compromise the system optical characteristics to an extent not recoverable.

### C.1.c(5) Physical Characteristics

#### Active TCS

The active TCS consists of electrical heaters bonded to the rear surface of the primary mirror. Each heater is independently controlled to a preset temperature value. In a similar manner, the heaters will provide thermal control of the main ring. The secondary mirror assembly is also provided with a similar active TCS. Adequate temperature sensors are used to monitor the controlled surfaces and provide input signals to the electrical heater controllers.

#### Passive TCS

The passive TCS consists of insulation blankets inside the OTA meteoroid shield and outside the main light baffle shell arranged in such a manner that the metering structure is thermally isolated from external environments. Insulation blankets are located behind the primary mirror, surrounding the main ring and secondary mirror assembly to maximize thermal isolation. Other areas, as necessary, contain insulation to provide and/or improve passive control. In addition to insulation, thermal control coatings are used on the exterior surface of the OTA. The characteristics of this coating will be determined at a later date.

## Reliability

Active thermal control elements will be 100 percent redundant. The TCS is designed to allow for "on station" maintainability wherever necessary by means of removable and replaceable insulation sections.

### C.1.d Pointing Control System

#### C.1.d(1) Requirements

The OTA pointing control system (PCS) shown in Fig. C.1-8 maintains the required accuracy and stability of the telescope line of sight. The PCS generates "coarse" pointing error signals of adequate sensitivity to enable the SSM to point the telescope optical axis to a specific stellar target within  $\pm 4.85$  microradians ( $\pm 1$  arc-second) accuracy (with the PCS not the SSM). A 0.29-milliradian (1-arc-minute) range contains the designated guide star.

#### C.1.d(2) System Description

The orientation of the space vehicle is controlled by signals from two sets of sensors: (1) signals from the SSM star trackers, coupled with an inertial navigation gyro system to provide coarse control of the vehicle orientation, and (2) signals from guide star sensors in the focal plane of the telescope which provide tracking error control signals for fine guidance of the telescope line of sight during the observation period. Upon acquisition of two guide stars, OTA pointing control is transferred from external control to the PCS.

The PCS consists of three major subassemblies: (1) the image dissector sensor assembly, (2) the differential velocity aberration (DVA) drives, and (3) the tracking actuator assembly.

#### C.1.d(3) Image Dissector Sensor Assembly

The image dissector sensor assembly contains the active star tracking components from the reticle plate through to the attachment for the f/96 camera scientific instrument assembly. It houses three image dissector assemblies, each of which is independently positionable in azimuth about the optical axis. Two of the three sensors are required for telescope tracking in the full performance mode, while the third sensor is included for redundancy. Operation in conjunction with the SSM gyros permits use of one star tracker for operation in a degraded, partial failure mode. A design goal is to minimize the azimuthal size of the tracker so that maximum use is made of the available guide field area in the event of failure of the azimuthal drive for any one head. Each image dissector head is capable of being positioned over a radius range of 2.3 to 3.5 milliradians (8 to 12 arc-minutes).

Each image dissector head includes the optical means to conform to the guide field of the telescope optical system and has a coarse search range of at least 0.29 milliradian (1 arc-minute) in diameter. The fine tracking range is capable of providing error signals to a least element of 0.005 microradian (0.001 arc-second) as described in Section C.5 of this report. Means are provided so that properly designed sensing elements in the f/96 cameras can derive error signals which register the thermal drift and similar errors of the guide stars with respect to the OTA/SIP structures. The image dissector sensor system is capable of giving acceptable guidance error signals with G3 class stars of 13 visual magnitude or dimmer.

Signal processing and coordinate transformations will be performed in the OTA electronics package associated with the image dissector sensor assembly for the functional block diagram of the signal processing subsystem. When tracking errors are less than 4.9 microradians (1 arc-second), tracking mirror command signals will be supplied to the SSM for long term line of sight correction. When tracking errors are greater than 4.9 microradians (1 arc-second) and less than 300 microradians (1 arc-minute), resolved error signals from the image dissector will be fed directly to the SSM.

The image dissector assembly is removable as a complete module, including the tracking field reticle plate, after removal of the f/96 camera. The housing and attachment are designed for astronaut handling ease, are self-locating and piloting, and require no alignment operations for replacement other than a system boresight calibration routine which is remotely commanded from the ground. The focus sensor is integrally mounted to the

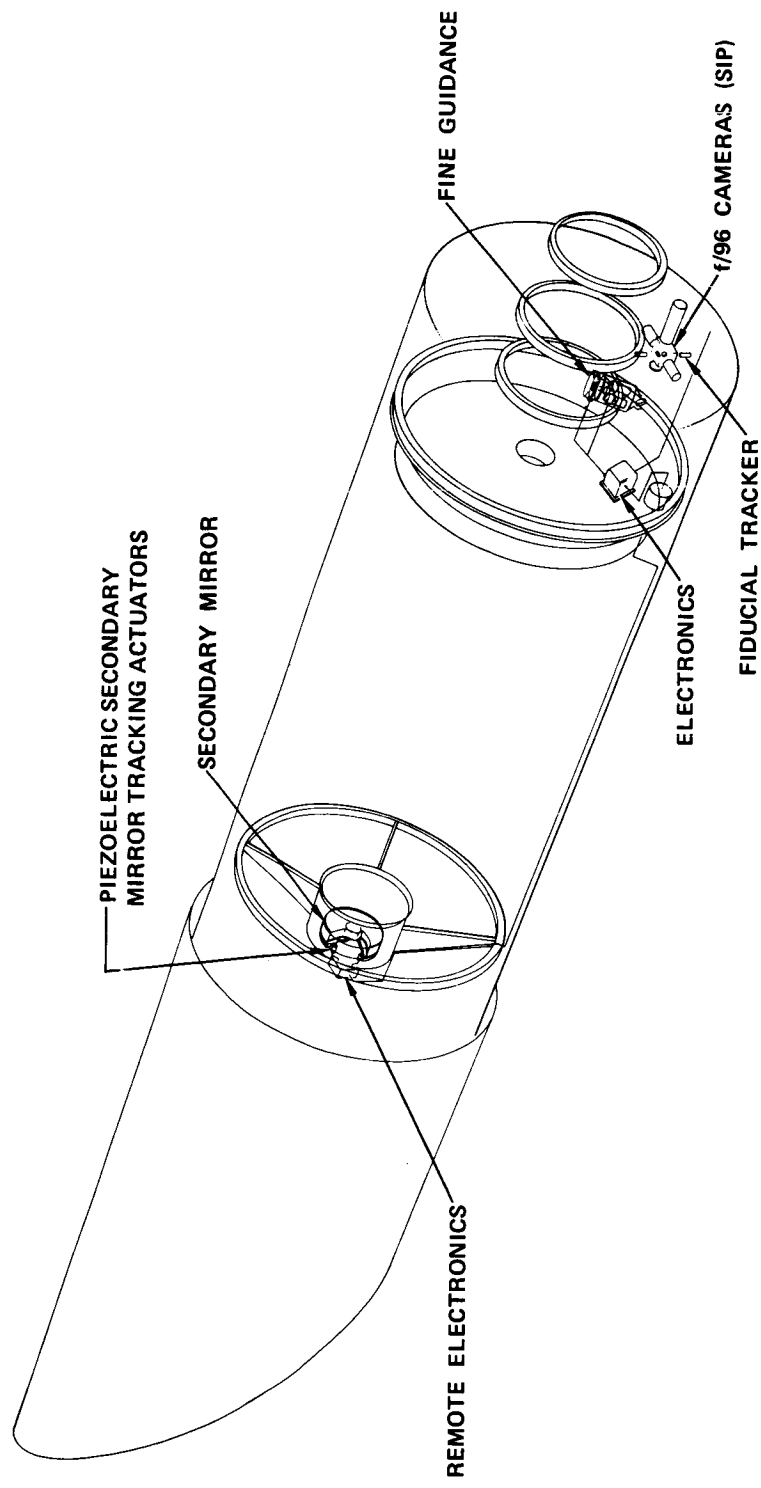


Fig. C.1-8 — OTA pointing control system

C.1-17

fine guidance housing so that its operation is coordinated with the focal surface established by the reticle plate. The image dissector assembly is attached to the DVA drive assembly, which in turn is attached to the folding optics assembly. The design is such that the integrated package of the folding optics, DVA drives, and image dissector sensor assembly move as a rigid body from a structural/thermal point of view, and thus must have high internal conductance and low emissivity surface with the minimum practical thermal expansion coefficient.

#### C.1.d(4) DVA Drives

A means is provided to allow the scientific data field to be shifted with respect to the guidance field visible to the image dissector sensor assembly, over a range of at least 9.7 microradians (2 arc-seconds). As a design goal, 48.5 microradians (10 arc-seconds) is desired to permit planetary imagery with filters in the f/96 cameras. The reproducibility of the setting of the DVA drive must be less than 0.005 microradian (0.001 arc-second). The least drive command quantum is 0.05 microradian (0.01 arc-second). The DVA is accomplished by means of a suitable glass plate matched to the telescope overall optical design and the image dissector sensor assembly optical design, which is mounted in a two-axis gimbal. The latter is driven by commands from the electronics package communicating with that of the image dissector sensor and the SSM.

The DVA drive assembly is removable as a complete module after removal of the image dissector sensor assembly and the f/96 camera assembly. It is attached to the folding optics assembly of the main optical system and will require no alignment operation for replacement, other than a system boresight calibration routine which is remotely commanded from the ground.

#### C.1.d(5) Tracking Actuator Assembly

The tracking actuator assembly is mounted between the secondary mirror alignment drives of the performance control system and the nine-point mount of the secondary mirror. Associated drive electronics are mounted nearby in the secondary mirror housing and are commanded by multiplexed signals from the image dissector sensor electronics (see Fig. C.1-2). The tracking drive is capable of moving the secondary mirror over an angular range of at least  $\pm 12.5$  microradians ( $\pm 2.5$  arc-seconds) with a least command resolution of 0.0024 microradian (0.0005 arc-second). The tracking drive is compensated in such a way as to minimize reaction forces transmitted to the telescope structure so that the net line of sight disturbance from this cause is less than 0.005 microradian (0.001 arc-second). Because replacement of the drive assembly requires de-orbiting of the telescope with the present system concept, its design must incorporate high reliability techniques and redundancy in circuits and commands so that a high system reliability is achieved for a 10-year operating period. Body pointing of the telescope by means of the SSM guidance system can be used as a degraded operating mode in case of failure of the tracking actuator assembly.

The drive is accomplished by means of piezoelectric actuators, as shown in Section C.5. In parallel with the tracking mirror drive, a reaction mass is driven by actuators in such a manner as to cancel the reaction forces produced by the tracking mirror drive to within 10 percent. Force transducers are included which measure the magnitude of the reaction forces transmitted to the telescope structure. Command signals are derived which cause the reaction mass to null out the reaction forces.

#### C.1.d(6) Interface Definition

The pointing control interface between the LST and SSM is a complex of electrical signals and dynamic feedback loops. The SSM is responsible for maneuvering the spacecraft until the guide stars for a desired target appear in the  $\pm 0.29$ -milliradian ( $\pm 1$  arc-minute) field of view of a set of coarse guide star trackers in the OTA. Error signals generated by the trackers are sent to the SSM, where torques are generated to reduce the error signal null. This will place the guide stars within the  $\pm 4.85$ -microradian ( $\pm 1$ -arc-second) field of view of a set of fine guide star trackers. The error signals from these trackers are converted into tip and tilt commands for the LST secondary mirror, to stabilize the image during data taking.

Movements of the secondary mirror from its null position are translated into error signals and sent to the SSM, where they are converted into torques to move the spacecraft in such a way that the mirror returns to its null position. Stabilization of the spacecraft in roll during data taking will be accomplished by the SSM, by using a signal from the fine star tracker to update rate gyros.

#### C.1.d(7) Performance

##### Accuracy

For photometric and spectroscopic measurements, the PCS will point the OTA axis to an orientation in space relative to the guide star locations to within an accuracy of 0.48 microradian (0.1 arc-second) rms.

##### Stability

During the observation period, the PCS will keep the OTA fixed with respect to data star locations within a variation of 0.024 microradian (0.005 arc-second) rms.

##### Power

The peak power requirements of the PCS are as follows:

Image dissectors	50 watts (2 units)
DVA drive	5 watts
Tracking actuators	30 watts

##### Initial Operation

The PCS operates in accordance with the design requirement and meets all performance requirements within 200 hours after launch. Except for thermal stabilization conditions, the PCS is capable of functional checkout immediately upon achieving orbit.

##### Reacquisition

During those observations where earth occultation occurs, reacquisition of the data image takes place within 60 seconds as limited by the telescope system, after both target stars are located in the coarse guidance sensor field of view by the SSM guidance system.

##### Malfunction Detection

The PCS incorporates in its design a calibration and monitoring subsystem to allow in-orbit adjustments of the system.

#### C.1.d(8) Physical Characteristics

The PCS has the following physical characteristics.

##### Weight

The PCS does not exceed 146 kilograms (322 pounds).

##### Maintainability

Module realignment under orbital conditions is consistent with initial telescope alignment. A test procedure is provided to ensure proper operation of the system to meet this specification after maintenance.

Manned maintenance is used to enhance the reliability and versatility of the LST. The term maintenance in this context means replacement of individual modules and replacement of instrumentation, as well as preventive care.

## C.1.e Performance Control System

### C.1.e(1) System Description

The OTA performance control system (Fig. C.1-9) consists of six subsystems: an angle sensor, a decenter sensor, a focus sensor, a figure sensor, primary mirror force actuators, and secondary mirror alignment actuators. Secondary mirror tracking actuators are included in the pointing control system.

Angle and decenter sensors are used to restore on-orbit system alignment to that which existed during the secondary and primary mirror manufacture.

The angle sensor determines the amount of angular misalignment present between the primary and secondary mirrors. The decenter sensor determines the amount of translation misalignment present between the primary and secondary mirrors. The focus sensor, mounted integrally with the image dissector sensor housing, determines how much defocus is present between the primary and secondary mirrors. Each of these three subsystems provides information to the secondary mirror alignment actuators. The actuators move the secondary mirror so that a null (zero error) condition is achieved by each of the above noted subsystems. A capability is provided to command alignment off of null if data from the figure sensor indicates that such a state is required.

The figure sensor monitors the wavefront errors within the telescope and provides information so that the primary mirror force actuators may make the necessary figure corrections. It is expected that the figure sensor information will be sent to the ground for data reduction and analysis. If corrections to the primary mirror force actuator are deemed necessary, the instructions will be sent to the OTA from the ground. All sensors are 100 percent redundant. The secondary mirror alignment actuators contain no single point failures for any single degree of freedom out of the required five. Fewer degrees of operating freedom can be used for operation in degraded modes.

### C.1.e(2) Interface Definition

The angle sensor and decenter sensor each consist of a sensor mounted directly to the primary mirror and targets mounted directly to the secondary mirror in its centrally obscured zone. The focus sensor, integrally mounted to the image dissector sensor housing, and the figure sensor both have access to the telescope optical path by means of the folding optics. The focus sensor targets (one roof pentaprism and one pentaprism) are mounted to the secondary mirror spider such that the focus sensor beam is properly transmitted through the telescope assembly. The figure sensor has no associated targets, since a starlight source is used to activate the sensor.

The secondary mirror alignment actuators are located behind the secondary mirror and are capable of moving the secondary mirror in at least 5 degrees of freedom (rotation z, rotation y, translation x, translation y, and translation z) without any single point failures.

The primary mirror force actuators are located between the primary mirror and the pressure bulkhead such that they will be capable of deflecting the primary mirror in a manner prescribed by the figure sensor and for gravity compensation during system ground testing.

The physical configuration for each of the subsystems will be identical to the configuration shown in Section C.6.

#### Power

Not more than 150 watts of conditioned power is supplied to the performance control system at any one time.

#### Operation

The performance control system operates only during nonviewing times of the telescope. It is anticipated that the angle sensor, decenter sensor, focus sensor, and the secondary mirror alignment actuators will be activated once per orbit, at an optimum time to minimize the frequency of correction. If the OTA is near thermal equilibrium, the

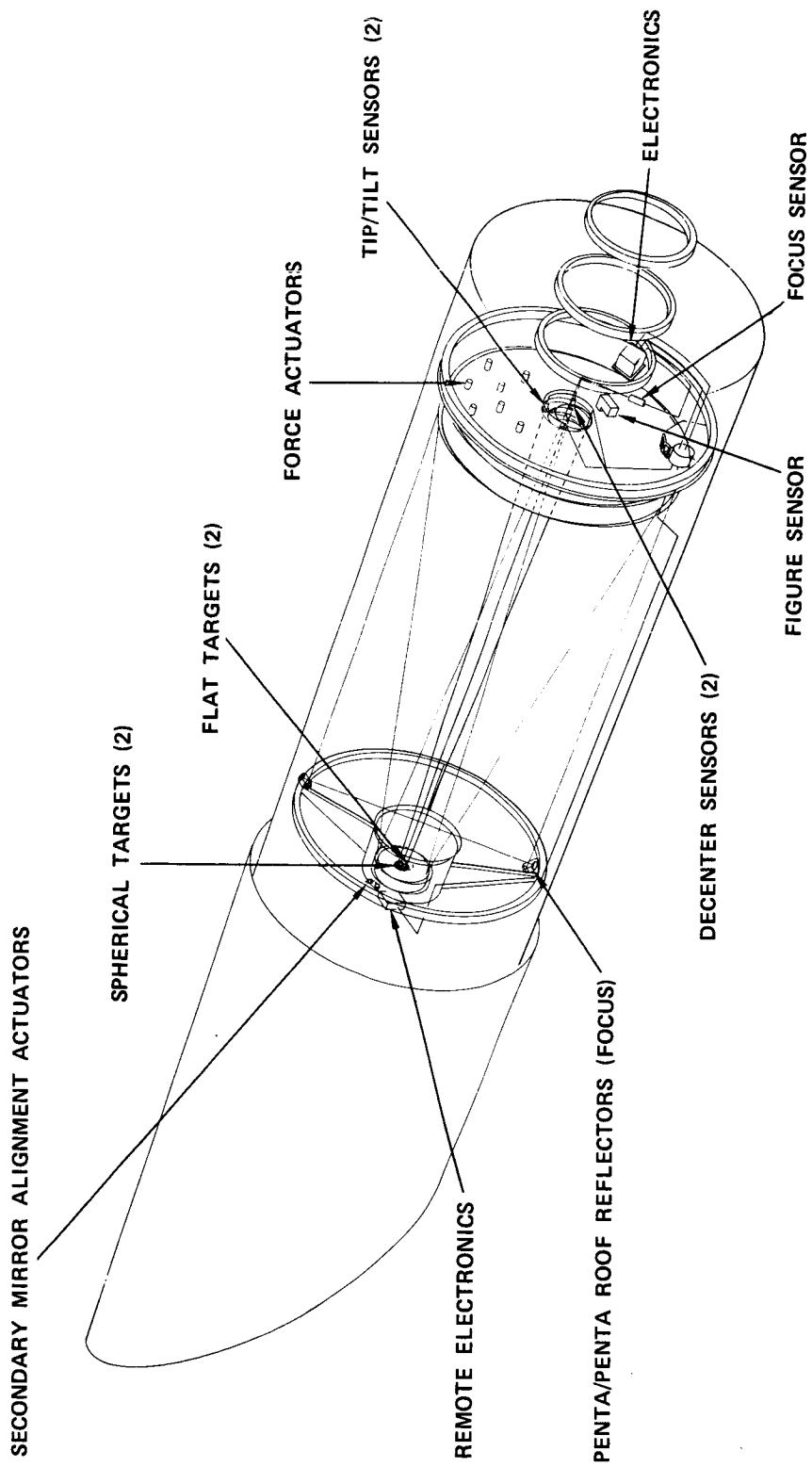


Fig. C.1-9 — Performance control system



frequency of correction may be less than once per orbit. During this time, these subsystems determine the amount of misalignment and send correction signals to the secondary mirror alignment actuators, which will correct the misalignment. It is expected that the figure sensor will be operated approximately monthly, or as required by use during nonviewing times of the telescope and the data obtained will be sent to the ground. Use of the figure sensor requires pointing the telescope to a star which is 6th visual magnitude or brighter.

#### Service Mounting

The mounting of each subsystem is such that no "on-vehicle" alignment is required upon replacement of any part of the subsystem.

#### C.1.e(3) Performance

The performance control system is capable of meeting the following performance criteria when measured at a wavelength of 633 nanometers.

#### Range

The performance control system is capable of operating over the following ranges:

Rotational range	0.7 milliradian
Translational range	1.25 millimeters
Focus range	±200 micrometers
Wavefront error	0.2 $\lambda$ rms

#### Accuracy

It is expected that the pointing control system will maintain the centering of the primary mirror to within 18 micrometers rms, the focus of the telescope at the determined best focus to within about 70 micrometers rms, and the tip of the secondary mirror to about 5 microradians. In addition, the overall OTA wavefront error can be monitored to better than 0.02  $\lambda$  rms.

#### Life and Duty Cycle

The performance control system is designed for a useful operational life of 10 years. The angle sensor, decenter sensor, focus sensor, and secondary mirror alignment actuators will be switched on before each use for 6 minutes to establish equilibrium. The use rate will be once every 90 minutes over the 10-year span. The primary mirror force actuators will be actuated once or twice upon reaching orbit conditions and a maximum of once a month thereafter during the life of the equipment.

#### Malfunction Detection

The performance control system has malfunction detection built in such that if any one of the subsystems develops a failure, a separate failure signal is generated and the failed subsystem reverts to a "no error" signal condition.

#### C.1.e(4) Physical Characteristics

#### Weight

Each major component of each subsystem does not exceed the weight noted in the following table:

Angle sensor	8.8 kilograms (19.5 pounds)
Angle target	0.2 kilogram (0.4 pound)
Decenter sensor	16.1 kilograms (35.5 pounds)
Decenter target	0.2 kilogram (0.4 pound)
Focus sensor	12.7 kilograms (28 pounds)
Focus target	0.2 kilogram (0.4 pound)

Figure sensor	17.4 kilograms (38.3 pounds)
Secondary mirror actuators (6)	1.7 kilograms (3.8 pounds)
Primary mirror force transducers (24)	8.2 kilograms (18 pounds)
Remote electronics (entire PCS)	45.0 kilograms (100 pounds)

The total performance control system weight will not exceed 138 kilograms (304 pounds) (no contingency).

### Size

The physical size of each subsystem is as shown in Figs. C.6-10, C.6-25, and C.6-28.

## C.1.f Telescope Protection/Diagnostic System

### C.1.f(1) System Description

The OTA protective/diagnostic system (Fig. C.1-10) consists of four major subsystems.

#### Extendible Sun Shield

The sun shield is designed to keep direct sunlight from entering the primary telescope tube. The sun shield is designed to reflect earth light when the angle of incidence is in the  $-z$ ,  $-x$  quadrant toward the origin.

#### Aperture Door Assembly

The aperture door assembly is designed to protect the optical surfaces from contamination entering the input end of the OTA during final OTA fabrication, shipping, launch, and manned orbital maintenance.

#### Pressure Bulkhead Door Assembly

The pressure bulkhead door is designed to protect the optical surfaces from contamination entering the SIP end of the OTA during final OTA fabrication, shipping, launch, and manned orbital maintenance.

#### Diagnostic Subsystem

The diagnostic subsystem consists of strain, vibration, temperature, and ultraviolet absorption sensors. It includes electronic sensors to monitor housekeeping functions and system status.

### C.1.f(2) Interface Definition

#### Extendible Sun Shield

The mechanical interface is at guide rails on the meteoroid shield. The rails are secured to the meteoroid shield, and the rolling elements to the sun shield. Limit switches provide electrical indication of status. The sun shield is actuated by drives mounted on the meteoroid shield (to be reviewed in phase B).

#### Aperture Door Assembly

The mechanical interfaces of the door sections (eight) are through hinges on the meteoroid shield and seals on the secondary mirror ring and baffle assembly. Limit switches provide electrical indication of status.

#### Pressure Bulkhead Door

The mechanical interface of the door will be cam, cam guide, and jackscrew assembly mounted to the pressure bulkhead. Limit switches provide electrical indication of status.

#### Diagnostic System

Diagnostic sensors are located throughout the OTA to monitor housekeeping activities. The electrical interface is accomplished through a series of cables to appropriate electronic subassemblies in the SSM.

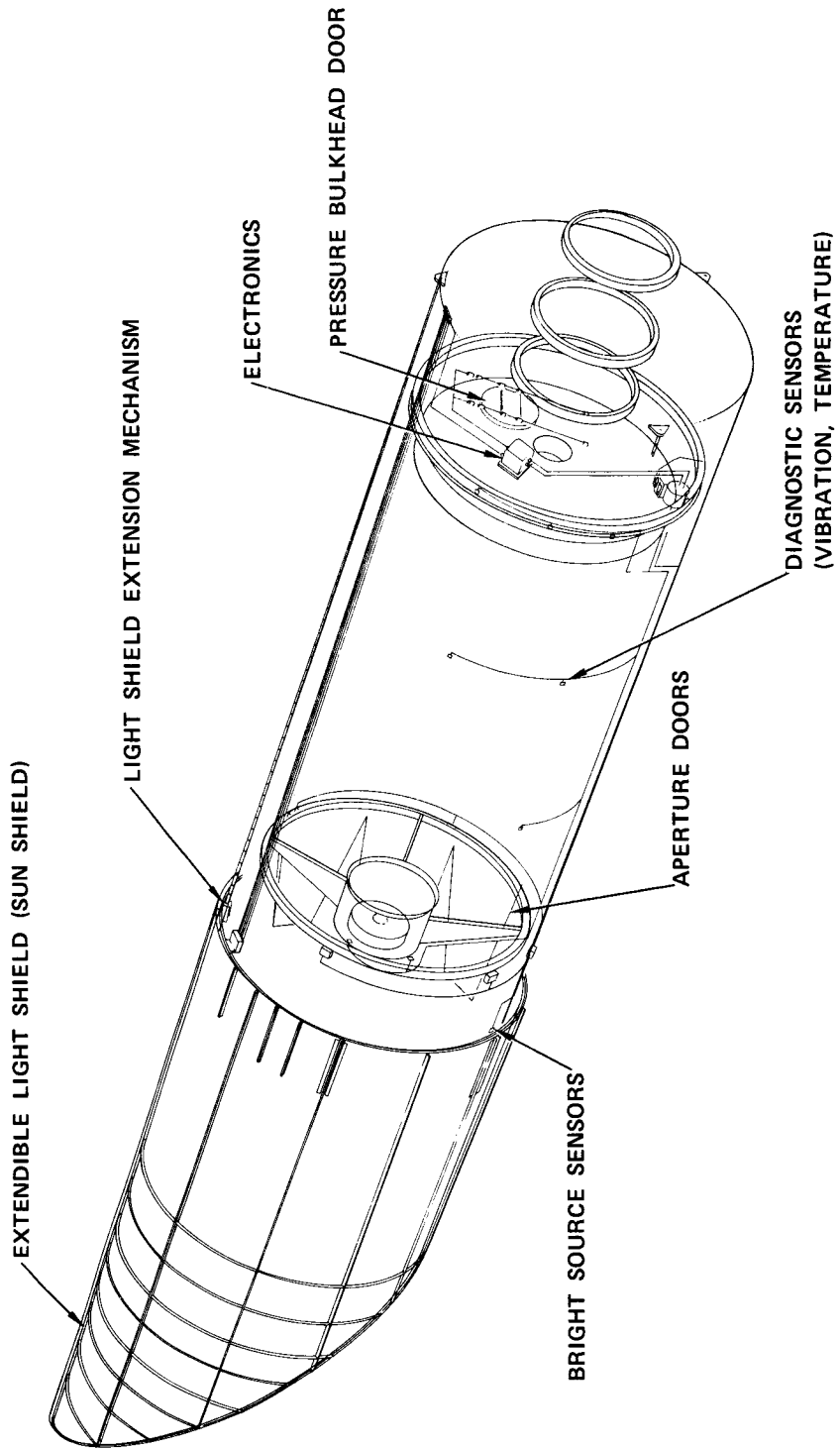


Fig. C.1-10 — Telescope protection/diagnostic system

### C.1.f(3) Performance

#### Failure Modes

The system is designed so as to eliminate single point failure modes. All critical components that could cause total failure will have backup modes if feasible. The pressure bulkhead door assembly and the aperture door assembly are designed such that if a failure occurs, the doors will remain in an open condition.

#### Extendible Sun Shield

Once in orbit, the shield will be activated by ground control and will be capable of extending 6.52 meters (25.7 inches) in such a time as to be consistent with LST stabilization requirements. The telescope is capable of operation with the shield in a fully extended mode (full specification compliance) or retracted mode (degraded performance). Limit switches are provided to determine status of extension.

#### Aperture Door Assembly

The aperture door assembly in the closed (launch) configuration assumes the shape of an axially segmented frustum of a cone. Once in orbit, the doors, which are hinged to the meteoroid shield, will be activated by ground control at a time consistent with LST stabilization and astronaut maintenance requirements. The door assembly can be closed automatically to avoid direct solar radiation. A bright source sensor located in the meteoroid shield monitors radiation level and initiates aperture door closure at a predetermined level.

#### Pressure Bulkhead Door

The pressure bulkhead door and its drive mechanism are attached to the pressure bulkhead. The door is open during the launch phase. The door opening mechanism is deactivated during manned orbital maintenance to avoid accidental depressurization of the SIP compartment.

### C.1.f(4) Physical Characteristics

#### Extendible Sun Shield

The sun shield is as shown in Fig. C.1-11.

#### Aperture Door Assembly

The aperture door has eight sections operated by jackscrews and motors as shown in Fig. C.1-12.

#### Pressure Bulkhead Assembly

The pressure bulkhead assembly is as shown in Fig. C.1-13.

### C.1.f(5) Maintainability

The aperture door and pressure bulkhead assemblies will be closed prior to maintenance.

### C.1.g Data Management System

#### C.1.g(1) System Description

The OTA data management system (Fig. C.1-14) consists of the data acquisition units and the command decoders, both of which are considered a part of the SSM. It is anticipated that both of these units will be supplied by the SSM contractor for inclusion in the OTA remote electronics package.

#### Power

The power required by the command decoder unit that is supplied by the SSM contractor will not exceed TBD watts of less than 50 vdc per unit. The power required by the data acquisition unit that is supplied by the SSM contractor will not exceed TBD watts of less than 50 vdc per unit.

#### Mounting

Each subsystem will be mounted so that no "on-vehicle" adjustments are required upon replacement of any part of either subsystem.

#### C.1.g(2) Performance

The command decoder is capable of handling the OTA command requirements noted in Table C.1-1. The data acquisition unit is capable of handling the OTA data noted in Table C.1-2.

### Life

The data handling system is designed for a useful operational life of 10 years.

### Malfunction Detection

The data management system has malfunction detection built in in such a way that if either of the subsystems develops a failure, a separate failure signal will be generated and the failed subsystem will revert to a "failsafe" condition.

#### C.1.g(3) Physical Characteristics

### Weight

The maximum weight of the command decoder subsystem is 0.9 kilogram (2 pounds). The maximum weight of the data acquisition unit is 2.2 kilograms (4.7 pounds).

### Size

The command decoder subsystem has a volume of  $5.0 \times 10^{-3}$  cubic meter (304 cubic inches). The data acquisition unit has a volume of  $1.9 \times 10^{-3}$  cubic meter (116 cubic inches).

### C.1.h Power Distribution System

#### C.1.h(1) System Description

The OTA power distribution system (Fig. C.1-15) consists of two electrical distribution units (EDU) which supply 16 power conditioning and control subsystems for the OTA and the power and control signal cables required to distribute power and command signals. One EDU is used continuously, while the second is available as a backup system. The EDU's control and supply the unconditioned SSM power to the 16 power conditioning and control subsystems. The 16 power conditioning and control subsystems provide power switching for individual loads, EMI filtering, voltage monitoring, overload monitoring, fault isolation, and command override.

#### C.1.h(2) Interface Definition

This system is located within the remote electronics package.

#### C.1.h(3) Performance

The EDU is capable of controlling and distributing a maximum of 1,084 watts of nominal 28 vdc power. No more than 2.0 watts of power is used to perform the control and distribution function noted above. The 16 power conditioning and control subsystems are capable of supplying the peak powers noted in Table C.1-3. Regulation, ripple, power consumption, turn on time, turn off time, etc., for the 16 power conditioning and control subsystems will be determined in later studies.

### Life and Duty Cycle

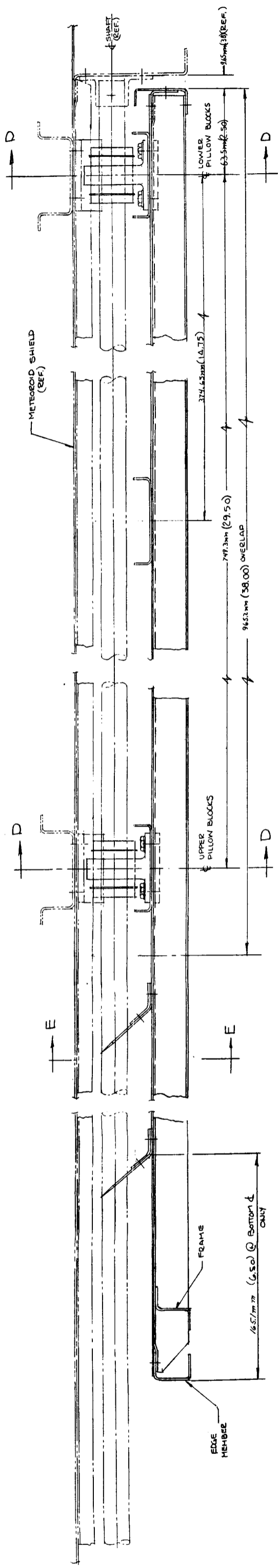
The power distribution system is designed for a useful operational life of 10 years. The EDU's are expected to be operated once each time the OTA is operated, whereas the 16 power conditioning and control subsystems will operate at least once each orbit during observations.

### Malfunction Detection

The performance control system malfunction detection is designed so that if any one of the subsystems develops a failure, a separate failure signal is generated and the failed subsystem reverts to a fail-safe condition.

#### C.1.h(4) Physical Characteristics

The EDU maximum weight is 31.8 kilograms (70.0 pounds), and the maximum volume is to be determined later. The 16 power conditioning and control subsystems do not exceed the size and weight noted in Table C.1-4. The maximum weight of the cabling is to be determined later.



C-C  
FULL SIZE  
(ROTATED 30°)

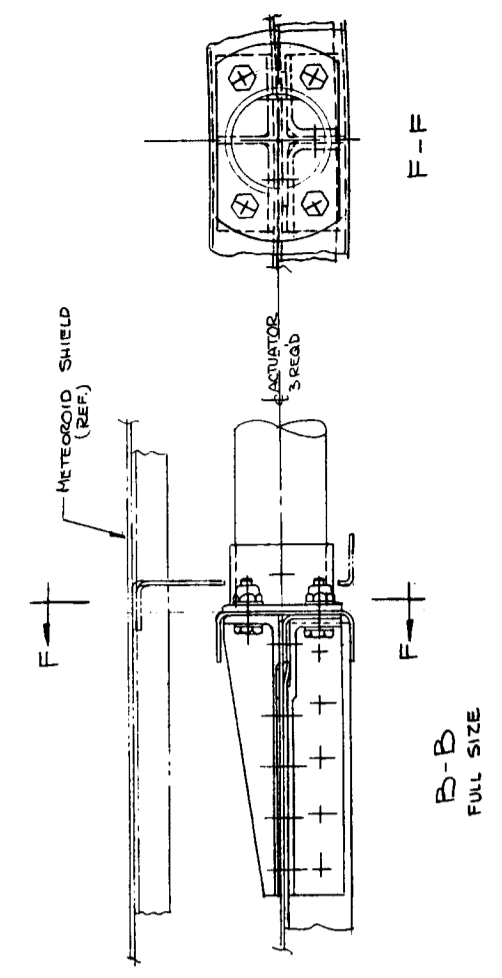
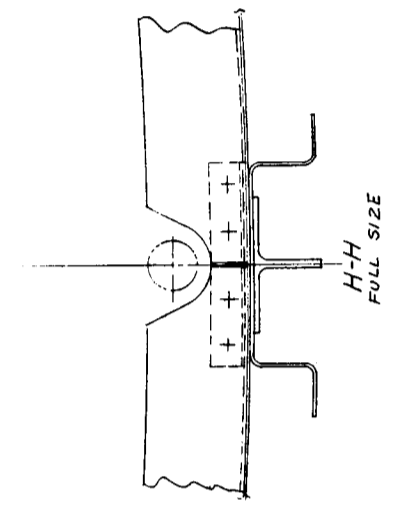
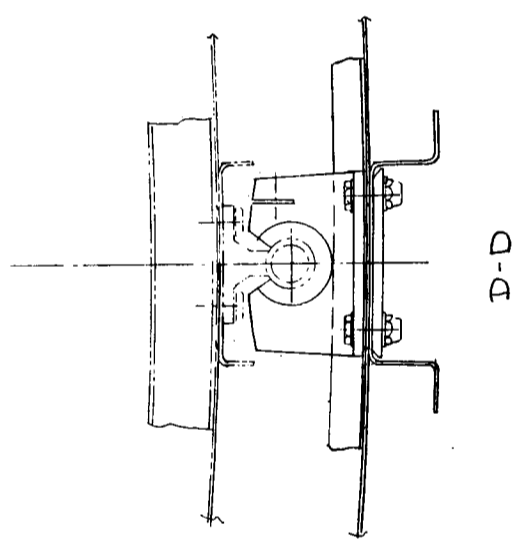
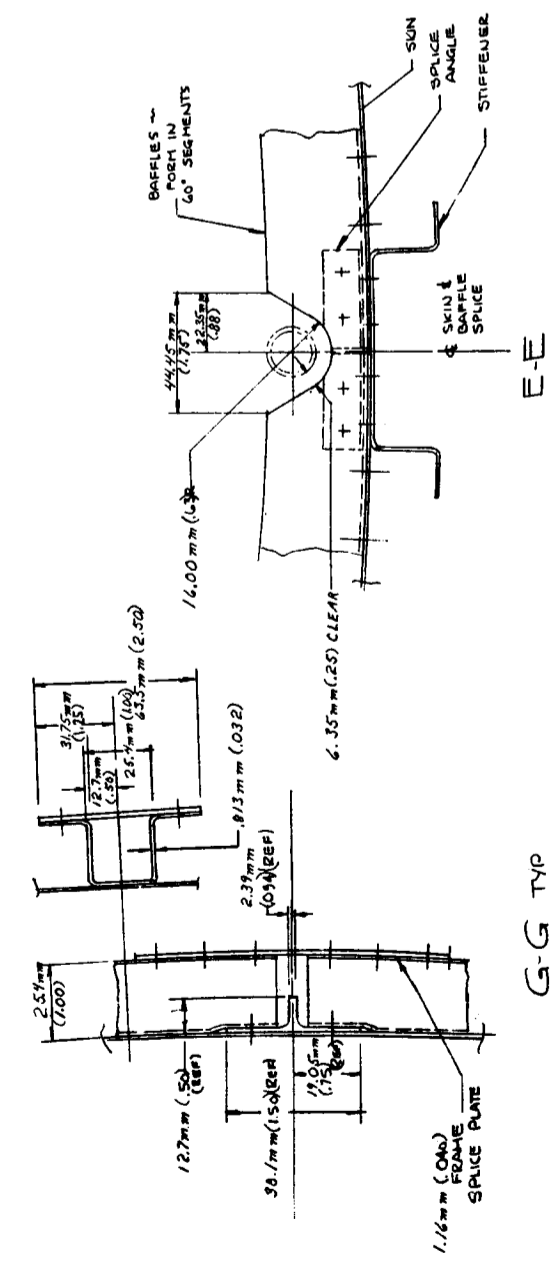


Fig. C.1-11 -- Sun shield assembly (dwg. no. SK-LST-018)

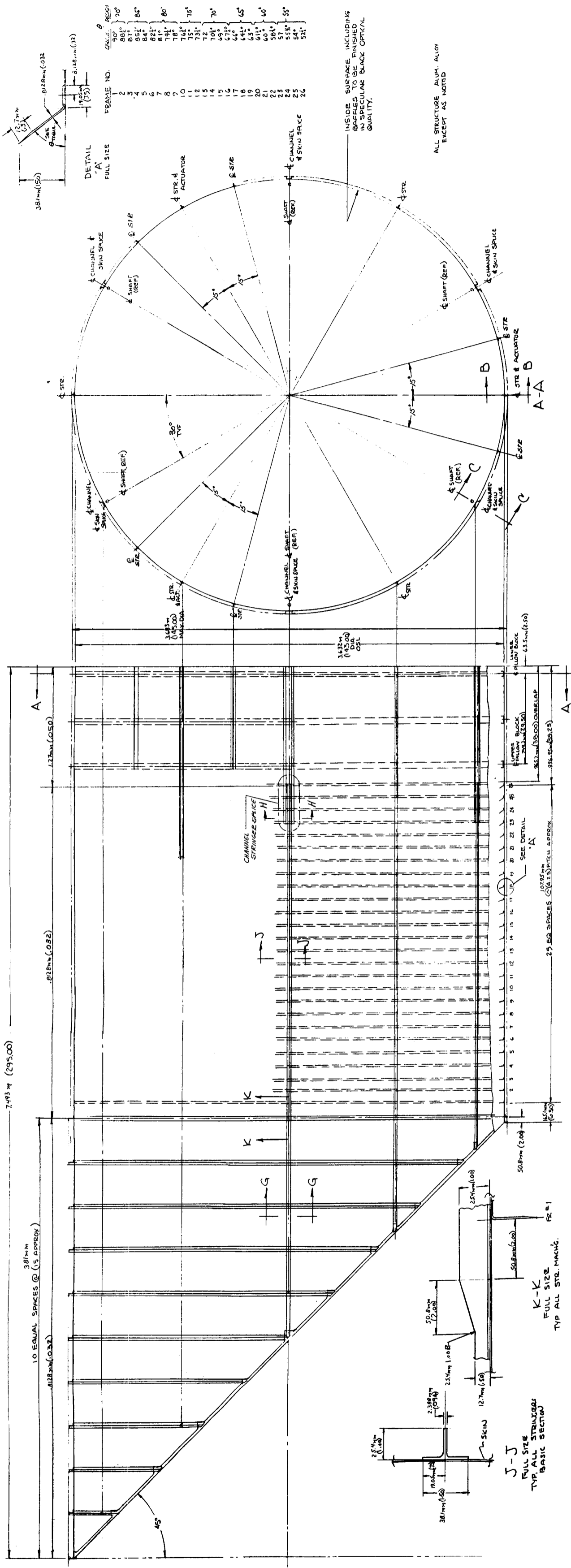


Fig. C.1-11 — Sun shield assembly (dwg. no. SK-LST-018) (Cont.)





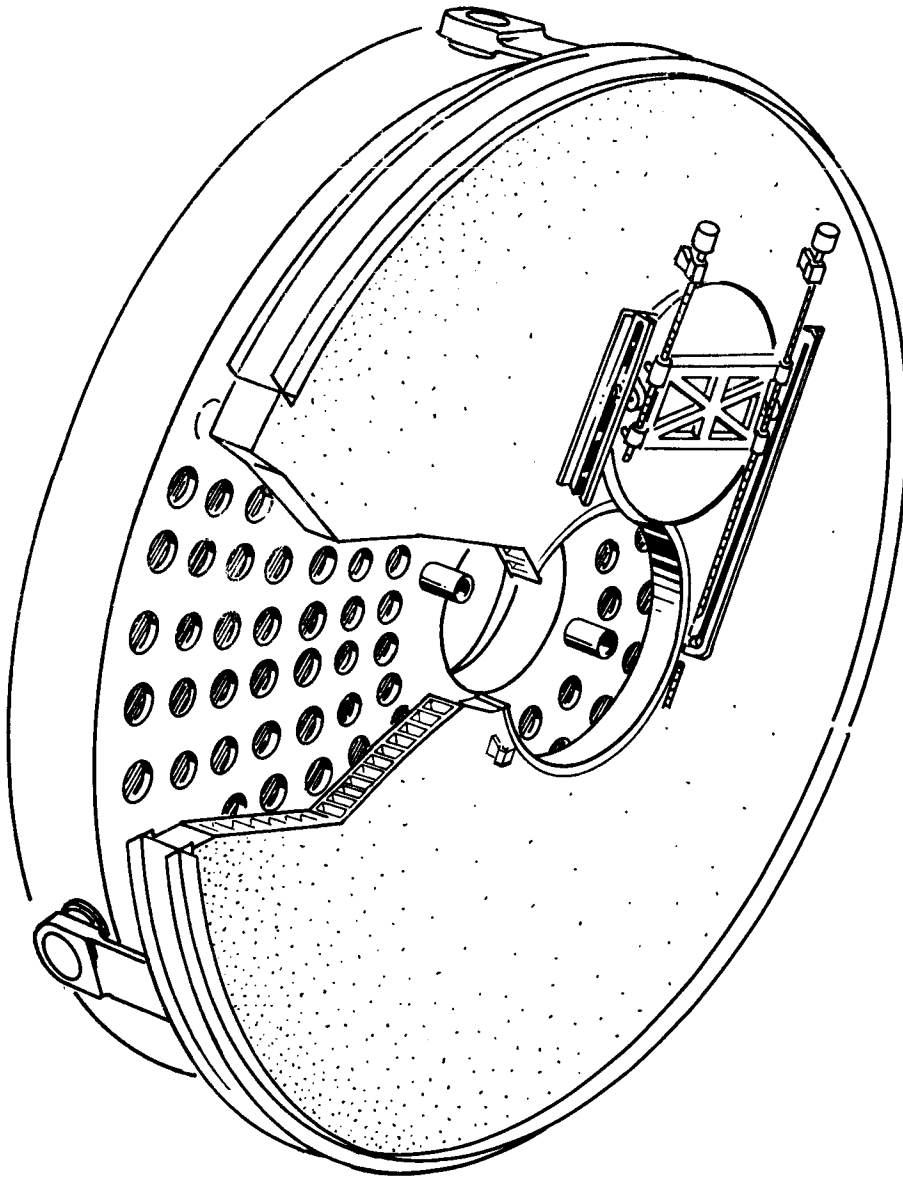
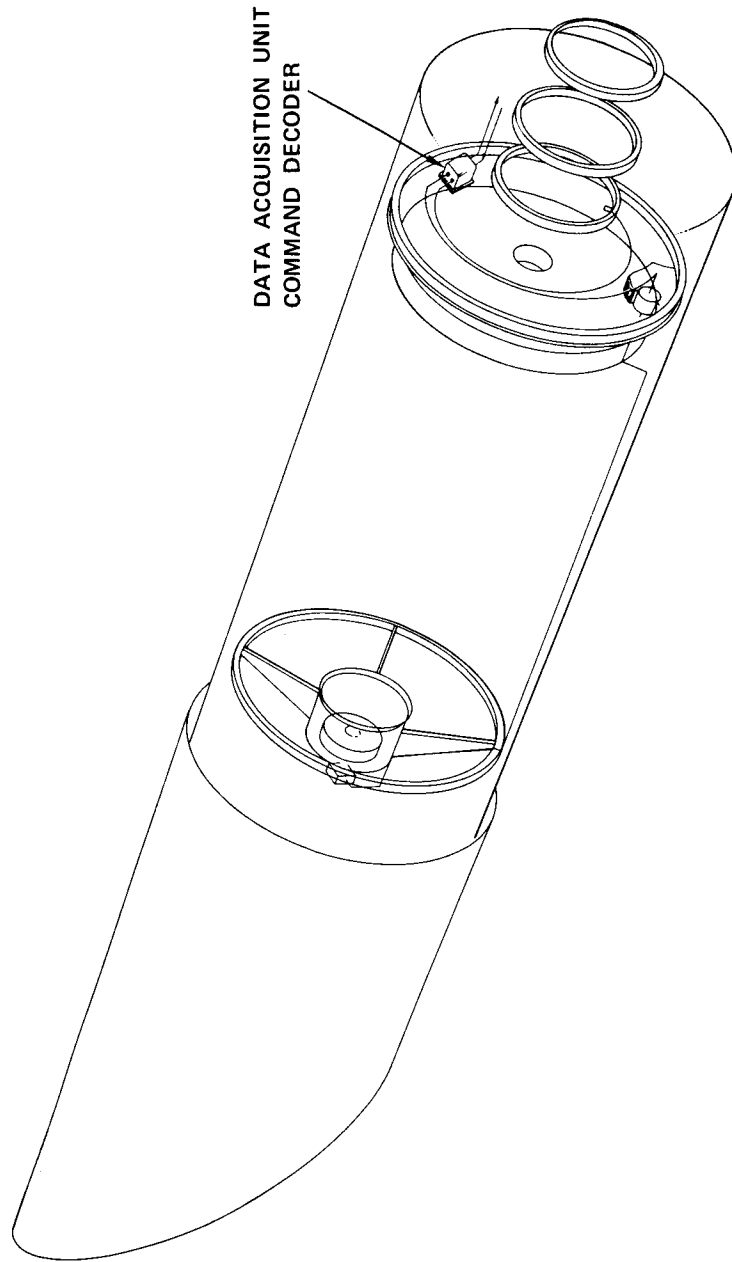


Fig. C.1-13 — Pressure bulkhead assembly



**Fig. C.1-14 — Data management system**

Table C.1-1 – OTA Command Requirements

	Commands
Power conditioning and control, off-on (16 units)	32
Secondary mirror alignment actuators, off-on (6 units)	12
Alignment matrix switch control	8
Figure sensor	2
Sun shield manual bypass controls	6
Aperture door manual bypass controls	4
Thermal electronics, control (27 units)	54
Primary mirror force actuators, control (25 units)	50
Guide sensor angles (6 units)	6
Guide sensor correction inputs (3 units)	14
Diagnostic sensor sequencer	12
	<hr/>
Total	200

Table C.1-2 – OTA Diagnostic Data Summary

Subsystem	Channels	Resolution, bits
Performance control (focus, angle, and decenter sensors)	82	6
	8	1
	6	10
Performance control (redundant unit) (focus, angle, and decenter sensors)	70	6
	8	1
Figure sensor	27	6
	1 (900 bytes)	8
Primary mirror force transducers	56	6
Thermal electronics	60	6
	27	1
Sun shield	6	6
	6	1
	1	8
Aperture doors	6	6
	4	1
Pointing and control	186	6
	3	18
	3	16
Diagnostic sensors	228	8
	18	6
<b>Total</b>	<b>806</b>	

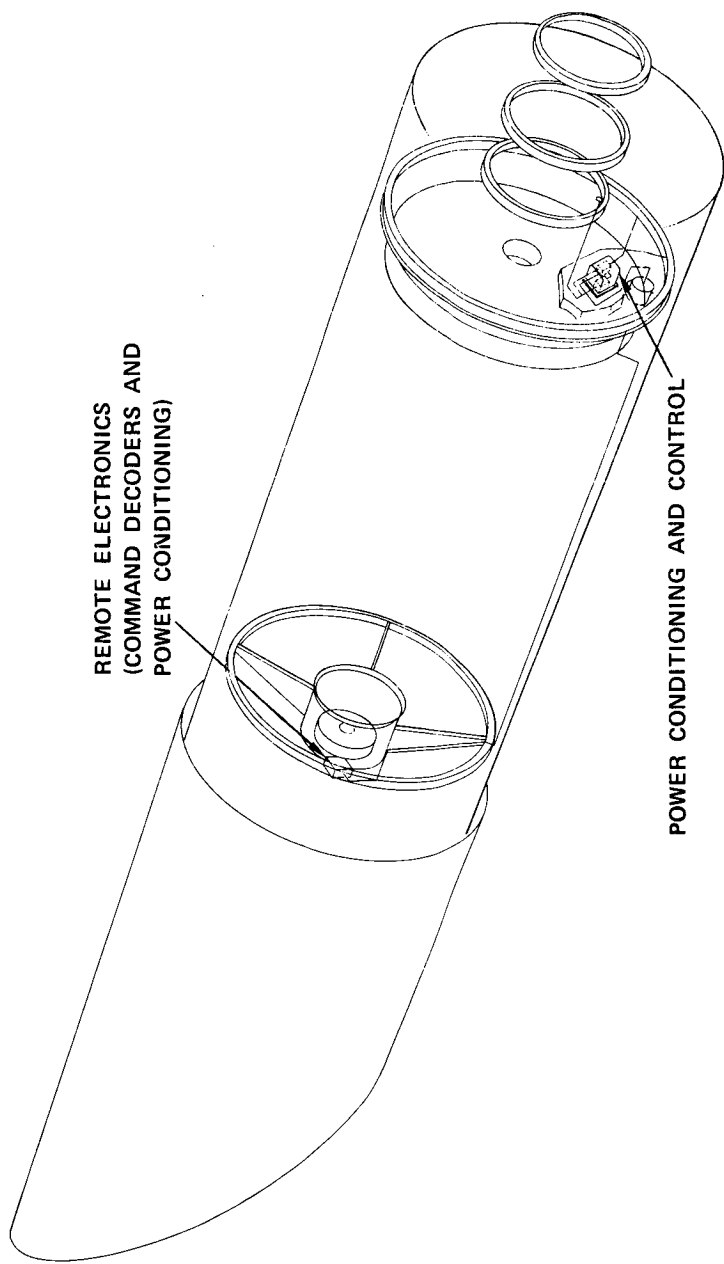


Fig. C.1-15 — Power distribution system

Table C.1-3 – Power Conditioning and Control Subsystem  
Power Handling Requirements

Power Conditioner (Subsystem)	Peak Power, watts
Decenter sensor	21
Angle sensor	21
Focus sensor	40
Alignment matrix switch	15
Secondary mirror alignment actuators	60
Figure sensor	40
Sun shield actuator	50
Aperture door actuators	30
Primary mirror force actuators (25)	100
Thermal electronics (27)	452
DVA drive (4)	10
Image dissector and electronics (2)	100
Tracking actuators (3)	30
Diagnostic sensors, temperature (160)	80
Diagnostic sensors, vibrations (18)	10
Diagnostic sensors, strain (50)	25

Table C.1-4—Power Conditioning and Control Subsystem  
Physical Characteristics

Subsystem	Weight		Volume	
	Kilograms	Pounds	$\times 10^{-4}$ Cubic Meters	Cubic Inches
Decenter sensor	0.45	1.0	2.46	15
Angle sensor	0.45	1.0	2.46	15
Focus sensor	0.91	2.0	5.74	35
Alignment matrix switch	0.45	1.0	2.46	15
Secondary mirror alignment actuators	1.36	3.0	7.37	45
Figure sensor	0.91	2.0	5.74	35
Sun shield actuator	2.27	5.0	22.94	140
Aperture door actuator	1.36	3.0	18.02	110
Primary mirror force actuator	4.54	10.0	32.77	200
Thermal electronics	4.54	10.0	32.77	200
DVA drive	0.45	1.0	3.28	20
Image dissector electronics	1.36	3.0	8.19	50
Tracking actuators	0.91	2.0	6.55	40
Diagnostic sensor, strain (50)	0.91	2.0	6.55	40
Diagnostic sensor, temperature (160)	1.36	3.0	13.11	80
Diagnostic sensor, vibration (18)	0.45	1.0	3.28	20

## C.2 STRUCTURAL DESIGN AND ANALYSIS

The structural design and analysis effort was directed toward the development and establishment of a feasible concept for future study. This concept includes (1) the metering truss, (2) the scientific instrument compartment truss, (3) the meteoroid shell, (4) the baffles, (5) the primary and secondary mirrors, together with their mounts, (6) the aperture door assembly, (7) the sun shield, and (8) the pressure bulkhead and its door. The following sections discuss the alternate candidate concepts considered and the evaluation procedure utilized to arrive at the recommended. Next treated are the structural system analysis and its results, e.g., the OTA/SSM dynamic response and the OTA thermal-structural response. Following this is a detailed treatment of the major structural subsystems (e.g., the metering truss, the SIP structure, and the mirror/mount design).

The summary of the structural design and analysis effort includes a description of the recommended design and the significant conclusions reached.

### C.2.a Review of Concepts Traded Off

#### C.2.a(1) Alternative Structural Systems

In the concept definition and evaluation phase of the LST design, system optimization tradeoffs of various structural concepts of a Ritchey-Chretien telescope have been conducted. These concepts are compatible with the Viking launch space envelope shown in Fig. C.2-7 and the Shuttle Payload Envelope. It should be noted that the OTA envelope at the light shield location has a near elliptical cross section with a mirror diameter of 3.5 meters (145 inches). This dimension was used as the maximum static envelope for the OTA configuration.

Fig. C.1-5 shows the SIP and OTA concept layout and identifies the major subassemblies. Those subassemblies specifically discussed in the structural system are catalogued in three major groups (see the family tree, Fig. C.1-1):

1. The structural support assembly, which includes the metering truss, the scientific instrument package truss, the meteoroid shell, and the baffles.
2. The main optics system which includes the primary mirror and secondary mirror, and
3. The telescope protection diagnostic system which includes the aperture door assembly, the sun shield assembly and the pressure bulkhead door.

The design goals and evaluation criteria leading to the preferred selection of each major subassembly are discussed in general in Sections C.2.b(1) and C.2.b(2), as well as the sections specifically dealing with the design of each subassembly.

#### Metering Truss.

In developing the preferred concept, the following general goals were set: (1) minimization of thermal movements, (2) development of a high, fixed, base frequency, (3) minimized use of ferromagnetic materials, (4) incorporation of an independent structure such that load sharing devices are not required, and (5) generation of minimum-weight concept.

The central objective of all of these goals was a better and more reliable optical performance, preferably within a range such that active system control is not required and, if required, is minimized.

The thermal analysis (see Section C.4) shows that adequate thermal control of a passively aligned secondary mirror is not feasible when conventional metallic metering structures are used. That is, the spacing and attitude of the secondary relative to the primary must be adjusted periodically to account for the thermally induced movements. In order to limit the frequency and degree of these adjustments, the design goal of minimizing thermal growth has been imposed on the structure.



Pointing and stability accuracies require the structural response of the vehicle to be virtually uncoupled from the pointing system. Preliminary analysis has set lower limits on desired subsystem frequencies, such that the composite-body response will not adversely affect image quality and pointing stability.

The interaction of ferromagnetic materials and the earth's magnetic field becomes a problem when induced torques in the telescope exceed the system's torque balancing capabilities, and when the ferromagnetic material's field interacts with sensitive instruments. The level of induced torque is dependent on the amount and distribution of magnetic materials and their magnetic strengths. Because a nickel-iron material (Invar) has good thermal characteristics, but questionable magnetic properties, its use must be minimized or properly balanced in terms of thermal and magnetic effects. Although the use of low-expansion composite materials has been advocated (chiefly in the interest of thermal-response characteristics) further study must be carried out on questions relating to manufacturing feasibility, manufacturing cost, dimensional stability, and such mechanical properties as precision elastic-limit equivalent, outgassing characteristics, hydroscopic effects, and reliability.

The need for reliable operation is obvious. Therefore, as a goal, a concept which requires no mechanical devices is desirable.

Three basic metering structure concepts and several variations of these were considered (see Fig. C.2-1). The selection of the preferred concept was based on the adequacy of that concept in satisfying all design goals and requirements, each to a degree consistent with requirement priority. Studies have indicated the superiority of the rigid truss structure; mainly for its adequate stiffness, its lack of launch or load sharing devices, its compatibility with thermal control requirements, the absence of ferromagnetic materials (or moderate use thereof, if Invar is considered a strut material), and its manufacturability.

A comparison of several metering concepts was conducted to evaluate the general feasibility of each approach.\* These concepts included a shell structure, several truss configurations, and a metering rod-shell arrangement.

#### Shell Metering Structure †

The metering shell considered (see Fig. C.2-1a) was a cylindrical Invar structure that supported the secondary mirror assembly via the spider. The construction is a closed semimonocoque consisting of longitudinal stringers and formed rings. The optimum sizing and spacing of the rings were not within the scope of the analysis, but for the purposes of the preliminary analysis, a reasonable configuration of adequate stiffness and strength was considered to determine weight and stiffness characteristics. The primary load carrying members are the stringers, and the rings are spaced at appropriate intervals to reduce buckling susceptibility.

Fig. C.2-2 (primary to secondary despace versus change in temperature for a diametral thermal gradient) and corresponding Fig. C.2-3 (for a thermal soak condition) indicate the metering structure's thermal sensitivity for various materials. Shells constructed of aluminum, beryllium, and titanium exceed the indicated allowable despace under very small temperature variations and therefore would require increased active alignment. The Invar shell is significantly better than the previously mentioned class but is not as attractive as the composite material shell or the athermalized truss. The athermalized truss can accommodate temperature changes two orders of magnitude greater than the aluminum shell and a factor of two greater than the graphite-epoxy shell. This characteristic was prime in the selection of the truss configuration.

The main advantages of the shell structure are (1) its superior stiffness-to-weight ratio as compared to all of the other concepts and (2) its small potential obscuration. Its main disadvantages are (1) poor thermo-structural response characteristics and susceptibility to induced alignment and focus errors caused by foundation motions and thermal gradients, (2) the total weight of the metal configuration, and (3) the amount of required ferromagnetic material (Invar concept).

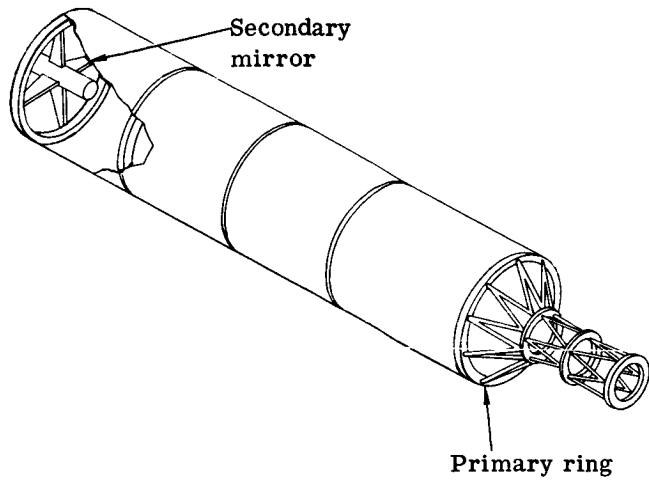
#### Metering Rods

The metering-rod concept has many variations in the number of rods and their load paths. The rods may serve as a connector between two rings of equal diameter at the primary and secondary, or they may connect to a smaller

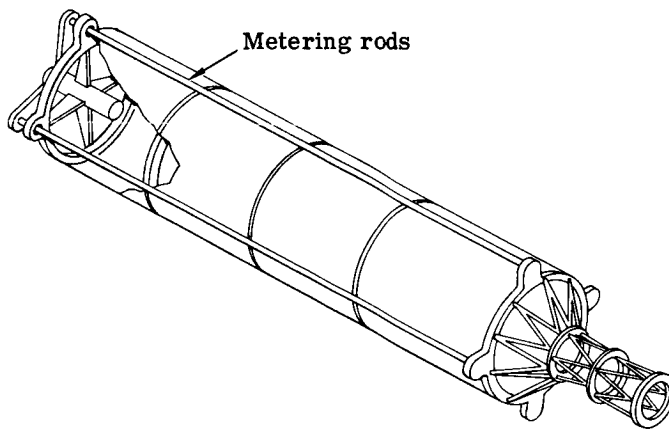
---

\*Itek Memo 278-1-53-72.

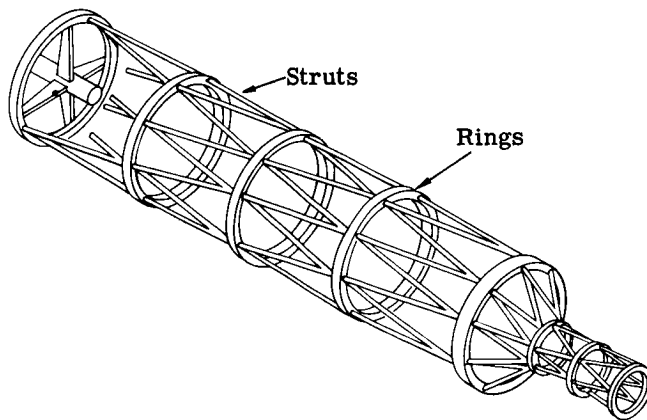
†NASW-1925 and Itek Memo 278-1-54-72.



(a) Shell



(b) Rod and shell



(c) Truss

Fig. C.2-1 — Metering structural concepts

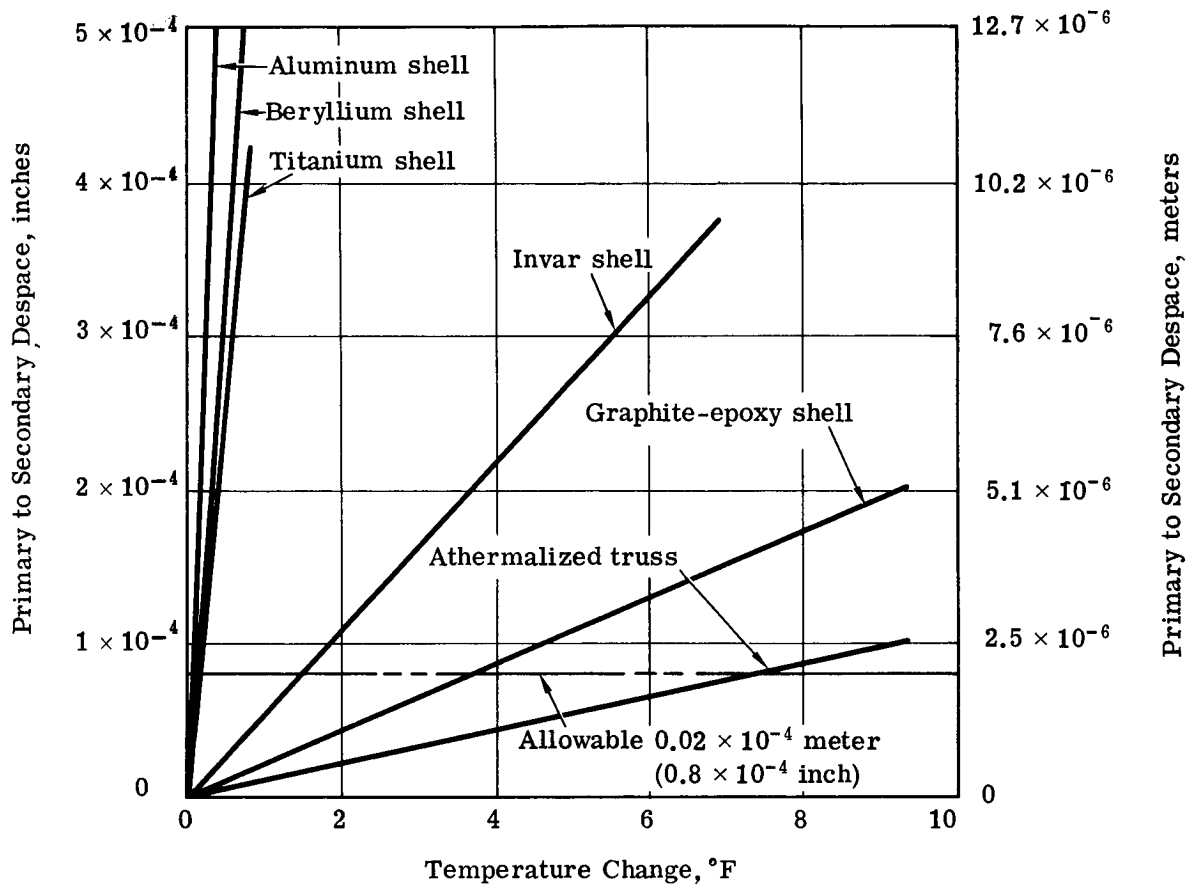


Fig. C.2-2 — Primary to secondary despace versus change in temperature; based on length of 5.5 meters (216.9 inches)

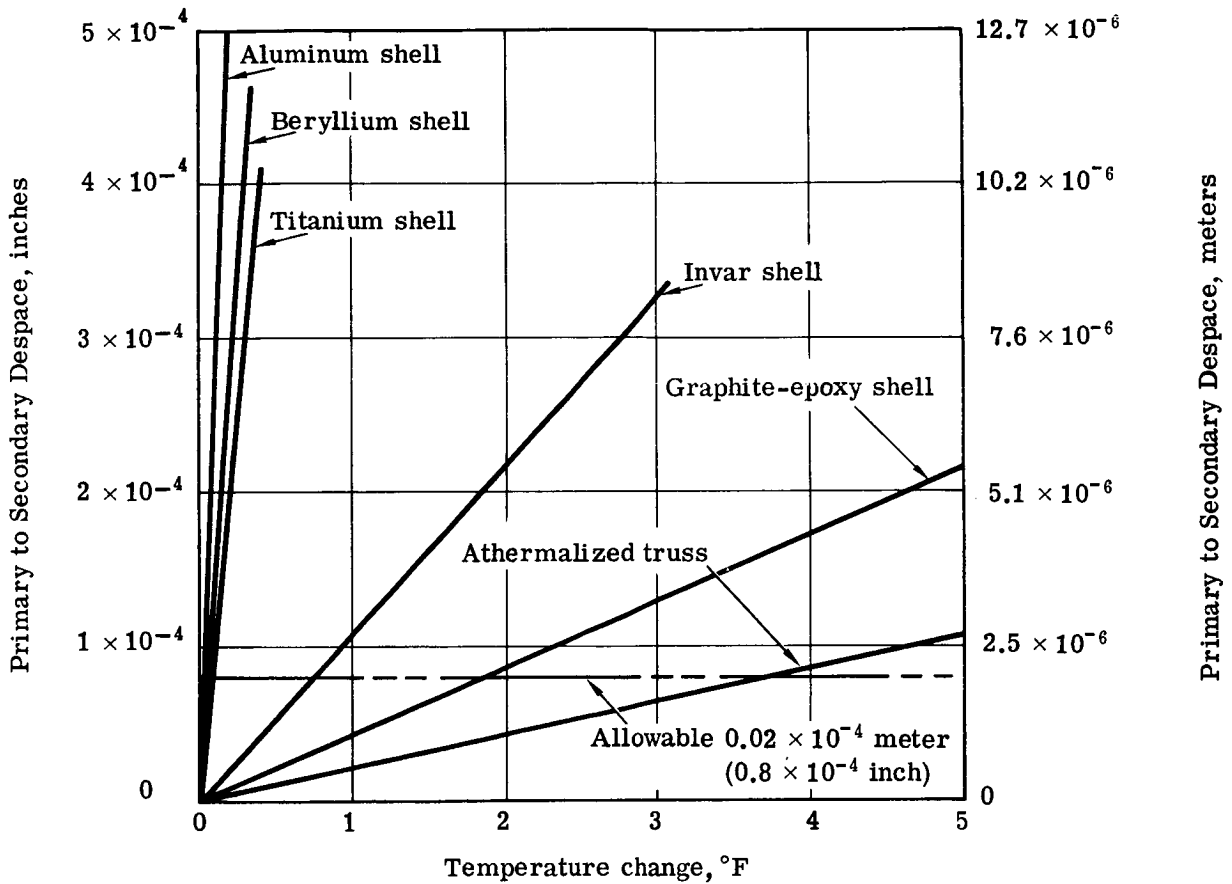


Fig. C.2-3 — Primary to secondary despace versus change in temperature with thermal soak loading versus change in temperature; based on length of 5.5 meters (216.9 inches)

intermediate ring. Because of the launch and stiffness requirements, the metering rods cannot function independently and require an auxiliary support system. This limitation is considered serious in its reliability and complexity implications.

An auxiliary support at the secondary spider location is required to provide a load path to transmit the launch and reentry loads and to provide lateral stiffness. Such support has been provided in other systems by mechanical bearing surfaces or flexure connections. The bearing surface transmits lateral loads and motion but allows axial slippage to account for relative thermal motions between the inner and outer structures. The flexure connection is designed to be stiff laterally and flexible in an axial direction. The degree of lateral stiffness is determined by the amount of relative thermal growth between the inner and outer structures.

As a preliminary step in the design of such a system, several existing arrangements have been reviewed and areas of necessary modification have been identified to improve these designs. In addition, a flexure concept has been devised, but this requires a great deal of additional work to demonstrate its feasibility, let alone desirability.

The use of low expansion glasses as metering structures appears attractive from a thermal standpoint, but presents a large number of structural questions. The ability of the glass to survive the severe loadings must be studied in great detail. In light of the great thermal advantage that can be obtained by the use of Cer-Vit or ULE, material properties and structural development studies are mandatory to adequately judge their suitability.

The metering-rod concept briefly studied consisted of four Invar rods connecting equal-diameter primary and secondary rings and reinforced laterally by an aluminum shell. The shell is of typical fabricated semimonocoque construction and is hard-fixed to the primary reference ring. Flexures provide the load path between the secondary and aluminum shell. As a design goal, no launch locking devices were included.

The fundamental disadvantages of this concept are (1) the inability to uncouple the axial and lateral responses of the system while maintaining acceptable stiffness levels through use of either launch locks or flexures and (2) the presence of heat leaks at the points of attachment.

#### Truss Metering Structure

The truss structure (see Fig. C.2-1) uses circular rings interconnected by struts. The secondary mirror assembly is supported by a four-legged spider that feeds its load into the top truss ring at the ring's quadrant points. To decrease the inward intrusion, and hence the obscuration and space envelope of the truss members, and to achieve a better stiffness-to-weight ratio, an eight-point structure (16 members per bay) was developed. It can be noted that as the number of members increases, the structure acquires some of the properties of a cylindrical shell, i.e., good symmetry and good stiffness. Detailed frequency calculations of several truss configurations were performed with a digital structural routine to optimize stiffness and weight characteristics. This analysis was performed to a level of detail sufficient to establish the feasibility of this concept. An in-depth discussion of the various truss concepts studied is given in Section C.2a(1) (Metering Truss Design).

Early in the concept-definition phase a comparison of the shell and truss concepts was made in terms of fixed base natural frequencies for various telescope systems, and it becomes instructive to consider the results here. Fig. C.2-4 shows the variation of metering structure frequency as a function of primary mirror focal ratio (which ratio may be interpreted as structural length). The curves show that shells of equal weight have higher fundamental natural frequencies for all cases. It also shows that the graphite-epoxy three-bay truss is superior to the Invar-titanium truss, although both trusses surpass the frequency design goal.

The most attractive feature of the truss concept is its potential of providing a structure that is thermally inert through use of materials with dissimilar coefficients of expansion for the rings and the struts. Proper selection of materials and spacing allow the axial growth of the truss members to be compensated by the radial growth of the rings.

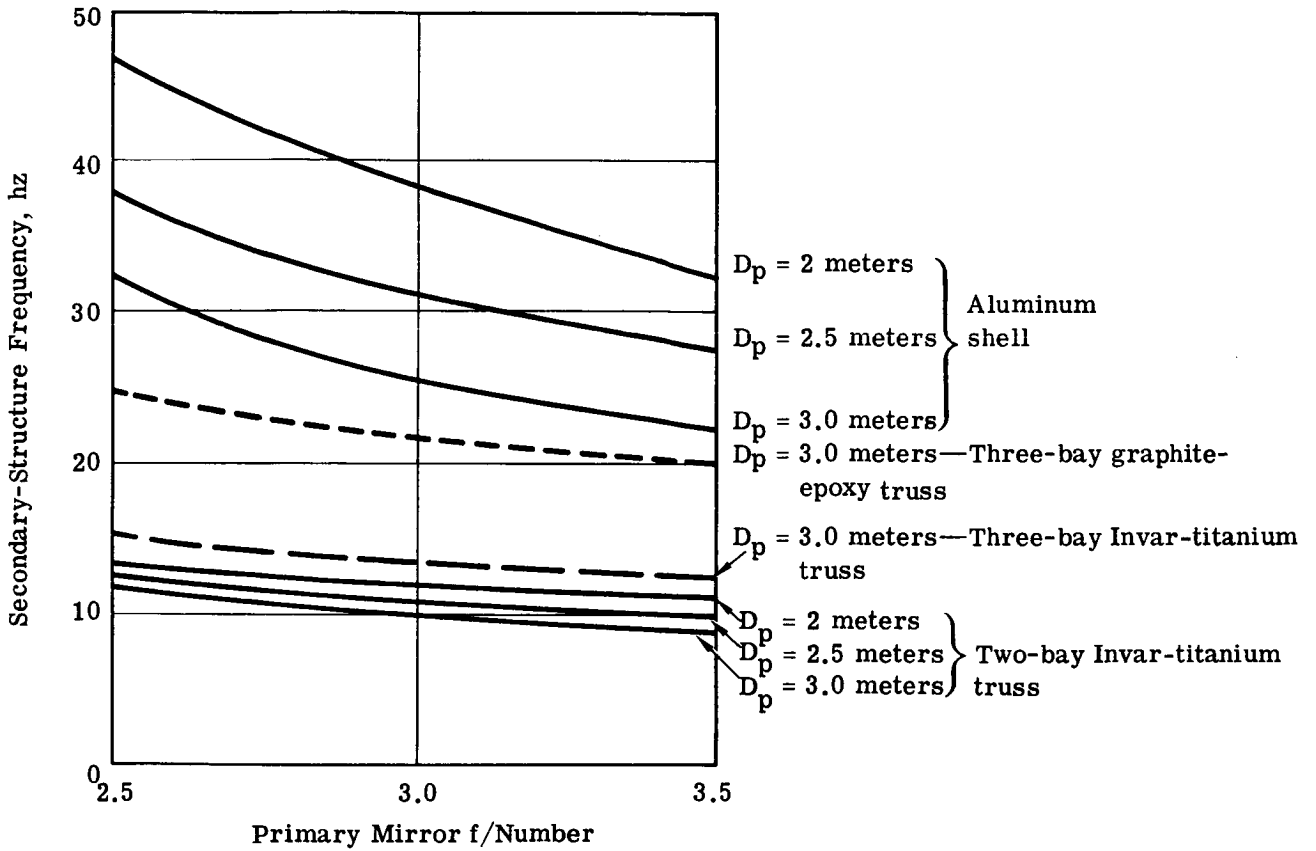


Fig. C.2-4 — Secondary metering structure natural frequency versus primary mirror f/number for shell and truss configurations and various primary mirror apertures

The main advantages of the design are that (1) it shows the most potential for accommodating thermal distortion minimization, (2) it does not require the inclusion of launch locks or load sharing devices, (3) its fabrication is within the current state of the art, and (4) it minimizes the use of ferromagnetic materials. Its major disadvantages are that it does not have (1) a superior stiffness-to-weight ratio or (2) the smallest space-envelope requirement.

#### Scientific Instrument Package Support Structure

The scientific instrument package (SIP) support structure provides the reference foundation for each instrument and ties these back to the telescope main structural ring and bulkhead. The development of the SIP structural concepts was directed toward satisfying the following design goals:

1. Minimized thermal deflections
2. Provision for easy access to instruments during replacement and maintenance operations
3. Holding fixed base fundamental frequency of the instrument above 25 hz
4. Minimized ferromagnetic effects
5. Minimized weight
6. Provision for incorporating future instruments and experiments.

The instrument package structure must not only perform in a manner similar to the secondary structure in terms of maintaining alignment and spacing during thermal and dynamic perturbations, but must also provide accessibility and maintainability.

The structural design concept described in Report GSFE X-670-70-480,<sup>7</sup> was reviewed for compliance with the design criteria and goals. The structural design was not adaptive to easy access and maintenance, and the structure could only satisfy operational alignment and spacing requirements by extremely tight control of thermal variations.

Several alternative approaches utilizing a truss configuration were developed to minimize thermal deflections. Two of these, centered about the use of the athermalized approach to control thermal movements were:

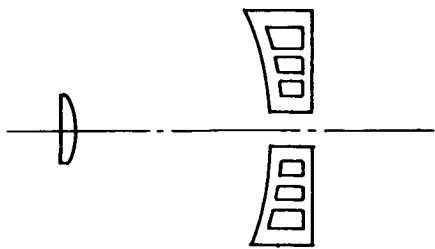
1. A truss configuration having titanium rings and Invar struts
2. A truss configuration having rings and struts, both fabricated from graphite-epoxy and made in such a way that their coefficients of linear thermal expansion were different and tailored to accomplish an athermalized design.

Because of the required precise alignment of the several optical planes in this area, the athermalizing approach was only marginally satisfactory. For this reason the third concept, utilization of zero expansion graphite-epoxy material was developed. This recommended concept and one variation of it is fully discussed in Section C.2.c(4).

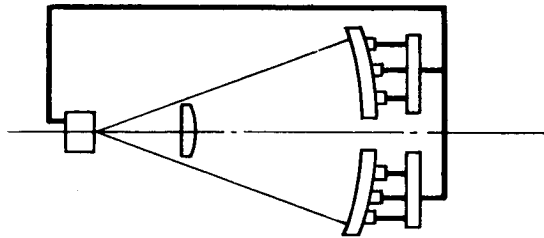
All of the above concepts provide eight open bays that allow maximum access and ease of maintenance. This approach is recommended for these reasons as well as for its ability to meet the stiffness and weight goals and future-growth potential.

#### Primary-Mirror Concepts

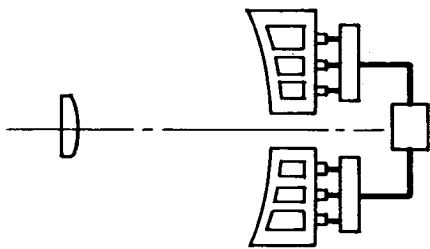
The basic mirror concepts may be classified as follows: segmented, deformable, and rigid (see Fig. C.2-5). This classification defines the method of limiting surface error to within allowable tolerances. The existence of these concepts is merely a way of questioning whether surface and wavefront error can be held by a rigid mirror of reasonable weight or whether surface corrections in space are required. This question can best be defined in terms of requirements for surface precision under imposed loads during manufacturing, testing, and mission operation.



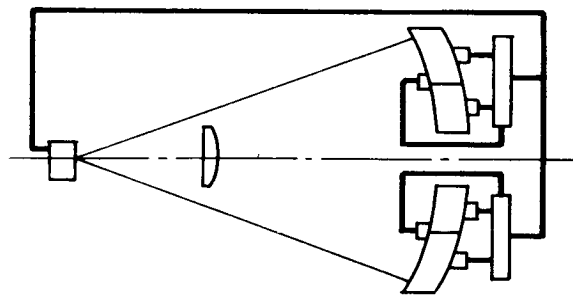
Rigid mirror



Thin deformable mirror



Augmented thick mirror



Segmented mirror

Fig. C.2-5 — Active and passive mirror configurations



Proponents of active mirrors (either segmented monoliths or thin deformable assemblies) have directed their attention to the following points. The discussion of each point provides the basis for selecting the preferred mirror concept, an augmented monolith.

1. There is some question about the ability of mirror material to return to its original shape after undergoing loading.

While this question is valid for metallic mirrors (and alone provides enough reason to disqualify metallic mirrors), recent findings of Woods<sup>1</sup> indicate no discernible permanent set in mirror materials (ULE, Cer-Vit, and fused silica) when stressed to levels approaching the material's rupture strength. The samples used were etched to remove all surface microscratches. This implies that if the mirror blank is properly etched and if design stresses are held to reasonable levels, permanent set due to loading will not occur.

2. There are no available data that indicate whether or not the mirror has sufficient long-term dimensional stability to maintain its surface quality over the life of the mission.

While there are no data indicating that silicate materials have good long-term dimensional stability, there also are no data indicating that they do not. This is an area for future study, to identify the problems if indeed they exist, and to work toward solutions.

3. As astronomers require larger and larger aperture systems to conduct their experiments, the feasibility of launching heavier and heavier payloads diminishes. The logical solution to this problem of the future, it is argued, is the thin deformable mirror. Therefore, adoption of this technique for smaller mirrors (3 meters and less) will provide important data and experience.

While the construction of very large aperture systems may present booster-capacity and mirror-fabrication problems, a 3-meter system has neither of these restrictions. It would then be inconsistent with the aims of the LST program to use the primary mirror as a prototype for larger systems if this application reduces the effectiveness of the system and increases its complexity.

5. The ability to achieve a uniform surface on a larger mirror decreases as the mirror diameter increases.

The size of a 3-meter primary mirror, taken by itself, cannot be considered to be a limiting factor in the fabrication process. Constructing the primary mirror of one of the presently available lightweight structures (cored Cer-Vit or fused ULE monolith) will satisfy all surface tolerance requirements.

In order to structurally evaluate the candidate mirror materials the mirror environment must be established. Metallic materials such as aluminum, titanium, and beryllium have desirable mechanical rigidity properties, but since their coefficients of thermal expansion are relatively large and variable, these materials were disqualified as candidates.

Due to the low allowable stress and low modulus of elasticity of glass ceramic materials, a large flexural moment of inertia is required (as a rule of thumb for terrestrial mirrors, a diameter-to-thickness ratio of 6:1 has proven successful). A 3-meter mirror would, therefore, have a thickness of 0.5 meter and a corresponding weight of about 9,000 kilograms (20,000 pounds). With the present state of design of the shuttle, this weight is prohibitive.

An obvious alternative to solid mirror design is the use of a cored rib approach in which a repeating cross section is similar to an I-beam. The webs resist shear and faceplates resist bending moments. A large mirror depth is required to maintain stress, strain, and total deflections within allowable levels. It is estimated that with the use of this type of lightweight construction approximately 75 percent of the mirror weight would be removed.

The materials and construction of a lightweight primary mirror are so interrelated that it is desirable to consider them in one tradeoff study. The two materials showing the most promise for this application are ULE titanium silicate and Cer-Vit. The methods of mirror construction are unique to each material. That is, a ULE mirror is assembled from component parts such as faceplates, ribs, corner blocks, and closure members. These are assembled to form the desired mirror geometry and welded together to form one monolithic assembly. The Cer-Vit mirror is made lightweight by conventional machining techniques in which undesirable material is removed from the back. Fig. C.2-6 shows the core construction and pertinent dimensions of the LST Cer-Vit mirror. However, it should be noted that neither Cer-Vit nor ULE was found to be structurally superior, thereby reducing the mirror material selection process by eliminating the structural parameter.

#### Mirror-Mount Concepts

The evaluation of mirror-mount concepts included criteria given in terms of the mount's effect on the optical element which it supports. Much of the technology leading to the mount parametric analysis had been previously developed. A significant portion of the state of the art of discrete point mounting arrangements has been compiled in Itek Report 71-9463-2. That work was heavily drawn upon during the current effort.

The historical development of the recommended axial leaf mount is covered in Section C.2.c(2) and need not be repeated here. What is significant to note is that the mounts were sized by an opto-structural analytical technique that ensures proper operation. In addition, the three-point configuration successfully supports the mirror during the launch and reentry loading phases, thereby obviating the need of additional load sharing devices. The mounting approach (viz., discrete point, universal type) has been proven feasible. Additional design and analytical efforts will develop an optimum configuration in terms of thermally induced mirror loads and compatibility with test mounting requirements.

#### Telescope Protective System

The telescope protective system consists basically of the aperture door assembly, sun shield, and pressure bulkhead door. Each has evolved through several design concepts in arriving at its present configuration.

#### Aperture Door Assembly

The earliest aperture door concept showed a simple lid hinged from the far end of the sun shield, whose design was originally a right circular cylinder. Although the concept was relatively simple from a mechanical standpoint, the requirement for electrical power to the sun shield and the weight penalty in providing adequate structural support so distant from the support appeared to offset the advantages. Later when the sun shield was truncated, an approach creating additional problems, this concept was set aside and a multi-petal door arrangement adopted.

The baseline aperture door consists principally of eight identical curved and bonded aluminum honeycomb segments that are hinged and cantilevered inboard from the meteoroid shield and opened or closed with electric-powered screwjacks. Honeycomb construction provides rigidity without excessive thickness and permits retraction into a small volume. Fabrication of honeycomb panels of this size is common in industry today.

Alternate door designs that need further evaluation are (1) conventional mechanically assembled types with sheet metal and fittings, (2) welded doors, and (3) door combinations of conventional and welded construction. These designs all use double skin construction to achieve rigidity. They contain no organic materials and thus avoid the outgassing characteristics of bonded honeycomb.

Since any of these four alternate designs will be satisfactory, the choice should be based on the usual parameters of weight, cost, rigidity, outgassing, etc. Honeycomb construction is most adaptable to the conical curvature of the door; however the need to provide curvature in each segment must be questioned, since flat or bent panels are usually more economical.

#### Sun Shield

The sun shield is an extendible light shield that fits concentrically over the meteoroid shield. At first the concept was simply that of a semimonocoque right circular cylinder. Later, in an attempt to improve the viewing field, the sun shield was truncated at 30 degrees. The forward tip of the sun shield was hinged and swung down

during launch to fit in the Titan-shroud space envelope. This configuration was later abandoned in favor of the present simpler sun shield design, which is truncated at 45 degrees with no hinged portion.

For actuation of the sunshade the chosen baseline is a set of motor-driven tubular extendible members. When retracted, these members wrap on storage drums; when extended they form slotted tubes of very limited column strength. Operating loads in the actuators are due to friction between the sunshade and the meteoroid shield. The magnitude of loads will be related to thermally induced strain, lubrication, materials, manufacturing tolerances, etc. Near the end of extension, and at full extension, the sunshade is weakly supported on a short couple and additional tension and compression loads will be induced in the actuators due to any lateral acceleration and uneven friction loads. When the magnitude of actuator loads (especially those due to thermally induced strain) is determined, a tradeoff of actuator types can be concluded. Alternate concepts include screwjacks or a cable system. These alternates appear to be more economical and are more efficient for carrying the loads, but since they do not retract, probably will require dynamic support along their length during launch.

#### Pressure Bulkhead Door

The pressure bulkhead door is machined from one piece of aluminum in the shape of a ring with a dished skin. The skin is chemically milled to final thickness. The result is a lightweight low-cost door configured to resist differential pressure in one direction. Aluminum honeycomb has been examined as an alternative to the dished skin. Its depth is one inch instead of two inches for the selected concept. There is no particular need to be restricted to a door of less than two inches, and the outgassing characteristics of bonded honeycomb can be avoided.

The door is positioned by translation rather than by rotation on a hinge in order to minimize the space requirements for its operation. The translation mechanism is based upon the precedent of the scientific airlock on Skylab, and upon such other components as airplane cockpit windows. The geometry of the cam that guides the door and the irreversible characteristics of a set of electrically driven screwjacks ensure that the door is locked when power is off.

#### C.2.b Structural System Analysis

The LST combined with the support system module (SSM) make up the entire spacecraft to be orbited around the earth. Since the spacecraft is presently designed to fit within the space envelope of the Viking shroud (see Fig. C.2-7), it will also fit in the cargo-bay area of the shuttle. The shuttle payload envelope is 4.57 meters (15 feet) in diameter and 18.29 meters (60 feet) long.

The LST structural system may be separated into two functional structural systems: the optical structural system and the nonoptical structural system (Fig. C.2-8a).<sup>\*</sup> The optical structural system consists of the optical metering truss and SIP structure. The nonoptical structure consists of the telescope protective system, as shown in Figs. C.2-8b and A1-1. The metering truss and SIP structure attach on opposite sides of the pressure bulkhead/main ring structure. The telescope protective structure encompasses the metering truss and SIP and interfaces with the SSM approximately 1.5 meters (59 inches) beyond the aft side of the pressure bulkhead. A second interface of the LST and SSM occurs between the OTA pressure bulkhead and SSM pressure cylinder.

The LST in the Titan III launch configuration interfaces with the vehicle through the SSM pressure cylinder. In the shuttle launch/reentry configuration the spacecraft is supported to the shuttle at three points, two on the OTA pressure bulkhead and a third on the SSM.

##### C.2.b(1) Structural System Requirements

Each subassembly has been evaluated in terms of general system design criteria and to the specific criteria pertinent to that subassembly.

The central objective of the OTA and SIP structural design is to efficiently maintain the positioning of the critical optical surfaces within allowable tolerances that ensure satisfactory optical performance throughout the mission. In addition, the structure must protect the optical system and the instruments from the adverse environment.

<sup>\*</sup>Final Briefing, LST Phase A Definition Study, Itek Document 72-8209-5, Dec 12, 1972, p. 9-5.

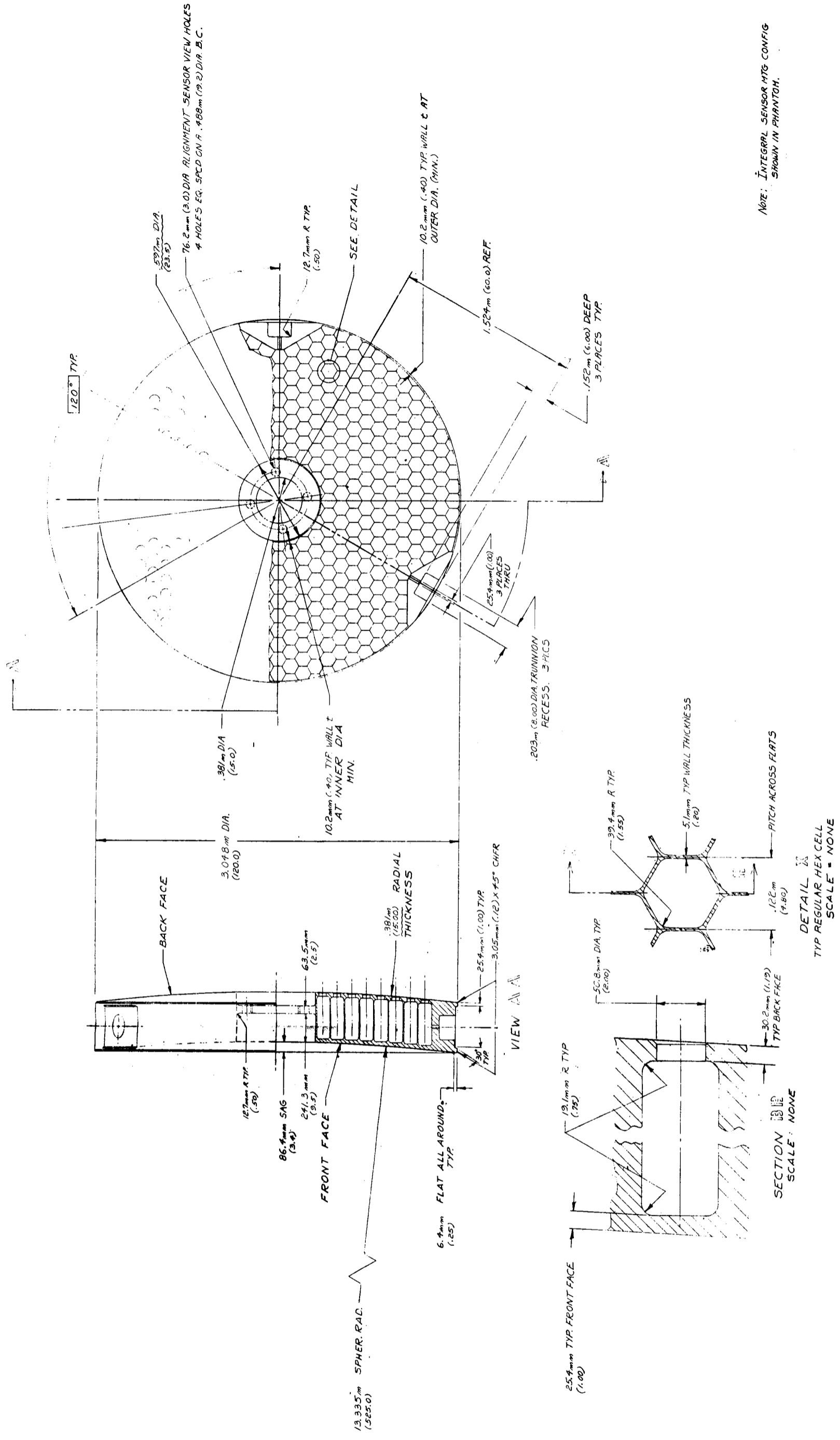


Fig. C.2-6 — Primary mirror configuration for structural mathematical model  
(with integral sensor mount)

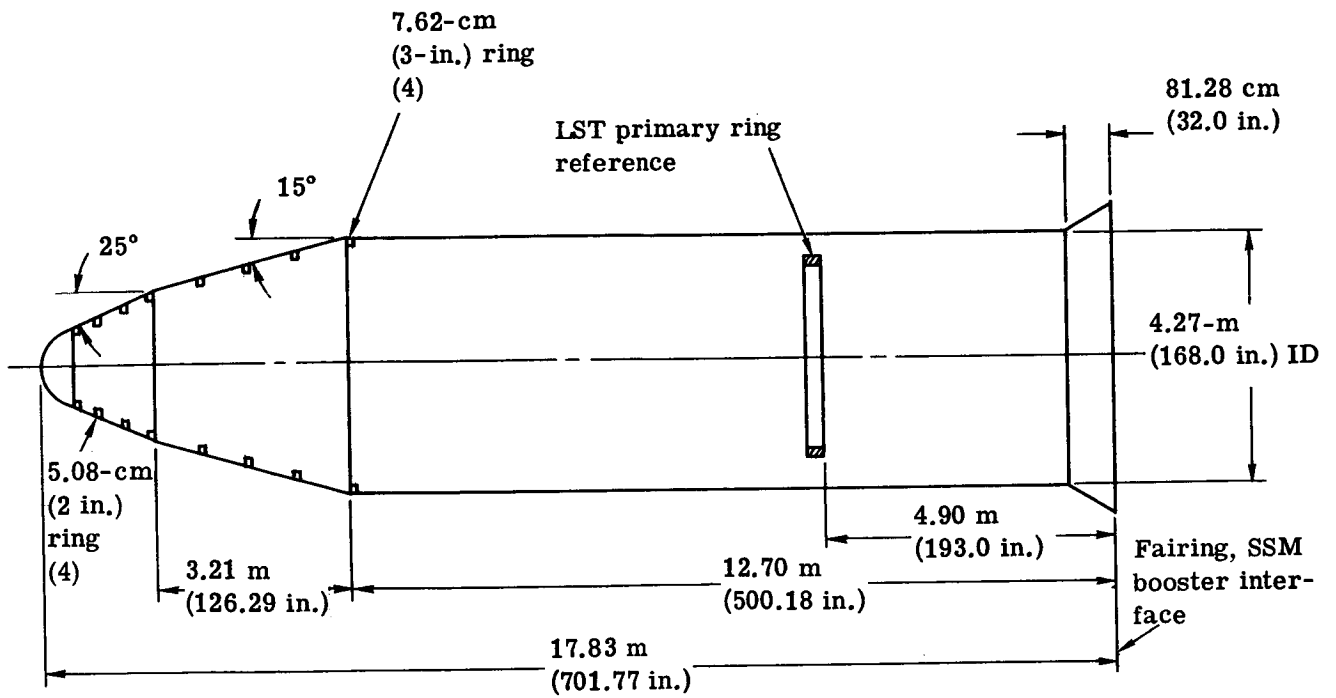


Fig. C.2-7 — Viking shroud payload envelope

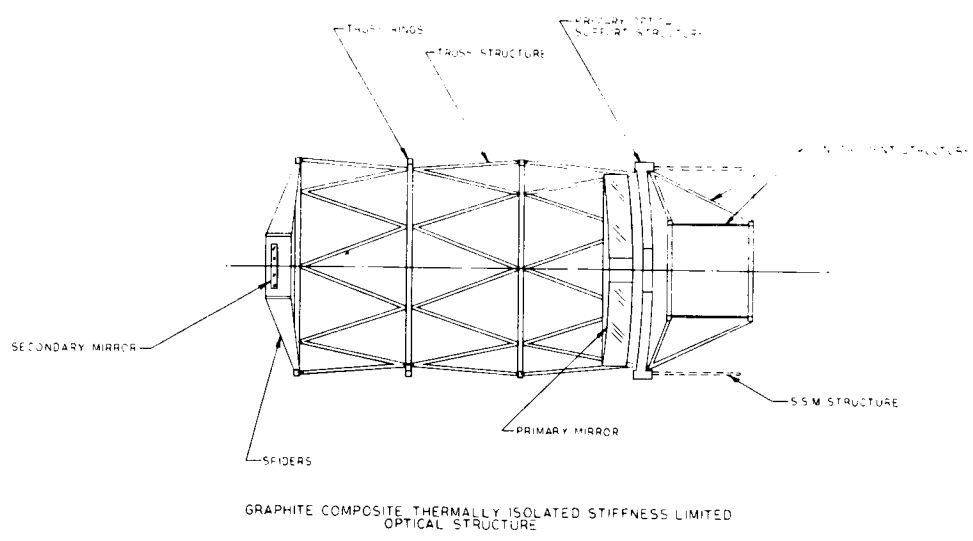
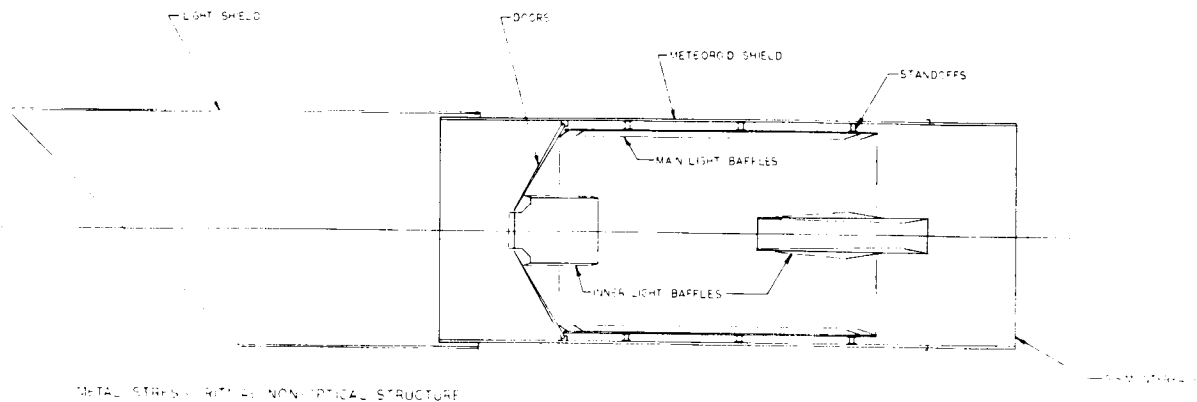
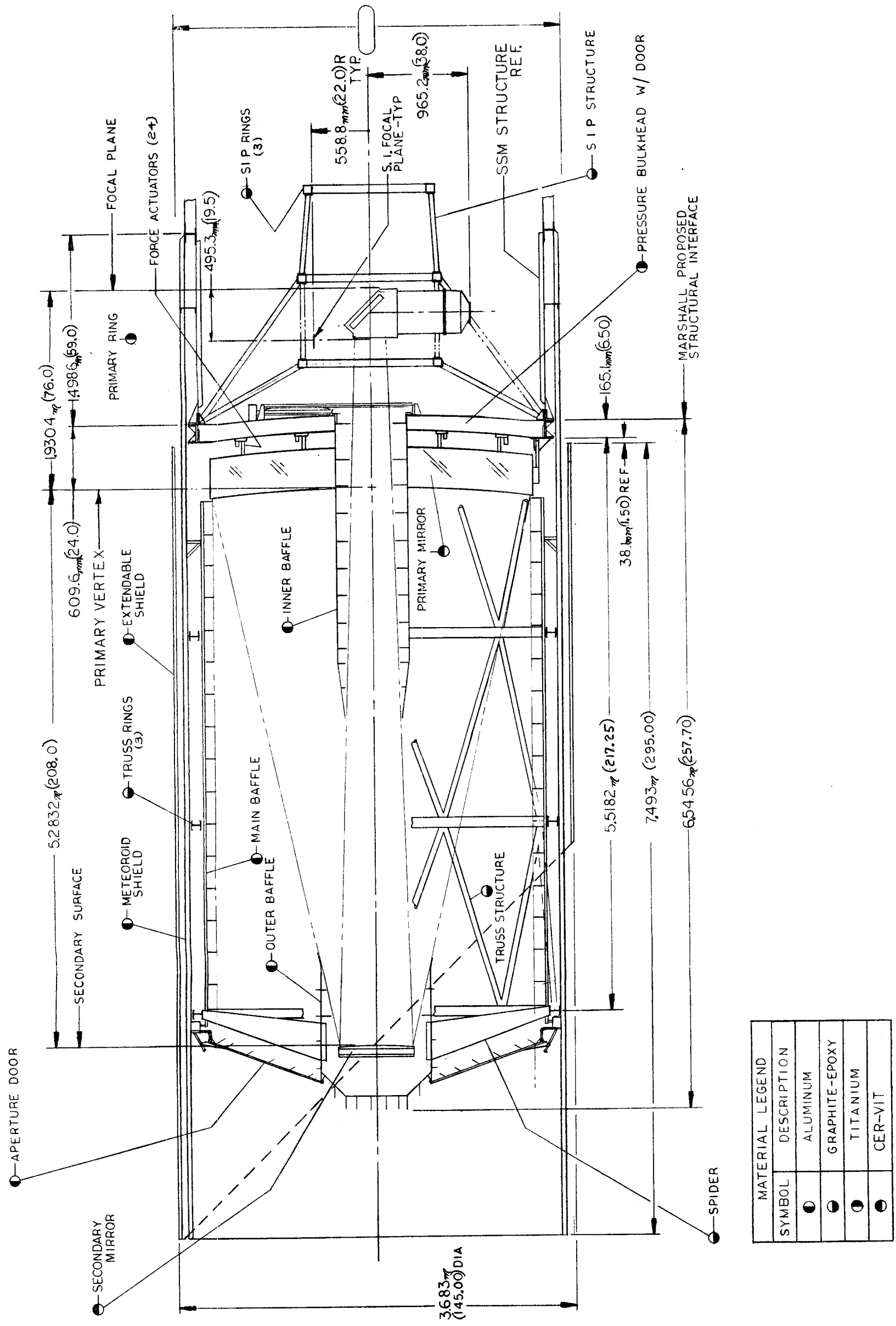


Fig. C.2-8a — Optical and nonoptical structural systems



MATERIAL LEGEND	
SYMBOL	DESCRIPTION
●	ALUMINUM
●	GRAPHITE-EPOXY
●	TITANIUM
●	CER-VIT

NOTE: DIMENSIONS SHOWN IN PARENTHESES ARE ENGLISH EQUIV

Fig. C.2-8b — OTA structural interface and configuration (drawing no. 185505)





### C.2.b(2) Optical Performance Tolerances

The maximum allowable movements of the critical optical surfaces and their locations are:

1. The secondary mirror must not exceed  $\pm 2$  micrometers ( $\pm 0.00008$  inch) pure axial motion relative to the primary mirror during operation. This motion corresponds to an rms wavefront error of  $0.02\lambda$ , where  $\lambda = 633$  nanometers.
2. The secondary mirror must not exceed  $\pm 10$  micrometers ( $\pm 0.0004$  inch) pure translation relative to the primary mirror during operation. This motion corresponds to an rms wavefront error of  $0.0055\lambda$ .
3. The secondary mirror must not exceed a tilt or a tip of 4.8 microradians (1 arc-second)-relative to the primary mirror during operation. These angular movements correspond to an rms wavefront error of  $0.004\lambda$ .
4. The focus at the locations of principal focus must not exceed  $\pm 5$  micrometers ( $\pm 0.0002$  inch) during operation.
5. The slit assembly must be held relative to the fine guidance to within  $\pm 1.8$  micrometers ( $\pm 0.00007$  inch) during operation.
6. The collimating mirror must be held to  $\pm 18$  micrometers ( $0.00070$  inch) relative to the slit assembly and to 7.5 microradians tip.
7. Each spectrograph must be held to  $\pm 15$  microradians tip.
8. The primary mirror mounts must not introduce forces which cause an rms wavefront error exceeding  $0.009\lambda$  during operation.
9. The secondary mirror mounts must not introduce forces causing an rms wavefront error exceeding  $0.0045\lambda$  during operation.
10. Interpanel g release deflections of mirrors must not exceed deflections equivalent to an rms deflection of  $0.005\lambda$ .

### C.2.b(3) General Design Goals

The general structural-design goals considered in the development of the recommended baseline concept were:

1. Minimization of payload weight to accommodate booster capabilities.
2. Minimization of ferromagnetic materials to limit induced torques generated from interaction with the earth's magnetic field and to limit deleterious electromagnetic effects on sensitive instruments.
3. Utilization, to the greatest possible degree, of independent structures, i.e., eliminate the need and use of load sharing devices.
4. Protection of the primary and secondary optical elements from a meteoroid environment on the basis of a 0.95 probability of no penetrations for a period of five years.
5. Development of a cost effective design incorporating potential for growth, accessibility, and ease of maintenance.
6. Development of a structure that minimizes obscuration and is consistent with launch envelopes described previously.

### Design Load Conditions

The design load conditions for the LST include (1) the Titan launch, (2) the shuttle launch and reentry environment, and (3) the ground handling environment. The limit loads for the launch and reentry are shown below.

#### Titan Launch

6.0 g axial + 1.5 g pitch

#### Shuttle Launch

3.3 g axial + 0.6 g pitch + 0.6 g yaw at cutoff  
-0.5 g axial - 4.0 g pitch  $\pm$  1.0 g yaw at reentry  
-1.3 g axial - 3.2 g pitch  $\pm$  0.5 g yaw at landing

A design load factor of 1.4 is introduced to the limit loads for an ultimate design load factor. The design loads should cause no permanent degradation, i.e., in the spacing and alignment of the optics or optical instruments. In order to attain this immunity the design goal is to keep optical-structures stresses below one-half of the material's microyield stress. The ground handling load environment is expected to be less severe than launch or reentry and not critical in the design.

The pressure compartment must withstand an internal pressure load of one atmosphere with a factor of 2 applied to obtain ultimate loads. The pressure bulkhead, which serves as a support for the metering truss, SIP structure, and primary mirror must be sufficiently rigid so as not to induce excessive strains on the optics under acceleration or pressure loads.

### Operational Dynamics

The operational dynamic environment is categorized by three areas of excitation.

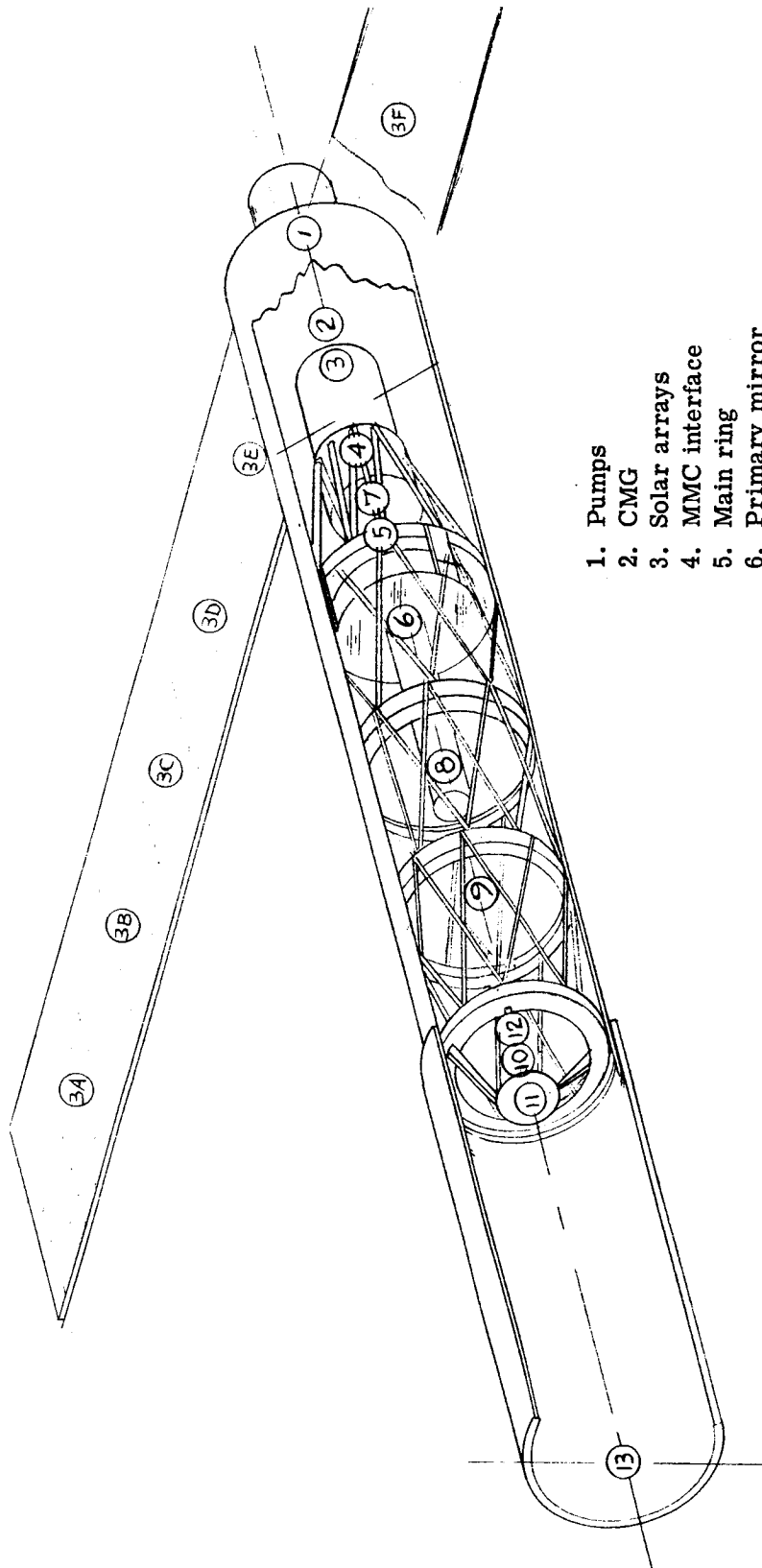
1. Disturbances generated by the telescope's associated spacecraft during launch, orbit and reentry.
2. Disturbances generated during pointing and stabilizing operations.
3. Disturbances generated from the OTA and SIP internal sources, e.g., inertial reaction induced by astronomical instruments.

To fully evaluate dynamic response to these excitations, a comprehensive study must be performed. This study would include a detailed knowledge of the magnitude and time histories of the excitations, mass, stiffness and damping characteristics of the entire orbiting vehicle. The analysis would be used to so allocate subsystem stiffness requirements as to ensure the dynamic response in the system.

A preliminary goal based on item 1 above is to minimize the dynamic response of the structural subsystems by keeping their fundamental frequency well above the fundamental frequency of the launch vehicle.

The initial LST dynamic model (see Fig. C.2-9) considered an all-metal structure in a free flight configuration. A separate analysis of the proposed solar panels indicated a degree of dynamic uncoupling sufficient to allow their inclusion in the payload model as a lumped mass at their interface. The metering truss and instrument package structure were assumed to be made of titanium and Invar and the outer protective structure made of aluminum. Analytical results showed that, exclusive of the rigid body modes, the first natural frequency was 16 hz with the corresponding mode a cantilevered bending of the metering truss at the primary ring. The second natural frequency was 18 hz with a similar mode bending, but of the instrument package structure (see Fig. C.2-10).

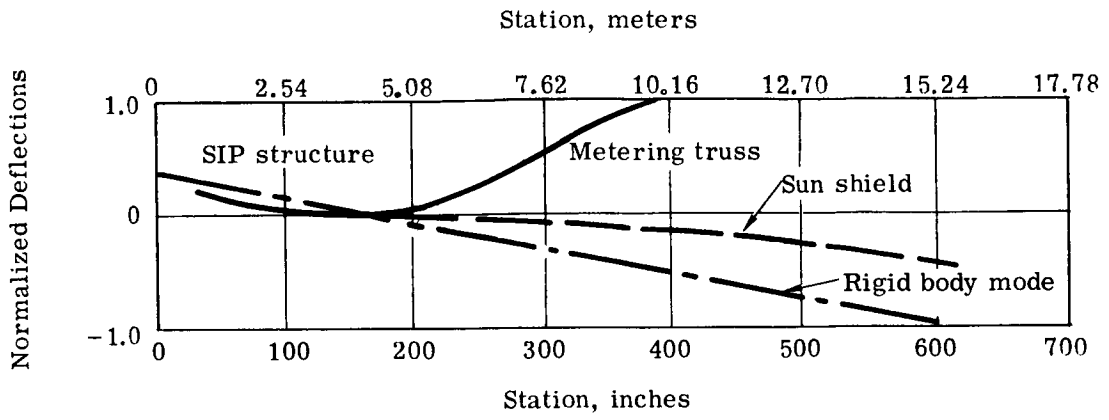
The subsequent analyses of the structural dynamics of the LST were confined to independent modeling of the metering truss and SIP structures and assuming the use of graphite-epoxy members. The discussion of those models is covered in detail in Sections C.2.c(3) and C.2.c(4). The results show the fundamental frequency of the metering truss to be 24 hz while that for the SIP structure was 28 hz, both in the lateral directions of bending. These updated configurations have not been applied to the overall LST dynamic model. Inasmuch as the lower system frequencies reflected the response of the secondary metering truss and the SIP structure, it is concluded that systems frequencies will increase with the inclusion of the recommended (stiffer) configurations. This increase will result in a more favorable dynamic response to excitations that fall into categories 2 and 3. Detailed dynamic analysis is reported in Itek Memo 278-1-26-72, Itek LST Dynamic Model Rev. A.



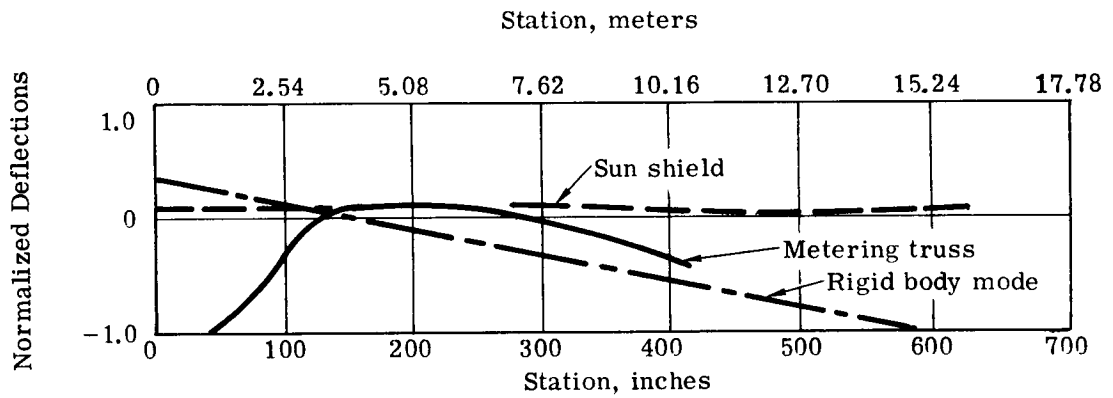
- 1. Pumps
- 2. CMG
- 3. Solar arrays
- 4. MMC interface
- 5. Main ring
- 6. Primary mirror
- 7. Instrument pack
- 8. Truss ring no. 1
- 9. Truss ring no. 2
- 10. Truss ring no. 3
- 11. Secondary assembly
- 12. Thermal shield
- 13. Light shield

\* Pumps were eliminated in later designs

Fig. C.2-9 — LST dynamic model



(a) Natural frequency 16 hz



(b) Natural frequency 18 hz

Fig. C.2-10 — LST dynamic model (all-metal structure)

## Thermal-Structural Response

As the design of each subsystem evolved, mathematical models were used extensively to predict thermally induced movements. These analyses were carried to a level sufficient to establish concept feasibility and are discussed in the following sections. The next step was to generate a mathematical model representing the entire OTA and SIP area in order to determine the effects of orbit environmental temperature variations on the structure and, in turn, on optical performance. The system model included the elastic interaction of the several subsystems. Feedback from this analysis could then be used in the evaluation of and provision for necessary remedial efforts in the various structural concepts.

Two distinct systems were analyzed for orbital temperature conditions: (1) an all-metal configuration, and (2) an all-graphite-epoxy configuration [see Sections C.2.c(3) and C.2.c(4) for detailed descriptions]. The analytical steps are shown in Fig. C.2-11. The initial step in this analysis was the establishment of a finite-element mathematical model, having sufficient detail to adequately simulate the real structure. Input for this analysis was generated from the system thermal model, which determined the environmental temperature distributions for various on-orbit attitudes. By using an appropriate structural program for determining the response to a given temperature distribution, the resulting displacements and forces were computed at various locations throughout the structure. At this point induced stresses were evaluated and found to be of little consequence to overall structural design. Relative displacements between the primary and secondary mirrors were used to determine the magnitude of tilt, decenter and defocus. Next, mirror/mount interface forces were used as input to the analytical mirror model in order to determine surface deflection vectors. To evaluate the associated noncorrectable wavefront errors, these optical surface movements were then used as input to existing Itek optical programs.

Table C.2-1 is a summary of some of the pertinent data generated from this study. Included are:

1. Induced rms surface errors at the primary mirror during a critical operational situation.
2. Thermal/optical sensitivity of the secondary mirror. This item indicates the range of allowable temperature increases to just match the allowable optical tolerances. The case shown (despace of the secondary relative to the primary) is the critical secondary-mirror design parameter.
3. The secondary metering structure's fixed base natural frequency.

### C.2.c Structural Subsystem Analysis

#### C.2.c(1) Primary Mirror

##### Primary Mirror Assembly

The subsystem with greatest overall impact on optical performance of a large aperture orbiting telescope is the primary mirror assembly. The primary mirror is the most massive and most critical in tolerance of any single component. It serves as the basis for the collection of all optical information and also as the principal mechanical and structural reference for the telescope. In addition, the ability of the mounting arrangement to successfully isolate the mirror from those factors inducing motions and deformation to the primary surface is central to overall system performance. Thus, for purposes of optimum design the primary mirror assembly is considered both conceptually and analytically as a single interrelated system (consisting of the mirror and its mounting arrangement) separate from other structural assemblies.

##### Design Specifications

Various primary mirror assembly concepts were studied by using design specifications that evolved as the most suitable for evaluation in terms of overall mission objectives:

1. The mirror must be of a minimum-weight design in order to accommodate launch vehicle payload capabilities while satisfying all stiffness requirements.

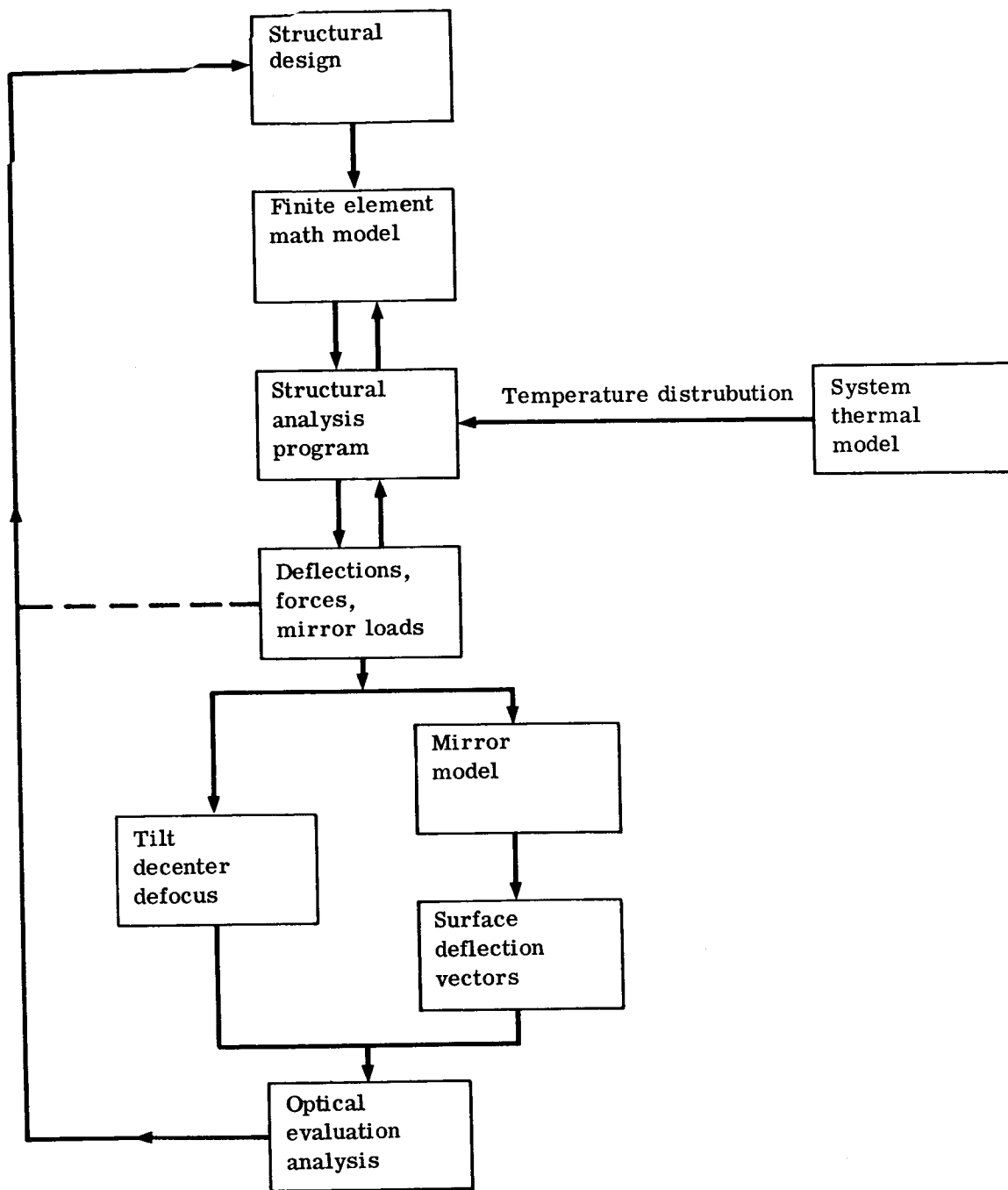


Fig. C.2-11 — Thermal structural response

Table C.2-1 – Selected Data From System Structural Model Analysis

Derived Parameter	Concept	
	All-Metal	Graphite-Epoxy OTA and SIP
Primary mirror rms surface error, micrometers	0.0007	0.0004
Thermal/optical sensitivity (despace), °C (°F)	-19 (3.1)	-13 (7.9)
Metering structure fixed base frequency, hz	13	24

2. The assembly must have a high natural frequency ( $>40$  Hz) to minimize effect on image motion.
3. The material chosen for the mirror must have good long-term stability.
4. On a basis of theoretical information concerning operational environment, materials with low and uniform expansion coefficient, high thermal conductivity, and high thermal diffusivity must be used.
5. Launch and reentry induced stresses to the mirror should be limited to 6.89 meganewtons/square meter (1,000 psi).
6. Intercell gravity release errors should be limited to  $0.005\lambda$  rms surface deformation ( $\lambda = 633$  nanometers).
7. Lap-loading induced stresses should be limited to 6.89 meganewtons/m<sup>2</sup> (1,000 psi).
8. The preferred mounting arrangement would be a universal type mount suitable for both launch and operational modes.
9. Induced mount stresses should be limited to values below 0.5x microyield stress (MYS).
10. Ferromagnetic mount materials should be avoided as much as possible.
11. Present mirror manufacturing limitations should be considered in the evaluation of all concepts.

#### Mirror Design

The initial step in the evaluation of a feasible design concept for the primary mirror was the selection of candidate materials that would satisfy the criteria for optimum performance. Two materials (ULE fused silica and Cer-Vit 101) were found to be exceptional in terms of overall material properties and were therefore chosen for consideration (see Section C.6 for detailed discussion of mirror material selection).

Since these materials are glass ceramics exhibiting relatively low strength and stiffness characteristics (thus making a solid mirror design weight prohibitive for present booster capabilities), only lightweight monolithic construction could be considered. This approach saves between 60 percent and 80 percent of mirror weight for mirrors of comparable overall dimensions. The unique fabrication techniques utilized in the manufacture of lightweight mirror blanks from each of the two candidate materials necessitated the development of two lightweight mirror designs with comparable optical performance.

The criteria considered most useful in the design of a lightweight mirror are intercell deflection due to zero g release, lap-loading (pressure of polishing tool), bending stiffness, and shear stiffness. Stress criteria are usually disregarded because past experience indicates that mirrors meeting any reasonable stiffness criteria exhibit relatively low stress levels and mirrors designed solely on the basis of stress fail to meet manufacturing stiffness requirements. Launch and reentry load factors are significant only as local stresses at the mirror/mount interface and have little effect on the gross integrity of the blank.

Intercell deflection due to zero g release and lap-loading must be maintained within specified tolerances (for the LST,  $\lambda/200$ ) to maintain the required figure. This requirement determines the necessary facesheet thickness for a specified monolithic cell size. Detailed analysis indicates the impact of any shear-stiffness criteria is minimal because blanks meeting bending criteria are more than adequate for shear loads. However, bending stiffness requirements cannot easily be established for a mirror to be used in a zero gravity environment. To adequately test an orbiting system in a 1 g field it would be advantageous to restrict deflections to within the operational performance budget. Unfortunately, the extremely stiff mirror blank necessary to achieve such an objective would result in a weight-prohibitive system. Therefore, it becomes necessary to design a test mount that simulates the zero g condition. Development of such mounts has been successfully accomplished for other large mirror assemblies whose



diameter exceeds 1.75 meters (69.0 inches). Alternatively, one could design an operational mount similar to the necessary optical test mount, but this solution would again result in excessive weight. It therefore becomes obvious that the only practical means of simulating the operational environment during testing is to use an acceptable operational mount and an appropriate method of simulating zero gravity conditions. Thus, the bending stiffness requirement is highly dependent on the design of a workable test mount (i.e., a lighter, more flexible mirror requires more extensive design of a test mount).

Several concepts were generated using the above criteria for both of the candidate materials. The best method of minimizing weight and maintaining stiffness was to limit the thickness of the faceplates as much as possible and to obtain greater stiffness by increasing core thickness. A 25.4-millimeter (1-inch) faceplate thickness was calculated to be acceptable under manufacturing requirements for both of the core cell configurations (ULE, Cer-Vit). Since a 50-millimeter (2-inch) access hole is required for machining the core geometry in a Cer-Vit mirror, and it is desirable to have equal weight in each faceplate, the backplate in all Cer-Vit designs was increased to 30.2 millimeters (1.19 inches). The tradeoff factor then encountered was a necessary increase in core thickness to obtain a stiffness consistent with test mount requirements and manufacturing limitations. This tradeoff necessarily results in a heavier mirror, given constant faceplate dimensions.

### Structural/Thermal Effects on Optical Quality

Itek has developed a method of predicting the optical surface degradation of large lightweight mirrors when subjected to structural and thermal environments, a process shown by the flow diagram of Fig. C.2-12.

Since lightweight cored mirrors are easily modeled in terms of finite number of grid points, a large mathematical model can be developed and analyzed by using one of several existing structural analysis digital routines (e.g., EASE, NASTRAN). By using all relevant thermal, structural, and boundary parameters as input, three-dimensional displacements and stresses can be determined at known locations on the mirror surface. Subsequently the mirror deformations for each loading condition can be optically evaluated by using an existing Itek program that accepts perturbed mirror surface deflection vectors, determines the best correctable surface based on these vectors, and computes the residual optical errors once the correction has been accomplished. The computed data are given in terms of rms surface errors. Tip, tilt, and contour maps of the deformed mirror surfaces are also generated.

### Mirror Model

A typical conceptual 3-meter (118-inch) primary mirror was modeled (see Fig. C.2-13) and analyzed by means of Itek's EASE structural-thermal digital program, using a CDC-6600 computer.

The mirror was divided into 768 nodes, 384 on each mirror surface. This model accounted in detail for the mirror's curvatures, its material, core grid pattern, and member sizes. The triangular element breakdown is given in Table C.2-2.

Table C.2-2 – Triangular-Element Model for 3-Meter (118-Inch) Primary Mirror

Location	Number of Triangles
Top surface	672
Bottom surface	672
Core parallel to y axis	504
Core parallel to z axis	504
Outer periphery	168
Inner periphery	24
	2,544

This degree of detail was necessary for an adequate representation of the mirror in a deformed mode thus permitting the effect of deformations on the optical wavefront to be accurately assessed.

### Mirror Stresses

Table C.2-3 gives the induced mirror maximum stress levels for an 8.4 g launch loading. The element numbers correspond to the specific finite elements in the mirror model experiencing the highest stress levels. For the 8.4 g

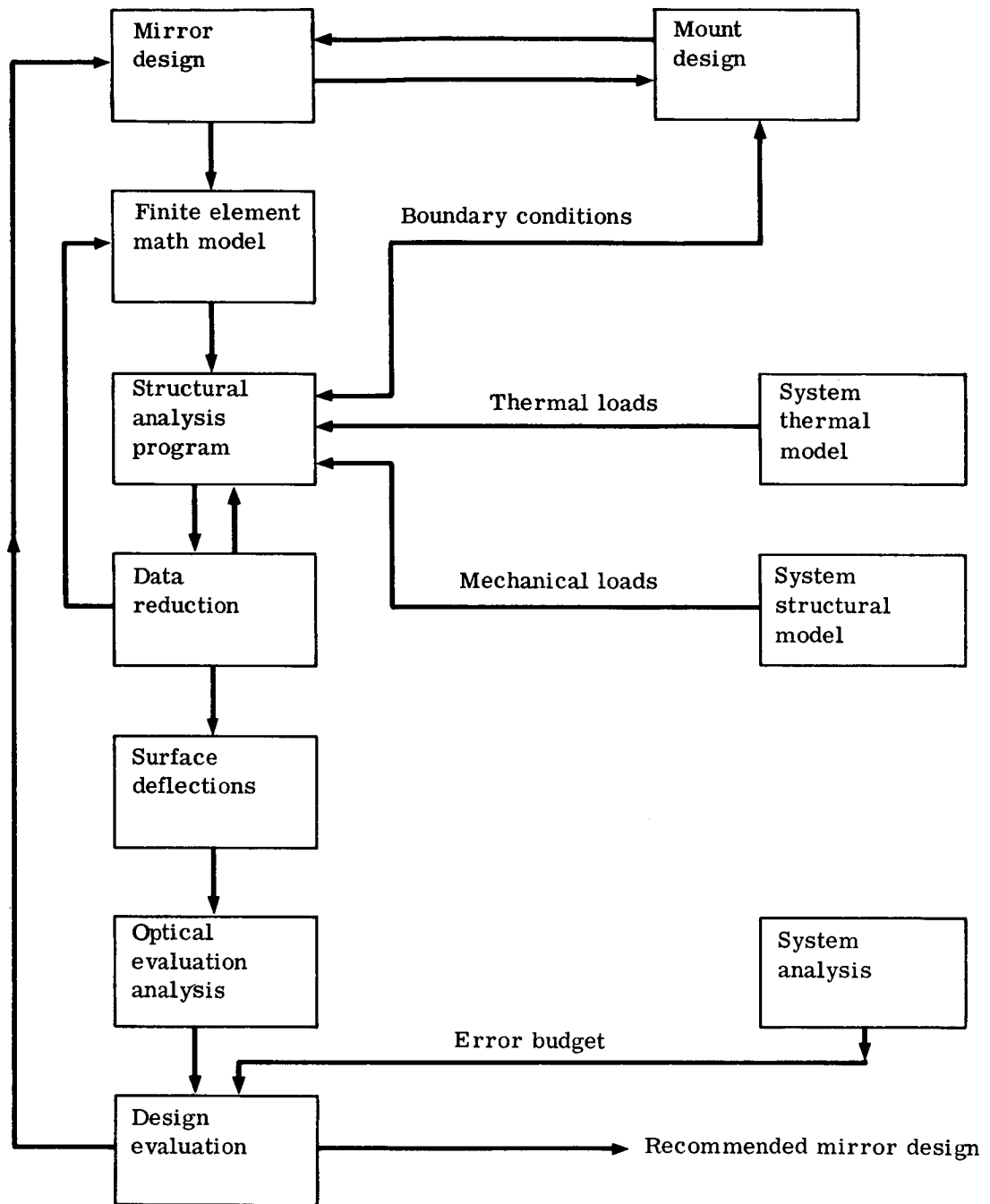


Fig. C.2-12 — Mirror analytical flow diagram

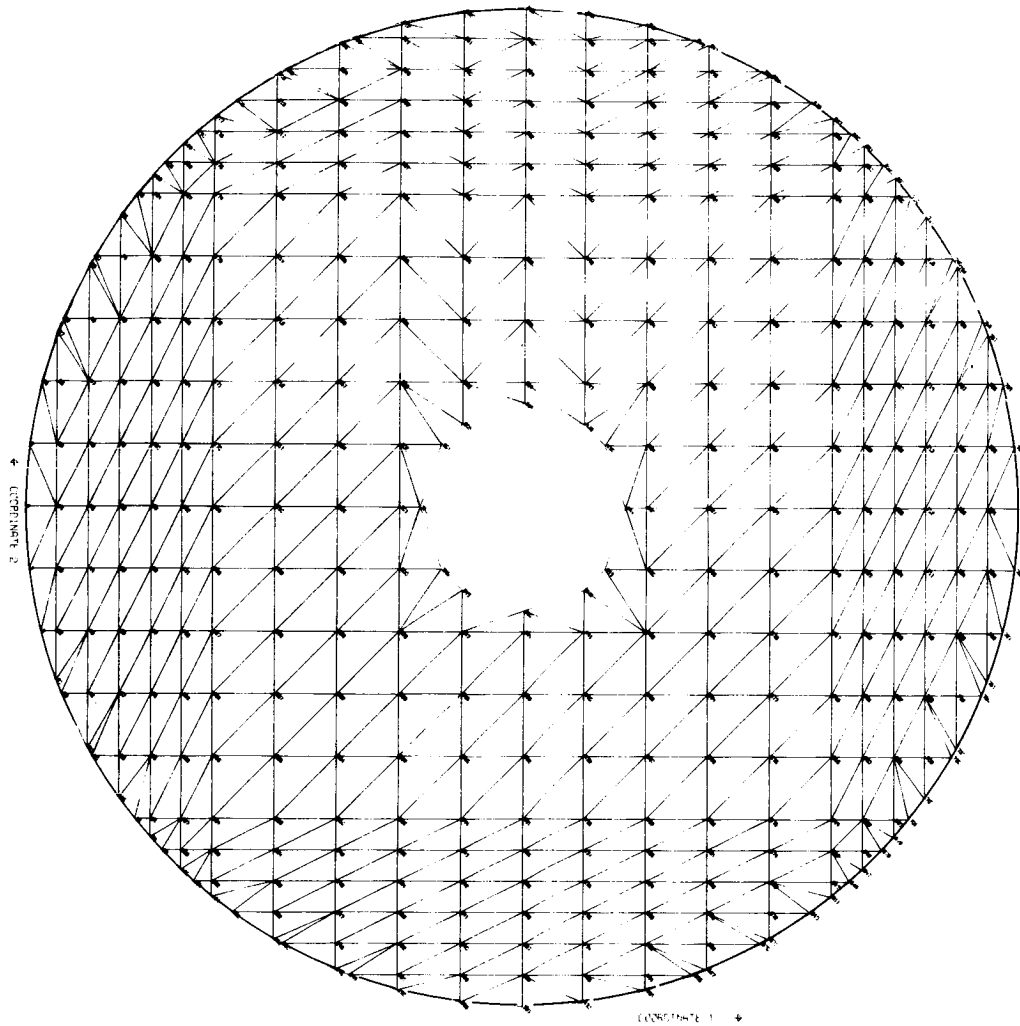


Fig. C.2-13 — 3-meter monolithic mirror

loading condition, the maximum internal stress (stress occurring away from the mirror periphery) is 0.79 meganewton per square meter and the maximum edge stress is 5.4 meganewtons per square meter. The internal stresses are well below the mirror allowable stress of 6.89 meganewtons per square meter; the edge stress, occurring at the reaction locations, approaches allowable limits. It should be noted that these stresses were based on point reactions whereas, in reality, the mount will distribute the reactive load over a finite area. This distribution will not greatly reduce the internal stresses, but will certainly reduce the edge stresses. Inspection of the elements around the highly stressed reactive points indicated a sharp drop in stress level. From this it is reasoned that the edge stress levels in the real mirror are considerably below allowable values.

Table C.2-3 – Launch-Induced Mirror Stresses

Stress Location Edge Element Number	Edge Stress, meganewtons per square meter	Internal Element Number	Internal Stress, meganewtons per square meter
1299	4.0	401	0.70
2374	4.5	403	0.79
2375	4.0	448	0.60
2436	5.4	450	0.59
2494	4.6	491	0.57

### C.2.c(2) Mirror Mount Design

The most important consideration in the design of a reliable mirror mount is the effect it has on the optical element it supports. It must effectively maintain the optical alignment of the system while isolating the mirror from any forces capable of causing mirror motions and surface deformations. These factors include launch dynamics, thermal excursions, orbital dynamic disturbances, long-term material instabilities, assembly-introduced strains and gravity release. The design criteria found useful in evaluating mount concepts by limiting these factors are as follows: (1) accommodate group handling, launch loads, and pressurization loads (stress levels below 1/2 microyield stress; (2) limit thermally induced surface errors to 0.0025 micrometer; (3) keep lateral, axial, and pitching natural frequencies in excess of 40 hertz.

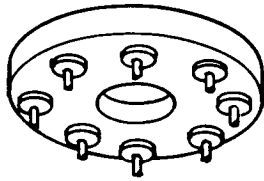
In general, the mirror could be supported in one of three configurations; back support, edge support, or a combination of the two. The mirror mounting arrangements shown in Fig. C.2-14 are discussed fully in Itek Report 71-9463-2, which indicated the superiority of a universal-type, three-point, edge-mounting arrangement. Only that type will be discussed in detail. It is interesting to note, however, that two other mounting concepts, each showing promise, were briefly considered during the study. These are (1) a three-point, articulated truss-type mount that minimizes thermally induced loads and (2) a six-point peripheral mount that minimizes the design problems associated with developing a simple test mount (one that simulates the zero gravity condition). It is believed that an optimum universal mount can be developed by incorporating the salient features of the above approaches with the recommended three-point mount. The resulting mount design (see Fig. C.2-15) would support the mirror at six points, which by truss action will terminate at three base points. The mounts themselves will have flexures incorporated to approach the articulated condition that transmits low thermal strains. Because feasibility of the three-point configuration was clearly demonstrated, the six-point concept was not further studied at that time.

#### Three-Discrete-Point Mount

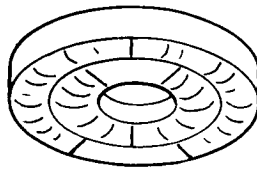
With this mount the mirror is supported at three points symmetrically located at the mirror's periphery. This type of mount results in unsymmetrical loads and deformations and causes the mirror to experience launch-induced stresses higher than those encountered with back-supported mounts. However, if the mounting arrangement is kinematic, or nearly kinematic, a large class of foundation movements results in mirror rigid-body motions that are optically correctable. Flexure mounts, or near-kinematic systems, can be devised to eliminate this problem because it provides the designer with a system that has predictable errors. Because of the predictable nature of the three-point, near-kinematic mount, various concepts of this system were studied. Fig. C.2-15 shows the basic mounting concepts that were evaluated: the tangent bar, the axial leaf, and the A-frame mounts.

#### Tangent Bar

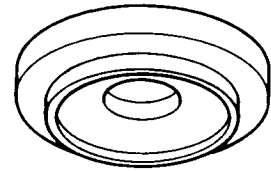
The mirror is supported on three tangential flexures stiff in both the axial and tangential directions and compliant in the radial direction. The attachments are located at equally spaced, peripheral points,  $2\pi/3$  radians



Many discrete points

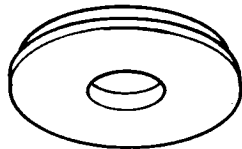


Segmented air bags

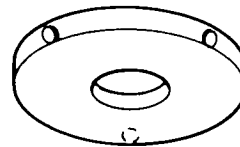


Continuous ring

(a) Back supported



Continuous edge ring



Three-point

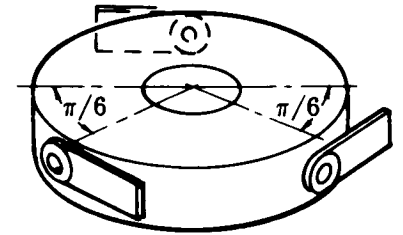
(b) Edge supported

Fig. C.2-14 — Mirror mounts

6-point connection →

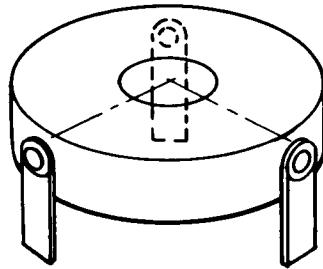
3-point base →

↙ Flexures

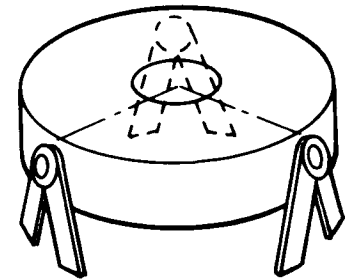


(a) 6-point

(b) Tangent bar, 3-point



(c) Axial leaf, 3-point



(d) A-frame, 3-point

Fig. C.2-15 — Point mount types

apart. It is pertinent to point out that compliance in the radial direction is the central feature of all near-kinematic mounts. The mount has adequate stiffness in selected directions to meet frequency and strength requirements, yet is sufficiently flexible in the critical radial direction to permit differential thermal movements with little induced strain.

#### Axial Bar

In this case, the mirror is supported at its three peripheral points by bar members whose longitudinal axes are parallel to the optical axis. This mount achieves its axial stiffness through column action and its tangential stiffness through flexure about the bar's stronger axis. The axial bar derives its radial compliance by offering its weaker flexural axis to radial motions.

#### A-Frame

The mirror is supported at three points as in the previous cases. This mount may be best understood as a variation of the axial bar mount in that its stiff axis is parallel to the optical axis. The major differences between the two types are that tangential stiffness is provided by truss action of the A-frame in the plane of its legs and that each mount has two attachment points at its foundation.

When considering the design of a mirror mount and its interaction with the mirror, it is necessary to include a detailed representation of the mirror in the basic mathematical model. The need for a detailed mirror-mount model is made evident and appreciated only when the sensitivity of the mirror to the mount stiffness is evaluated, i.e., the mirror is extremely conscious of, and susceptible to, mount strains and movements. For this reason, reference is made to the previous discussion of the mirror model.

The mirror boundary conditions were selected to match the candidate three-point mounts, which are radially compliant and axially and tangentially stiff. Therefore, the mirror was grounded at three peripheral nodes  $2\pi/3$  radians apart in the axial and tangential directions and unrestrained in all other directions.

After the mirror mathematical model was constructed, a set of mirror deformations was digitally generated for a series of selected loading cases. These deformation sets were optically evaluated to establish sensitivity to each of the loading cases. To effectively use the sensitivity data, superposition of dissimilar loadings (e.g., radial loads with tangential moments) were arithmetically developed. From these data, a mount evaluation chart was developed that included the effects of optical tolerances, thermal data, launch loadings, and required stiffness.

Materials chosen for consideration in the mount application were Invar and titanium, the former due to its low thermal expansion coefficient and the latter for its high microyield strength and dimensional stability. Because the use of Invar allows greater latitude in allowable thermal gradients and the microyield strength is high enough for the accommodation of launch-induced stresses, Invar was selected as the recommended material.

An examination of the three candidate three-point mount concepts by means of equivalent cross sectional dimensions indicate that tangent bars and axial-leaves produce lower rms surface errors than those produced by A-frame mounts (see Itek Report 71-9463-2 for a more detailed discussion). Furthermore, the utilization of axial-leaves in lieu of tangent bars results in a smaller main ring configuration and therefore a smaller overall payload diameter. Thus, the axial-leaf concept was given primary consideration. Further analysis into this fixed-end concept indicated that reduction of induced mirror moments could better be accomplished by the utilization of a bearing surface, e.g., a spherical ball insert for attachment purposes. More detailed investigation is necessary to evaluate the possible advantages of using A-frame links, i.e., a mount that allows relative articulation of the link legs; this concept presently shows promise. This concept limits the induced mirror load sources to frictional in that it virtually eliminates bending; however it does add a degree of mechanical complexity.

Environmental temperature changes result in variable thermal excursions in the mirror, mounts, and main ring-pressure bulkhead. The mounting arrangement must accommodate the relative growth between the mirror and the ring-bulkhead in order to minimize the induced strains. In addition to the thermal gradient this growth is proportional to the respective radii and material coefficients of thermal expansion of the mirror and the main ring.

A linear relationship can be established between the radial mount force and the temperature gradient by assuming that the radii of the mirror and ring are approximately equal and by introducing a constant which is a function of mount geometry and material properties.\* Fig. C.2-16 shows the relationship between this stiffness/expansivity constant and the radial mount force for various thermal gradients.

Active thermal control of the primary mirror and the main ring will result in a maximum radial gradient of 2°C. For the selected mount concept the stiffness/expansivity constant is equal to 24.2 N/m/°C which results in a maximum radial mount force of 22.5 newtons.

Extensive structural modeling of the optical telescope assembly which took into account the effects of both the secondary support structure and the scientific instrumentation support structure was utilized to determine the loads into the mount under operational environmental temperature conditions. Several models which reflected each of the various structures and materials under consideration were analyzed. The results indicated that the maximum radial mount force would be 40.5 newtons for an Invar-titanium structure and 22.5 newtons for a graphite-epoxy composite structure with titanium ring. Examination of Fig. C.2-17, which relates radial force to rms surface error, shows that all of the computed radial mount forces would result in surface errors well within the established budget.

Launch induced stresses are derived by assuming rigid body motion of the primary mirror during the loading phase. The dynamic loading factors which were applied to the mirror were ±6.0 g longitudinal, and ±1.5 g lateral. The critical design stresses computed for an axial leaf, spherical ball insert mount were:

Maximum bending stress	= 26.2 MN/m <sup>2</sup>
Maximum axial stress	= 24.7 MN/m <sup>2</sup>
Critical stability stress	= 385 MN/m <sup>2</sup>

The design criteria dictate that launch induced stresses be below one-half the microyield stress of the mount material. Since the microyield stress of Invar is 122 MN/m<sup>2</sup> it is evident that the proposed mount arrangement can adequately support the primary mirror during launch.

Fulfillment of dynamic design requirements for maintaining optical alignment dictates that the minimum lateral, axial, and pitching frequency for the mount arrangement be 40 Hz. For the proposed mount design the natural frequencies are:

$f_n$ lateral	= 172.6 Hz
$f_n$ axial	= 468.1 Hz
$f_n$ pitch	= 569.5 Hz

These values easily satisfy the design requirements.

Earlier primary-mirror concepts proposed the utilization of integral external mounting trunnions. However, consultation with mirror manufacturers indicated that the integration of external trunnions to any mirror blank would result in additional fabrication complexity and cost. Therefore, a study was initiated in order to develop alternate mount attachment concepts.

The 5 concepts shown in Fig. C.2-18 were devised to satisfy the design criteria, requirements, and goals established in Itek Reports 71-9463-2 and 71-8209-1. A brief discussion of these concepts follows.

---

\*This constant,  $p = \frac{\alpha E b h^3}{4L^3}$  (N/m/°C) has been referred to as the stiffness/expansivity constant and was previously introduced in referenced Itek Report 71-9463-2.



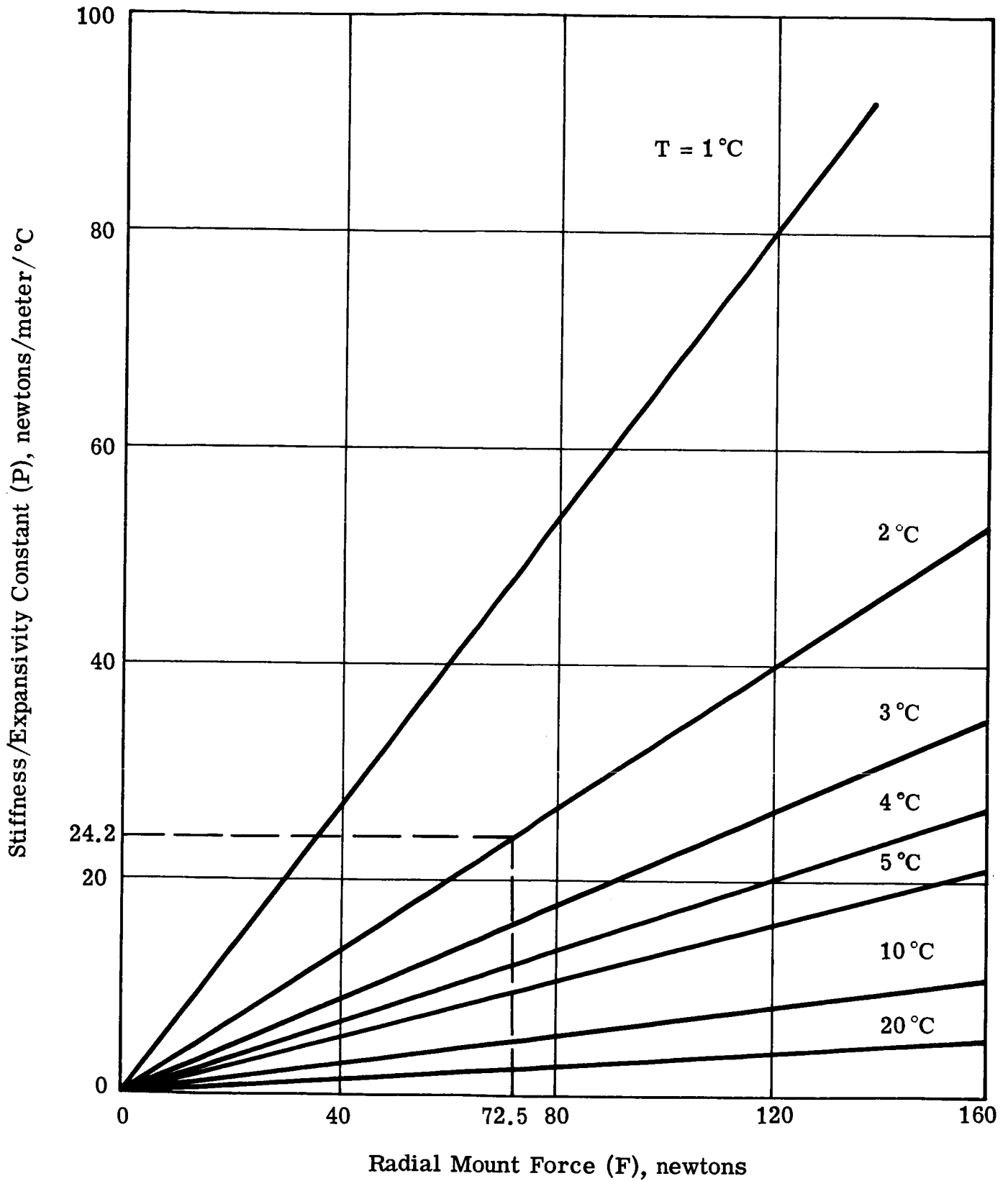


Fig. C.2-16 — Axial-leaf, cantilevered, 3-meter mirror radial mount force versus stiffness/expansivity constant for a 3-meter mirror subjected to various temperatures

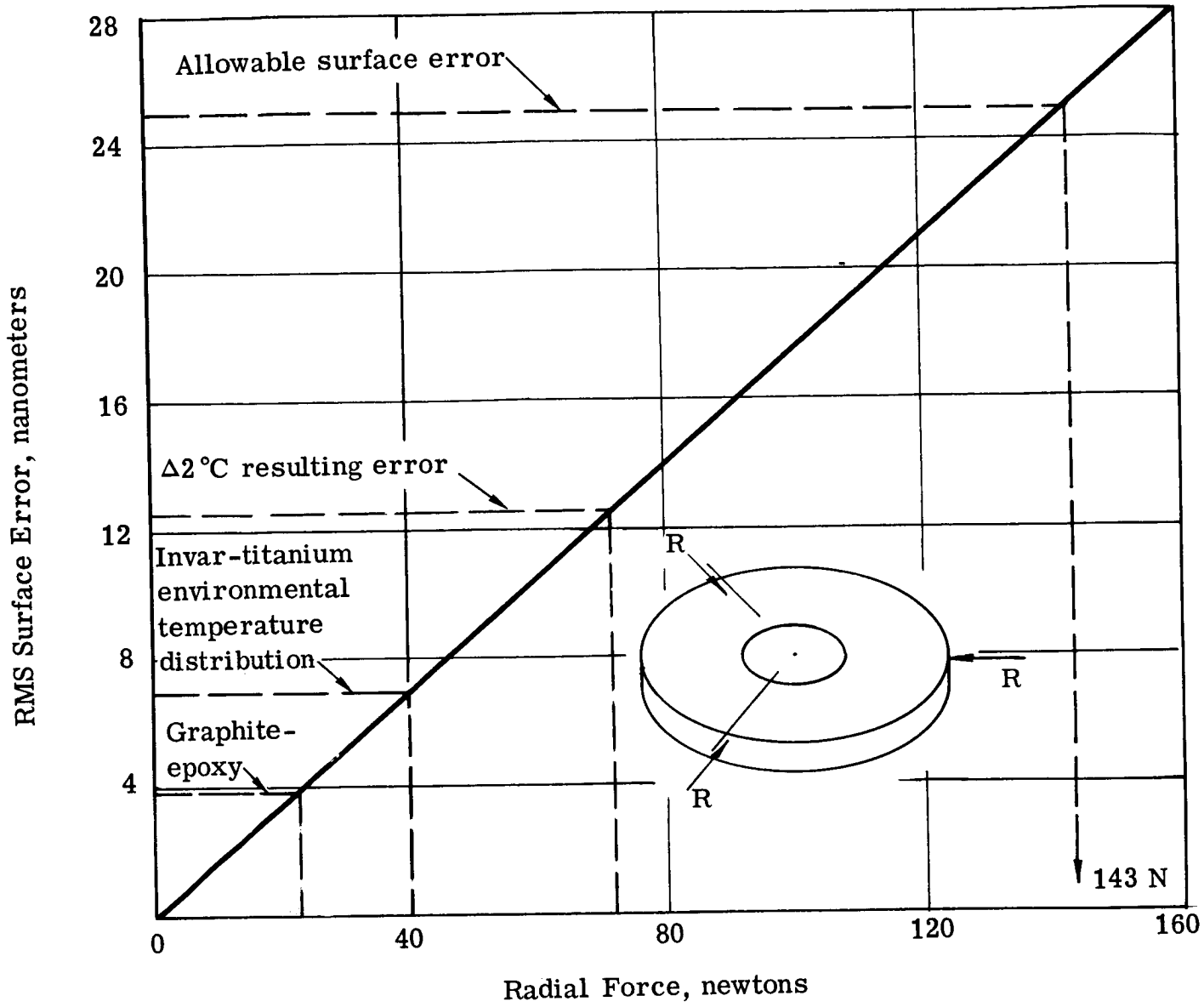
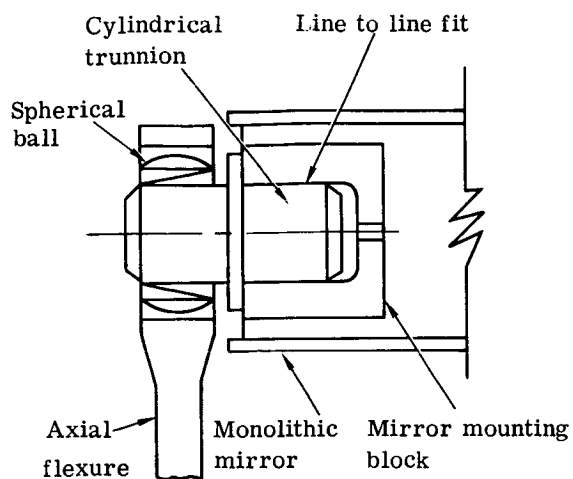
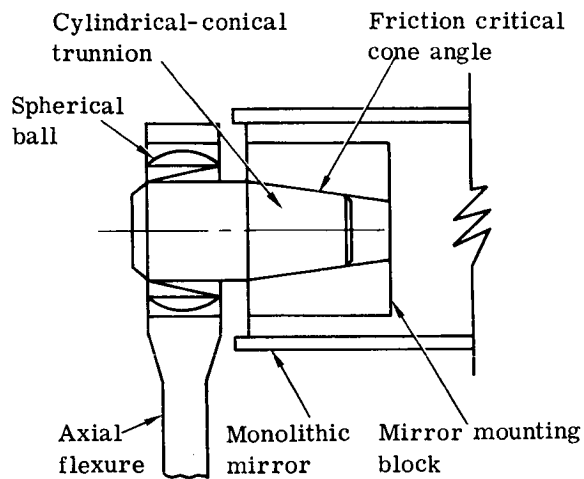


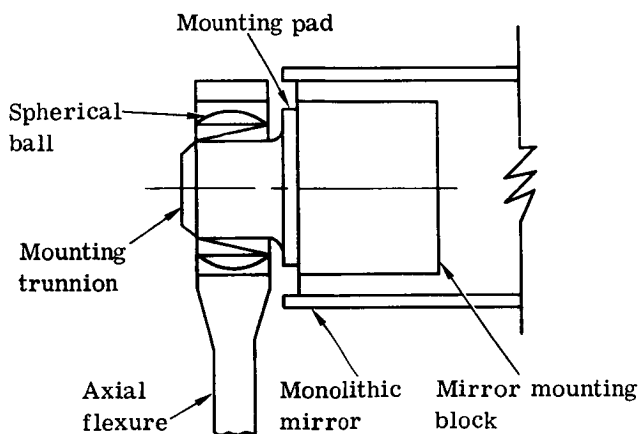
Fig. C.2-17 — RMS surface error of a 3-meter monolithic mirror for radial loads at three points



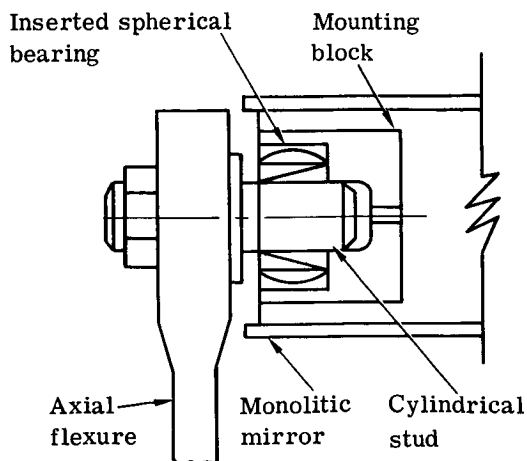
(a) Attachable cylindrical trunnion



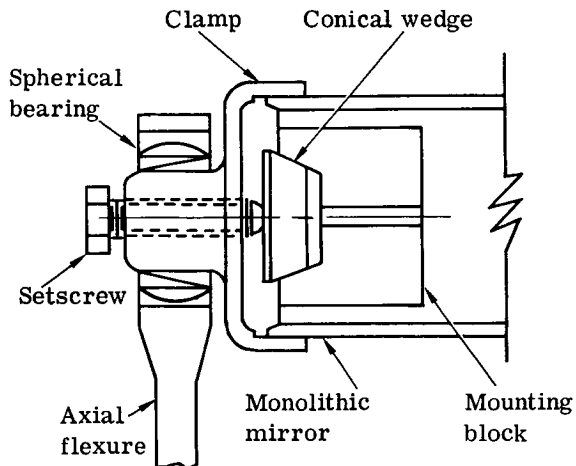
(b) Taper-key attachable trunnion



(c) Pad-mounted trunnion



(d) Inserted-bearing mount



(e) Clamped-edge mount

Fig. C.2-18 — Mirror-mount attachment concepts

### Attachable Cylindrical Trunnion

In Fig. C.2-18a a cylindrical trunnion is inserted into the mounting hole in the mirror blank by means of a line-to-line fit (either sliding, preloaded joint, or bonded) and in turn is attached to a flexure mount by means of a preloaded special bearing. The bearing is accepted by the flight flexure which terminates at the main ring. The internal blocks were slightly enlarged to account for the mounting bore.

### Taper Key Attachable Trunnion

In Fig. C.2-18b a machined coaxial trunnion tapered to the critical locking angle is inserted into a similarly tapered hole in the mirror to provide a rigid connection by means of static friction. The trunnion is then attached by a spherical preloaded bearing to a flexure mount.

### Pad-Mounted Trunnion

(See Fig. C.2-18c.) This mount consists of a single-piece, cylindrical trunnion and pad which would be bonded to the exterior of the mirror mounting blocks. The flexure mount again is connected to the trunnion by means of a spherical bearing. The block is indicated as solid as it needs no mounting bore.

### Inserted Bearing Mount

(See Fig. C.2-18d.) In this design, the flexure mounts are rigidly connected to cylindrical bars inserted into spherical bearings that have been inserted into the mirror and are attached by means of a bearing preload. This mounting concept induces the least edge moment into the mirror but effects of bearing preload must be evaluated.

### Clamped Edge Mount

(See Fig. C.2-18c.) In this design, a clamping apparatus is tightened upon the edges of the mirror by means of a tightening screw. The clamp is secured to the flexure mount by means of a spherical bearing. This concept introduces undesirable mirror tensile stresses at the conical wedge interface. Effects of the clamp on the mirror must be further studied.

## C.2.c(3) Metering Truss Design

The primary consideration in the design of the LST metering structure (Itek dwg. 911390) was to maintain spatial stability of the secondary mirror with respect to the primary mirror during dynamic and thermal operating conditions. The opto/structural design tolerances required are:

1. Allowable despace of secondary mirror relative to primary mirror =  $\pm 2$  micrometers
2. Allowable decenter of secondary mirror relative to primary mirror =  $\pm 10$  micrometers
3. Allowable tilt of secondary mirror =  $\pm 4.85$  microradians ( $\pm 1$  arc-second)
4. Fundamental lateral fixed base frequency greater than 15 hz.

Preliminary studies (see Itek Reports 71-8209-1 and 70-9443-1) indicated a preference for a rigid truss structure mainly for its adequate stiffness, its lack of launch or load-sharing devices, its compatibility with thermal control requirements, and its manufacturability. In developing the preferred design, four major variations of this concept were considered:

1. An eight-point (16 members per bay) Invar-titanium truss
2. A twelve-point (24 members per bay) Invar-titanium truss
3. An eight-point aluminum-titanium truss
4. An eight-point composite material (graphite-epoxy) truss.

The major tool in the analysis of each concept was the EAC/EASE digital program.\*

---

\*The EAC/EASE (Elastic Analysis for Structural Engineering) computer program provides static structural analyses of linear three-dimensional systems using an application of the direct stiffness method.

Before discussing these analyses and their results, it is instructive to consider the "athermalizing" effort that is easily incorporated into a truss design comprised of ring and strut members with varying coefficients of linear thermal expansion. This approach selects the truss configuration (axial positioning of the rings and hence the number and orientation of the struts) such that the thermally induced axial growth of each truss member is compensated by the thermally induced radial growth of the rings. This compensating mechanism results in a radical reduction in axial growth of the secondary mirror location relative to the primary mirror location and hence a thermally inert structure. Preliminary geometries were established using the relationships given in Table IIB-27 of Itek Report 71-8209-1, dated 15 October 1971 and will not be repeated here. These geometries were then refined by computer analyses of the mathematical models to be discussed.

#### Metering Truss Analysis

Each metering structure configuration was evaluated in terms of thermo-structural response, weight, stiffness (fundamental natural frequency) ease of manufacture, and space requirements. The thermo-structural response characteristics of the candidate concepts were determined by subjecting them to the following temperature distributions:

1. Uniform soak of 5.55°C (10°F) – that is, the entire structure experiences a 5.55°C change in temperature from its base temperature.
2. An axial temperature gradient of 5.55°C – that is, the structure experiences a linear axial gradient from the primary ring to the secondary mirror support spider. There is no circumferential variation.
3. A circumferential temperature gradient of 5.55°C – that is, the structure experiences a linear diametral temperature variation from one side to the other with no axial variation.

In addition, orbiting temperature distributions were determined for the recommended case.

#### Eight-Point Invar-Titanium Truss

The eight-point Invar-titanium truss (see Fig. C.2-19, a typical computer plot of the mathematical models utilized) was the first concept considered in depth. This structure consisted of four titanium rings including the primary ring/pressure bulkhead, connected by tubular Invar struts. The secondary assembly was supported by a four-legged Invar spider extending from the foremost ring.

Fig. C.2-19 shows the node points and their interconnecting beam elements. Node 81 represents the location of the secondary mirror. Several computer runs were made with varying geometries in an attempt to optimize the configuration for each material combination. The resulting effective coefficient of thermal expansion\* was found to be  $0.057 \times 10^{-6}$  m/m/°C for a uniform temperature soak. Corresponding effective coefficients of thermal expansion values of  $0.412 \times 10^{-6}$  and  $0.86 \times 10^{-6}$  m/m/°C for axial gradients and circumferential gradients, respectively, were also determined.

An approximation of the first fundamental lateral and axial frequencies from the EASE program displacement data yielded a lateral frequency of 13 hz and an axial frequency of 22 hz. The lateral frequency can be increased by judiciously varying the section properties from bay to bay along the truss to improve the overall stiffness.

---

\*The effective coefficient of thermal expansion ( $\lambda^*$ ) is defined as

$$\lambda^* = \frac{\delta}{\ell \Delta T} \text{ in which}$$

$\delta$  is the calculated dilation of the structure of axial length  $\ell$  undergoing a soak temperature of  $\Delta T$ .

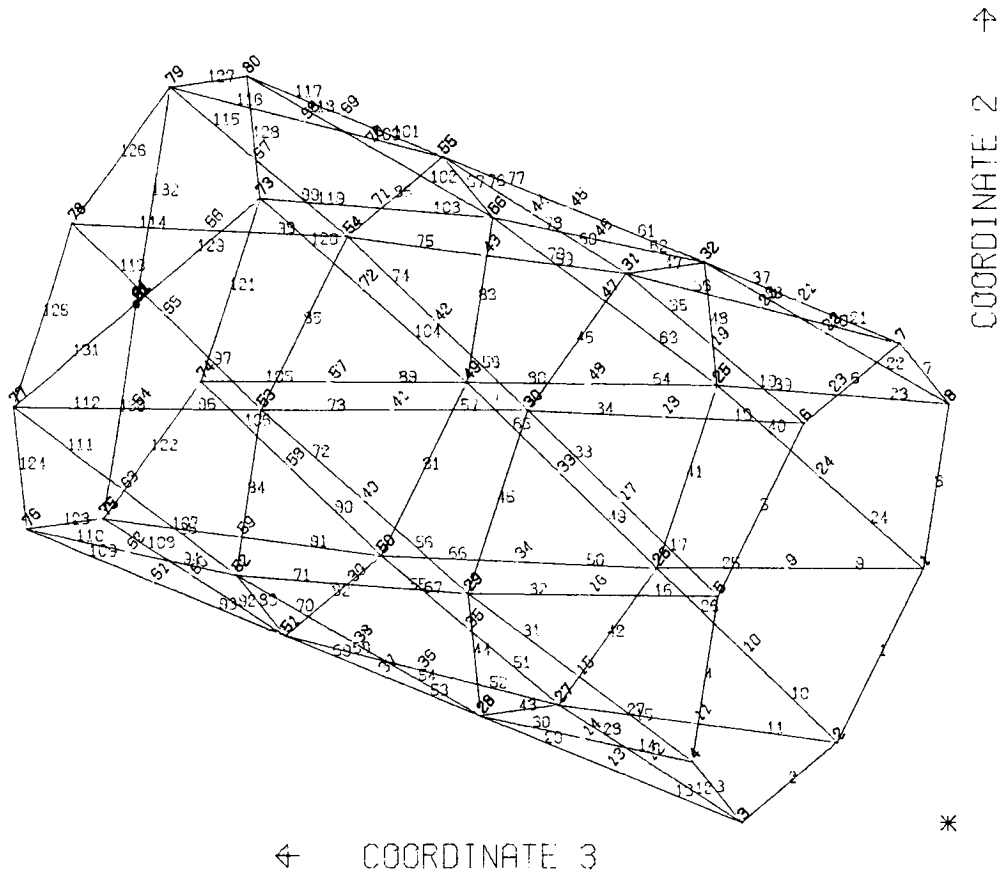


Fig. C.2-19 — Computer drawing of eight-point Invar-titanium truss

### Twelve-Point Invar-Titanium Truss

The twelve-point, five-bay (24 struts per bay) concept was developed in an attempt to increase the stiffness of the structure, to decrease the required annular volume, and to configure a truss whose strut pickup points are compatible with the four-legged spider and the three-point primary mounts. This latter goal was desired to reduce induced bending at the primary ring. Fig. C.2-20 is a sketch of this configuration indicating the need for 5 rings due to strut angle increase.

As the number of members increases, the structure acquires some of the properties of a cylindrical shell, i.e., radial symmetry, good stiffness, and increased weight. Thus with the increase in structural members required, this concept became a tradeoff of frequency and weight. The resulting effective coefficient of thermal expansion was  $0.207 \times 10^{-6} \text{ m/m/}^\circ\text{C}$  for a uniform soak. Other data are given in Tables C.2-4 and C.2-5.

### Eight-Point Aluminum-Titanium Truss

An aluminum-titanium truss concept was considered in an effort to decrease the amount of ferromagnetic materials in the structure. The interaction of ferromagnetic materials and the earth's magnetic field becomes a problem when induced torques in the telescope exceed the system's torque balancing capabilities. The level of induced torque is dependent on the amount and distribution of magnetic materials and their magnetic strengths. Because Invar has questionable magnetic properties a substitute structure with aluminum rings and titanium struts evolved. Proper athermalization of this concept required a six-bay, seven-ring structure with 16 members per bay.

The analysis to date has indicated a lateral frequency of 16 hz and an axial frequency of the same value. This decrease in axial frequency is due to the lower modulus of elasticity of aluminum as compared to that of Invar. However, it is felt that the frequencies of this concept can be increased by increasing the sections of the titanium struts. This increase of course, will result in additional weight. This concept weighs 220 kilograms (484 pounds) as compared to 349 kilograms (767 pounds) for the 8-point, Invar-titanium truss. It is further felt that if this configuration's weight approached that of the Invar-titanium truss its natural frequency would increase to a comparable and acceptable level.

### Eight-Point Graphite-Epoxy Truss

A graphite-epoxy composite material concept was also studied but with greater emphasis since its low thermal expansion, lightweight, and nonferromagnetic characteristics made it an ideal candidate material. The structural aspects of this design were the same as the eight point Invar-titanium concept except for the sectional properties of the struts.

The coefficients of thermal expansion and longitudinal elastic modulus are a function of lamina orientation (Fig. C.2-21). In the process of optimizing the design the coefficient of thermal expansion was used as the independent variable with the resulting study becoming a tradeoff between elastic modulus and thermal coefficient. Proper athermalization of this concept required a ratio of ring to strut coefficient of thermal expansion of 9:1.

The optimum laminate for our structure was found to be  $(0/90)_2$  for the struts and  $(0_2/\pm 15)_8$  for the rings and spider. Thermal and dynamic analyses for this structure show a fundamental lateral frequency of 24 hz, an axial frequency of 29, and an effective coefficient of thermal expansion of  $0.074 \times 10^{-6} \text{ m/m/}^\circ\text{C}$ .

The metering truss structural concept is a series of circular rings interconnected by struts. The secondary mirror assembly is supported by a four-legged spider that feeds its load into the top truss ring at the ring's quadrant points. To decrease the inward intrusion, and hence obscuration and space envelope of the truss members, and to achieve a favorable stiffness to weight ratio, a three-bay, eight-point truss was finally selected.

The most attractive feature of the truss concept is its potential of providing a structure whose overall axial growth is thermally inert through judicious manipulation of coefficients of expansion for the rings and struts. Detailed thermal response and frequency calculations of several truss configurations and material combinations were performed to optimize its stiffness and thermal characteristics. This analysis was performed to a level of detail sufficient to establish this approach as a feasible concept.

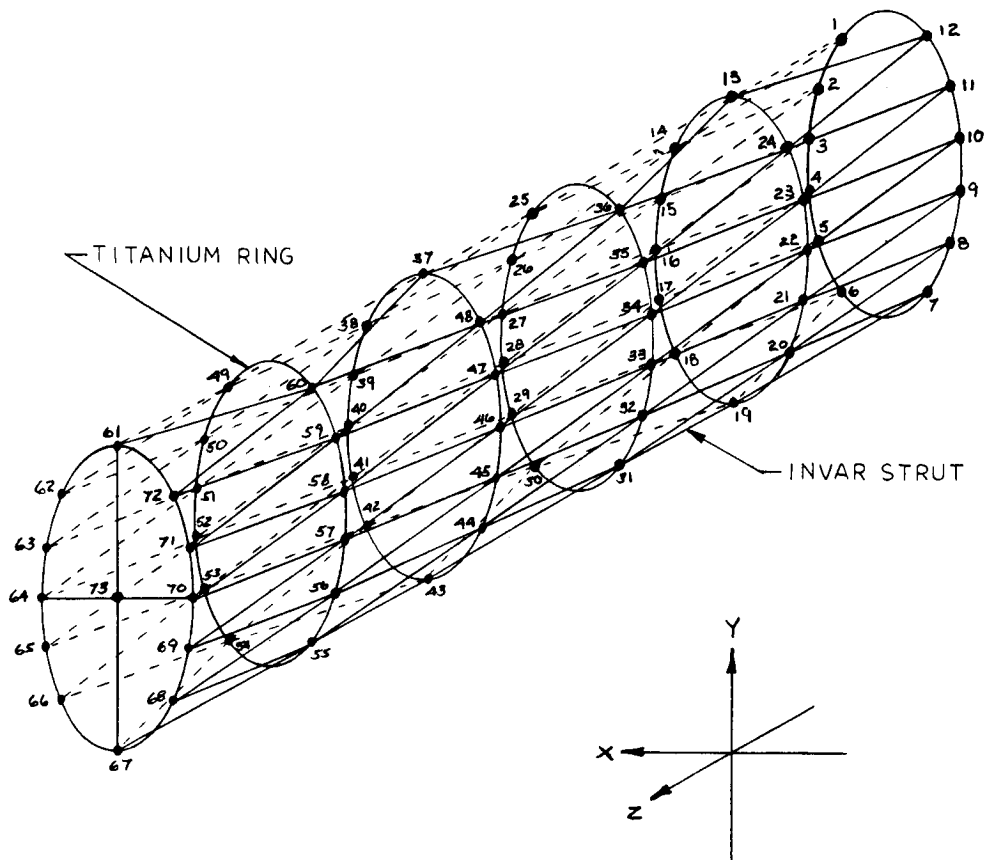


Fig. C.2-20 — OTA secondary metering structure



Table C.2.4 — Comparative Truss Characteristics

	Uniform Temperature Soak		Axial Gradient		Circumferential Gradient			
	$\alpha_{\text{eff}} \times 10^{-6}$	$\Delta T_{\text{all}}$	$\alpha_{\text{eff}} \times 10^{-6}$	$\Delta T_{\text{all}}$	Defocus		Tilt	
					$\alpha_{\text{eff}} \times 10^{-6}$	$\Delta T_{\text{all}}$	$\alpha_{\text{eff}} \times 10^{-6}$	
Invar-titanium 8-point truss	0.057 (0.032)	6.2 (11.2)	0.41 (0.23)	1.7 (3.1)	0.06 (0.03)	12.4 (22.4)	0.86 (0.48)	2.4 (4.4)
Invar-titanium 12-point truss	0.207 (0.115)	1.7 (3.1)	0.34 (0.19)	2.1 (3.8)	0.21 (0.12)	3.4 (6.1)	0.29 (0.16)	6.9 (12.5)
Aluminum-titanium 8-point truss	0.63 (0.35)	0.6 (1.0)	1.1 (0.62)	0.63 (1.1)	0.94 (0.52)	0.78 (1.4)	1.5 (0.83)	1.4 (2.5)
Graphite-epoxy 8-point truss	0.074 (0.041)	4.8 (8.7)	0.16 (0.09)	4.4 (7.9)	0.07 (0.04)	9.7 (17.4)	0.18 (0.10)	11.7 (21.1)

Note:  $\alpha_{\text{eff}}$  in meters/meter/°C and in./in./°F.  
 $\Delta T$  in °C and °F.

Table C.2-5 — Comparative Truss Characteristics

	Rings		Spider		Struts		Bay Length, meters (inches)	Total Length, meters (inches)	Frequency, hz.		
	Area, m <sup>2</sup> (in. <sup>2</sup> )	Material	Area, m <sup>2</sup> (in. <sup>2</sup> )	Material	Area, m <sup>2</sup> (in. <sup>2</sup> )	Material			Y	Z	Weight,* kilograms (pounds)
Invar-titanium 8-point truss	5.28x10 <sup>-4</sup> (0.820)	Titanium	1.85x10 <sup>-3</sup> (2.875)	Invar	1.97x10 <sup>-4</sup> (0.306)	Invar	1.87 (73.5)	5.73 (225.4)	13	22	348 (767)
Invar-titanium 12-point truss	4.73x10 <sup>-4</sup> (0.734)	Titanium	1.85x10 <sup>-3</sup> (2.875)	Invar	1.80x10 <sup>-4</sup> (0.280)	Invar	1.15 (45.3)	5.75 (226.5)	16	30	401 (884)
Invar-titanium 12-point truss	4.73x10 <sup>-4</sup> (0.734)	Titanium	9.47x10 <sup>-4</sup> (1.469)	Titanium	1.80x10 <sup>-4</sup> (0.280)	Invar	1.15 (45.3)	5.75 (226.5)	17	26	374 (825)
Aluminum-titanium 8-point truss	5.28x10 <sup>-4</sup> (0.820)	Aluminum	9.47x10 <sup>-4</sup> (1.469)	Aluminum	1.97x10 <sup>-4</sup> (0.306)	Titanium	0.859 (33.8)	5.73 (225.4)	16	16	220 (484)
Graphite-epoxy 8-point truss	5.28x10 <sup>-4</sup> (0.820)	Graphite-epoxy $\alpha=3.08\dagger$ $E=24.1\dagger$	9.47x10 <sup>-4</sup> (1.469)	Graphite-epoxy $\alpha=3.08\dagger$ $E=24.1\dagger$	2.2x10 <sup>-4</sup> (0.342)	Graphite-epoxy $\alpha=-.342\dagger$ $E=15.5\dagger$	1.87 (73.5)	5.73 (225.4)	24	29	81.6 (180)

\* Weight does not include secondary mirror assembly and miscellaneous fittings.

†  $\alpha$  in meters/meter/°C.‡  $E$  in newtons/meter<sup>2</sup> x 10<sup>10</sup>.

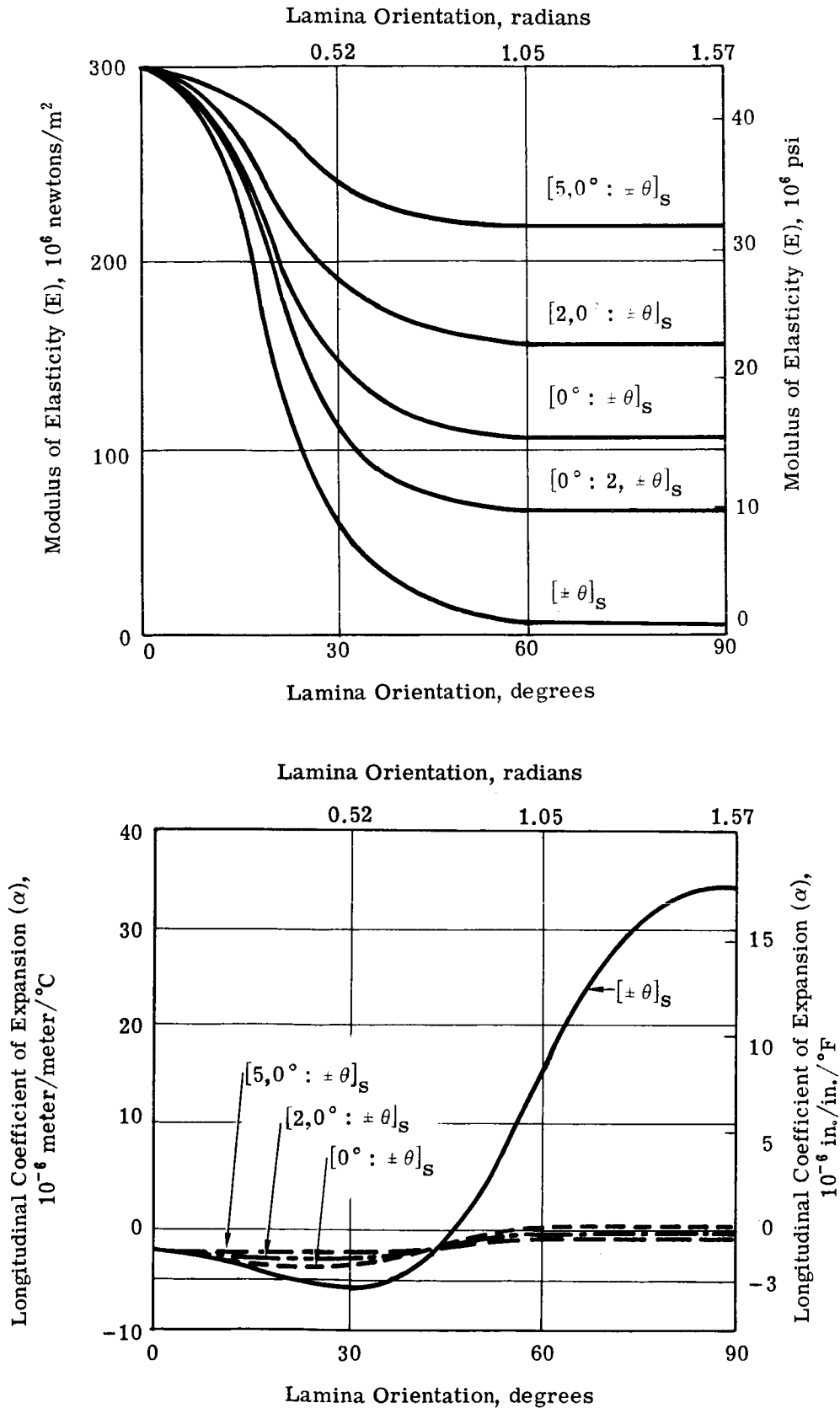


Fig. C.2-21 — Modulus of elasticity and longitudinal coefficient of expansion versus lamina orientation of eight-point graphite-epoxy truss

The material selection for the baseline truss concept is graphite-epoxy composite material. In addition to being lightweight and nonferromagnetic the composite can be tailored to meet the thermal and structural design goals. Its major drawbacks are increased material and manufacturing costs due to the state of the art nature of graphite-epoxy structures.

The thermal response to the metering truss under orbital thermal conditions is shown in Fig. C.2-22, which shows the relative despace, decenter, and tilt between the primary and secondary mirrors. Comparison between the required tolerances in Section C.2.c(3) and the results of Fig. C.2-22 show that they are well within tolerances.

#### C.2.c(4) Scientific Instrument Package Support Structure

##### Description and General Philosophy

This section describes the development concept of the scientific instrument package (SIP) concept that is structurally compatible with the main ring and the forward end of the telescope. It should be noted that the forward end of the telescope attaches to the titanium main ring and bulkhead (see Fig. A.1-1), via eight points. These eight points represent the graphite-epoxy composite truss that separates and supports the secondary mirror from the primary mirror.

In order to reduce the number of load points into the primary ring and take full advantage of any possible negating effects from the SIP structure interacting with the OTA structure, it followed that the SIP structure should attach to the primary ring by eight points and have the same orientation as the OTA truss and SSM structure's main longerons.

The SIP structure consists of two instrument sections: (1) an axial bay and (2) a radial bay. The following instruments shown in Fig. A.1-1 are housed in these two sections:

1. Axial Bay
  - (1) Faint object spectrograph (0.115 to 0.220 micrometer)
  - (2) Echelle spectrograph (0.180 to 0.350 micrometer)
  - (3) Echelle spectrograph (0.115 to 0.180 micrometer)
  - (4) Collimator assembly
  
2. Radial Bay
  - ( 1) Faint object spectrograph (0.660 to 1.00 micrometer)
  - ( 2) Faint object spectrograph (0.220 to 0.350 micrometer, 0.350 to 0.660 micrometer)
  - ( 3) Slit-jaw camera
  - ( 4) f/12 camera
  - ( 5) Mid-infrared interferometer
  - ( 6) Slit mechanism
  - ( 7) Filter mechanism
  - ( 8) f/96 camera assembly
  - ( 9) Fine guidance sensor
  - (10) Focus sensor
  - (11) Figure sensor
  - (12) Fix fold assembly
  - (13) Fixed head star trackers (3)
  - (14) Reference gyro

##### Design Criteria and Requirements

The primary requirement is to design a structure that will support the SIP instruments and be relatively insensitive to a varying thermal environment in order to maintain optical alignment of the instruments during an observation. In the radial bay the slit assembly will have to be held relative to the fine guidance to within 1.8 micrometers and the focus at the principal focus to 5 micrometers. In the axial bay the collimating mirror will have to be held to 18 micrometers laterally relative to the slit and to 7.5 microradians tip. The spectrographs will have to be held to 15 microradians tip. In addition, this structure will have to be strong enough to survive the design limit loads of 6.0 g, 1.5 g during launch and reentry and be stiff enough (have a natural frequency in excess of 25 hz) to avoid excitation during LST operation. Finally, the design should be such to provide accessibility and maintainability as well as growth potential.

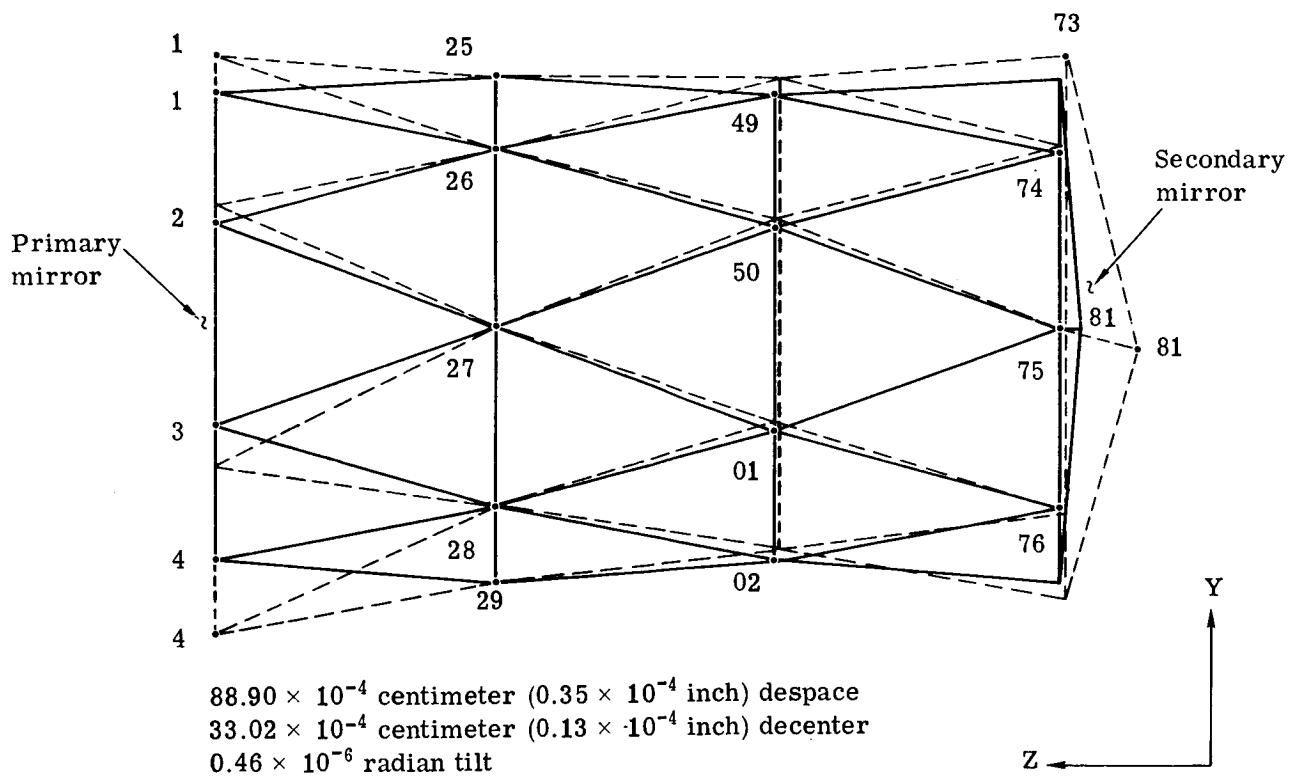


Fig. C.2-22 —Orbital thermal condition response

## Design Evolution

As the instrumentation configuration evolved, several structural arrangements were developed that were consistent with meeting the criteria and requirements. In general, these configurations were open truss work structures that optimized accessibility and ease of maintenance. An example of these is shown in Fig. C.2-23. This design was characterized by a basket-like, on axis instrument bay structure that served as the foundation for this discrete optical assemblies depicted. The entire structural assembly fundamental frequency was below 20 hz. This objectionable feature in conjunction with repackaging of the instrument complement led to the following three concepts.

### Concept 1 (Athermalized Radial Bay)

Starting with the desired layout of the instruments in both the radial and axial bays we proceeded to build a structure to support them remembering the need for maintainability and replaceability (see Fig. C.2-24). The radial bay consists of an eight-point spider space trusswork that supports two titanium rings. These two titanium rings, which are about 1.3 meter (4.3 feet) in diameter, attach to each other by an Invar cylindrical shell about 1.1 meter (3.5 feet) in length. The eight-point spider is connected to the primary ring opposite the OTA truss attachments. Connected to the farthest ring (second ring) away from the primary ring is a belleville shaped plate enclosing the radial bay at one end. The axial bay is formed by attaching four posts to the plate of the radial bay with struts from the second ring laterally supporting these posts individually. All the instruments in the radial bay area were mounted to the cylindrical Invar shell.

A cursory review and analysis of this design showed that the heat generated from these components (e.g., f/12 instrument) could cause large excursions in temperature and associated movements which are not desirable. In the axial bay we provided easy replaceability and maintainability by allowing the instrument to be removed radially. Space envelope limitations dictated a structure that was weak torsionally unless the instruments could be used to tie the four posts together. This approach is not desirable because of the probability of inducing strains into the instruments themselves causing optical degradation. In addition, the collimator sits flimsily on top of these four posts. In order to limit the excursions of the structure caused by a varying thermal environment, the truss is designed with Invar and titanium members to create an athermalized design which also is a heavy design. The philosophy of athermalized truss structure is discussed in Section C.2.c(3).

### Concept 2 (Athermalized Radial Bay, Trussed Axial Bay)

A second concept leaving the radial bay as it is except for removing the belleville shaped plate is shown in Fig. C.2-25. The axial bay has been redesigned by adding a third ring that encompasses the instruments in the axial bay. That ring is connected to the second ring via a trusswork made of Invar circular tubes. With this third ring around the instruments, removal will have to be axially instead of radially which does not present any problem. The axial bay now is structurally sound and provides a better support for the f/96 instrument. The radial bay still represents the same thermal problems but now with the plate gone there are no expedient means for independently supporting the fold mirror assembly.

### Present Design (G/E Truss Configuration)

The present design (see Fig. C.2.26) achieves satisfaction of the goals to have a stiff, lightweight, thermally inactive structure, in addition to possessing qualities of ease of maintenance and replaceability of the instruments. It was thus decided to make the SIP structure from graphite-epoxy composite materials which are light in weight and allow you to design in the desired thermal properties by selecting the layup of the plies (see Table C.2-6). In order to prevent heat pockets in the radial bay, the Invar cylindrical plate was replaced with a graphite-epoxy composite truss. The SIP structure now consists of three rings, two in the radial bay interconnected to each other by a trusswork and supported from the primary ring by an eight-point truss. The third ring is in the axial bay and is attached to the radial bay by a trusswork from its adjacent ring. In the radial bay, four trussed beams reach inward to independently support the folding mirror assembly. The fine guidance assembly is supported by the radial bay rings via appropriate bracketry and is also bolted to the folding mirror assembly to form one integral unit. The three rings are graphite-epoxy composite I sections. The interconnecting and supporting trusswork are tubes of graphite-epoxy composites of indicated diameter.

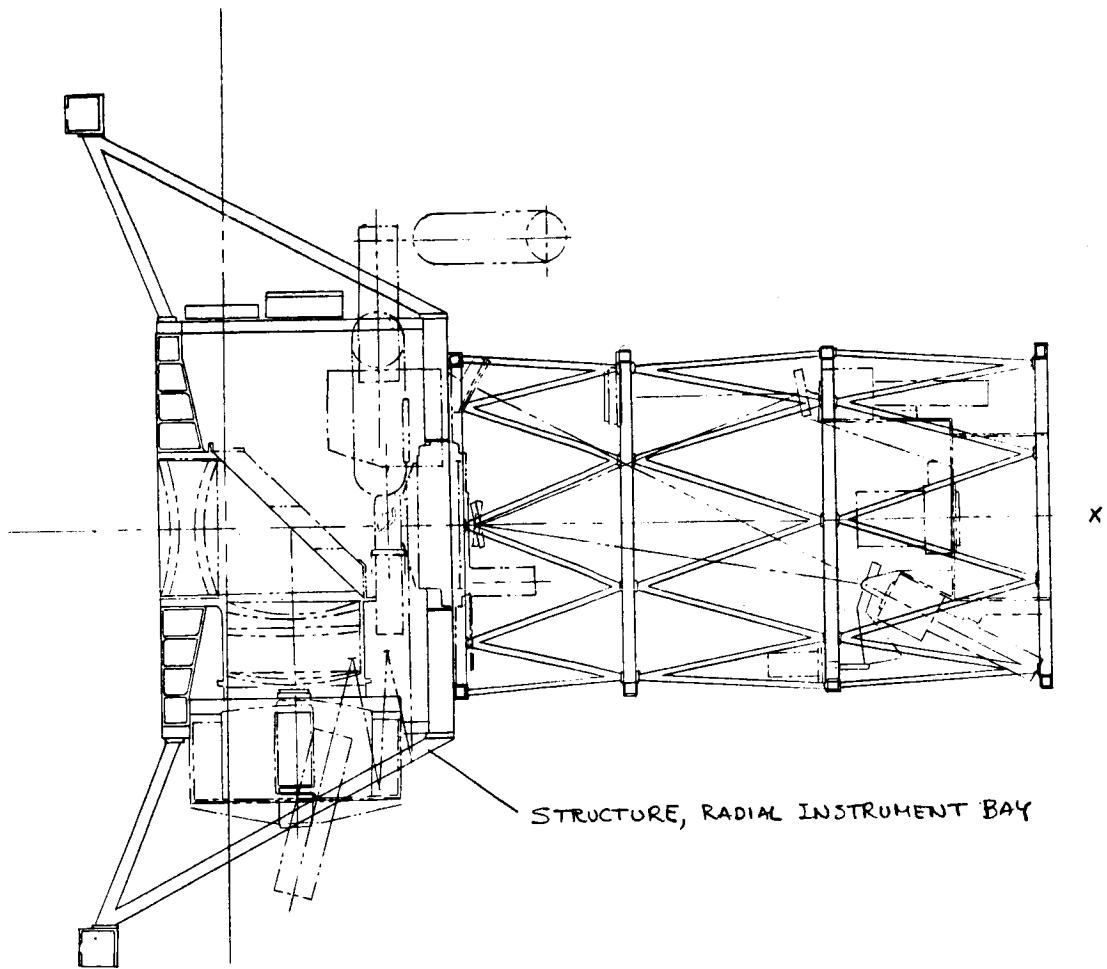


Fig. C.2-23 — Early SIP structural configuration

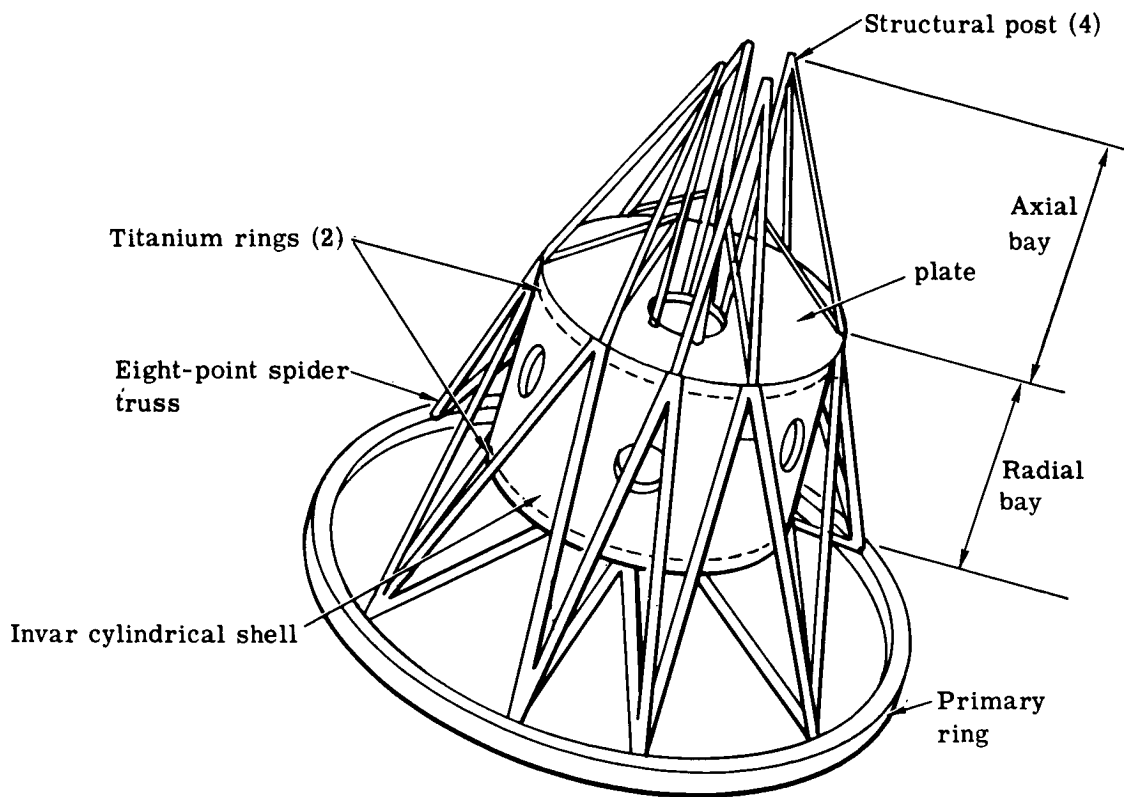


Fig. C.2-24 — Athermalized radial bay, cantilevered axial bay SIP structure



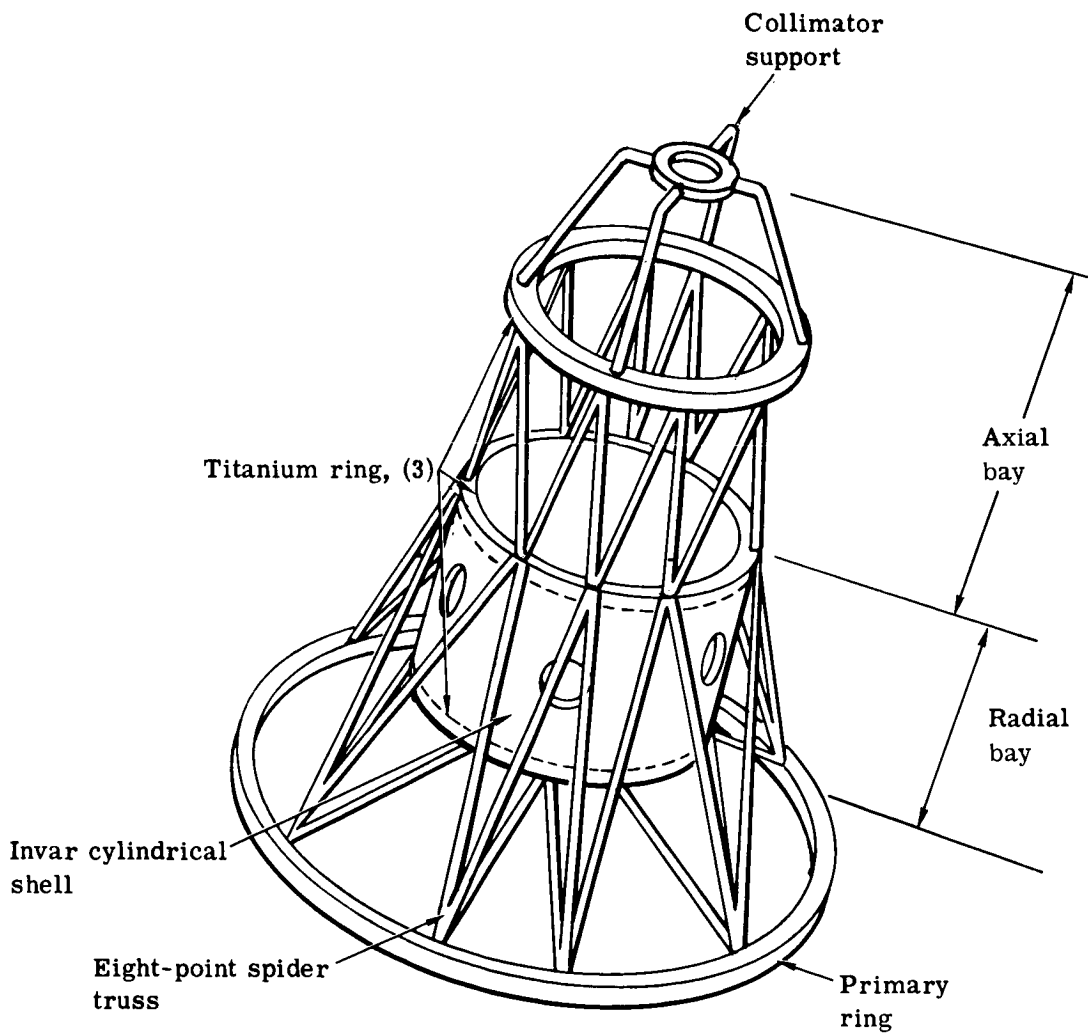


Fig. C.2-25 — Athermalized radial bay, trussed axial bay SIP structure

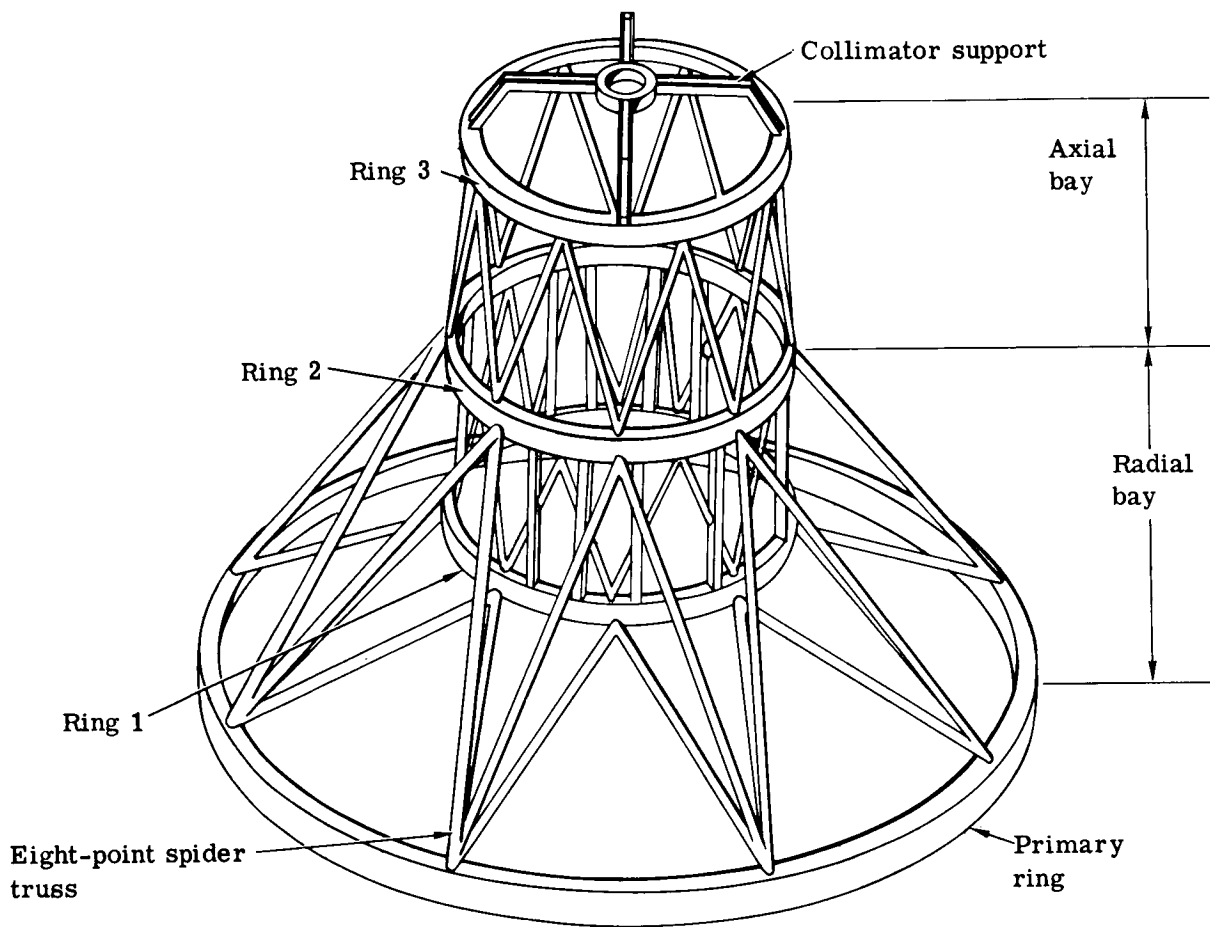


Fig. C.2-26 — Graphite-epoxy truss configuration (present design)

Table C.2-6 – SIP Structure Material Properties Used-

Material	Young's Modulus, newtons/meter <sup>2</sup> (psi)	Thermal Coefficient of Expansion meters/meter/°C (m/m/°F)	Density, kg/m <sup>3</sup> (lb/in <sup>3</sup> )
Titanium	110 x 10 <sup>9</sup> (16.0 x 10 <sup>6</sup> )	8.64 x 10 <sup>-6</sup> (4.8 x 10 <sup>-6</sup> )	4.43 x 10 <sup>3</sup> (0.16)
Graphite-Epoxy Composite	105.5 x 10 <sup>9</sup> (15.3 x 10 <sup>6</sup> )	0.0 (0.0)	1.66 x 10 <sup>3</sup> (0.06)
Graphite-Epoxy Composite (3° tolerance)	105.5 x 10 <sup>9</sup> (15.3 x 10 <sup>6</sup> )	0.126 x 10 <sup>-6</sup> (0.07 x 10 <sup>-6</sup> )	1.66 x 10 <sup>3</sup> (0.06)

### Analytical Model

An 89-node, 214-beam model of the SIP structure (see Fig. C.2-27) was generated for use on both the EASE and STARDYNE computer programs. To this general computer model individual modifications, as described in the following sections, are made to tailor this general model for the particular analysis being performed.

### Structural Analysis

The graphite-epoxy composite SIP structure has been analyzed for deformation and stresses caused by a varying thermal environment. Results of those analyses can be found in Table C.2-7. In addition, the STARDYNE structural model was used to calculate the SIP structure natural frequencies and associated mode shapes as well as launch and reentry stresses.

### Thermal Sensitivity Analysis

The thermal analysis department has subdivided the analysis and design of the thermal control of the SIP structure into three categories: (1) constant  $Q$ , (2) constant  $T$ , (3) and insulated structure. A brief explanation of these categories will be given here but a more thorough explanation can be found in the thermal analysis section. The constant  $Q$  category requires the heat output constant from all the cameras whether they are on or not. This concept necessarily uses a large amount of energy. The second category, constant  $T$ , is to have a thermal shroud around and enclosing the SIP structure and the passive portions of the instruments. The heat generating components of the instruments are located outside the shroud. With this design the temperature will be maintained inside the shroud at  $70^\circ$  and allow outside temperatures on the shroud to go where they may. The third concept, the isolated structure, is similar to the previous concept with the following exceptions. Instead of having a thermal shroud, the individual members and the passive elements of the instruments are insulated maintaining them to  $21.1^\circ\text{C}$  ( $70^\circ\text{F}$ ) and allowing the camera temperatures to vary as they may whether they are operating or not.

During the phase A study, several thermal sensitivity analyses on the SIP structure were conducted to determine whether the development of a relatively thermally insensitive instrument support structure was possible. The SIP temperature distribution can, as in the case of the instruments operating or constant  $Q$  case, vary significantly between different locations. A graphite-epoxy composite SIP structure was considered to be an effective means of controlling the structure's thermal movements. Since graphite-epoxy composite consists of a layup of lamina in calculated orientations to obtain the desired properties, the effects of fabrication tolerances must be evaluated. It was determined from consultation with vendors that a tolerance of  $3^\circ$  in layup angle is reasonable from both a fabrication and a quality control standpoint. This tolerance can produce a change in  $\alpha$  from zero to  $0.126 \times 10^{-6}$  meter/meter/ $^\circ\text{C}$  ( $0.07 \times 10^{-6}$  inch/inch/ $^\circ\text{F}$ ). Consequently, an  $\alpha = 0.126 \times 10^{-6}$  meter/meter/ $^\circ\text{C}$  was used in the analysis of the SIP structure.

Thermal analyses of the SIP assembly provided the temperature distributions to the SIP structure (see Fig. C.2-28). This temperature distribution was refined and made compatible with the SIP structural model (see Table C.2-7) and thermal response analyses made.

### Static Analysis

In order to perform a stress analysis of the SIP structure the computer model was revised in the following manner: the eight points that attach to the primary ring were restrained from translation in the X, Y, and Z directions and the masses of the instruments were added in their proper locations. To obtain unit stresses, a 1-g load was individually applied in the three mutually perpendicular directions. See Table C.2-8 for applied weights. The analysis, in turn, also accounted for the dead weight of the SIP structure. Taking the 1-g loads and applying the given design-limit load factors of 6.0, 1.5, 1.5 in the appropriate directions, stress levels of less than  $6.2 \times 10^7$  newtons/meter<sup>2</sup> (9000 psi) were achieved, this level being well below that allowable.

### Resonant Frequency

The structural model used for the stress analysis was also analyzed for fixed base natural frequencies. This analysis, which included the mass of the various instruments and the mass of the graphite-epoxy composite structure, indicated a fundamental frequency of 28 hz. The response mode associated with this frequency showed translation of the collimator support structure and spectrograph support structure in the Y direction.

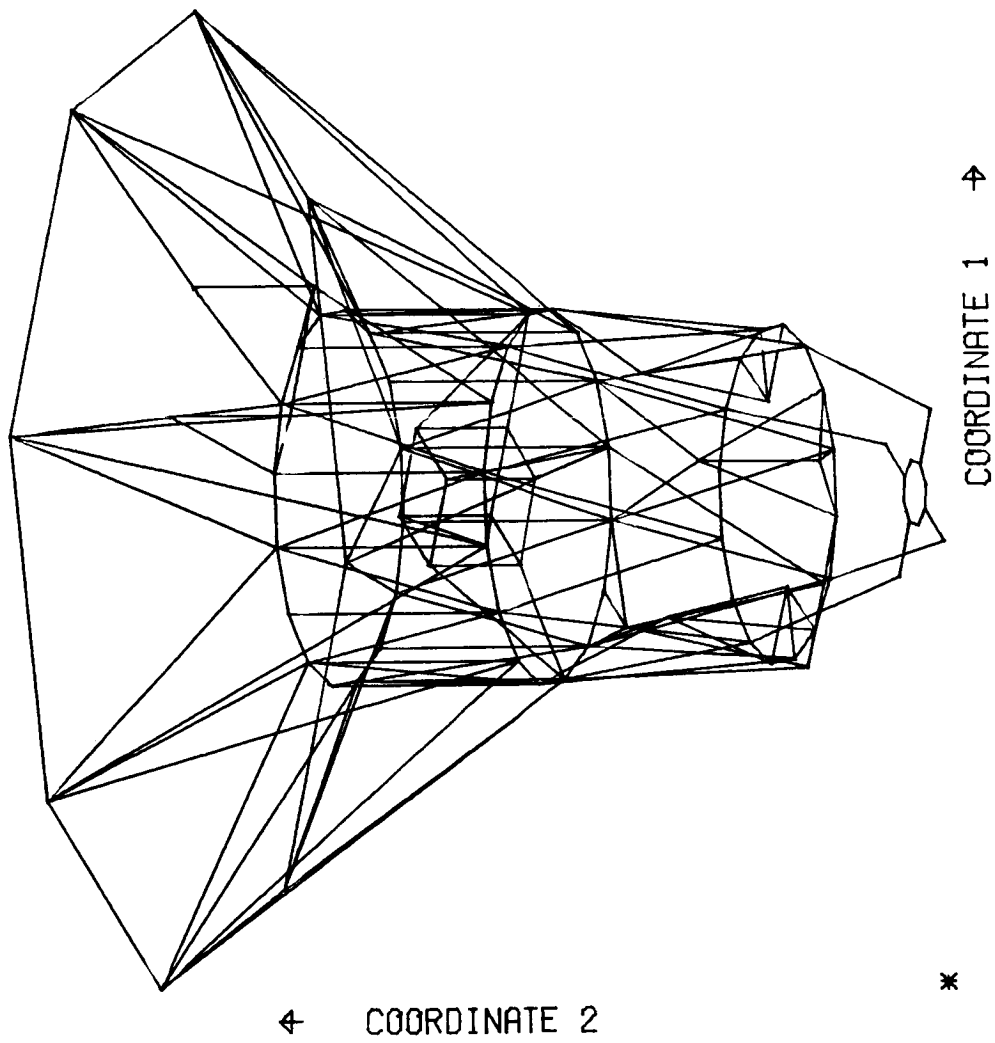


Fig. C.2-27 — Plot of SIP structural mathematical model

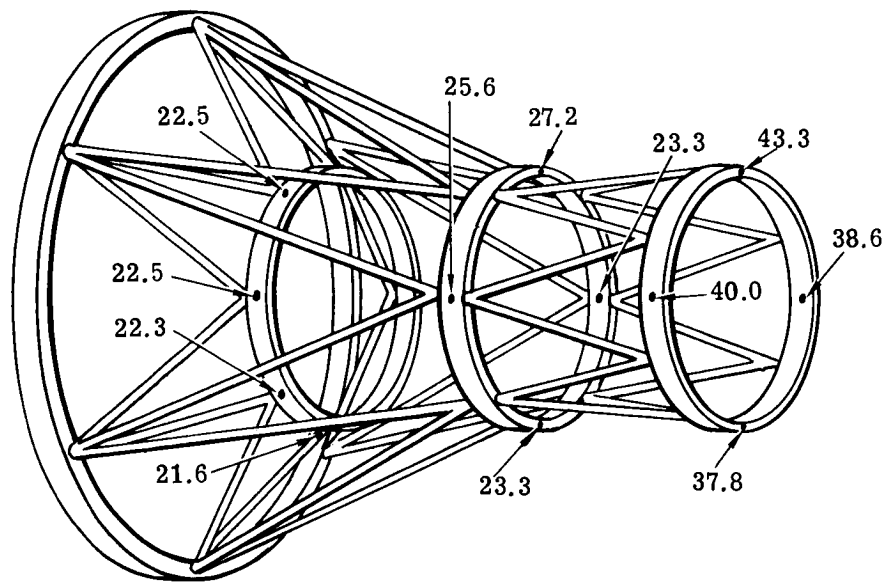


Fig. C.2-28 — SIP temperature distribution—constant Q system

Table C.2-7 – Thermal Operating Environment – Constant Q

Node	Radial Bay Temperature		Node	Axial Bay Temperature	
	°C	°F		°C	°F
1	21.1	70.0	54	38.3	101.0
2	21.1	70.0	55	38.3	101.0
3	21.1	70.0	56	43.3	110.0
4	21.1	70.0	57	41.7	107.0
5	21.1	70.0	58	41.1	106.0
6	21.1	70.0	59	40.6	105.0
7	21.1	70.0	60	40.6	105.0
8	21.1	70.0	61	40.0	104.0
9	21.7	71.0	62	39.4	103.0
10	21.7	71.0	63	38.3	101.0
11	22.8	73.0	64	38.3	101.0
12	22.8	73.0	65	38.9	102.0
13	22.8	73.0	66	38.9	102.0
14	22.8	73.0	67	39.4	103.0
15	22.2	72.0	68	39.4	103.0
16	21.7	71.0	69	39.4	103.0
17	22.8	73.0	70	41.7	107.0
18	22.5	72.5	71	44.4	112.0
19	22.2	72.0	72	42.2	108.0
20	21.9	71.5	73	42.2	108.0
21	21.7	71.0	74	45.6	114.0
22	21.9	71.5	75	48.3	119.0
23	22.2	72.0	76	44.4	112.0
24	22.2	72.0	77	42.2	108.0
25	22.5	72.5	78	42.2	108.0
26	22.8	73.0	79	42.2	108.0
27	23.9	75.0	80	43.3	110.0
28	23.9	75.0	81	45.6	114.0
29	23.9	75.0	82	46.7	116.0
30	24.4	76.0	83	48.3	119.0
31	24.4	76.0	84	43.3	110.0
32	24.4	76.0	85	42.2	108.0
33	25.0	77.0	86	44.4	112.0
34	25.6	78.0	87	43.3	110.0
35	25.6	78.0	88	42.2	108.0
36	25.6	78.0	89	44.4	112.0
37	27.2	81.0			
38	26.7	80.0			
39	26.1	79.0			
40	25.6	78.0			
41	25.0	77.0			
42	24.4	76.0			
43	23.9	75.0			
44	23.3	74.0			
45	23.3	74.0			
46	23.3	74.0			
47	23.3	74.0			
48	23.3	74.0			
49	23.9	75.0			
50	25.6	78.0			
51	26.7	80.0			
52	28.3	83.0			
53	23.3	74.0			

Table C.2-8 – Applied Weight Breakdown for Radial and Axial Bays

Radial bay	Kilograms	Pounds
Faint object spectrograph (660 to 1,000 nm)	54	120
Faint object spectrograph (220 to 350 nm, 350 to 660 nm)	54	120
Slit-jaw camera	45	100
f/12 camera	66	145
Mid-infrared interferometer	23	50
Slit mechanism	7	15
Filter mechanism	5	12
f/96 camera assembly	240	530
Fine guidance	91	200
Focus sensor	5	10
Figure sensor	5	10
Fix fold assembly	23	50
Axial bay		
Faint object spectrograph (115 to 220 nm)	57	125
Echelle spectrograph (180 to 350 nm)	57	125
Echelle spectrograph (115 to 180 nm)	57	125
Collimator assembly	11	24
Total	800	1,761



## Discussion of Results

### Weight

The theoretical computer calculated weight of the SIP structure minus the weight of the instruments and the primary ring is 143 kilograms (316 pounds). To this must be added the weight of structural fittings and instrument mounting surfaces plus a contingency factor. It would seem that an overall weight of the SIP structure without a contingency factor would be approximately 181 kilograms (400 pounds).

### Static and Dynamic

The maximum stress levels attained after the structure was subjected to the design limit loads of 6 g and 1.5 g in the axial and lateral directions was  $62 \times 10^2$  newtons/meter<sup>2</sup> (9,000 psi).

The first frequency, an adequate 28 hz, indicates that for the present stiffness not stress is the designing criterion.

### Thermal

Table C.2-9 summarizes the results of the structural analysis for the deformations caused by the constant Q condition. The results (which are favorable) are compared to the allowable motions and fall well within the limits. [See Fig. C.2-29.]

Table C.2-9 – Comparison of Actual and Allowable Motions Due to Thermal Loads

	Allowable	Actual constant Q
Collimating mirror	18 micrometers in the Y – Z plane 7.5 microradians tilt	1.5 micrometers in the Y – Z plane 1.3 microradians tilt
Spectrography body	15 microradians tilt	4 microradians tilt

### Conclusion

A review of the data has shown the graphite-epoxy composite SIP structure to be a lightweight and stiff design. The thermal control concept with constant Q, which exhibited the widest variations in temperatures was analyzed and found to be well within the allowable limits. Thus, having a structure that exhibits both ease of instrument replacement and maintainability and being thermally insensitive should have the design freedom to satisfy completely the packaging requirements of the instruments.

### C.2.c(5) Telescope Protective System

The telescope protective system serves to protect the sensitive optical elements from environmental contamination and undesirable stray sources of light. Primary to this system is the aperture door assembly, the sun shield, and the pressure bulkhead door. Associated with the telescope protective system are a few structural subsystems which function both as structural support elements as well as protective structures. These are the meteoroid shield, baffles, and pressure bulkhead.

#### Meteoroid Shield

The meteoroid shield (see Fig. C.2-30) is an aluminum skin-stringer-frame structure 9.19 meters (362 inches) long and 3.52 meters (138.5 inches) in diameter. It provides the outer covering for the primary and secondary mirror systems. It not only acts as a meteoroid bumper but also serves to support the sunshade (SK-LST-018) and its deployment mechanism, the main baffle assembly (SK-LST-008), six desaturation magnets, the super insulation, and

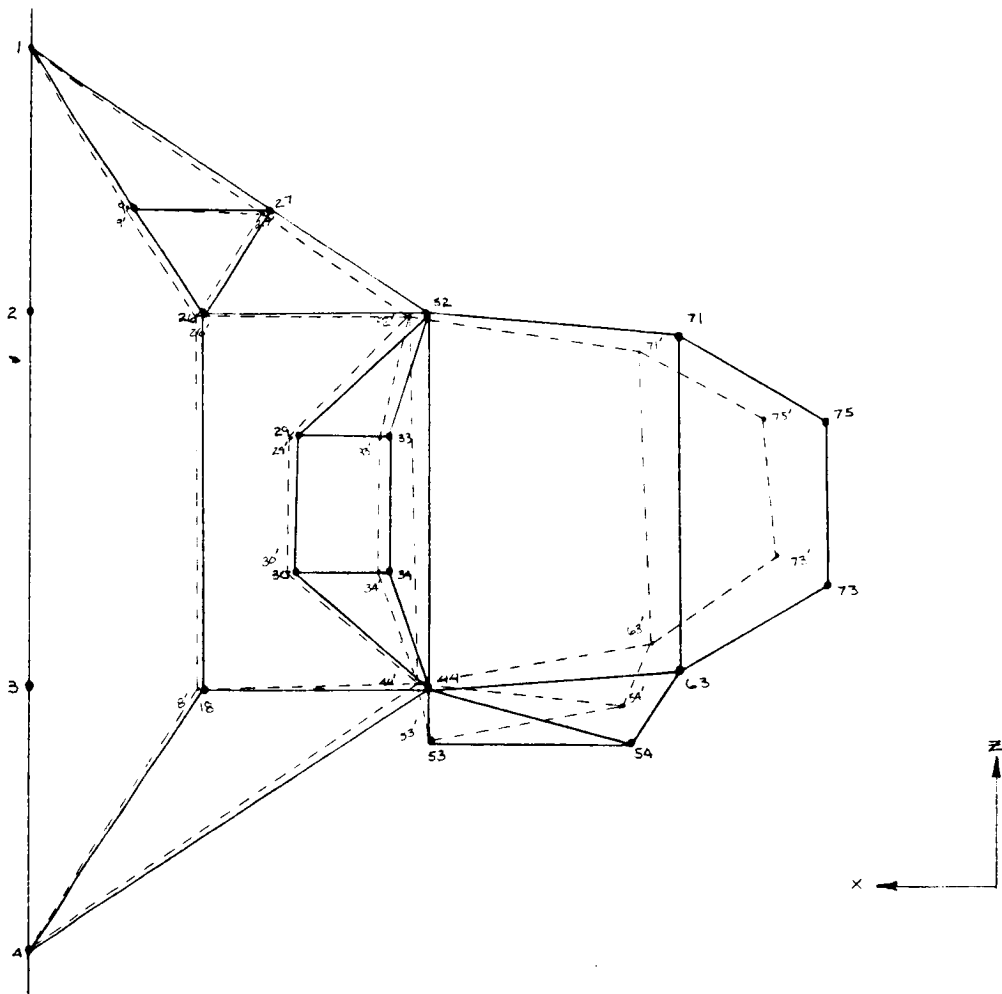


Fig. C.2-29 — Thermal response of structures, constant Q

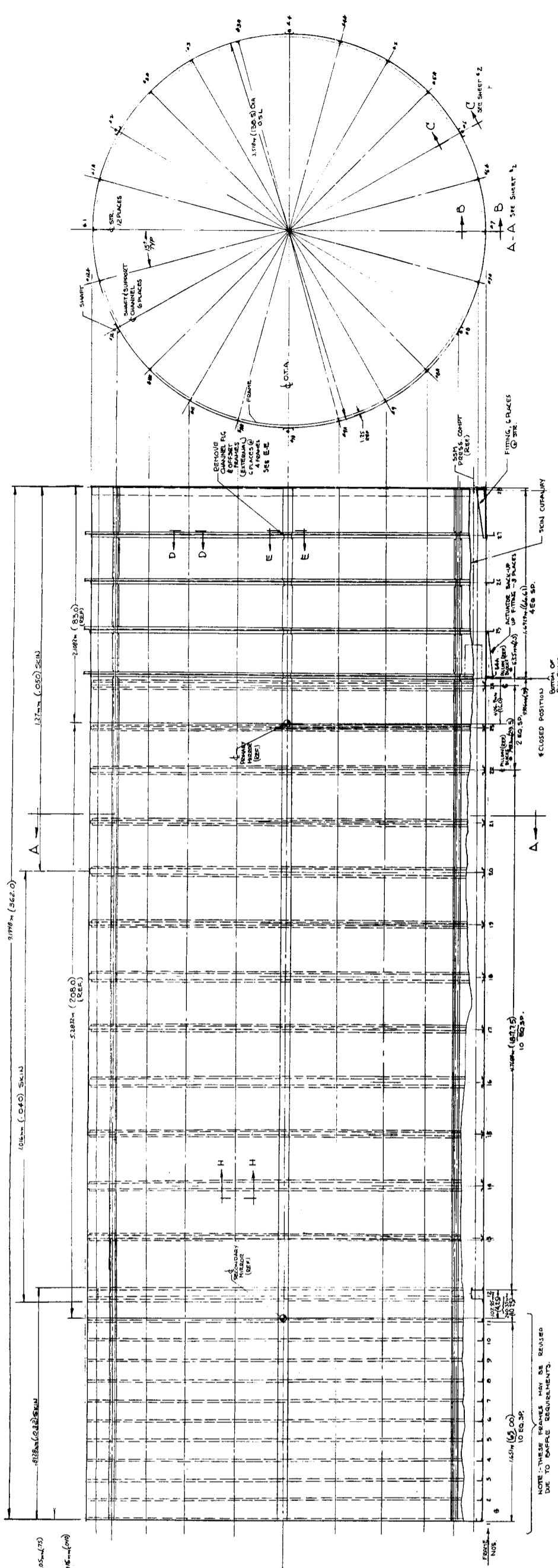


Fig. C.2-30 — Meteoroid shield, extended configuration

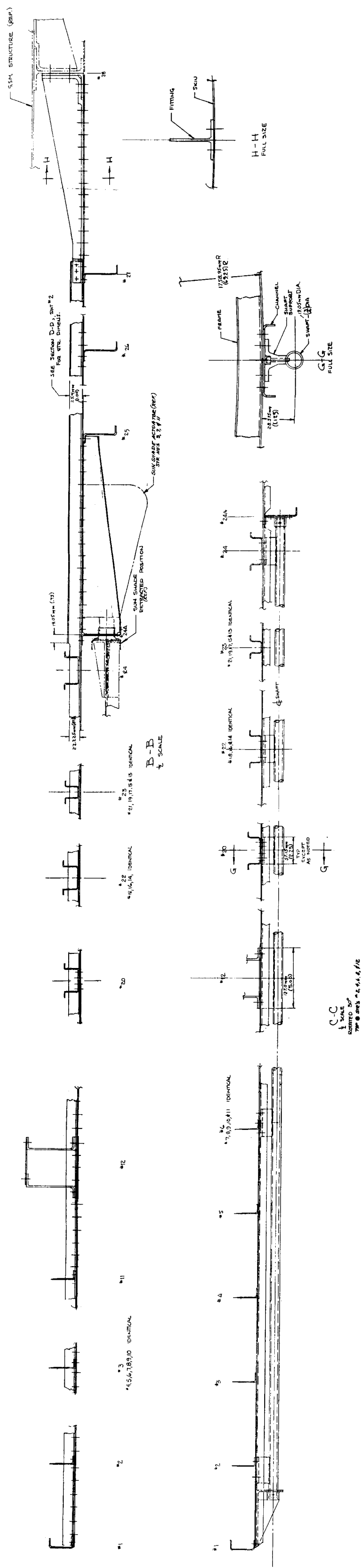


Fig. C.2-30 — Meteoroid shield, extended configuration (Cont.)

the aperture door assemblies (see Fig. C.1-12). The meteoroid shield is supported only at its aft end where it interfaces with the SSM. This method of support is chosen to provide structural as well as thermal isolation from the primary and secondary optical systems.

The meteoroid protection requirements on structural component thicknesses are presented in Itek memo "Telescope Tube Meteoroid Hazard" and indicate a required total radial aluminum thickness of 1.778 millimeters (0.070 inch) based on a protection probability of 0.95 for 5 years. The proposed design indicates total thicknesses of 1.829 millimeters (0.072 inch) for most locations. In many cases, the thicknesses are considerably greater due to presence of doublers, metering truss, stiffening rings and longerons, and sun shield structure.

The critical case is the 3 g lateral load situation occurring upon return to earth in the shuttle vehicle. Lateral loads from the main baffle structure (see Fig. C.2-31) are introduced into the meteoroid shell structure at two ring frames while fore and aft baffle loads are introduced into the shield at the aft baffle support only, through four struts spaced at 90° around the circumference of the shell.

The sun shade (see Fig. C.1-11) is in the fully retracted position during the launch and return cases. The axial sunshade loads are reacted at the aft end of the shade into three actuator supports which are located on the exterior periphery of the meteoroid shield. The lateral loads are introduced into two ring frames in the shield of which the aft support point is the same location used in reacting the axial loads. The forward reaction point is near a ring frame in the meteoroid shield about 3.53 meters (138.8 inches) forward of the aft support. This forward support point allows the 45-degree cut section of the sunshade to overhang the forward support.

There are eight telescope aperture doors (see Fig. C.1-12) supported internally from the inside of the meteoroid shield. These doors, with their seals, provide light closures to the telescope optical system but are structurally and thermally isolated from the telescope components by being supported from the meteoroid shield. Lateral loads from the doors are carried into the ring frames while the axial loads are introduced into fittings or intercostals and sheared into the skin.

Details of this analysis (meteoroid shield) as well as those pertaining to the sunshade, aperture door, main baffle, and pressure bulkhead door are given in data reported in Martin-Marietta letter from K.W. Kohlenburg to J. J. Cleary, 29 Sept 1972.

#### Sunshade

The sunshade (see Fig. C.1-11) is an open-ended circular shell, with the forward end cut at 45 degrees. The shape is maintained with ring frames that are external in the 45 degree region and internal elsewhere. Internal frames exposed when the sunshade is extended serve as baffles.

The sunshade is supported laterally on the meteoroid shield at two rearward frames 0.75 meter (29.5 inches) apart. Six sets of roller bushings in pillow blocks on the sunshade at these two positions engage shafts mounted externally on the meteoroid shield. In the stowed position, additional lateral support is provided at another position about 3.53 meters (138.85 inches) forward of the rearmost frame (see Fig. C.2-32). All stringers are external. Axial loads are taken at three stringers where actuators mounted on the meteoroid shield are attached. The actuators are synchronized and assist in providing axial alignment during extension or retraction.

The design concept of the sunshade deployment mechanism is a stem push/pull drive. This method is one that is workable and appears well suited for the job. However, this is not necessarily the final design since the method of extending and retracting the sunshade has not been studied in sufficient depth. Various other concepts may be employed and the final optimum choice should await further study. Other methods include a perforated tape pulley drive, a cable drive, a ballscrew drive, and a rack and gear drive. Associated with the drive mechanisms are various schemes to guide the sunshade during operation.

#### Main Baffle

The main baffle (see Figs. C.2-31 and C.2-33) is a cylindrical shell with open ends having internal rings (blades) and external longerons, simply supported at two stations inside the meteoroid shield. The outside is wrapped with

insulation to aid in temperature control of the truss structure supporting the secondary mirror. Fittings at the support stations, and clearances, accommodate thermally induced strain between the meteoroid shield and the main baffle. Heat flow through the support fittings is minimized by use of shims of low conductance. Strength of the fittings is governed by the launch and return loads. Axial loads are reacted at the aft support station only to shorten the load path to the boost vehicle structural interface ring. Skin and ring sheet metal gauges are the minimum for ease of fabrication. Rings are sized, shaped, and spaced, and all internal surfaces are specular black of optical quality.

#### Aperture Door Assembly

The aperture door (see Fig. C.1-12) consists of eight segments supported by the meteoroid shield and the secondary mirror support structure. In the closed position, the segments are sealed around their perimeter. Segments are opened or closed four at a time by electric-powered screwjacks. Operating loads occur in a negligible gravity field and are relatively insignificant. Inertial loads at launch govern structural design. Each segment is fabricated of bonded aluminum honeycomb for rigidity, hinged through two fittings to the meteoroid shield, and connected to a screwjack. Lateral loads along the hinge are considered reacted at only one place as a limiting condition. Stops in the screwjacks index segments in the open and closed positions. When open, the segments nest inside the meteoroid shield and expose baffles that contribute to stray light suppression.

#### Pressure Bulkhead Door

The pressure bulkhead door (see Fig. C.2-34) is the same mechanical concept as the scientific airlock on Skylab. The door is attached with links to a carriage that is driven by two electrically powered screws and is guided into position with cams against a seal. The door is compactly stowed in a parallel position adjacent to the bulkhead. The entire assembly is attached to the pressure bulkhead. The door is a one-piece, machined structure to minimize weight and cost. It is designed for a limit pressure differential of one atmosphere with a factor of safety of 2.0.

#### Pressure Bulkhead

The pressure bulkhead structure serves as a support base for the metering truss, primary mirror, and SIP structure. The bulkhead also interfaces with and makes up one end of the SSM pressurized cylinder. The present design is a shallow titanium honeycomb spherical dome with the pressure door at the center. Two titanium rings rigidly connect to the opposite faces of the bulkhead and become an integral part of it.

During the shuttle launch and reentry phases, the LST is supported at the bulkhead at two points 180 degrees apart on either side of the shuttle [see Section C.2.c(6)] Two shuttle support fittings are incorporated into the bulkhead core at these points to help distribute the loads.

The pressure load condition on the bulkhead governs the structural design. Under a pressure loading, the rotations around the edge of the bulkhead must be controlled so as not to induce unacceptable levels of stress in the primary mirror, mirror flexures, metering truss, or SIP structure. The deflections of the bulkhead must also remain within tolerable limits to prevent any undesirable interaction between the primary mirror and force actuators located on the bulkhead. Preliminary analyses have demonstrated the feasibility of the proposed concept.

#### C.2.c(6) Shuttle Reentry

The OTA may after a period of time be retrieved from orbit by the shuttle spacecraft for refurbishing or realignment. The cargo bay area of the shuttle will have provisions to accept the OTA. The present design philosophy is to provide a cradle in the shuttle that will engage the OTA at two points 180° apart in the area of the pressure bulkhead/main ring (see Fig. C.2-35). Two titanium fitting inserts in the pressure bulkhead receive and engage with pins from the shuttle to secure the OTA in the three translational directions. This location should coincide reasonably close to the center of gravity to minimize the unbalanced rotational forces. A third point of attachment will be provided on the SSM structure a distance away. The OTA reentry loads will be transmitted to the shuttle through these three points, which are statically determinate.



OTHER METHODS CONSIDERED ARE:

- a. SHEAR PINS
- J. ROLLERS

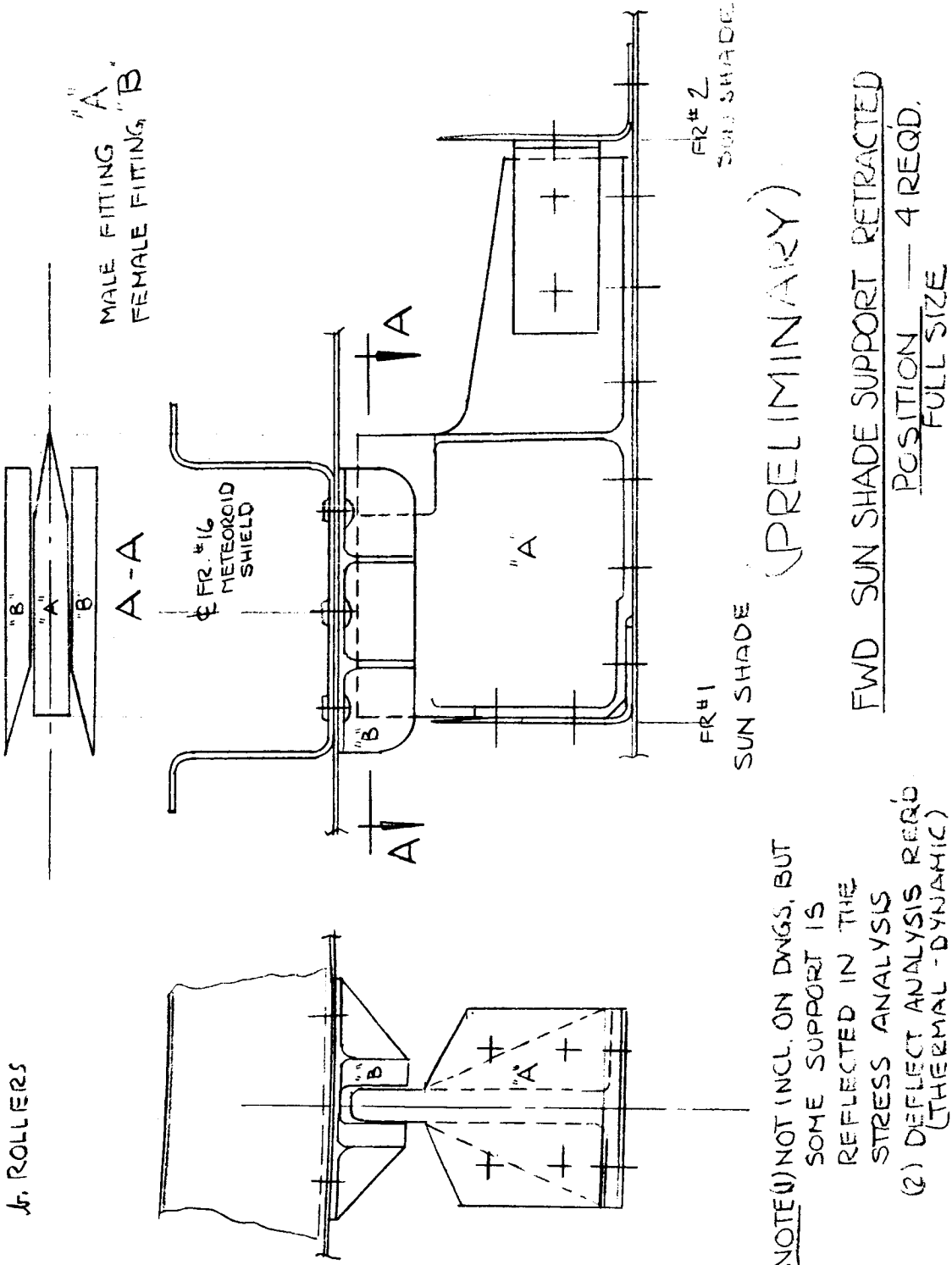


Fig. C.2-32 — Forward sunshade support in retracted position



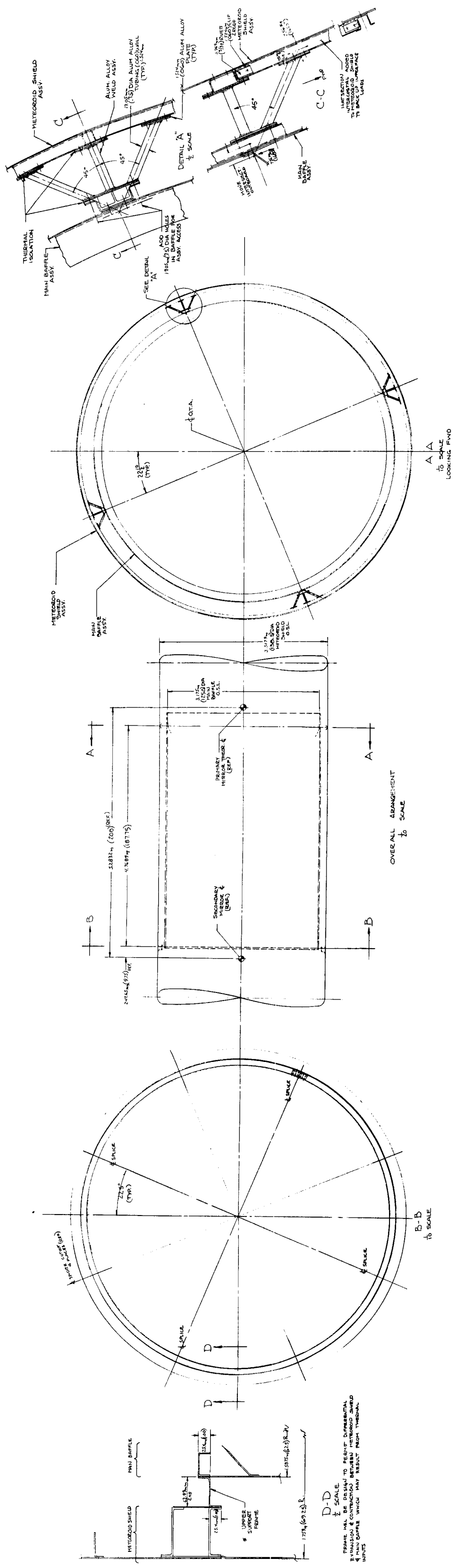


Fig. C.2-33 — Baffle attachment to meteoroid shield

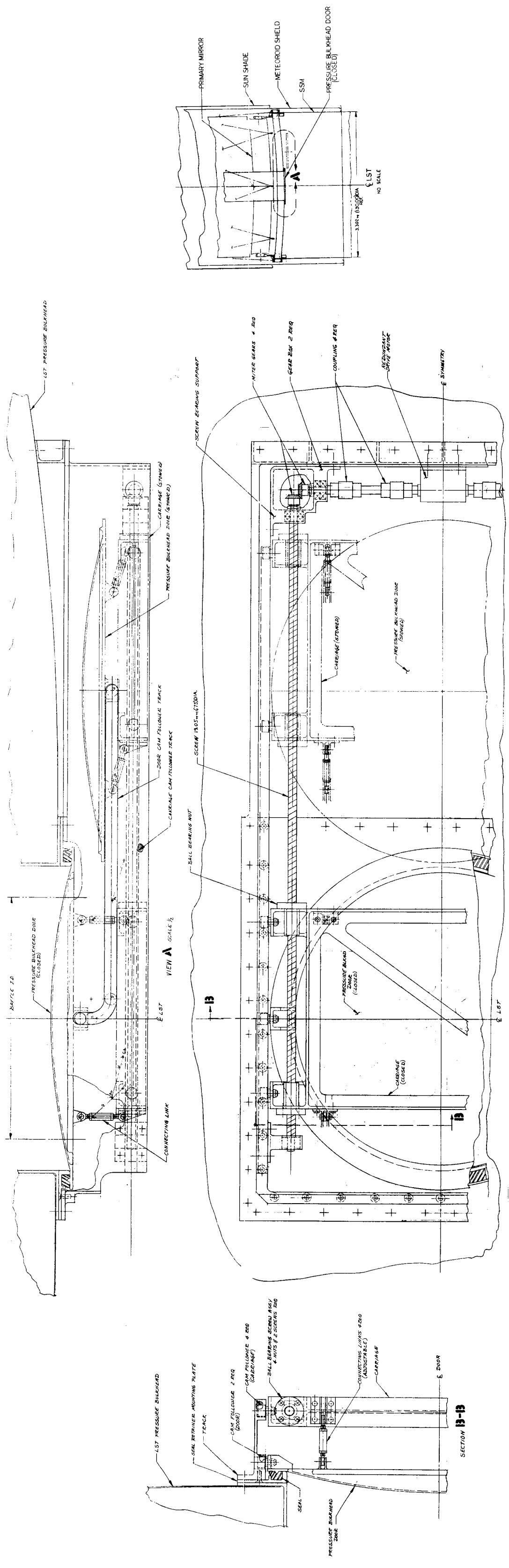


Fig. C.2-34 — Pressure bulkhead door and mechanism

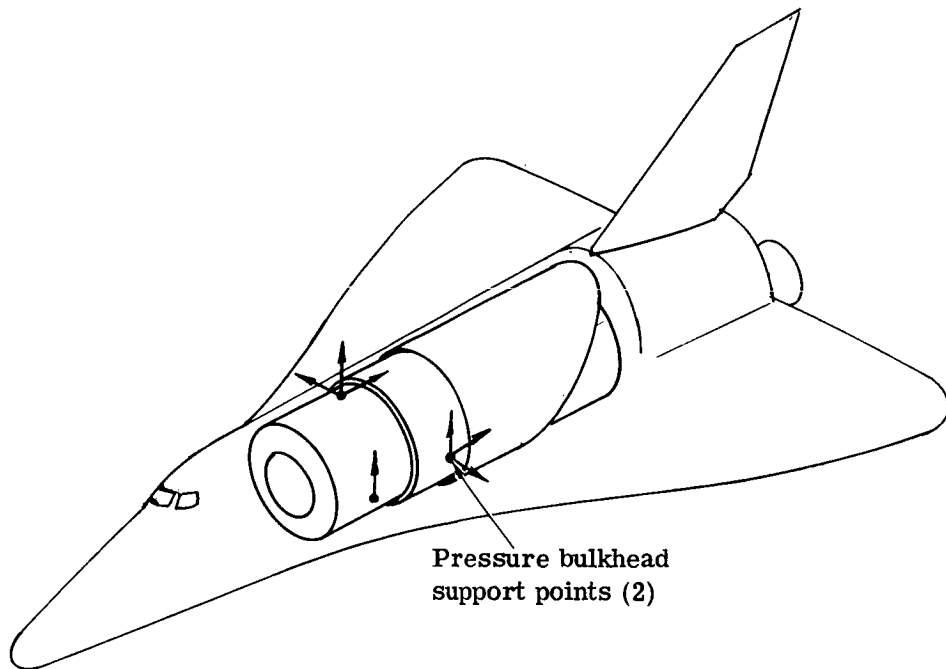


Fig. C.2-35 — Shuttle support points

### C.2.c(7) Manufacturing Plan

A preliminary manufacturing and assembly sequence has been established (Fig. C.2-36). An essential step prior to final assembly of the graphite-epoxy composite metering and SIP truss structure is to test the members to ensure that their coefficients of thermal expansion fall within acceptable ranges. The actual assembly sequence as shown may be deviated from to accommodate optical testing and alignment requirements. Inherent to the manufacture and assembly of any complex structure such as the OTA are the requirements for numerous test and fabrication mounts as well as assembly fixtures.

### C.2.d Summary

The three structural systems that make up the OTA – namely (1) the optical metering truss, (2) SIP, and (3) telescope protective system – have been effectively designed to be structurally independent and thermally isolated from one another. Table C.2-9 shows the OTA and SIP structure thermal response summary. The metering truss design has been analytically demonstrated to meet the optical requirements for the orbital thermal condition. The primary mirror rms surface errors are obtained via a series of mathematical modeling and analytical techniques that include the entire optical structure, thermal and structural analysis, a detailed mirror model analysis, and a mirror surface error analysis. The SIP structure thermal response data also show compliance with optical requirements.

The optical metering truss supports only the optics whereas the SIP structure supports the associated optical instrumentation. Thermal isolation of the metering truss and SIP is accomplished by both insulating the structure and using an athermalizing truss design. A three-bay, eight-point mount truss with graphite-epoxy members appears to be a most suitable design for the metering truss. The SIP truss structure is also governed by the same general requirements as the metering truss, but to a lesser degree. Consequently, a graphite-epoxy composite truss design is also recommended. This truss has the added feature of satisfying the accessibility and maintainability requirements for the SIP. Structural isolation is accomplished by providing independent load paths. The pressure bulkhead and main ring form the main structural support base for both the metering truss and SIP.

The primary mirror, which serves as the optical reference, is the most critical component and has the greatest overall impact on the optical performance of the system. Here, the recommended design is a monolithic, Cer-Vit mirror supported by a three-point axial-leaf mounting system. A series of force actuators is provided to augment the capability of the primary mirror in minimizing surface degradations caused by various unpredictable forces. Although uncertainties exist about the nature of the degrading forces, estimates can still be made as to the required corrective actuator forces.

The nonoptical protective system includes the meteoroid shield, sunshade, baffles, and aperture doors. The meteoroid shield acts as the main support member for the sunshade, baffles, and aperture doors and is itself supported by the SSM. In general, an aluminum semimonocoque construction is used except for the aperture doors, which are an eight-segmented aluminum honeycomb design supported by the meteoroid shield and operated by screwjacks. The design concept for the sunshade is an open-ended circular shell truncated at 45 degrees and can be extended and retracted from the meteoroid shield. The pressurizable portion of the OTA structure includes the pressure bulkhead and SSM pressurized instrument bay, where servicing of instruments can readily be made by astronauts. In summary, a chart of the recommended system is shown on Table C.2-10.

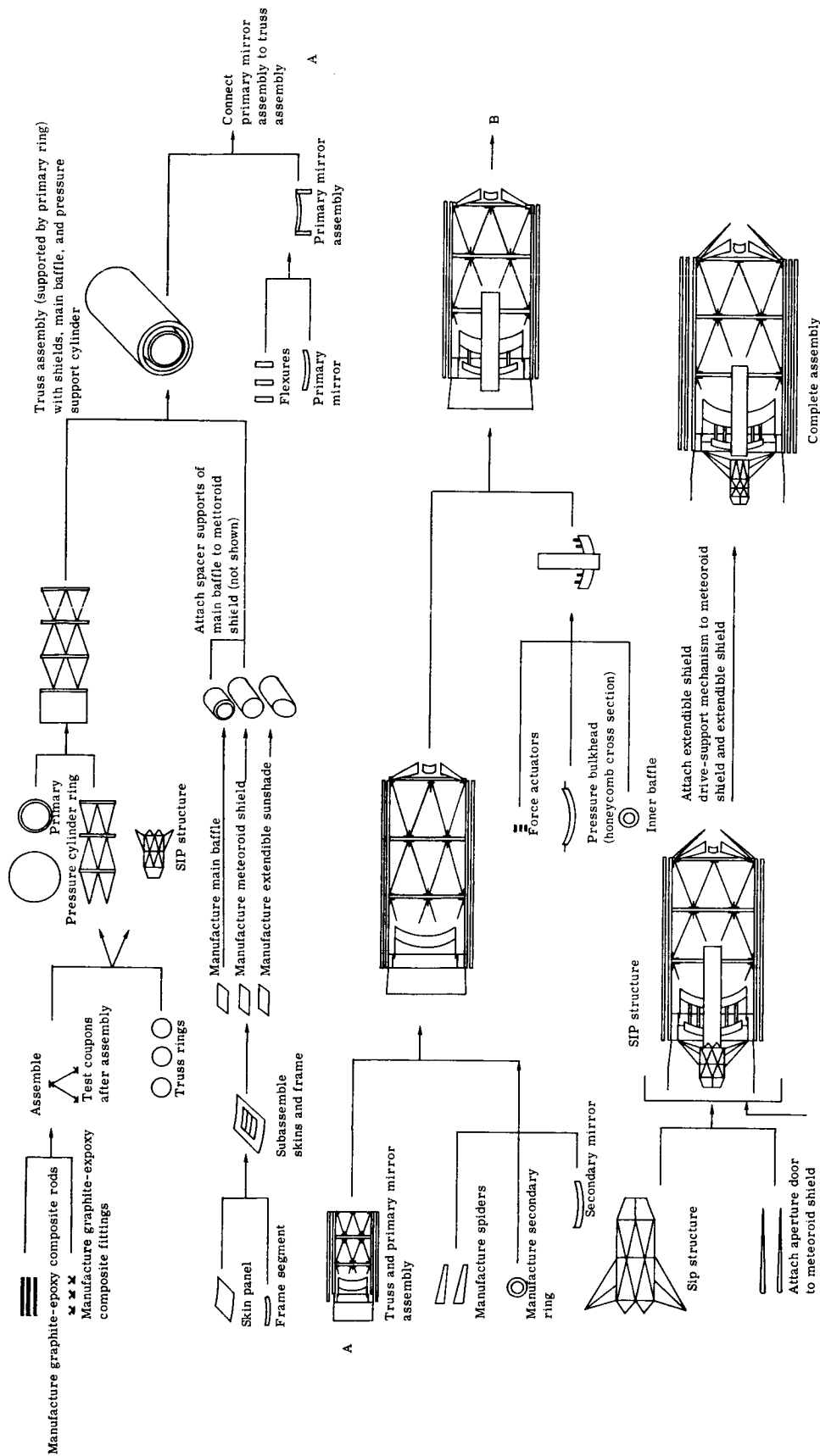


Fig. C.2-36 — Manufacturing and assembly sequence for composite metering and SIP truss structure

Table C.2-9 — OTA and SIP Structure Thermal Response Summary

Item	Allowable	Predicted	Remarks
Graphite-epoxy metering truss (secondary mirror relative to primary mirror)	±10 micrometers	0.33 micrometer	Orbital thermal condition
		4.8 micrometers	10°F diametral gradient
Despace	±2 micrometers	0.88 micrometer	Orbital thermal condition
		2.3 micrometers	-12 °C (10 °F) soak
		2.6 micrometers	-12 °C (10 °F) axial gradient
		1.2 micrometers	-12 °C (10 °F) diametral gradient
Tip/tilt	4.85 × 10 <sup>-6</sup> radian (1 arc-second)	0.46 × 10 <sup>-6</sup> radian	Orbital thermal condition
		0.46 × 10 <sup>-6</sup> radian	-12 °C (10 °F) diametral gradient
Primary mirror rms surface error	0.0045 micrometer	0.0004 micrometer	Orbital thermal condition on OTA/SIP model
Collimating mirror	18 micrometers	1.5 micrometers	Instrument operating
		7.5 × 10 <sup>-6</sup> radian	
Translation			
Tip/tilt			
Spectrograph body	±15 × 10 <sup>-6</sup> radian	4 × 10 <sup>-6</sup> radian	Instrument operating
Tip/tilt			
Focal plane	5 micrometers	0.5 micrometer	
Translation			

Table C.2-10 – Recommended System

Primary reference ring	Titanium, insulated
Mirrors	Lightweight monolithic Cer-Vit
Mirror mount	3 axial flexures, universal, Invar
Metering structure	Thermally isolated athermalized truss, graphite-epoxy
Pressure bulkhead	Titanium honeycomb Augmentation actuators
Secondary mirror mount	4-legged graphite-epoxy spider 5-degree-of-freedom alignment mechanism
Thermal control	
Active	Primary mirror, secondary mirror, reference ring
Passive	Metering structure (super insulation), meteoroid shell (paint pattern to control soak temperature)
Internal baffles	Aluminum, attached to pressure bulkhead and spider
Main light baffle	Aluminum shell supported by meteoroid shell and thermally isolated from metering structure
Meteoroid shell	Semimonocoque aluminum shell
Extendible light shield	Semimonocoque aluminum, cut at 45 degrees and supported by meteoroid shell with extension mechanism
SIP structure	Truss and ring configuration, graphite-epoxy, attached to primary reference ring

### C.3 OPTICAL SYSTEM DESIGN

The LST will have the highest resolution of any telescope ever constructed. The space environment eliminates the atmospheric limitations to the system performance and makes it useful to build as large and as perfect a telescope as desired. The theoretical factor governing the resolution is the aperture diameter, which has been set at 3 meters. All other factors will be minimized or made insignificant to permit the entire system to take full advantage of that aperture.

The optical quality for a nearly perfect optical system essentially is diffraction-limited if the wavefront is perfect to  $1/4 \lambda$  peak to valley (J.W. Strutt, Lord Rayleigh). In the past decade, it has been found that the rms of the wavefront error is a more practical criterion. The current goal is a value of  $0.05\lambda$  rms at 633 nanometers, which is roughly equivalent to the  $1/4 \lambda$  peak to valley. For the LST, the goal is to achieve this quality when all possible sources of image degradation are included, thereby developing a total imaging system that will give the best possible performance with a 3-meter aperture.

If the wavefront is nearly perfect, the performance will then be dependent on diffraction. The outside diameter of the aperture has the most influence, but obstructions inside the aperture also affect the image. Optical systems that have no central obstruction include refractors and off-axis reflectors; neither are suitable for the LST. The selected design is a Cassegrain system, but with an obscuration that is as small as feasible. The operational image quality of the LST will very closely match the diffraction pattern of the aperture geometry.

The telescope described in this section will achieve this near perfect performance. It has a basic Ritchey-Chretien optical design to give excellent performance over a 2-arc-minute data field and adequate performance over a 24-arc-minute guide-star tracking field. The telescope will have a relatively fast  $f/2.2$  primary to keep the structure short. The secondary will have a magnification of 5.5 to give a relative aperture of  $f/12$  at the primary image plane. The image of the basic telescope at fixed points beyond 2 arc-minutes is astigmatic, but the instruments and/or relay optics are designed to eliminate the effects of this aberration. The discussion of optical quality in most of this section refers to the telescope wavefront (i.e., at the  $f/12$  focus) over the portion of the field covered by the high resolution camera.

The primary mirror is one of the more critical elements in the LST. The choice of material (Cer-Vit), surface shape ( $f/2.2$  hyperboloid), and manufacturing techniques are discussed in this section. The secondary mirror is less demanding but it too is a critical optical element and is discussed in some detail.

The reflective coating is considered in detail. The baseline design is aluminum overcoated with magnesium fluoride. It is designed to last the life of the instrument rather than to be recoated periodically.

The techniques used to control stray light are a sunshade, to permit use in sunlight, and well designed but basically conventional interior baffling. High-quality mirrors have been made to excellent quality in terms of overall surface figure, ripple, and scattering; but only the first characteristic has been measured and controlled quantitatively. For the LST application, the effects of ripple and scattering are being investigated closely, so we are expecting to measure and control them quantitatively.

There are a number of mirrors near the image plane to direct the light to the various instruments. Some of these will have a nonflat shape to correct the small but finite astigmatism at the edge of the data field. Other aspects of the optical elements associated with the auxiliary optical devices are discussed in those appropriate sections.

#### C.3.a Detailed Optical Design

The telescope design is a Ritchey-Chretien  $f/12$  with an  $f/2.2$  primary, as shown in Fig. C.3-1. This design will give excellent image quality over the 5-arc-minute-diameter data field with no corrector lenses.

This design has evolved over the past two years of study of the LST program, as discussed in Section B.2.c. The Ritchey-Chretien version of the Cassegrain is usually chosen for demanding applications since the use of a slightly nonparabolic primary permits complete correction of third-order coma. Since all mirror systems can have zero aberrations on axis, this gives the best possible performance over the fields appropriate to the LST. The effect



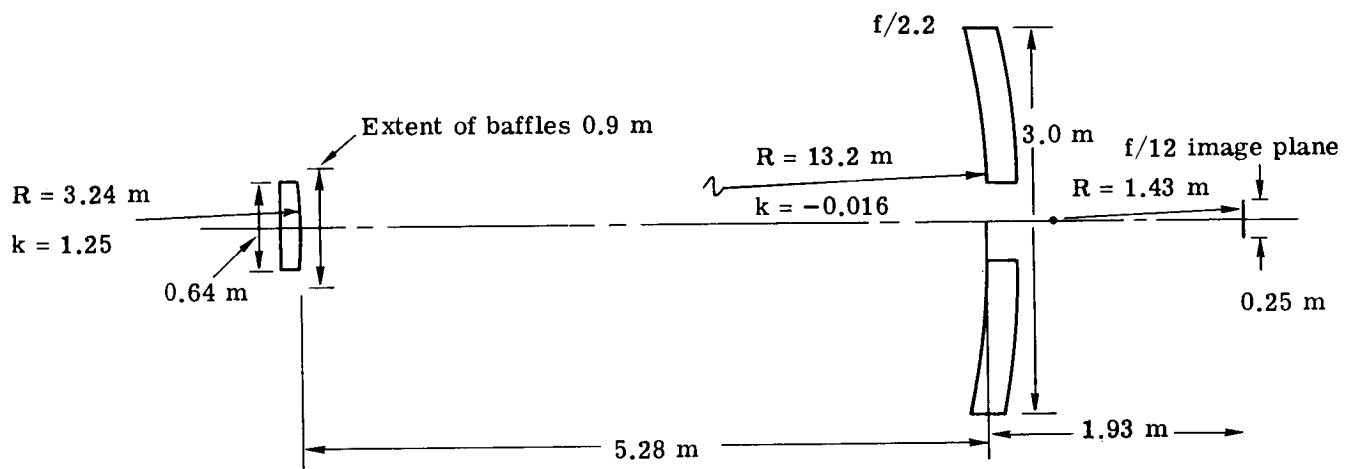


Fig. C.3-1 — LST telescope design (Ritchey-Chretien)

of the wavefront error and image smear on system resolution are presented in this report in sections on the error analyses and budgets.

The performance of the telescope is a strong function of the aperture diameter, a weaker function of the obscuration diameter, and is almost independent of the primary focal length and secondary magnification over a substantial range of values. One of the parameters that drives the design is the vertex back focal length, i.e., the distance between the primary mirror vertex and the focal plane. For the LST, this distance must include the primary mirror thickness, room to mount the tracking field corrector elements, and room for the instruments. A value of 1.93 meters was set by these considerations and is used in the design.

The actual design is given in Tables C.3-1 and C.3-2. The first is the computer printout with optical parameters and the second a listing of system and component parameters. The aberration curves are not shown since the aberration at the edge of the high resolution data field is negligible.

The choice of  $f/12$  for the system relative aperture was dictated by the image size and scale and by the effect of secondary magnification on alignment tolerances. The choice of  $f/12$  is a compromise among many factors, none of which is critically dependent on the actual value chosen.

The choice of  $f/2.2$  for the primary mirror is of considerable interest. This is a relatively fast mirror for an astronomical telescope. The short focal length mirror will keep the telescope section short, making vibration control easier and providing more room for the instrument package and the spacecraft control equipment. The determining factor is the fabrication; it is felt that  $f/2.2$  is the fastest that a mirror can be made using current technology and still meet the exacting surface requirements.

The optical performance in the data field is primarily a function of the telescope aperture size and shape. There will be no vignetting, so the aperture is controlled by the outside diameter, the central obstruction, and the secondary supports. Fig. C.3-2 presents the effect of the central obscuration diameter on the modulation transfer function of the LST. The aperture is the most significant single parameter, since the optical performance is a direct function of aperture. All theoretically perfect performance values scale directly with aperture and, since other sources of performance degradation are small, the LST performance will likewise scale with aperture. The aperture of 3 meters was selected as a goal at the Woods Hole Summer Study.\* That value has received considerable attention in terms of feasibility in the more detailed studies since, and it is still a viable diameter today. The outside diameter of the baseline LST is constrained by the assumed launch vehicle geometry. The walls of the telescope have been made quite thin (see elsewhere in this report) so there is still room for the 3-meter aperture.

The other parameter in the aperture is the central obstruction. Its effect on performance is well known and has been documented in detail in earlier reports. It reduces the performance in the mid-frequencies on the modulation transfer function curve, as illustrated in Fig. C.3-2, and reduces the Strehl criteria performance, as shown in Fig. C.3-3. The central obscuration diameter (usually given as a ratio to the outside aperture diameter) is dictated by the baffle geometry required to prevent light from entering the telescope focal plane directly from the object field. It is, thus, a function of the telescope geometry. In the range of parameters suitable for the LST, the field size and primary focal length have the greatest effect on the baffle. Both of these are already set at the minimum practical values and the baffling needed gives a central obscuration diameter of 30 percent, i.e., 0.9 meter.

The design of the telescope affects both the data image and the tracking image. It is common practice to use a group of refractive elements near the image plane to correct the off-axis aberrations of a Ritchey-Chretien telescope. If that were to be done for the LST, the group would have the center missing, as has been discussed in earlier reports. However, the baseline LST design uses a unique tracker device that operates with the curved, astigmatic image surfaces.

---

\*NASA SP-213, July 1969.

**Table C.3-1 — LST Optical Parameters**  
 (Linear dimensions in centimeters; angular  
 dimensions in radians)

SYSTEM DATA					
F-NUMBER =	12.0000019	ENTRANCE PUPIL DISTANCE =	-0.0000000		
FOCAL LENGTH =	3600.0005761	EXIT PUPIL DISTANCE =	-123.8572219		
BACK FOCUS =	720.8829051	GAUSSIAN IMAGE HEIGHT =	12.5640020		
TOTAL LENGTH =	720.8829051	DP/DV =	0.0000000		
OBJECT HEIGHT =	=0.523E+15	AXIAL BEAM RADIUS =	150.0000000		
CHIEF RAY ANGLE =	0.0034900	CHIEF RAY HEIGHT =	0.0000000		
AXIAL RAY ANGLE =	0.0000000				
-----					
WAVELENGTHS	LOWER 0.4500	MAJOR 0.5500	UPPER 0.7500		
-----					
SURFACE DATA					
SURFACE NUMBER	RADIUS OF CURVATURE	THICKNESS	GLASS TYPE AND/OR N(D)	V(D)	APERTURE DIAMETER
OBJECT	INFINITE	0.150E+18			
1	-1320.0000 CONIC CONSTANT =	-527.8382 -1.0168429	AIR		503.0601
2	-323.6616 CONIC CONSTANT =	720.8829 -2.2539509	AIR		64.6133
IMAGE	-139.3026				

Table C.3-2 — Design Specifications, Baseline 3-Meter LST

Basic parameters

$D_p$	= 3.0 meters	Entrance pupil diameter
$B$	= 1.93 meters	Vertex back focus
$\eta$	= 0.64	Normalized vertex back focus
$F_p$	= 2.2	Primary mirror focal ratio
$F$	= 12	System focal ratio
$\theta_t$	= 6.95 milliradians	Tracking field of view diameter
$A_t$	= 339 square arc-minutes	Tracking field area
$m$	= 5.4545	Magnification

Primary mirror parameters

$R_p$	= -13.2 meters	Radius of curvature
$K_p$	= -0.0168429	Conic constant
$k_p$	= -1.0168429	Conic constant in Itek notation
$D_{hp}$	= 0.555 meter	Minimum diameter, hole in primary

Secondary mirror parameters

$R_s$	= -3.236616 meters	Radius of curvature
$K_s$	= -1.2539509	Conic constant
$k_s$	= -2.2539509	Conic constant in Itek notation
$D_s$	= 0.640 meter	Clear aperture diameter

General parameters

$S$	= 5.27838 meters	Mirror separation
$f$	= 36 meters	System focal length
$e$	= 0.30	Central obstruction diameter ratio (fully baffled)
$l_{ep}$	= 8.4474 meters	Exit pupil distance from image plane

Secondary mirror alignment

$L_{wo}$	= -1.29144 meters	Neutral point location (from secondary)
$I_{wo}$	= 0.05644 meter	Neutral point location (from prime focus)
$\sigma_D$	= 0.000552 wave rms/micrometer decenter ( $\lambda = 633$ nanometers)	Decenter sensitivity (decenter of neutral point)

Image parameters

$D_I$	= 0.25135 meter	Tracking field diameter (uncorrected)
$R_I$	= -1.4269 meters	Radius of curvature, surface of best image quality, data field

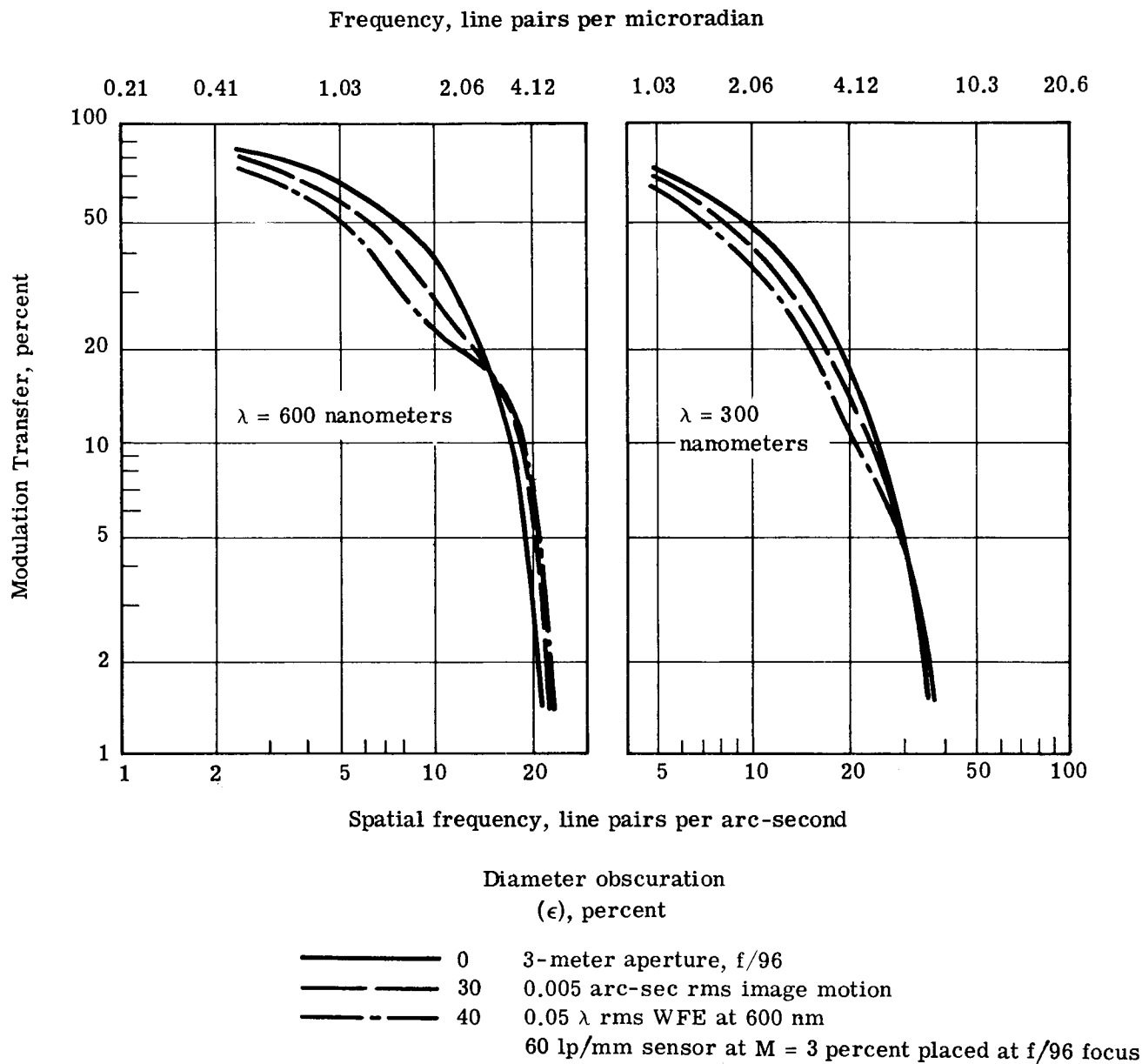
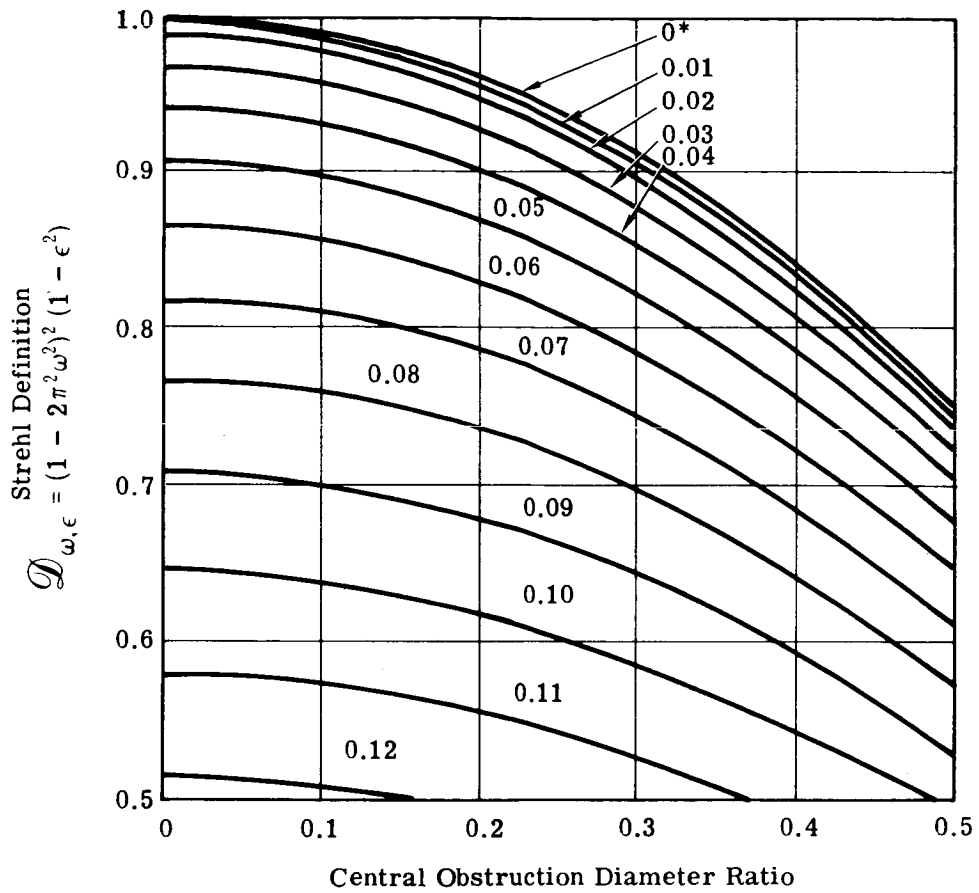


Fig. C.3-2 — Effect of central obscuration diameter on modulation transfer function of high resolution camera. [This graph is taken from a previous report (see footnote on page B.3-2); the quantities are defined and discussed there.]



\* RMS wavefront error

Fig. C.3-3 — Strehl definition as function of rms wavefront error and central obscuration diameter ratio

One of the residual aberrations in the telescope design is field curvature. The image curves towards the mirrors in an arc of approximately 139 centimeters radius. This is shown in Fig. C.3-4, which presents the departure from the paraxial image plane of the image formed by the two mirrors above. As shown, astigmatism is also present as a residual aberration; i.e., the sagittal and tangential rays focus in separate curves. While the best image by conventional terms lies midway between these curves, the nature of Itek's guidance system accounts for this separation of image planes and results in a guidance sensitivity as high as if there were no astigmatism at all.

Another residual aberration in the LST design is distortion. If the system is used for astrometry, this lack of linearity of image displacement from the optic axis must be known very accurately. The formulation for the fractional distortion\* is

$$\frac{\delta y}{y} = \frac{\alpha^2 (F - \eta)}{4m^2 (F_p + \eta)^2} [(m^2 - 2) F + (3m^2 - 2) \eta]$$

where  $\alpha$  = the field angle  
 $F$  = the system focal ratio = 12  
 $F_p$  = the primary mirror focal ratio = 2.2  
 $m$  = the magnification = 5.4545  
 $\eta$  = the normalized vertex back focal length = 0.64

Plots of the distortion are given in Figs. C.3-5 and C.3-6. Fig. C.3-5 presents the fractional distortion, i.e., the departure from the Gaussian image height in units of the Gaussian image height. Fig. C.3-6 presents these same values but as actual micrometers of distortion rather than fractional distortion. The distortion is seen to be about 0.05 micrometers at a 0.725-milliradian (2.5-arc-minute) field angle.

### C.3.b Primary Mirror

The primary mirror of the optical telescope assembly (OTA) will be a 3-meter (118-inch) aperture, f/2.2, lightweight hyperboloid, fabricated of Cer-Vit. This choice of material, mirror mounting, thermal considerations, etc., are discussed in their separate sections within this report. This section concentrates on fabrication and testing of the mirror.

Itek has produced mirrors of similar speed and quality although to date not of such a diameter. However, the process of quality optical polishing is not strictly size-limited. Successful manufacture will be ensured by a relatively simple scale-up of the procedures used on smaller mirrors such as the 1.83-meter (72-inch), f/2.2 parabola that Itek is presently under contract to NASA to fabricate to  $\lambda/64$  quality. The overall figure quality of  $\lambda/64$  has been accomplished before the optician or the test techniques reached their limits; work was stopped when the mirror reached a quality suitable for the application. Previously, the small scale ripple and surface scattering were not considered to be critical parameters because the finished mirrors were made and tested qualitatively to be very good in this regard. It is quite possible that the mirrors have been of a quality suitable for the LST. However, these factors have not been specified nor accurately measured, so they are discussed in the fabrication and testing sections below.

---

\*Wetherell, W.B., and Rimmer, M.P., General Analysis of Aplanatic Cassegrain, Gregorian, and Schwarzschild Telescopes, Appl. Opt. 11:12, 2817 (Dec 1972).

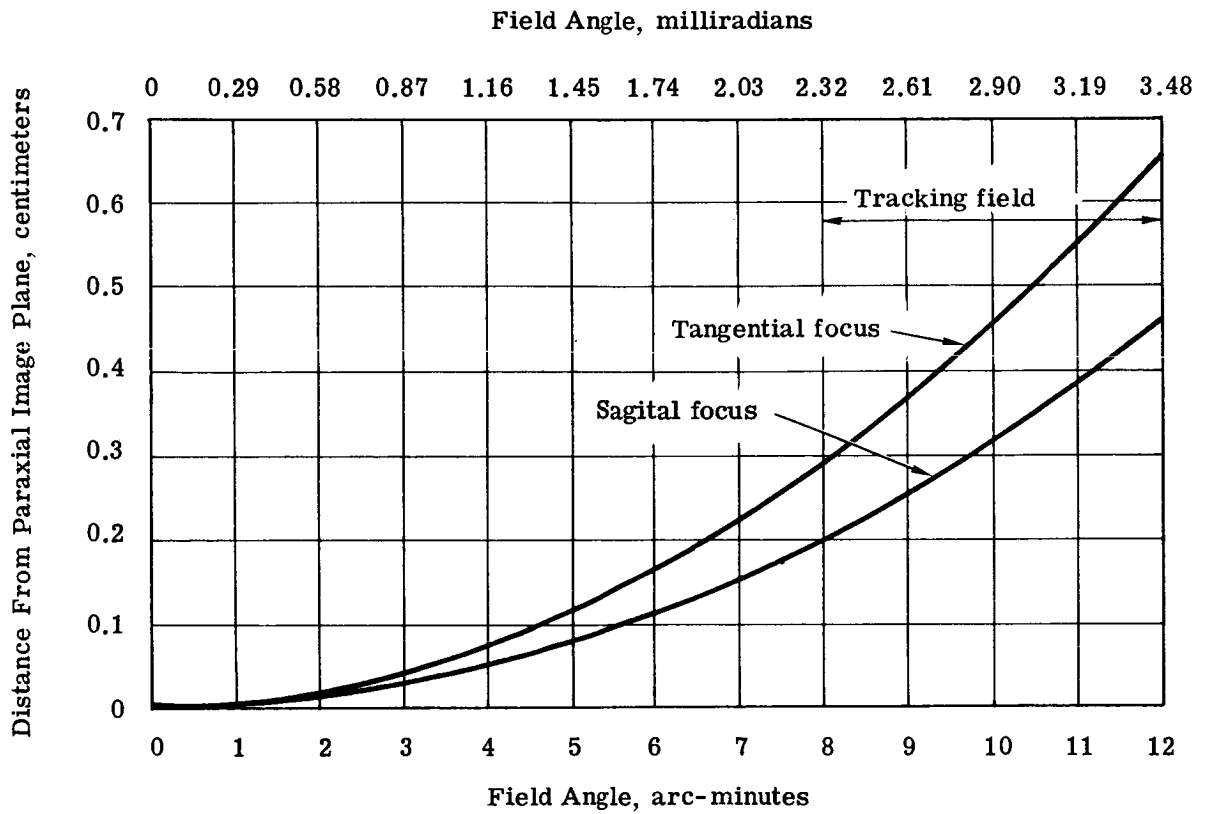


Fig. C.3-4 — Telescope field curvature



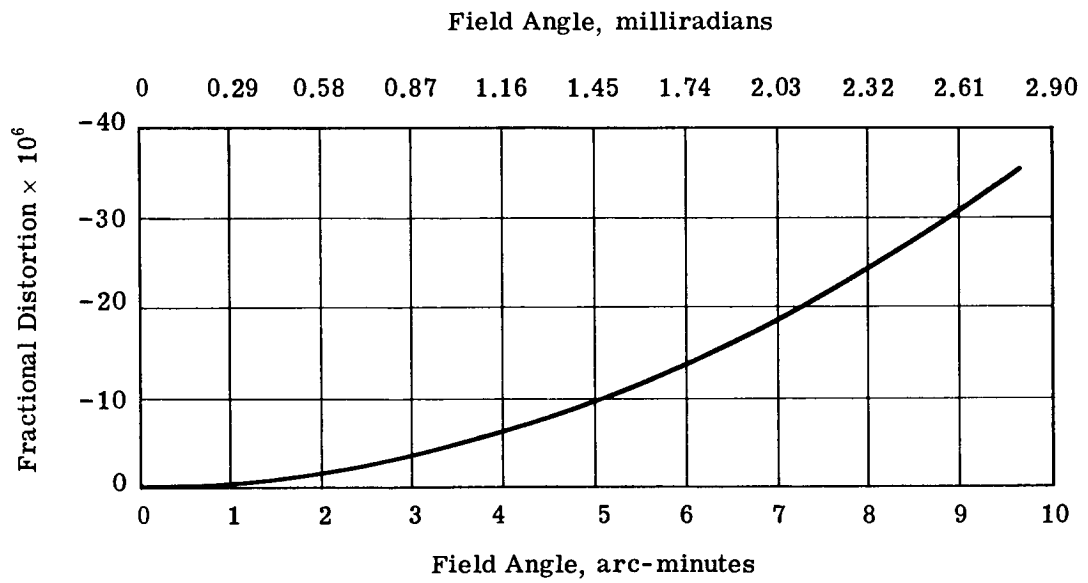


Fig. C.3-5 — Fractional distortion at  $f/12$  focus

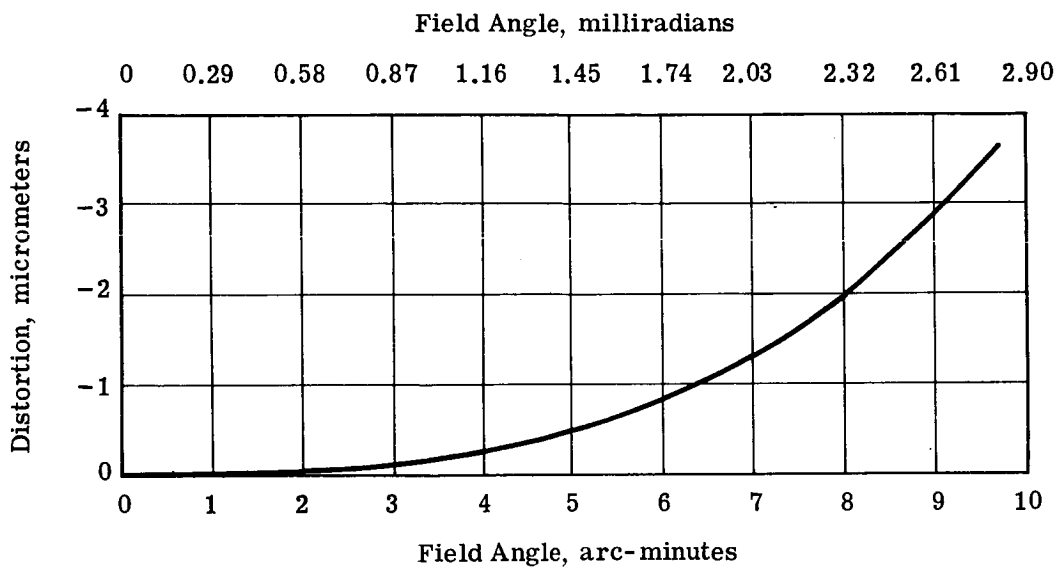


Fig. C.3-6 — Distortion at f/12 focus

### C.3.b(1) Fast Aspheric Mirror Surfacing

#### Production of the Required Parabola

The successful production of the LST primary consists mainly of achieving the correct figure (or aspheric curve) on the mirror and producing a smooth, or nonscattering, surface. The primary mirror of the LST will be very nearly a paraboloid of revolution, hence the applicability of the methods considered here.

One technique for producing the aspheric curve is to generate to the radius of a sphere and then remove material from the center and edge of the piece. The sphere is tangent to the finished asphere at the 7/10 zone. After generating to this radius, the center and edge of the mirror are high relative to the desired asphere, but only 1/4 as high as if the piece had been ground to the vertex sphere. Once the sphere generating is done, the edge is rolled off and the center is worked down to create the desired surface.

#### Removal of High Frequency Surface Structure

The macrostructure of the primary mirror surface is of concern to the astronomical community. There is the possibility that a mirror surface with a low amplitude ( $0.01\lambda$  rms), moderately high frequency (on the order of 1 cycle per centimeter) surface ripple might deviate radiation into a very narrow beam about the image.\*

It has been found that this macrostructure can be controlled by removing the tiles from the aluminum grinding tool and replacing them with a sheet of rubber, thereby increasing the tool flexibility. This flexible tool is then used to work out any scratches and any high frequency surface ripple that may have been left in previous figuring. The techniques have been developed such that overall surface figure, macrostructure, and microstructure can all be controlled. These techniques can be improved further if quantitative tests on the 1.83-meter mirror indicate the need for better control.

### C.3.b(2) Fast Aspheric Mirror Testing

The real problem of producing a surface of  $\lambda/64$  rms quality lies not in the polishing techniques but in ascertaining when such a surface quality is reached, i.e., in the testing. Present data reduction and test techniques, when used with extreme care in the taking and reduction of the data, can reliably measure rms surface error to the order of  $\lambda/100$ .

#### Testing the Primary

It has been found that making a null (or compensating) lens an integral part of the Itek laser unequal path interferometer (LUPI) is the most satisfactory method for testing large, fast aspheric mirrors. Fig. C.3-7 is a schematic of null lens/LUPI combination. After passing through the interferometer beam splitter, the laser light is brought to focus by the first null lens element, producing a spherical wavefront. The diverging wavefront is then reconverged by the second null lens element. It is this element that introduces most of the asphericity into the wavefront. The third element produces a slight additional correction, making a wavefront that matches the desired asphere exactly. By exactly it is meant that this type of null lens can easily be designed to match the asphere to  $\lambda/1,000$  peak to valley on the surface.

The null lens is fabricated to very tight tolerances and it is possible to estimate and remove residual wavefront errors introduced by imperfect fabrication of the null lens. This is accomplished by using standard Itek procedures and software.

The interferometer produces a set of fringes that are photographed, measured, and analyzed. The procedure is conceptually straightforward, but in operation is quite complex and, thus, is done with the aid of a computer. The technique has been recently described in the literature.†

---

\*Some discussion on this subject can be found in the Itek report on contract NASw-2313, Large Space Telescope, Image Quality Analysis (Dec 1972), Section 3.

†M.P. Rimmer, L.M. King, and D.G. Fox, Computer Program for the Analysis of Interferometric Test Data, Appl. Opt., 11:12, 2790 (Dec 1972).

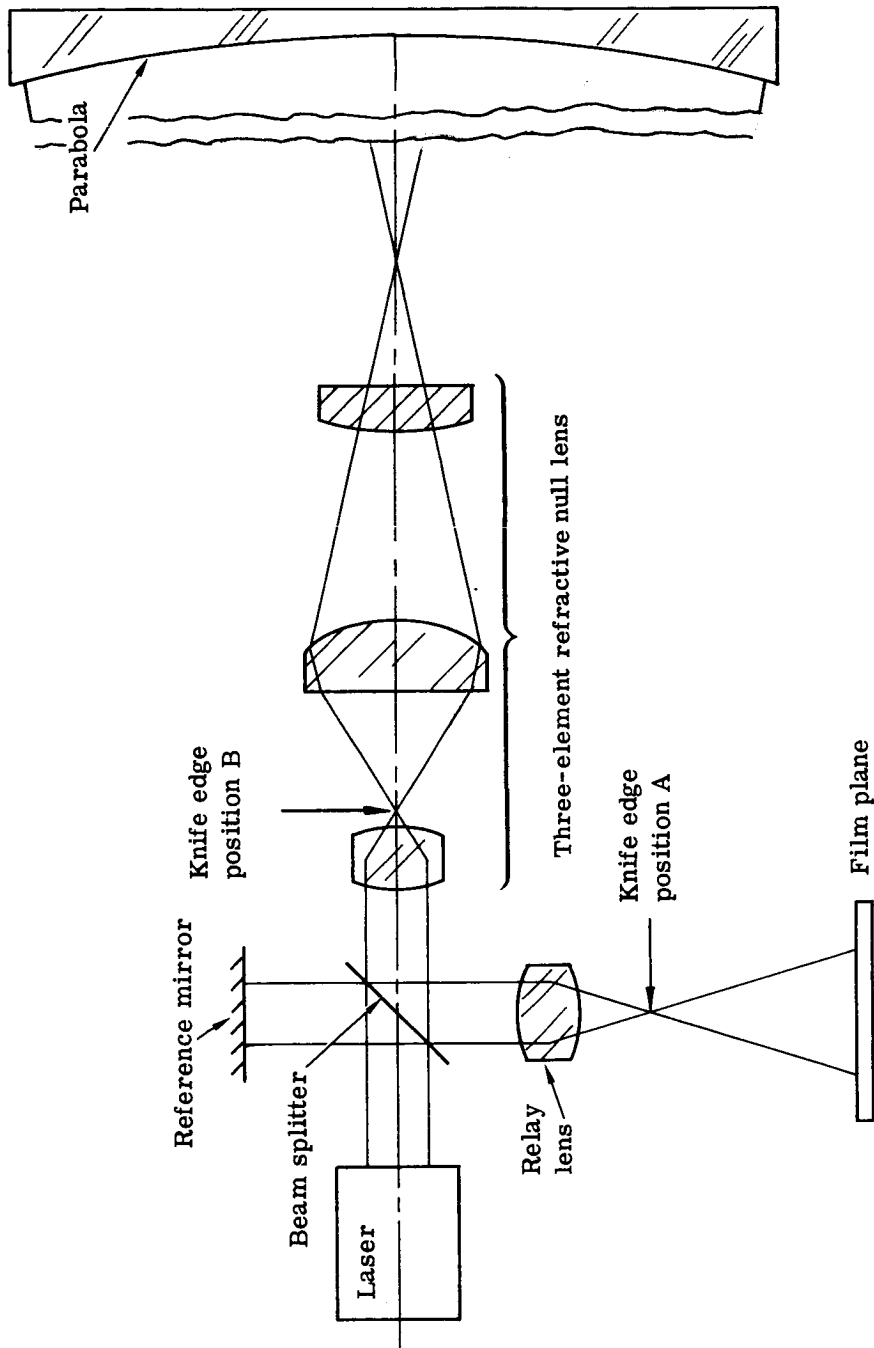


Fig. C.3-7 — Null lens interferometer

### Testing for Removal of High Frequency Surface Structure

The tests described so far determine the overall or low spatial frequency figure errors in the mirror. The interferometric tests are not the most useful nor necessarily the most sensitive method of determining high spatial frequency errors. Their sensitivity to this type of surface defect could be increased greatly by employing multiple beam interferometry, which is being considered for this application. However, other tests are presently more readily available with more sensitivity to the defects under consideration. Fig. C.3-8 shows an interferogram of a mirror surface (a) and a knife-edge test (b). The knife-edge picture was made by placing the knife at position A in Fig. C.3-7 and covering the interferometer reference flat. These photographs were taken at a time when zonal errors were being polished out, and the knife-edge photograph (Fig. C.3-8b) shows up the locations of these zones much more clearly than does the interferogram of the mirror in the identical state of figuring. Knife-edge tests are routine during fabrication. Although Itek has not used the Zernike or Lyot phase contrast tests during large mirror fabrication, these tests may be easily implemented by replacing the knife-edge with the proper phase plate.

Itek has been involved in testing mirrors for surface scattering within programs unrelated to the LST. The entire field is making the transition from qualitative to quantitative testing.

The test technology exists that will allow the fabrication of a 3-meter, f/2.2 asphere to an overall figure quality of  $\lambda/64$  rms or better. In addition, tests such as the knife-edge or phase contrast methods are strictly compatible with the null lens test methods currently in use at Itek. These methods should allow the rapid assessment of the progress made during low scatter and superpolishing stages of optical fabrication.

### C.3.c Secondary Mirror

The secondary mirror of the OTA will be a 71-centimeter (28-inch) diameter convex hyperboloid, fabricated of Cer-Vit. It will be figured to produce an f/12 image at the Cassegrain focus.

The mirror mounting, thermal considerations, etc., are each considered in their separate sections of this report. This section concentrates on (a) the actual fabrication and testing of the secondary and (b) the final figuring of the secondary against the primary and the resultant wavefront error budget.

Itek has produced mirrors similar to the LST secondary and, although the task is at least as difficult as the manufacture of the primary, no severe problems are expected in fabricating this particular piece. Although its smaller size will ease production, the fact that it has a convex surface complicates the testing considerably.

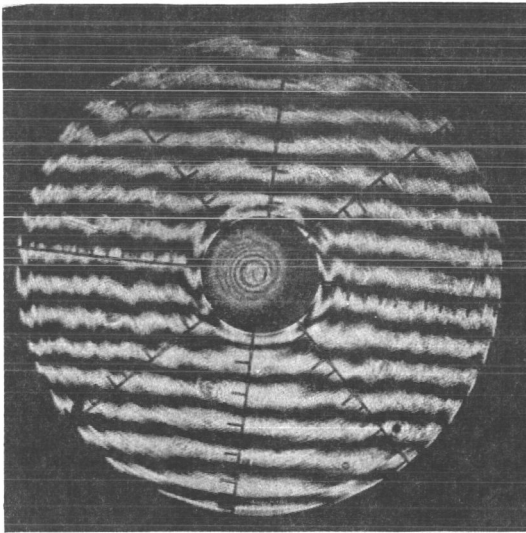
#### C.3.c(1) Convex Aspheric Mirror Surfacing

The production of the convex hyperbolic secondary will be accomplished by using standard Itek techniques. The blank will first be ground and polished to the base sphere (tested against test plates). It will then be polished to the design asphere and Hindle-tested. As stated in Section C.3.b, the problem is not the polishing, but the accurate testing of the piece.

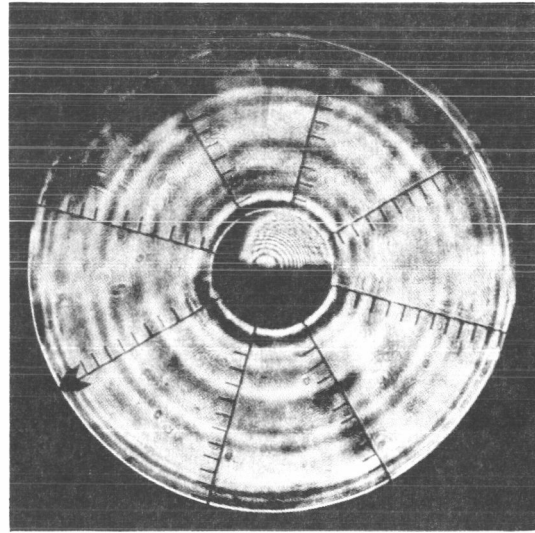
#### C.3.c(2) Testing of Convex Aspheres

The Hindle null test, one of several standard tests used at Itek for testing convex surfaces, will ensure production of the secondary to about 0.01 wave rms. It has the advantage of being twice as sensitive to errors in the secondary as to the test optics, which is not the case for the primary mirror. Thus the figure quality of the secondary can be made somewhat better than that of the primary.

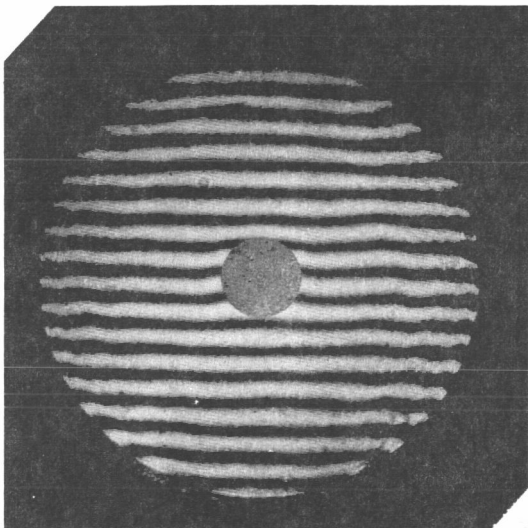
The Hindle null test works on the assumption that the convex secondary is a hyperbola. By placing an interferometer with a diverging lens at the focus in front of the secondary, a virtual image is formed at the focus behind the secondary. A sphere is placed so that its center of curvature lies at this virtual focus, causing the wavefront to return via the secondary to the interferometer.



(a) Interferogram of large parabola. Overall mirror shape is good. Optician is about to concentrate on reducing ripple



(b) Foucaultgram of mirror as shown in (a)



(c) Typical large parabola at conclusion of optical polishing. The mirror exceeds the program requirements, so work was stopped at this point

(Foucault knife-edge patterns are usually examined visually. Meaningful photographs of the pattern formed on a smooth mirror are difficult to obtain and none is available.)

Fig. C.3-8 — Tests showing surface ripple on parabolic mirrors

### C.3.c(3) Final Figuring of the Secondary Against the Primary

The best telescope performance can be obtained by further testing of the entire telescope. The manufacturing concept calls for final figuring of the secondary mirror to null out the wavefront error of the system. This requires measurement in an autocollimation test with a LUPI and the appropriate data reduction. The accuracy with which the optical system can be tested and manufactured with this technique is evaluated in Table B.3-1.

Compensation for errors in the primary by figuring of the secondary can theoretically be perfect for one point in the field (logically the point of the optical axis). Compensation will be less than perfect for other points in the field. Thus, this technique is useful only for narrow field of view systems such as the LST.

### C.3.d Folding Optics

To distribute the telescope image to the various instruments (spectrographs, guidance sensors, f/96 relay, etc.), one or several folding mirrors are used just in front of the primary image plane. These mirrors allow the instruments to be spread out around the optical axis. To ensure that the mountings of these mirrors do not obstruct the guidance field, they are mounted directly to a glass plate that is normal to the telescope axis on the front side of the folding optics assembly. The glass plate is perforated and baffled to allow ultraviolet light to be transmitted without loss. Refractive effects of the plate on the guidance field are included in the optical design and are expected to be slight if low scatter surfacing techniques are used. This glass plate with its attached mirrors can be removed as a unit, as shown in Fig. C.3-9, from the assembly. Work described below has been carried out to show how the primary Ritchey-Chretien astigmatism can be corrected by using weak spherical surfaces on those mirrors that relay images to instruments requiring unaberrated image planes.

The former concept of one small mirror that rotates to fold the data field to selected instruments or moves aside to allow the light to pass to other instruments has been considered and is presented in NASA GSFC X-670-70-480. This is shown schematically in Fig. C.3-10. Although this concept provides great flexibility, it has the significant shortcoming that a failure of the translating/rotating mirror in an intermediate position would prevent further observations.

A more reliable configuration, based on sharing of the available field, is shown in Fig. C.3-11. At the center of the data field is a fixed fold mirror that brings a 0.174-milliradian (0.6-arc-minute) image to the high resolution f/96 camera.

By offsetting the telescope about 1.59 milliradians (5.5 arc-minutes), the beam is brought to the 1.39-milliradian (4.8-arc-minute) f/12 cameras via a stationary fold mirror. The image quality is lower since it is off axis, but at f/12 the image tube will be the resolution-limiting factor. The image quality can be improved by adding correcting optics if later analysis indicates that this would be desirable.

Offsetting the telescope in the other direction allows the light to pass to the various spectrographs, and another offset (e.g., out of the plane of the page) illuminates other instruments.

Small stationary spherical mirrors are used to bring light to the infrared spectrographs and the focus and figure sensors, all of which require negligible field. The spherical surface, properly tilted, gives excellent correction over a small field, even though it may be several milliradians (arc-minutes) off axis.

The concept shown illustrates the most desirable arrangement from a stability viewpoint. A later, slightly different, version is shown in Fig. A.1-1.

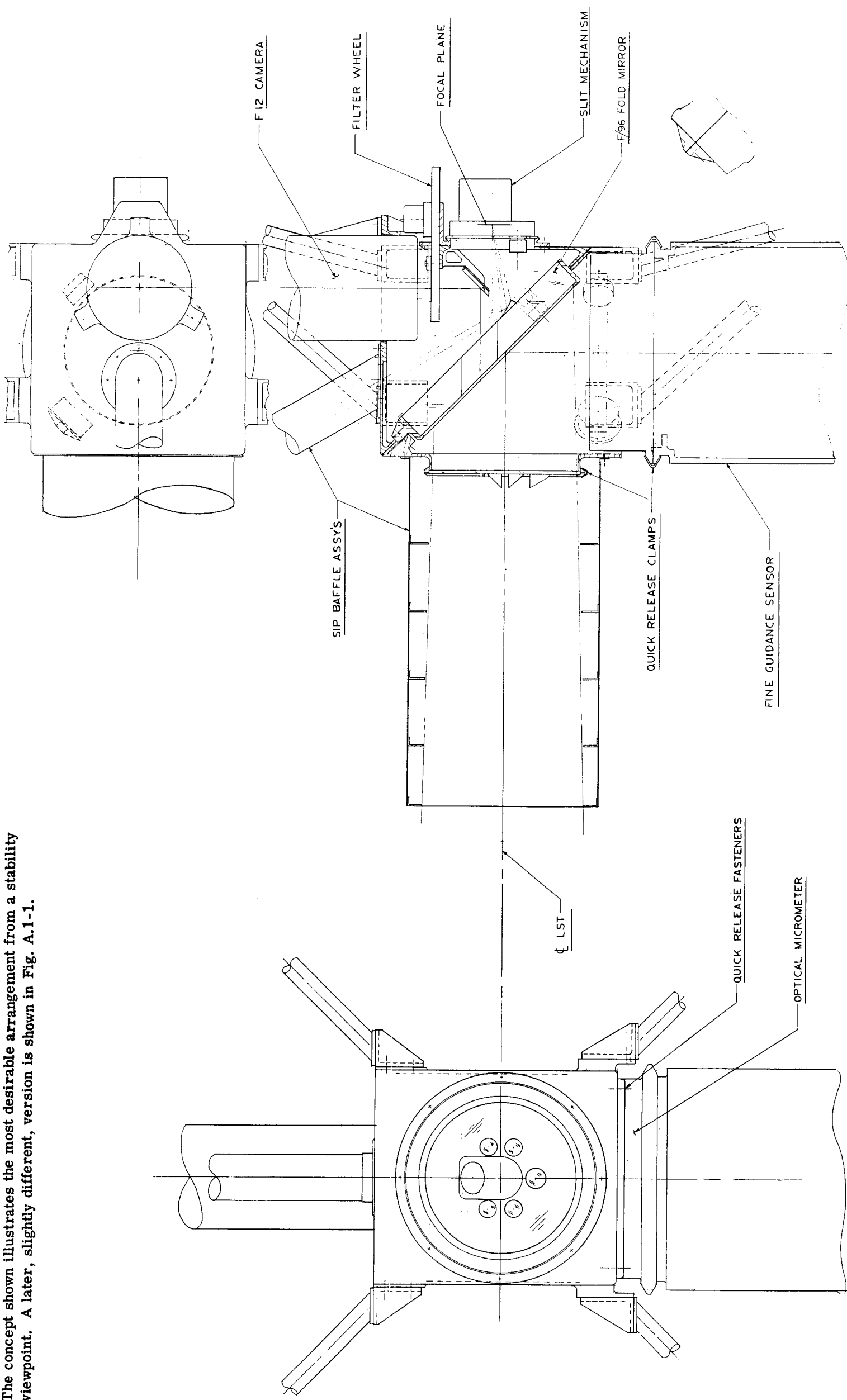


Fig. C.3-9 — Fold optics layout (drawing no. 185514)



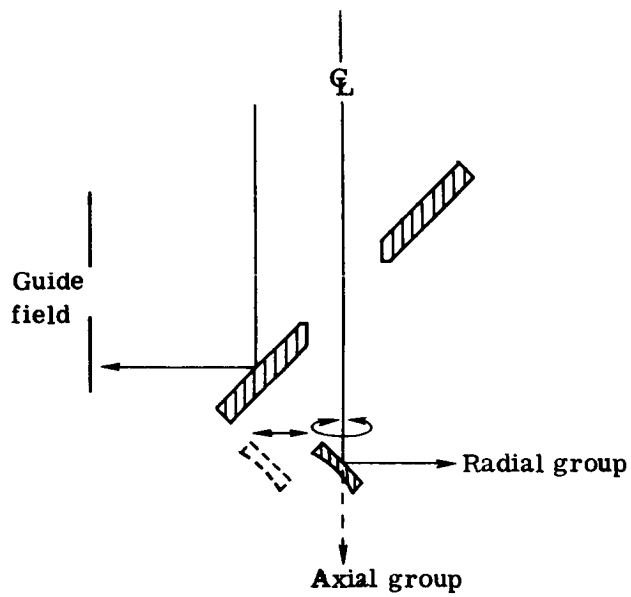


Fig. C.3-10 — Former focal plane layout (Goddard)

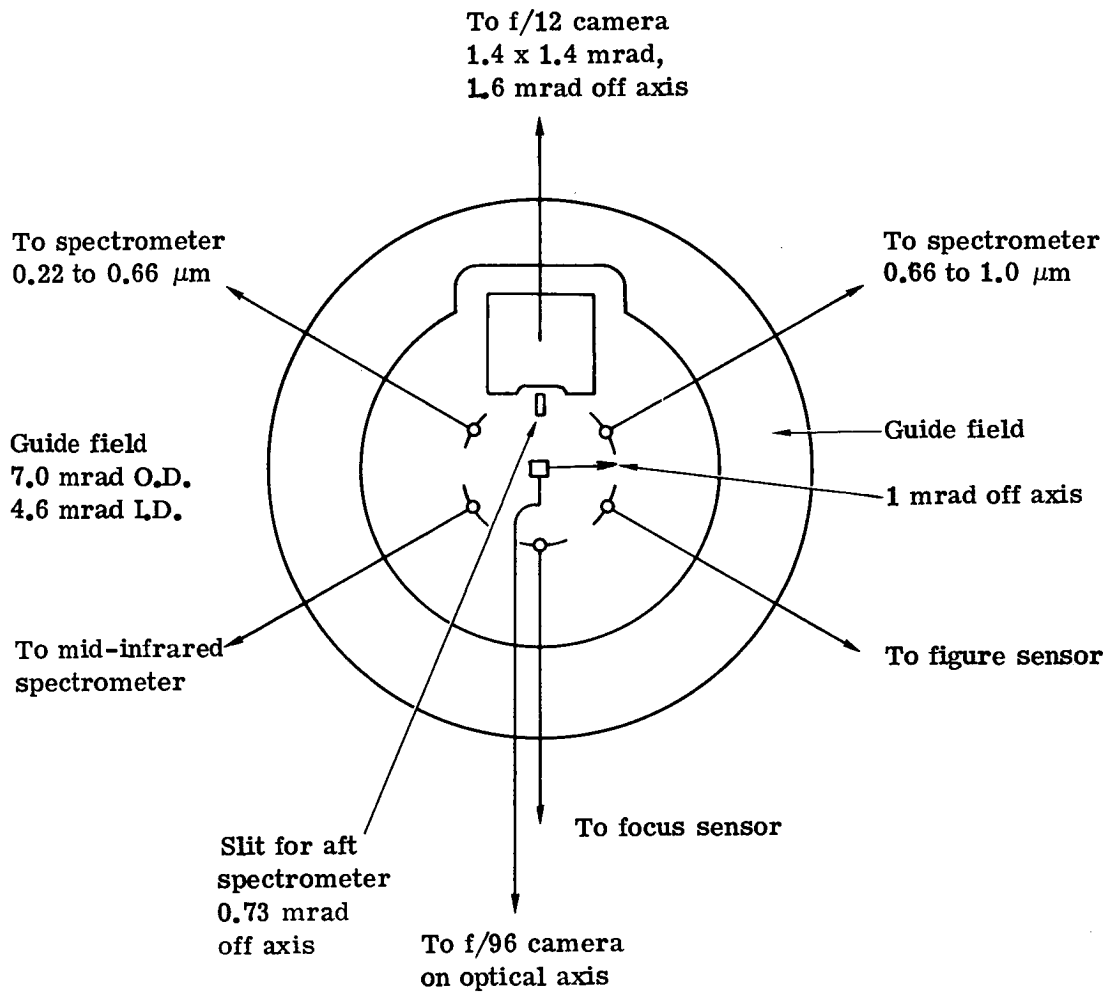


Fig. C.3-11 — f/12 image plane format

The aberration introduced into a beam striking a spherical mirror at a large angle of obliquity is predominantly astigmatism. A 0.78-radian (45-degree) diagonal with a spherical surface, suitably placed inside focus will cancel the astigmatism at one point in the field of a Ritchey-Chretien telescope. To apply this corrector scheme to the LST, it has been necessary to determine how rapidly the correction is degraded at field points surrounding the locally corrected field point.

A family of nine such tilted-surface configurations was evaluated with Itek's optical program for the  $f/2.2/f/12$  LST. Combinations investigated were of field radii 1.5, 2.9, and 5.8 milliradians (5, 10, and 20 arc-minutes) off axis and 30, 60, and 90 centimeters inside focus. The diagonal mirror curvature that minimized the astigmatism was determined. The residual wavefront error was then determined around several concentric circles surrounding the corrected points. A flat focal surface was assumed for each circle, suitably tilted and defocused to minimize the error of the inner and outer field points. Since some field curvature is present, this causes the residual error of the corrected point to increase as the image plane is refocused to provide the best compromise image over the wider field.

The results are given in Table C.3-3. Fig. C.3-12 is plotted for the 90-centimeter inside focus case and for field points radial to the optical axis. The variation of the curves for the 30- and 60-centimeter inside focus cases are too small to plot. The behavior of the curves out of the plane of the paper can be found by referring to the  $\bar{h}, r$  column of Table C.3-3. It will be seen that those skew field wavefront errors are comparable to, or slightly smaller than the  $\bar{h}-r$  values in all cases.

For visual instruments, one might budget 0.02 wave rms to design wavefront error; Fig. C.3-11 shows that, at 1.5 milliradians (5 arc-minutes) field height, the local field is over 0.29 milliradian (1 arc-minute) diameter; but, at 2.9 milliradians (10 arc-minutes) field height, the local field is only 0.58 milliradian (0.2 arc-minute) diameter. (The growth of higher order aberrations at larger field angles prevents extremely good local correction with only a spherical surfaced diagonal.) An infrared instrument might have a 0.05 wave rms design wavefront error, in which case some usable local field is available beyond 4.4 milliradians (15 arc-minutes) field height.

Thus, a focal area layout (Fig. C.3-13) of considerably higher reliability than that considered previously has been obtained. There is no moving fold mirror to fail and limit observational flexibility, which advantage must be weighed against the disadvantage that it would be necessary to offset the LST between each observation if one object is to be analyzed by several instruments in sequence in different bays. However, this will rarely be the observing program, so it is relatively unimportant.

The fold mirrors should be of the highest quality attainable in order to introduce virtually no wavefront error. They will, in all probability, be fabricated to better than  $1/100$  wavelength rms. While this is certainly not a trivial task, the ability to polish small mirrors to such tolerances is well established.

### C.3.e Material Selection

Constant development in the technology of producing large diameter, lightweight mirror blanks demands a continuous surveillance of the industry in order to rationally select the appropriate material for any particular application. Specifically, the LST requires a primary mirror of 3-meter (120-inch) diameter to be figured to a minimum surface error of  $\lambda/64$  rms, which quality is to be maintained for a 10-year orbital lifetime in a controlled thermal environment of  $\pm 3^\circ\text{C}$ .

There are several materials that can be considered for this application: Corning ULE (titanium silicate), Owen-Illinois Cer-Vit, fused silica, and Zero-Dur. Due to the overall size requirement, the need for a lightweight blank, and the desire to minimize the sensitivity to thermal variation, the choice was reduced to two prime candidates, Cer-Vit and ULE. This subsection is confined to a comparison of those two materials.

Table C.3-3 – Astigmatic Correction Values for Various Local Field Radii\*

$\bar{h}$ , mrad	B, cm	r, mrad	WFE, $\lambda$ rms			
			$\bar{h}$	$\bar{h} + r$	$\bar{h}, r$	$\bar{h} - r$
1.45	90	0.58	0.053	0.116	0.089	0.078
		0.29	0.014	0.054	0.043	0.042
		0.145	0.006	0.027	0.022	0.022
	60	0.58	0.053	0.120	0.089	0.080
		0.29	0.014	0.056	0.043	0.043
		0.145	0.006	0.028	0.022	0.022
	30	0.58	0.053	0.132	0.089	0.087
		0.29	0.014	0.061	0.043	0.048
		0.145	0.006	0.030	0.022	0.025
2.9	90	0.29	0.023	0.112	0.087	0.092
		0.145	0.019	0.059	0.046	0.048
		0.072	0.018	0.035	0.028	0.027
	60	0.29	0.023	0.117	0.087	0.098
		0.145	0.019	0.062	0.046	0.050
		0.072	0.018	0.036	0.028	0.028
	30	0.29	0.023	0.134	0.087	0.116
		0.145	0.019	0.070	0.046	0.058
		0.072	0.018	0.040	0.028	0.081
5.8	90	0.145	0.068	0.146	0.108	0.112
		0.072	0.068	0.099	0.080	0.075
	60	0.145	0.068	0.157	0.108	0.123
		0.072	0.068	0.104	0.080	0.078
	30	0.145	0.066	0.191	0.106	0.156
		0.072	0.066	0.118	0.078	0.089

\*  $\bar{h}$  is the distance from the telescope optical axis to the center of the local field

r is the radius of the local field

B is the distance that the fold mirror is from the parallel focal plane

$\lambda$  is the wavelength,  $\lambda = 550$  nanometers.

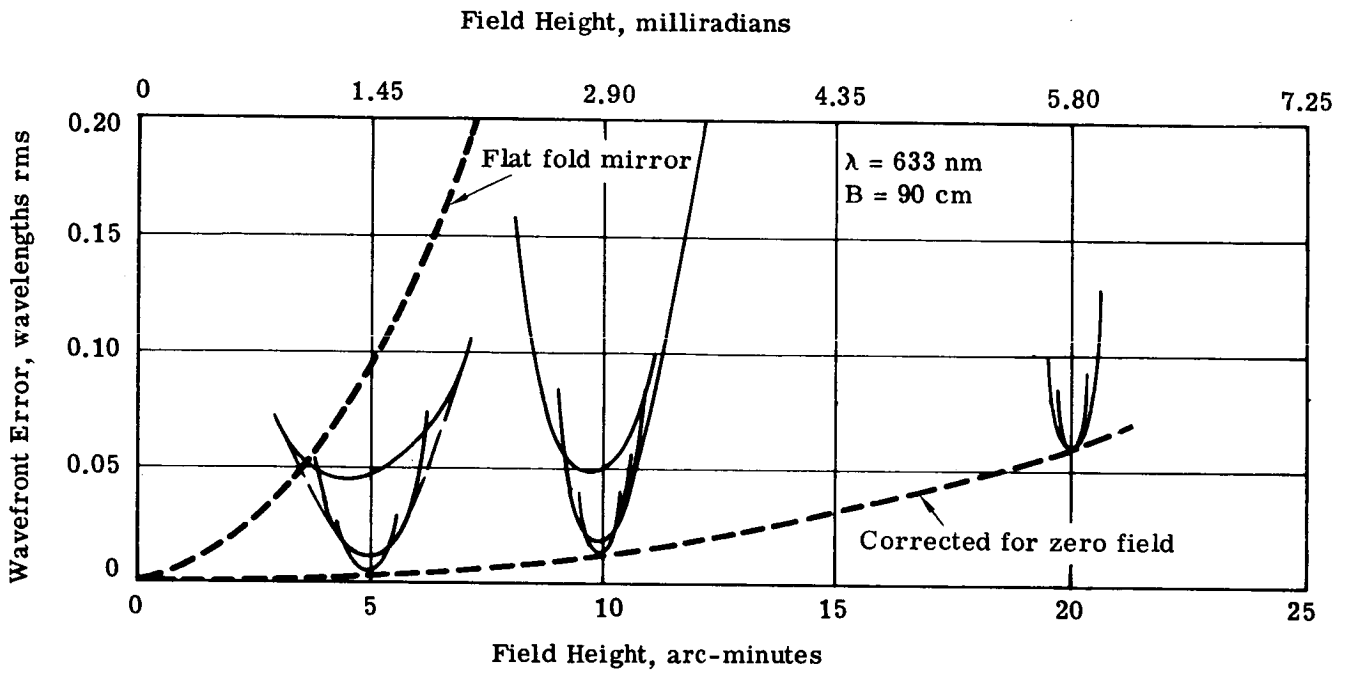


Fig. C.3-12 — Local field correction, using spherical fold mirrors 90 centimeters in front of focus

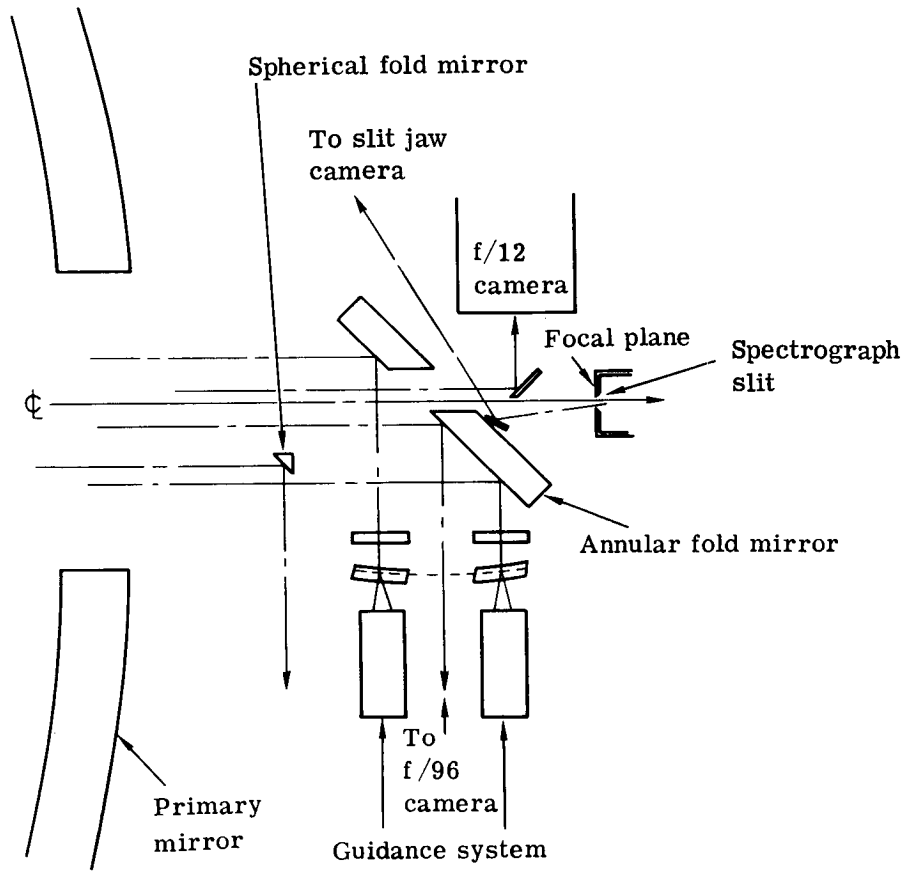


Fig. C.3-13 — Focal plane layout

To investigate adequately the many facets of producing a suitable mirror blank, one must start from a basic design that incorporates the particular character of each material. Designs of mirror blanks for both materials, which were discussed with the individual suppliers, are used as a comparable reference baseline.

Critical parameters in the evaluation are, of course, the physical characteristics of each material and the influence of these parameters on the end item product. The discussion is divided into optical influences, structural or mechanical influences, and the economics/productivity factors.

The study has indicated that the selection process is not a simple decision. Both materials have comparable qualities. There is no outstanding characteristic that would make the selection process obvious. In an attempt to provide a fair and intelligent recommendation, an evaluation matrix was developed and is included in Table C.3-4.

Attention is focused on quantitative comparison of the engineering design parameters obtainable at the present state of the art in fabricating lightweight mirror structures of the two low thermal expansion glasses: ULE titanium silicate (7971) and Cer-Vit (C-101). The production of a durable, highly specular surface on these materials is well within the existing state of the optician's art. The major constituent of both materials is  $\text{SiO}_2$  and chemical attack is unlikely. Similarly, radiation damage will probably not be a significant factor and, hence, has not been addressed in this preliminary analysis.

Finally, quantitative comparisons combining fundamental physical property differences with the differences in lightweight structural configurations preferred for each material (e.g., welded ULE versus machined Cer-Vit) are attempted.

### C.3.e(1) Composition and Molecular Structure

#### ULE Titanium Silicate

The production method for Code 7971, which consists of  $\text{SiO}_2$  plus approximately 7 percent of  $\text{TiO}_2$  is essentially identical to that for Code 7940 (fused silica), with the reactant mixture being  $\text{SiCl}_4$  and  $\text{TiCl}_4$ .

One useful effect obtained is that the temperature at which the thermal expansion coefficient ( $\alpha$ ) passes through zero is shifted into the 5-35°C range. Material having a coefficient of  $0 \pm 0.03 \times 10^{-6}/^\circ\text{C}$ , 5-35°C is now a standard product. The addition of  $\text{TiO}_2$  introduces a potential source of inhomogeneity, and variations of  $0.02 \times 10^{-6}/^\circ\text{C}$ , 5-35°C between the center and edge of each boule are consistently observed.

#### Cer-Vit

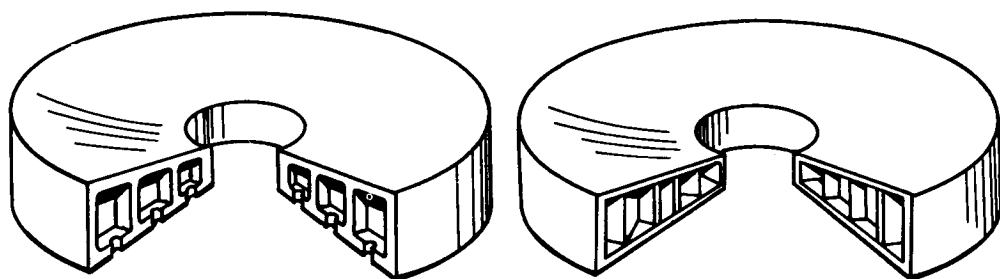
Cer-Vit begins as a lithium-aluminum-silicate glass, melted and poured, using conventional glass technology (with a pouring temperature much higher than for soda-lime glass and comparable to boro-silicate glass). After solidification, it is subject to a temperature/time cycle that causes nucleation and growth of crystals in the glass matrix. In C-101, the final crystal size is substantially smaller than the wavelength of visible light. The material remains transparent, light yellow in color, and only slightly hazy. Birefringence measurements have been made through a 0.60-meter (24-inch) thickness without difficulty.

The C-101 material is formulated and treated to yield a low thermal expansion coefficient, comparable to that of ULE — i.e.,  $0 \pm 0.03 \times 10^{-6}/^\circ\text{C}$ . The final value of  $\alpha$  is dependent on both composition and heat treatment. Subsequent reheat treatment can be accomplished, but can only raise the value of  $\alpha$ .

Good practice in melting, stirring, and pouring will result in good homogeneity in a finished blank, as partially evidenced by the 3- to 5-micrometer/centimeter strain birefringence often achieved through all the major portions of a large blank. Destructive testing of one large blank showed no detectable variation in  $\alpha$  for a measurement precision of  $0.02 \times 10^{-6}/^\circ\text{C}$ .

Table C.3-4 -- Material Comparison

Parameter	Cer-Vit	ULE
Coefficient of expansion $\alpha$ at 35°C, centimeter per centimeter per °C	$0 \pm 0.03 \times 10^{-6}$	$0 \pm 0.03 \times 10^{-6}$
Modulus	$13.0 \times 10^6$	$9.7 \times 10^6$
Birefringence, micrometers per centimeter	10	40
Material stability	Good	Good
Design flexibility	Good	Poor





### C.3.e(2) Fabrication Methods for Lightweight Structures

#### ULE Titanium Silicate

The fusion of pure silica requires heating the entire structure to prevent fracturing. The thermal expansion of ULE, however, is sufficiently low that it may be welded to itself at one point in a structure, while the major portion of the structure remains at room temperature, much as in the fusion welding of steel. This makes practical the preassembly of a fully fused, ribbed core structure, subsequently joined to front and back plates as for the eggcrate structure. The additional joining obtained at the rib intersections contributes measurably to the overall stiffness of a blank of given size and weight.

#### Cer-Vit

Cer-Vit, in the glass stage, is cast by the same techniques used for high temperature glasses. Care must be used in mold design; intricate shapes are difficult to achieve because of the shrinkage on solidification and cooling and the further shrinkage in the nucleation and microcrystal stages during heat treatment. Thus, direct casting of lightweight structures is difficult and better success has been achieved by machining, using metal bonded diamond tools, directly from solid disks.

The final finishing of the internal surfaces of lightweight Cer-Vit mirrors is accomplished by chemical milling with hydrofluoric acid, and as now practiced contributes substantially to weight reduction as well as the removal of any microcracks that may be left by the machining operations. The major structural difference of the machining approach relative to the egg-crate approach is the necessity of perforation of the back plate to provide machining access to remove core material.

### C.3.e(3) Physical Properties

#### Expansion Coefficient

The development of lightweight mirror structures of ULE and Cer-Vit has been driven by the need to obtain near-theoretical optical performance in large spaceborne optical systems for which precise control of temperature, temperature distribution, or extraneous heat fluxes might be impossible. ULE and Cer-Vit have been tailored to achieve low  $\alpha$  with the same ultimate goal of identically zero. The residuals now reflect only differences in the precision of and confidence in the measurement methods used and in process control tolerances.

#### Homogeneity

Since the target for ULE and Cer-Vit is a mean value of zero  $\alpha$ , small deviations from the mean may represent large percentage variations. Reduction of these deviations may be of more interest than the mean value within a given piece.

Beyond those physical properties previously discussed in this section, there are other less definable parameters that must be evaluated to display a comprehensive coverage of the material selection problems.

### C.3.e(4) Current Capabilities

While many advancements have been made throughout the industry over the past years in the development of large-diameter lightweight mirror blanks, the optical community has just as actively placed more stringent demands on the blank suppliers. The requirements outlined for the large space telescope have continued that trend. While many mirror blanks have been produced of equivalent and larger diameter than the LST, they have not been produced with the weight restrictions or the long-term maintenance of an ultra-high quality surface as the LST. The LST requirement then is to produce a large diameter, minimum weight, minimum sensitivity, and an extremely high quality optical primary mirror that will retain its performance over a 10-year lifetime.

#### Titanium Silicate

The ability to produce a mirror blank of the required specifications of ULE is of concern basically in four areas. To date, the fabrication of the total thickness of a lightweight mirror has been restricted because of size and

weight to a core matrix not exceeding 0.30 meter (12 inches). The requirement for the core thickness of the LST primary would be 0.41 meter (16 inches); with the two faceplates added the mirror thickness is 0.48 meter (18.75 inches). While this requirement does not demand any special advance in the technology of mirror blank fabrication, it does require a substantial retooling effort, along with the inevitable learning curve that results in an increased capability. The cost of the retooling would be reflected in the procurement of the initial blank.

A second area of concern is the current ability to fabricate the front and back plates from a single piece. At this point, the largest diameter, single, ULE plate that has been produced is one of approximately 2.54 meters (100 inches). To produce the front and back plates for the LST primary mirror blank, there are alternatives. The conventional approach is to segment several hexagonal shaped pieces and fuse them together to build up essentially a single plate of the required diameter. This process results in a series of vertical seams where the segmented pieces are joined. The concern with this technique is, of course, the alpha variation from one segment to the next, as well as the effect that may result from bubbles and inclusions normally inherent in the joining of the vertical seams. The second choice is to continue the technology required to flow a single piece of ULE out to the required diameter. This process, while successful on diameters up to 2.54 meters (100 inches), has not been attempted on any larger diameters. The process essentially is to subject a single piece of ULE of appropriate thickness to pressure and temperatures that will cause the material to flow out to the proper diameter and thickness. Again, there does not seem to be any obvious restriction to this technology. Rather, it is a case of this demand not being previously placed upon the supplier.

The third area of concern covers the techniques that would be employed to accomplish a fused connection first between the inserts at the three support points of the mounting system and then between them and the basic core matrix of the mirror blank. Several methods have been reviewed with the manufacturer. While many techniques have been used over the years in a variety of configurations, the concept of fusing the highly stressed pickup points to the core matrix, as well as the front and back plate, has not been fully developed. To accomplish this successfully would require some additional detail design and development.

The final area of significant concern is in the slumping process. The requirement for the large space telescope blank requires that two important parameters be considered during this process. The design of the LST optical system requires a very fast primary mirror. Mirror radius equivalent to an  $f/2.2$ , plus the additional thickness in the overall height of the blank, presents a new and demanding set of circumstances to complete the slumping process satisfactorily. These demands, while new and extremely stringent, are again not beyond the state of the art. They are, however, beyond the current capability and pose a serious problem in developing a high degree of confidence for a timely delivery.

#### Cer-Vit Capabilities

The development of a large diameter, lightweight mirror blank of Cer-Vit is a substantially different process from that of the ULE. The process basically is to pour a solid blank of the required diameter and thickness and then accomplish the lightweighting process by essentially machining out hexagonal shaped cores from the back surface of the mirror blank. This process is essentially a machining operation, using diamond tools.

In the development of the original solid blank, it is customary to control the temperature cycle to produce a blank having a negative expansion coefficient. Upon defining a specification for a particular blank, the original blank is reheat-treated to obtain the required expansion coefficient. This process is irreversible and, while the reheat cycle is well planned, well instrumented, and closely controlled, there does exist the danger of exceeding the allowable limits of the cycle.

The second area of concern is in the coring of the hexagonal pattern to lightweight the blank. While sample cores have been produced of the depth required for the LST blank, present information does not reveal that Owens-Illinois has produced a completely cored blank of this diameter. Substantial caution must be exercised in the

machining process to avoid a catastrophic failure as well as to maintain the close tolerances required to produce a uniform cross section. The tooling required to produce the lightweighted blank per specifications has been developed, manufactured, and tested at Owens-Illinois. To lightweight a blank of this size, additional tooling would be reproduced to the current design to facilitate a reasonable delivery cycle. It is estimated that approximately three cores would be machined simultaneously.

#### C.3.e(5) Summary

Two materials, Cer-Vit and ULE, are satisfactory candidates for the LST primary mirror. The selection at this time is based upon the current size capability of the vendor and, thus, is Owens-Illinois Cer-Vit.

#### C.3.f Stray Light Suppression

The LST will be able to observe only very faint (e.g.,  $m \sim 30$ ) objects if the sky is sufficiently dark and if stray light within the system can be controlled. There is nothing that can be done about the sky, other than to select wavelength and direction. Sky light consists of radiation from stars, galaxies, and nebulae, sunlight reflected from the earth's residual atmosphere, and emissions from the residual atmosphere. It may be that some control can be exercised over the gaseous cloud that accompanies the LST in orbit, reflecting sunlight and emitting radiation, but how much remains to be determined.

Inside the LST, one may hope to exercise control over various stray light sources that could degrade image contrast or restrict faint object detection. A mirror surface that scatters light makes each star seem fainter and, at the same time, increases the apparent sky background through which the star must be seen.

After discussing the measuring of scattered light, superfinishing of optical surfaces to minimize scattering is considered (Fig. C.3-14). Contamination of the optics by residual gases or outgassing can produce similar degrading effects, as shown in the next subsection.

The control or suppression of stray light in the LST will follow the usual techniques for baffling a Cassegrain telescope. The baffles and surface finishes will be more complex than usual in order to achieve the very low stray light levels that are needed to make full utilization of the telescope. The major effort has been devoted to techniques that will permit operations when the telescope is in sunlight – a rather unusual situation for an astronomical telescope.

The control of stray light has been considered in previous Itek studies \*† and in a concurrent study at The University of Arizona.‡ This work has been reviewed and augmented by some on-going work at Itek. While it is presently not possible to predict quantitatively the stray light levels nor to select optimum techniques, a baseline configuration has been selected by means of conservative conceptual analyses. Most of the baseline configuration is expected to remain firm throughout the LST program; the one item that might change is the sunshade. When present work at The University of Arizona is completed, it will be possible to draw more firmly based conclusions.

---

\*Large Space Telescope Continuation of a Technology Study, Itek 71-9463-2, 3 Sept 1971.

†Technology Study for a Large Orbiting Telescope, Itek 70-9443-1, 15 May 1970.

‡The University of Arizona, Midterm Progress Report, NASA Contract NAS 8-27804 Stray Light Suppression Study for Large Space Telescope.

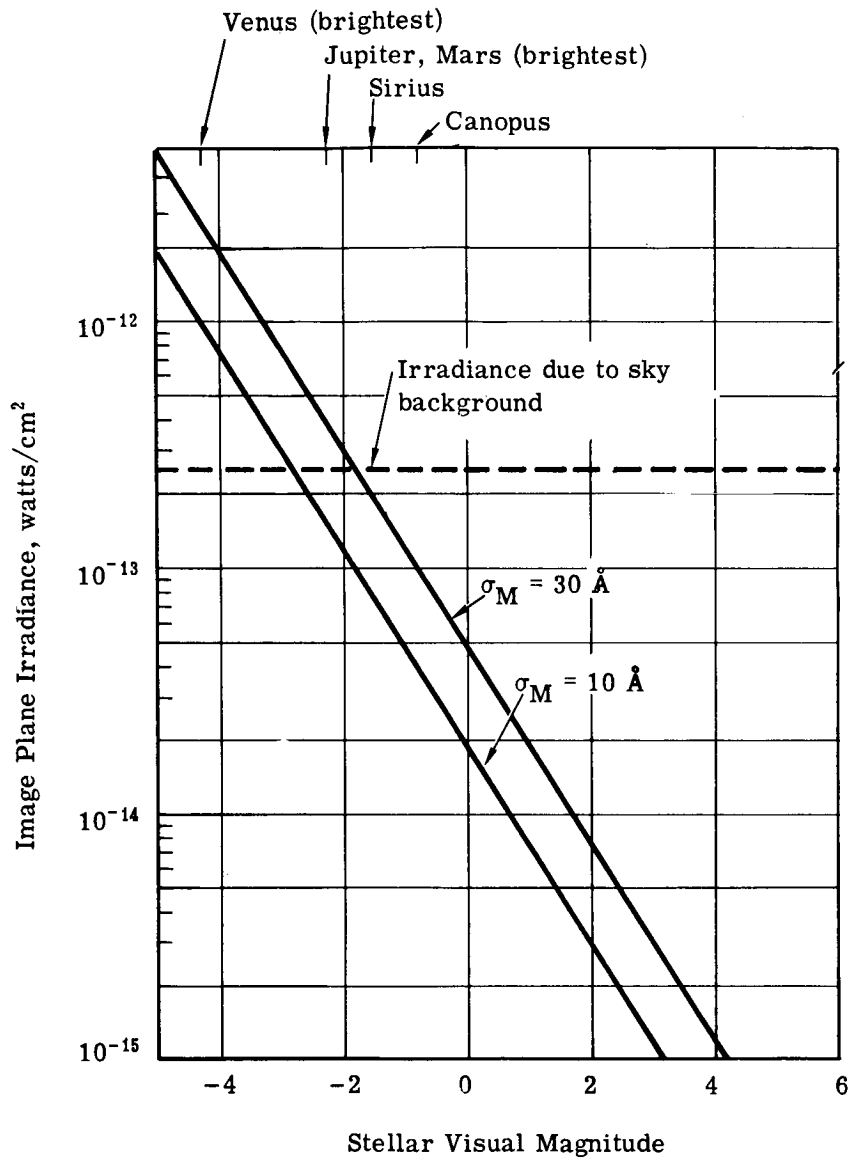


Fig. C.3-14 — Irradiance in LST image plane as a function of visual magnitude of a stray light source at edge of data field

The basic baffling is provided by the long narrow cone in front of the primary, the shorter cone in front of the secondary, and the opaque wall of the telescope, as seen in Fig. A.1-1. There had been some question as to whether or not to baffle the edge of the tracking field fully, but the tracking field is now smaller and the baseline design is baffled fully. The two-cone baffle will subtend a large solid angle at the image plane and so will be carefully designed with secondary baffles such as those shown in Fig. A.1-1. The baseline design does not vignette the tracking field, so a small amount of the rear section of the telescope tube can be seen from the image plane via the telescope mirrors. In the detailed design, this rear section will be kept very dark or (better) the baffles will be extended if the tracking field can tolerate a small amount of vignetting.

The inside of the telescope tube will be baffled with ring baffles as indicated in Fig. A.1-1. The design shown is based upon simple rings that allow single reflection deeper into the telescope but not onto the primary mirrors. The slant angle follows The University of Arizona report recommendation. The depth is only 7.62 centimeters (3 inches), a compromise forced by the LST restricted outside diameter.

The telescope walls are thinner just in front of the secondary, permitting deeper baffles. However, the doors must be stored in this region. The doors will have baffles to match those on the tube which it is expected will be about as effective as other parts of the baffle, since the area of the exposed gaps at the edges of the doors will be kept small as compared to the overall baffle area. The baffling in the extendible portions of the tube will be similar to that inside the main telescope body. The detailed design might be somewhat different owing to different optical and structural details, but the configurations will be similar, as shown in Fig. A.1-1. The final design will consider more complex baffles (such as the honeycomb treatment suggested in Itek report 71-9463-2, page 3-40), more advanced design criteria, and the possibility of using the space between the baffle and the outer shield as a light trap. The optical characteristics of the baffle edges will have a substantial effect on the design and performance of the overall baffle configuration.

The Denver Division of Martin-Marietta Corporation has developed a process that, when applied to an aluminum alloy, produces a surface that has been proven to be the blackest (low reflectance) surface known to date. From 0.27 to 120 micrometers (far ultraviolet to far-infrared), the reflectance of the surface is less than 0.015, except for a region between 1.2 and 3 and 4.5 to 6 micrometers. In the visible, the reflectance is less than 0.010.

Most of the development has been conducted on 6061-T6, a commonly used aluminum alloy. Coatings have been made on 7075, 2024, 2012, and Invar; in general they are comparable to the 6061. The materials have been tested by Martin-Marietta for outgassing and environment effects for space use, and are used by them for space applications. This coating has been applied to the edges, and is reported to give less stray light than razor edges, as shown in Fig. C.3-15.

The surface treatment of the secondary support spider will include small baffles and possibly honeycomb material. This structure is particularly sensitive to stray light since the image plane can view this region through the two telescope mirrors. Thus, some of the light scattered by this structure will reach the image plane without further attenuation. Even with the best of baffling, this structure will be a source of stray light and it is expected that the levels will not be maintained with moonlight shining directly on the secondary spider structure. The University of Arizona has recently suggested a black mirror surface for the spider, an interesting alternative to the small baffles.

The front of the telescope is configured to be an effective sunshade. The baseline design is based on the recommendation given in The University of Arizona report. The choice of design is not critical to the successful operation of the LST, but it will affect the available time of operation for various levels of stray light. The University of Arizona report discusses some aspects of this subject, and additional consideration has been given to it at Itek. Both concur that the relative merits of the two techniques depend on many factors that cannot now be quantitatively evaluated in sufficient detail for an optimum design. These factors include (1) the level of light due to particles or a cloud in front of the telescope; (2) the mechanical (discussed elsewhere in this report) and operational feasibility of intermeshing a low light level, long exposure experiment with one or more high light level experiments; (3) the feasibility of rotating the LST to provide a moonshade when needed; and (4) the detailed design and optical performance of the sunshield.

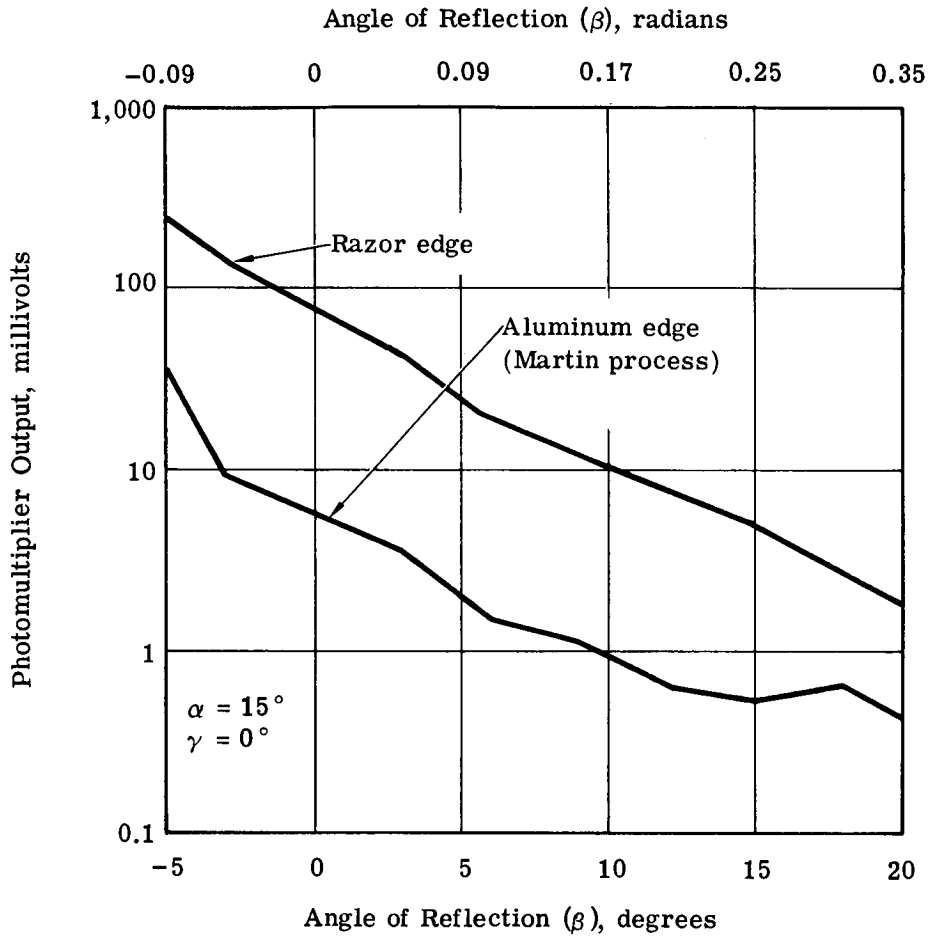


Fig. C.3-15 — Stray light from baffled edges

The assumptions in the baseline design are that there is no cloud in front of the LST, that the longer time of low level operations is very desirable, that the special low scatter inside coating of the sunshield is feasible, and that a folding front section is not practical. The sunshade shown in Fig. A.1-1 has a 0.785 radian (45-degree) angle, a compromise based upon the best estimates of the factors involved. The interior surface will have a coating that has a very low diffuse reflectance, and the front edge will be configured to control the diffracted light.

The primary and secondary mirrors will scatter light, some of which will reach the image plane directly without further attenuation. This will be a source of stray light by two mechanisms, by large angle over 0.017 radian (1 degree) scattering of residual stray light from the telescope walls, and by small angle scattering of light from stars or planets in or near the field of view. The first problem interrelates with the baffle, and will be addressed quantitatively later in the program. The second problem is less complex, and some results are based upon a small amount of preliminary data in the visual region. Since this problem is minor, the baseline mirror is assumed to have a good normal finish on it. There are other factors yet to be considered, e.g., the large angle scattering and the performance in the short wavelength regions. The final specification of the mirrors will have to await further investigation. It is expected that supersmooth surfacing techniques will be available for use on large mirrors in the next few years. Such a finish will be used on the LST unless some undesirable characteristics (such as low ultraviolet reflectance) prevent its use.

### C.3.g Effect of Contamination on Optical Surfaces

This section discusses a variety of information assembled in a literature search conducted in the following areas [see Section C.3.g(2)]: the vacuum-ultraviolet, outgassing, and optical contamination.

#### C.3.g(1) Source of Contaminants

1. Rocket exhaust contamination
2. Organic compound contamination due to outgassing
3. Reaction of primary contamination sources to form secondary sources
4. Manned interface

It is hoped that the techniques of protecting optical components from exhaust contaminants and other space-vehicular sources will be sufficient to shield adequately the LST optical components. At any rate, we are not concerned with source 1 at this time. It is almost impossible to predict just what source 3 reactions may or may not occur. This is due to the uncertainty in deposition rates, the proportions of different contaminants present, and perhaps to other variables. Source 4 is another unknown that may introduce contaminants when maintenance crews investigate, repair, or clean the LST. Its effect also is not examined presently.

As far as source 2 is concerned, the probable outgassing contaminants of the LST optical components are as yet unknown. In addition, although there are considerable data on outgassing materials available in the literature,<sup>1-5</sup> almost no data are available concerning the vacuum-ultraviolet contamination properties of such materials (although some general vacuum-ultraviolet absorption is presented in reference 2). Hence, the vacuum-ultraviolet effects of those specific materials outgassed from the LST elements will probably have to be measured. This judgment is reiterated in the conclusions of a recent study<sup>6</sup> by Teledyne Brown Engineering: "Much additional work, both analytical and experimental, is required to provide the information and techniques. . . [that are] essential to a complete analysis of the problem. . . In conclusion, it appears that the present state of knowledge of the optical effects of potential contaminants is probably inadequate to permit an analysis of the kind outlined above." However, to obtain some ballpark degradation numbers, this section contains a brief analysis using some presently available data.

Chemical or physical adsorption of particles are not considered in this subsection. Instead, treatment concentrates on (1) adhesion of contaminants and (2) radiation induced film growth. This is justified by a recent analysis by Scialdone,<sup>15</sup> who calculated that adsorption should constitute only 0.0001 to 0.01 of the total surface contamination due to returning outgassed flux.

Concerning adhesion of contaminants, contamination may present itself in droplet or thin film form. Depending on the surface tension, certain materials that condense on a surface do not form a uniform layer but form small discrete droplets so that scattering of light is more dominant than absorption. These droplets are not necessarily uniform in size, shape, or areal distribution. Hence, a theoretical analysis of the scattering properties is extremely difficult, although some work<sup>8-10</sup> has been done on the subject. Most information of practical value will probably have to be obtained through direct measurements rather than from calculations.

Figs. C.3-16 and C.3-17 represent such data. Fig. C.3-16 is a plot of degradation (percent decrease in reflectance) at 121.6 nanometers versus thickness for DC704 diffusion pump oil deposited on a  $MgF_2$ -overcoated aluminum-coated mirror. The shaded area in the lower left-hand corner represents an uncertainty of  $\pm 2$  percent in measurements, although the rest of the data are apparently reliable. Since DC704 has an effective molecular size of 12 nanometers, 4-5 monolayers represents a thickness of about 50-60 nanometers, corresponding to a degradation of only about 4 percent.

Fig. C.3-17 is a plot of reflectance versus wavelength for DC705 diffusion pump oil (in droplet form) deposited on an  $Al_2O_3$ -overcoated aluminum-coated mirror. The modulation of the reflectance curves is due to thin-film interference from the overcoating and is an important consideration when calculating contamination effects. (It may be noted that  $Al_2O_3$  will not be used as an overcoating for the LST and is shown here only for discussion.) It may be seen that for a 5.0-nanometer equivalent weight oil thickness, the loss of reflectivity is as much as 30 percent at the lower wavelengths (200.0 nanometers). Because the total diffuse reflectance was the same as the initial specular reflectance, the reduction in reflectance was solely due to scattering. At 121.6 nanometers, the loss (excluding absorption) presumably is the same or greater. It may be seen (from Fig. C.3-16) that for DC704 oil it takes up to 13 monolayers (15.6 nanometers) equivalent weight thickness to produce the same 30 percent degradation. A graph extrapolation of Fig. C.3-16 indicates a 75 percent reflectivity loss for a 35.0-nanometer thickness. For thin films of typical organic compounds on reflecting surfaces, an Itek in-house theoretical analysis has indicated that degradation (due to absorption) should be no worse than 75 percent (in the vacuum-ultraviolet) if the contaminant layer is 65.0 nanometers thick or less, although worst cases may permit no more than 20.0 nanometers or less.

There are several articles<sup>1,11-14</sup> that discuss the second mechanism, radiation-induced film growth. Strong ultraviolet radiation can cause photopolymerization, a process by which a compound is changed into another compound having the same elements but a higher molecular weight and different physical properties (e.g., it may become less volatile). However, since the LST will not be facing the sun at any time, this possible effect of solar ultraviolet radiation should not be significant.

As far as solar proton radiation is concerned, that too should be minimal, although it is possible that some proton radiation will pass right through the walls of the telescope. Gillette and Kenyon<sup>14</sup> studied the effects on telescope mirror reflective surfaces of proton radiation in a synchronous orbit (an altitude of 35,000 kilometers). They found that, if organic molecules impinge upon the optical surfaces, some proton-induced polymerization (i.e., individual molecules affixed to the mirror surface by individual protons) can cause losses in reflectance. (See Fig. C.3-18.) Since the LST will be in a different orbit (an altitude of 750 kilometers) from the telescope examined by Gillette and Kenyon, the charged particle densities will be different for the LST. Further study in this area is warranted.

Some other considerations that may have an effect on LST contamination are the following. By making several conservative assumptions (each one representing a worst-case), Scialdone<sup>7, 15</sup> has developed a rather elaborate theory for predicting spacecraft self-contamination. Fig. C.3-19 is a plot (obtained from calculations using that theory) of returning flux versus altitude. Here,  $\phi_D$  is the emitted flux and  $\phi''$  is the returned flux. The results are also given in terms of the number of returning molecules to the number emitted. Note that at 750 kilometers, the LST orbit altitude, the number returning is approximately one-millionth of those emitted. It should be mentioned that these numbers are calculated for the region in front of the moving spacecraft. (Scialdone calls this the condensation region.) A rarefaction region forms at the rear of the spacecraft. If Scialdone's calculations are correct, then outgassed material emitted in this region should not return to the LST.



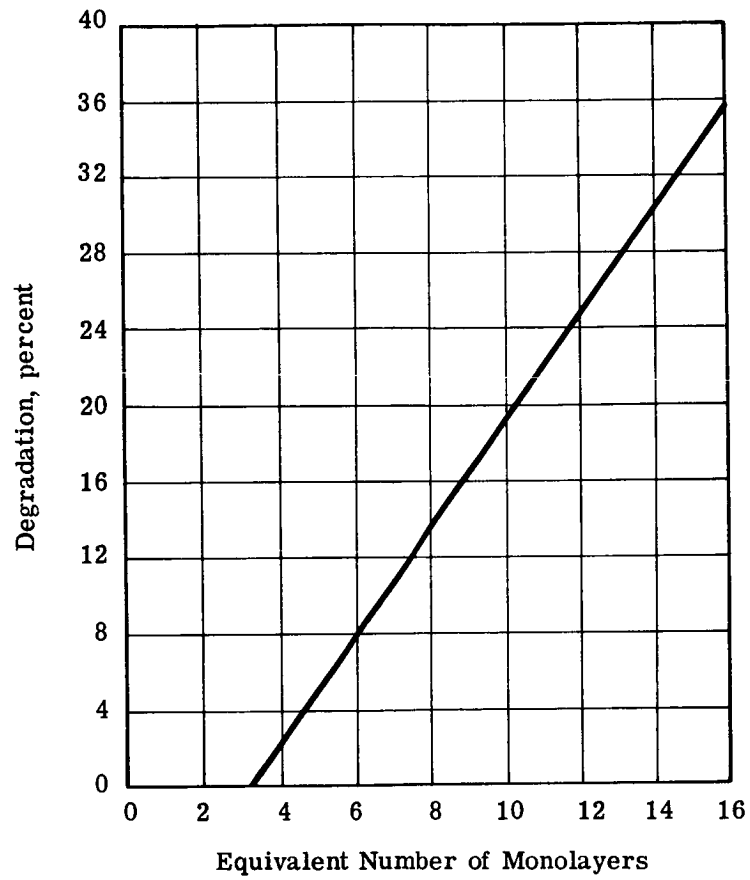


Fig. C.3-16 — Percentage of degradation in equivalent number of monolayers

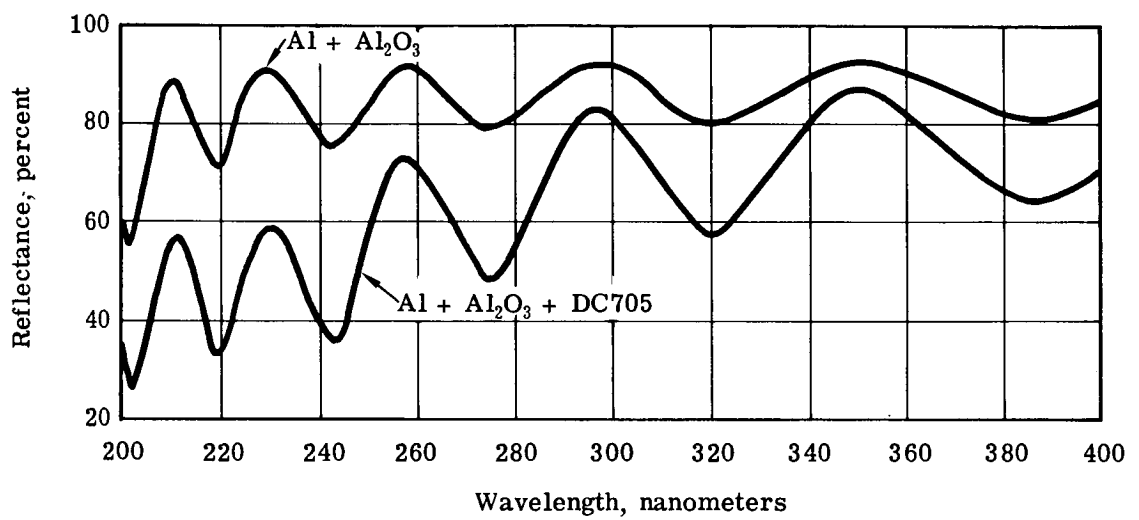
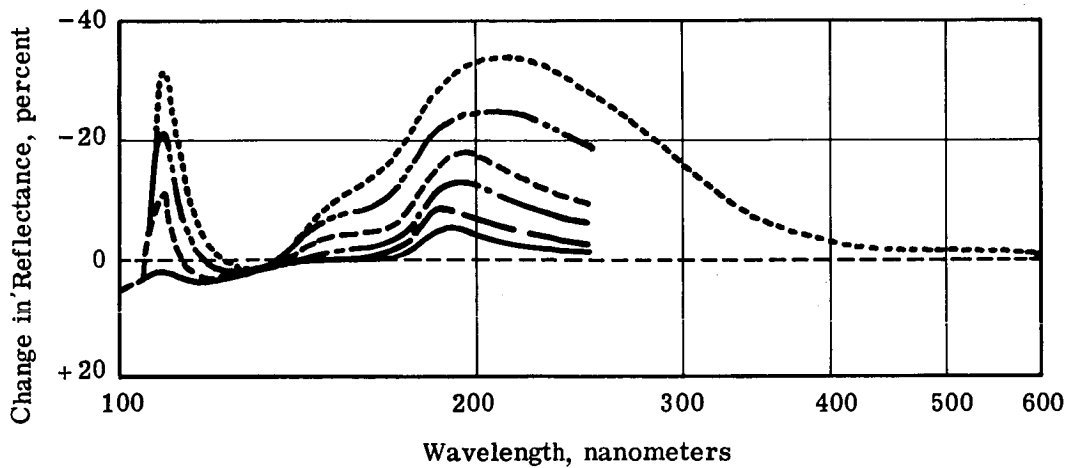


Fig. C.3-17 — Measured reflectance of Al + Al<sub>2</sub>O<sub>3</sub> as a function of wavelength



Flux =  $1.4 \times 10^{11}$  protons/cm<sup>2</sup>/sec

- After  $2 \times 10^{14}$  protons/cm<sup>2</sup>
- After  $5 \times 10^{14}$  protons/cm<sup>2</sup>
- - - - After  $1 \times 10^{15}$  protons/cm<sup>2</sup>
- After  $2 \times 10^{15}$  protons/cm<sup>2</sup>
- After  $5.3 \times 10^{15}$  protons/cm<sup>2</sup>
- After  $1 \times 10^{16}$  protons/cm<sup>2</sup>

Fig. C.3-18 — Reflectance changes of a MgF<sub>2</sub>/Al-coated Cer-Vit mirror

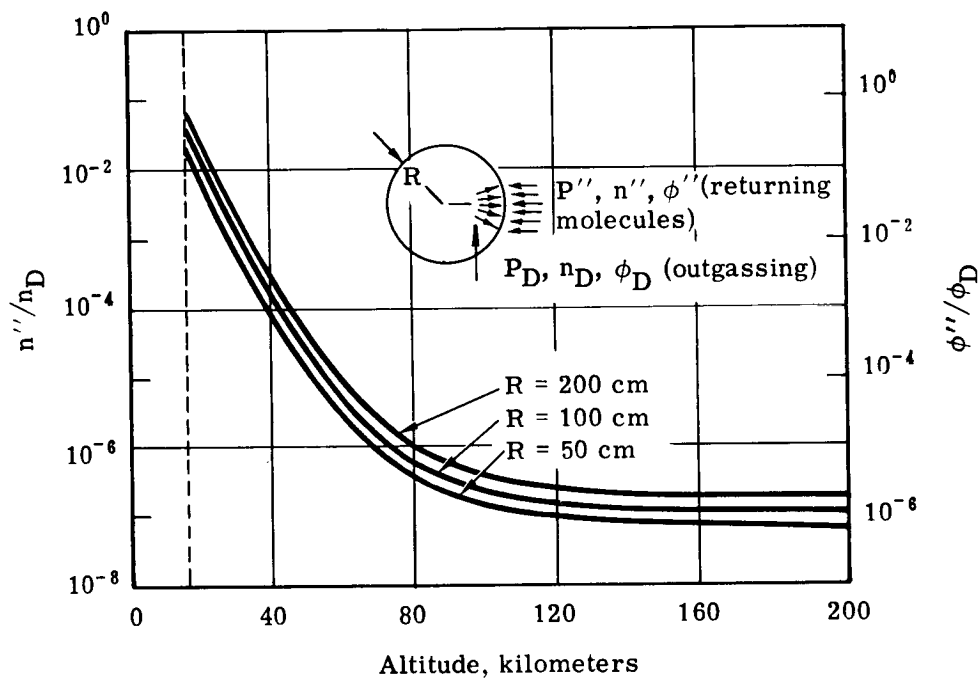


Fig. C.3-19 — Returning flux versus altitude

Outgassed material that has condensed on optical components may not be the only source of image degradation. Light scattering may occur from a molecular cloud surrounding the LST. The optical thickness  $W$  of such a cloud is given by  $W = \sigma \dot{m} / 4\pi\nu R$ , where  $\sigma$  is the molecular absorption cross section for the particular outgassed molecules at the wavelength of interest,  $\dot{m}$  is the outgassed mass per unit time (i.e.,  $m = \dot{N} M/A$ , where  $\dot{N}$  is the number of molecules emitted per unit time,  $M$  is the molecular weight, and  $A$  is Avogadro's number),  $\nu = (8kt/\pi M)^{1/2}$  is the mean thermal velocity of the outgassed molecule at absolute temperature  $T$  ( $k$  is Boltzmann's constant), and  $R$  is spacecraft radius.

For all the theory of Scialdone however, useful numbers, such as the rate of condensation and time for the formation of a monolayer (and not just ratios of emitted to returned flux), will be obtained only when emission rates of LST spacecraft components are actually measured.

### C.3.g(2) References

1. See, for instance, the symposium report *Optical Contamination in Space*, Optical Society of America, Rocky Mountain Section, Aug 1969.
2. McPherson, D.G., *Apollo Telescope Mount Extended Applications Study Program-ATM Contamination Study*, Final Report, NASA contract NASw-1386, Mar 10, 1967.
3. Austin, J.O., *Category and Contamination Ranking Lists for OSO Materials*, Ball Brothers Report No. TR69-08, Mar 1969.
4. Dunipace, D.W., et al., *A Rapid, Sensitive Materials Contamination Screening Technique*, in *Advanced Techniques for Material Investigation and Fabrication*, 14th Symposium of Science Advanced Materials Process Engineering, Nov 1968, p. I-3-6.
5. Muraca, R.F., and Whittich, J.S., *Polymers for Space Applications*, Stanford Research Institute, Final Report, Sept 1967.
6. Scarborough, J. M., *Large Space Telescope Contamination Study*, Teledyne Interim Report ASD-PD-1527 (May 1972).
7. Scialdone, J. J., *Self-Contamination and Environment of an Orbiting Spacecraft*, NASA TN D-6645 (May 1972).
8. Bennett, H. E., and Porteus, J. O., *J. Opt. Soc. Am.* 51:123 (1961).
9. Davies, H., *Proc. IEEE* 101:209 (1954).
10. Bennett, H.E., and Bennett, J.M., in G. Hass and R. Thun, Eds., *Physics of Thin Films* (Academic Press Inc., New York, 1967), Vol. 4, pp. 12-21.
11. Shapiro, H., and Hanyok, J., *Monomolecular Contamination of Optical Surfaces*, NASA TN D-4612 (NASA contract NAS1-7627), June 1968.
12. Hass, G., and Hunter, W.R, *Laboratory Experiments to Study Surface Contamination and Degradation of Optical Coatings and Materials in Simulated Space Environments*, *Appl. Opt.* 9: 2101 (1970).
13. Hollahan, J.R., et al., *Restoration of Optical Properties of Surfaces by Radiofrequency Excited Oxygen*, Boeing Report No. D1-82-0935, Nov 1969.
14. Gillette, R.B., and Kenyon, B.A., *A Study of Proton-Induced Effects on Reflective Surfaces of Space Mirrors*, NASA CR-1532, Feb 1970.
15. Scialdone, J.J., *Predicting Spacecraft Self-Contamination in Space and in a Test Chamber*, NASA TN D-6682, May 1972.

### C.3.h Optical Coatings

Since the large orbiting telescope is expected to operate as a general purpose instrument, optical coatings that would operate over as broad a wavelength range as possible were investigated. The usefulness of coating materials over the range of 0.1 to 100 micrometers was evaluated. No materials transmit throughout this entire region.<sup>1, 2</sup> Since the optical system must be primarily reflective in form, efforts were concentrated on metallics. Data available in the literature show the reflectivity of the most commonly used metals over a 0.22- to 40-micrometer region.<sup>3</sup> Aluminum is the only metal that maintains a high ( $\geq 86$  percent) reflectivity in this region. The reflectivity of aluminum in the far infrared also shows it to be well behaved.<sup>4</sup>

If reflectance below 200 nanometers is not required, an aluminum film overcoated with  $\text{Al}_2\text{O}_3$  or  $\text{SiO}_2$  can be used. These films are quite durable and can be cleaned without damage. For some components of the LST, this may be the coating of choice. When reflectance is required in the region below 200 nanometers,  $\text{MgF}_2$  or LiF-overcoated aluminum are the only choices. The spectral performance of these two combinations is shown in Fig. C.3-20. The 250-nanometer thickness of the  $\text{MgF}_2$  represents the thinnest layer that provides adequate protection from degradation due to atmospheric oxygen. Neither of these coatings can be regarded as cleanable, and both require special handling precautions.  $\text{MgF}_2$  is normally thought of as a durable hard film because of its use as an antireflection coating. For this application, it is soft because it must be deposited at room temperature rather than at  $250^\circ\text{C}$ . Aluminum loses its reflectivity if it is heated and any protective coating must be deposited on an unheated substrate.

The decision between these is almost automatic once the system requirements have been defined. Since  $\text{MgF}_2$  provides higher reflectance above 120 nanometers and has less tendency to degrade on exposure to atmospheric humidity, the decision to use LiF as an overcoating material would only be made if the region between 95.0 and 115 nanometers was of overriding importance.

Generally, the effect of thickness is quite pronounced at low wavelengths and the thickness can be tailored to provide the vacuum-ultraviolet reflectance that is optimum for each specific application. Films of  $\text{MgF}_2$  of these thicknesses have little or no effect on the reflectance of aluminum mirrors at higher wavelengths. From spectral scan data taken in the infrared (2.5 to 50 micrometers), using an uncoated surface and one coated with 100.0 nanometers of  $\text{MgF}_2$ , no change was noted in the transmitted light. It was concluded that no anomalous transmission effects are presented. Hass<sup>5</sup> reports the following: "... That very thin layers of absorbing materials have little effect on the infrared reflectance of metals, but decrease the transmittance of infrared transparent materials strongly, is of general importance. This is not only true of  $\text{SiO}_2$ , but also applies to films of any infrared absorbing material, such as thin layers of absorbed water or grease. The effect shown here leads to the conclusion that in the infrared, equipment windows and lenses have to be cleaned more carefully and frequently than front surface mirrors." On the basis of this information, it is expected that there will be virtually no effect on reflecting optics in the infrared owing to the small effect on transmittance shown by the overcoating materials.

The most significant coating problem consists not of choosing the correct coating materials but rather of depositing them in a manner that achieves the maximum reflectance obtainable at the wavelengths of interest. There are two major parts to this problem: excluding oxygen from the film and controlling film thickness accurately.

Two solutions to excluding oxygen from the film have been reported. Hutcheson *et al.*<sup>6</sup> evaporate aluminum at rates in excess of 30.0 nanometers/second in a vacuum of  $5 \times 10^{-6}$  torr and immediately overcoat with dielectric. The other approach developed by Feurbacher *et al.*<sup>7</sup> consists of evaporating in vacua of  $3 \times 10^{-9}$  torr at rates of 1.0 nanometer/second and permits a time lapse of as much as 15 minutes between the completion of the aluminum evaporation and the commencement of overcoating. The results obtained by Feurbacher *et al.* are substantially better than the most recent data from Hutcheson *et al.*

To obtain high reflectance at the shortest wavelength possible with either  $\text{MgF}_2$  or LiF, it is necessary to control the optical thickness of the overcoating precisely. The commonly used methods to accomplish this are quartz crystal monitors and optical monitoring at near-ultraviolet wavelengths. Both of these methods have

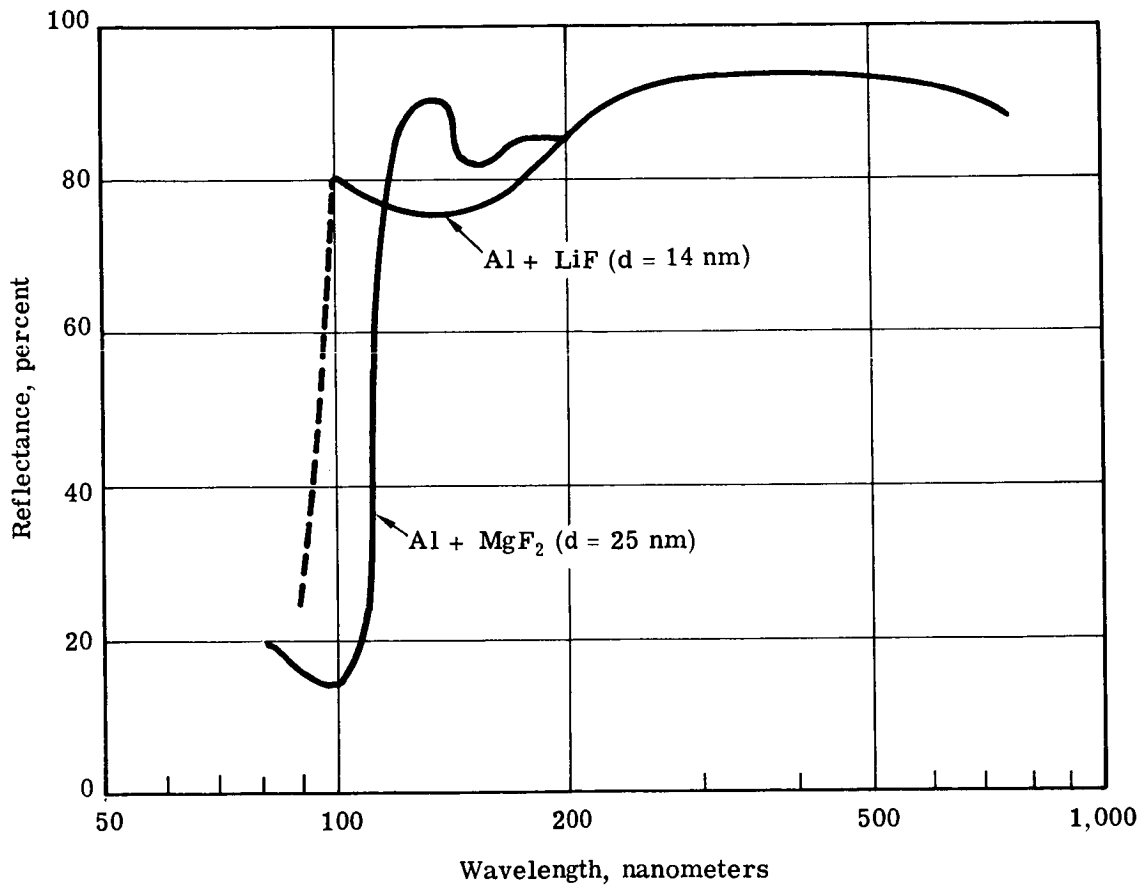


Fig. C.3-20 — Spectral performance of MgF<sub>2</sub> and LiF overcoated aluminum

shortcomings that make precise control of the optical thickness of the very thin overcoating layers difficult. Hutcheson *et al.*<sup>8</sup> have developed a method that utilizes the 121.6-nanometer line of hydrogen to produce a sensitive monitoring system. A system with this sensitivity makes it possible to evaporate the dielectric overcoating at higher rates than previously, without loss of thickness control. Using this technique Hutcheson and his co-workers were able to produce MgF<sub>2</sub> overcoated aluminum mirrors by evaporating MgF<sub>2</sub> at 45 Å/sec. with higher reflectance than they had previously obtained. They regard this as the optimum rate for MgF<sub>2</sub>.

The need to exclude oxygen presents special problems when it is necessary to coat large optics. In order to coat a 3-meter mirror with Al at a rate of 30.0 nanometers/second it would be necessary to use many sources placed in fairly close proximity to the optic. The sources must be baffled to confine the evaporant to a narrow cone angle in order to avoid the high scatter that results when aluminum is incident on the substrate at high angles. The locations of the sources must be carefully calculated and the output balanced in order to ensure even distribution. There will also be a requirement to monitor the output of the sources in order to control the thickness of the Al layer. These requirements could be greatly simplified by coating at 1.0 nanometer/second and  $3 \times 10^{-9}$  torr, however, vacua of this order are not easily obtained in systems with 3-meter openings.

This is because elastomer seals, such as Viton O rings, are significant outgassing sources. Also after a prolonged pumping period a diffusion gradient is established across the seal to allow water and other atmospheric gases to enter the chamber.<sup>9</sup> This problem can be eliminated by using metal gasket seals or reduced by using double O rings with a guard vacuum between them.

The limit for Viton seals is generally regarded to be  $5 \times 10^{-8}$  torr, which is two orders of magnitude better than the conditions used by Hutcheson *et al.* The possibility of coating at  $5 \times 10^{-8}$  at a rate less than 4.0 nanometers/second should be investigated in an effort to develop a coating that has excellent performance in the vacuum ultraviolet and can be deposited reliably and economically on large optics.

The other problem to be considered is the effect of contamination and the space environment on the performance of the reflecting surface. These possible sources of contamination cannot be neglected. The following effects are possible:

1. Erosion, roughening of the surface due to impinging of space originated material
2. Radiation, physical changes due to irradiation by space originated material causing changes in optical properties
3. Effluents, spacecraft-originated materials that will coat and reduce the optical efficiency.

The design of the space vehicle will determine the effluents present during the mission. The orbit will determine primarily the erosion and radiational effects. The primary mirror, because of its orientation, will be affected by space-originated effects. Internal system elements may be more proximate to and affected by outgassing products. Many portions of the optical system could be serviceable and even replaceable in orbit. This is not true of the primary mirror.

These effects will probably have to be measured. If it is established that the vacuum ultraviolet reflectance of the mirrors will be unavoidably degraded by the operating environment, it may be necessary to profile all short wavelength studies as early in the flight as possible.



## REFERENCES

1. American Institute of Physics Handbook, 2d ed. (McGraw-Hill Book Co., Inc., New York, 1963), Section 6.
2. Hass, G., and Ritter, E., Optical Film Materials and Their Applications, J. Vac. Sci. Technol., 4(2) (Mar/Apr 1967).
3. Drummeter, L., Jr., and Hass, G., Solar Absorptance and Thermal Emittance of Evaporated Coating, Phys. Thin Films, Vol 2 Academic Press, New York, 1964.
4. Cummings, R., Itek Corporation, personal communication.
5. Hass, G., Filmed Surfaces for Reflecting Optics, J. Opt. Soc. Am. 45(11) (Nov 1955).
6. Hutcheson, E.T., Hass, G., and Cox, J.T., Effect of Deposition Rate and Substrate Temperature on the Vacuum Ultraviolet Reflectance of  $MgF_2$  - and  $LiF$  - Overcoated Mirrors, Appl. Opt. 11(10) (Oct 1972)
7. Feurbacher, B., Fitton, B. and Steinman, W., High Efficiency Reflecting Surfaces for the Vacuum Ultraviolet, European Space Research Organization, European Space Research and Technology Centre, Internal Working Paper No. 380 (June 1969)
8. Hutcheson, E.T., Cox, J.T., Hass, G., and Hunter, W.R., Monitoring the Thickness of Thin  $MgF_2$  and  $LiF$  Films on Al by Reflectance Measurements Using the  $1216 \text{ \AA}$  Line of Hydrogen, Appl. Opt. 11(7) (July 1972)
9. Santeler, D.J., Jones, D.W., Holkeboer, D.H., and Pagano, F., Vacuum Technology and Space Simulation, NASA SP-105, 1966.

## C.4 THERMAL DESIGN

The thermal design of the optical telescope assembly (OTA) is governed by the orbital environment, the error budget for optical system performance, and the rationale adopted for maintaining reliability of the entire system. To a lesser extent, the thermal interfaces between the various units of the orbiting LST (see Section-C.9) influence the thermal design. An additional, implied requirement for the design is the minimization of required thermal control power. In the present study program, it has been possible to identify the thermo-optical requirements, perform tradeoffs between different approaches to athermalization, define some of the thermal design requirements for the relationship between the OTA and the system support module (SSM), define two possible approaches to the thermal control and interface between the scientific instrument package and the SSM, and perform an initial design of a key thermal problem, the cooling of the image tubes in the spacecraft environment.

The spacecraft environment requirements drive the image tube cooling system, and are directly related to the manned maintenance rationale used in terms of the environment that must be available within the spacecraft. Future work must examine this rationale more closely than has been possible in the present effort and in particular must examine the reliability requirements that must be satisfied by the image tubes, the impact of the tube thermal control means used on this reliability, and review in more depth alternate thermal control systems as related to the SSM environment.

### C.4.a Thermo-Optical Requirements

The starting point in the design of the LST thermal control system is the optical wavefront and pointing error budgets. These budgets represent best estimates of how to apportion the LST system degradation. The budgets are then combined with calculated thermal sensitivities to determine tolerable temperature variation. Given these tolerable degradations, the thermal control system is configured so as not to exceed the requirements.

The creation of an error budget always leads to the question of defining how to add the errors. It was decided to add individual mirror error contributors arithmetically when their magnitude and direction were known and to rss individual components when only their magnitudes were known to develop a total error budget. There is only one real way to determine how close this will be to reality: to trace rays completely through an environmentally perturbed analytical LST mathematical model and calculate the degradation to the final wavefront. However, as a precursor to that final step, the error has been budgeted in what is considered to be a realistic manner.

The thermo-optical design requirements have been reviewed and updated to reflect the latest design changes in truss and mirror materials. Table C.4-1 presents the current allocation of thermal error sources and the associated thermal requirement. The general allocation of error sources identical to Itek's previous work; however, the primary mirror requirements have been loosened somewhat, whereas the secondary mirror allowables have been correspondingly tightened to reflect a more up-to-date error allocation.

### C.4.b Manufacturing Implications

The question of manufacturing implications has been considered in terms of the system thermal requirements. In this respect, two general classes of problems must be resolved: mirror figuring and general structural fabrication.

In terms of mirror figuring, the primary and secondary have been designed for nominal room temperature operation. The problems associated with cold mirror performance are manifold if the mirror is figured at room temperature and operated at an unheated system equilibrium temperature that may be as low as  $-82^{\circ}\text{C}$  ( $-115^{\circ}\text{F}$ ) and have as large a potential temperature variation as  $12.8^{\circ}\text{C}$  ( $55^{\circ}\text{F}$ ), depending on orbital orientation. Figuring the mirror for the cold condition implies numerous thermal cycles between figuring and interferometric testing which complicates the overall manufacturing sequence. Therefore, the manufacturing, testing, and operation of the mirror must be done under controlled conditions at a room temperature of  $21^{\circ}\text{C}$  ( $70^{\circ}\text{F}$ ) to counter the effect of thermal coefficient of expansion variation known to occur randomly within large mirror blanks. The current estimate of this effect indicates an optical sensitivity of  $0.0024 \lambda/^{\circ}\text{C}$  for a 3-meter Cer-Vit blank.

Table C.4-1 – Thermo-Optical Design Requirements  
 Primary and Secondary Mirror Budget:  $0.026\lambda^*$

Element	Optical Degradation, Wavelengths rms		Thermal Requirement, °C
	Systematic	Random	
Primary mirror			
Axial gradient	0.00157		9
Radial gradient	0.00433		3.25
Soak ( $\propto$ variation)		$\pm 0.0105$	$\pm 4.4$
Axial gradient variation		$\pm 0.0155$	$\pm 1.2$
Secondary mirror			
Axial gradient	0.00015		4.5
Radial gradient	0.001		3.3
Soak ( $\propto$ variation)		$\pm 0.0004$	$\pm 0.5$
Axial gradient variation		$\pm 0.0006$	$\pm 0.25$
	<u>0.00705</u>	<u>0.01875 rms</u>	
Total optical degradation	0.0258		
Focus maintenance	0.020		2.75†
Primary-secondary distance change			1.5‡

\* $\lambda$  = 633 nanometers. Optical characteristics:  $D = 3.0$  meters,  $F_p = 2.2$ ,  $F_s = 12.0$ .

† Graphite-epoxy.

‡ Invar-titanium.

In addition to mirror thermal expansion coefficient ( $\alpha$ ) effects, there is also the general problem of fabricating a large optical metering structure at room temperature and deliberately operating that structure at the temperature levels mentioned above. Since an unheated metering structure will be used, system refocusing capability has been included as a part of the overall system design. Periodic refocusing permits reduction of the thermal requirements on the truss structure and thermal concern in this area is only to provide a reasonable degree of orbital stability. The orbital stability requirements are dictated by the desire to reduce periodic refocusing to once per 40-minute time period or longer for cases near steady state.

#### C.4.c Maintenance Constraints

In terms of the OTA, no significant maintenance constraints are imposed on the thermal design. A set of aperture doors is provided immediately forward of the secondary mirror spider. These doors are open during all normal orbital conditions. Normal maintenance operations will not require entry into the telescope compartment and the door would be closed (probably on ground command) prior to the commencement of any maintenance operations. Closure of the aperture doors will result in a decrease in system power (to heat mirrors).

The major maintenance constraints occur in the instrument compartment. The baseline concept is for manned maintenance in a shirtsleeve environment. Further complicating the baseline approach is the laminar airflow system. Evaluation of the baseline concepts indicates that they have the potential of excellent compatibility with the proposed laminar airflow system.

Since it is likely that the pressure shell wall will be designed to run cold, makeup heaters supplied from the maintenance vehicle will be required. This area should be reviewed during the next phase of the program.

#### C.4.d Review of Thermal Control Concepts

The thermal control concept developed for the LST is based on a combination of active thermal control for the optical elements and passive thermal control for the supporting structure. Specifically, the primary mirror, secondary mirror, and main support ring are actively controlled at  $21 \pm 0.3^\circ\text{C}$  ( $70 \pm 0.5^\circ\text{F}$ ) by means of multizone electrical heaters. Furthermore, these items are thermally isolated from the surroundings by the use of multilayer insulating blankets to reduce thermal power consumption. Passive thermal control of the main supporting structure (between primary and secondary mirrors) is accomplished by multilayer insulating blankets surrounding and isolating the truss from the internal light baffle and the external meteoroid shell. The passive thermal control concept also incorporates a low  $\alpha_S/\epsilon$  thermal finish on the exterior of the meteoroid shell.

This concept is the logical outcome of conceptual tradeoff studies conducted in previous programs (NASw-1925 and NASw-2174). Briefly, this thermal control concept has evolved from attempting to maintain the entire telescope at a fixed temperature of  $21^\circ\text{C}$  ( $70^\circ\text{F}$ ) requiring several kilowatts of thermal power to a system that maintains only the critical optical components at  $21^\circ\text{C}$  ( $70^\circ\text{F}$ ). Induced thermal motions of the metering structure are attenuated by insulation, and the attenuated motion is actively corrected by means of a diagnostic sensor system linked to the secondary mirror.

An alternate concept for mirror thermal control (which has not been examined) is the specular core concept presently employed in Itek's photoheliograph study. The advantage of this approach for the LST is that the axial gradients within the primary may be reduced by an increase in apparent mirror core conductance due to internal specular radiation. This alternative may be explored in future studies since thermal gradient reduction reduces the thermal errors of the mirror.

The remaining element of the original tradeoff matrix is the selection of the external thermal control finish. The low  $\alpha_S/\epsilon$  finish has been selected to provide for thermal control of the main ring independent of telescope orientation relative to the sun. As the  $\alpha_S/\epsilon$  ratio increases, the main support ring will receive sufficient thermal loading, even with insulation, to exceed the active thermal control setpoint. For an  $\alpha_S/\epsilon$  ratio of 1, prior studies indicated a maximum ring temperature of  $29^\circ\text{C}$  ( $84^\circ\text{F}$ ). For the present baseline concept, an  $\alpha_S/\epsilon$  ratio of 0.285 has been selected. This ratio is typical of a number of available thermal control finishes.

Three general thermal control concepts have been investigated for the OTA scientific instrument package (SIP) instrumentation compartment of the LST. The first concept may be categorized as a constant Q system based on constant power outputs from all major thermal sources within the compartment, thus reducing or eliminating the effect of unknown instrument usage or sequencing. The second concept is a constant T system based on maintaining the instrument support structure at a constant temperature independent of instrument usage. The last concept is a passive (insulated truss) concept, using no active thermal control.

The constant Q concept results in a system that is independent of instrumentation sequences (instrument power dissipation is replaced by identical heater power when instruments are off) and that may be designed to be reasonably insensitive to orbital variations. The major disadvantages are the large continuous power drain imposed by this mode of operation and the unavoidable structural temperature gradients that develop. This also leads to unwanted heat conducted into the main ring. Even if the gradients are ignored or eliminated, the estimated power requirement of approximately 660 watts, based on the GSFC Baseline System on which all tubes are coded, appears excessive.

The constant T concept results in a system operating at a fixed constant structural temperature based on an intermediate thermal shield containing a number of thermostatically controlled electric heaters that provide a constant 21°C (70°F) background for the structures at lower power. The major disadvantages are the complexity of the shield, which would require suitable penetrations for all cameras. Some thermal perturbations will occur, however, depending on the instrument usage sequence. This thermal transient cannot be predicted until a baseline instrument operational sequence is established.

The insulated truss concept results in a design having none of the complexity associated with a thermal shield. However, positive temperature control is not obtained. Orbital perturbations and instrument cycling effects are attenuated by the insulation or a low emissivity coating to a level consistent with design requirements for an ultralow expansion (graphite-epoxy) structure.

These concepts are discussed in greater detail in Section C.4.j.

#### C.4.e Baseline Concept

To meet all of the previously noted system requirements, a baseline concept for thermal control has been developed. This concept consists of active and passive elements, described below. The overall thermal control system is illustrated in Fig. C.1-7.

##### C.4.e(1) Active Elements

The principle of the baseline design is to provide active thermal controls for the primary mirror, the secondary mirror, and the main support ring. Both the primary and secondary mirrors are actively controlled to maintain them at or near their manufacturing and figuring temperature. This approach is conservative; however, it reduces the potentially deleterious effects of coefficient of expansion variation over the 3-meter aperture primary to values that are within the error budget. Active control of both optical elements is based on the use of multizone, thermostatically controlled electrical heaters bonded to the rear surface of the respective mirrors. The temperature setpoint has been selected as  $21 \pm 0.3^\circ\text{C}$  ( $70 \pm 0.5^\circ\text{F}$ ).

While not an optical element, the main support ring is considered to be sufficiently critical to telescope performance to warrant active thermal control. As it is the supporting member of the primary mirror and the instrument section and is fabricated from a more thermally sensitive material (titanium alloy), active control is necessary. As in the case of the optical elements, the thermal control is provided by multizone thermostatically controlled electrical heaters operating at a  $21 \pm 0.3^\circ\text{C}$  ( $70 \pm 0.5^\circ\text{F}$ ).

Although not part of the active thermal system, it should be noted that all of the active elements, the mirrors and the main ring, are thermally insulated from their surroundings to the maximum extent possible by means of multilayer insulation (aluminized Mylar film) known as superinsulation.

#### C.4.e(2) Passive Elements

The baseline design includes passive thermal control of two kinds, superinsulation and external thermal control finishes. The supporting structure between the primary and secondary mirrors consists of a three-bay graphite epoxy composite truss from the main support ring forward. At the upper end of this structure, a spider is positioned to support the secondary mirror. The passive baseline concept provides the maximum thermal isolation possible for this supporting structure. The effect of thermal isolation is to reduce the orbital variations in truss structural temperatures to a level compatible with the system fixed focus operational requirement (dictated by primary-secondary spacing change).

Thermal isolation of the truss is accomplished by sandwiching it between two superinsulation blankets that are themselves supported by the internal light baffle and by the external meteoroid shell. The spider supporting the secondary mirror and its five-degree-of-freedom mount is not insulated since the use of a thermal blanket in this area is detrimental to system optical performance.

The thermal control finish on the exterior meteoroid shell has the following characteristics:  $\alpha_S = 0.25$ ,  $\epsilon_{IR} = 0.88$ , and  $\alpha_S/\epsilon = 0.284$ . This thermal finish will provide a cold external environment for the LST walls in order to maintain thermal control of the active elements within the system at all times regardless of solar orientation. However, it must be recognized that thermal finish property optimization has not been done. The allowable variation has been bracketed. Future study is necessary to establish an optimum finish that will reduce thermal power by increasing the external temperature level and provide a heat sink for the active elements under maximum thermal loads.

#### C.4.e(3) Instrument Compartment

The baseline thermal control concept for the SIP/OTA instrument compartment is predicted on two general requirements: thermal control of the various instrument cameras located within the compartment and maintaining thermal stability of the supporting structure during all operational conditions.

The problems associated with thermal control of the instrument cameras have been evaluated and a baseline control concept selected. The cameras will be designed to radiate focus coil heat from the camera shell to the SSM pressure shell wall. The camera tube will be cooled by a thermoelectric module connected to a copper sleeve surrounding the tube envelope. The thermoelectric waste heat and pumping power are also radiated by the camera shell to the SSM pressure shell wall.

The requirement for manned maintenance implies a 21°C (70°F) temperature during the service interval at least. To prevent condensation from contaminating the instrument compartment, all objects within that compartment must be at a temperature above the dewpoint. [The dewpoint will vary between 21°C (70°F) and 7.2°C (45°F), with a probable value of about 10°C (50°F).] If moisture is allowed to condense, it could be a source of contamination for a long period after the service visit. Wall temperatures of 21°C (70°F) imply an image tube radiation temperature of the order of 49°C (120°F) and high power consumption in the Peltier coolers. If the astronaut were to wear a suit with a self-contained atmosphere during service so that his effluents would not condense within the SSM, it would be possible to operate the walls at a much lower temperature, reducing the tube temperature and the amount of Peltier cooling required. From a purely image tube point of view, the preferred SSM temperature would be of the order of -20 to -30°C (-4 to -22°F), resulting in no active cooling needed for image tubes. It is recommended that further study be made of the choice of SSM temperature setpoint and wall temperature control methods in order to arrive at a better compromise for cooling the main payload, the image tubes.

#### C.4.f System Thermal Model

##### C.4.f(1) Description

The fundamental purpose of the thermal model is to provide the necessary temperature information for comparison with the thermo-optical design requirements. These requirements require model detail fine enough to

predict three-dimensional temperatures, temperature changes, and gradient changes. The thermal model of the 3-meter LST is designed to meet these requirements and consists of 156 nodes, 832 radiation connections, 298 conduction connections, and 15 heat input tables.

The primary mirror is subdivided into three axial planes, four circumferential sections, and three radial rings to show axial and radial gradients; the secondary mirror is subdivided similarly, except that there is no circumferential breakdown. The truss is modeled as seven axial rings and four circumferential sectors per ring to show the thermal tip and tilt and axial growth rates. The overall thermal model is subdivided into 10 rings and four circumferential sectors. See Fig. C.4-1 and Table C.4-2.

The primary mirror that was analyzed is a cored monolith having the dimensions and nodal breakdown shown in Fig. C.4-2. Heat transfer within the mirror core involves radiation interchange as well as conduction. The primary light baffle extends through the central hole in the primary mirror, from which it is thermally isolated, except for the radiation interchanges. The mirror is mounted to the main truss beam (primary mounting ring) by three flexural supports. Heater control is simulated at the rear surface of the mirror in 12 zones that correspond to the rear surface nodes.

The metering truss structure model breakdown is shown in Fig. C.4-3. It is constructed of graphite-epoxy tubes and three ring beams. The truss is set in the annular area between the internal light baffle and the meteoroid shield. It is thermally isolated by multilayer insulation considered to have an effective emissivity of 0.01. The primary mount ring of the truss has four circumferential zones of heater control.

The secondary mirror area includes the secondary mirror, its mount, active mount assembly structure, secondary light baffling, and protecting cover. The secondary mirror is a cored monolith and has the nodal detail and dimensions shown in Fig. C.4-4. Heaters are simulated in three radial zones at the rear of the mirror. The back of the mirror and its mounting structure are protected from aperture thermal effects by an insulated cover.

The truncated, retractable light shield consists of two cylindrical rings, four sections per ring, and the truncated portion that has been modeled as an eight-sector ring.

#### C.4.f(2) Orbital Conditions

The analysis used a 741-kilometer (400-nautical-mile) altitude and 30-degree inclination orbit for the determination of incident external fluxes (solar, albedo, and earthshine). Since the baseline orbit is approximately 611 kilometers (330 nautical miles), the calculated incident albedo and earthshine fluxes are slightly lower for the assumed orbit. However, the overall effect of these differences is negligible on system performance.

The boundary conditions for the LST are the external surface properties and the orbital heat fluxes. The external  $\alpha/\epsilon$  ratio used in the analysis was 0.284, where  $\alpha = 0.25$ , to represent the solar absorptance of the spacecraft surface coating and  $\epsilon = 0.88$ , to represent the infrared emittance.

The fluxes on the spacecraft are a function of its position in the orbital plane and include the direct solar flux, earth albedo, and earth infrared emission. The direct solar, albedo, and earthshine fluxes to the external surfaces of the telescope were calculated with the aid of an orbital heat flux program.\* The following constants were used:

1. Solar	1,395 watts/m <sup>2</sup>
2. Albedo (taken as 0.39)	540 watts/m <sup>2</sup>
3. Earth infrared	210 watts/m <sup>2</sup>

An eight-sided telescope (two surfaces per node of the thermal model) was used and these flux inputs were adjusted for thermal model nodal area, absorptivity, and emissivity to yield the proper energy inputs for each exterior node as a function of orbit position.

\*G.A. McCue, Program for Determining the Thermal Environment and Temperature.

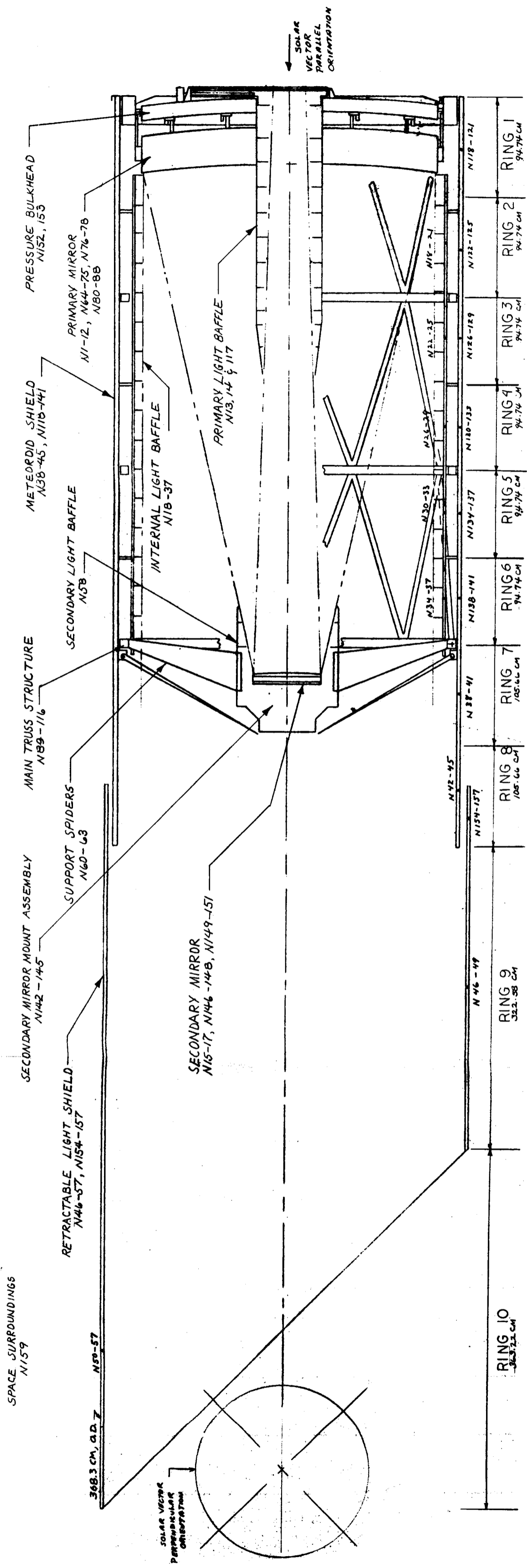


Fig. C.4-1 — LST telescope thermal model



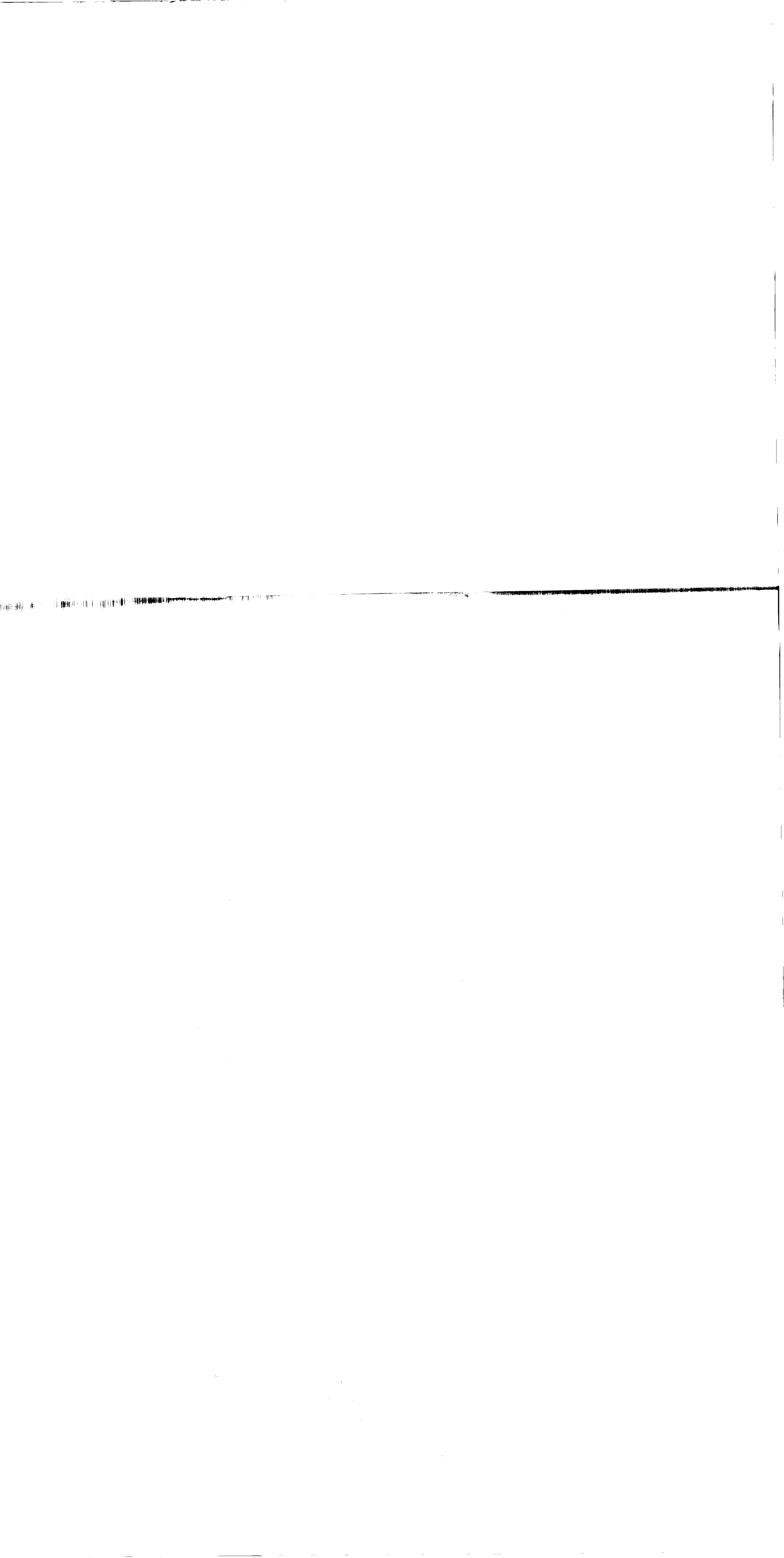


Table C.4-2 – Thermal Nodal Information

Assembly	Material	Surface Emissivities	Number of Nodes and Breakdown
Primary mirror	Cer-Vit	0.04 front surface 0.81 back face	36 (3 axial x 3 radial x 4 circumferential)
Secondary mirror	Cer-Vit	0.04 front surface 0.81 back face	9 (3 axial x 3 radial)
Internal light baffle	Aluminum	0.99 inside, outside insulated	20 (5 axial x 4 circumferential)
Primary light baffle	Aluminum	0.99	3 (axial)
Secondary light baffle	Aluminum	0.99	1
Primary ring	Titanium	0.05	4 (circumferential)
Main truss	Graphite-epoxy	0.95	24 (6 axial x 4 circumferential)
Meteoroid shield	Aluminum	0.88* outside, inside insulated	32 (8 axial x 4 circumferential)
Retractable light shield	Aluminum	0.88* outside 0.99 inside	16 (2 axial x 4 circumferential, 1 axial x 8 circumferential)
Support spiders	Graphite-epoxy	0.95	4 (1 each)
Pressure bulkhead	Titanium, honeycomb	0.05	1
Pressure bulkhead ring	Titanium	0.05	1
Secondary mirror mount	Invar-aluminum	0.99 cover insulated	4 (cover actuators, tangent bars, support ring)
Deep space			1

\* Infrared emissivity; solar absorptance is 0.25.

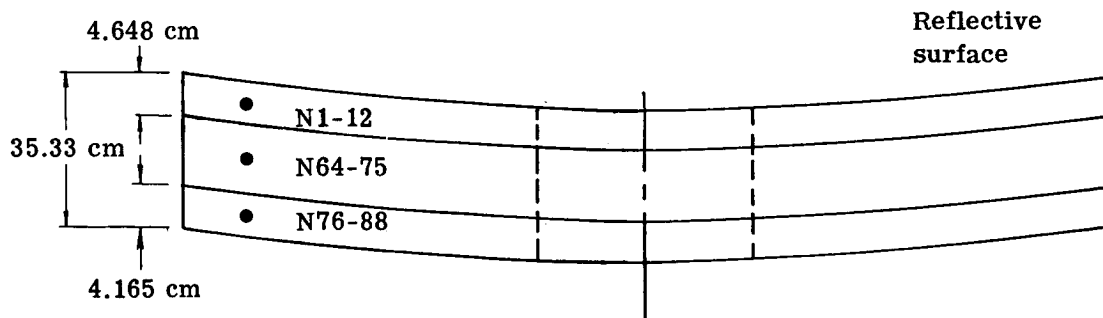
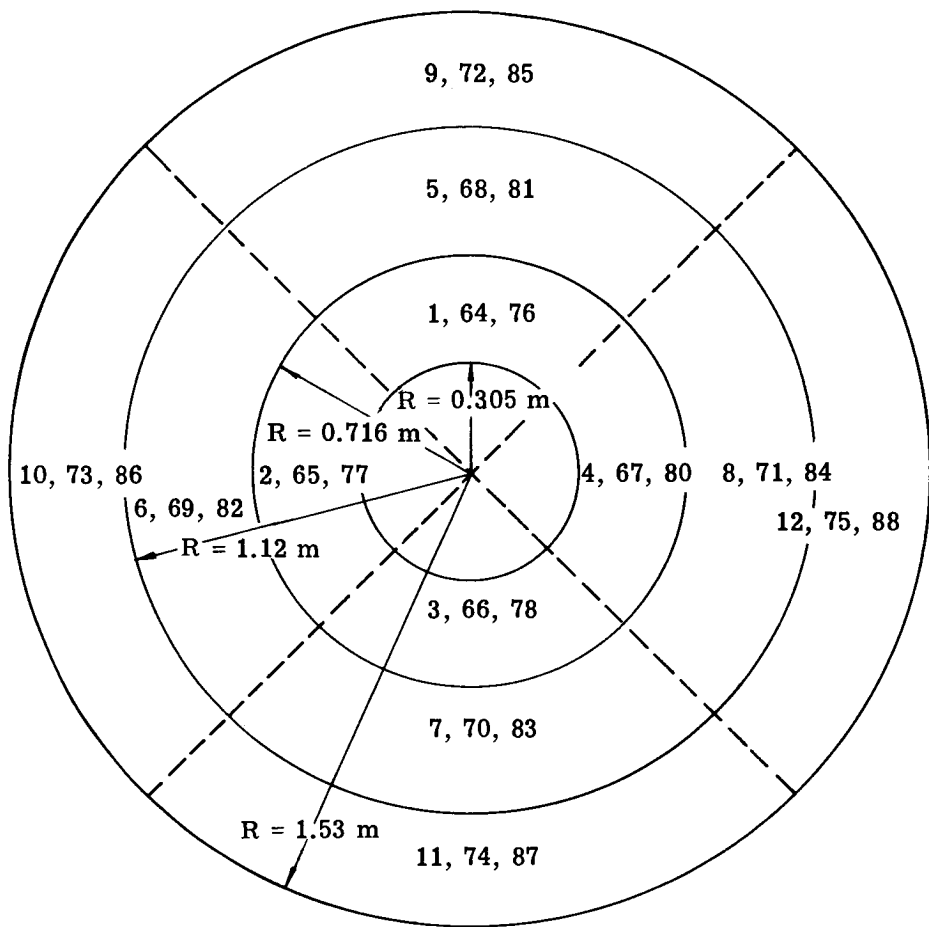
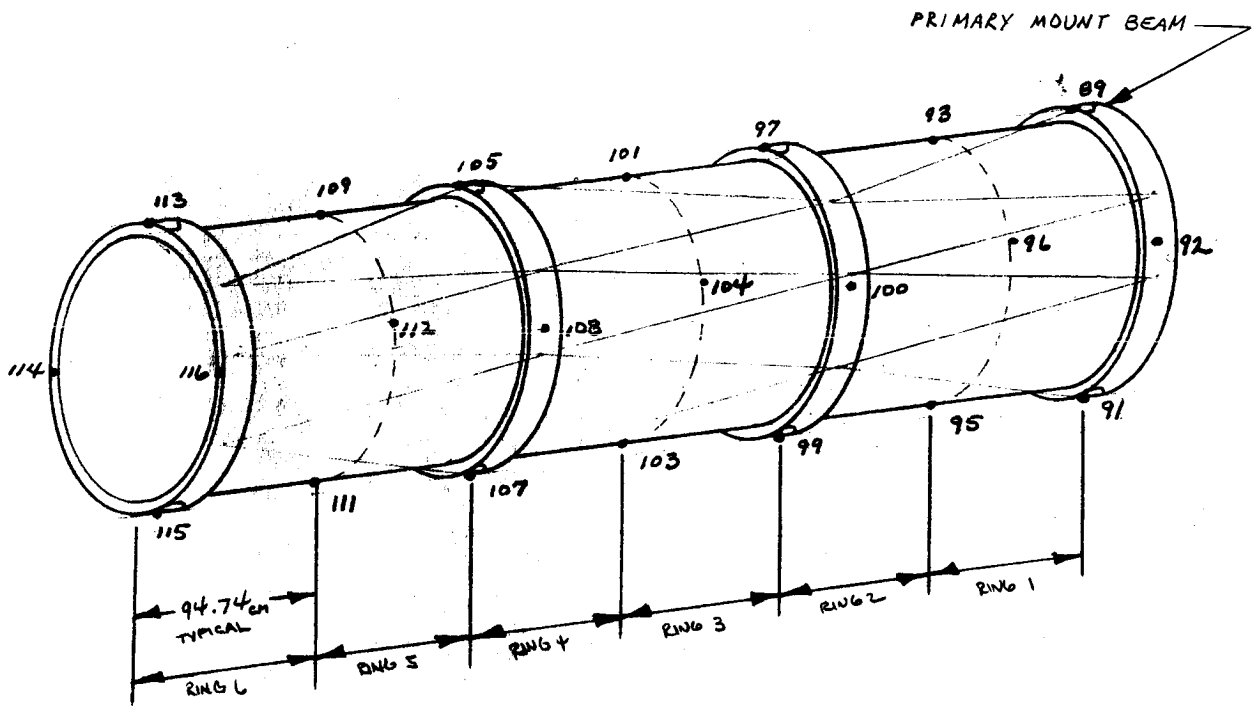


Fig. C.4-2 — Nodal model of primary mirror



NOTE: 4 TRUSS MEMBERS/NODE

Fig. C.4-3 — Nodal network for truss structure

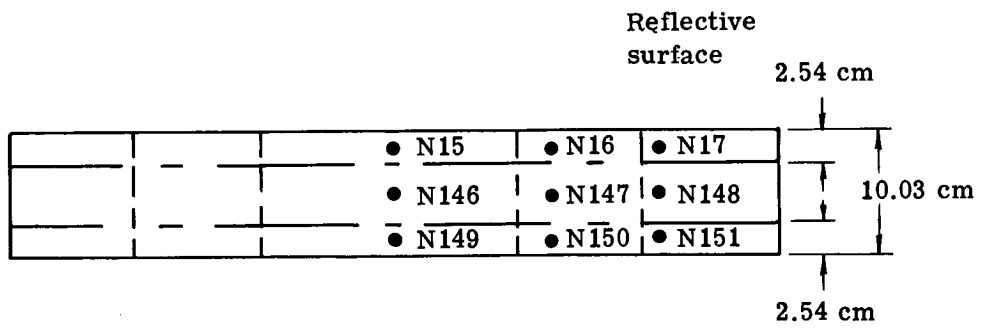
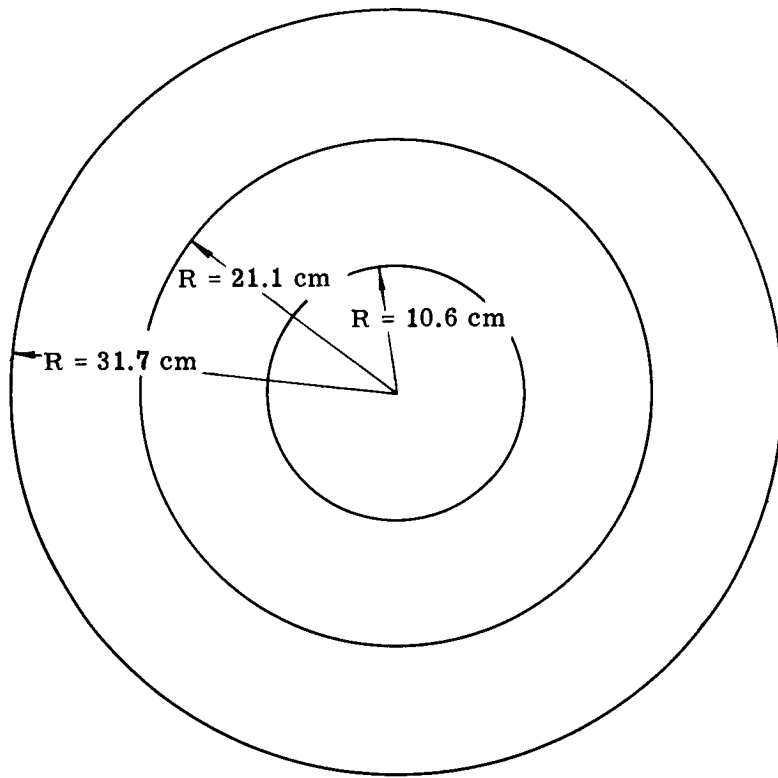


Fig. C.4-4 — Nodal model for secondary mirror

The aperture fluxes were entered as follows. For the two external orientations chosen, there are no direct solar inputs; i.e., the telescope aperture is either parallel or faces away from the solar vector. However, the telescope interior receives albedo and earth infrared input to varying degrees, depending on orbit positions. As the telescope progresses along its orbit, different nodes of the telescope interior view the earth and receive input loads. The heat fluxes to these internal nodes were determined at selected orbital positions.

#### C.4.f(3) LST Orientations

Two basic vehicle orientations have been investigated: where the LST optical axis is perpendicular to the solar vector and where the optical axis of the telescope is parallel to the solar vector. These orientations have been selected to provide the bracketing cases of possible telescope orientation. The perpendicular orientation produces the maximum solar loading, the larger temperature gradient across the telescope, and the minimum power requirements. The parallel orientation produces the minimum solar loading and maximum power requirements. These orientations are illustrated in Fig. C.4-5.

In addition to the two basic orientations described above, the effect of a change in telescope orientation (slew) was investigated. Again, a maximum thermal perturbation was considered by simulating a slew from the parallel orientation to the perpendicular orientation.

#### C.4.f(4) Analysis Results

The effects of the various orbital orientations on the thermal model of the telescope are described in succeeding sections. An evaluation is presented to compare analytical results with previously developed thermal design criteria.

The boundary conditions described represent conservative bracketing conditions to yield maximum temperature effects for comparison with the design requirements. For each orientation, the telescope was run for 20 orbital periods to give quasi-steady-state conditions; i.e., while there are temperature transients during an orbit, the temperature effects from orbit to orbit repeat quite closely. The significant temperature effects are due to vehicle orientation. Therefore, comparisons have been made with the two orientations mentioned previously (parallel and perpendicular to the sun vector).

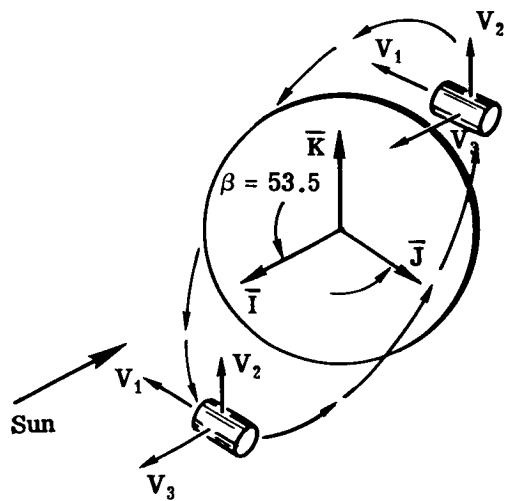
To evaluate the LST system thermal response of the various components, a transient thermal model run was made for a period of 165.6 hours (100 orbits), starting with an initial launch temperature of 21°C (70°F). This period was sufficient to determine the time required for various components to reach thermal equilibrium. Table C.4-3 presents the equilibrium time for selected components. The majority of the components reach thermal equilibrium approximately 60 hours after launch. The primary and secondary mirror temperatures reach equilibrium between 120 and 160 hours. Typical temperature histories for the transient analysis are presented in Figs. C.4-6 and C.4-7 for the primary mirror face and truss structure, respectively.

#### C.4.g Active Thermal Control System

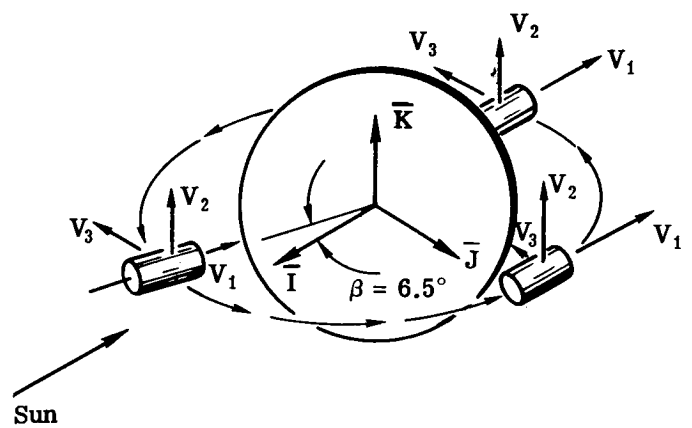
Performance of the active thermal control system has been evaluated for both orbital orientations by means of the thermal model of the OTA. Results for the main optical elements are given in Table C.4-4. Included for comparison purposes in the table are the thermal design requirements derived from the system error budget. It is significant that in some cases (particularly for the primary mirror), there is no remaining margin in terms of allowable thermal error contributors. On an overall basis, the allowable wavefront error of  $0.026\lambda$  is being maintained.

Table C.4-5 presents the computer calculated thermal control power input to the three actively controlled regions of the OTA.

Typical computer-generated plots of selected nodal time/temperature history for the last two orbits are presented in Figs. C.4-8 through C.4-11 for the perpendicular OTA orientation. Comparable plots for a parallel



(a) Orbit 2, orientation 1



(b) Orbit 1, orientation 2

Fig. C.4-5 — Orbit and orientation

TEMPERATURE HISTORY

KEY

4	NODE 1	PRIM. MIR.	FACILEST THERMAL MODEL - BASELINE DESIGN - DWG. NO. 105510195503, SEPT 72
+	NODE 5	"	"
X	NODE 9	"	PARALLEL TO SUN, - SUMMER SOLTICE
			100 ORBITS

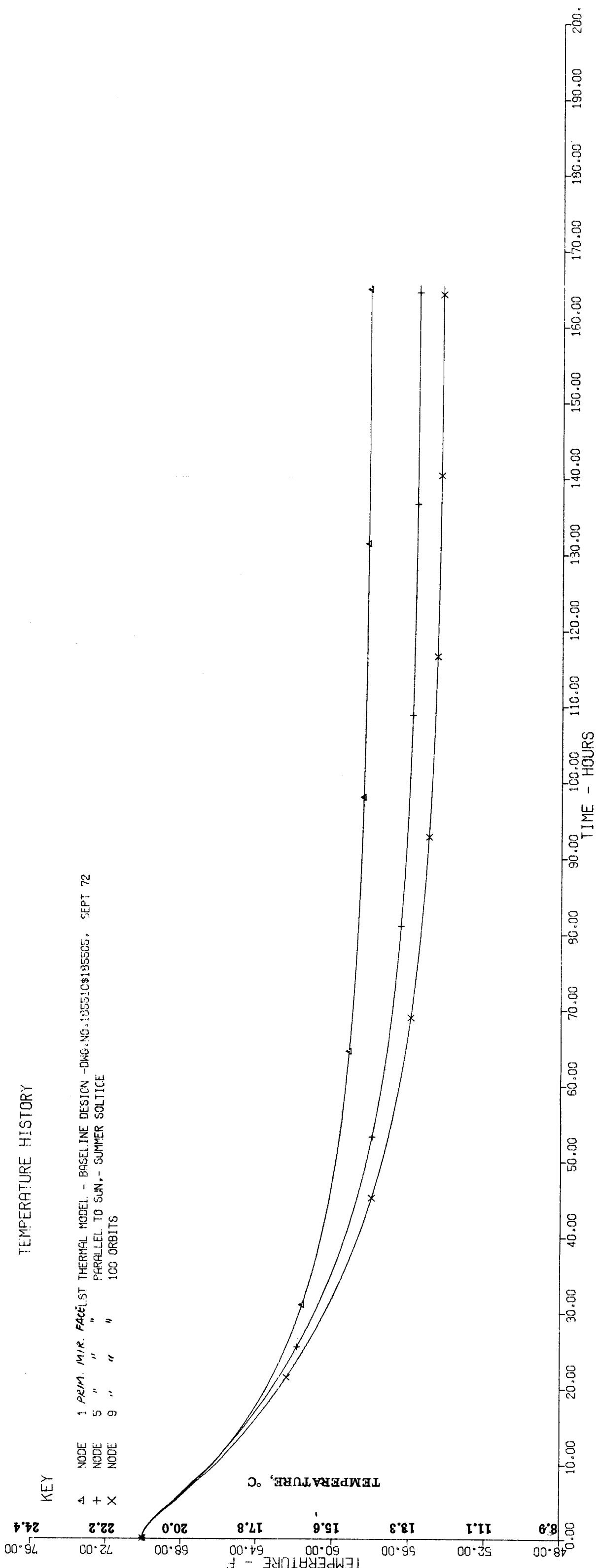


Fig. C.4-6 — Temperature history of primary mirror face



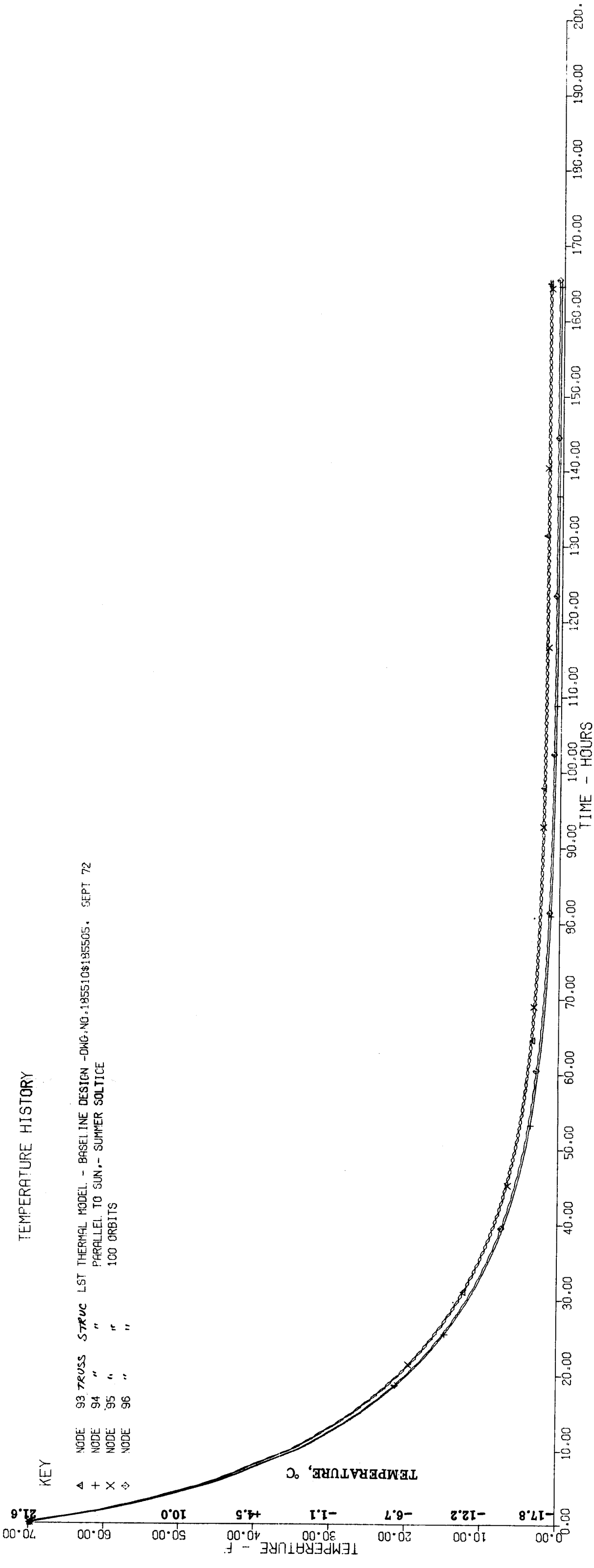


Fig. C.4-7 — Temperature history of truss structure

Table C.4-3 – System Equilibrium Time\*

Item	Approximate Time, hours
Primary mirror	120
Secondary mirror	160
Truss structure	60 to 110
Support spiders	60
Inner light baffles (primary and secondary)	30
Internal light baffle	40
Meteoroid shield	10

\*Time for component to reach thermal equilibrium from 21.1°C (70°F) launch (~ S time constants).

Table C.4-4 – Mirror Temperature Effects, °C

Item	Design Requirement	Perpendicular to Solar Vector	Parallel to Solar Vector
Primary mirror			
Average temperature change (soak)	±4.4	±3.31	±4.4
Maximum axial gradient	9.0	6.55	8.85
Maximum variation, axial gradient	±1.2	±0.75	±1.15
Maximum radial gradient	3.25	2.28	2.96
Secondary mirror			
Average temperature change (soak)	±0.5	±0.277	±0.338
Maximum axial gradient	4.5	1.0	1.0
Maximum variation axial gradient	±0.25	±0.084	±0.201
Maximum radial gradient	3.3	0.28	0.287

Table C.4-5 – Heater Power in Watts to Maintain  $21 \pm 0.3^{\circ}\text{C}$  ( $70 \pm 0.5^{\circ}\text{F}$ )

Thermal Control Region	Case	
	Perpendicular to Sun	Parallel to Sun
Primary mirror	59.61	79.21
Main support ring*	12.75	18.22
Secondary mirror	<u>1.09</u>	<u>1.42</u>
Totals	73.45	98.85

\*Excluding losses to SSM pressure shell.

TEMPERATURE HISTORY

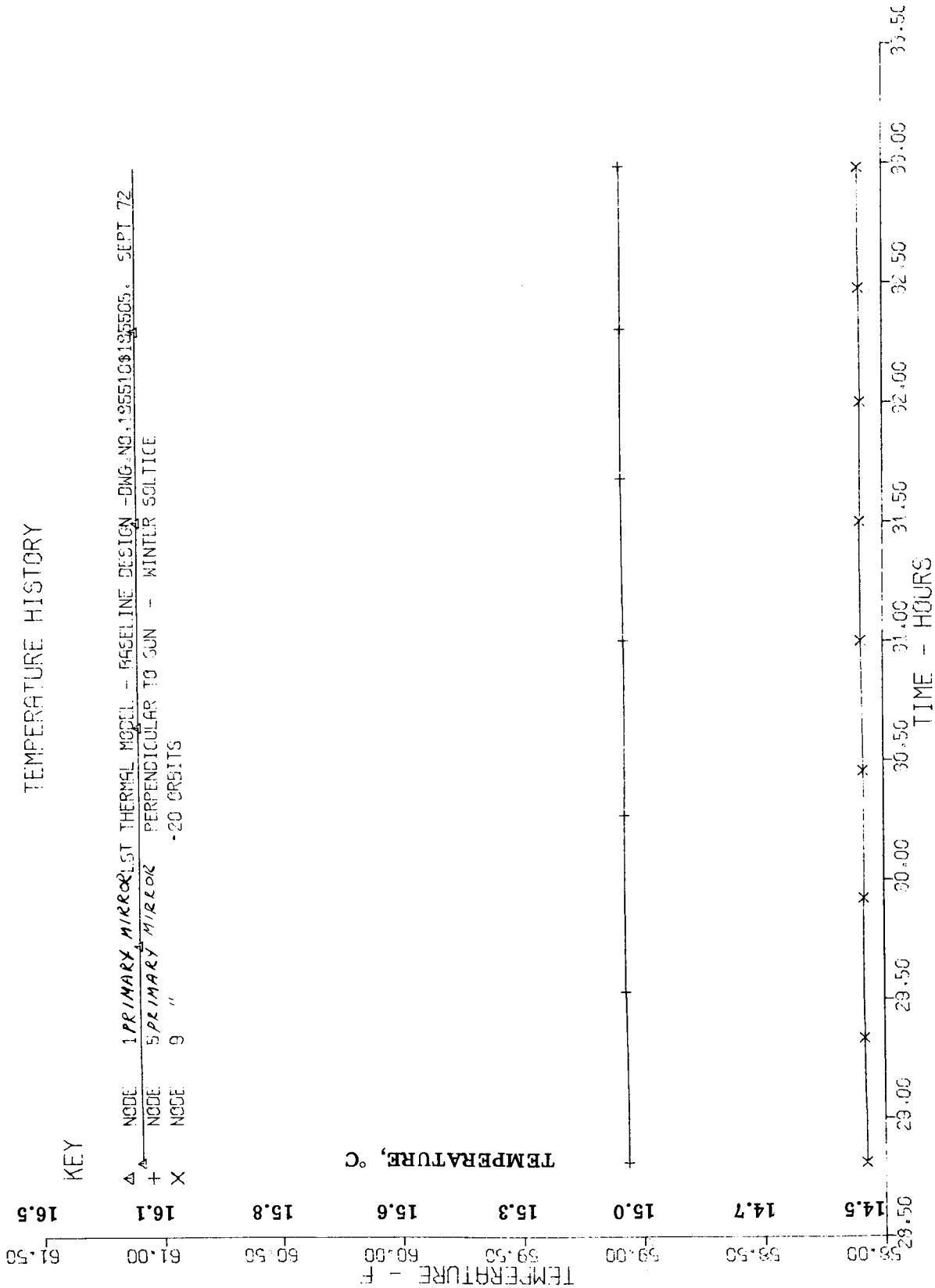
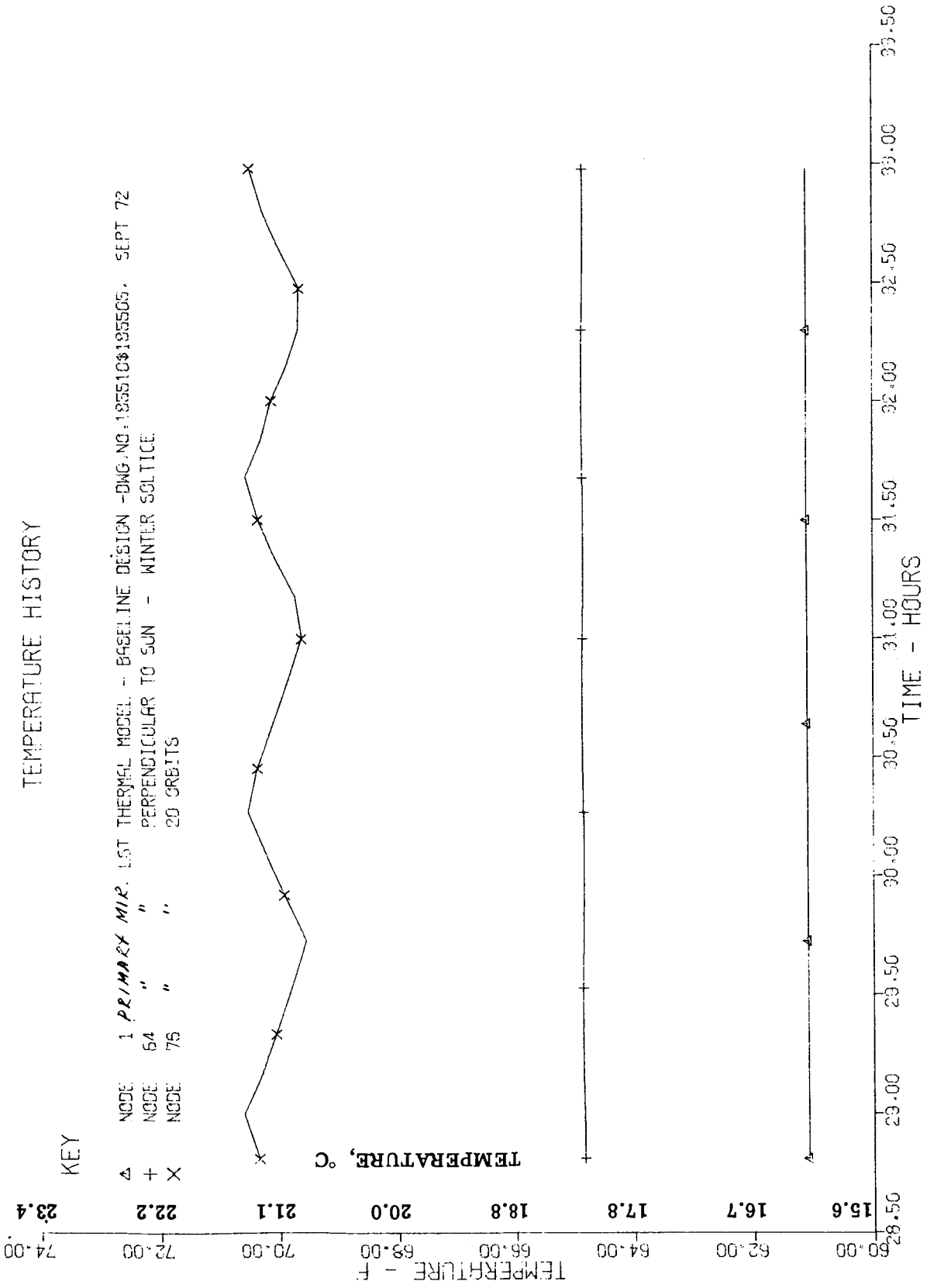


Fig. C.4-8 — Time/temperature history of primary mirror in perpendicular operation

# TEMPERATURE HISTORY



KEY  
 4 NODE 1 PRIMARY MIR. LST THERMAL MODEL - BASELINE DESIGN - DWG. NO. 1355103195505. SEPT 72  
 + NODE 64 " " PERPENDICULAR TO SUN - WINTER SOLTICE  
 X NODE 75 " " 20 GREYS

Fig. C.4-9 — Time/temperature history of primary mirror in perpendicular operation

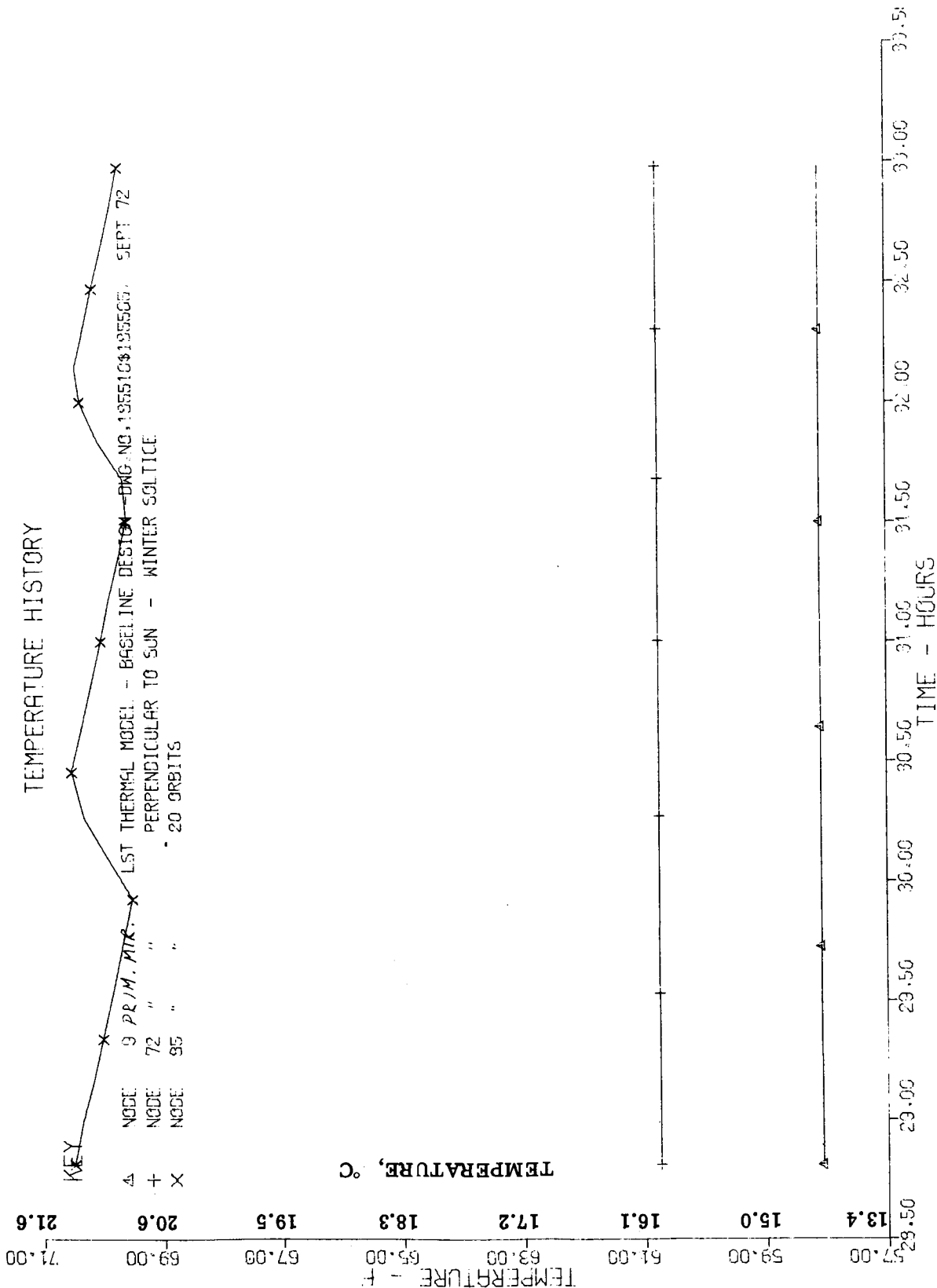


Fig. C.4-10 — Time/temperature history of primary mirror in perpendicular operation

# TEMPERATURE HISTORY

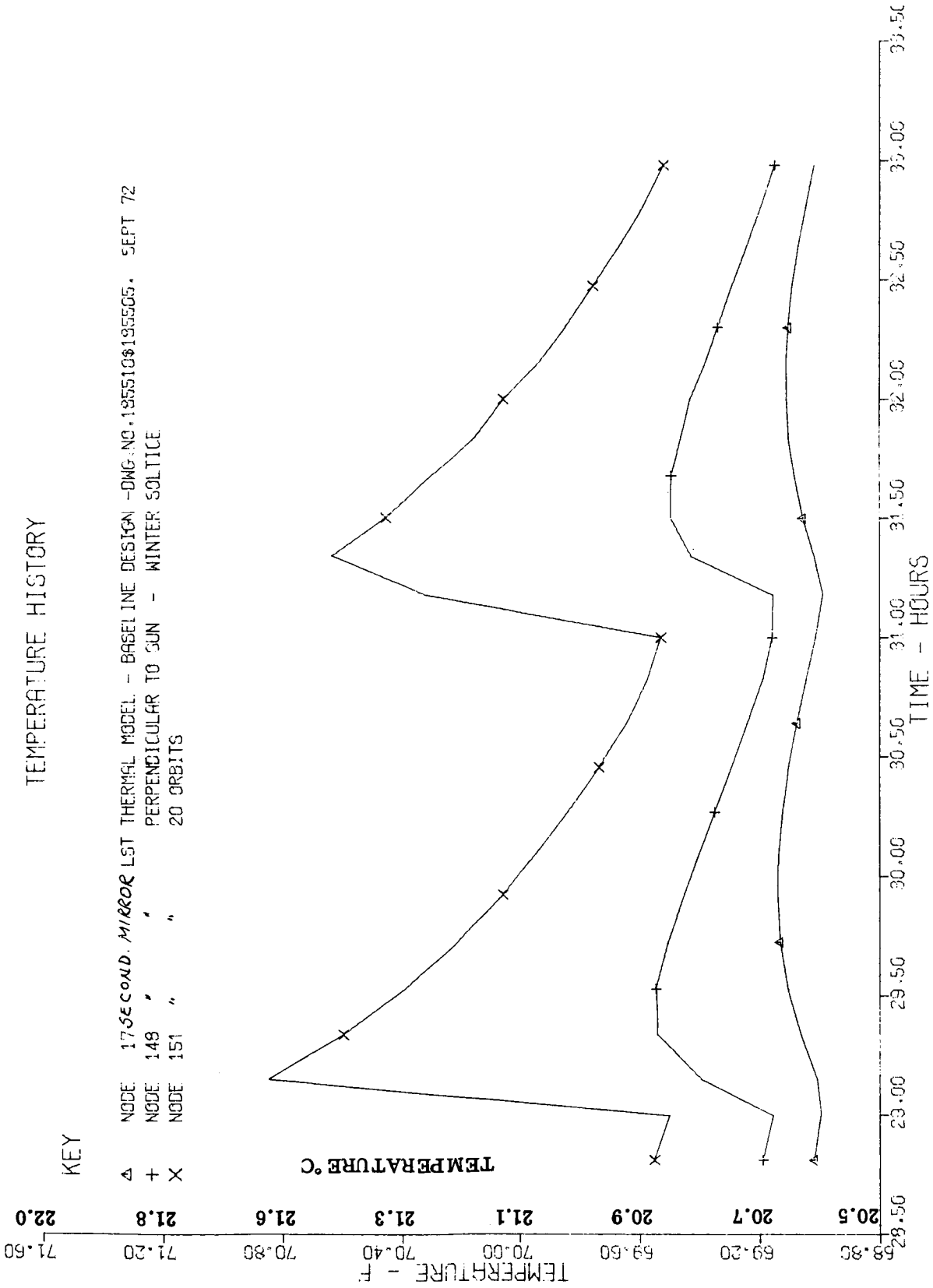


Fig. C.4-11 — Time/temperature history of secondary mirror in perpendicular operation



orientation are presented as Figs. C.4-12 through C.4-15. These figures depict radial gradients in the primary mirror face, axial gradients in the primary mirror at two radial positions, and the axial gradient in the secondary mirror. Operation of the active electrical heaters is clearly evident in the cyclical behavior of nodes 76, 85, and 151. Although not plotted, a review of the orbital temperature history of the main support ring indicates similar behavior.

Future studies of the active elements should consider all of the implications of thermal controller setpoint deadband selection since it does effect the performance of the optical system randomly.

#### C.4.h Passive Thermal Control System

Verification of the thermal performance of the passive thermal control system is based primarily on an evaluation of the nodal response of the various truss members within the model. A review of the available data indicates that the maximum orbital nodal temperature variation in the perpendicular orientation is approximately  $1^{\circ}\text{C}$ ; it occurs at the secondary mirror spiders (nodes 60-63). A similar examination of the available data for the parallel orientation results in a temperature variation of less than  $0.4^{\circ}\text{C}$ . Comparison with the required truss stability requirement of  $2.75^{\circ}\text{C}$  reveals that this is well within the allowable value.

Figs. C.4-16 through C.4-25 represent plots of time/temperature history for perpendicular and parallel telescope orientations. Circumferential temperature distributions immediately above the main support ring are shown in Figs. C.4-16 and C.4-21; those near the secondary mirror are shown in Figs. C.4-17 and C.4-22. Axial temperature distributions along the truss are shown in Figs. C.4-18 and C.4-23. Secondary spider structural temperatures are given in Figs. C.4-19 and C.4-24. The temperature history of a typical circumferential segment of the outer meteoroid shell is represented in Figs. C.4-20 and C.4-25.

Of great interest in the evaluation of the performance of the passive thermal control system is the structural thermal response to a change of orientation of the telescope. A worst-case simulation of this condition has been analytically simulated. The telescope was assumed to be at thermal equilibrium in the parallel solar orientation and was then slewed to the perpendicular orientation. As expected, the equilibrium time for the primary mirror was on the order of 100 hours [note, however, that the maximum mirror  $\Delta T$  is approximately  $1.7^{\circ}\text{C}$  ( $3^{\circ}\text{F}$ )]. On the other hand, the secondary mirror had no detectable time constant (considered reasonable in light of the small gradients developed in the secondary mirror).

Of major concern, then, is the response of the truss elements. In general, their response characteristics are inversely related to the distance from the primary mirror; i.e., truss elements near the secondary mirror respond faster to the change in position. Review of the time/temperature plots for the truss indicate equilibrium times of from 20 hours for the secondary spiders, to 30 hours for the forward truss elements, to 60 hours for the truss elements near the main support ring. These responses are illustrated in Figs. C.4-26 through C.4-28.

Fig. C.4-29 presents the dimensional changes resulting from normal orbital temperature perturbations. For the worst-case slew simulation, active correction of the secondary mirror will be required no more than once per 20 minutes to maintain system performance. Further studies are recommended for small slew maneuvers to define the active correction requirements.

#### C.4.i Thermal Design and Analysis of the Instrumentation Compartment

The development of the thermal control concept for the instrument compartment, as part of the overall thermal design effort of the LST, must take into account not only the thermal perturbations resulting from orbital operation and orientation but also the random operation of individual instruments as well. Specific requirements for the instrument cameras are discussed elsewhere.

This section presents three thermal design concepts and the results of the supporting analysis conducted to verify their performance. The analysis for this task was based on a thermal model of the entire rear section (from the primary ring) of the LST.

# TEMPERATURE HISTORY

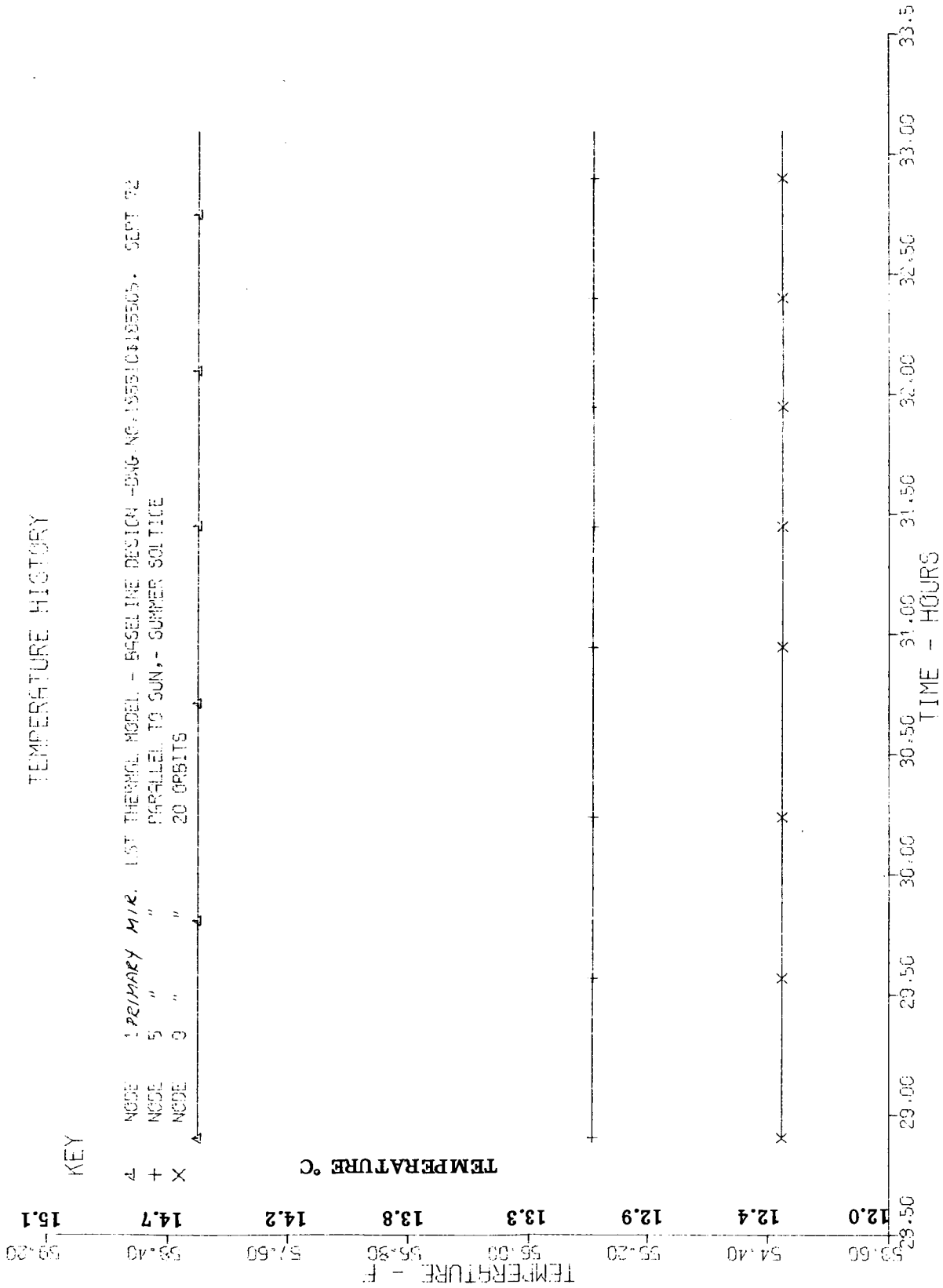


Fig. C.4-12 — Time/temperature history of primary mirror in parallel operation

TEMPERATURE HISTORY

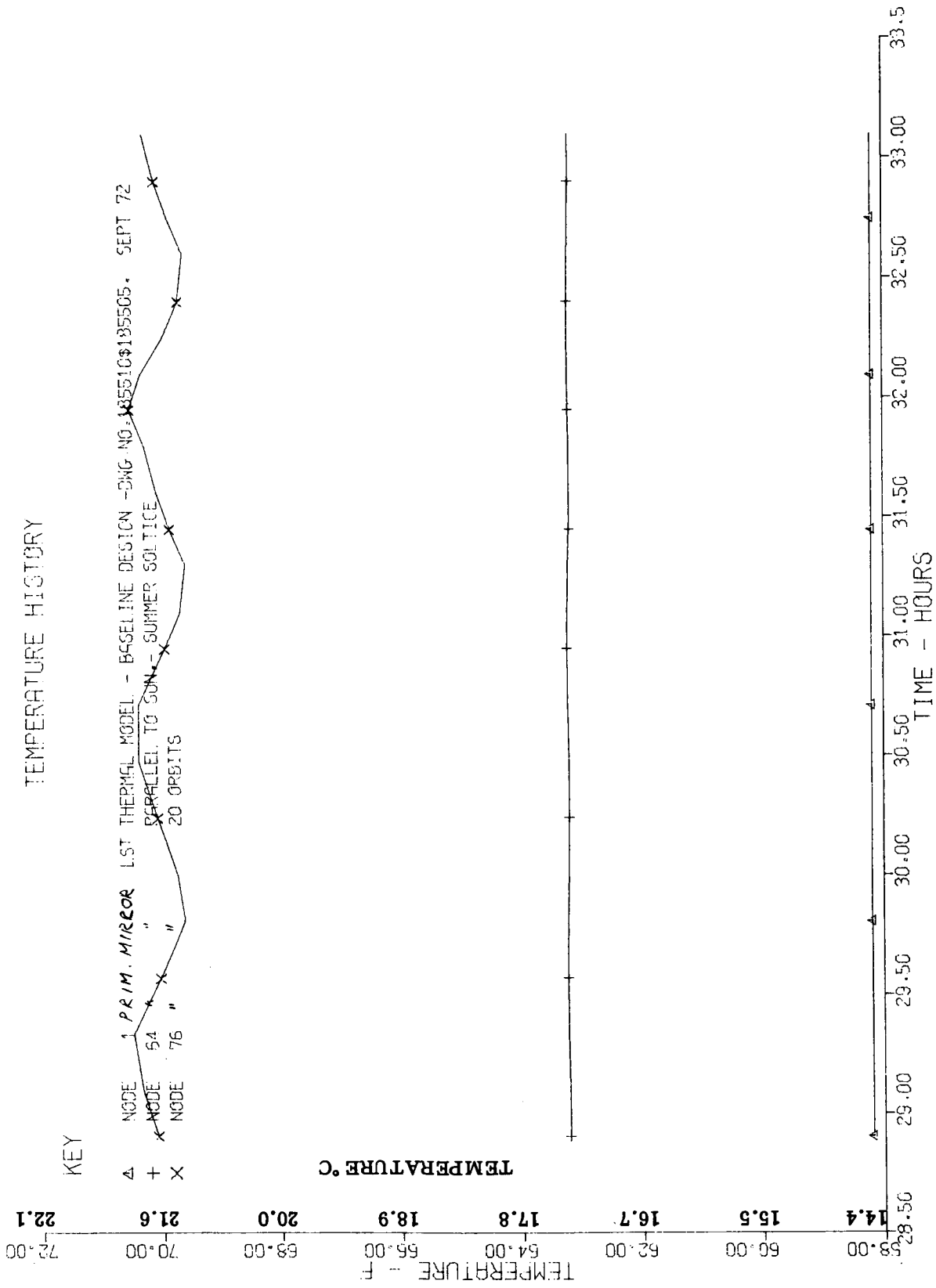


Fig. C.4-13 — Time/temperature history of primary mirror in parallel operation

# TEMPERATURE HISTORY

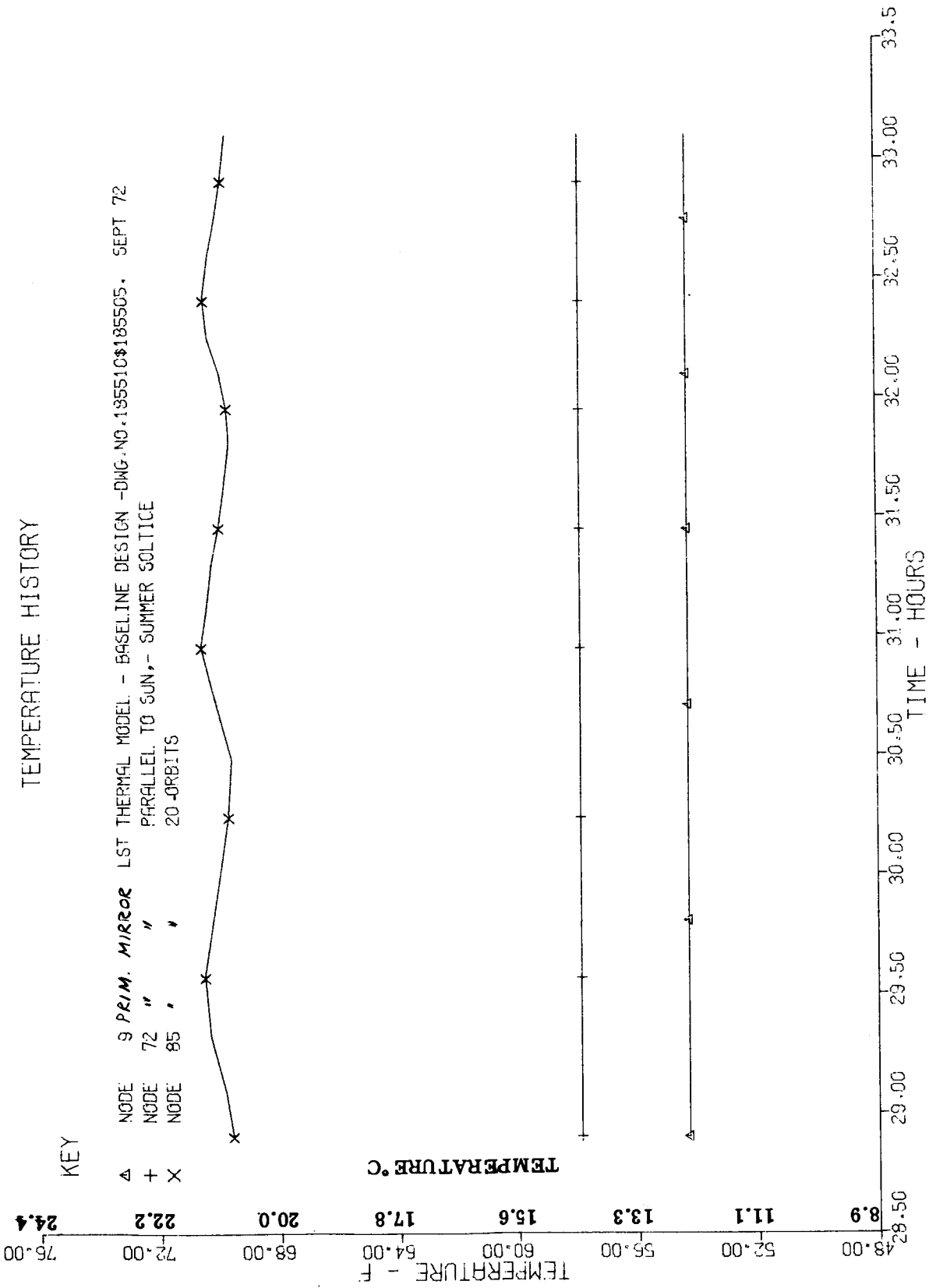


Fig. C.4-14 — Time/temperature history of primary mirror in parallel operation

# TEMPERATURE HISTORY

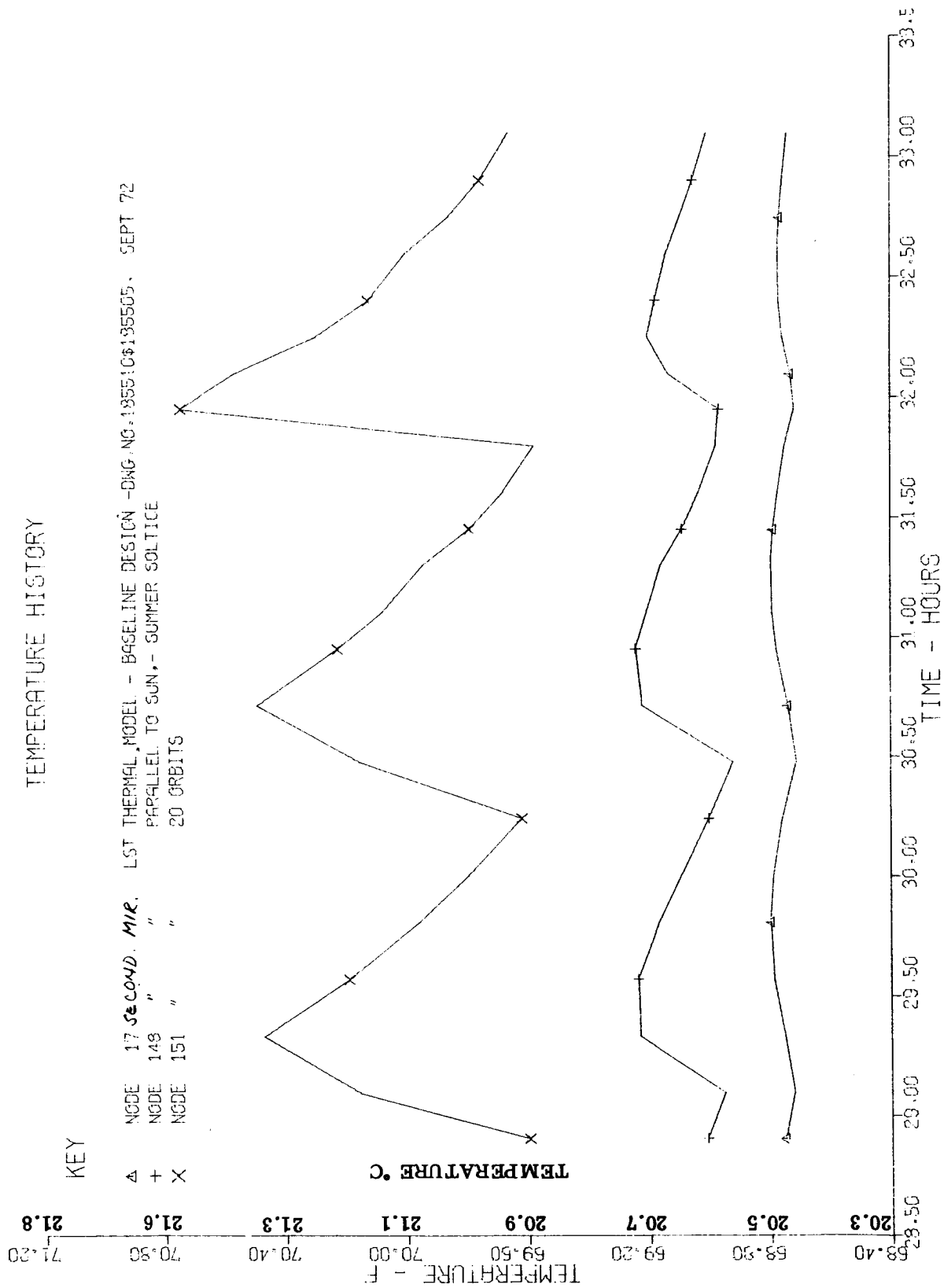


Fig. C.4-15 — Time/temperature history of secondary mirror in parallel operation



# TEMPERATURE HISTORY

## KEY

△	NODE 113	TRUSS STRUC.	1ST THERMAL MODEL - BASELINE DESIGN - DWG. NO. 1955103195505, SEPT 72
+	NODE 114	"	"
x	NODE 115	"	PERPENDICULAR TO SUN - WINTER SOLTICE
◇	NODE 116	"	20 ORBITS

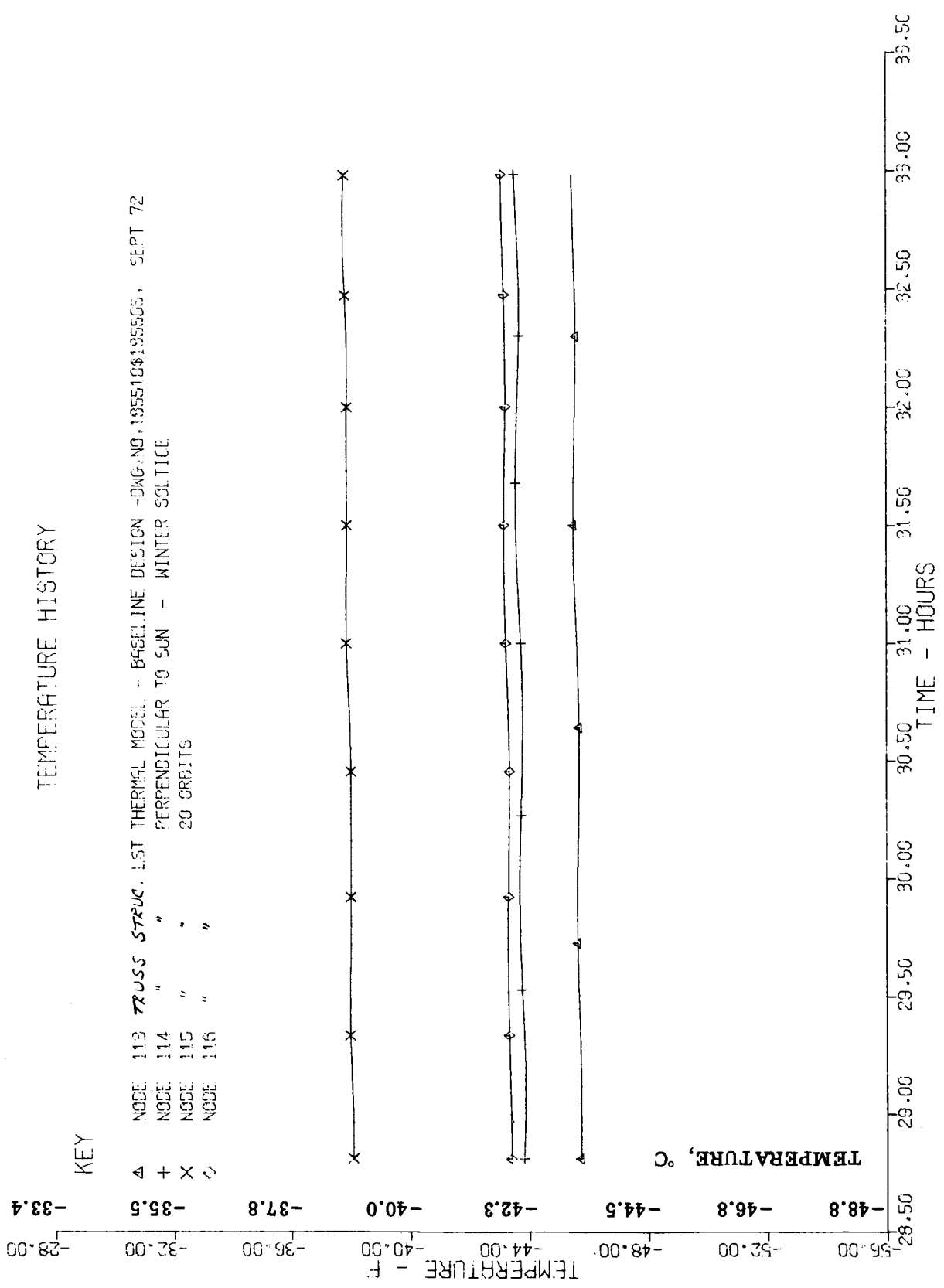


Fig. C.4-17 — Time/temperature history of truss structure in perpendicular operation; circumferential distribution

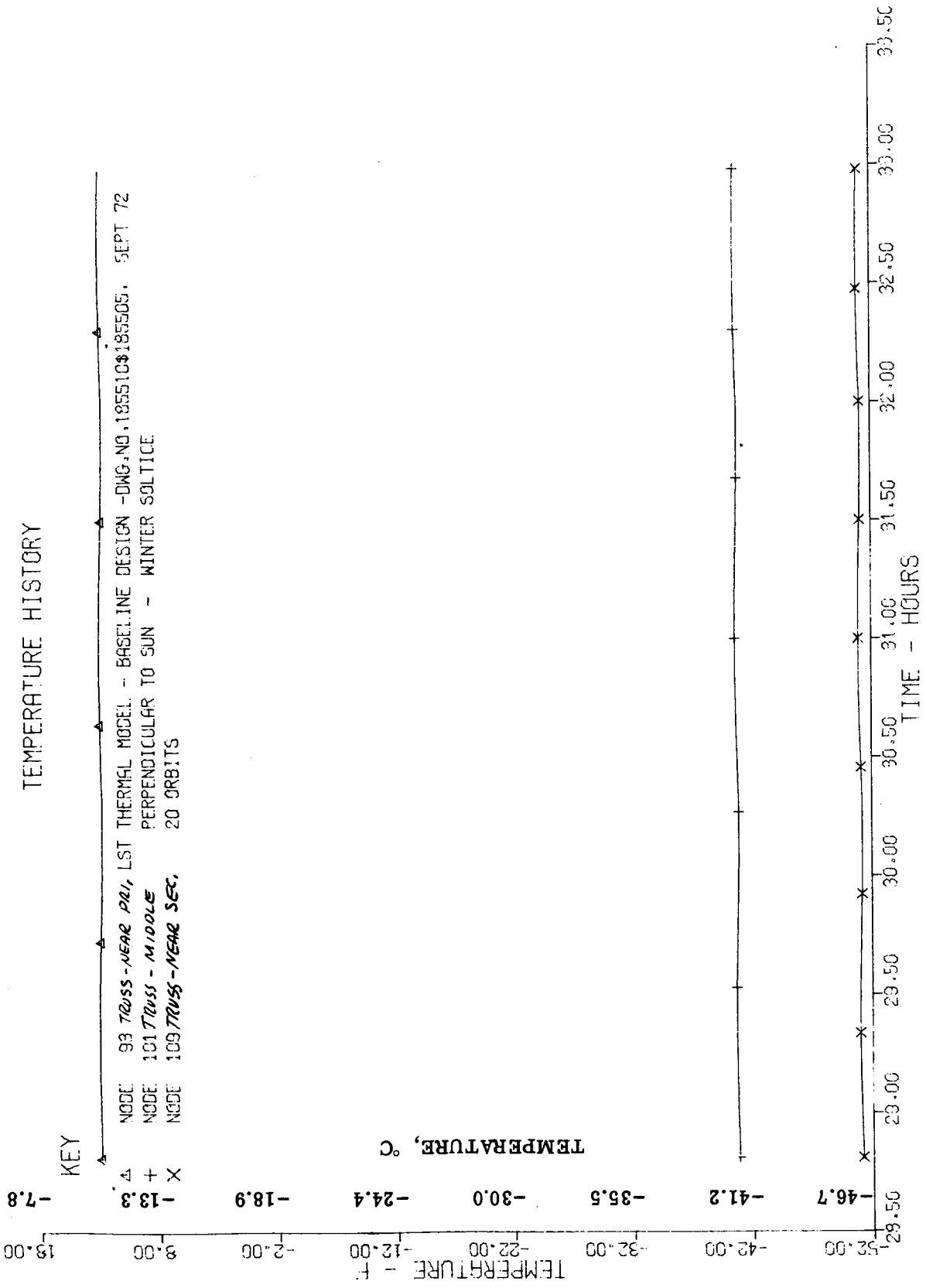


Fig. C.4-18 — Time/temperature history of secondary spider in perpendicular operation; axial distribution



TEMPERATURE HISTORY

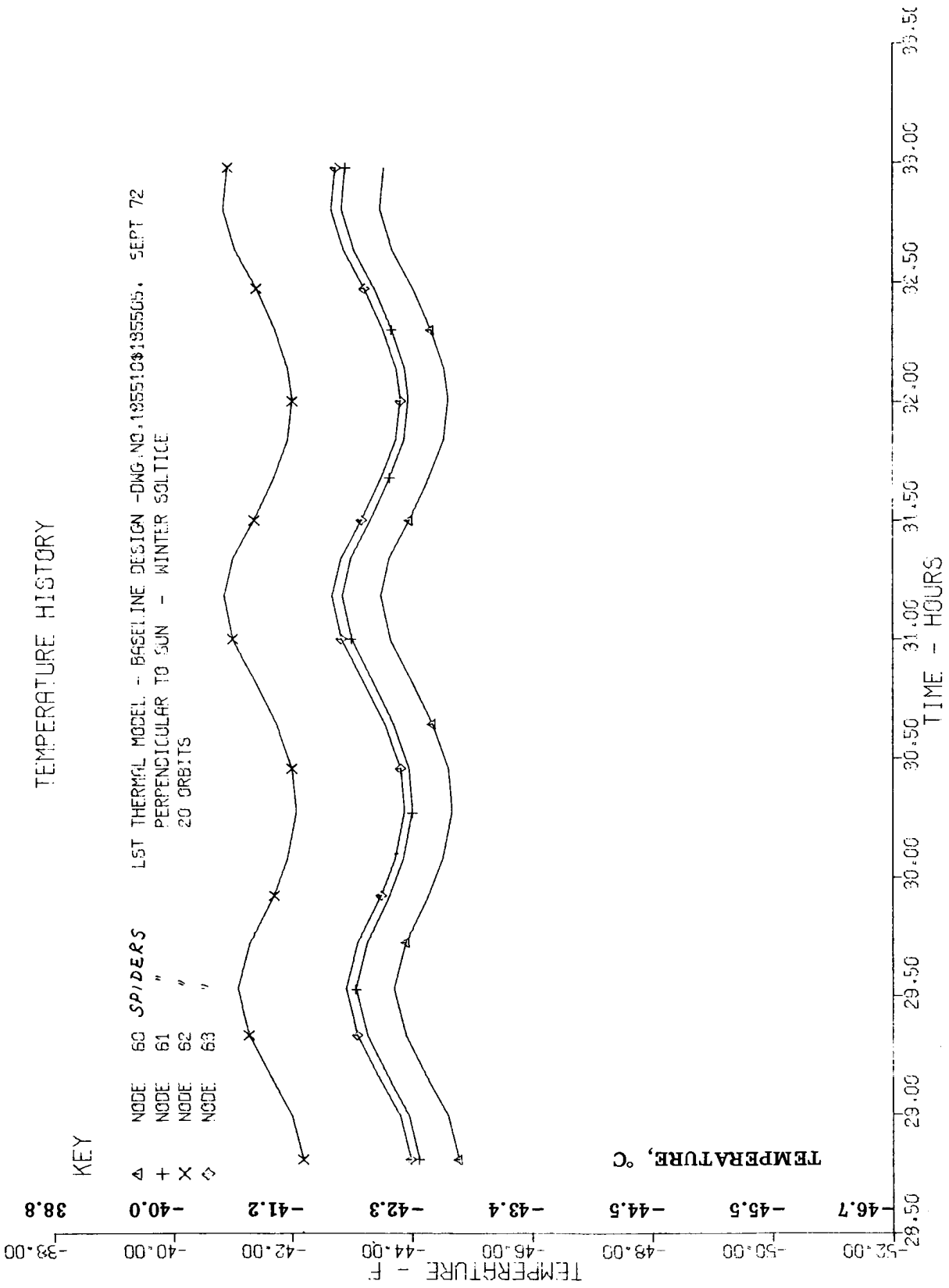


Fig. C.4-19 — Time/temperature history of secondary spider in perpendicular operation

# TEMPERATURE HISTORY

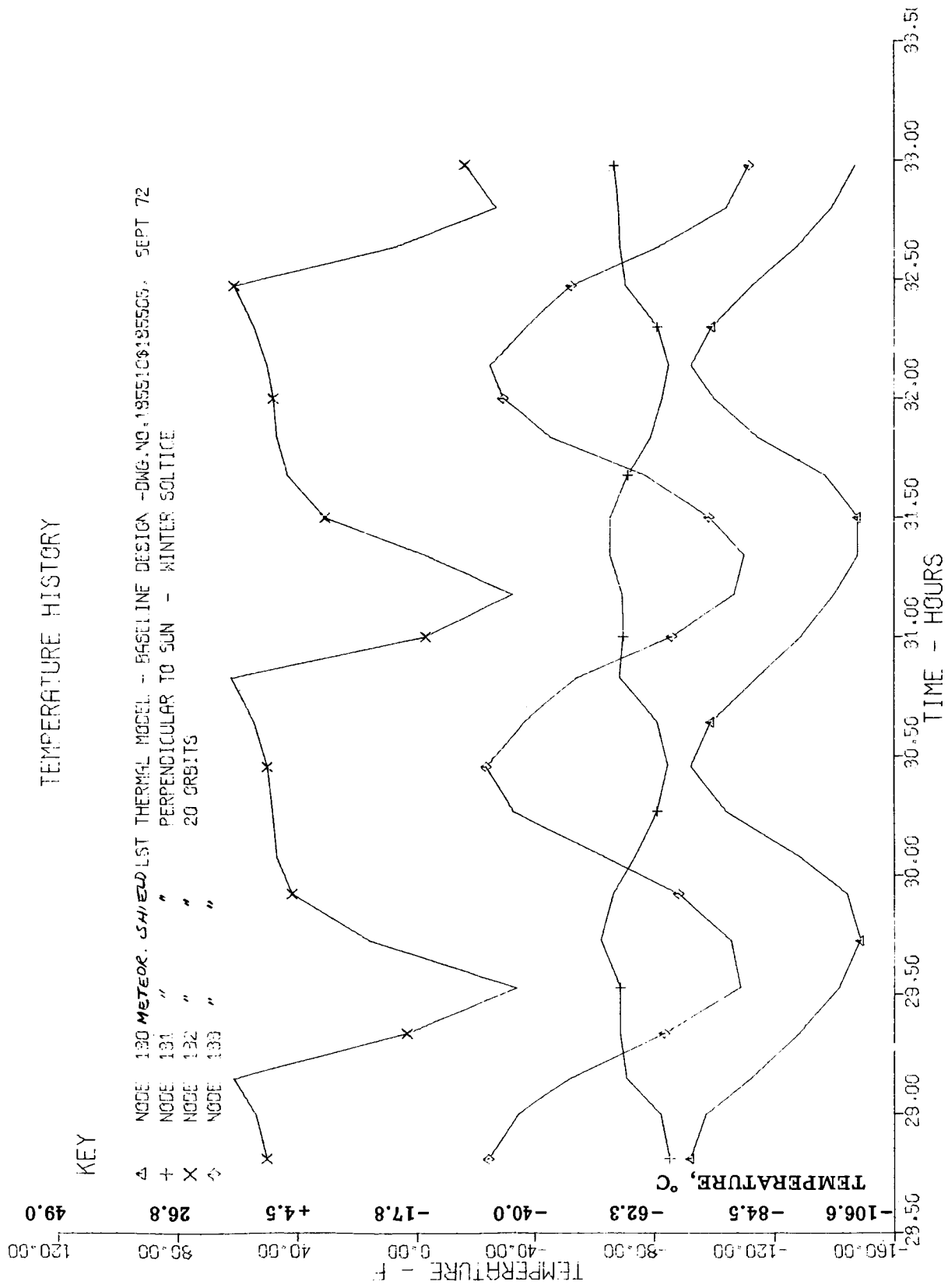


Fig. C.4-20 — Time/temperature history of meteoroid shell in perpendicular operation

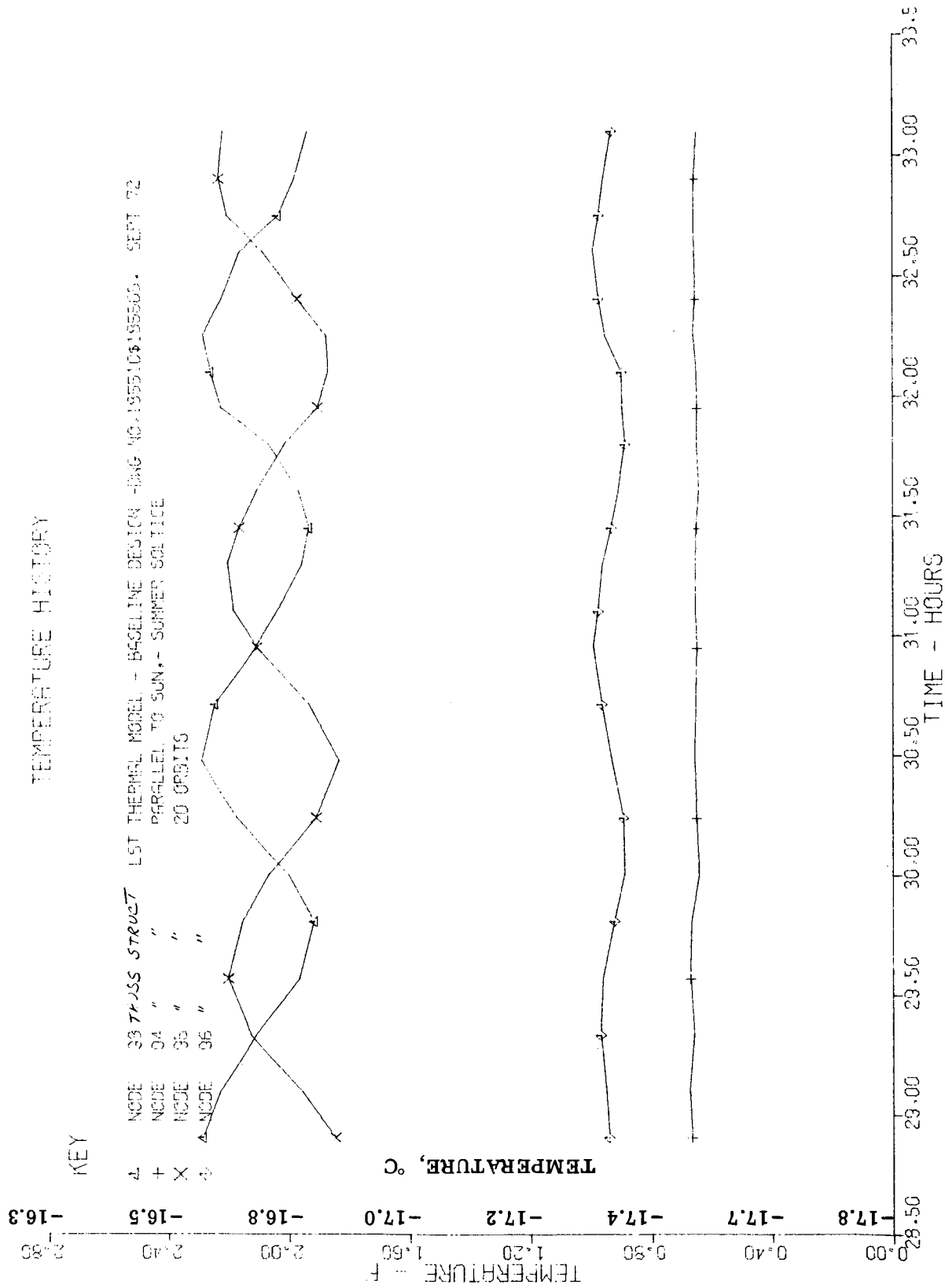


Fig. C.4-21 — Time/temperature history of truss structure in parallel operation; circumferential distribution



TEMPERATURE HISTORY

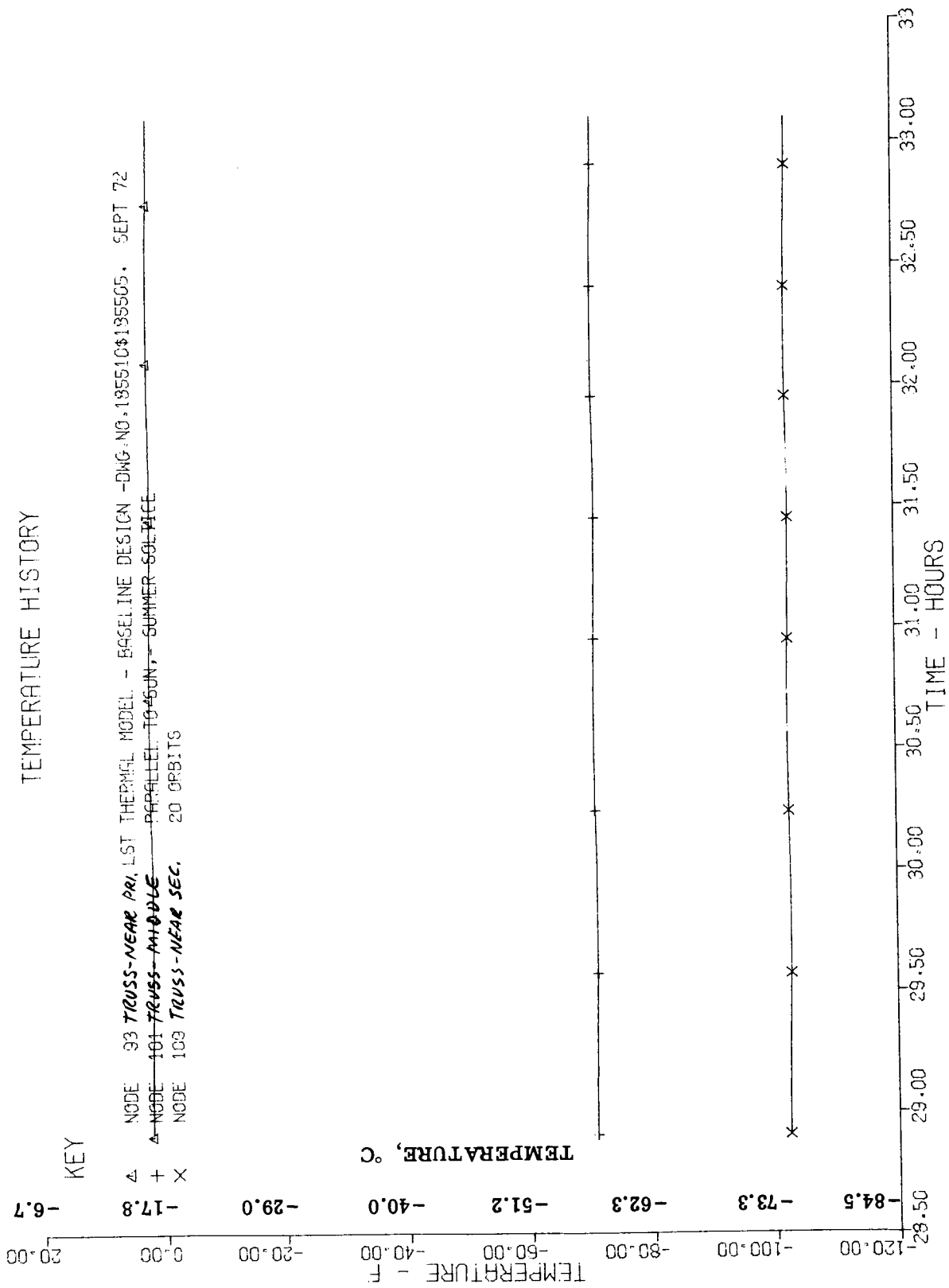


Fig. C.4-23 -- Time/temperature history of truss structure in parallel operation; axial distribution

TEMPERATURE HISTORY

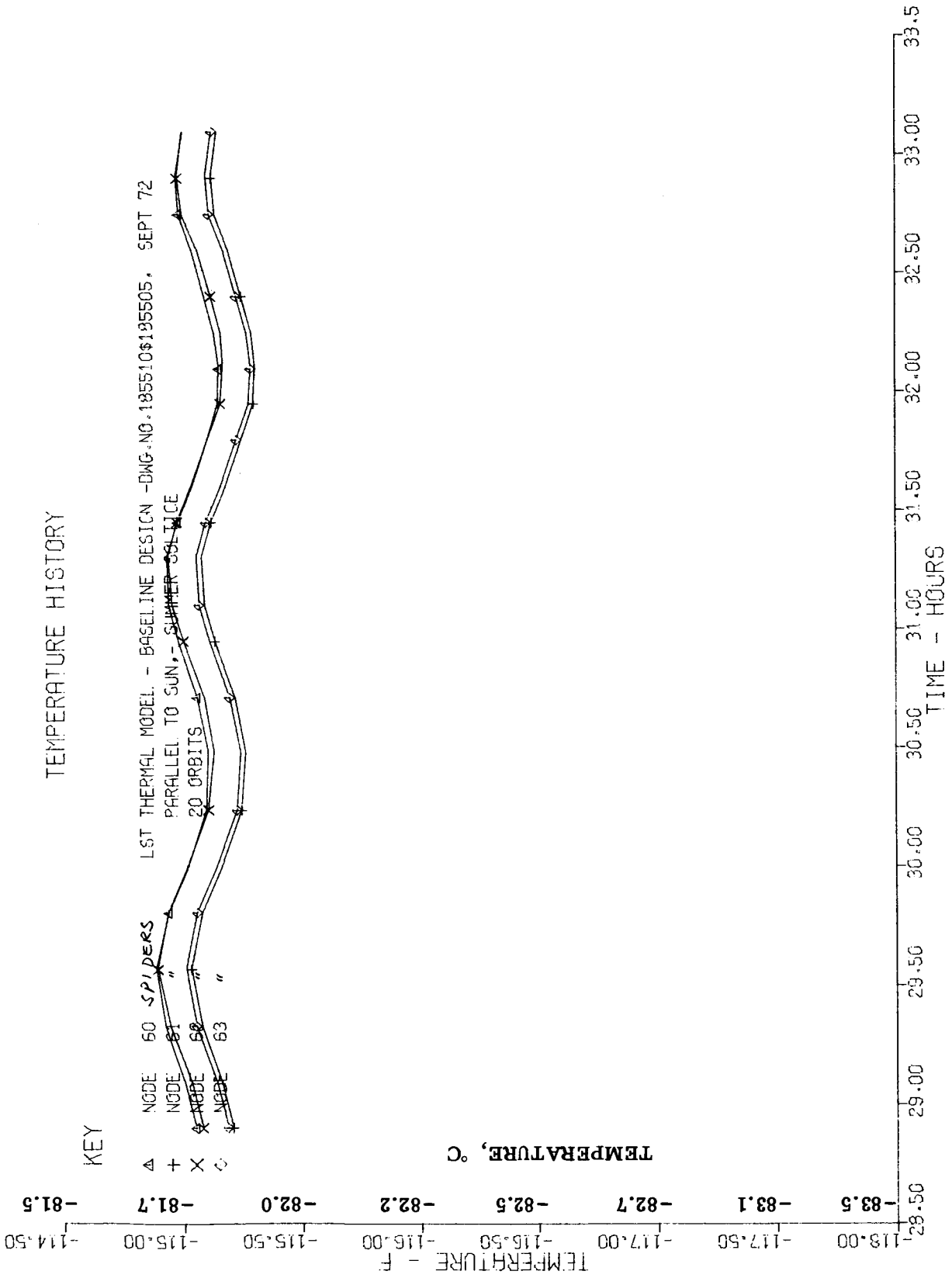


Fig. C.4-24 — Time/temperature history of secondary spider in parallel operation

TEMPERATURE HISTORY

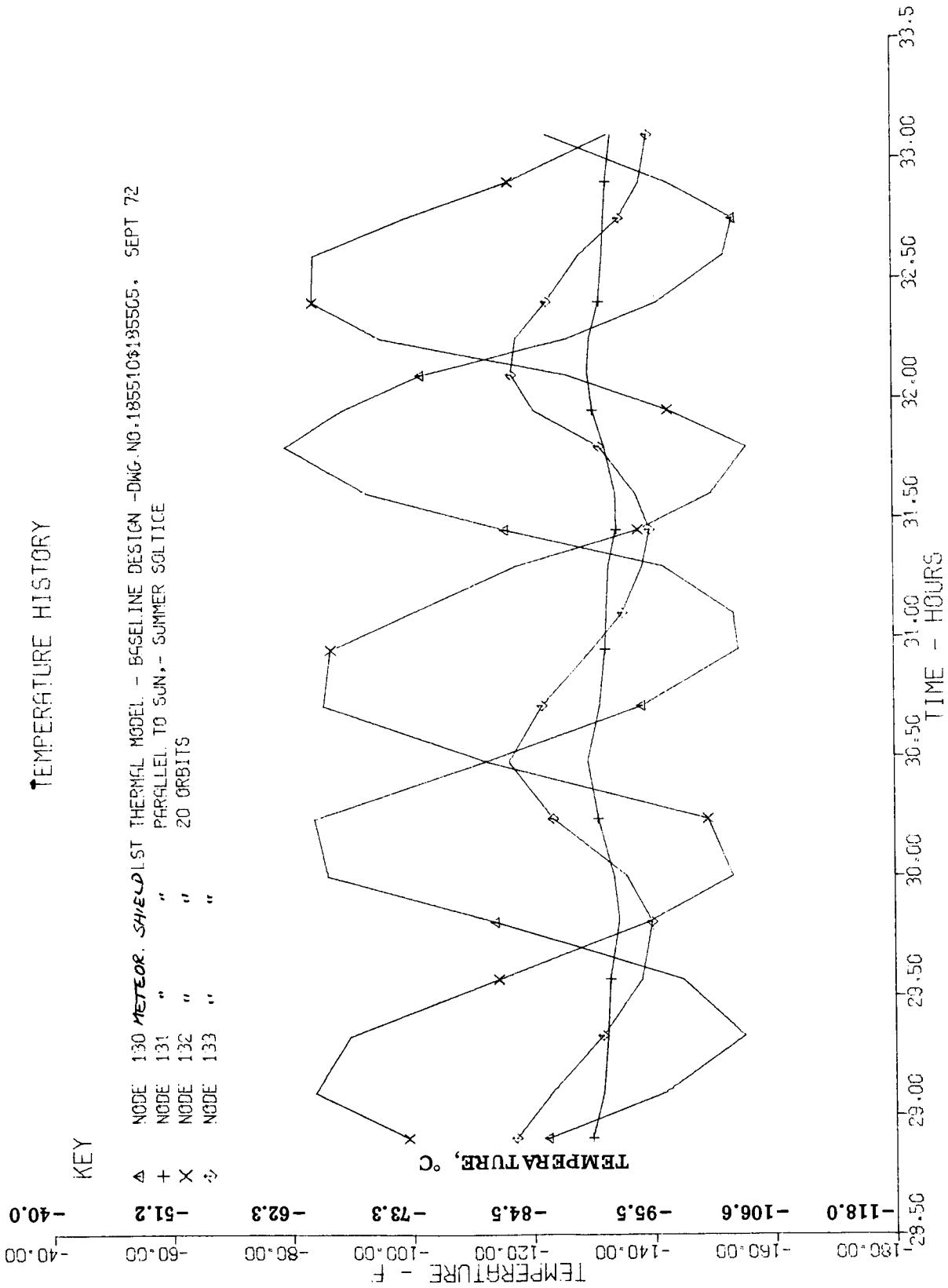


Fig. C.4-25 — Time/temperature history of meteoroid shell in parallel operation

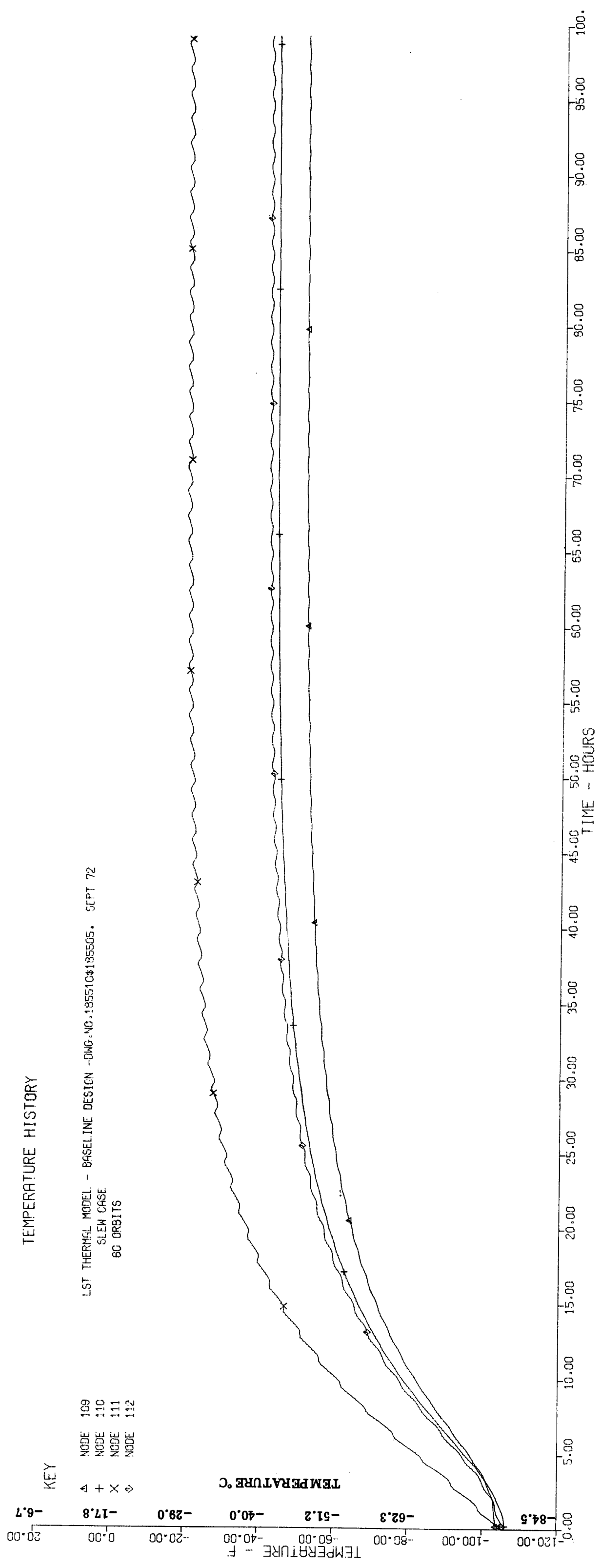


Fig. C.4-27 — Response time of forward truss elements



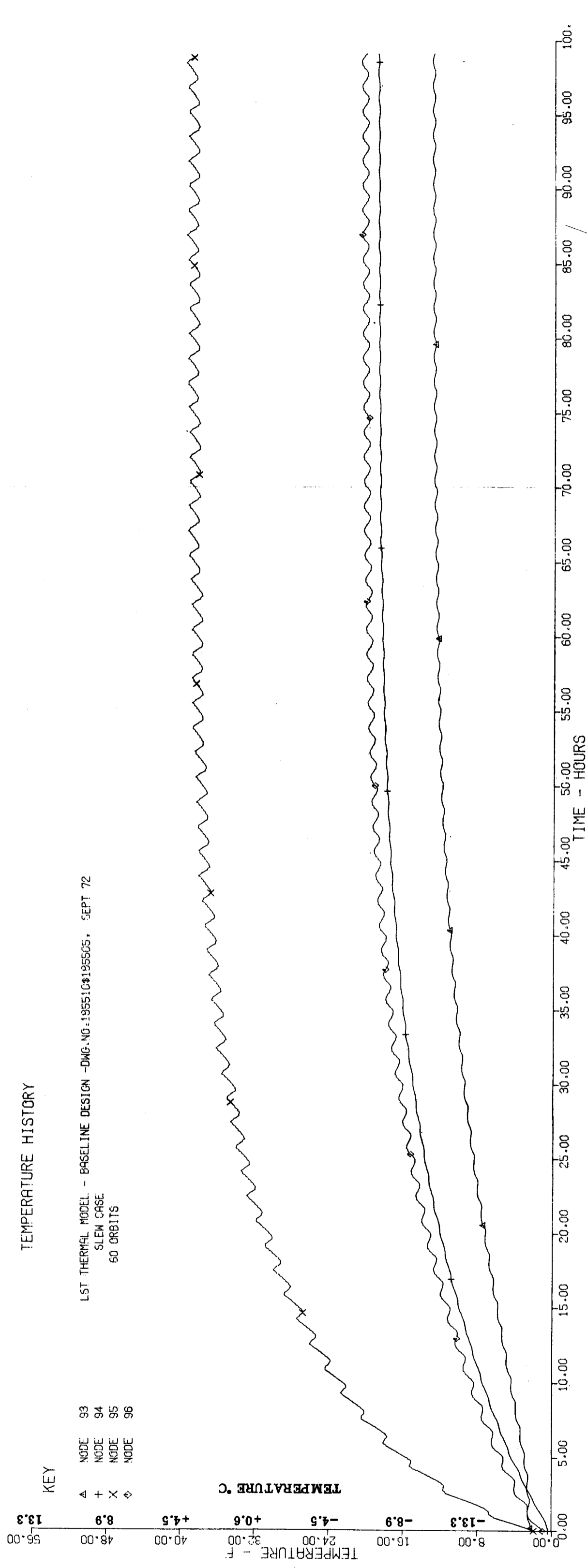


Fig. C.4-28 — Response time of truss elements near main support ring

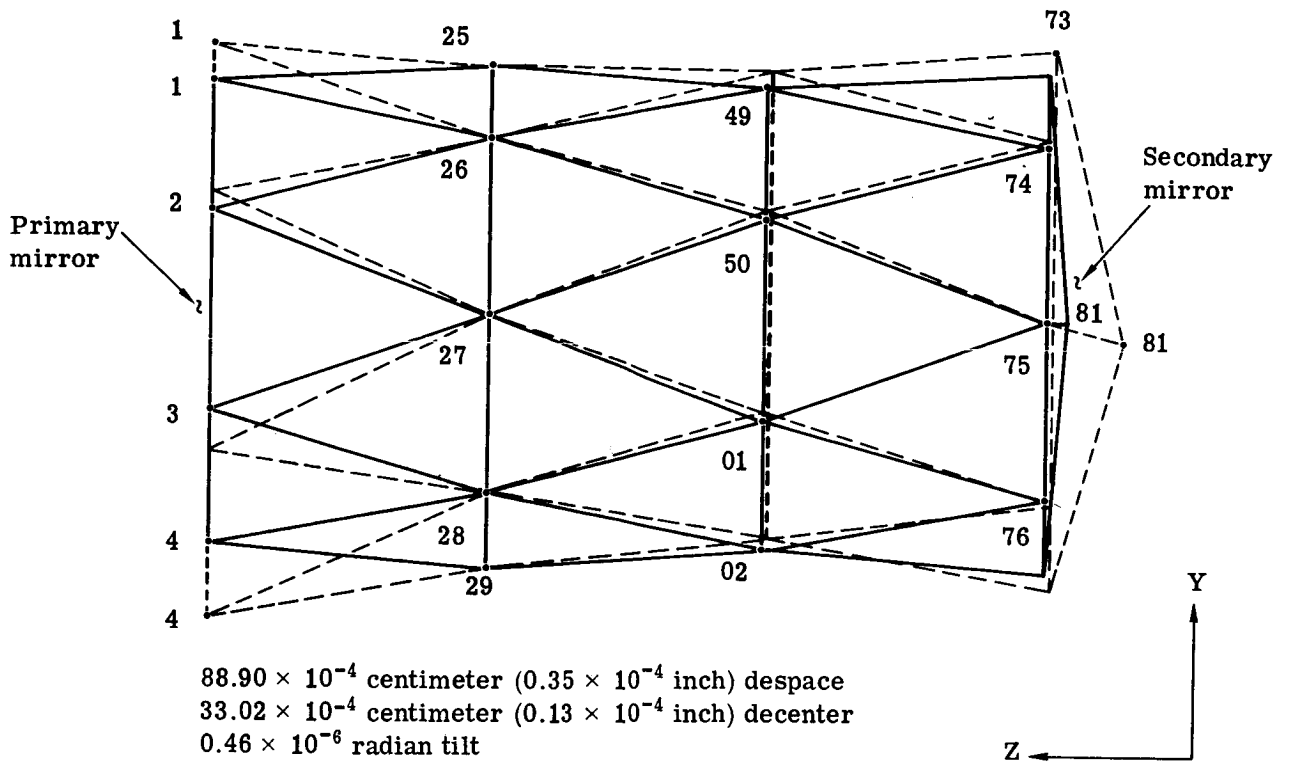


Fig. C.4-29 — Orbital thermal condition response

#### C.4.i(1) Thermal Requirements

Specific requirements for the entire SIP are not available at this time. Since it is not possible to completely develop and verify a design concept without them, we have developed our own requirements based on our understanding of potential system impacts.

#### C.4.i(2) Structural Temperatures

The thermally induced structural motions in the instrument compartment are of primary importance in the overall performance of the LST. These motions affect the performance characteristics of the various scientific instruments and the fine guidance system.

Although the specific requirements for the various instruments have not been defined, some information regarding stability of the fine guidance package is available. Using the artificial star, the allowable motion of the fine guidance package is 10  $\mu$ meters. The conversion of this allowable motion into an allowable temperature is a function of the type of structure assumed. For a composite truss,  $\alpha = 0.126 \times 10^{-6} / ^\circ\text{C}$  ( $\alpha = \pm 0.07 \times 10^{-6} / ^\circ\text{F}$ ), an allowable temperature variation of approximately 55.6 $^\circ\text{C}$  (100 $^\circ\text{F}$ ) is estimated. If however, an Invar structure is assumed, the allowable temperature decreases by an order of magnitude to 5.6 $^\circ\text{C}$  (10 $^\circ\text{F}$ ). Use of other metal structures having higher coefficients of thermal expansion would decrease the allowable temperature variation accordingly. From a realistic standpoint, the determination of structural deformations will be performed by means of a structural model of the instrument compartment and the evaluation of these deformations will be made then [see Section C.2.c(4)]. Although not defined, it is clearly a requirement that the variation in structural temperature with time be minimized. The maximum allowable deformation will be governed by instrument performance.

#### C.4.i(3) Camera Cooling

The concern here is to verify that the camera case (which acts as a radiator) temperatures are not excessive during camera operation. An upper bound on camera case temperatures of 350 $^\circ\text{K}$  has been established. It is a design goal to demonstrate operation of the cameras at as low a temperature as possible to reduce the thermoelectric cooling required for the individual image tubes.

Heat must be pumped uphill from the sensor cathode to radiators by means of Peltier coolers. Therefore the temperature level of these radiators is determined by the sink temperature of the SSM walls. In future studies, it will be important to trade off SSM operating temperatures versus tube cooling power and reliability, considering the impact of manned maintenance environment (dewpoints, etc.).

#### C.4.j Thermal Control Concepts

##### C.4.j(1) Constant T System

It is proposed that the entire instrument compartment structure and instruments be enclosed within a thermostatically controlled at 21.1 $^\circ\text{C}$  (70 $^\circ\text{F}$ ) aluminum shell. The major thermal power sources, the cameras, would be outside the thermal shroud and be free to radiate to the pressure shell wall. The thermal shroud would be polished on the external surfaces to provide a low emittance ( $\epsilon = 0.04$ ) to the pressure shell walls, thereby reducing thermal control power. The interior of the shroud would be coated to provide a high emittance, thereby closely coupling the internal structure to the temperature-controlled walls of the shroud.

For thermal control, the pressure shell walls are insulated with a low performance insulation ( $\epsilon^* \approx 0.09$ ) to provide a cold background. The insulation characteristics initially were selected to provide a thermally balanced system rejecting 300 watts from the shroud.

This concept provides a close control on the temperature of the structure and the associated instruments or structure-mounted components. Because of this control, the design is quite insensitive to material substitutions or variations in the thermal coefficient of expansion.

Since this concept encloses the entire structure within a metal shroud, there may be maintenance problems. The shroud will require careful design to allow for the removal of various sections to permit access to specific instruments or components. Because the cameras will be fully exposed, there appear to be no access problems. This design is fully compatible with the proposed laminar airflow concept. It should also be noted that supplementary pressure shell wall heaters may be required if parts of the thermal shroud are removed during maintenance operations.

#### C.4.j(2) Insulated Structure System

The proposed concept is based on the structure and instruments being isolated from the walls of the pressure shell by using multilayer insulating blankets, still allowing the cameras to radiate to the wall to reject the operating power. Since the primary structure is thermally decoupled from the cooler pressure shell, it will experience attenuated thermal transients that may occur at the wall.

The pressure shell wall is thermally decoupled from the outer wall of the vehicle by means of a high performance multilayer insulating blanket ( $\epsilon^* \approx 0.01$ ) to reduce the overall thermal leakage and external temperature transients.

A further degree of thermal control may be imposed by providing thermostatically controlled electric heaters on the instruments themselves, if it proves necessary to maintain the instruments at a fixed temperature.

In contrast to the thermal shroud concept, manned maintenance does not appear to present a problem. Access to all instruments and components can be accomplished by careful removal of a multilayer insulating blanket. Compatibility with the laminar airflow requirement may be accomplished by enclosing the open regions of the light bundle within thin, removable, metal shells to provide a continuous air path from end to end. The use of supplemental wall heaters during maintenance will probably be required.

#### C.4.j(3) Constant Q System

The proposed thermal control method would maintain the SIP inner wall at temperatures below or near  $20^\circ\text{C}$  ( $68^\circ\text{F}$ ) while radiating the power dissipated in the scientific instruments and in the thermoelectric coolers to the wall. When certain instruments are switched off, their power dissipation will have to be made up by  $I^2R$  heaters, on the instruments. The compartment walls will be insulated with a low performance insulation system whose average  $\epsilon^*$  will produce a system energy balance and maintain the wall temperature near  $20^\circ\text{C}$  ( $68^\circ\text{F}$ ) maximum for hot conditions. Heaters will provide a near constant energy source within the SIP. If the heaters are located in the photocathode camera radiators, the temperature distribution will remain nearly constant on the truss structure and cancel displacements caused by duty cycling of the cameras. Because of the low coefficient of expansion of the graphite-epoxy material [ $0.126 \times 10^{-6}/^\circ\text{C}$  ( $0.07 \times 10^{-6}/^\circ\text{F}$ )] the philosophy is to make all radiating surfaces black and allow the support structure temperatures to run hot with gradients.

The manned maintenance of this system presents no problems in terms of accessibility since it is similar to the insulated structure. The laminar airflow problem may be solved in a fashion identical to that suggested for the insulated structure.

The remaining maintenance problem concerns the effect of turning off the constant power sources within the compartment, which results in a cooldown of the pressure shell from its nominal value of  $21.1^\circ\text{C}$  ( $70^\circ\text{F}$ ). Supplemental heaters must be provided to account for the 660+ watts being released by the 10 cameras. The alternate systems, which incorporate more efficient insulation systems, require less power for the same condition.

#### C.4.k SIP Thermal Model

A detailed thermal model of the instrument compartment was made, consisting of 147 nodes with approximately 840 radiation connections and 230 conduction connections, depending on specific configuration. The detailed thermal model of the scientific subsystem module can be categorized as follows:

1. Outer thermal control surface (meteoroid shell), which is divided into 16 nodes (500-515) (Fig. C.4-30). The material of the structure is assumed to be aluminum (6061-T6), subject to the following boundary conditions:

- a. Orbital beam fluxes for a 740-kilometer (400-nautical mile) orbit
- b. Heat loss from surface to 4°K space
- c.  $\alpha_S/\epsilon = 0.135/0.92 = 0.146$

2. Pressure shell wall, which is divided into 16 nodes (516-531) (Fig. C.4-31). The material of the structure is assumed to be aluminum (6061-T6)

3. SIP support structure—radial truss, which is divided into 28 nodes and consists of a titanium primary ring (nodes 532-539) and a graphite-epoxy truss network (Fig. C.4-32). The primary ring temperature is held at 21.1°C (70°F) while the remainder of the structure is not controlled directly and receives heat input from operating cameras and the surroundings.

4. SIP support structure – axial truss, whose nodal identification is shown in Fig. C.4-33. This truss network supports the Echelle spectrographs and a faint object spectrograph (0.115 to 0.22 micrometer). Heat inputs to the truss are produced by conduction from these instruments and radiation from the surroundings. A contact conductance of  $629 \times 10^6$  joules/hr-m<sup>2</sup>°C (1,000 Btu/hr-ft<sup>2</sup>·°F) is assumed for all instrument mounting connections.

5. Fine guidance housing, which is divided into 16 nodes (580-595) (Fig. C.4-34). The structure is a solid graphite-epoxy cylinder. This structure houses the fine guidance system and the f/12 camera. The following instruments are mounted on the exterior of the cylinder:

- a. Faint object spectrograph 0.66 to 1.0 micrometer
- b. Faint object spectrograph 0.22 to 0.35 micrometer, 0.35 to 0.66 micrometer
- c. Mid-infrared interferometer

6. Cameras. The nodal identification for the cameras contained in the scientific instrument package is as follows:

Node	Camera
597	Echelle spectrograph (0.115 to 0.18 micrometer)
602	Echelle spectrograph (0.18 to 0.35 micrometer)
606	f/96 camera
607	f/96 camera
608	f/96 camera
617	Faint object spectrograph (0.115 to 0.22 micrometer)
620	Faint object spectrograph (0.22 to 0.35 micrometer, 0.35 to 0.66 micrometer)
622	Faint object spectrograph (0.66 to 1.0 micrometer)
624	Mid-infrared interferometer
625	f/30 slit jaw camera
614	f/12 camera

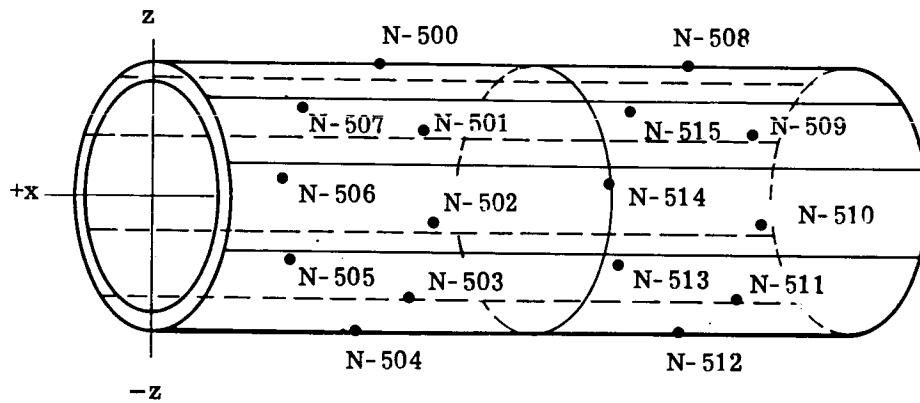


Fig. C.4-30 — Outer thermal control surface—nodal network

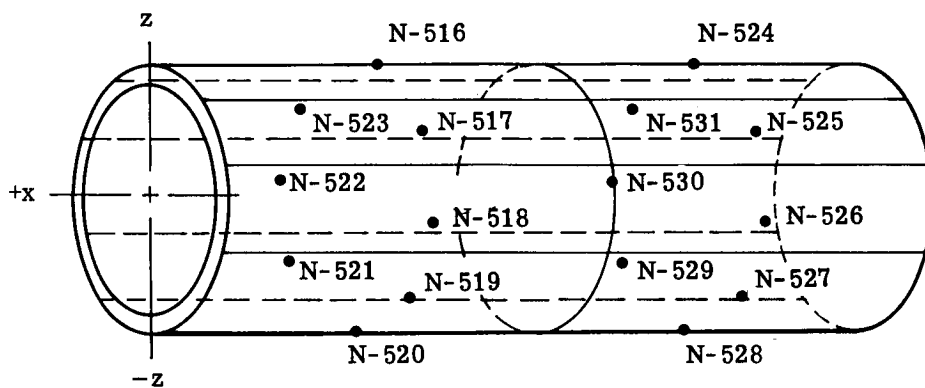


Fig. C.4-31 — Pressure cylinder wall—nodal network

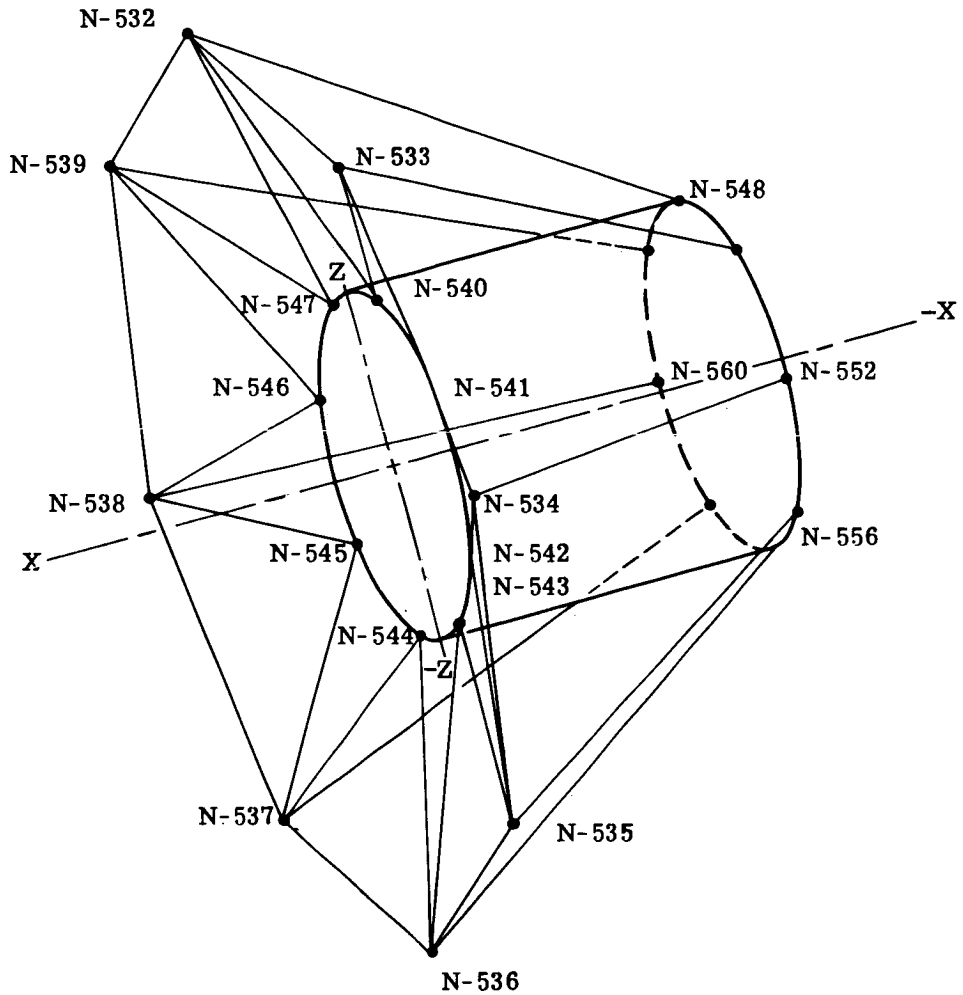


Fig. C.4-32 — Radial truss—nodal network



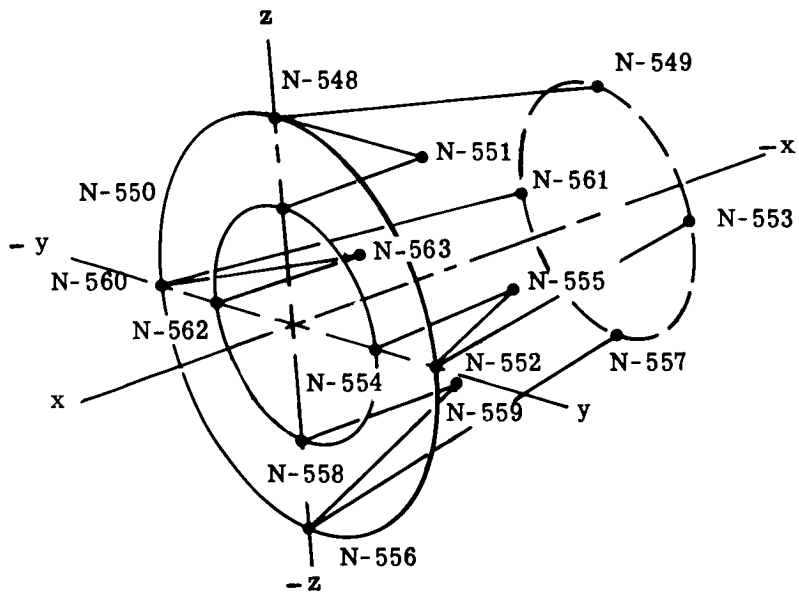


Fig. C.4-33 — Axial truss—nodal network

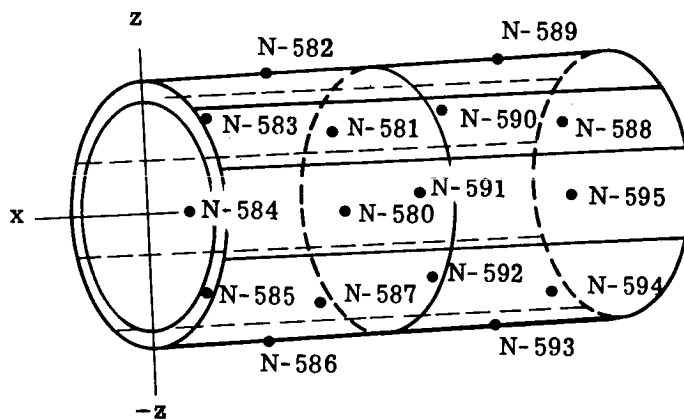


Fig. C.4-34 — Fine guidance housing—nodal network

For analysis purposes, the following camera power dissipations are assumed: 76 watts for 50-millimeter format cameras (f/96 and f/12) and 59 watts for 25-millimeter format cameras. This power is based on the instrument integration time only since the readout is assumed to be negligible (5 minutes) and it includes the best estimate of thermoelectric power for tube cooling.

#### Structural Changes

The current SIP structural concept is not reflected in the thermal model because of the structural concept evolution after the model had been made. The major difference is in the radial bay internal region. The model is based on the prior concept of a cylindrical shell supported between two truss and ring members (see Figs. C.4-32 and C.4-34). The current structural concept has replaced the cylindrical shell with a truss structure [see Section C.2.c(4)].

Relative to the concepts previously discussed and subsequently evaluated, the thermal model results in terms of temperature distributions and heater power are considered valid for the shroud and the insulated structure concepts. However, the validity of the temperature distributions calculated for the constant power output system is somewhat doubtful, but, these doubts can be ignored since this concept is considered the least promising thermal control approach.

#### C.4.1 Results of Thermal Model Studies

##### C.4.1(1) Constant Q System

As indicated above, the temperature distributions determined for this system are questionable. Structural temperatures in excess of 43.3°C (110°F) were calculated. Fig. C.4-35 presents typical temperatures for the constant Q system. The complete temperature distribution for this concept was used as input for a worst-case structural deformation analysis [discussed in Section C.2.c(4)]. Even if these structural temperatures are ignored, this concept is considered to be least promising for a thermal control system owing to the higher power required to maintain a constant thermal power output.

The current estimate for the constant Q system is 660 watts peak power for all cameras.

##### C.4.1(2) Constant T System

The constant temperature system has been examined for both the hot and cold orbital conditions (Fig. C.4-36), representing the extremes in terms of induced thermal gradients and maximum thermal control power, respectively. A camera operational duty cycle was imposed on the model to examine transient thermal effects.

The duty cycle consisted of an initial 24-hour period with no instrument power, followed by 10-hour operation of all three f/96 cameras. The system was then unpowered for 6 hours, following which one of the aft spectrographs was powered for 10 hours.

Typical results of this operation for the enclosed shroud concept, in terms of structural temperature response, are presented in Fig. C.4-36 for the initial and final structural temperatures during the operation of the f/96 camera complement in the hot orbit. The initial temperatures are indicated and the change after the 10-hour operating period is given by the value beneath each. Temperature changes in no case exceeded 0.11°C (0.2°F) during this period. The camera temperatures increased from 13.3°C (56°F) to 40.5°C (105°F) however, they are isolated from the instrument and structure radiationally by the thermal shroud and conductively by a high thermal resistance mounting configuration.

The thermal power required to maintain the thermal shroud at 21.1°C (70°F) is estimated to be 65 watts average. The thermal power requirements are discussed in greater detail elsewhere in this report.

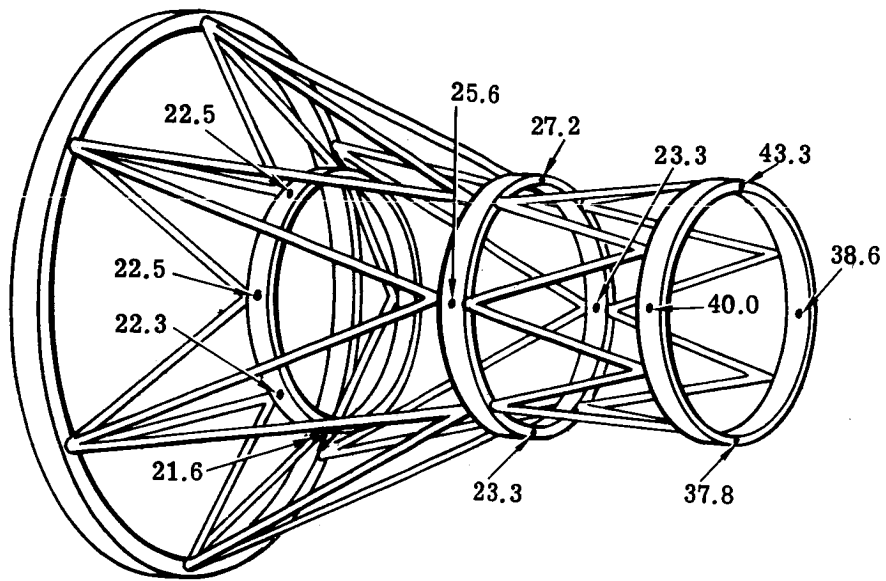


Fig. C.4-35 — SIP temperature distribution — constant Q system

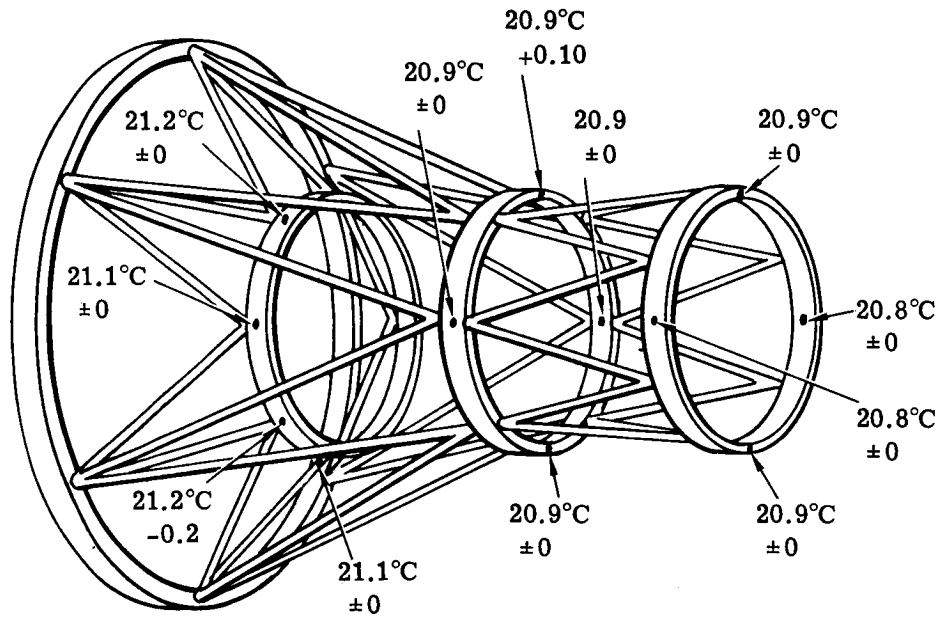


Fig. C.4-36 — SIP temperature distribution — constant T system

### C.4.1(3) Insulated Structure System

The insulated structure system was investigated similarly to the constant temperature system discussed above. The identical duty cycle was imposed on the camera complement. Fig. C.4-37 presents the structural temperatures immediately before and at the termination of f/96 camera operation. Although the temperatures were slightly lower (reflecting the lack of thermal control on the structure), the characteristic change during this period was less than  $0.28^{\circ}\text{C}$  ( $0.5^{\circ}\text{F}$ ). It is interesting to note an axial gradient of approximately  $0.83^{\circ}\text{C}$  ( $1.5^{\circ}\text{F}$ ) from the main mounting ring, owing to the lack of direct thermal control on the structure.

The direct thermal control power to maintain the instrument array at  $21.1^{\circ}\text{C}$  ( $70^{\circ}\text{F}$ ) has been estimated to be 14 watts average.

To illustrate the effects of instrument duty cycle on the cameras and their respective instruments, Table C.4-6 presents the temperature history of the baseline instrument complement during the previously mentioned 50-hour time period. This particular run did not include instrument heaters. The results indicate that the f/96 camera temperature increased to approximately  $46^{\circ}\text{C}$  ( $115^{\circ}\text{F}$ ) during the 10-hour time span. The data also reveal that the cameras were almost at a steady state temperature at this time [temperature increase less than  $0.57^{\circ}\text{C}$  ( $1^{\circ}\text{F}$ ) per hour]. Over the last 16 hours of the run, the cameras cooled down and were within  $1.11^{\circ}\text{C}$  ( $2^{\circ}\text{F}$ ) of their initial temperature.

The secondary effects on the other cameras within the system after the release of 2,780 watt-hours of power within the SIP are of note: all cameras increased in temperature, with the greatest effects appearing at the three aft-mounted cameras closest to the f/96 array.

A comparison of the results of this study with those of the camera cooling study indicates that the cameras operate significantly cooler than predicted. This is partly the result of sink temperatures below the  $21.1^{\circ}\text{C}$  ( $70^{\circ}\text{F}$ ) postulated in the camera cooling study. It is also the result of using a lower power consumption estimate for the thermal model cameras. This lower dissipation is based on discussions with a thermoelectric module manufacturer wherein it was determined that module efficiency of 20 percent was attainable for present applications. For this analysis, an efficiency of 16 percent was used.

### C.4.1(4) Discussion of Results

It is recommended that the SIP thermal control system be studied further because both the thermal shroud and the insulated structure concepts are thermally feasible, offer reasonably positive control of structural temperatures, and are currently compatible with the laminar airflow requirement.

The outstanding problems presented by the shroud concept are the following. (1) The maintenance difficulties resulting from surrounding the truss up to the primary ring with an additional fixed structure enclosing the instrument complement are increased (probably solvable by design of a multipanel shroud with suitable removable access ports). (2) Heat rejection requirements for the f/12 camera (in its present location) require more detailed design and analysis. This problem must be resolved in concert with the design of the thermal shroud.

2. Heat rejection requirements for the f/12 camera (in its present location) require more detailed design and analysis. This problem must be resolved in concert with the design of the thermal shroud.

The insulated structure concept also is feasible, but with greatly improved instrumented service access. As such, it provides an alternate that appears viable with an ultralow expansion structure (graphite-epoxy composite), although it does not provide direct thermal control.

In the process of evaluating and reviewing the thermal model data, it was observed that the predicted thermal control power for the recommended baseline concept was much lower than expected. A review of the model revealed a major heat leak from the main support ring to the pressure shell wall, which caused it to run warm.

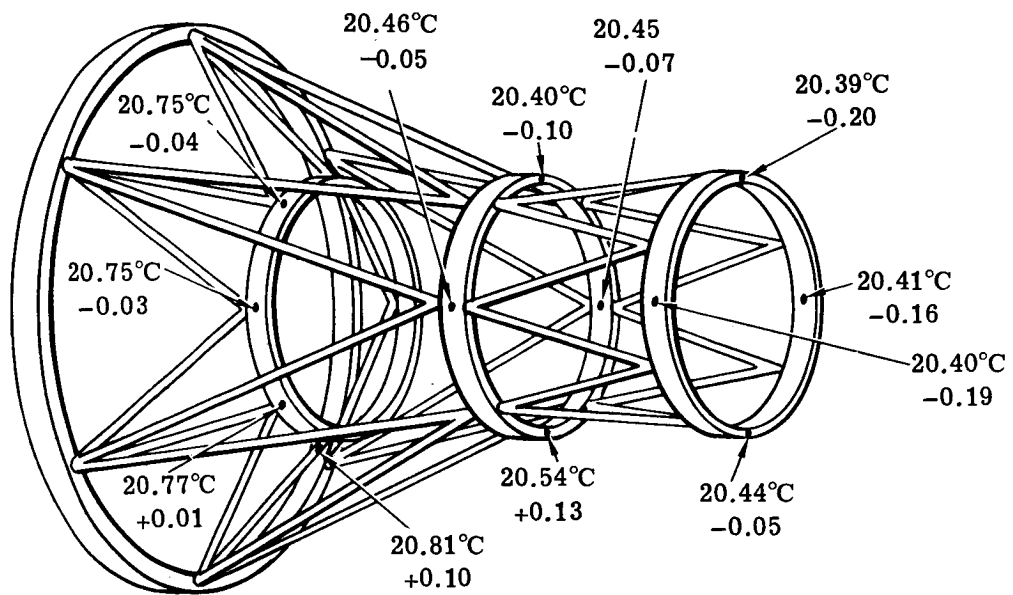


Fig. C.4-37 — SIP temperature distribution —insulated structure

Table C.4-6 – Transient Camera and Instrument Temperature Distribution –  
Insulated Truss Concept

Node	Temperature							
	24 hours		34 hours		40 hours		50 hours	
	°C	°F	°C	°F	°C	°F	°C	°F
596	20.0	68.1	19.7	67.4	19.6	67.3	19.4	66.9
597	13.4	56.2	16.8	62.2	16.1	61.0	15.6	60.0
601	20.0	68.1	19.7	67.4	19.6	67.2	20.4	68.8
602	13.4	56.1	15.7	60.3	15.7	60.2	34.4	93.9
606	16.6	61.9	45.2	113.3	21.6	70.8	17.6	63.7
607	16.8	62.1	46.2	115.1	22.0	71.7	17.7	63.9
608	16.8	62.1	45.4	113.8	21.7	71.1	17.8	64.0
609	20.7	69.3	21.5	70.7	21.7	71.1	21.6	70.8
614	21.0	69.9	21.0	69.9	21.0	69.9	21.0	69.8
616	20.3	68.5	20.2	68.3	20.1	68.2	19.9	67.8
617	13.4	56.2	17.2	63.0	16.3	61.4	15.6	60.0
620	17.6	63.5	18.0	64.5	18.3	64.9	18.0	64.4
621	20.6	69.0	20.3	68.6	20.2	68.4	20.0	68.1
622	17.4	63.4	18.0	64.3	18.2	64.7	18.0	64.3
623	20.6	69.1	20.3	68.5	20.2	68.4	20.0	68.0
625	16.8	62.3	17.8	64.0	18.0	64.4	17.8	64.0
626	20.6	69.1	20.4	68.7	20.3	68.6	20.3	68.5



Examination of the structural design indicates this is because the pressure shell wall is hard-mounted to the main ring for load carrying purposes. The magnitude of the leak is indicated in Table C.4-7, which summarizes the direct as well as the secondary thermal power requirements for the system. If the leak is reduced (say by increasing the thermal resistance to the shell), the direct thermal power required for maintaining the shroud at 21.1°C (70°F) will be increased and the net power reduction will be minimal. Using the insulated structure, reduction of the thermal leak will reduce the wall temperature and decrease the floating structural temperatures accordingly. This area should be given careful study as soon as possible since it impacts on the overall design.

#### C.4.m Thermal Control Power

The thermal control power required to maintain the OTA and instrument compartments at the required temperature levels has been determined during the course of the analytical studies described previously. The results of this power study are summarized in Table C.4-7, which also indicates the parameters assumed for the GSFC scientific instrument compliment. Also included in this table is an estimate of power required for a system cooling only the visible-spectrum sensors.

These power values clearly indicate the impact of the various SIP thermal control schemes on the direct thermal control power in the instrument compartment and on the main support ring thermal control power (due to the high thermal coupling with the SSM walls).

#### C.4.n Summary of Results

The results of the thermal studies conducted in this program can be categorized for the OTA and instrument compartment separately as follows.

1. We have developed for the OTA a realistic thermal control concept that meets all current system requirements. It is recommended that (a) future work be directed toward optimizing the thermal control coating to reduce thermal power further and (b) transient thermal reactions induced by telescope orientation changes be studied in greater depth to define the limitations associated with focus and alignment maintenance after the maneuvers.

2. We have investigated several thermal control concepts for the SIP structure and instruments and have found them all to be conceptually feasible. It is recommended that these studies be continued, with the goal of reducing thermal control power without impacting system performance while simplifying interfaces with the SIP and OTA. It is clear from these studies that the maintenance implications in the instrument compartment play a key determining role in the choice of the thermal control system.

Table C.4.7 – Thermal Control Power

	Constant Temperature System	Constant Q System (all cameras cooled)	Insulated Truss System	Constant Q System (3 cameras cooled)
Optics	81	81	81	81
Thermal shroud	65	0	0	0
Instrument heaters	0	0	14	0
Constant power sources	0	660	0	308
Main support ring	368	0	178	18+
Thermoelectric coolers	150	0	150	0
Total thermal power (watts)	664	741	423	407+

Scientific Instrument Parameters

Camera Compliment

- 4 – 50 x 50-millimeter tubes
- 6 – 25 x 25-millimeter tubes

Operating Power

- 50 millimeters 26 watts
- 25 millimeters 9 watts

Thermoelectric Cooling Power

- 50 watts each (Cambion Inc.)

Cooled Cameras (Minimum)

- f/96 0.45 to 1.1 micrometers
- F.O. spectrum 0.35 to 0.66 micrometer
- F.O. spectrum 0.66 to 1.0 micrometer

## C.5 STABILIZATION AND CONTROL DESIGN

The stabilization and control system of the LST is one of the two principal systems directly affecting the optical performance of the telescope, the other being the optics.

The NASA Bluebook gave as a design goal a line-of-sight stabilization capability of 0.024 microradian. Subsequent work indicated that this, interpreted to be the rms value during an observation, is a worthwhile goal, especially for ultraviolet imagery, where motion much in excess of this value begins to eat into the inherent capability of the optics.

During the study program, NASA Headquarters Astronomy Committee directed that the final image seen by the high resolution cameras have a means for structural drift compensation during long time exposures. Additionally, a means must be provided for positioning a fine spectrograph slit to at least 0.12 microradian (0.025 arc-second) with respect to any specific astronomical feature.

It is expected that net image integration times up to 10 hours in length may be required. This means that the system must have a capability to maintain stabilization up to 40 hours, since the 10-hour integration time must be accumulated by fractions of an orbit.

Whether or not spectroscopy requires the same stabilization as does imagery has not yet been determined. Generally speaking, however, it would appear that pointing correctly is critical to spectroscopy, whereas stabilization is critical to imagery. Table C.5-1 summarizes the requirements.

To stabilize the line of sight, the telescope is locked onto two guide stars near the target object. The two guide stars are chosen so that they can be imaged within the field of view of the telescope along with the data object. They must be spaced relative to each other and the target object to provide pitch, yaw, and roll guiding information through fine guidance sensors located in the vicinity of the focal plane. Line-of-sight motion can occur in a number of different forms from many different causes. The telescope can move as one rigid body; flexing of the structure can cause relative motions between the primary mirror, the secondary mirror, fold mirrors and relays, and the fine guidance and scientific data sensors.

Preliminary data indicate that the vehicle pointing actuators can be expected to introduce larger disturbances to the line of sight than the gravity gradient and other orbital disturbances. Hence, higher control bandwidths are needed than would be required to stabilize in the presence of the orbital disturbances alone. Temperature changes within the structure and the mirrors will produce very significant motions during the course of a long observation period. Therefore, it is essential that the guide sensors and the scientific data sensors be mechanically and optically linked together as closely as possible so that closed loop control of the line of sight between the guide stars and the guide sensors guarantees line-of-sight stability to the data object as well.

The major features of the reference design for the stabilization and control system are shown in Fig. C.5-1. The heart of the focal plane guidance sensor, from which the guide signals are derived, is a reticle grating at the focal plane on a dimensionally stable, fused-quartz substrate. The guide signals are generated at this grating by a division of the light in the guide star image. The field of view for the high resolution cameras, which is relayed to a larger magnification, is linked through the relay to the guide sensor grating by means of fiducials (artificial stars) on the grating and sensors at the high resolution image tubes. The slits for the high resolution spectrographs are placed close to the grating and linked mechanically by a rugged, box-shaped structure holding both the grating and the slit assembly.

The error signals from the focal plane guidance sensors are used to control the fine positioning of the secondary mirror over a very small range. Through this loop, the line of sight can be corrected at higher frequencies than is possible in pointing of the spacecraft as a whole. Thus, fine trimming of the spacecraft pointing is achieved through control of the secondary mirror.

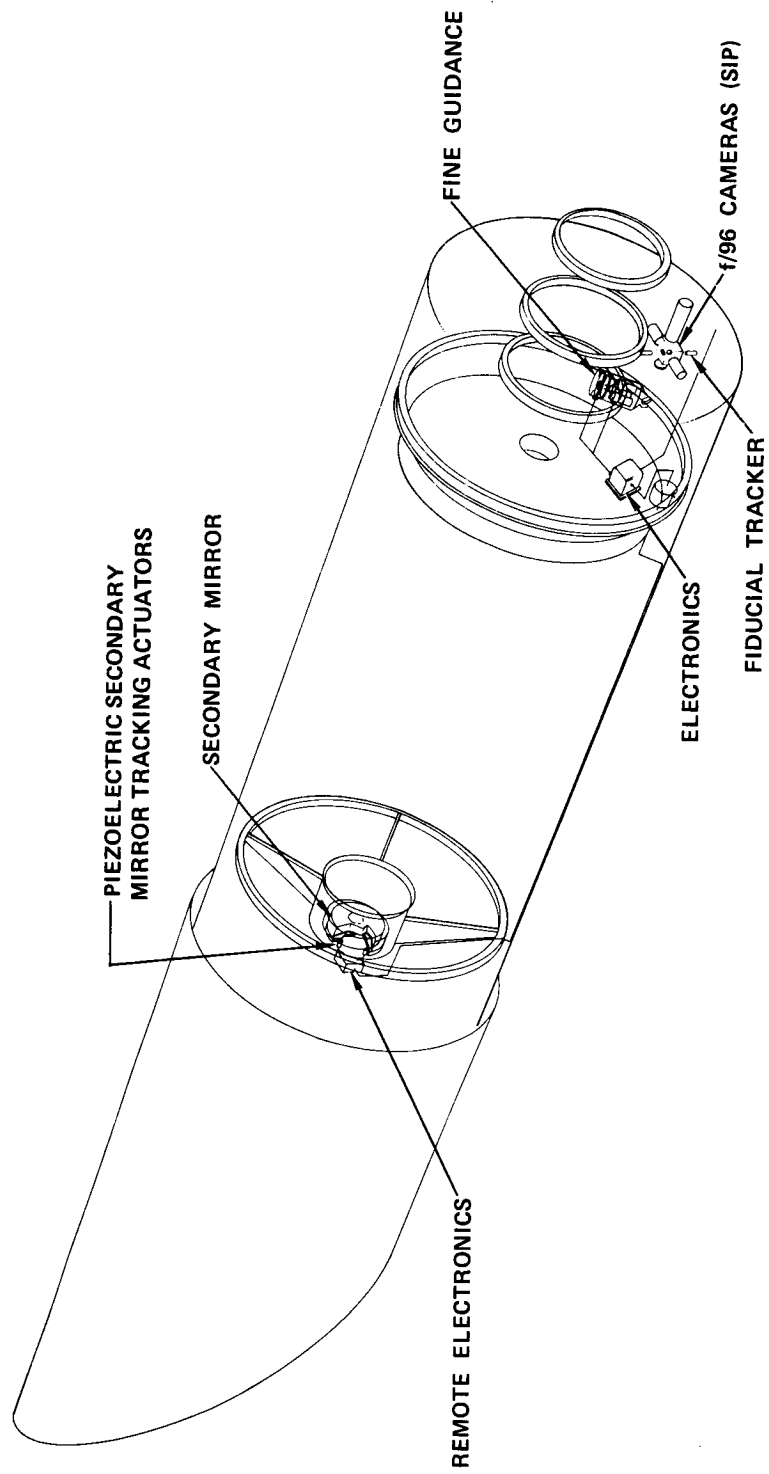


Fig. C.5-1 — OTA pointing control system

Table C.5-1 – OTA Pointing and Stabilization Requirements

	Imagery	Spectroscopy
Longest observation period	40 hours (10 hours net)	40 hours (10 hours net)
Pointing	±5 microradians	±0.12 microradian
Stabilization	~0.024 microradian rms	Not defined

The remainder of this section includes more detailed explanation of the reference design, including:

1. A discussion of the overall pointing and stabilization requirements, including the allocation of errors to different major classes of line-of-sight disturbance and the interaction between various sensors and actuators in bringing the line of sight to the desired portion of the sky (Discussion of Requirements).

2. The rationale for the reference design (Configuration of a High Stability System).

3. Design of the focal plane guidance sensor, including calculations of the guide field area requirements, tradeoffs made in the course of the design, a detailed description of the focal plane guidance sensor of the reference system and how it operates, and descriptions of the parameter choices and the expected performance. (Design of the Focal Plane Guidance Sensor).

4. Design of the secondary mirror control system, including basic considerations leading to the use of the secondary mirror for fine guidance, the design of the actuator system, the tie-in with the focal plane guidance sensor, the control dynamics of the system, and a description of a one-dimensional computer simulation of the fine guidance of the telescope. This simulation included modeling of the spacecraft and telescope structure, the servo control characteristics, important noise sources within the fine guidance sensor and the mirror actuator system, and the nonlinear gain function of the fine guidance sensor (Design of the Secondary Mirror Control System).

5. Error budgets for the fine guidance system within the OTA and for the dimensional stability of the telescope during an observation from the point of view of the image motion requirements (Error Budgets).

The analysis indicates that, with the focal plane guidance sensor of the reference design, the photoelectron noise in the error signal (the major noise source in the fine guidance control system within the telescope itself) will be on the order of 0.0055 microradian rms or less for more than 90 percent of potential target locations in the sky. By virtue of the configuration chosen, the residual effects of dimensional changes within the structure are of second order and the implied thermal stability requirements are very much in line with the requirements for maintaining optical alignment. Actuation of the secondary mirror to provide compensation for residual errors in the spacecraft stabilization gives a significant boost to the available closed-loop bandwidth for the overall stabilization system, and a simulation using input disturbances expected from the attitude control actuators indicated that the attainable 4-hertz equivalent noise bandwidth would be adequate for stabilization. Finally, preliminary study at Itek\* and other studies have indicated that, in the reference design concept, vibrational levels in the structure can be kept to a tolerable level, from the point of view of line-of-sight motion, by the use of nonexotic isolators at the sources of vibration, principally the control moment gyros.

---

\*Large Space Telescope System Definition Study (RAM Concept), Optical Telescope Assembly (OTA), Itek 72-8209-1, 10 Feb 1972, p. IIB-158 ff.

### C.5.a Discussion of Requirements

The image stabilization goal is 0.024 microradian rms. An initial allocation of this error was made by giving equal portions to the SSM and the OTA. Within the SSM, it is suggested that equal portions of the error should be allocated to low-frequency, rigid-body disturbances to attitude and to high-frequency, vibrational disturbances causing relative motions between the optical components. Within the OTA, an equal-portion allocation has been made to the generation of the guide signal and the low-frequency dimensional stability of the structure. This equipartition of the stabilization error into four classes is shown graphically in Table C.5-2.

It is assumed that the vehicle attitude control system can stabilize the vehicle, using input from the fine guidance sensor, to within 5 microradians, the limit of accommodation of the secondary mirror fine stabilization system. An additional, but extremely important, constraint upon the vehicle system is that the vehicle motions, after being corrected by the secondary mirror system, do not leave excessive errors in the line-of-sight stabilization. The secondary mirror system is limited in its ability to correct the line of sight because of its bandwidth.

Because of the separation of bandwidths of the spacecraft attitude control system and the secondary mirror control system, the two control loops can be closely represented in a cascaded form in which the secondary mirror control system filters the residual error from the vehicle actuator control system. The vehicle stabilization requirements are that the vehicle be stabilized to within  $\pm 5$  microradians (the range of accommodation of the secondary mirror) and, furthermore, that the residual error, after filtering by the secondary mirror function, not exceed 0.012 microradian rms. The cascaded representation of the two control loops and the effective filtering function of the secondary mirror control system are shown in Fig. C.5-2. (Fig. C.5-42, later in the text, gives a more accurate representation of the interaction of the two loops.)

Fig. C.5-3 summarizes the ranges for the different components and the points of handoff between components. To some extent, the vehicle actuators must stabilize the vehicle to the full stabilization requirement in that disturbances with frequency content that cannot be measured and corrected by the focal plane sensor/secondary mirror system must not be permitted. The outboard star tracker must point the vehicle within the search field of view of the focal plane sensor. The coarse acquisition mode of this sensor must then bring the line of sight within the range of a specific line crossing on the reticle. The photon counting mode of this sensor provides nonlinear acquisition information to the point of aligning the star image on a peak of the grating, at which point the function becomes linear and useful in fine stabilization. The optical micrometer (described in more detail in a later portion of the text) can be used for pointing the telescope to increments finer than permitted by the grating alone and to extend the linear range of the stabilization mode of the focal plane sensor.

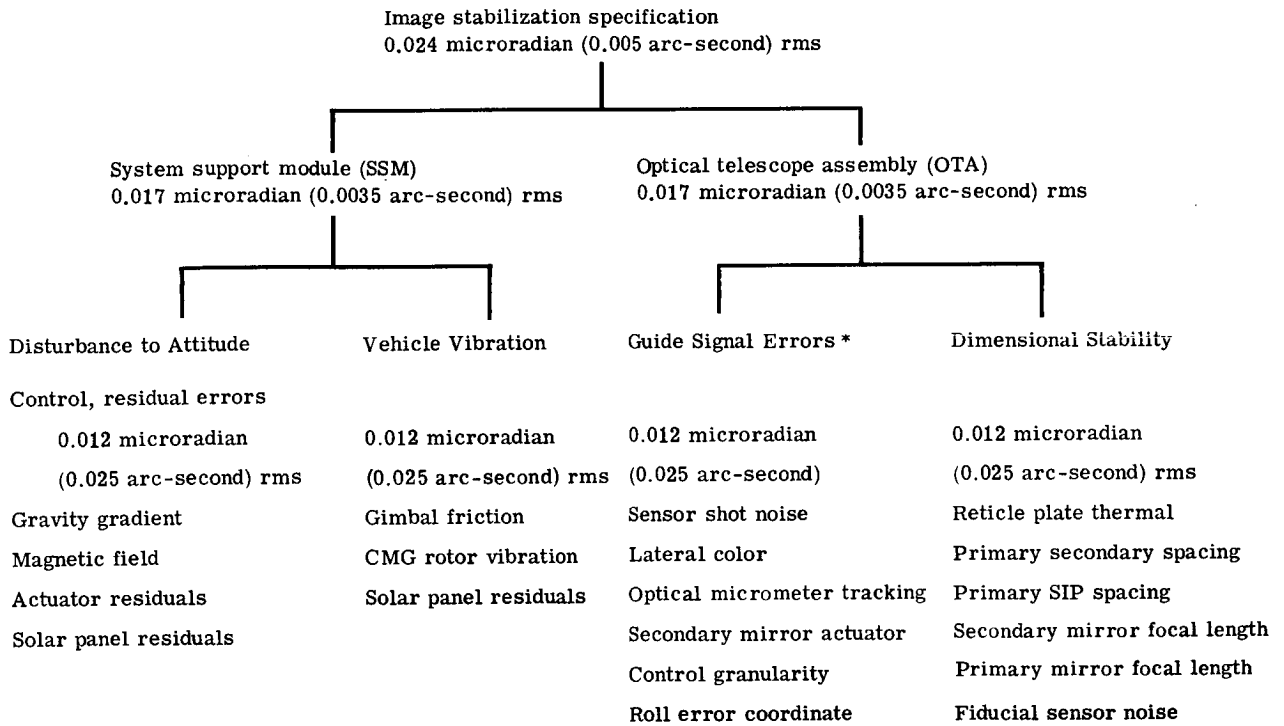
### C.5.b Configuration of a High-Stability System

The major components of the pointing control system (shown in greater detail in Fig. C.5-4) are the guide sensor assembly, which generates fine guidance signals, and the secondary mirror actuation system for line-of-sight stabilization, which compensates minor errors of the system support module (SSM) attitude control system. In addition, the OTA structure carries the electromagnets of the SSM momentum dumping system (see Fig. C.5-5). In conjunction with sensors near the high resolution cameras of the scientific instrument package (SIP), artificial stars within the guide sensor assembly provide the pointing control system with signals that indicate the line-of-sight error caused by structural deflection within the SIP during an observation.

The system shown is a high stability configuration devised to overcome the basic problems to be solved by the fine pointing control system: the limited stabilization ability of the vehicle's attitude control system and the dimensional instability within the optical structure. The following is a qualitative explanation of the system. Ranges, accuracies, and design data for the various components and the system as a whole are given in later sections.

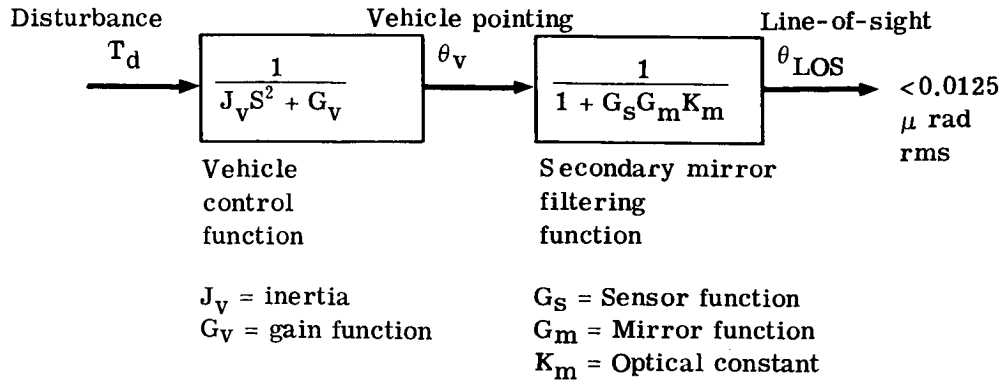
The telescope uses two guide stars adjacent to the data object for generation of attitude control signals. The guide signals from the guide star sensors provide commands to the vehicle stabilization system. Since the vehicle's attitude control system may be limited in its ability to stabilize the vehicle line of sight to the required tolerance [0.024 microradian (0.005 arc-second) rms total], the guide sensors also furnish commands to actuators that support the secondary mirror, and the secondary mirror is tipped to compensate for the slight errors in the vehicle

Table C.5-2 – Image Stabilization Error Budget



\*Based on 2 hertz control gain crossover frequency

### Cascaded Representation



### Secondary Mirror Filtering Function

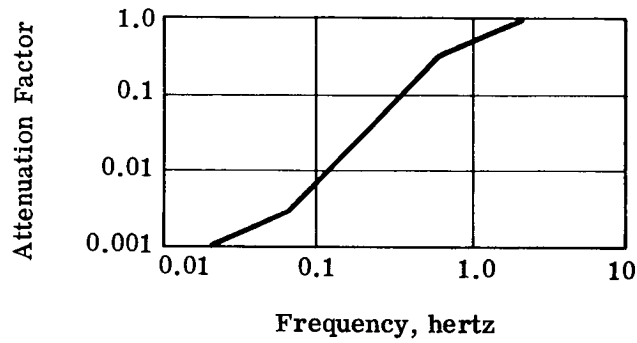


Fig. C.5-2 — Cascaded representation of vehicle and secondary mirror control loops

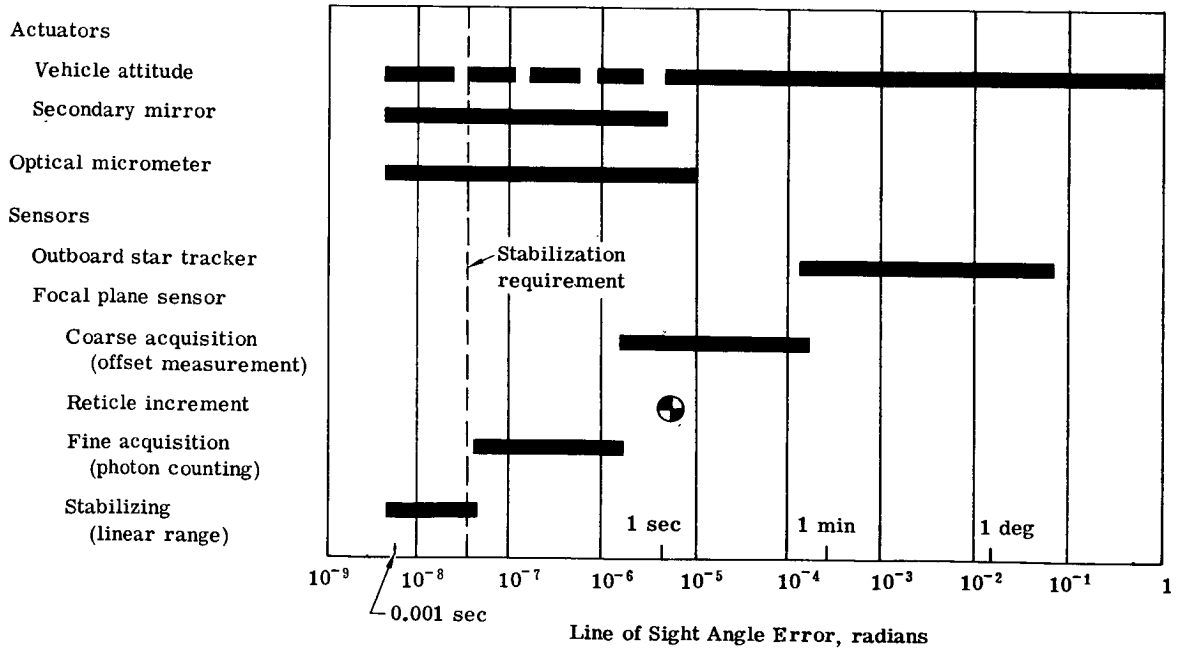


Fig. C.5-3 — Accommodation ranges for various components of the pointing and stabilization system



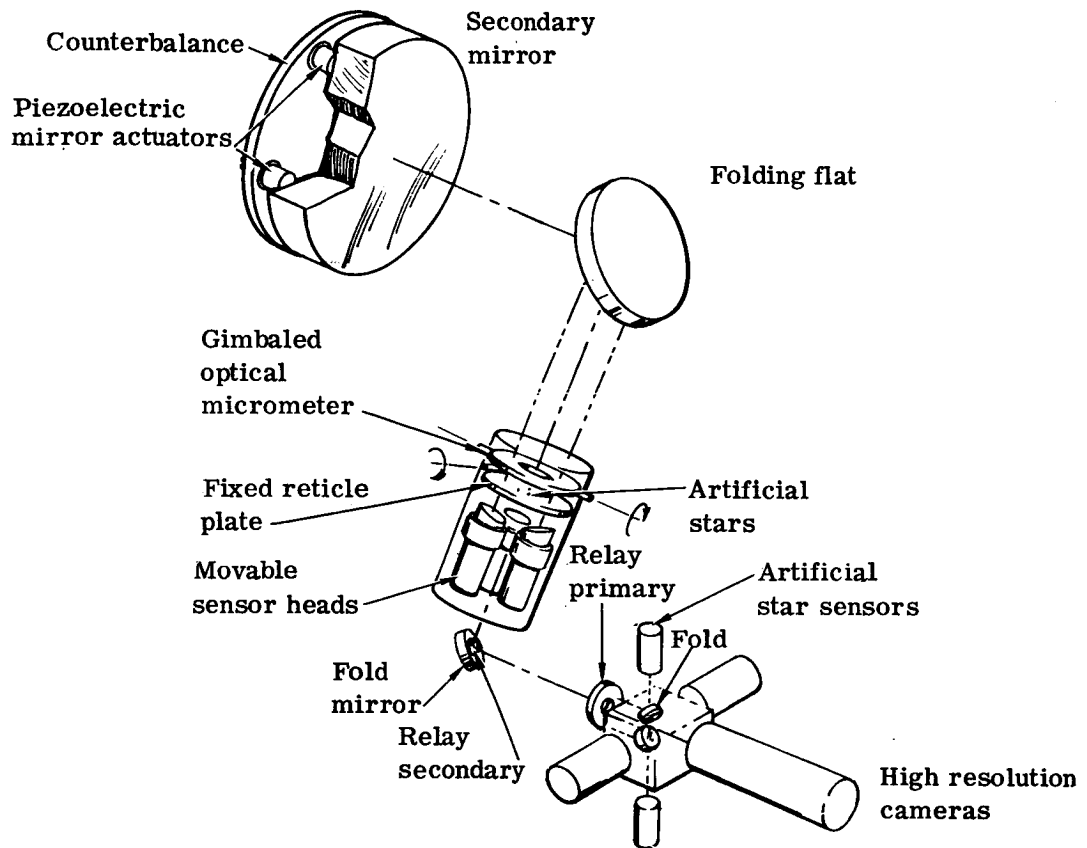


Fig. C.5-4 - Pointing control system

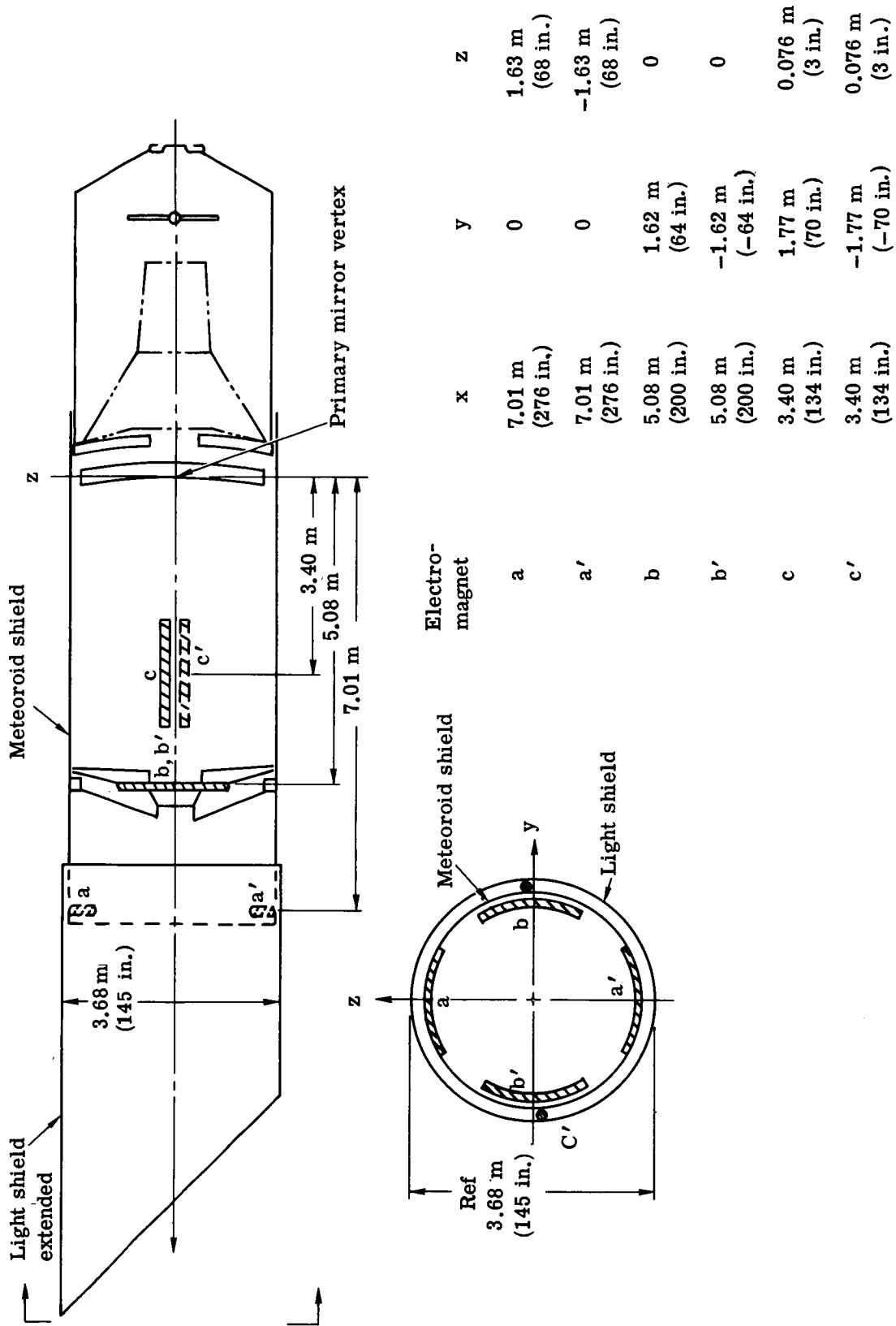


Fig. C.5-5 — Proposed location of electromagnets

attitude. As light to both the guide stars and the data star is deflected equally by the tipping of the secondary mirror, control of the secondary mirror provides closed loop stabilization of the line of sight to the data star at a higher bandwidth than is possible with the vehicle attitude control system alone.

To ensure that a structural resonance in the secondary mirror support structure does not create a servo stability problem, actuators at the secondary mirror also drive a counterbalance in a direction opposite the tip of the secondary mirror so that, in effect, the forces and moments required to tip the mirror come not from the support structure but from the counterbalance.

As a general design principle, the optics for the high resolution imaging camera should be shared as much as possible with the guide sensors that control the attitude so that internal deflections within the optical path produce the same effect on both the data field and the guide field. It is not practical, however, to place the guidance sensors at the  $f/96$  image plane with its limited field coverage because of the relatively large field required for the guide sensor system. As a compromise, the guide field is placed at the  $f/12$  Cassegrain focus, while the high resolution imaging field is relayed to the  $f/96$  focus. Optics common to both fields are the primary, secondary, and fold mirrors. Other features of the system configuration are designed to offset the effects of this compromise.

The heart of the guide sensor is a reticle plate at the  $f/12$  focus. The guide signal is generated optically at the reticle plate, which is made of a fused silica substrate having a very low thermal coefficient of expansion

The high resolution imagery field passes through a hole in the center of the reticle plate. At the edges of the hole are artificial star sources at the  $f/12$  focal plane. The  $f/12$  image of the high resolution imagery field is reimaged at  $f/96$  by the  $f/96$  relay, which also images the artificial stars at  $f/96$ . Sensors at the  $f/96$  plane detect apparent motions of the artificial stars caused by structural deflections that affect the relaying of the image to the  $f/96$  plane.

An apparent movement of the artificial stars can be compensated by introducing an offset between the guide field and the high resolution imagery field by means of the optical micrometer. This device is a plane-parallel glass plate that is placed in the optical path just ahead of the reticle plate and is large enough to cover the entire guide field. It is mounted on gimbals so that it can be tipped slightly. The high resolution imagery field passes through a hole in the center of the optical micrometer so that only the guide field is affected by tipping of the plate. Although this plate is an optical element not common to both the guide field and data field, its positioning is not too critical, since the plate is designed to introduce at most a relatively small differential motion of the two fields.

The optical micrometer is used also to compensate for the differential velocity aberration effects between the guide stars and the data star that are caused by acceleration of the telescope with respect to the stars. It is also used to interpolate between the reticle lines on the reticle plate; otherwise the telescope would be limited to pointing at discrete positions. A further use of the optical micrometer is to compensate for parallax motion between a planet under study and the guide stars being used.

The diffraction-limited field of view of the Ritchey-Chretien system is quite small. It is not large enough to accommodate the guide field without additional correction. The predominant aberration in the guide field is astigmatism, which causes the guide star to be imaged as perpendicular lines at separate (sagittal and tangential) focal planes. It is desirable to avoid optical elements with power ahead of the focal plane, since such elements would not be common to both the data guide field and the high resolution imagery field (such elements would block ultraviolet light were they placed in the data field). Deflection of the structure holding these elements would cause unknown differential motions between the guide field and the data field.

The reticle consists of prismatic grooves on the reticle plate that divide the light of the star image according to the exact location of the image on the groove. The different parts of the divided beam are sent to a differential sensor that then determines the pointing error. Compensation for astigmatism is accomplished by using a radial-circumferential groove reticle pattern. The surface containing the radial grooves is actually separated from the surface containing the circumferential grooves by the separation distance between the tangential and sagittal focal surfaces. At the same time, curvature of the image field is accommodated by curving the surfaces that carry the reticle grooves to conform to the curved focal surfaces. The astigmatism-compensating prismatic grating is illustrated in Fig. C.5-6.

Because of the discrete spacing of the reticle lines, the first of two guide stars will be centered on both a radial and a circumferential groove. However, the second star can be centered only on either a radial or a circumferential groove, but not on both. Yaw and pitch information will thus come predominantly from the first star, whereas roll information will be provided by the second star. One's first inclination would be to control the secondary mirror, keep the first star at its null position, and to supply roll signals to the vehicle from the second star. In the presence of a roll error, however, the data star image would then be offset from the desired position. Therefore, to minimize the motions of the data star image, the secondary mirror system will be commanded to null the radial position of the first (yaw and pitch) star image and to equalize the circumferential errors of the images of the two guide stars. This is illustrated in Fig. C.5-7.

The high resolution spectrographs do not have access to the artificial stars in the reticle plate. To ensure a stable relationship between the reticle plate and the spectrographs, the reticle plate, its fold mirror, and the spectrograph slit assembly (which is the critical component of the spectrographs relative to image stability) are attached to an Invar box (Fig. C.5-8) to form the core of the instrument package structure. The rigidity of this box makes it possible to keep a star image centered on a very narrow spectrograph slit without necessitating unrealistically tight temperature control. Should temperature changes of the supporting structure cause the box as a whole to move during an observation, no relative image motion will be introduced between the slit and the reticle. unrealistically tight temperature control. The concept shown illustrates the most desirable arrangement from a stability viewpoint. A later, slightly different version is shown in Fig. A.1-1. Should temperature changes of the supporting structure cause the box as a whole to move during an observation, no relative image motion will be introduced between the slit and the reticle.

### C.5.c Design of the Focal Plane Guidance Sensor

Several aspects of the design of the focal plane guidance sensor were considered in some detail during the course of the study. A careful analysis was made to determine realistic requirements of the size of the guide field needed to provide sufficiently high acquisition probability for targets in any part of the sky. A tracker design tradeoff was made in which a number of different designs were very seriously considered. An initial configuration of the chosen basic concept was generated for the LST application, critical parameters were chosen, and the performance in the fine guidance mode was predicted by analysis. Finally, the logic was worked out for the use of the guidance sensors in acquisition, coarse mode pointing, and fine mode guiding. Each of these topics is discussed in detail in this section.

#### C.5.c(1) Guide Field Area Requirements\*

It became evident during the course of this study that the instrumentation configuration would suffer from an oversized guide field, necessitating a determination of its maximum permissible area.

The key to minimizing the guide field area required is to use a star tracker system with a maximum sensitivity so that the dimmer, more abundant stars can be used for guiding. It is imperative that the trackers operate on a near-diffraction-limited image and use the most sensitive detectors available, i.e., photomultipliers. Fig. C.5-9 shows the equivalent object space noise angle for the optical system/sensor combination proposed as a function of visual stellar magnitude and bandwidth. Derivation of this function is given elsewhere. The OTA/SSM interface provides that the sensors will be used in a 4-hz noise bandwidth system, so that the 4-hz curve from Fig. C.5-9 applies.

Fig. C.5-10 gives the cumulative star density (inverse) as a function of visual stellar magnitude. †

In the visual magnitude system, stars are about twice as numerous as in the photographic magnitude system for the same numerical magnitude value, which was taken into account in plotting the data. For example, the graph shows that for stars of visual magnitude 16 or brighter, there will be, on the average, one star for every  $8.5 \times 10^{-6}$  steradian (10 square arc-minutes) of sky in the region of the galactic pole.

---

\*The work reported here is described in detail in "Guide Field Requirements of the LST," LST-72-62.

†Allen, C.W., *Astrophysical Quantities* (The Athlone Press, University of London, 1955), 2nd edition, p. 234.

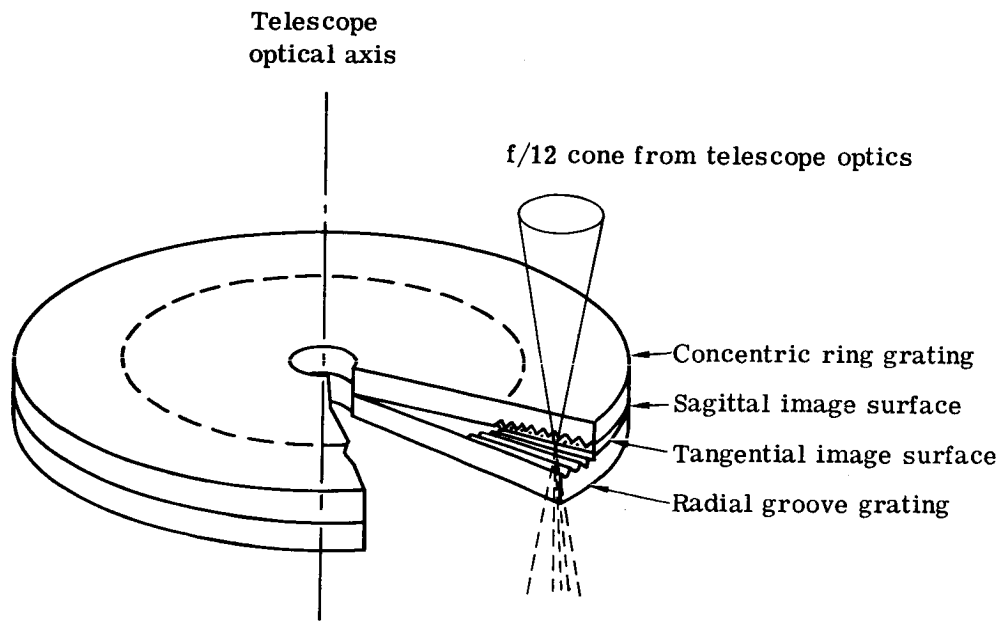


Fig. C.5-6 — Astigmatism-compensating prismatic grating

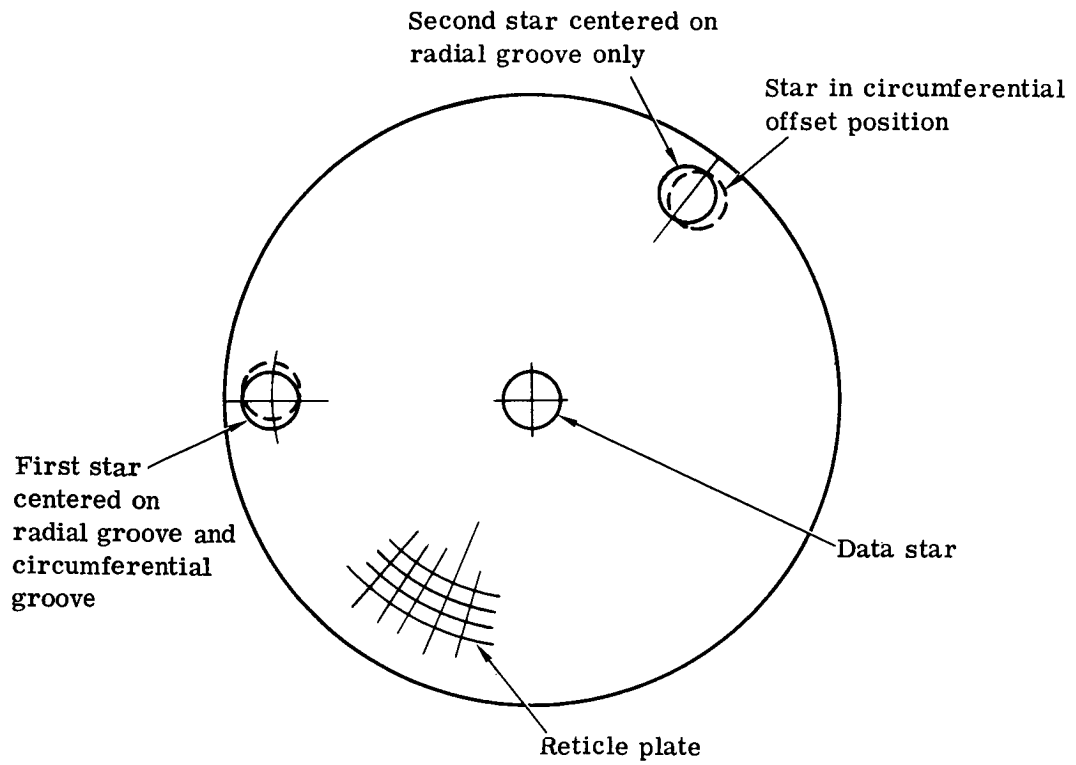


Fig. C.5-7 — Use of reticle plate in generating attitude control signals

The concept shown illustrates the most desirable arrangement from a stability viewpoint. A later, slightly different, version is shown in Fig. A.1-1.

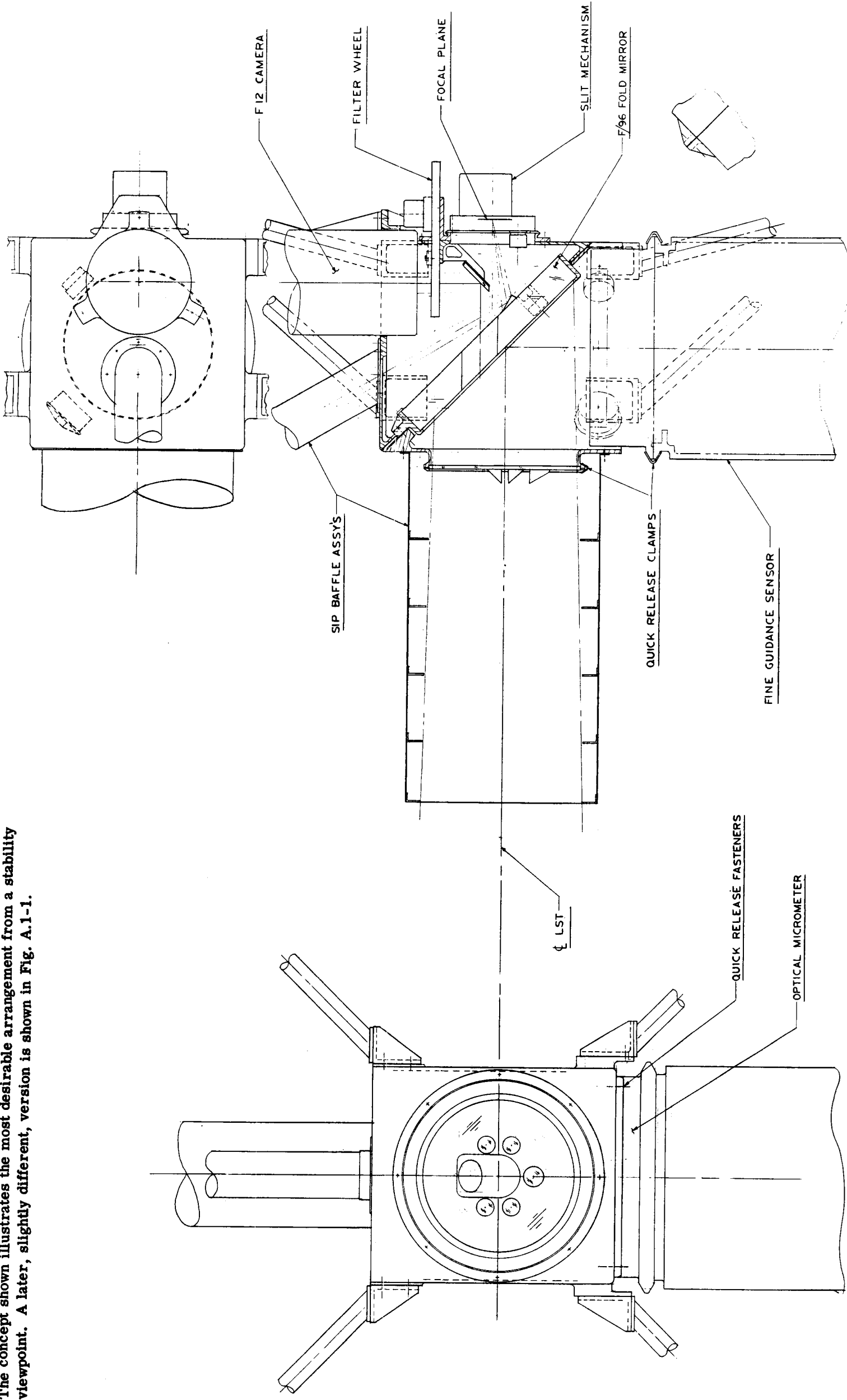
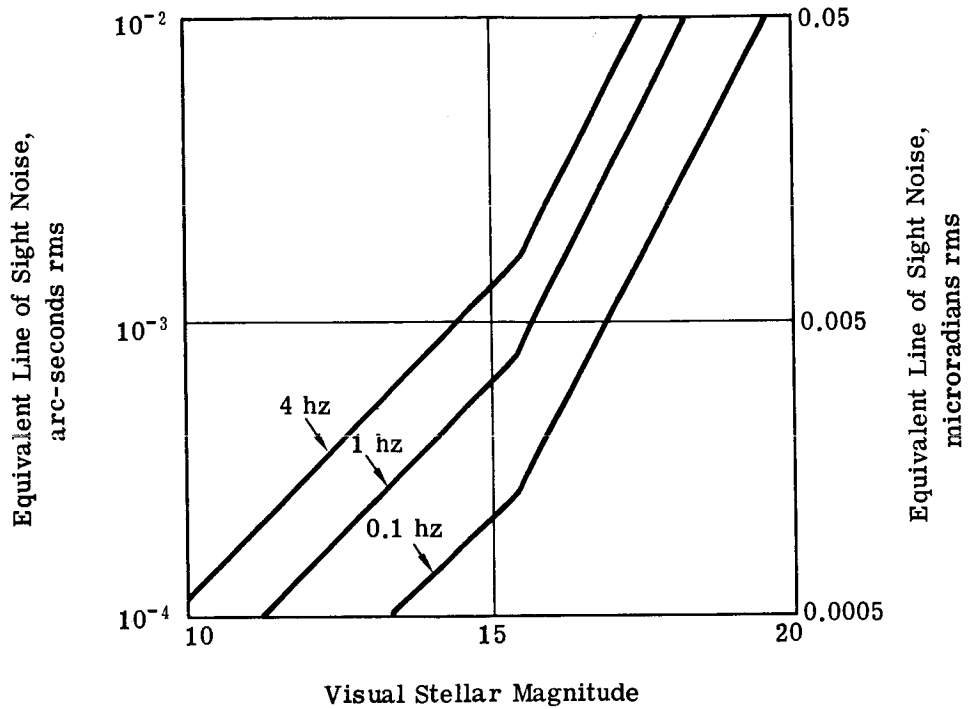


Fig. C.5-8 — Fold optics layout (dwg. no. 185514)



3-meter aperture  
 30 percent obscuration  
 $0.1\lambda$  WFE (633 nm)  
 40 percent optical transmission  
 G3 target star  
 S-20 photocathode (200  $\mu$ amp/lumen)  
 60 percent multiplier counting efficiency  
 30 percent/0.1 microradian optical energy transfer function  
 2-millimeter dissector aperture

Fig. C.5-9 — Photoelectron noise limit to fine guiding, at several bandwidths



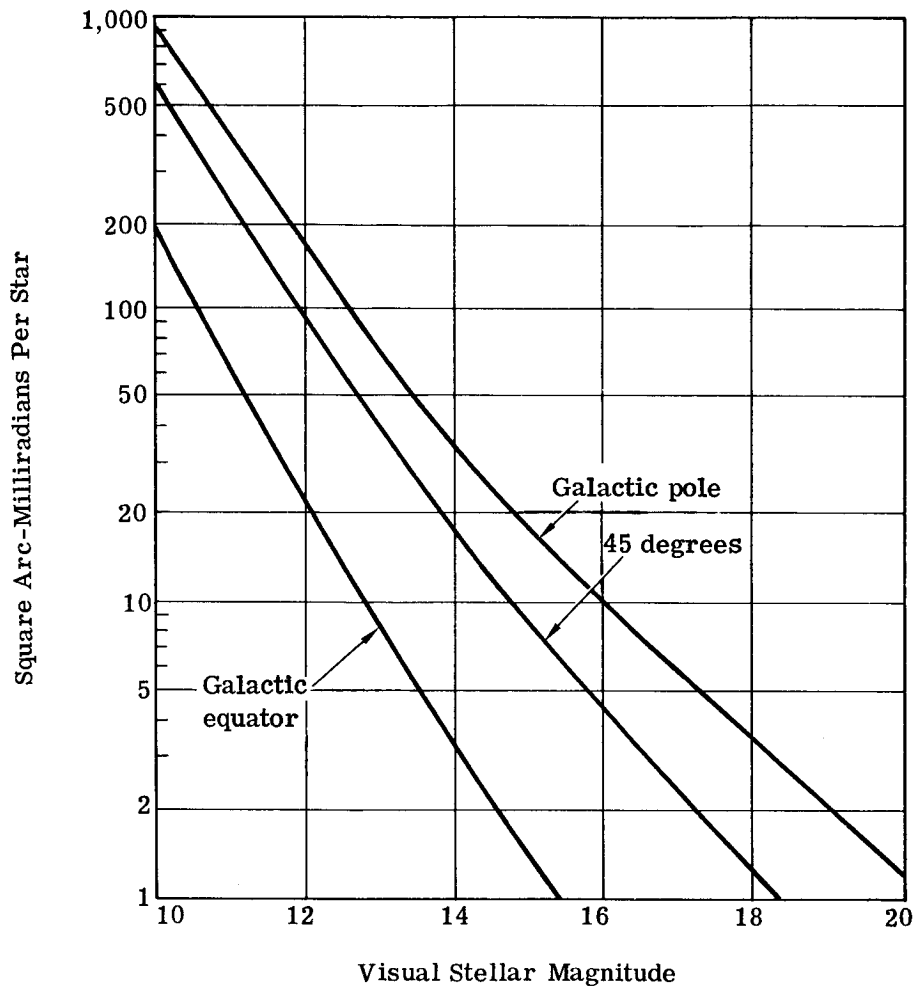


Fig. C.5-10 — Cumulative star density as a function of visual stellar magnitude

The Poisson distribution for discrete events applies to the data of Fig. C.5-10 to determine acquisition probability as a function of guide field area. The probability of finding  $n$  stars in a given area is

$$P(n) = \frac{N^n}{n!} e^{-N}$$

where  $N$  is the average number of stars in an area of the size of the guide field (from Fig. C.5-10). The probability of not finding any stars is

$$P(<1) = P(0) = e^{-N}$$

The probability of not finding two or more stars is

$$P(<2) = P(0) + P(1) = (1 + N)e^{-N}$$

Future study may show that roll control of the spacecraft is such that one guide star is sufficient. However, it is presently assumed that two stars with a certain degree of separation are required to provide yaw, pitch, and roll information. Analysis has shown that as the angular separation between the guide star images in the focal plane becomes less than  $\pi/2$  radians (90 degrees), the roll information accuracy quickly degenerates. Therefore, the criterion has been used that an acceptable second star must lie at least  $\pi/2$  radians away from the first star in the image plane, as is illustrated in Fig. C.5-11.

In the more general case, two stars must be separated by a certain distance to be usable. If one of the  $n$  stars found in a particular location is selected for the first sensor, at least one of the  $n-1$  remaining stars must fall outside an area fraction  $\alpha$  of the guide field. From the binomial distribution, the probability that none of the  $n-1$  remaining stars will fall outside area fraction  $\alpha$  is  $\alpha^{n-1}$ , so that the probability that one or more will fall outside the area is  $1 - \alpha^{n-1}$ .

The probability of finding two or more stars in the area can be written in series form:

$$P(>1) = \sum_{n=2}^{\infty} \frac{N^n}{n!} e^{-N}$$

This can be modified to express the probability of finding two or more stars in a satisfactory geometric arrangement:

$$P(>1) = \sum_{\substack{\text{suitably} \\ \text{arranged}}}^{\infty} \frac{N^n}{n!} \exp \left[ -N(1 - \alpha^{n-1}) \right]$$

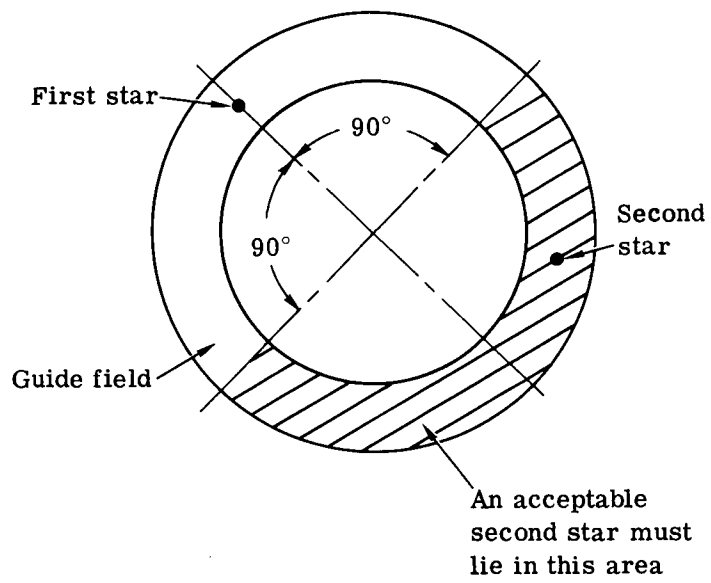


Fig. C.5-11 — Relative location of two guide stars in guide field

The series expansion of  $e^N$  can be used to simplify this. Expressed as the probability of not finding at least two stars suitably arranged, it becomes

$$P(<2) = e^{-N} \left( 1 + \frac{e^{\alpha N} - 1}{\alpha} \right)$$

suitably  
arranged

As area fraction  $\alpha$  approaches zero, l'Hopital's rule can be used to show that this expression approaches the expression given previously for the probability of not finding at least two stars in an unrestricted arrangement  $P(<2)$ .

A slightly more convenient form of the preceding equation is

$$P(<2) = \frac{1}{\alpha} \left[ e^{-N(1-\alpha)} - (1-\alpha)e^{-N} \right]$$

suitably  
arranged

where, once again,  $N$  is the average number of stars to be found in an area the size of the guide field, and  $\alpha$  expresses the required separation between guide stars.

The probability of not finding at least two stars distributed as in Fig. C.5-11 ( $\alpha = 1/2$ ) is found to be

$$P(<2) = 2e^{-N/2} - e^{-N}$$

suitably  
arranged

The probabilities of not finding at least one star and two stars suitably situated ( $\alpha = 1/2$ ) are plotted as functions of the average number of stars in the guide field in Fig. C.5-12. Fig. C.5-13 gives the line-of-sight error equivalent to the noise of one sensor as a function of the percentage of possible targets in the galactic polar region for guide fields of several different areas.

To determine what guide field is adequate, a criterion is needed. A suggested criterion (Fig. C.5-14) is that when 90 percent of the potential targets in the galactic polar region are covered, the noise from the sensor begins to be an important part of the guide signal budget, namely half, or 0.006 microradian (0.0012 arc-second). The effect of having twice or half this guide field is shown by the dashed lines in Fig. C.5-14. This criterion suggests, from Fig. C.5-13, that a minimum guide field would cover about 11 square milliradians (130 square arc-minutes) of sky.

The guide area suggested for the LST is shown in relationship to the rest of the image plane format in Fig. C.5-15. This guide field has an area of approximately 19.5 square milliradians (230 square arc-minutes) and, if fully baffled, gives the telescope a minimum obscuration of 29 percent.

In the proposed guide sensor system, the first star provides the yaw and pitch information and the second star provides the roll information. The error at the data star is greater than the error from each sensor alone by a factor that depends on the separation between the two guide stars. This function is plotted in Fig. C.5-16. At a minimum angular separation of 90 degrees, the sensor noise seen at the data star is 1.4 times the noise of a single sensor.

Fig. C.5-17 gives the noise from the two guide sensors for the proposed 19.5 square milliradians (230-square arc-minute) guide field as a function of the percent of targets covered in the galactic polar region. A 90-degree separation between the guide stars is assumed. For 90 percent of the targets, the indicated noise error is 0.005 microradian (0.0011 arc-second) rms and, for 90 percent of the targets, guide stars brighter than 14th magnitude are available.

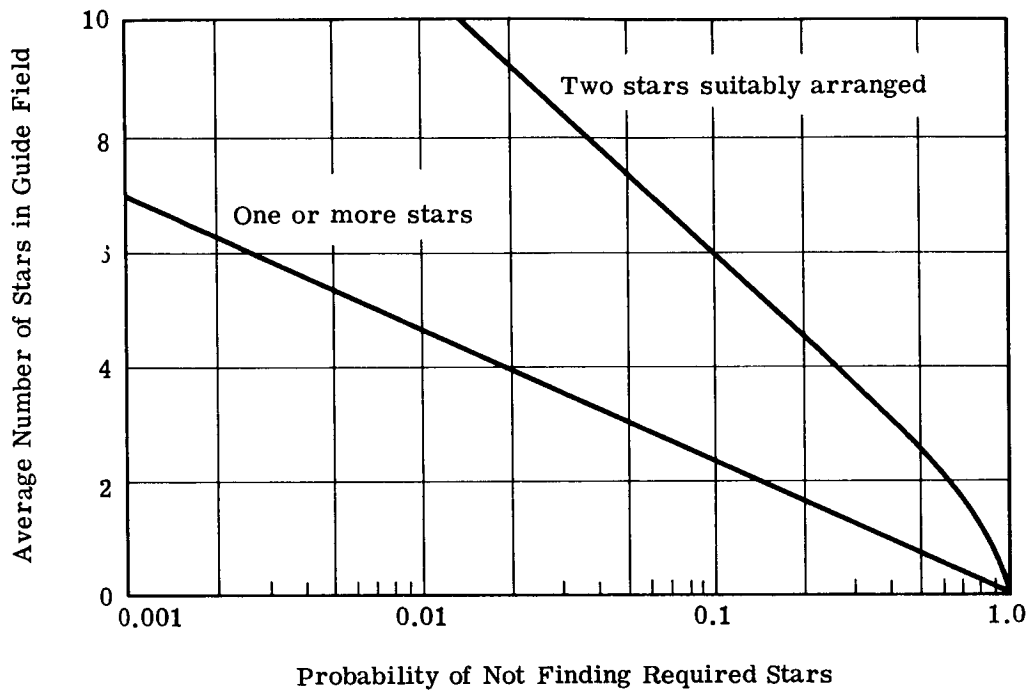


Fig. C.5-12 — Poisson statistics for guide stars

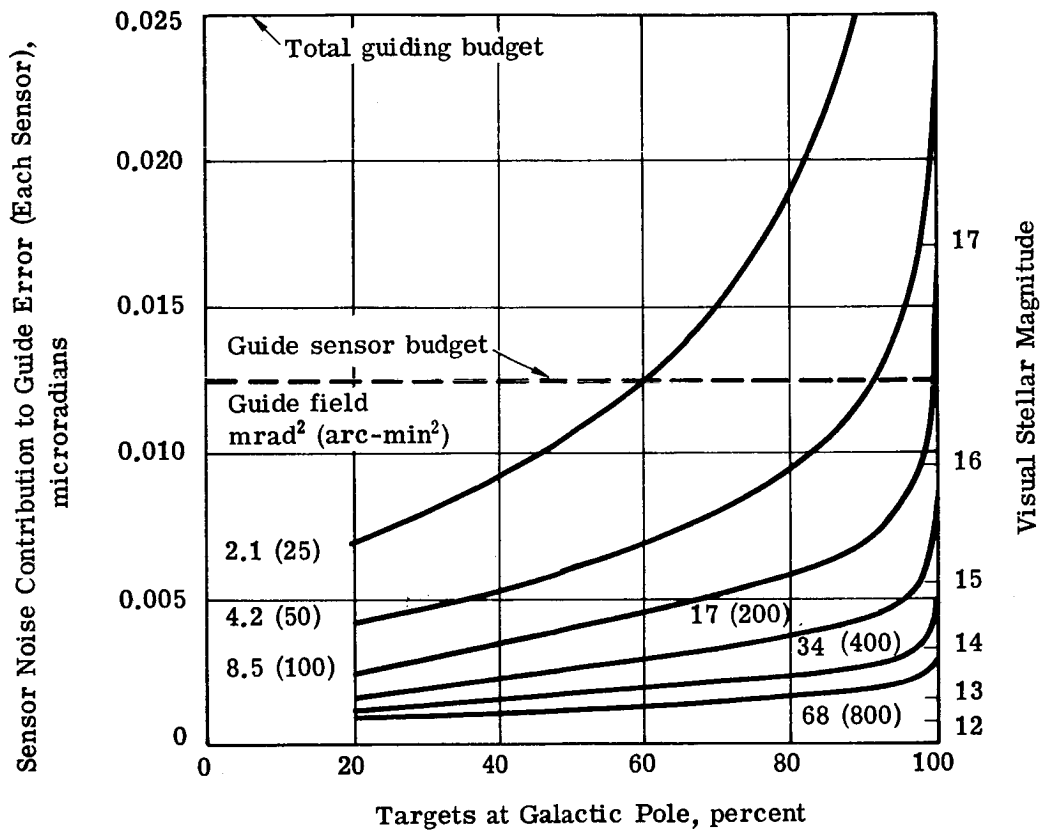


Fig. C.5-13 — Sensor noise distribution for a given guide field area, galactic pole viewing

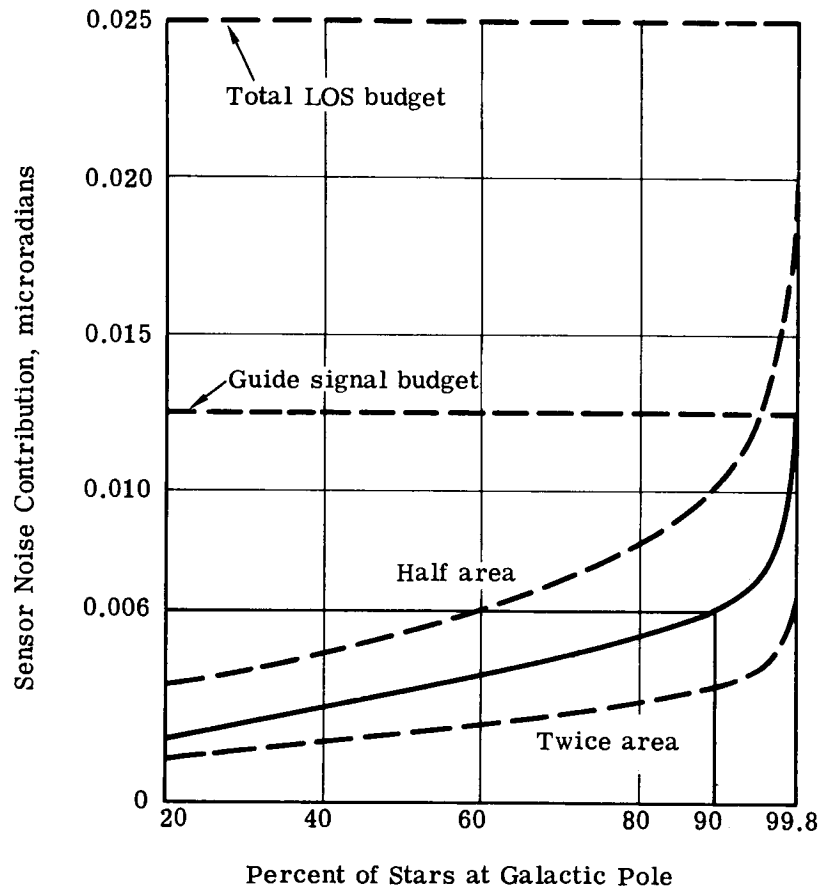


Fig. C.5-14 — Sensor noise contribution to line of sight error for minimum area configurations

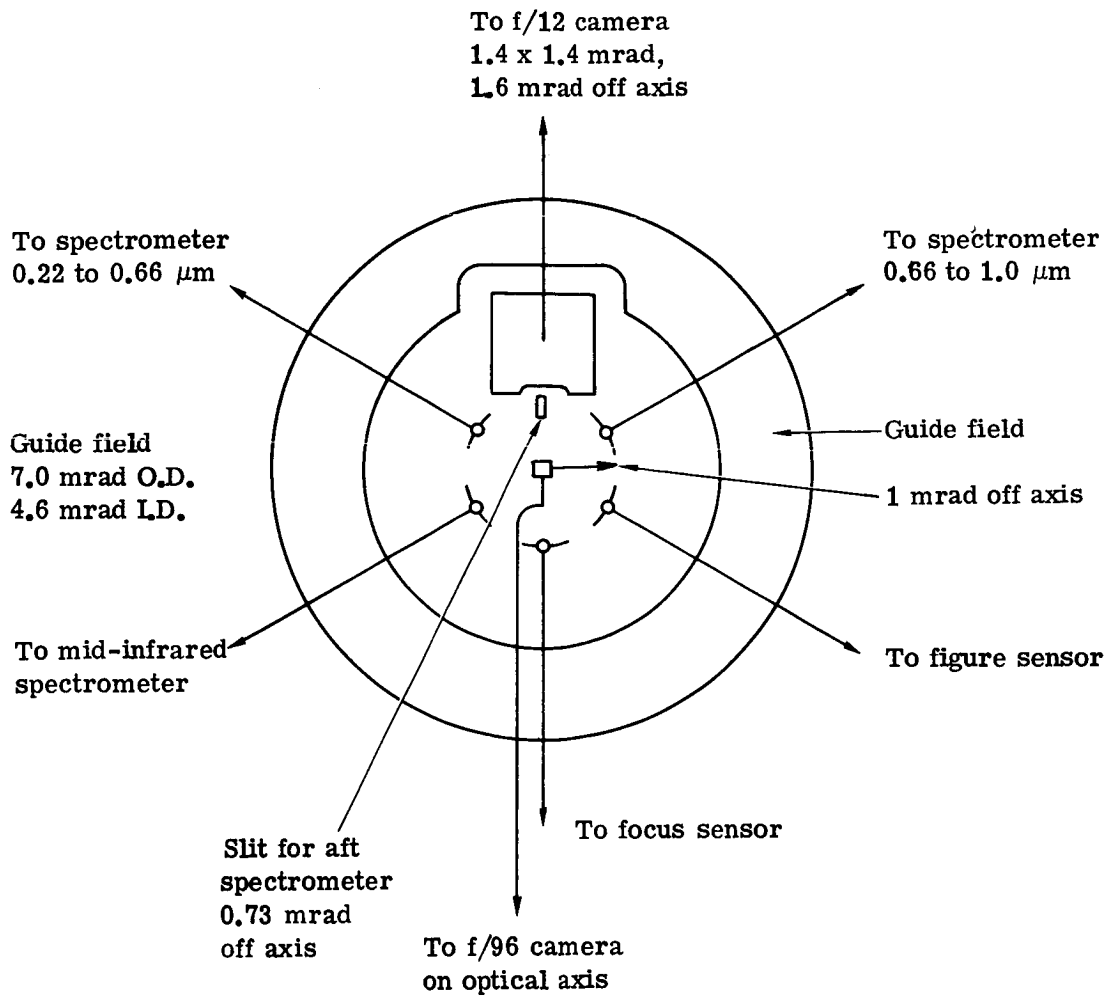


Fig. C.5-15 — Image plane format, in object space coordinates



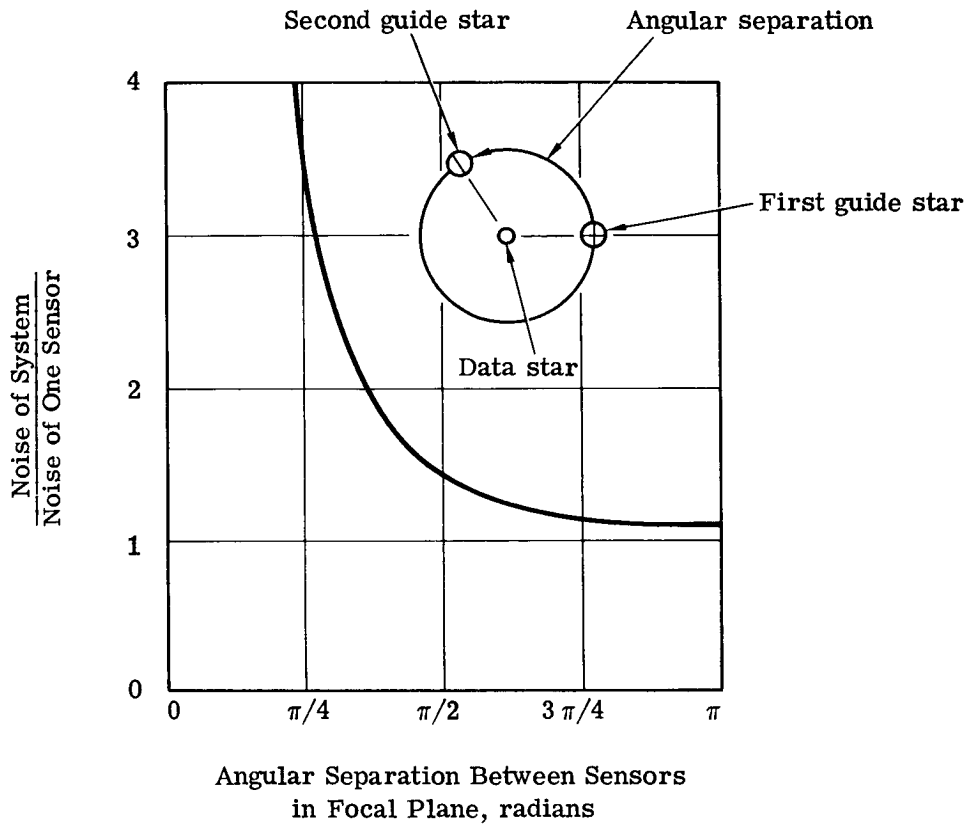


Fig. C.5-16 — Guide signal noise of fine guidance system relative to noise from one sensor (system using two guide stars of equal brightness)

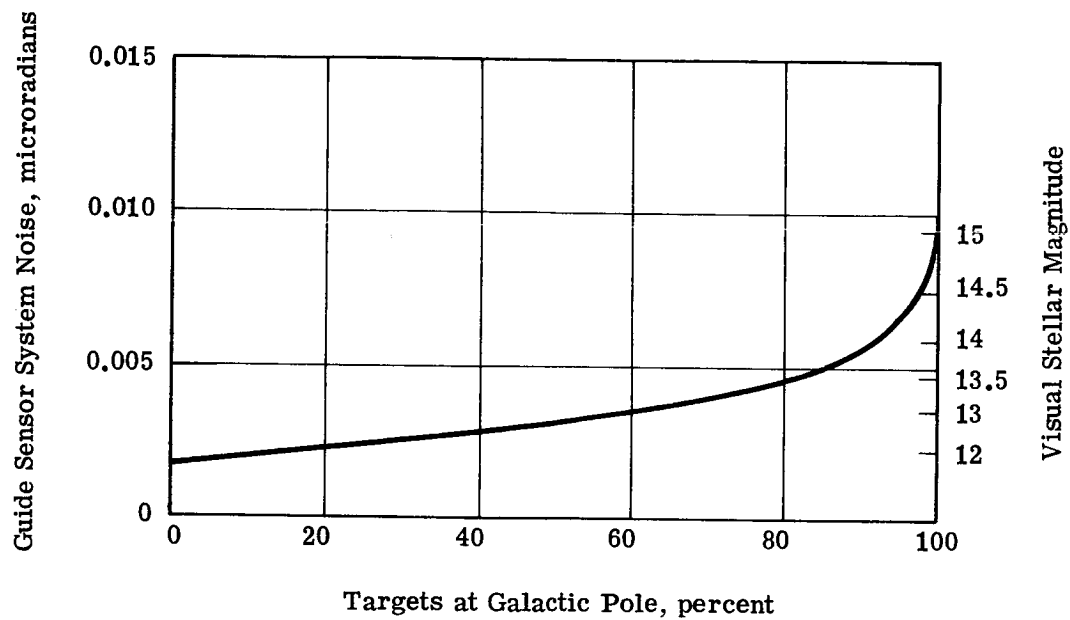


Fig. C.5-17 — Guide signal noise from two-sensor system, 4-hertz bandwidth, 4-channel image dissector

### C.5.c(2) Tracker Selection

Of the five types of star-tracking sensors evaluated for an LST, one has been selected as the baseline tracker. Table C.5-3 lists the prime properties used for evaluation for each type.

#### Reticle With Four Image Disectors

A reticle tracker incorporating a stationary, high transmission refractive reticle to determine fine guiding (tracking) accuracy and an image disector seems to offer the greatest potential in most respects. It works as an image disector tracker in the coarse acquisition and pointing mode and as an optical quadrant beam splitter tracker in the fine guiding mode. (It is described in detail elsewhere.) The noise-limited accuracy is near ideal, with the only differences being a slight degradation in optical spread function owing to aberrations in the reticle and lower transmission owing to a more complex optical path. Technology for manufacturing the reticle, which is made of fused silica, is believed adequate. Once it is manufactured, it should stay in place and define a mechanical reference with very low drift.

The main disadvantage with the reticle tracker is the lack of continuous offset capability. Due to the granular nature of the reticle, pointing will be designatable to within only  $\pm 5$  microradians ( $\pm 1$  arc-second). Intermediate offsets or variable offsets (such as for differential velocity aberration corrections) necessitate the incorporation of auxiliary systems of at least one of two types: either a mechanically tilted plate in front of the tracker (which would reintroduce the problems of a mechanism) or of electronic image steering in the scientific data recording cameras. Since 0.48 microradian (0.1 arc-second) amounts to only 0.15 millimeter at  $f/100$ , this would result in a trivial increase in electronic complexity. This concept should be verified experimentally at an early date.

#### Beam Splitter With Two Image Disectors

This type of star tracking sensor (Fig. C.5-18) uses a beam splitter to provide dual fields of view, with each relayed to an image disector faceplate. Two fields of view at different magnifications are needed, since the required tracking accuracy (about  $1/30,000$  of the minimum field of view for the entire error budget) is beyond the capability of a single tracker. Positioning of the tracker head is necessary to cover the annular field of view. In addition to the uncertainties of positioning, there is also possible drift owing to mechanical motion of elements of the electron optics caused by thermal shift, drift of electronic circuits, and beam deflection as a result of electrostatic charging effects inside the image disector. The sensitivity is less by a factor of four owing to division of light energy (factor of two) and the less efficient method of modulation and demodulation of the position information (factor of two).

The main advantage of this type of operation is in the ease of obtaining continuously variable offset in tracking angle, which allows accurate pointing designation and easy accommodation of differential velocity aberration correction and planetary motion compensation.

#### Single Image Disector With Dual Field of View

This type of star tracking sensor is similar to the beam splitter with two image disectors, but it optically superimposes on the same image plane, two fields of view at different magnification, thus providing the coarse and fine channels with a single image disector (Fig. C.5-19). There are a number of optical methods for superimposing fields of view, some involving beam splitters or holes in either a pupil plane or an image plane. All suffer from one of two disadvantages: either the light is shared between coarse and fine optical channels (reducing signal current) or there is a discontinuity when light is transferred from the coarse channel to the fine channel (creating a handoff problem). In addition, each channel must operate in the presence of the background from both channels.

#### Quadrant Prism Splitters With Four Photomultiplier Tubes

This concept, used on the orbiting astronomical observatory (OAO), is highly accurate so far as noise-limited sensitivity is concerned, since resolution may be made nearly diffraction-limited and use of available photons is very efficient. To provide variable offset, it is necessary to position the tracker head at the desired location for the

Table C.5-3 – Star Tracking Sensors

	Type of Tracker				
	Field-Variable Focal Length With One Image Dissector	Quadrant Prism Splitter With Four Photomultiplier Tubes	Single Image Dissector With Dual Field of View	Beam Splitter With Two Image Dissectors	Reticule With Four Image Dissectors
Tracking accuracy noise limit (relative sensitivity)	0.45	1	0.2–0.45	0.25	0.9
Stability limit	Circuit drifts and electron optics	Positioning mechanism	Circuit drifts and electron optics	Circuit drifts and electron optics	Solid glass and metal
Servo loop compatibility handoff	No handoff	No handoff	Problems for some optical schemes	No handoff	No handoff
Linearity	Poor	Very poor	Excellent	Excellent	Fair
Manufacturability	?	OK	OK	OK	OK
Size, weight, power	Not a significant discriminant				
Ability to reacquire original guide star after pointing at another guide star	Low	Low	Low	Low	High

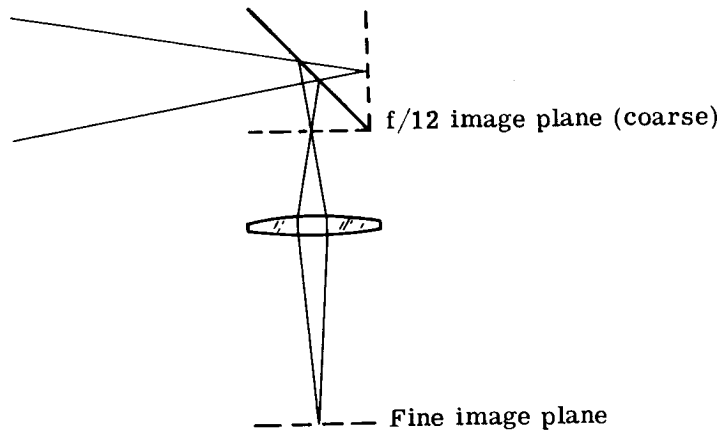
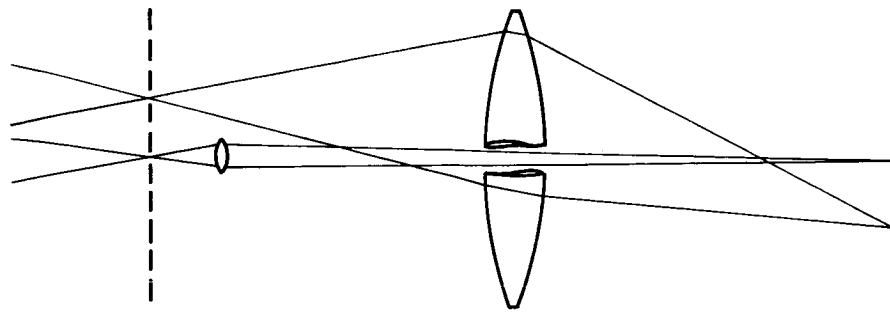
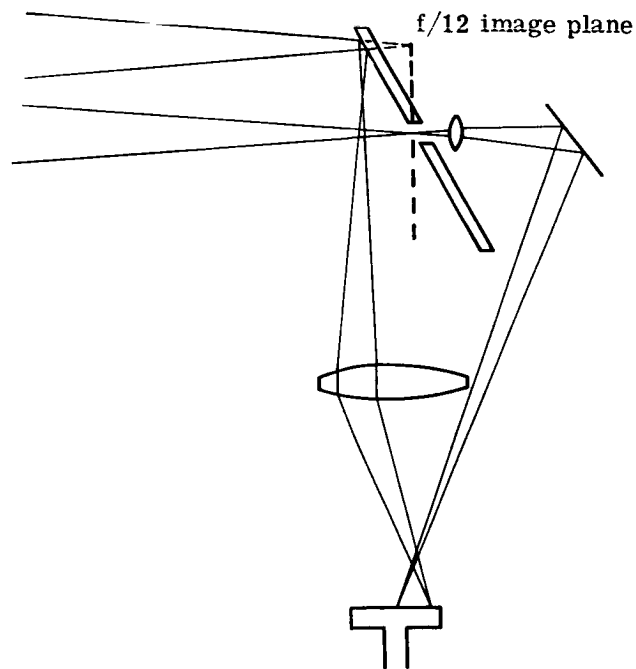


Fig. C.5-18 — Beam splitter with two image dissectors



f/12 image plane

(a)



(b)

Fig. C.5-19 — Single image dissector with dual field of view

tracked star. It is difficult to build a mechanism that will be accurate enough to position the tracker head correctly and solid enough to prevent any drift over the long exposure time. Drift would have to be around 0.1 micrometer to meet a reasonable error budget at  $f/12$ . The overall tracking accuracy is likely to be limited by this mechanism. The design, fabrication, and mechanical calibration of such a mechanism would also be a difficult task.

#### Field-Variable Focal Length Relay With One Image Dissector

This type of star tracking sensor is a variation of a dual magnification optical relay, where a continuously variable magnification is created by using an aspherical relay element, as shown in Fig. C.5-20. A single image dissector with electrical nutation is used. Sensitivity is somewhat less with the optical quadrant beam splitter, primarily because the method of modulation and demodulation is less efficient. Initial optical analysis also indicates that aberrations in the aspherical element are high without correction. It is not yet clear whether this optical relay method is usable or not, but in any case it will present a difficult problem of optical analysis and design and will be difficult to fabricate. Difficulties will be incurred as well in designing a servo loop, because the effective focal length, which is a factor in servo loop gain, is a variable across the field of view. The main advantages of such a relay are that no coarse/fine handoff is required and energy need not be shared between coarse and fine channels.

#### C.5.c(3) Reticle/Image Dissector Tracker

##### Description

The arrangements of the key elements in the star tracker suggested for use on the LST are shown in Fig. C.5-21. The  $f/12$  image plane contains an annular plate reticle that refracts light from the off-axis guide stars and passes the on-axis data field for further relay to the scientific instruments. The annular tracking field is defined by the size of the annular reticle, which has an outside diameter of 7 milliradians (24 arc-minutes) and an inside diameter of 4.65 milliradians (16 arc-minutes). Behind the reticle plate are three tracker heads, two for operations and the third for redundancy. Each consists of relay optics and an image dissector and each is positioned with a mechanism that gives motion about the optical axis and about an offset axis in order to provide placement in both radial and tangential directions. Electronics are located with the image dissector. The reticle is shown in detail in Fig. C.5-6. Since the telescope is astigmatic off axis, the tangential and sagittal focal surfaces are separated by an amount that varies over the tracking field of view. This is compensated by placing two reticle plates in the  $f/12$  plane, one conforming to each of the astigmatic focal surfaces.

The method of deriving information may be seen in Fig. C.5-22. The incoming cone from the main telescope passes through the refractive reticle (represented here by the two prisms). The ridges of the prisms are parallel to the radial and tangential images, respectively, and are in the radial and tangential image planes. The width of the ridge lines is much smaller than that of the star image, and the spacing between ridge lines is much larger. Each prism thus may deflect light in either of two directions, producing a total of four possible light beams. In the coarse tracking mode, when the star image is located randomly with respect to the reticle, only one of the four beams will normally contain light. In the fine tracking mode, the star image is held on both the tangential and sagittal prism ridge and all four beams are illuminated. The relay optics perform the functions of relaying the tracking field of view onto the image dissector and of separating the light according to which of the four possible combinations of refractions it has undergone.

The overall format of the image dissector photosensitive surface is shown in Fig. C.5-23, with the four displaced fields of view sitting side by side. A star image at the  $f/12$  plane has four images on the image dissector. Which of the four contains light and how the light is divided is determined by the placement of the star image relative to the reticle ridges. As a star image moves in the  $f/12$  plane, the four deflected images move in unison, maintaining the square pattern. The image dissector is made with four apertures, each serving as the entrance to an electron multiplier and arranged in the same pattern as the four optical images. Thus, by electrically deflecting the image dissectors, the four deflected star electron images may always be directed into their proper multiplier aperture.

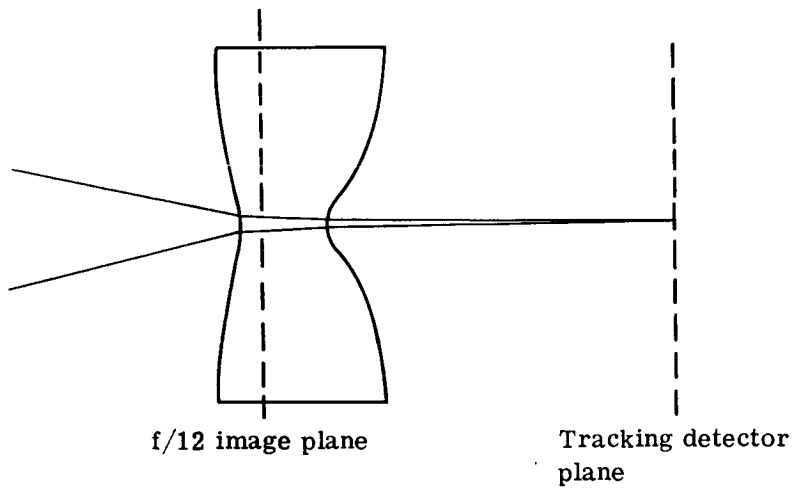


Fig. C.5-20 — Field-variable focal length relay



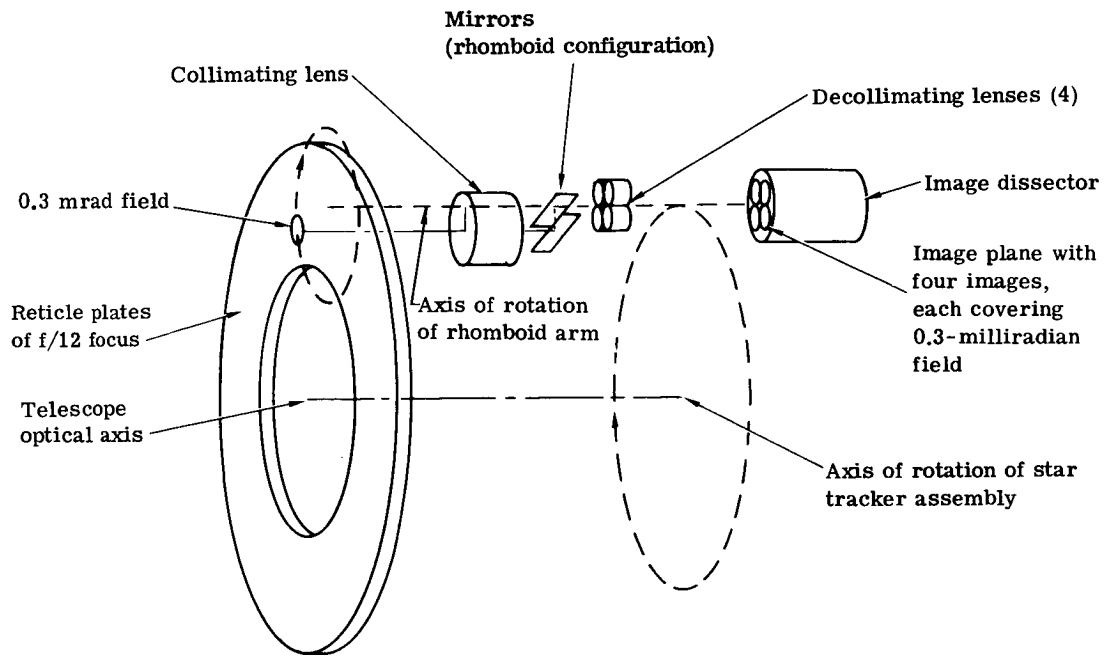


Fig. C.5-21 — Star tracker schematic

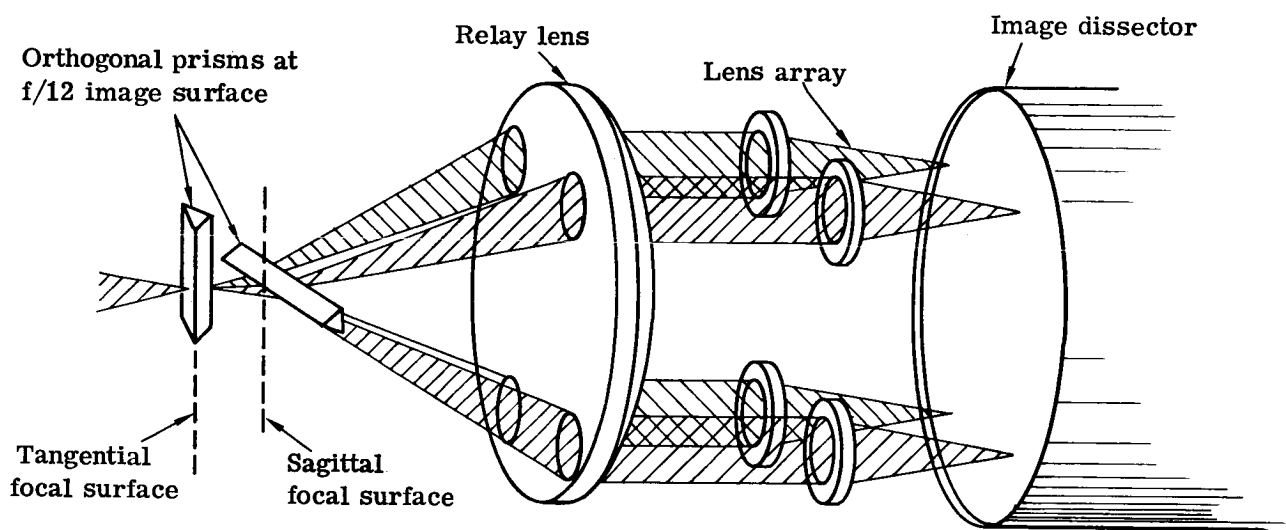


Fig. C.5-22 — Fine guidance mode schematic

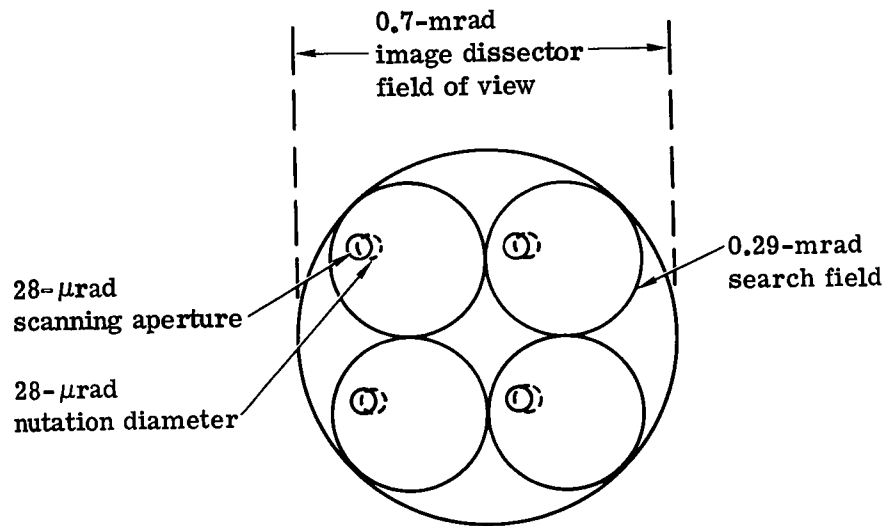


Fig. C.5-23 — Format on image dissector

The location of the fourfold image of the guide star depends only on the gross location of the guide star with respect to the reticle and is used to derive coarse tracking information. The relative division of light in the fourfold guide star image depends only on the phase location of the guide star relative to the spatial periodicity of the reticle and is used to derive fine tracking information. Since the division of light occurs at the reticle, which is inherently astigmatism corrected due to its construction, a motion that is insignificant in terms of spot size on the image dissector will cause a large change in relative light flux among the four elements of the fourfold guide star image.

By observing the location of the four images with the image dissector, it is possible to locate a star image anywhere in the field of view to within an uncertainty less than the reticle spacing and approaching the optical spot size. If the output of the four multipliers is summed together, the same signal appears in the summed output without regard to where the light is with respect to the light-dividing reticle or how the light is split among the four images. This is the coarse tracking mode.

By observing the relative amounts of light in the four images by comparing the count rates from the multipliers, it is possible to determine the position relative to a reticle ridge to within a very small fraction of the diffraction limited optical spot. This is the fine tracking mode. A discussion of the exact method of deriving location information and a quantitative discussion of tracking accuracy in the two modes is given in another section.

A layout of the tracker head and positioning mechanism is shown in Fig. C.5-24.

Signals from the four electron multipliers are read in a digital mode: i.e., rather than the average electron rate (current), pulse events are recorded. As discussed below, this results in much lower noise. Most of the signal processing is done digitally and is virtually noiseless as compared with the noise inherent in the photoelectron statistics.

### Operation

The operation of the star tracker consists of a sequence of four steps:

1. Designations of target stars
2. Positioning of two tracking heads to designated locations
3. Lock-on sequence
4. Fine tracking.

### Designation

The guide stars should have a visual magnitude of about 10-15 (the brighter, the better). Their selection is subject to a few limitations to maintain proper tracker operation. The amount and direction of offset from the data object must be such that the guide stars fall within the tracking field of view and are sufficiently separated as to provide useful tracking data. The separation may be from 1.57 to 3.14 radians (90 to 180 degrees) in angle, measured about the optical axis. If the tracker is designed for operations at visual magnitude of 13, the brightest star usable will have a visual magnitude of 10 if counting efficiency is not to be degraded owing to overlap of pulses. Since the tracker will probably be unable to distinguish between stars of nearly the same brightness, it will be necessary to select guide stars such that there are no other stars within 1 arc-minute (the  $3\sigma$  diameter of the SSM pointing uncertainty) that are within a set brightness range. If the brightness determination capability of the tracker is  $\pm\frac{1}{4}$  magnitude, no more than 3 percent of the potential target stars will be unusable in the galactic plane and proportionately less in areas of the sky containing fewer stars. Since the tracking field has been sized for operation in the galactic polar regions, this is not of significance.

Double stars are a potential problem. Fig. C.5-25 shows the tracking fine error signal as a function of star displacement. The effect of a double star is to broaden the transfer characteristic and create a dead band that may be several orders of magnitude wider than the desired tracking accuracy. Known doubles may be excluded from selection as guide stars. Those whose separation is between the resolution of ground-based observatories and the resolution of an LST are most troublesome because they will not be known a priori as doubles. It will thus be necessary to include a double check as part of the acquisition and lock-on sequence.

## Head Positioning

Each guide head looks at an area covering a field angle of approximately 0.3 milliradian (1 arc-minute). The guide head must be positioned mechanically both circumferentially and radially in the guide field to the position at which the guide star is expected to appear when the spacecraft is positioned by the initial pointing system. How this is done is shown schematically in Fig. C.5-21. The entire guide head can be moved to the desired circumferential position. The light from the reticle passes through a rhomboidal image moving system that can be rotated to provide the radial motion. Encoders for both rotating mechanisms are used in positioning the mechanisms with the required accuracy. The positioning tolerance criterion is that the mechanism can repeatedly position the guide head at any given reticle line crossing.

There are three guide heads: two are used in any given observation and the third is redundant. If one of the guide heads becomes immobilized through a mechanism failure, then that particular portion of the guide field may no longer be used. Consequently, the acquisition probability for any given target is diminished. If two guide heads fail, the stabilization performance then depends on the ability of the SSM guidance system to stabilize in roll.

The entire guide sensor mechanism is shown in Fig. C.5-24.

## Critical Parameters Discussion

Baseline values have been chosen for a number of key parameters of the tracker that have a significant effect on performance or on interfaces. Several of these are discussed below.

### Field of View and Formatting

The minimum field of view for a tracker is set by the pointing uncertainty of the SSM. This is 290 microradians (1.0 arc-minute) specified as the  $3\sigma$  diameter of a two-dimensional Gaussian probability distribution. In the  $f/12$  plane, this is a circle 10.5 millimeters in diameter, which is a convenient size for handling with a unity magnification relay. The largest field of view considered would cover the entire tracking field of view, which is an annulus 7 milliradians (24 arc-minutes) in diameter. At  $f/12$ , this annulus has an outside diameter of 250 millimeters and would have to be optically reduced by a large factor to place on the useful format of any reasonable sized image dissection. To avoid any ambiguity as to which field of view a point image falls into, it is necessary that the field of view shear provided by the reticle be at least equal to the diameter of the SSM uncertainty.

The simplest arrangement of the four displaced fields of view places them immediately adjacent as shown in Fig. C.5-25. This requires an image format that (if circular) has a diameter  $1 + \sqrt{2}$  times the diameter of the individual fields of view or 25 millimeters at  $f/12$ . This is a reasonably convenient format size, because image dissectors of that size are available. The extent to which the entire format might be optically reduced to use a smaller tube (which would reduce the size and power of the tracking head) is limited by the desire to locate the dot absolutely within a small fraction of the field of view in order to provide a high density of possible aiming points. To have reticle ridge spacings corresponding to 9.7 microradians (2 arc-seconds) in object space, it is necessary to be able to locate the dot absolutely to  $\pm 4.85$  microradians ( $\pm 1$  arc-second). This is 175 micrometers or about 1/150 of the entire format. If this is interpreted as the  $3\sigma$  radius of a two-dimensional Gaussian distribution, then the rms uncertainty must be held to about 1/500 of the format, a rather tight requirement. The baseline format is accordingly taken as 25 millimeters, and the feasibility of reducing tube size will not be resolved until the performance of a detailed design analysis or the testing of a breadboard tracker.

### Reticle

The reticle consists of two annular plates, one having straight radial grooves and the other having concentric circular ring grooves. In each case, the face containing the grooves is spherical, with the radial and circular grooves

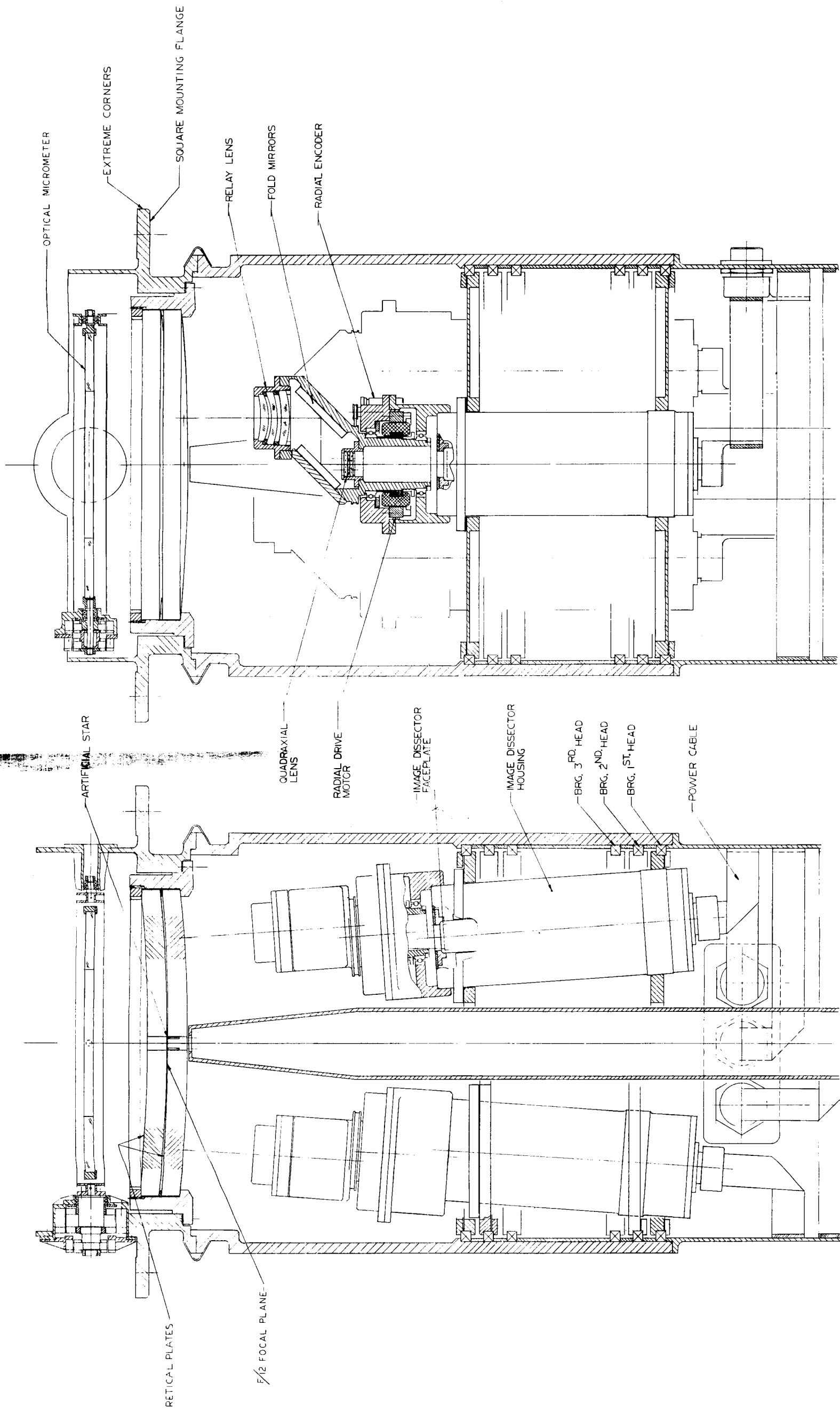


Fig. C.5-24 — LST fine guidance sensor assembly (dwg. no. 915230)

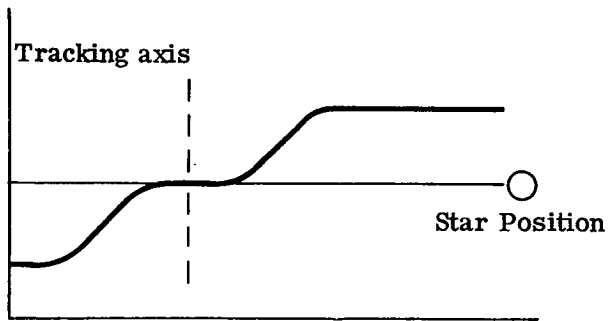
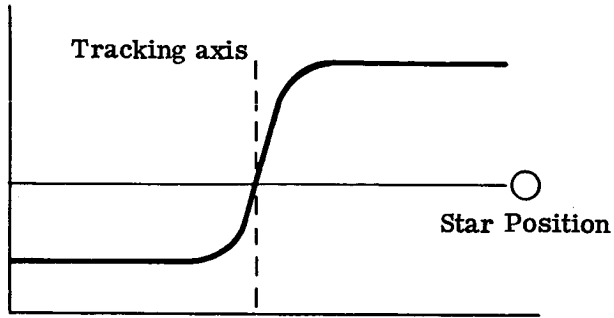


Fig. C.5-25 — Error transfer characteristics for single stars and double stars

conforming to the sagittal and tangential focal surfaces, respectively. The parameters of this reticle affecting first-order performance are the angle of the facets, the groove spacings, the sharpness of the grooves, and the optical transmission. Mission considerations require pointing capability to within  $\pm 4.85$  microradians ( $\pm 1$  arc-second). At  $f/12$ , this corresponds to a spacing between peaks of 350 micrometers, or a frequency of 2.9 grooves per millimeter. This number may be a constant for the tangential plate but it is only a nominal number for the sagittal plate since it covers a ratio of radii of 1.5. If the nominal spacing is taken to be that at the mean radius, then the inner and outer radii correspond to pointing capabilities of  $\pm 3.9$  and  $\pm 5.8$  microradians ( $\pm 0.8$  and  $\pm 1.2$  arc-seconds), respectively.

The angle,  $\alpha$ , to the average surface made by the individual facets of the grooves is determined by the amount of separation required and the focal length,  $F$ , of the relay field lens. The image plane separation in either dimension is

$$\Delta x = 2(n-1)\alpha F$$

For typical optical materials having  $n \approx 1.5$  and for a field lens focal length of around 100 millimeters, the angle is about 5 or 6 degrees to provide a separation equal to the 10.5-millimeter diameter of the SSM pointing uncertainty.

The sharpness of the ridges of the reticle may affect tracking accuracy if the grooves are so rounded as to increase the spread functions. The astigmatic spot from the telescope will have a width (at the half-amplitude points) of at least 7 micrometers. A common rule of thumb is to have cascaded spread function widths differ by a factor of three if the effect of the smaller one is to be negligible in determining the overall function. Thus, if the radius of curvature can be kept smaller than the telescope's spot by a factor of around three or so, the spreading effect of the reticle will be negligible. This appears to be well within the capabilities of conventional diffraction grating technology.

#### Image Dissector

A number of properties of the image dissector affect the performance of the tracking head and its interfaces. The most basic choice is that of electron optics configuration. While hybrid combinations are possible, the normal configurations have focus and deflection either both electrostatic or both electromagnetic.

There are several key differences to be traded off in this case. For a 25-millimeter format, the outside diameter and length are comparable. The weight, however, will be several pounds heavier for the electromagnetic tube since the vacuum and light metal grids of the electrostatic electron optics are replaced with copper coils to generate magnetic fields. In addition, the coils continuously dissipate several watts of power. On the other hand, tubes with electromagnetic focusing have better and more uniform resolution.

The spread function of the electron optics (diameter at half-amplitude) is about 12 to 15 micrometers and is fairly constant over the format. The spread function for an electrostatic tube is about 20 to 50 micrometers for reasonable voltages and varies over the useful format by a factor of two or so, being worse at the periphery of the format.

There is also substantially more mapping distortion in electrostatic focus tubes than in electromagnetic focus tubes. This may result in incorrect placement of points in the electron image of up to 1 percent or so of the correct radius for electromagnetic focus and up to 10 percent for electrostatic tubes. As a result of distortion, a pattern of four optical images falling on the corners of a perfect square on the photocathode produces a distorted figure at the electron image plane, the exact shape of which varies with location in the format. For very small distortions, the only effect is in coarse acquisition, made when all four channels are summed. In this case, there may be an apparent displacement of the coarse image when the light shifts from one channel to another. If necessary, this effect may be mapped and corrected for.



In the case of electrostatic focus, the distortion is so large that for some locations of the four-dot pattern on the format, it is not possible to get all four electron beams into their respective apertures. This is because the electron images no longer form the corners of a square; the holes inside the tube that form the multiplier entrance apertures still do. Itek feels that the advantages of low distortion and high resolution of electromagnetic focus outweigh the advantages of lower power and weight of electrostatic focus.

This configuration therefore is the baseline choice for an image dissector for star tracking. The diameters of the four apertures have an upper limit that is set by astronomical background and dark current [Section C.5.c(6)] of about 2 millimeters. The lower limit is set by the need to have the aperture at least three to so times the diameter of the optical spread function in order to collect electrons efficiently and provide a broad unambiguous error transfer characteristic for the servo loop. The image of the astigmatic circle of least confusion is about 75 micrometers, providing a lower limit for aperture diameter of 0.225 millimeter. A further consideration is the desire to have the aperture as large as possible in order to reduce the extent to which distortion must be mapped and electronically corrected for. As a baseline, the aperture diameter selected is 1 millimeter.

The most applicable photocathode appears to be a bi-alkali (CsKSb) photocathode. It is fairly consistently available from various manufacturers, is stable over long time periods, and has low dark current ( $2 \times 10^{-17}$  amp/cm<sup>2</sup> at 20°C) and high sensitivity to stars in the middle of the range of spectral classification (approximately  $2 \times 10^{-4}$  amp/lumen for 5,500°K blackbody radiation).

Counting efficiency depends on the three main factors. About 5 percent of the counts will be lost just owing to the probability of zero output events from a dynode following Poisson statistics with a mean gain of three. In addition, the mesh providing the high accelerating field at the photocathode transmits about 80 to 90 percent of the electrons unless the mesh is so coarse that resolution is compromised. If pulse height discrimination is used to eliminate spurious dark pulses originating in the multiplier, about 80 to 85 percent of the output pulses will cross the threshold and be counted. The net counting efficiency is thus about 60 to 70 percent. A fourth possible loss, due to the spread function being wider than the aperture, is not significant here owing to the rather large (1-millimeter-diameter) aperture.

#### C.5.c(5) Coarse Acquisition Accuracy

The method of operation of the tracker head requires that the image dissector be able to determine which reticle ridge the star image is falling on in order that the tracker have absolute pointing capability. Due to the inherent discreteness of the fixed reticle, pointing may be designated no more accurately than plus or minus one-half of the reticle peak spacing. The lower limit on reticle spacing is set by the ability of the image dissector to determine the absolute positions of the star image. For reliability, the spacing must be safely larger than the amount by which position calibration may drift over a period of time, which may be up to several years if no on-board calibration is used or as short as a few minutes if the tracker is recalibrated before each acquisition.

Several sources of potential long or short term drift in calibration have been identified:

1. Statistical noise of the same type discussed as a limit to tracking accuracy will also act as a very short term (depending on the electrical bandwidth) source of apparent drift. Since the image of the astigmatic plane of least confusion is much larger than the diffraction limit and will be further degraded by the optical relay and image tube electron optics, this limit will probably be at least 20 times worse than the fine tracking accuracy, if comparable bandwidths are used.

2. The ability to position the tracking head mechanically in the field of view and to maintain its optical alignment normal to the spherical image surface will have a tolerance that will show up as a shift of the reticle image on the image dissector faceplate. This uncertainty occurs each time that the tracking head is normal.

3. Since the temperature in the instrument bay will not be perfectly uniform or constant, mechanical components will move in response to thermal transients during each orbit. Movement may occur in the positioning mechanism, in the mounts holding the image dissector or its deflection yoke, or in the electric field forming grids inside the image tubes.

4. The electronic circuits generating the voltages and currents that produce the deflection of the electron image inside the image dissector are subject to both short term fluctuations due to thermal changes during orbit and long term drift due to aging.

5. The earth's magnetic field deflects the image dissector electron image producing an apparent movement of the reticle. This may be reduced by magnetic shielding, but not eliminated. The amount and direction of the deflection depend on spacecraft orientation and orbital phase. There is also some defocusing effect, but this is small and of much less effect.

6. Hysteresis in the tracker may occur owing to any of several effects. If magnetic deflection is used, it is impossible to remove magnetic materials completely from the system, and they will have some hysteresis. By using compensation techniques, the effect may be greatly reduced, though. In addition, electrostatic charging of dielectric materials inside the image dissector may produce an apparent image shift that depends on past history of deflections and on image content.

7. Distortion is produced by both the relay optics and the image dissector. To the extent that distortion is not mapped and compensated for, there is an apparent image shift which is variable over the field of view but is constant over the life of the tracker.

To provide an absolute pointing capability of  $\pm 4.8$  microradians ( $\pm 1$  arc-second), the tube must be able to distinguish between lines that are 350 micrometers apart. To achieve this, it is necessary that the root sum square of the estimated individual potential amounts of drift be less than one-half of the ridge separation by a safety factor of perhaps three to account for the unlikely possibility of all deflections being large and in the same direction. This establishes a maximum of 58 micrometers as the root sum square and 175 micrometers as the worst case.

Table C.5-4, an initial budget for the individual potential drifts, has been prepared for a tracking head that incorporates a magnetic focus image dissector with a 25-millimeter usable format diameter. Each is reasonable in an instrument that is carefully designed and built for low drift. In particular, extreme care will have to be exercised in designing the method of rigidly mounting the image dissector and its yoke and in designing magnetic components so as to minimize the effects of hysteresis and the earth's field. Maintaining low electrical drift may require carrying a standard voltage reference cell as part of the instrumentation. The budget assumes that the distortion is mapped and electronically corrected for in absolute pointing determinations. The budget indicates that it is probably possible to give  $\pm 4.85$  microradians ( $\pm 1$  arc-second) designation capability. It may also be possible to reduce the size of the tube to cut the weight and power.

#### C.5.c(6) Tracking Mode Signal-to-Noise Ratio

Two methods of modulation and demodulation are considered and compared. In the first (Fig. C.5-22), a refractive prism reticle is used to divide the focused optical spot into four parts whose relative strength depends on the centering of the optical spot on the reticle. An image dissector (or four photomultipliers) is used to measure the relative strengths of the four beams. Fig. C.5-22 details how the focused optical star image falls on a prism peak on the reticle and is divided into four beams. If the star image is perfectly centered, the four beams are of equal intensity. If the star image is off center, the intensity differences may be used to derive error signals.

In the second method (Fig. C.5-26), the star image falls directly on the photocathode of an image dissector that scans the image in a manner that produces a position indicator. The focused light image produces a focused electron image that is located on the aperture plate. In the tracking mode, the star image is steered by an average

Table C.5-4 – Absolute Pointing Budget for Image Dissector Tracking

Drift Source	Drift Budget, micrometers
Resolution shot noise	1
Positioning mechanism	10
Mechanical drift	25
Uncompensated distortion	5
Hysteresis	10
Stray magnetic fields	10
Circuit drifts	<u>25</u>
RSS	40
(Allowable)	(858)
Worst case	86
(Allowable)	(175)

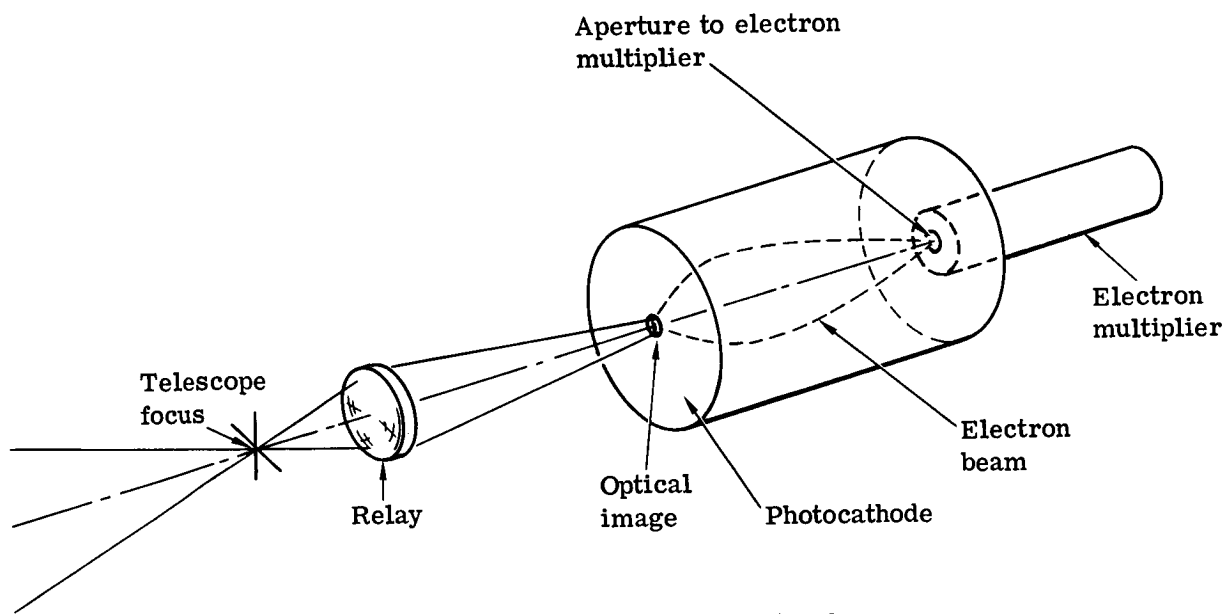


Fig. C.5-26 — Image dissector tracker

electric or magnetic field so that it enters the aperture that is also the entrance to an electron multiplier. A circular nutation of the electron image is created by time-varying electric or magnetic fields so that the electron image moves around the edge of the circular aperture. So long as the average position is exactly centered on the aperture, a steady direct current enters the multiplier. If the image is slightly off center, a sinusoidal signal is added to the average whose amplitude and phase represent the magnitude and direction of deviation from the average. This sinusoid is demodulated and used to correct the average offset value until the error signal becomes zero. The average offset is then read out as the location of the star being tracked.

This optical position sensor thus incorporates a closed loop that operates at a bandwidth about an order of magnitude higher than the secondary mirror tracking loop; it should not be confused with it. The jitter accuracy limit is set by shot noise in the demodulated signal that is unavoidably fed around the loop as an error signal and causes a corresponding jitter in the average that is read out as the position signal. If four optical spots nutating in unison around four apertures are present, the four multiplier outputs are summed and operation is the same.

### Signal Current

The useful current for a given guide star is a direct function of the radiation collected and the image dissector sensitivity. The current is

$$I_O = 2.65 \times 10^{-(6 + 0.4m_v)} A_C \tau S \eta$$

where

- $m_v$  = star visual magnitude
- $A_C$  = collecting area =  $\pi D^2/4$
- $\tau$  = optical transmission including effects of obscuration, scattering, absorption, and reflection
- $S$  = photocathode sensitivity to light of the color class of the guide star
- $\eta$  = counting efficiency of the image dissector aperture/multiplier

The mean electron event rate  $\dot{\eta}$  is found from the current and the electron charge:

$$\dot{\eta} = 2.65 \times 10^{-(6 + 0.4m_v)} A_C \tau S \eta / e$$

If tracking is accomplished on a guide star of visual magnitude 13 and color class G3, with a 3-meter-diameter aperture, 40 percent transmission, 200-microamp/lumen photocathode sensitivity to 5,500°K radiation, and 60 percent counting efficiency, these expressions become

$$I_O = 5.65 \times 10^{-15} \text{ amp} = 3.53 \times 10^4 \text{ electrons/sec}$$

### Dark Current and Noise Sources

To verify that the subsequent analysis is valid, it is necessary to examine the amount of dark current flowing through the sensor, i.e., the output current or count rate measured when no star is present. It must be less by a factor of three or so than the current due to the dimmest guide star used in order that the tracking jitter be due solely to the noise in the signal current generated by the guide star.

Three sources of dark current may be present. The image dissector is subject to random internal emissions that come from the photocathode, from stray areas inside the tube on which photocathode material was unintentionally deposited, and from field emission at sharp edges on high voltage grids. Second, there may be ohmic leakage along the glass or ceramic walls of the multiplier structure and through the mount. Third, the diffuse background surrounding the guide star is also imaged and detected.

The most fundamental of these is the sky background since it is an inherent part of the problem rather than a property of the proposed solution. The astronomical background in earth orbit is made up of diffuse sunlight scattered by debris in the solar system and of other stars dimmer than the guide star. The scattered sunlight is a function of pointing angle with respect to the sun and ranges from a minimum radiance of  $N_B = 3.5 \times 10^{-5}$  lumen/m<sup>2</sup>-steradian (visual magnitude of 23.75/arc-second<sup>2</sup>) to a practical maximum for the LST of  $6.2 \times 10^{-4}$  lumen/m<sup>2</sup>-steradian when viewing in the ecliptic plane 0.79 radian (45 degrees) from the sun. The effective photocathode current produced by this background in an aperture of area  $A_c$  with a focal ratio of  $N_f$  is

$$I_b = \frac{\pi}{4} \frac{N_b}{N_f^2} \tau S \eta A_c$$

If it is necessary that the background current be no more than 1/10 the current from a star of visual magnitude 13 when tracking against the brightest background, then the maximum diameter aperture that may be used in the image dissector is

$$D_A = 0.176 N_f$$

At  $f/12$ , the maximum diameter is about 2 millimeters. This maximum size aperture subtends a solid angle of  $2.42 \times 10^{-9}$  steradian at any focal ratio. This angle is sufficiently small that there will normally be no unresolved stars adding to the background. If one is present, its effect will normally be to cause a constant slight offset in pointing direction. For viewing toward the galactic center, the probability of having a second star of visual magnitude brighter than 15.5 in the maximum aperture is less than 5 percent and is proportionately less with smaller apertures and lower background.

The photocathode current density at  $f/12$  due to the lowest background level listed above is

$$J_B = \frac{I_B}{A_c} = \frac{\pi}{4} \left( \frac{N_B}{N_f^2} \right) \tau S \eta = 1.22 \times 10^{-15} \text{ amp/cm}^2$$

This is the approximate effective dark current at 20°C from a state of the art S-20 photocathode/electron optics structure in image intensifiers with high red response. Dark current may be one to two orders of magnitude lower in tubes optimized for sensitivity to 5,500°K radiation and designed for low background emission. Therefore, dark emission inside the tube is easily made negligible as compared to photocurrent from the astronomical background.

It may be concluded that by proper selection of aperture size and proper design and fabrication of photocathode and high voltage grids, background may be made to at least 10 times less than the signal current from a star of visual magnitude 13. The final source of noise to be considered is leakage current at the output. Anode leakage produces a finite current owing to the high voltage gradient between the anode pin and lower voltage pins nearby. The leakage is probably due to surface leakage along the glass and is accentuated by contaminants on the surface. Typical amounts are  $10^{-10}$  to  $10^{-9}$  ampere. The noise in it, though, is several orders of magnitude less than the peak current owing to the individual photoelectron pulses (about  $10^{-6}$  ampere for  $B = 10^7$  hz and  $G = 10^6$ ).

It is clear that by selecting the photon counting mode of operation and by properly designing the tube, all sources of noise other than shot noise in the signal current may be made negligible.

#### Optical Line Spread Function

In the stabilized condition, the guide star image is held on the peak of the reticle prism so that equal amounts of energy from the image go to the four quadrants of the detector. As the line of sight deviates from this condition,

the energy is transferred from one quadrant to another. This transfer function for each of the astigmatic images is given in Fig. C.5-27 as computed for the LST for 0.6-micrometer-wavelength light.

The line spread function is the energy distribution across the width of the astigmatic image (Fig. C.5-27). This latter curve is simply the slope of the former. The computed data show that the line spread function  $F_1$  has a peak value  $F_1(0)$  of 38 percent per tenth of a microradian line-of-sight deviation, or  $3.8 \times 10^6$  per radian.

Several factors were not taken into account in computing the line spread function. The computation assumed a perfectly made telescope, not including effects of manufacturing errors, misalignment, and thermal disturbances. Slight chromatic degradations from the reticle plate were not included, but the point spread function has been computed at the long wavelength end of the spectrum, so that a spectrally averaged curve would show a somewhat higher peak. Defects in the reticle grating were not considered. To allow for these degradations, a somewhat lower peak value for the line transfer function ( $3.0 \times 10^6$ ) was chosen for the line-of-sight noise calculations that follow.

### Image Dissector Tracking

The method of signal modulation may be seen by referring to Fig. C.5-28. The focused electron image of the star is nutated in a circle whose radius is equal to that of the circular aperture by deflection currents (assuming magnetic scan) of

$$I_{dx} = I_{do} \cos 2\pi FT$$

$$I_{dy} = I_{do} \sin 2\pi FT$$

If the average values of the deflection currents are such that the center of nutation coincides with the center of the circular aperture, a steady current flows into the aperture and is multiplied by the electron multiplier. If the current approaching the aperture is  $I_0$ , the average current into the aperture is  $I_0/2$ .

If the center of nutation is displaced by a small  $\Delta r$  at an angle of  $\phi$ ,

$$\Delta x = \Delta r \cos \phi$$

$$\Delta y = \Delta r \sin \phi$$

A sinusoidal error signal is now superimposed on the current entering the aperture. In addition, there is shot noise in the current owing to statistical fluctuation in the number of photoelectrons emitted, which is

$$I_{s,rms} = e I_0 B^{1/2}$$

The total current through the aperture for small displacements is

$$I_s = I_0 \left[ \frac{1}{2} - F_1(0) \Delta r \cos (2\pi Ft - \phi) \right] + I_{s,rms}$$

This consists of a dc component, shot noise, and a sinusoid whose amplitude and phase carry the information on magnitude and direction of displacement.

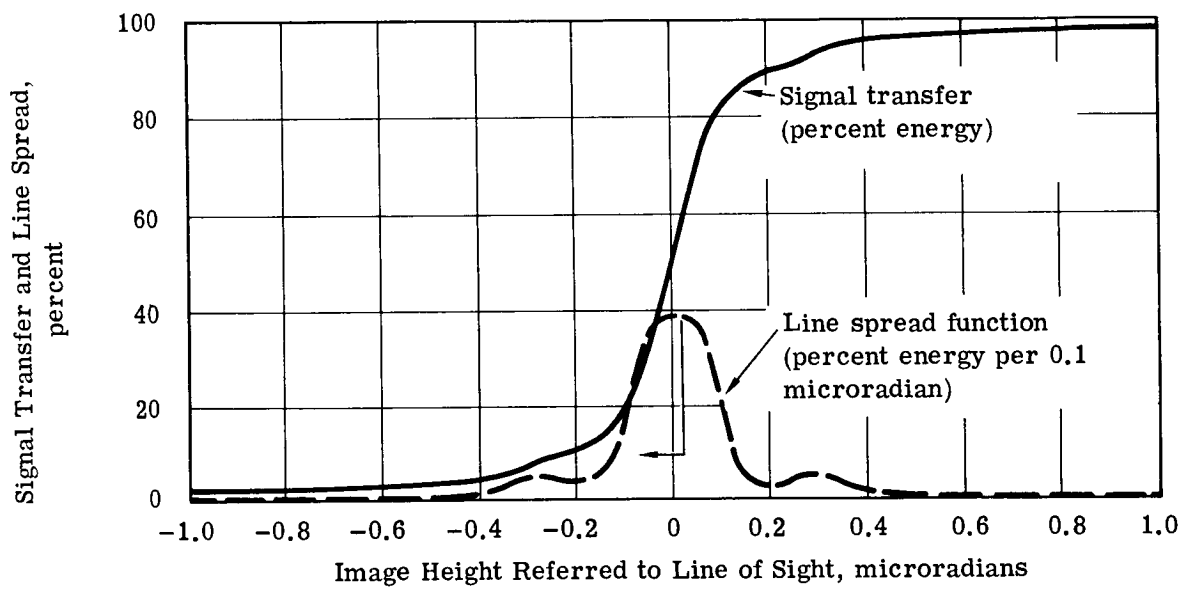
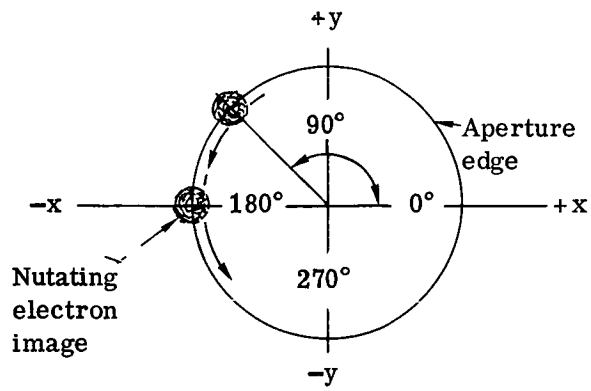
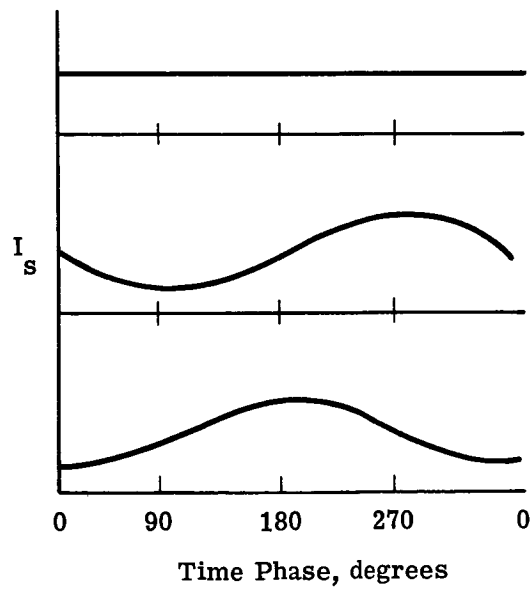


Fig. C.5-27 — Line spread function and signal transfer function for astigmatic images at LST focal plane (3.5 milliradians off axis,  $\lambda = 633$  nanometers)





(a) Optical spot moving around edge of aperture



(b) Output current waveforms

Fig. C.5-28 — Image dissector tracker—method of signal modulation

The method of demodulation is to multiply  $I_s$  by the two deflection waveforms, and average this, removing the existing dc component to produce two new dc components whose magnitudes represent  $\Delta x$  and  $\Delta y$ .

To recover the x error signal, for instance, the demodulated output signal  $I_x$  is

$$I_x = I_s I_{dx}$$

$$I_x = \frac{I_{do} \bar{I}_o}{2} \cos 2\pi Ft - I_{dx} \bar{I}_o F_1(0) \Delta r (\cos^2 2\pi Ft \cos \phi - \sin 2\pi Ft \cos 2\pi Ft \cos \phi)$$

$$+ I_{do} I_{s,rms} \cos 2\pi Ft$$

After low pass filtering of bandwidth  $B$ , the values of the mean and the rms of this are

$$\bar{I}_x = - \frac{I_{do} I_o F_1(0) \Delta r \cos \phi}{2}$$

$$= - \frac{I_{do} I_o F_1(0)}{2} \Delta x$$

$$I_{x,rms} = I_{do} I_{s,rms} / \sqrt{2} = I_{do} \frac{(e I_o B)^{1/2}}{2^{1/2}}$$

The signal to noise (S/N) ratio is

$$S/N_x = \bar{I}_x / I_{x,rms} = \left( \frac{I_o}{2eB} \right)^{1/2} F_1(0) \Delta x$$

Similarly, to recover the y error signal

$$\bar{I}_y = - \frac{I_{do} \bar{I}_o F_1(0)}{2} \Delta y$$

$$I_{y,rms} = I_{do} \left( \frac{e I_o B}{2} \right)^{1/2}$$

$$S/N_y = \left( \frac{I_o}{2eB} \right)^{1/2} F_1(0) \Delta y$$

### Reticle Tracking

The method of modulation was shown in Fig. C.5-22, which indicates the star being split into four separate beams. Each of the four is fed into a photomultiplier (all of which may be in a common bottle with steerable electron optics in the form of a multiple aperture image dissector). The information is demodulated by subtracting the outputs of the four photomultipliers:

$$\bar{I}_x = (I_1 G_1 + I_2 G_2) - (I_3 G_3 + I_4 G_4)$$

$$\bar{I}_y = (I_1 G_1 + I_3 G_3) - (I_2 G_2 + I_4 G_4)$$

Since the reticle is simply shifting light from one beam to the other as the optical spot is displaced with respect to the reticle intersection, the difference currents may be given by

$$\bar{I}_x = 2 \bar{I}_0 G F_1(0) \Delta x$$

$$\bar{I}_y = 2 \bar{I}_0 G F_1(0) \Delta y$$

where

$$I_0 = I_1 + I_2 + I_3 + I_4$$

$$G = G_1 = G_2 = G_3 = G_4$$

The noises in these currents due to shot noise are

$$I_{x,rms} = I_{y,rms} = (2 e I_0 B)^{1/2} G$$

The signal to noise ratios are

$$S/N_x = \left( \frac{2 I_0}{eB} \right)^{1/2} F_1(0) \Delta x$$

$$S/N_y = \left( \frac{2 I_0}{eB} \right)^{1/2} F_1(0) \Delta y$$

The error signals may be derived just as well by counting the individual pulses representing photoelectrons and adding and subtracting them. The statistically limited accuracy is not changed and possible losses of accuracy due to leakage current, nonuniform gain in the four channels, cosmic ray events, and multiplier dark current affecting the analog processing are eliminated. The signal transfers in terms of count rates  $n$  become

$$\bar{n}_x = 2 \dot{n}_0 T F_1(0) \Delta x$$

$$\bar{n}_y = 2 \dot{n}_0 T F_1(0) \Delta y$$

$$n_{x,rms} = n_{y,rms} = (\dot{n}_0 T)^{1/2}$$

$$S/N_x = 2 (\dot{n}_0 T)^{1/2} F_1(0) \Delta x$$

$$S/N_y = 2 (\dot{n}_0 T)^{1/2} F_1(0) \Delta y$$

on making the substitutions  $I = \dot{n}e$  and  $B = 1/2T$  and eliminating  $G$  since the multiplier multiplies charge but not events.

If an image dissector incorporating only one aperture is used, it will sequentially sample the four beams (by image steering) at a rate higher than the data rate. The average currents  $\bar{I}$  will thus be smaller by a factor of four (or equivalently, the sampling time  $T$  will be shorter by a factor of four). In this case, the transfer signals and signal-to-noise ratios will be

$$\bar{I}_x = \frac{I_0}{2} G F_1(0) \Delta x$$

$$\bar{n}_x = \frac{\dot{n}}{2} F_1(0) \Delta x$$

$$S/N_x = \left( \frac{I_0}{2eB} \right)^{1/2} F_1(0) \Delta x = (\dot{n} T)^{1/2} F_1(0) \Delta x$$

The expressions for  $y$  are similar.

### Tracking Jitter

The rms jitter is obtained by solving for  $\Delta x$  with  $S/N = 1$ . For the image dissector tracking mode

$$\Delta x = \Delta y = \frac{(2eB/I_0)^{1/2}}{F_1(0)} = \frac{1}{(\dot{n} T)^{1/2} F_1(0)}$$

For the refractive reticle tracking mode with four multipliers

$$\Delta x = \Delta y = \frac{(eB/2I_0)^{1/2}}{F_1(0)} = \frac{1}{2(\dot{n}_0 T)^{1/2} F_1(0)}$$

For the refractive reticle tracking mode with a single time-shared electron multiplier,

$$\Delta x = \Delta y = \frac{(2eB/I_0)^{1/2}}{F_1(0)} = \frac{1}{(\dot{n} T)^{1/2} F_1(0)}$$

Note that in each case the jitter is directly dependent upon  $F_1(0)$ , the slope of the optical energy line transfer function or the peak of the line spread function. This stresses the importance of high image quality and reticle sharpness.

In terms of the signal currents from a star of visual magnitude 13 and a peak value of  $3 \times 10^6$ /radian for the line spread function, the jitter for the image dissector tracking is

$$\begin{aligned} \Delta x = \Delta y &= 2.5 \times 10^{-9} \sqrt{B} \text{ radian} \\ &= 1.77 \times 10^{-9} / \sqrt{T} \text{ radian} \end{aligned}$$

For a refractive reticle tracker with four multipliers

$$\begin{aligned} \Delta x = \Delta y &= 1.25 \times 10^{-9} \sqrt{B} \text{ radian} \\ &= 0.885 \times 10^{-9} / \sqrt{T} \text{ radian} \end{aligned}$$

For a refractive reticle tracker with a single time-shared multiplier,

$$\begin{aligned}\Delta x = \Delta y &= 2.5 \times 10^{-9} \sqrt{B} \text{ radian} \\ &= 1.77 \lambda \cdot 10^{-9} / \sqrt{T} \text{ radian}\end{aligned}$$

The tracking accuracy of a tracker incorporating four multipliers is shown for operation in the reticle mode in Fig. C.5-29 and the image dissector mode in Fig. C.5-30.

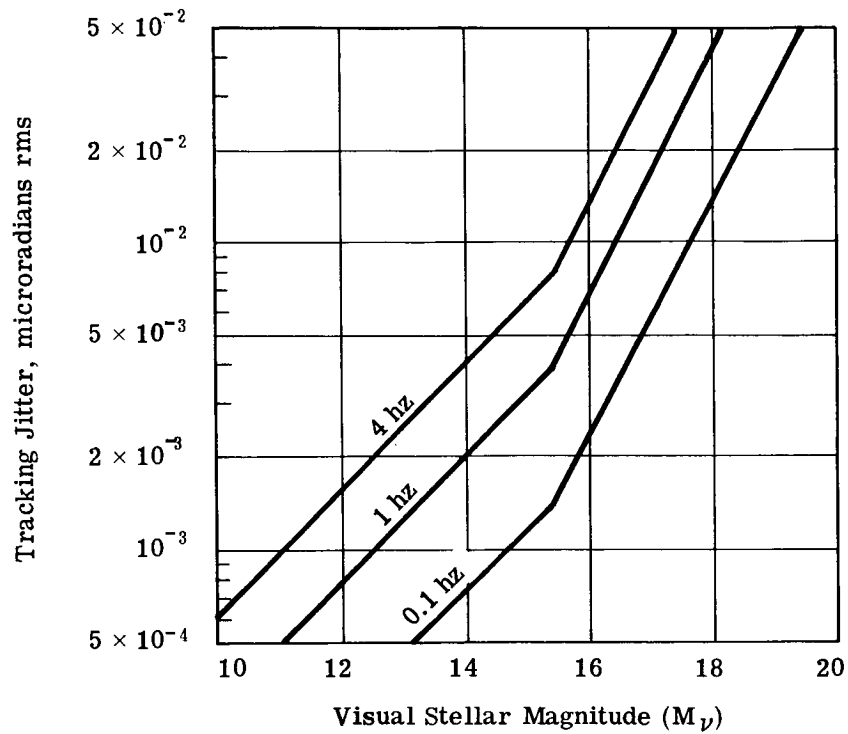
#### C.5.c(7) Technology for Production of Prismatic Gratings

The techniques used in production of prismatic gratings directly influence the steepness of the transfer function of the star tracking sensor. Defects resulting from these techniques reduce the amount of available tracking field area and open a possibility of having accidental or false coincidences of guide star and tracking intersection of prisms. To date, two bodies of existing technology have been identified, and with deeper study, it is probable that more will be uncovered. These two existing sources of gratings are (1) producers of replicated diffraction gratings and (2) producers of Fresnel lenses. Diffraction grating techniques have been briefly investigated and have proven surprisingly successful for an initial brief study. Modern techniques for producing Fresnel lenses using hot diamond ruling techniques have great potential in reducing the number of surface defects in the final replica. The following photographs reveal some of these technology problems.

Fig. C.5-31 shows a dark field photomicrograph of a prismatic grating produced by standard replication techniques from an aluminum master. This master was produced by ruling a block of aluminum with a heavily loaded diamond point of 2.09 radians (120 degrees) included angle. The grating shown is an epoxy replica taken from the monolithic aluminum master. Therefore the peaks of the replica grooves correspond to the point of the original diamond, while the valleys are the result of the coming together of successive rulings. The dark field picture is taken by using a narrow cone of illumination in a conventional microscope. Since the 0.52-radian (30-degree) prism angles would deflect all the light away from the microscope objective, a perfect prismatic grating would result in a perfectly black picture. Every surface of the grating that is approximately normal to the microscope axis will transmit light and appear as a bright area. Therefore, the light areas on this photomicrograph display the imperfections in the grating replica. It can be seen that the lines have alternating intensities, indicating that the peaks and valleys have different optical quality, because the peaks are best. Unfortunately, it is difficult to interpret exactly from this type of picture how sharp these peaks are because of the low magnification and diffraction effects.

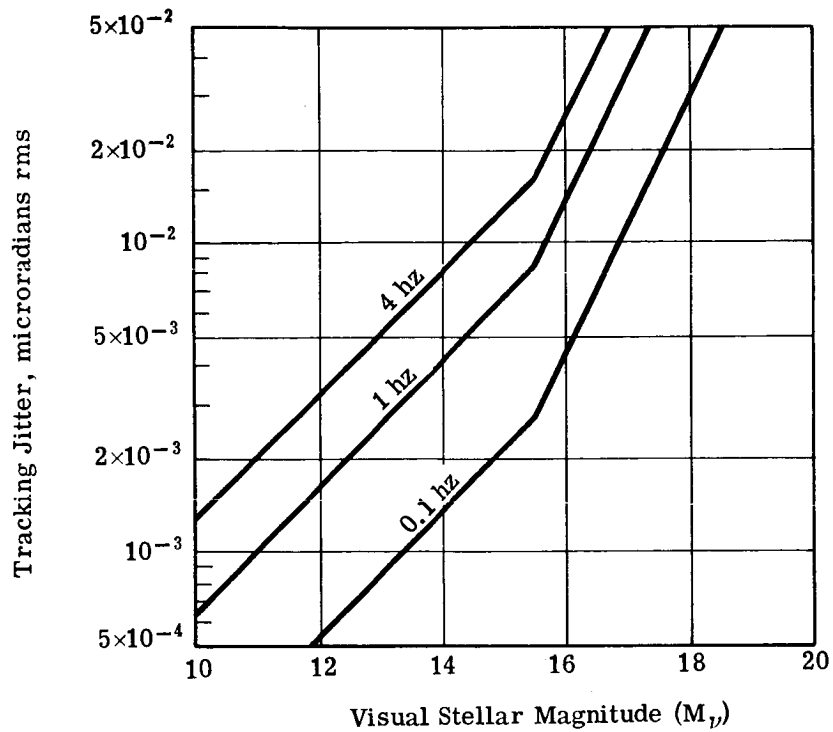
In an attempt to improve the visibility of the groove profile, pictures were made in a scanning electron microscope of the prismatic grating surface. Fig. C.5-32 was taken at approximately the same magnification as Fig. C.5-31. The photograph was taken near the edge of the glass substrate near a point where some of the replica grating was torn away in sawing the sample. Therefore, it is possible to observe a cut section through the grating in some places. The arrow indicates the section that was further magnified in the next picture (Fig. C.5.33). At this magnification (75X), it is not possible to resolve the shape of the prism edges.

Fig. C.5-33 shows this prism section at a magnification of 1,000X. In this particular area, it can be seen that the edge is small as compared to the width of the prism (0.1 millimeter), if the sharp bright line is an indication of the width of the true edge, 0.3 millimeter on the picture or about 0.3 micrometer on the grating itself. The fluffy material below is the fractured epoxy that is still sticking to the glass substrate. It is clear that if the overall grating edges can be produced to this quality, they will have negligible effect on the star image, which is of the order of 14 micrometers in the  $f/12$  focal plane. More microscopic work must be done to verify the interpretation of this kind of image and that the bright line is not broadened due to field fringing or such effects.



3-meter telescope aperture  
 30 percent obscuration  
 $0.1\lambda$  WFE  
 40 percent optical transmission  
 G3 target star  
 S-20 photocathode (200  $\mu$ amp/lumen)  
 60 percent multiplier counting efficiency  
 30 percent per 0.1  $\mu$ rad optical energy transfer function  
 2-millimeter image dissector aperture

Fig. C.5-29 — Photoelectron noise limit to tracking accuracy, refractive reticle mode



3-meter telescope aperture  
 30 percent obscuration  
 0.1λ WFE  
 40 percent optical transmission  
 G3 target star  
 S-20 photocathode (200 μamp/lumen)  
 60 percent multiplier counting efficiency  
 30 percent per 0.1 μrad optical energy transfer function  
 2-millimeter image dissector aperture

Fig. C.5-30 — Photoelectron noise limit to tracking accuracy, image dissector mode

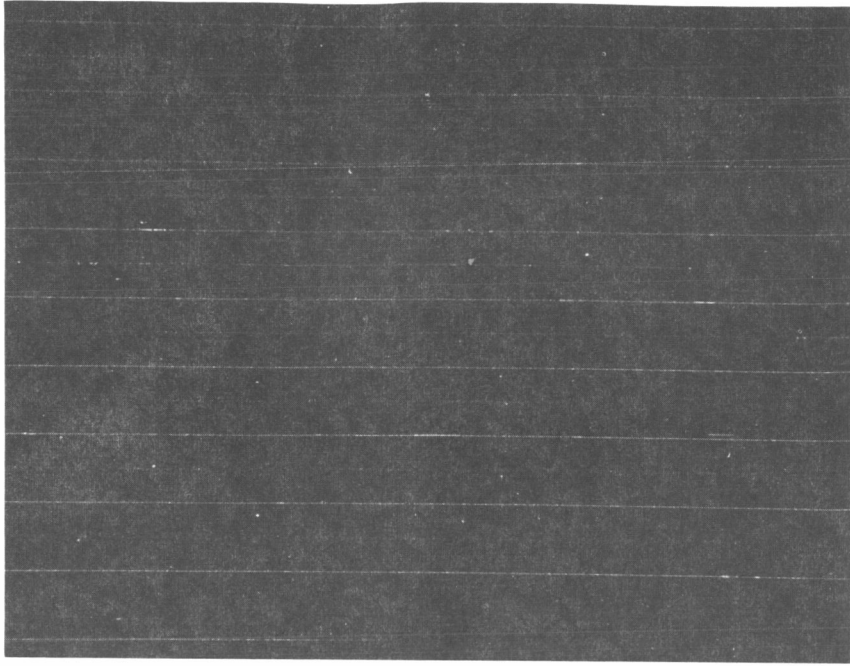


Fig. C.5-31 — Dark field optical photomicrograph of prismatic grating (92 $\times$ )

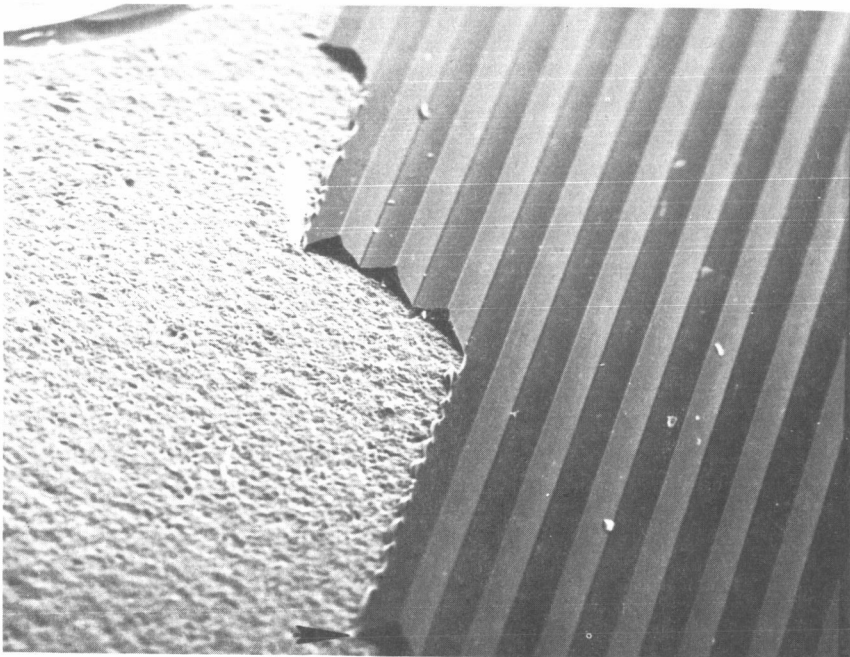


Fig. C.5-32 — Scanning electron microscope photograph of prismatic grating (83 $\times$ )



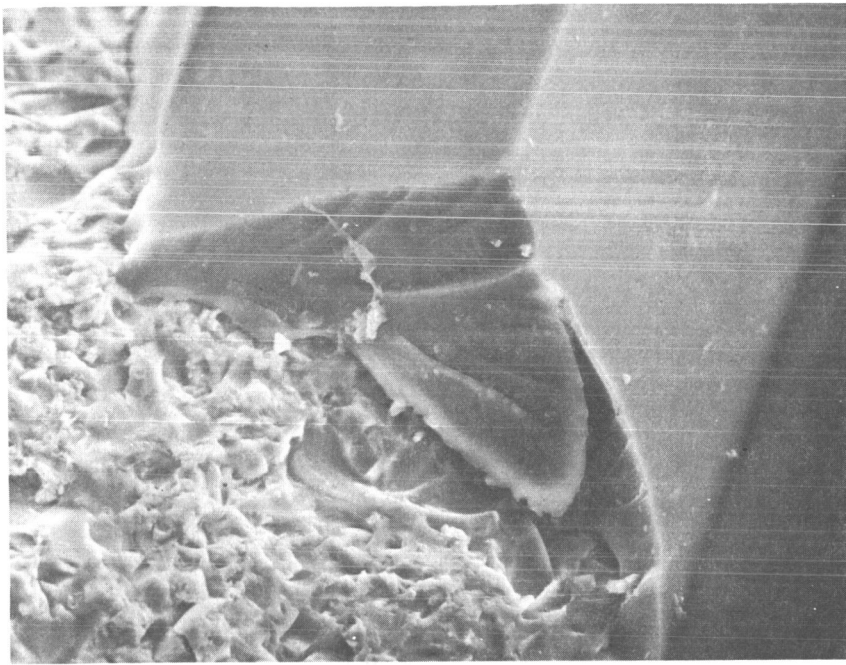


Fig. C.5-33 — Scanning electron microscope photograph of edge pointed out in Fig. C.5-32 (1,000 $\times$ )



Fig. C.5-34 — Scanning electron microscope photograph of surface defects of master grating occlusions replicated in prismatic grating (1,660 $\times$ )

Fig. C.5-34 shows some of the characteristic surface defects encountered on this grating. It is suspected that these are caused by the dragging of occlusions or dirt between the diamond and the metal surface being ruled. To be sure of their origin, stereo photographs would have to be taken to verify whether these defects project out from the replica or the opposite. Since the hot diamond techniques used in the production of Fresnel lenses also result in much better surface finishes, these bear future investigation. It is possible that less sharp edges would result.

Existing grating technologies used in this series of pictures and related transfer function measurements clearly establish the feasibility of producing prism edges that are small compared to the scale of an  $f/12$  star image for the LST. These gratings could be useful in the offset fine guidance system proposed by Itek.

#### C.5.c(8) Optical Micrometer for Guide Field

The optical micrometer for the guide field (Fig. C.5-24) consists of a plane parallel refracting plate that covers the entire area in front of the guide field. The plate is mounted on gimbals so that it can be tipped to offset slightly the light passing through the plate to the guide field. The central portion of the plate, in front of the data field, is cut away so that the data field is unaffected by the plate. Thus, the plate can be used to produce a differential shift of the positions of the data and guide fields.

The optical micrometer has four potential functions: (1) to compensate internal deflections within the  $f/96$  relay path to the high resolution imagery cameras as detected by the artificial star sensors, (2) to compensate for differential velocity aberrations, (3) to compensate for planet motions relative to the guide stars during planetary observation, and (4) to provide pointing interpolation between the grid lines of the reticle plate.

Thermally induced deflection in the  $f/96$  relay path during an observation will be equivalent to a fraction of a milliradian line-of-sight motion. Tipping of the optical micrometer, which then causes a change in the telescope pointing, is an open loop alternative to compensating for thermal drift by closed loop motion of a component within the  $f/96$  relay system.

Differential velocity aberration between the guide stars and the data star will be, at most, about 0.1 microradian (0.02 arc-second) (see Fig. C.5-35) for a 3.49-milliradian (12-arc-minute) field of view.

The planet motions to be accommodated are treated in "Planetary Motion During Full-Spectrum Exposure," LST-72-100, and "Observation of Planets, Asteroids, and Comets," LST-72-105a. It appears that all the planets can be observed in white light with an exposure time short enough that the planetary motion is a fraction of a milliradian. For narrow band observation (e.g., 3 nanometers at 200 nanometers wavelength), motions of some of the planets during the exposure time required are of several or many milliradians magnitude. An attending problem is that of the rotation of the planet itself about its own axis, which causes relative motion of one part of the planet with respect to another.

Table C.5-5 gives motions that might be accommodated by the optical micrometer for full spectrum exposure, limited spectrum exposure (3 nanometers at 200 nanometers), and exposure limited to the time in which differential motion within the planet itself is 0.025 microradian (0.005 arc-second). Because of the differential motions from planet rotation, it would appear from Table C.5-5 that the ability to accommodate motions greater than about 20 microradians (4 arc-seconds) would have limited use. At the same time, a 20-microradian (4-arc-second) range of the optical micrometer represents a range beyond which accuracy of the micrometer [at 20 microradians (4 arc-seconds), it must be accurate to about 1 part in 4,000] and lateral color aberrations become problems of significance.

The reticle grid is to have a spacing corresponding to about 10 microradians (2 arc-seconds) in object space. To point the telescope to any location and still have the guide star fall on a reticle groove requires at least a 10-microradian (2-arc-second) total range in the optical micrometer for interpolation.

From the considerations given above, it is proposed to use an optical micrometer with a total range of about 20 microradians (4 arc-seconds) equivalent line-of-sight motion [10 microradians ( $\pm 2$  arc-seconds) about the mean position].

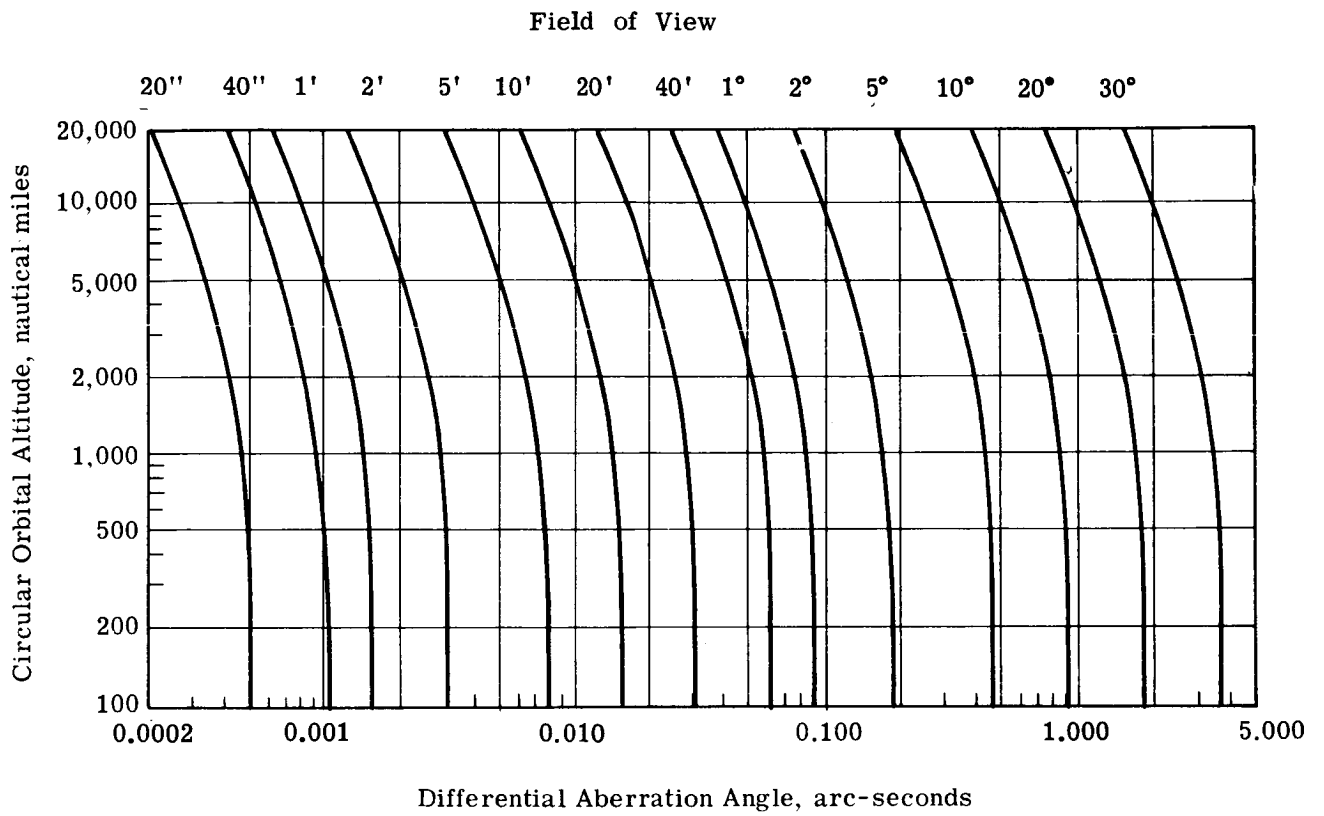


Fig. C.5-35 — Maximum value of differential aberration versus orbital altitude for several separations of two stars

Table C.5-5 – Planetary Motions To Be Accommodated by Optical Micrometer, Microradians (Arc-Seconds)

	Mars	Venus	Mercury	Jupiter	Saturn	Uranus	Neptune	Pluto
Full exposure, full spectrum	<0.005 (<0.001)	<0.005 (<0.001)	<0.005 (<0.001)	<0.005 (<0.001)	0.0068 (0.0014)	0.009 (0.002)	0.0170 (0.0035)	0.076 (0.016)
Full exposure 3-nanometer band at 200 nanometers	0.383 (0.079)	0.155 (0.032)	(2.1)	10.2 (2.8)	21.8 (4.5)	29.6 (6.1)	50.4 (10.4)	223 (46)
Exposure limited by 0.025-microradian (0.005-arc-second) rotational motion of planet	335 (69)	281 (58)	0.58 (0.12)	0.0320 (0.0066)	0.0470 (0.0097)	0.145 (0.030)	0.228 (0.047)	17.9 (3.7)

The first-order equations that apply to the operation of the optical micrometer are

$$\delta = t\alpha(n - 1)/n$$

$$\Delta\delta/\delta = \Delta n/n/(n - 1)$$

where  $\delta$  = displacement introduced by a tip of the plate  
 $\Delta\delta$  = lateral color smear accompanying the tip  
 $\alpha$  = angle of tip of the plate  
 $t$  = thickness of the plate  
 $n$  = index of refraction of the plate  
 $\Delta n$  = variation of index over the spectral region of interest

For a micrometer range of  $\pm 10$  microradians ( $\pm 2$  arc-seconds), the required focal plane motion is  $\delta = 0.3$  millimeter. Over a spectral range of 0.4- to 0.6-micrometer wavelength, fused silica has a mean index of  $n = 1.46$  and an index variation of  $\Delta n = 0.012$ . For a thickness  $t = 20$  millimeters, the angle of tip to cover the 10 microradians ( $\pm 2$  arc-seconds) is 0.0477 radian. At the edge of the plate (a 125-millimeter radius), the motion required is  $\pm 60$  millimeters. The lateral color smear ratio is  $\Delta\delta/\delta = 0.018$ . For a normal (nonplanetary) observation, the maximum plate deviation would be the 5 microradians (1 arc-second) interpolation distance to the nearest grid line, over which range the lateral color smear would be 0.09 microradian (0.018 arc-second), a relatively small fraction of the Airy disk size of 0.5 microradian (0.1 arc-second). The effect of this smear is to round out the guide signal transfer function somewhat (Fig. C.5-36), although the maximum slope, and consequently the sensitivity at null, is affected only to a negligible degree. The chief effect is that the scale constant of the optical micrometer becomes a function of the spectrum of the particular guide star being used and the spectral sensitivity of the guide detector; a reasonable tolerance for calibration of the scale factor must be taken into account in the error budget.

The monochromatic scale factor for the plate can be determined to within 40 parts per million simply by measuring the thickness of the plate and its index of refraction. For the effects of color smear to be very small in the case of planet tracking [e.g., 0.005 microradian (0.001 arc-second)], the centroid of the smeared image must be determined to a small fraction of the amount of color smear [e.g., 1.4 percent for tracking a planet through the full 20-microradian (4-arc-second) range of the optical micrometer]. For star observation in which the maximum motion to be accommodated is on the order of 0.1 microradian (0.02 arc-second), the problem of knowing the scale factor is much less severe.

The sensor that measures the tilt of the plate must be linear to about 0.025 percent over the 20-microradian (4-arc-second) range to give a 0.005-microradian (0.001-arc-second) error. For the more limited excursions of star observations, the error of the sensor probably would not be reduced in proportion.

Factors that have not been evaluated are the linearity of the optical function of the optical micrometer and whether or not compensation must be made for the nonlinearity in the control of the plate tip.

#### C.5.c(9) Lock-On Sequence and Fine Track

A general configuration and operating sequence for a reticle star tracker was developed for use aboard an LST. A coarse positioning mode aims the telescope to within 1 microradian (0.2 arc-second), at which point the fine positioning mode takes over to aim the telescope precisely.

Fig. C.5-37 is a functional block diagram showing the major system components, which include

1. Sequencer/controller, that receives the desired position and positioning mode commands and sends an error vector to the secondary mirror positioning loop. It controls the scan sequence and nutation generators and

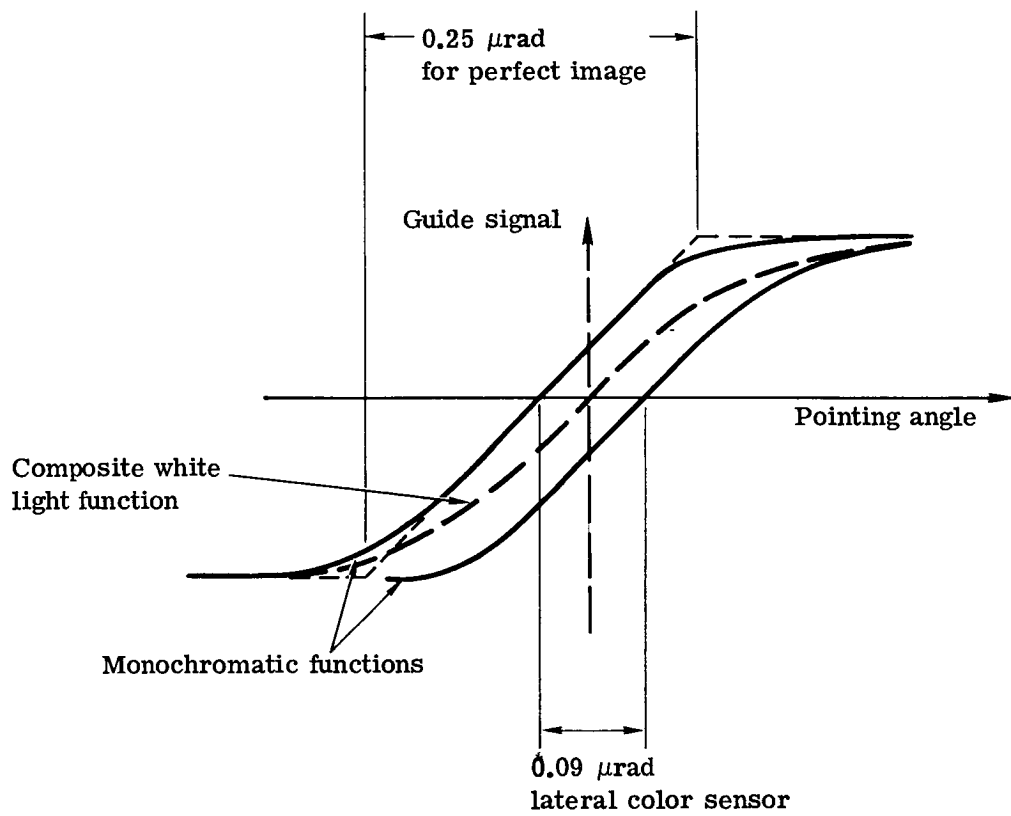


Fig. C.5-36 — Effect of lateral color smear on guide signal transfer function

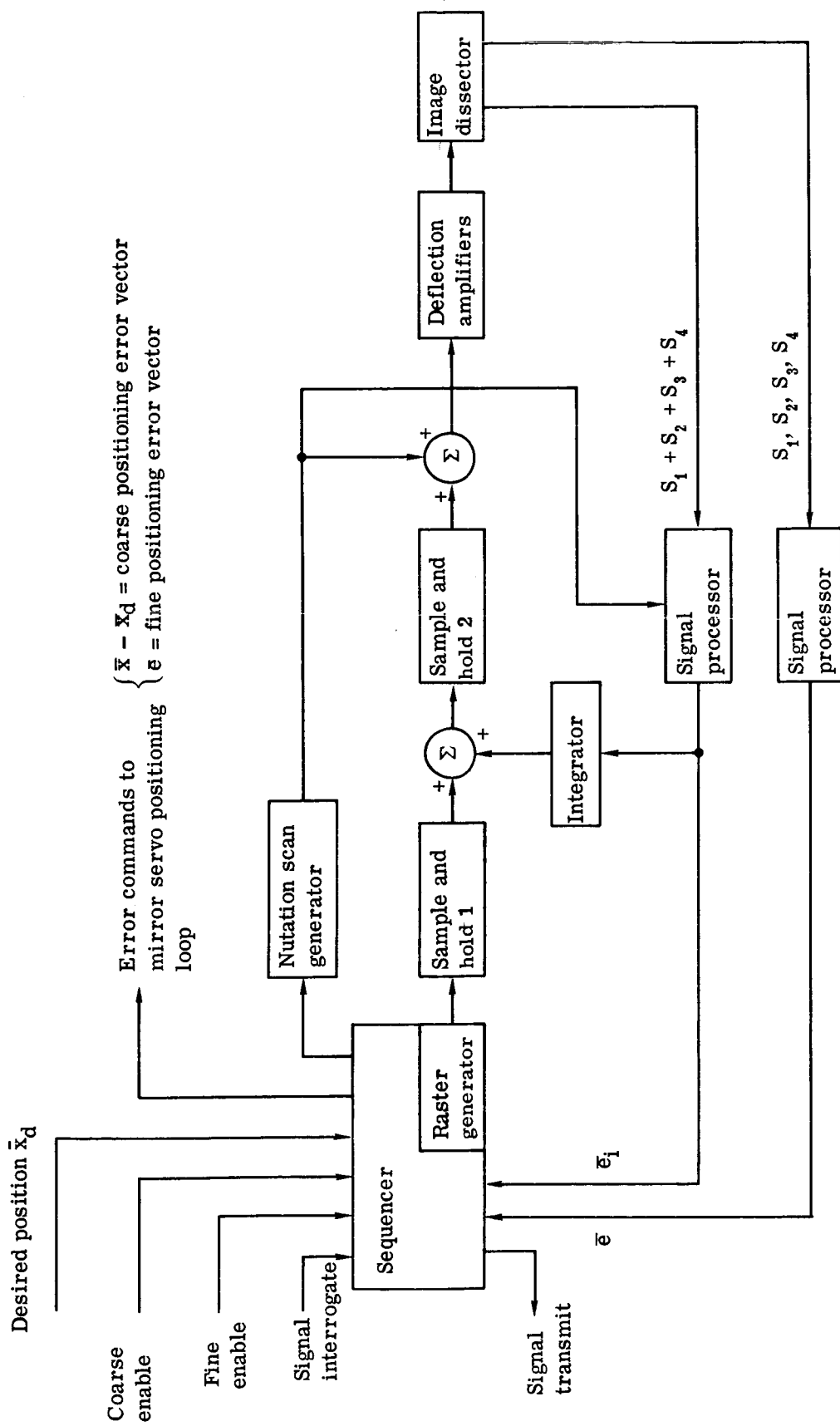


Fig. C.5-37 — Functional diagram of reticle star tracker

determines how to process the image dissector output. The major decision points and feedback loops of this device are indicated in Fig. C.5-37 and the following paragraphs.

2. A four-channel image dissector tube and associated deflection amplifiers
3. A reticle that divides the star image into four parts whose ratio depends on the star's precise position
4. A nutation scan generator that superimposes a circular nutation on the scan sequence.
5. Two signal processors, one for each of the positioning modes.

As presently envisioned, the individual guide head will track the x and y coordinate positions independently of each other.

#### Coarse Positioning Mode

Figs. C.5-38 and C.5-39 show the system operation in the coarse positioning mode. The outputs of the four image intensifier channels are summed together so that they act as a single aperture. This aperture is scanned over the photocathode. A high frequency circular nutation whose diameter is equal to the aperture diameter is superimposed on this scan and the output is synchronously demodulated to detect the desired star. The output of the signal processor is an error vector indicating the offset between the center of nutation and the center of aperture.

Fig. C.5-38 shows the initial acquisition phase. The scan is stepped digitally across the photocathode. When a star is detected, the magnitude of the step is decreased and the stepping is continued until the demodulated output indicates that the star image is sufficiently within the aperture to activate a linear servo loop.

The scan generator output is then clamped to its current value and a linear servo positioning loop is activated (Fig. C.5-39). Integrating the error vector output of the signal processor and adding it to the clamped scan generator output results in a feedback loop positioning the center of the nutation on the center of the aperture. When the error vector output of the signal processor is within the desired bounds, the current position of the telescope can be determined from the direct current output of the image dissector deflection amplifiers.

The indicated current position can then be compared with the desired position and a command signal sent to the secondary mirror positioning loop. The bandwidth of the position sensing loop should be much higher (an order of magnitude or more) than that of the mirror positioning loop so that it may continue to track accurately the present position as the secondary mirror adjusts it to the desired position.

#### Fine Positioning Mode

When the indicated and the desired positions are within the necessary tolerances, the fine positioning mode can be activated (Fig. C.5-40). The coarse positioning mode should ideally be accurate enough to position the star image on the reticle so that it is split into four images, but this is not necessary for handoff.

The nutation scan generator is shut off, and the direct current voltage on the deflection amplifier is clamped and held digitally. An error vector is generated by comparing the relative intensities in the four channels, which in turn indicates the offset of the star from the reticle ridge. This is fed to the secondary mirror positioning loop, which attempts to null the offset. When this error vector is within the desired tolerances, a lock-on signal is sent to the guidance computer.

The tracker will remain in this mode until a standby or shutdown command is received.

#### Flow Chart for Operating Sequence

Fig. C.5-41 is a flow chart of the operation of the tracking head as directed by the sequencer in going through its acquisition and lock-on routine. The amount of logic involved is rather modest; Itek expects that it will be included in the tracking head rather than be supplied by central computation facilities in order to have the tracking heads as self-contained as possible and to reduce mechanical cable loading.



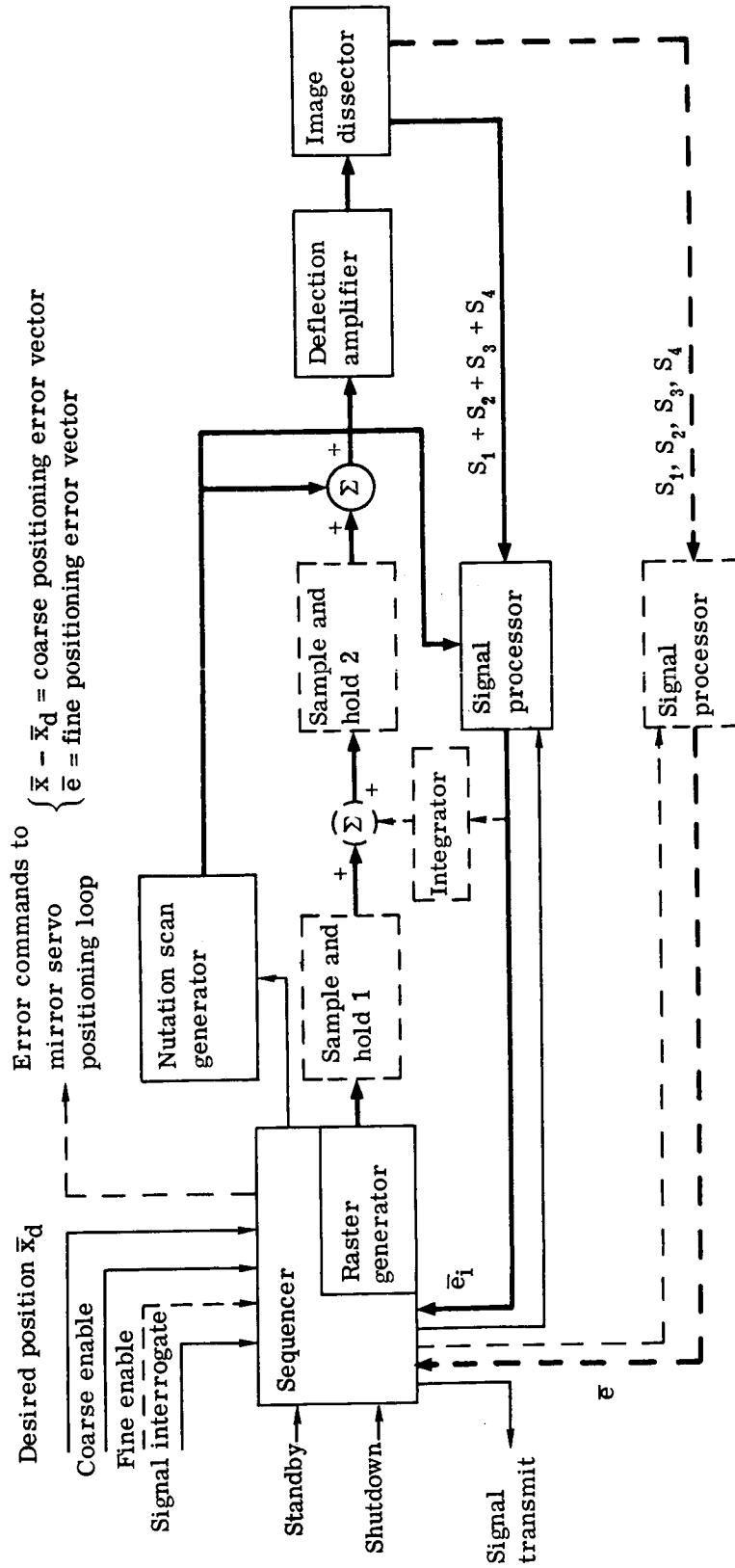


Fig. C.5-38 — Reticle star tracker, coarse positioning: initial acquisition

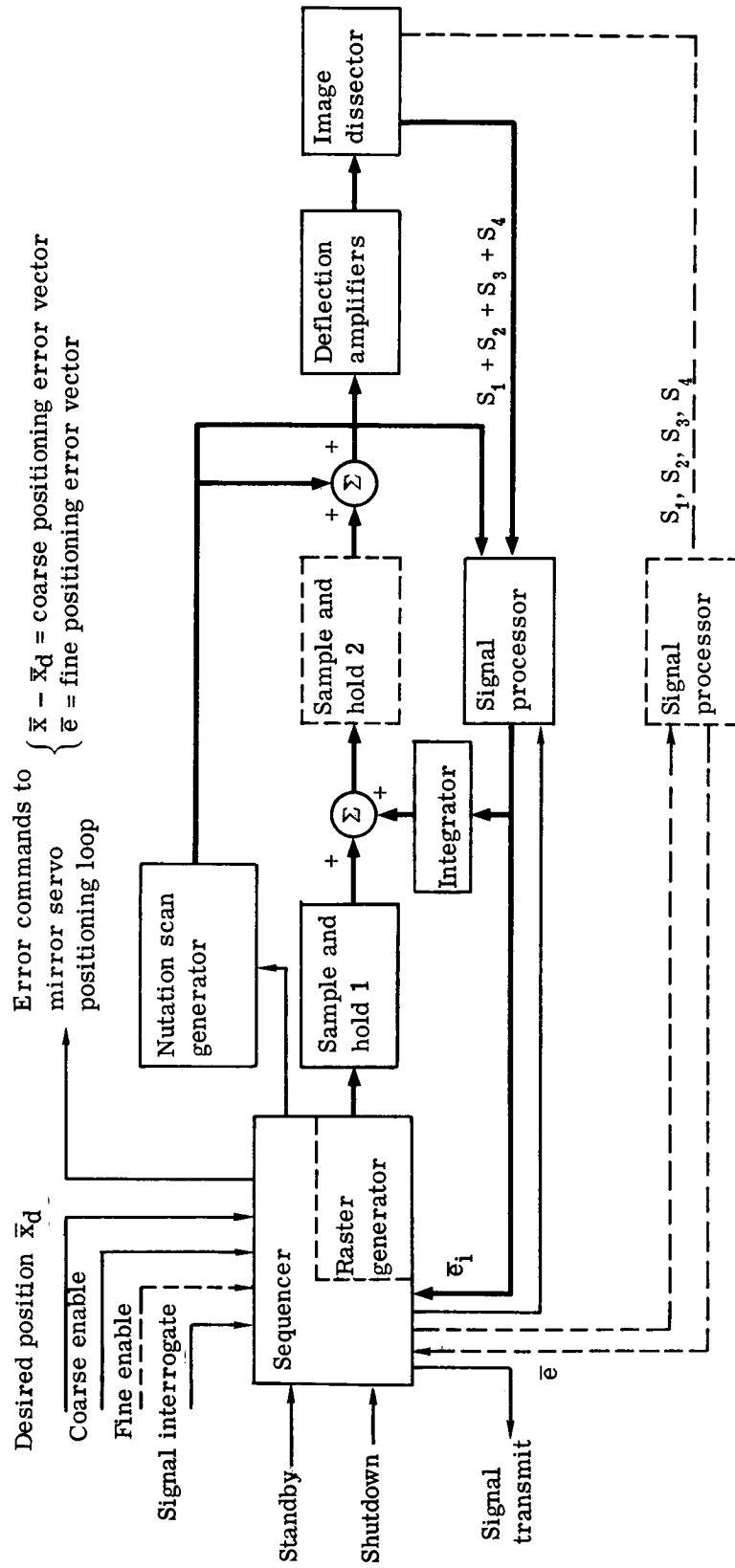


Fig. C.5-39 --- Reticle star tracker, coarse positioning: linear servo tracking

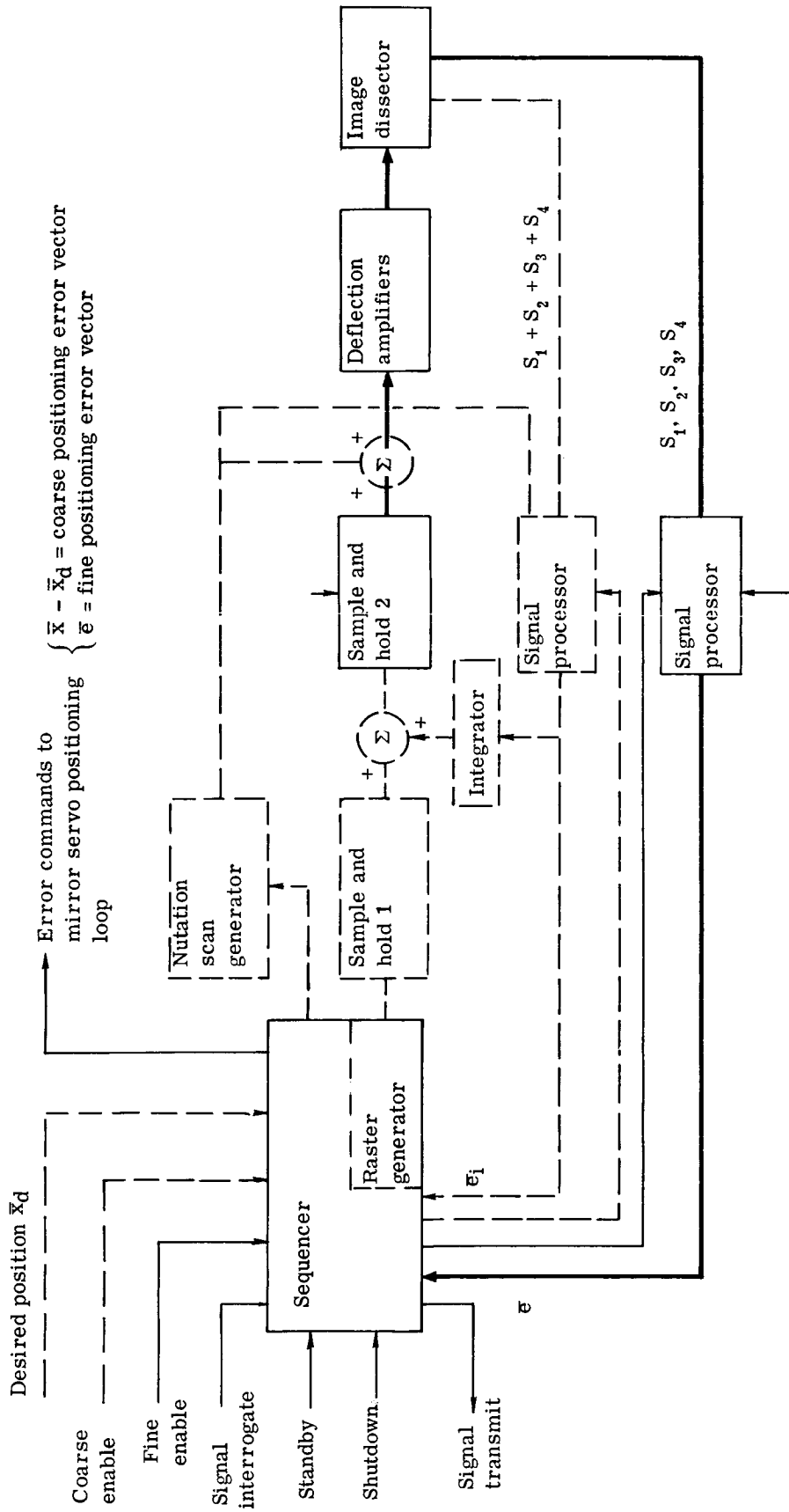


Fig. C.5-40 — Reticle star tracker, fine positioning

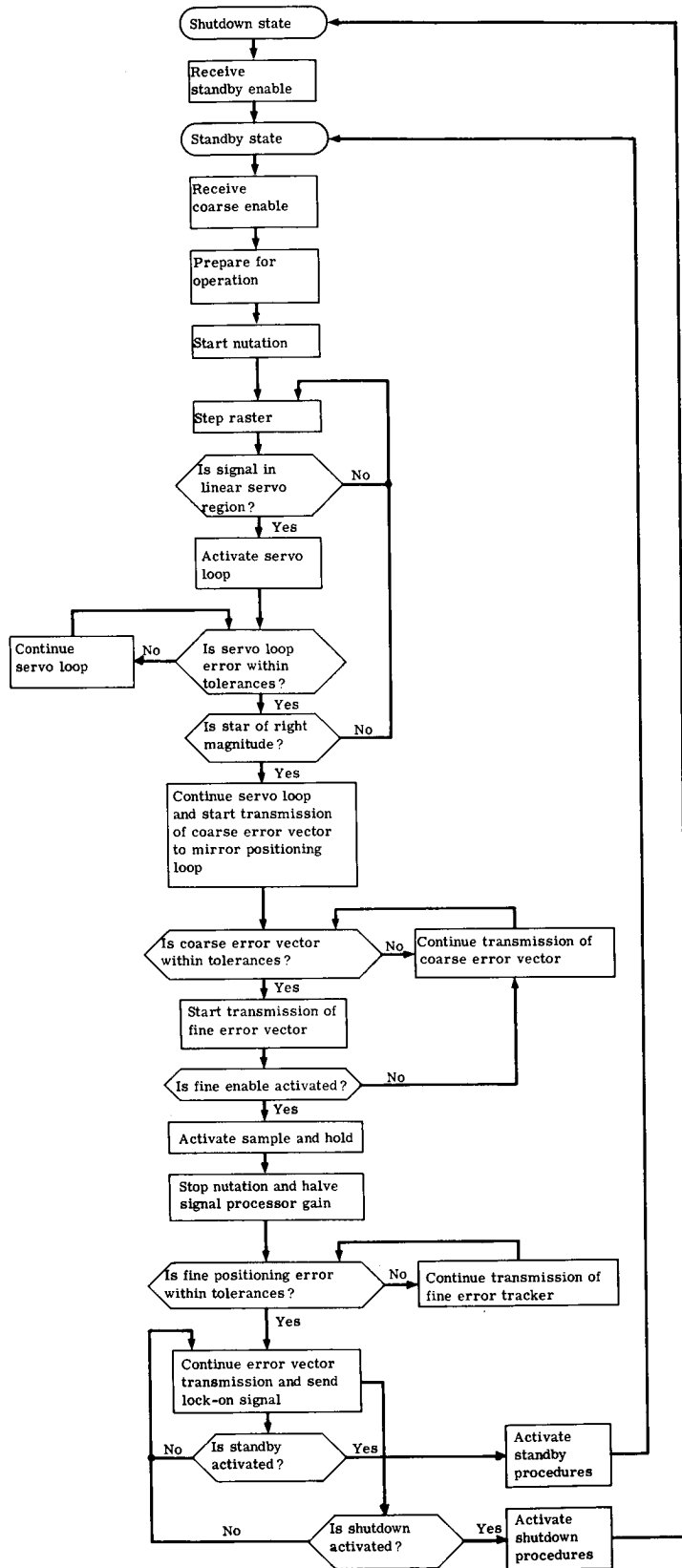


Fig. C.5-41 — Flow chart of tracker head acquisition/lock-on sequence

The startup requires turning on power to go into standby for a period of warmup. When a coarse enable command is received, the tracker activates those portions indicated in Fig.C.5-37, including beginning the electrical nutation of the image dissector. Next, the field of view scan is begun by digitally stepping the position of the nutation circle. This may be either a raster scan or an outgoing spiral scan, and has substantial overlap in order that pointing instabilities in the SSM not allow the star image to make an end run around the moving instantaneous search field of view, which is twice the aperture diameter.

When the nutated field of view of the image dissector aperture approaches the star image, a square wave will begin to appear at the summed output of the four multipliers. At this point, a ratio comparison is made of the average and fundamental components in order to indicate how far from the center of the nutation circle the star image is. When it is close enough for the tracker to give a useful position transducer constant, the digital scan is halted and a linear servo loop is activated.

The configuration of active elements is now indicated by Fig. C.5-38. The servo loop pulls the tracker in onto the target star and, while doing so, monitors the magnitude of the error signal. When the error signal falls below specified bounds, the average count rate is compared with the count rate expected. If the wrong star has been located, the digital search is reactivated. If not, the tracking head continues as a linear servo and the position of the star is transmitted.

If the head has been positioned so that the desired position of the star is the center of the field of view, then the actual coordinates with respect to the center represent a coarse error signal that may be used for positioning the vehicle and/or the secondary mirror. If unknown doubles are expected to be a problem, a doublecheck (not shown in Fig. C.5-41) may be performed before transmission of error signals. This may be done by introducing a known perturbation in apparent star position (such as by modulating the radius of the nutation circle) and measuring the output response. If the response is lower for some angles of orientation than others, it indicates that a situation such as is shown in Fig. C.5-25 exists, and that a double star (which is not an allowable guide star) has been found.

In normal operation, the linear servo mode of operation will continue until the vehicle is properly pointed and the coarse error has fallen below a specified tolerance. When coarse error is within bounds, transmission of the fine error signal begins, and may, if desired, also be used to trim vehicle and secondary mirror position. When a fine tracking enable command is received, the position of the scanning apertures is fixed with a digital sample and hold and the linear servo loop is deactivated. The scan nutation is turned off and, since the signal current is therefore doubled, gain is cut in half to keep the loop gain constant. The configuration becomes that shown in Fig. C.5-39. The tracking head is now transmitting the fine error signal as determined by comparing the relative amounts of light in the four refracted beams. It is serving solely as a position transducer in the secondary mirror tracking loop.

#### C.5.d Design of the Secondary Mirror Control System

Early in the study, consideration was given to basically different methods of achieving the line-of-sight stabilization required. The most powerful method, that of isolating the telescope from the rest of the spacecraft, introduced significant problems and seemed undesirable unless it was shown to be required. Available data and subsequent analysis indicated that existing actuators could stabilize the vehicle enough that the residual errors could be compensated internally to the telescope through use of the fine guidance sensor and a moving optical component. It appeared that the largest unstabilizing disturbance came from the stabilization actuators themselves, and correction of these disturbances required a higher servo bandwidth than was achievable in the vehicle control system. Table C.5-6 lists three basic stabilizations considered and some of the problems characteristic to each. It is important to note that the reference design represents what was felt to be the least complex approach that would meet the requirements.

The present approach provides within the telescope a backup fine tracking method capable of wider bandwidths than the vehicle itself. This approach would have the secondary mirror of the telescope moved by means of actuators. There are two advantages to moving the secondary mirror for fine tracking. (1) The entire image plane,

Table C.5-6 – Fine Stabilization Options (Reference System)  
in Descending Order of Effectiveness

Fine stabilize isolated telescope structure

- Heavy
- Structurally complex
- Problem with pressurized compartment
- Launch locks required
- Costly development

Fine stabilize optical component (reference design)

- Requires vibration sources be isolated
- Limited accommodation of pointing errors

Fine stabilize entire spacecraft

- Requires vibration sources be isolated

including the offset guide field, is moved as a unit, preventing significant defocus or differential distortion. (2) The image position can be maintained in all  $f/12$  planes in a closed control loop via the offset guidance. Alternative methods of moving an optical element near the focal plane either did not satisfy the above conditions or imposed and excessive precision requirement on the open loop compensating elements in the system. (These elements are used to provide correction to differential velocity aberration and to thermal drift of the instrument structure, both of which need only modest precision in the system described here.) Alternative approaches to internal stabilization that were very briefly considered are indicated in Table C.5-7.

In the reference design, fine stabilization is achieved by controlling the secondary mirror to compensate for errors in the vehicle angle. The secondary mirror directly controls the line of sight, then, and the secondary mirror angle is used to command the vehicle actuators. The operation of the concept is illustrated in Fig. C.5-42. Conceptually, the fine guidance sensor controls the secondary mirror and, the secondary mirror controls the vehicle in the fine guiding mode. The loop closed by the secondary mirror has a faster response than the loop closed by the vehicle actuator. The line-of-sight correction thus is very nearly equal to the vehicle angle error. Consequently, the feedback to the vehicle actuator is virtually the vehicle angle error, meaning that the cascaded representation given previously in Fig. C.5-2 is a good approximation.

The remainder of this section describes aspects of the secondary mirror control system concept that were studied in detail. First of all, an initial design of the secondary mirror actuator system was generated, including the counterbalance and force feedback system that prevents the transmission of forces and moments to the structure. A method of processing of the signals from the focal plane guidance sensors was worked out to give the necessary three-axis overall control information and the two-axis control information for the secondary mirror. A linear servo analysis was carried out to arrive at a useful set of servo parameters for the one-dimensional stabilization case, assuming an overall LST stabilization concept and considering likely disturbances. Finally, a one-dimensional computer simulation of the telescope fine guidance control system was made to test the concept in terms of its performance under expected disturbance levels and the control bandwidth attainable with the secondary mirror control system. For the purpose of analysis, the model assumed servo parameters for the overall LST stabilization control system derived in the preceding sections. Included in the model were the first nine lateral dynamic modes of the structure (one-dimensional model), the secondary mirror with its actuators, counterbalance (with 10 percent imbalance), and force feedback sensors with their added structural compliance, the nonlinear gain function of the fine guidance sensor, and amplifier and guide sensor noise. This portion of the design study demonstrates the overall feasibility of the reference design of the OTA fine stabilization system.

#### C.5.d(1) Secondary Mirror Actuation System for Line-of-Sight Stabilization

To achieve the required accuracy of line-of-sight stabilization, in the presence of anticipated motions of the vehicle, the studies have shown that the secondary mirror should be rotated to achieve line-of-sight deflections of 4.85 microradians ( $\pm 1$  arc-second), which would require 12.10-microradian ( $\pm 2.5$ -arc-second) rotations of the secondary mirror. The fine pointing loop controlling the secondary mirror should have a gain crossover frequency of 2 Hz, which corresponds to a noise bandwidth of about 4 Hz.\* To achieve this gain crossover frequency, the simulations have indicated that it will be necessary to isolate the secondary mirror actuation forces from the telescope structure lest instability result from the structural resonance effects of the telescope.

Fig. C.5-43 shows a schematic system diagram of the secondary mirror actuator proposed for rotating the mirror while the mirror actuation forces are isolated from the telescope. This force isolation actuation system works in the following manner. A counterweight is coupled to the mirror through a series of piezoelectric transducers. The transducers move the counterweight in opposition to the mirror such that the counterweight reaction forces drive the mirror and only small residual forces are transmitted to the structure.

---

\*Approximate Analysis of Allowable LST Vehicle Pointing Errors, LST-72-57, 14 Apr. 1972.

Table C.5-7 — Alternate Fine Stabilization Approaches Within OTA  
(Capabilities With Each Optical Element)

	Effective for Whole Field	Closed Loop Correction	Range of Accommodation	Structural Disturbance	Attainable Bandwidth
Primary mirror	Yes	Yes	$\pm 5 \mu\text{rad}$	Large	Very low
Secondary mirror	Yes	Yes	$\pm 5 \mu\text{rad}$	Moderate	2 hz (reference design)
Folding mirror	No	Yes	$\pm 5 \mu\text{rad}$	Slight	> 2 hz
Optical components within instruments	No	No	$\pm 0.5 \mu\text{rad}^*$	Slight	> 2 hz
Electron optics in imaging tubes	No	No	$\pm 0.5 \mu\text{rad}^*$	None	Noise limited

\* 1 percent precision with open loop control.



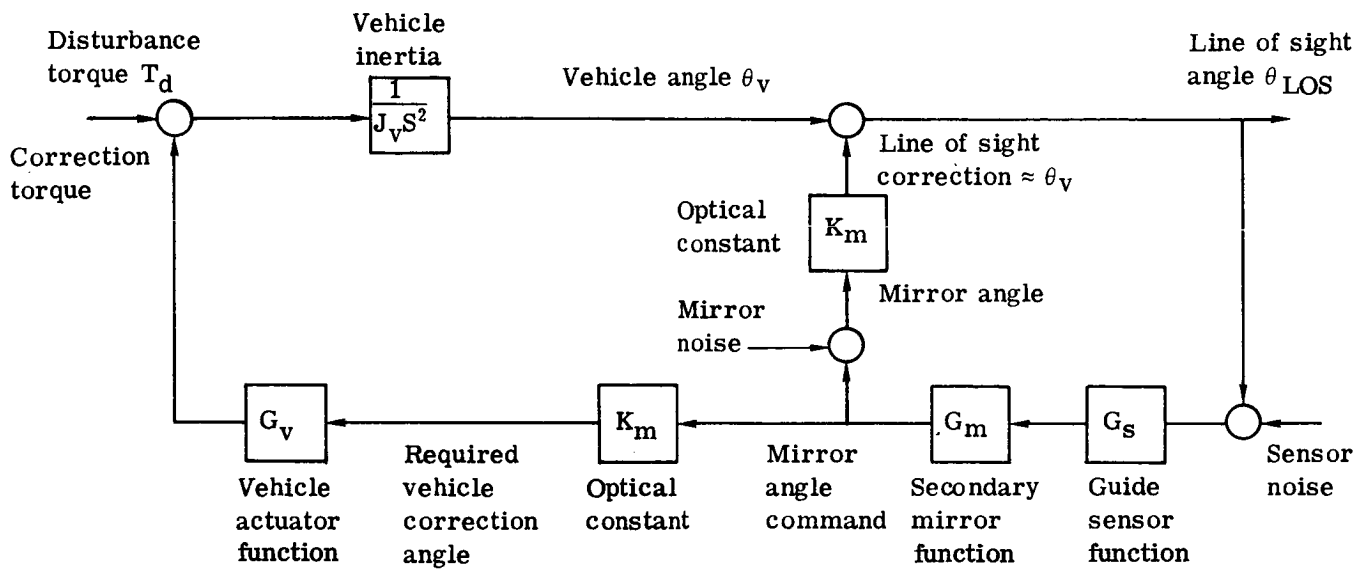


Fig. C.5-42 – Fine stabilization control system (concept)

Three sets of actuators of the form shown in Fig. C.5-43 are used to drive the mirror symmetrically at three points. Transducers  $A_{w1}$ ,  $A_{w2}$ , and  $A_m$  are piezoelectric actuators of equal length and essentially the same sensitivity (linear deflection per applied voltage). Transducer  $S_1$  is a piezoelectric compression-type force sensor and  $S_2$  is a piezoelectric bender-type force sensor. The bender transducer  $S_2$  has much greater sensitivity than the compression transducer  $S_1$  and a very much higher compliance. Transducer  $S_2$  is actually a three-point suspended beam, but for simplicity is represented as a cantilever beam. As shown, the bender force transducer  $S_2$  is fastened to the telescope structure and is coupled by flexures to the series combinations of  $A_{w1}$  and  $A_{w2}$  and  $A_m$  and  $S_1$ , which in turn are coupled by flexures to the counterweight and mirror, respectively.

The counterweight has half the inertia of the mirror, and so must be driven through twice the angular excursion as the mirror to achieve force balancing. This is implemented by using cascaded actuators  $A_{w1}$  and  $A_{w2}$  to drive the counterweight and actuator  $A_m$  to drive the mirror. They all have essentially the same deflection per applied voltage. If the system were exactly balanced, there would be no reaction forces transmitted through the bender piezoelectric sensor  $S_2$  to the structure.

To compensate for any unbalance in this actuation system, force feedback is used to reduce further the forces on the structure. The bender piezoelectric sensor  $S_2$  measures the force being transmitted to the telescope structure and feeds its signal through the force isolation loop amplifier, back into the power amplifier that drives the counterweight actuators  $A_{w1}$  and  $A_{w2}$ . This negative force feedback changes the counterweight motion in such a way as to minimize the dynamic reaction force transmitted to the structure.

A second damping force feedback loop is used to damp out high frequency oscillations between the mirror and counterweight owing to compliance in the interconnecting structure. The compression piezoelectric sensor  $S_1$  detects the forces associated with this oscillation and feeds its signal through the damping signal amplifier and into the two power amplifiers, to drive all three actuators  $A_{w1}$ ,  $A_{w2}$ , and  $A_m$ . The gain in this damping feedback loop (actuator deflection rate per unit input force) is very much less than for the force isolation loop.

Fig. C.5-44 gives a mechanical layout of the mirror fine pointing actuation system.\* Fig. C.5-45 shows an exploded view of one set of actuators. The three-point suspended beam is the bender force sensor  $S_2$ . It has an effective length of 150 millimeters between the outer flexure points, a width  $w$  of 25 millimeters, and a thickness  $T$  in the direction of beam deflection of 15 millimeters. The compression-type piezoelectric transducers are cylindrical shells, with a length of 20 millimeters and a wall thickness of 5 millimeters. Actuators  $A_{w1}$  and  $A_m$  are 65 millimeters in diameter. Actuator  $A_{w2}$  and sensor  $S_1$  are 50 millimeters in diameter. As shown, the smaller transducers are located inside the larger ones.

For preliminary analysis, it is assumed that the mirror and directly connected structure weigh 54.4 kilograms (120 pounds) and that the counterweight weighs half this amount, or 27.2 kilograms (60 pounds). The counterweight inertia is assumed to be half that of the mirror, which is estimated to be 1.44 kilograms/meters<sup>2</sup>. The stiffness of the telescope structure supporting the mirror is assumed to be such as to achieve 40-hz resonant frequency for resonance relative to the mirror counterweight inertia. The compliance of the bender force sensors (0.12 micrometer/N) adds to the structural compliance to reduce this resonant frequency from 40 to 35 hz.

The bender sensors can support a total acceleration load of only 2.5 g on the mirror and counterweight before the rated tensile strength of the piezoelectrical crystal is exceeded. To keep the crystal stresses from exceeding this value, the motions of the bender are restricted by stops that limit the motions to  $\pm 0.075$  millimeter ( $\sim \pm 0.003$  inch). These stops are indicated in Fig. C.5-45.

---

\*A detailed analysis of the performance of this actuation system is presented in Biernson, G., Memorandum LST-72-126, Discussion and Analysis of Secondary Mirror Actuation System, Sept 15, 1972.

If the transducer compliance were to represent the total compliance between the mirror and counterweight, the natural frequency of mechanical oscillation between mirror and counterweight would be 1,500 hz. This is the resonance that is damped by the damping feedback loop. On the other hand, the resonance should be appreciably lower than this value because of compliance in other structural members. For this analysis, this resultant resonant frequency of 500 hz has been conservatively assumed.

The open and closed loop frequency responses of the force isolation feedback loop are shown in Fig. C.5-46. (These simplified responses ignore the effect of the high frequency resonance damped by the damping feedback loop.) The force isolation loop gain exceeds unity gain at frequencies above 1 hz. Hence, the force isolation feedback attenuates structural forces at frequencies greater than 1 hz.

The effect of the force isolation actuation system in attenuating structural forces is shown in Fig. C.5-47. This is a frequency response plot relating mirror angular accelerations  $\ddot{\theta}_m$  to the resultant structural reaction torque  $T_{st}$ . With a conventional actuator, the structural reaction torque would be equal to  $J\ddot{\theta}_m$  (upper dashed curve), where  $J$  is the inertia of the mirror and its directly coupled structure.

With the force isolation system, if the force isolation feedback loop were opened, the structural force  $T_{st}$  would be equal to  $\delta J\ddot{\theta}_m$ , where  $\delta$  is the relative error in matching the sensitivities of the actuators that drive the mirror and the counterweight. It is conservatively assumed that these sensitivities can be matched to an accuracy of at least 10 percent so that  $\delta < 0.1$ . Thus, by the dynamic balancing effect it can be conservatively assumed that the structural reaction torque is reduced by at least a factor of 10.

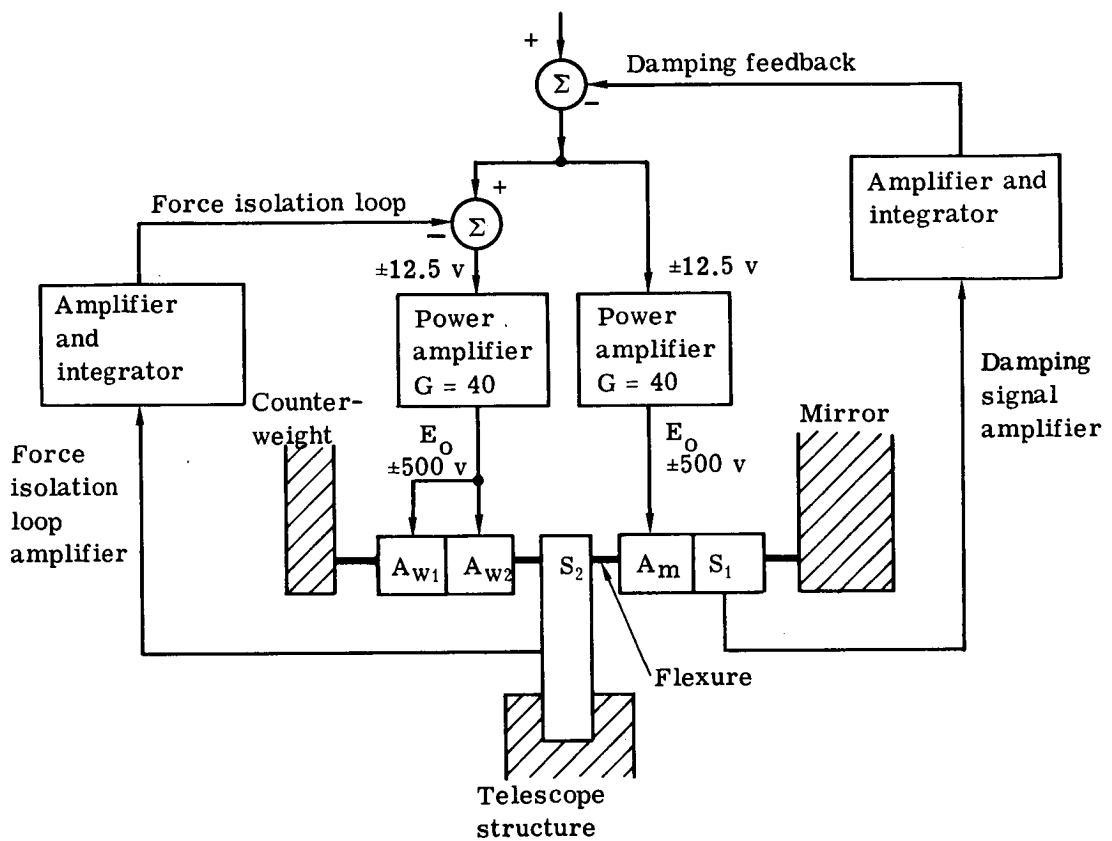
Closing the force isolation feedback loop produces attenuation proportional to frequency at frequencies above the gain crossover frequency (1.0 hz) of the force isolation feedback loop, as shown by the crosshatched area in Fig. C.5-47. This force isolation feedback thus provides an additional attenuation greater than a factor of 10 at frequencies between 10 and 120 hz, which is the frequency region of the major resonances of the telescope structure. Thus, it can be conservatively assumed that the frequency response peaks of those structural resonances in the secondary mirror control loop will be attenuated by at least a factor of 100 by the force isolation actuation system.

Random electronic noise in the amplifiers that amplify the force sensor signals produces jitter in the mirror and counterweight. To evaluate the effects of amplifier noise as well as amplifier drive and low-frequency dynamic properties, preliminary designs of the amplifiers were made. Fig. C.5-48 shows a block diagram of the signal processing for the actuation system and the related tracking loop amplifier. Fig. C.5-49 shows the circuitry of the force isolation feedback amplifier, which amplifies the signal from the bender sensor  $S_2$ . (The amplifier for the damping loop, which amplifies the signal from the compressor sensor  $S_1$  is not presented here because it is very much less critical.)

The piezoelectric crystals all use PZT-4 because this material has reasonably high sensitivity and little change of characteristics with temperature. Greater sensitivity (charge per unit of force, or deflection per applied voltage) and lower impedance up to a factor of two can be achieved with other materials (PZT-5A, PZT-5H) at the expense of much more variability of characteristics with temperature.

Actuators  $A_{w1}$ ,  $A_{w2}$  and  $A_m$  (which are 20 millimeters long) consist of stacks of 40 piezoelectric crystals each, 0.5 millimeter thick, connected in parallel. For PZT-4, the crystal is depolarized with a negative voltage gradient in excess of 1,400 volts/millimeter, which corresponds to 700 volts across the 0.5 millimeter elements. It is proposed that the crystals be driven over a voltage swing of  $\pm 400$  volts, which is less than 60 percent of the polarization level. To avoid atmospheric voltage breakdown under rarified atmospheres, it will be necessary to enclose the actuators in some medium such as a flexible coating.

Driving the actuator stacks with a voltage swing of  $\pm 420$  volts moves the mirror by  $\pm 5$  micrometers at the actuation point and the counterweight by  $\pm 10$  micrometers. The combined effect of the three actuator sets rotates the mirror through an angle of 24.23 microradians ( $\pm 5$  arc-seconds) thereby producing line-of-sight deflections of



$A_{w1}$ ,  $A_{w2}$ ,  $A_m$  — piezoelectric actuators (equal sensitivity)  
 $S_1$  — piezoelectric compression force sensor  
 $S_2$  — piezoelectric bender force sensor

Fig. C.5-43 — Dynamic force isolation actuation system for LST secondary mirror

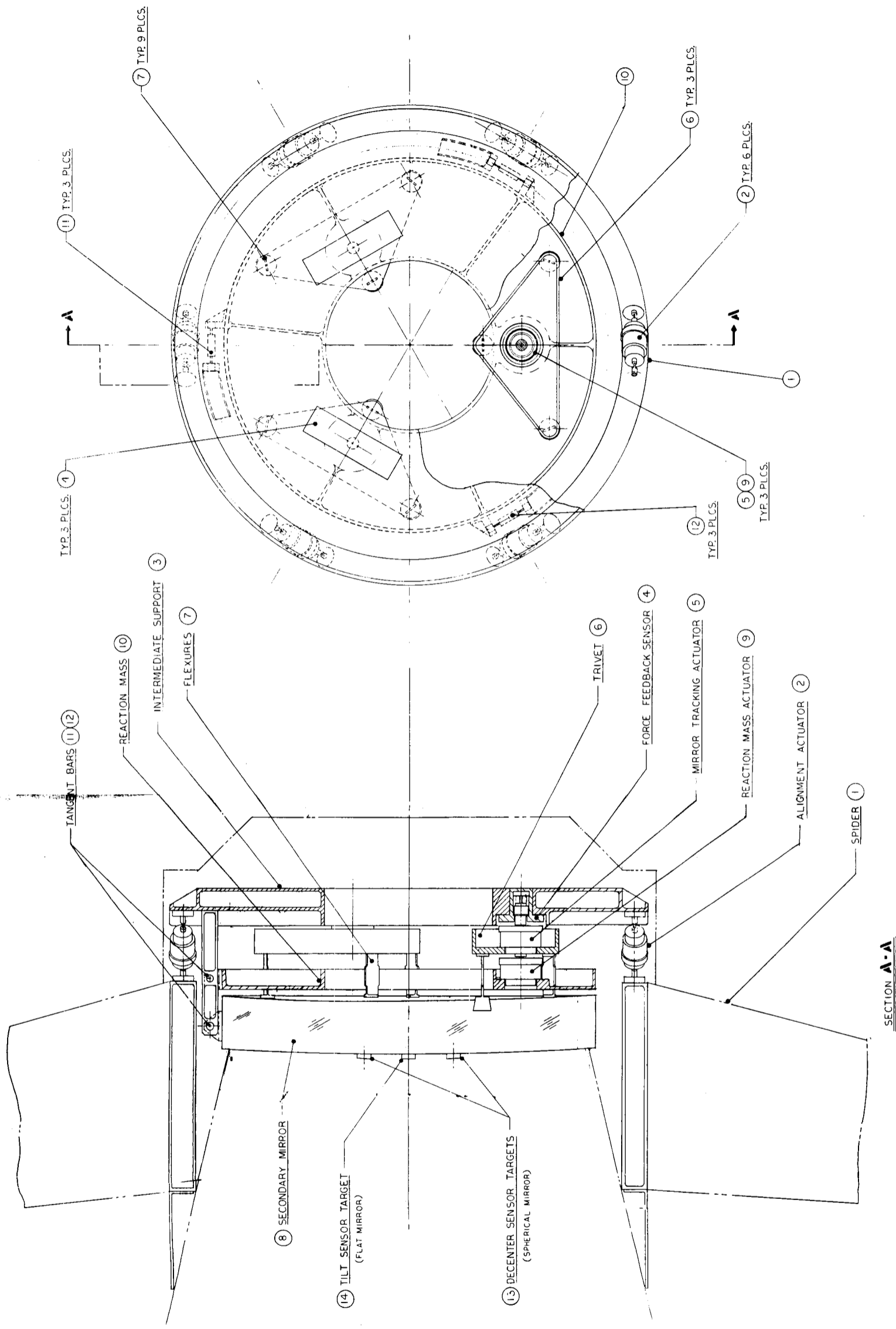
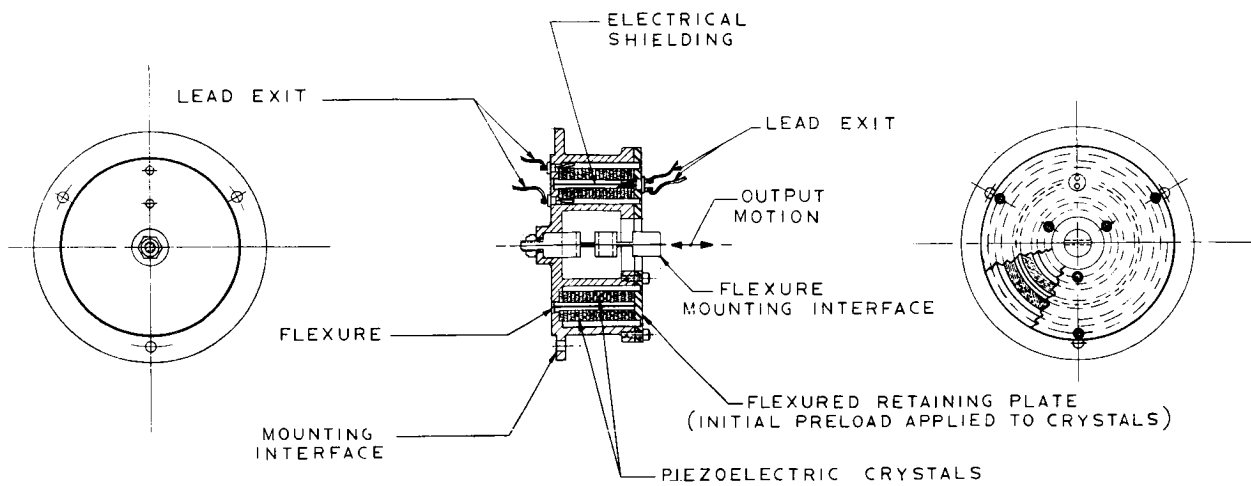
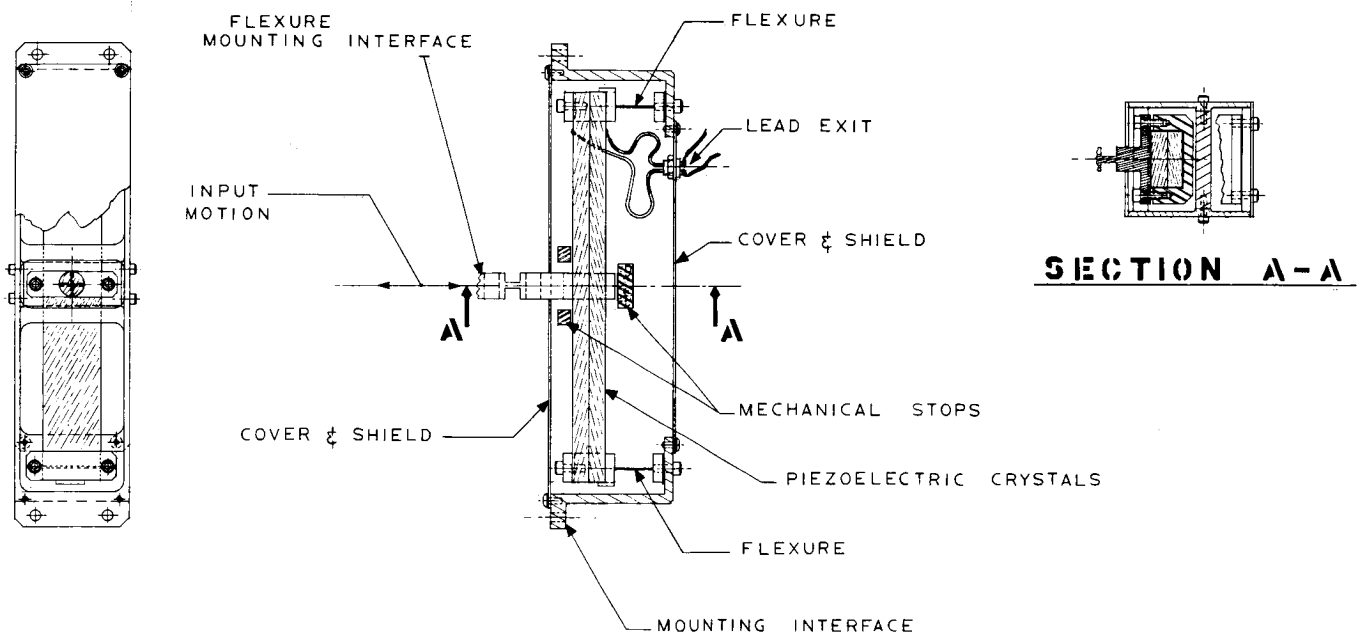


Fig. C.5-44 — Secondary mirror actuator configuration (dwg. no. 911329)



(a) Actuator



(b) Force Sensor

Fig. C.5-45 — Piezoelectric transducers (dwg. nos. 915925, 915926)

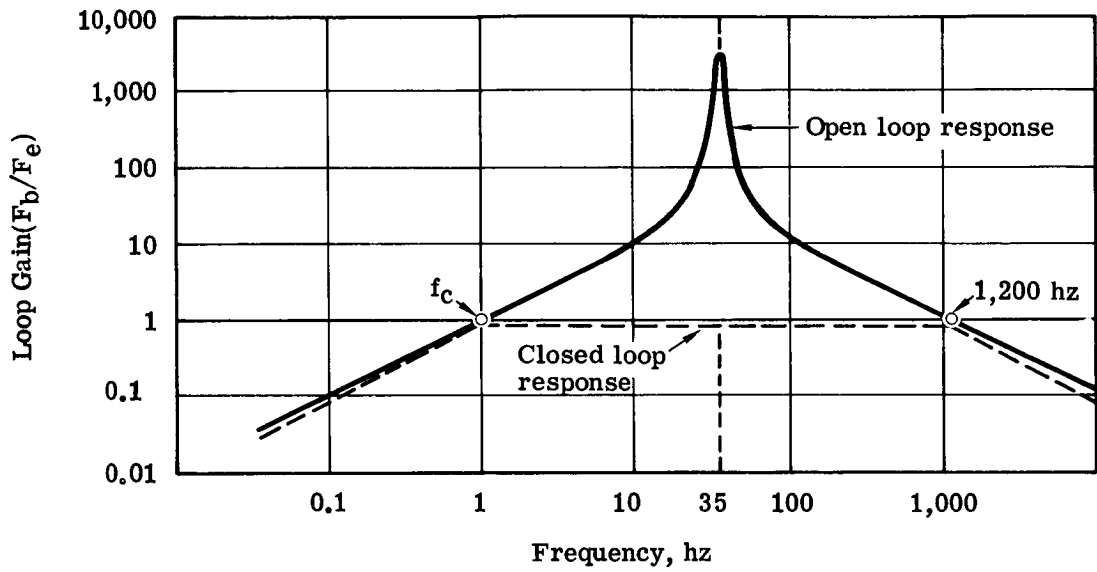


Fig. C.5-46 — Approximate open loop and closed loop responses of force isolation loop

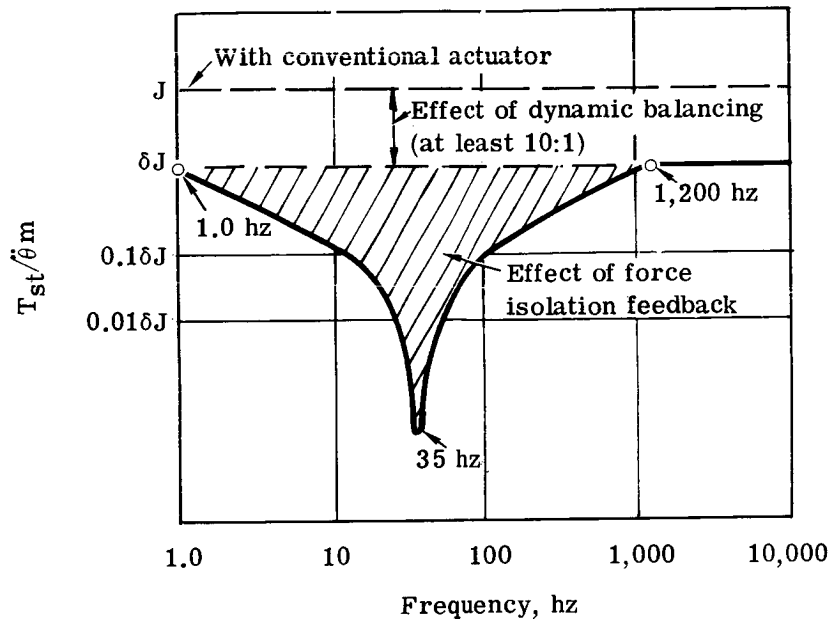


Fig. C.5-47 — Frequency response relating to mirror angular acceleration to the corresponding reaction torque,  $T_{st}$ , exerted on the telescope structure



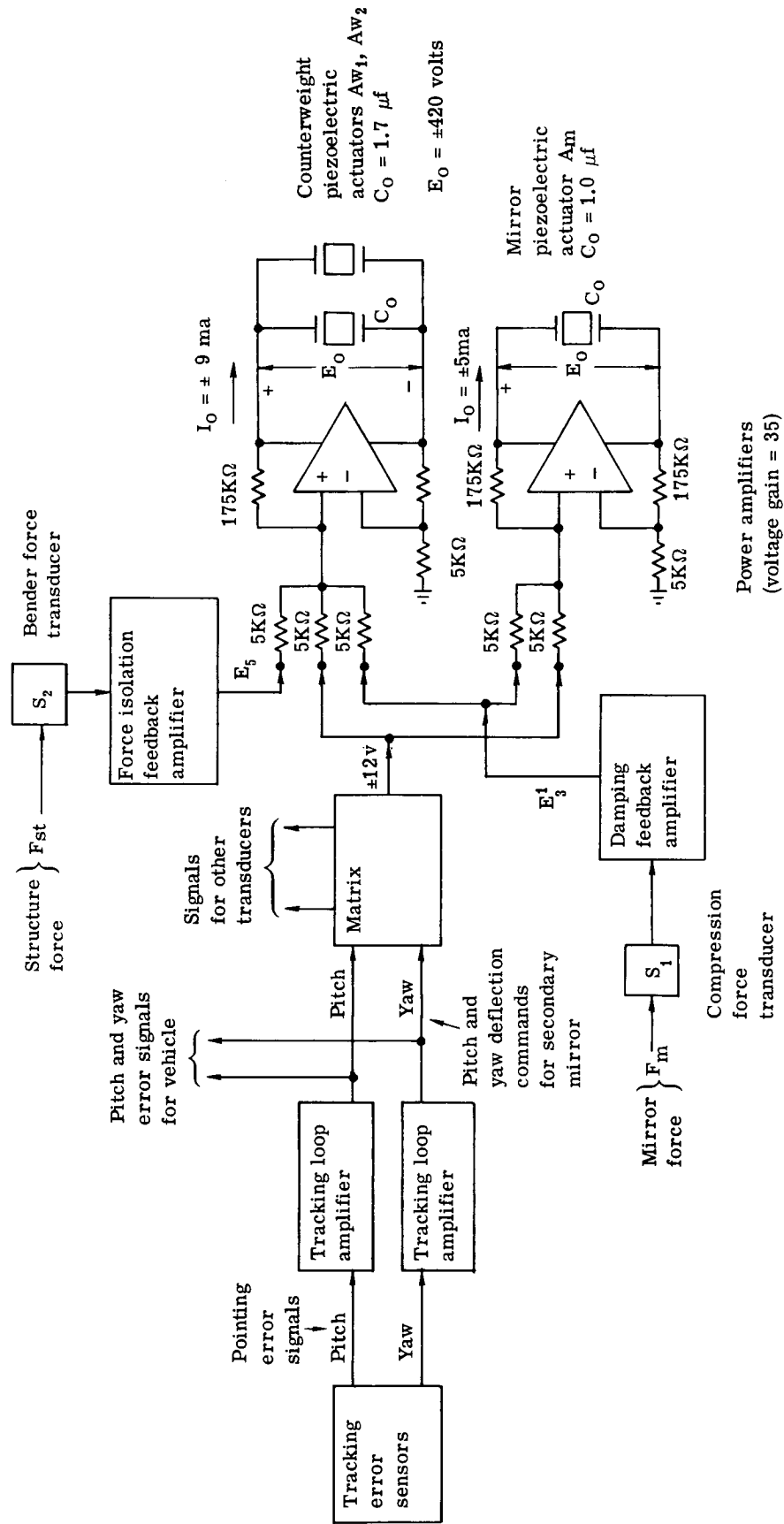


Fig. C.5-48 — Signal diagram of secondary mirror actuation system

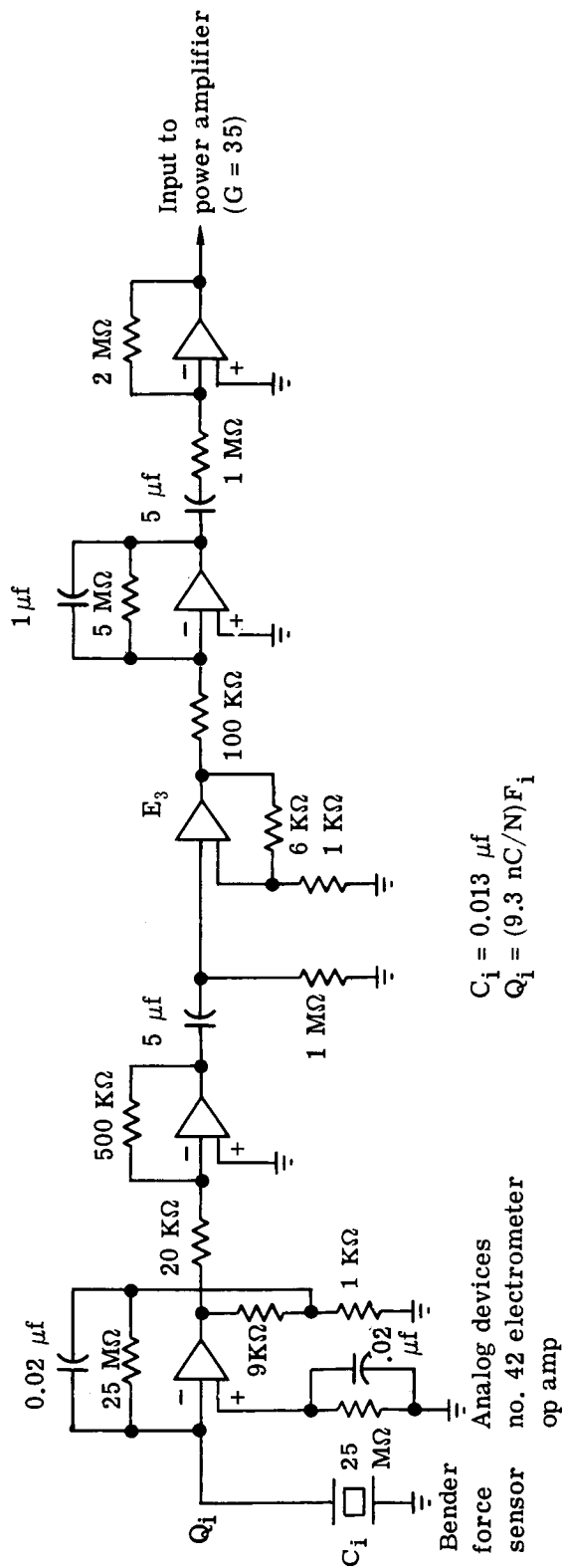


Fig. C.5-49 — Force isolation feedback amplifier

9.70 microradians ( $\pm 2$  arc-seconds). This is a factor of two greater than the 4.85-microradian ( $\pm 1$ -arc-second) range that the studies indicate should be adequate. Not only does this give a good safety factor when dealing with extreme situations and deterioration of the vehicle control system, but as is shown it also can be instrumental in allowing redundancy in the mirror actuation system.

The counterweight actuators  $A_{w1}$  and  $A_{w2}$  have a combined capacitance of 1.2 microfarad. The mirror actuator  $A_m$  has the capacitance of 1.0 microfarad. To drive these actuators sinusoidally over the whole  $\pm 420$ -volt range at a frequency of 2.0 hz (the gain crossover frequency of the fine pointing loop) requires a current swing of  $\pm 9$  milliamperes for the power amplifier that drives the counterweight actuators and a current swing of  $\pm 5$  milliamperes for the power amplifier that drives the mirror actuator. These current capabilities should be quite adequate for the amplifiers.

The compression sensor  $S_1$  consists of a stack of four elements, each 5 millimeters thick. It has a sensitivity (charge per applied force) of  $Q/F = 1.2$  nanocoulombs per newton and a capacitance of 0.007 microfarad. The bender sensor  $S_2$  consists of two slabs electrically connected in parallel. Bending the beam compresses one slab and expands the other. The resultant stresses produce the piezoelectric signals. This sensor has a charge sensitivity of  $Q/F = 9.3$  nanocoulomb/newton and a capacitance of 0.013 microfarad.

The transfer functions of the amplifiers for the feedback loops between input force  $F$  and output voltage  $E_o$  applied to the piezoelectric actuators are

#### Force Isolation Loop

$$\frac{E_o}{F_{st}} = \frac{570,000 \text{ (volts/second) / newton}}{S(1 + 1/\tau_1 S)(1 + 1/\tau_2 S)^3}$$

where  $\tau_1 = 0.5$  second  
 $\tau_2 = 5$  seconds

#### Damping Feedback Loop

$$\frac{E_o}{F_m} = \frac{2,500 \text{ (volts/second) / newton}}{S(1 + 1/\tau_3 S)(1 + 1/\tau_4 S)^2}$$

where  $\tau_3 = 0.0033$  second  
 $\tau_4 = 0.005$  second

The variable  $F_{st}$  is the force on the structure (in newtons) measured by bender sensor  $S_2$ .  $F_m$  is the force on the mirror measured by the compression sensor  $S_1$ .

The input noise for the force isolation feedback amplifier of Fig. C.5-49 produces (for the three sets of actuators) an rms jitter of the mirror of 0.00017 microradian, which corresponds to a line-of-sight jitter of 0.000017 arc-second, which is negligible. The jitter of the counterweight is very much greater than this. The counterweight actuation point jitters over a peak-to-peak excursion of 0.2 micrometer, which is 1.2 percent of the peak-to-peak operating range of the actuators ( $\pm 10$  micrometers). The angular jitter of the counterweight is 0.068 microradian (0.014 arc-second), peak-to-peak. These jitter values are quite small relative to the tracking accuracy requirements of the telescope. (The jitter due to the damping feedback loop is very much less than these values).

#### Redundancy

To minimize noise, the force feedback amplifiers should be located close to sensors  $S_1$  and  $S_2$ . To avoid the requirements of conducting relatively high voltages ( $\pm 420$  volts) over long distances, the power amplifiers that drive the actuators (and their corresponding high voltage power supplies) should be located close to the actuators. Hence, these amplifiers and power supplies should be mounted on the secondary mirror assembly, which necessitates redundancy of these circuits because maintenance is extremely difficult to implement there.

The counterweight actuators  $A_{w1}$  and  $A_{w2}$  can be driven by separate power amplifiers, and the mirror actuator (which contains 40 elements connected in parallel) can be electrically separated into two parts driven by separate amplifiers. Likewise the bender sensor  $S_2$  (which contains two parallel sensing elements) and the compression sensor  $S_1$  (which contains 4 parallel elements) can each be electrically separated into two portions that drive separate feedback amplifiers. The signals from the feedback amplifiers and the signals to the actuators can be fed back to the pressurized compartment, where interconnections can be changed in case of failure. If one of the power amplifiers fails, the actuation system can still operate but with a line-of-sight deflection capability of 4.85 microradians ( $\pm 1$  arc-second) rather than 9.70 microradians ( $\pm 2$  arc-seconds).

#### C.5.d(2) Signal Processing To Form Tracking Signals

Fig. C.5-50 shows how the tangential and radial error signals from a pair of guide star sensors are processed to produce the pitch and yaw error signals that drive the secondary mirror servo amplifiers and the roll control servo for vehicle control. One guide star tracker (1) derives both radial and tangential error signals ( $\Delta\rho_1, \Delta\phi_1$ ) and the other tracker (2) derives only a tangential error signal  $\Delta\phi_2$ .

The constants  $K_1$  to  $K_9$  are telemetered digitally from the ground and can have either positive or negative values. These constants are a function of the radial and angular settings and the sensitivities of the guide star trackers. (The equipment for measuring these sensitivities is described later.) The constants  $K_1$  to  $K_4$  resolve the tangential and radial error components ( $\Delta\phi_1, \Delta\rho_1$ ) from guide star sensor (1) in terms of the pitch and yaw coordinates. Constants  $K_5$  and  $K_6$  resolve ( $\Delta\phi_1, \Delta\rho_1$ ) in terms of the tangential error signal  $\Delta\phi_2$  from guide star sensor (2), forming the signal  $\Delta\phi_{12}$ . This is subtracted from  $\Delta\phi_2$  and multiplied by constant  $K_7$  to form the roll error signal.

The signals (a) and (b) represent the pitch and yaw tracking errors of guide star sensor (1). If there were no roll, one would want the system to minimize these error signals. However, with roll there must be tracking errors in guide star sensor (1) in order to minimize tracking errors in the data field. Accordingly, the roll error signal is filtered and multiplied by constants  $K_8$  and  $K_9$  to form appropriate roll correction signals to add to the yaw and pitch error signals.

Fig. C.5-51 shows how the fine and coarse tangential and radial error signals are formed by a guide star tracker. The guide star image is fed through the tilt plate that adds constant offset corrections ( $\bar{P}, \bar{Y}$ ) in pitch and yaw having values over a range of 4.85 microradians ( $\pm 1.0$  arc-second) and much smaller variable corrections ( $P, Y$ ) that correct for differential velocity aberrations (DVA). The constant offset corrections  $\bar{P}, \bar{Y}$  are telemetered from the ground station and allow the reticle tracker to operate at null at any point within the (2-second) spacing of the grooves in the reticle plate.

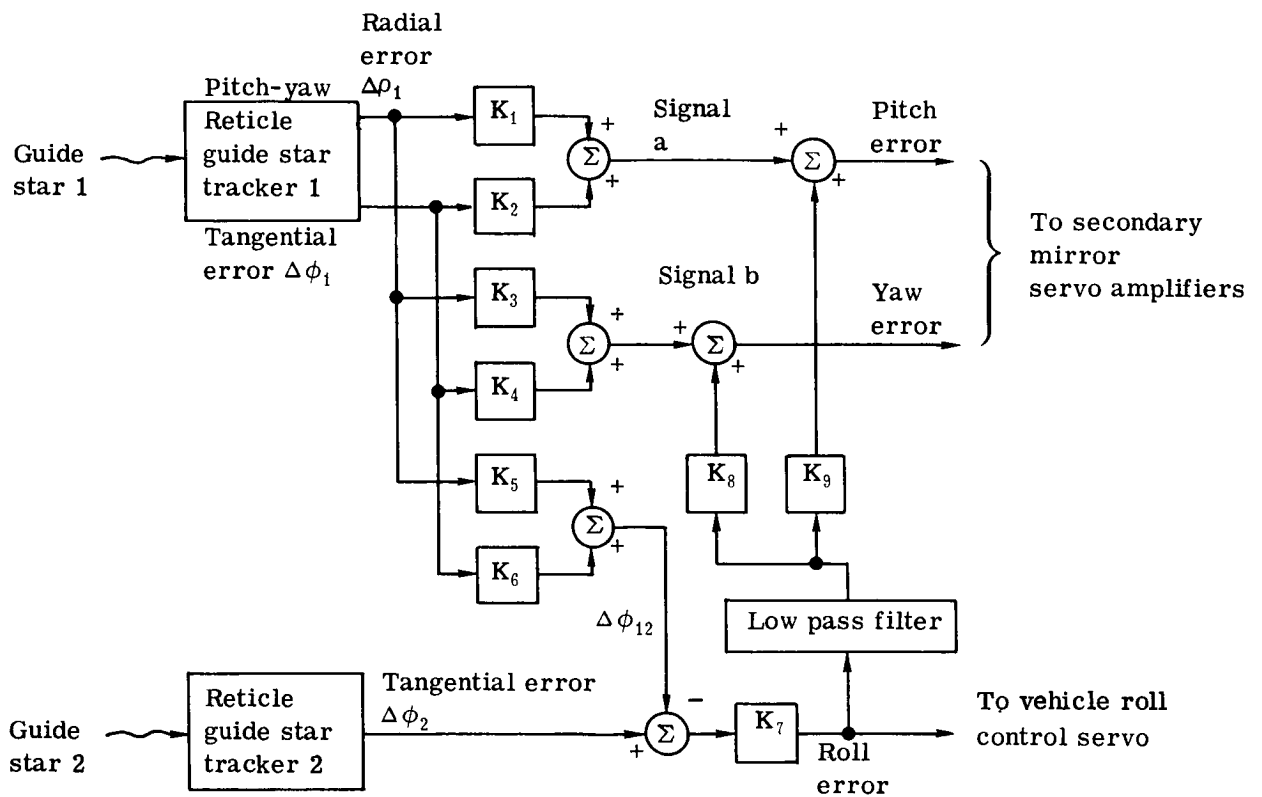
The DVA digital computation employs the following simple computation routine:

$$P_n = P_{n-1} + K(Y_{n-1} + Y_{n-2})$$

$$Y_n = Y_{n-1} - K(P_n + P_{n-1})$$

$$K = \pi \Delta\tau / T$$

The variables  $P_n, Y_n$  are the pitch and yaw DVA corrections for the  $n^{\text{th}}$  computation cycle and  $P_{n-1}, Y_{n-1}, Y_{n-2}$  are the corresponding values for previous cycles. The parameter  $K$  is a constant equal to  $\pi\Delta\tau/T$ , where  $T$  is the orbital period and  $\Delta\tau$  is the time increment for a computation cycle. To achieve the proper values of this computation, the ground station telemeters the parameters  $P_0, Y_0, T_0$  and  $\Delta\tau$  to the LST space vehicle, where  $P_0$  and  $Y_0$  are the initial values of  $P$  and  $Y$ , the parameter  $T_0$  is the instant at which computation starts, and  $\Delta\tau$  is the computation interval, which establishes the frequency. The constant  $K$  is hard-wired into the computation, and so this computation employs only addition and subtraction (no multiplication). Thus, the digital computation is very simple.



$K_1$  to  $K_9$  — telemetered constants  $f(\delta_1, \phi_1, \delta_2, \phi_2)$

Fig. C.5-50 — Guide error signal coordinate transformation process

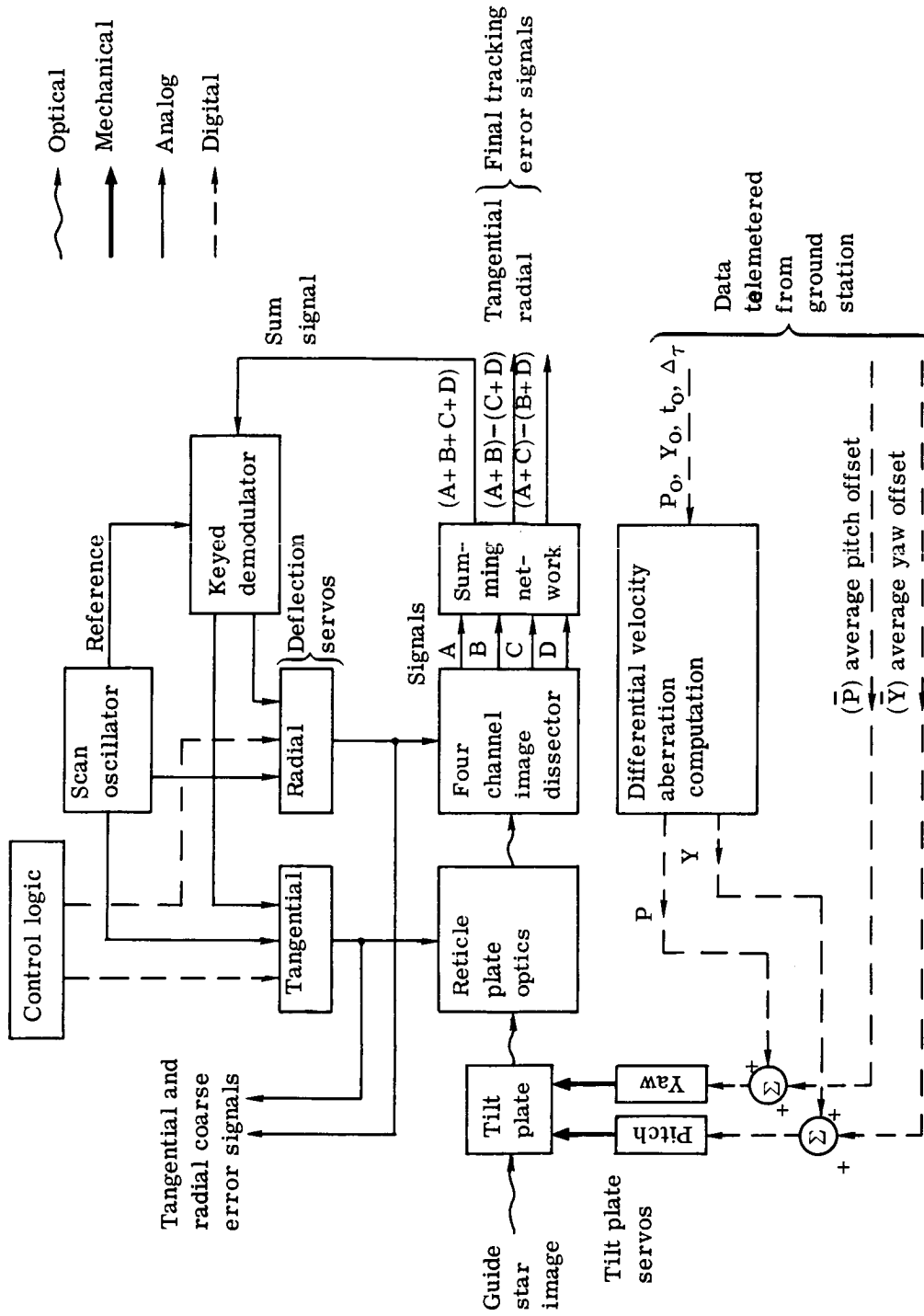


Fig. C.5-51 — Signal processing for fine and coarse tracking

The image of the star is projected through the tilt plate to the reticle plate optics, which focuses it at the photosurface of the four-channel image dissector. This image dissector has four apertures. Behind each one is a separate photomultiplier section. The signals from these four channels are represented in Fig. C.5-51 as A, B, C, and D. The holes are located such that, as the optical image moves across a line of the reticle plate, the electronic image in the photomultiplier tube moves from one aperture to another.

During coarse tracking, signals A, B, C, and D are summed together so that the system operates nearly independently of the grating lines of the reticle plate. By means of a sinusoidal signal from the scan oscillator, the aperture is scanned around the image in a circular manner. The resultant modulation on the sum signal ( $A + B + C + D$ ) is fed to a keyed demodulator that derives tangential and radial error signals that are fed to the tangential and radial deflection servos. These servos vary the tangential and radial deflection voltages of the image dissector in such a manner as to null the image dissector tracking error. The resultant radial and tangential deflection signals are used to form the error signals that control the telescope pointing during the acquisition phase. These are converted into the pitch and yaw coordinates (by multiplying them by constants  $K_1$ ,  $K_2$ ,  $K_3$ , and  $K_4$ , as shown in Fig. C.5-50 to form the pitch and yaw error signals, which control the vehicle orientation.

The coarse tracking error signals move the line of sight of the telescope to null the tangential and radial deflection signals of the image dissector. The accuracy of coarse control is sufficient to assess that the image of guide star (1) is significantly less than  $\pm 1$  second from the appropriate tangential and radial lines on the reticle plate. This ensures that the system will track this guide star at the appropriate intersection when the system switches to fine track. [Note that the spacing of the reticle lines is 9.70 microradians (2 arc-seconds).]

When the telescope is tracking accurately with the coarse error signal, the scan oscillator is switched off and the apertures (assumed to be 6 seconds in diameter) are centered over the guide star image. The fine tracking tangential and radial error signals are formed by comparing signals A, B, C, D from the four channels, these error signals being  $(A + B) - (C + D)$  and  $(A + C) - (B + D)$ . These signals are converted to pitch and yaw error signals (as shown in Fig. C.5-50 and used for fine tracking.

To calculate the pitch, yaw, and roll error signals accurately by the signal processing of Fig. C.5-50, the ground station must know the error slopes of the guide star trackers in order to compute the proper values for the telemetered constants. Fig. C.5-52 shows circuitry for measuring these error slopes.

The oscillator generates a sinusoidal signal at a frequency greater than the gain crossover frequency of the fine tracking loop, but which can be followed by the tilt plate servo. This signal is multiplied by constants  $K_{10}$  and  $K_{11}$  to form signals that perturb the pitch and yaw tilt plate servos in such a way as to produce a sinusoidal deflection of the image in the radial or tangential direction of a particular guide star sensor.

The corresponding radial or tangential fine tracking signal is then subtracted from a signal that is the oscillator signal multiplied by constant  $K_{12}$ . The resultant signal is then coherently detected to form an error signal, which is used to vary constant  $K_{12}$  in such a way as to null that error signal. The final value for  $K_{12}$  is then telemetered to the ground station and gives a measure of the error slope of the guide star sensor.

Fig. C.5-53 shows the assumed concept of the control of the vehicle in pitch or yaw during the acquisition phase when it is being positioned by the coarse error signal. The pitch or yaw course tracking error signal is derived, as shown in Fig. C.5-51, from a single guide star tracker and is resolved in terms of pitch and yaw coordinates by the constants  $K_1$  to  $K_4$ , as shown in Fig. C.5-50. (Control of the vehicle in roll during acquisition is performed by signals from an auxiliary star tracker.)

The pitch or yaw coarse tracking error signal is fed through the vehicle tracking amplifier to a gyro feedback loop closed around the vehicle. The gyro feedback is desirable to provide fine rate control during acquisition.

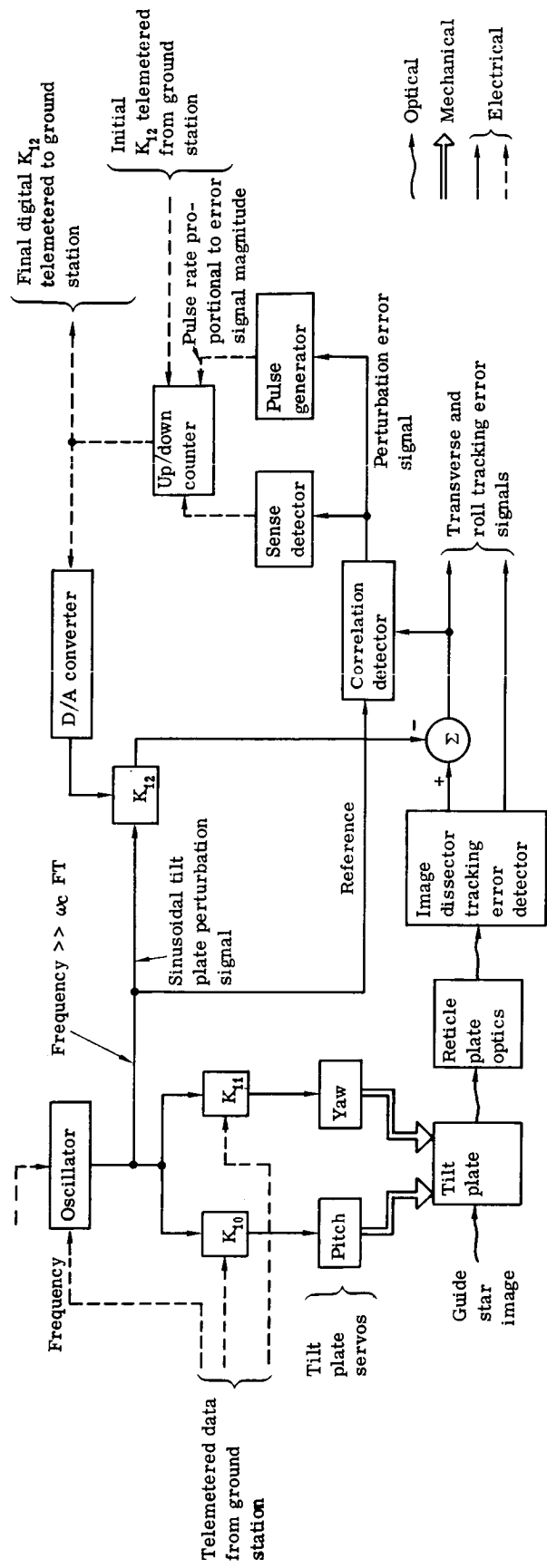


Fig. C.5-52 — Signal processing to measure slope of guide star tracking error detector



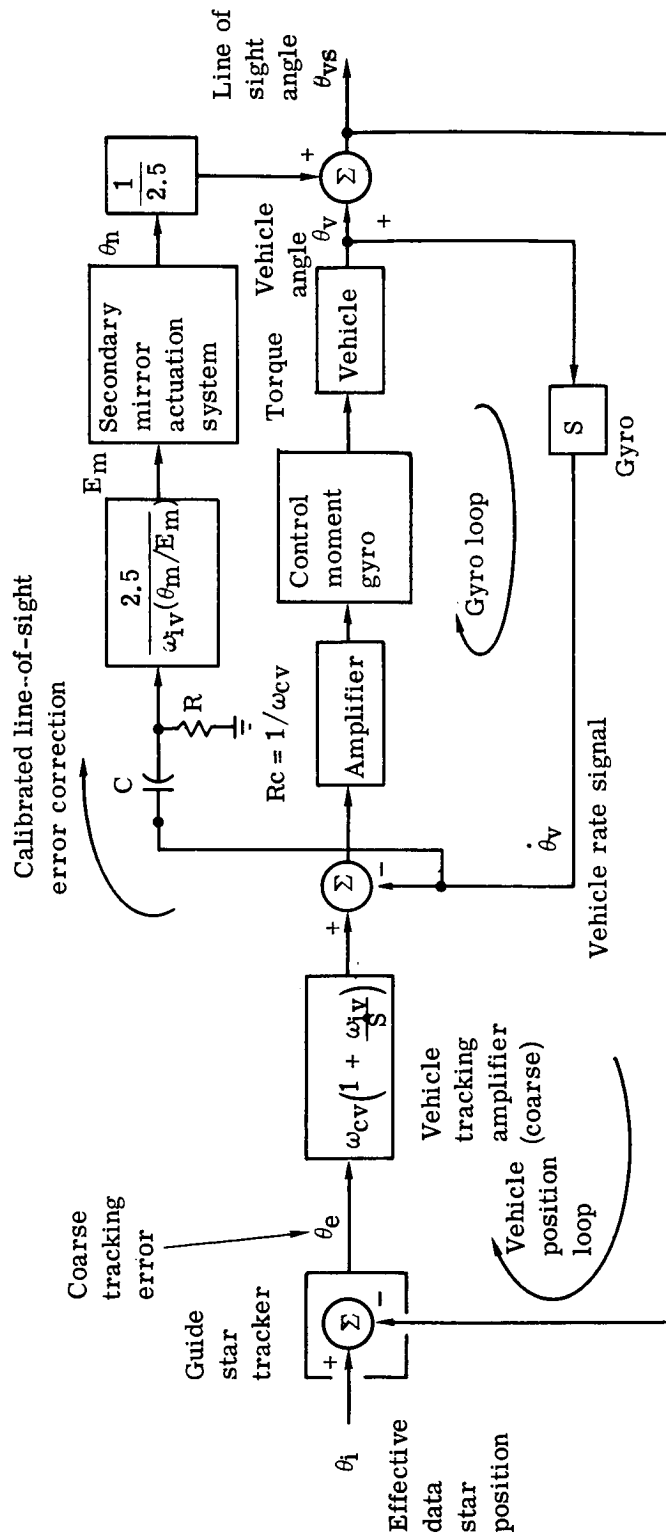


Fig. C.5-53 — Vehicle control loop for coarse tracking

During fine tracking, a lead network is used to achieve the effect of rate feedback. However, this approach is undesirable during coarse tracking because the coarse tracking signal experiences discrete steps when the guide star image moves over a line on the reticle plate. This causes the electronic guide star image in the image dissector to pass through a different aperture and misalignments of the apertures produce a small step change of tracking error. If a lead network were used during coarse tracking, it would differentiate these steps and produce strong jitter of the vehicle position.

Rate gyros can readily be achieved with sufficient accuracy for the acquisition phase. However, for pitch and yaw fine tracking, much greater gyro accuracy is necessary. Studies by the MIT Draper Laboratory suggest that adequate gyro accuracy may be achievable for fine tracking. For the present, however the approach assumed is the more conservative one of deriving the complete fine tracking signals from the guide star trackers by the use of lead networks in the vehicle control loops.

The vehicle control loop will probably experience jitter that is appreciable in relation to the 4.85 microradian ( $\pm 1$ -arc-second) maximum error limits of coarse tracking that are required if the guide stars are to lock onto the proper intersection on the reticle plate. Accordingly, in the final portion of the acquisition phase, the secondary mirror control would be actuated to reduce the line-of-sight errors. The rate signal from the gyro would be fed as a calibrated command signal into the secondary mirror to cancel out the major component of dynamic error (which is proportional to line-of-sight acceleration). This should reduce dynamic coarse tracking errors below 4.85 microradians ( $\pm 0.1$  arc-second).

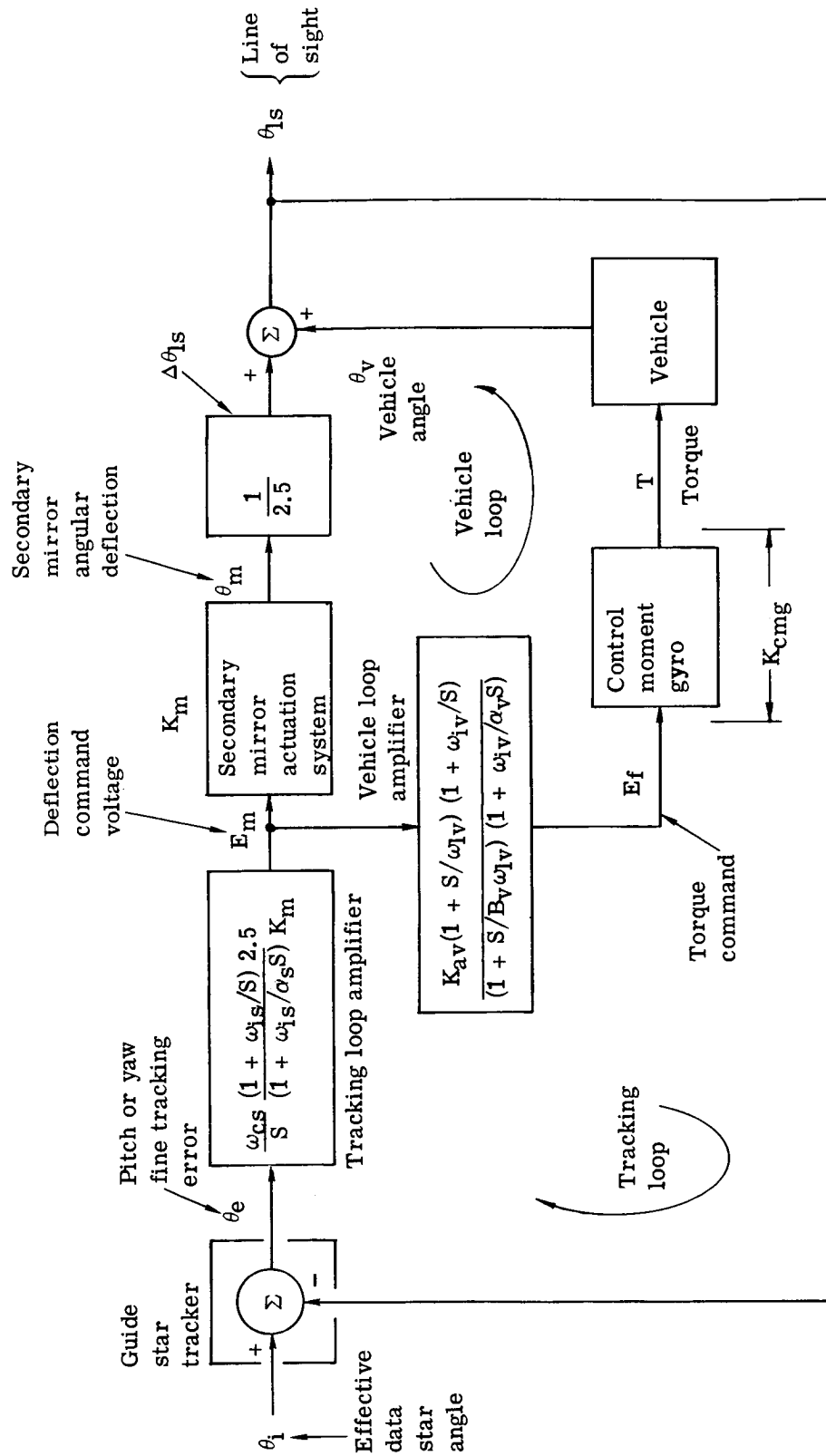
The parameter  $W_{cv}$  is the gain crossover frequency of the vehicle control loop, and  $W_{iv}$  is the upper break frequency of the integral network in that loop. We assume that  $W_{iv}$  is approximately equal to  $W_{cv}/3$ , and  $W_{cv}$  is 0.6 radian/second (about 0.1 hz).

Fig. C.5-54 is a block diagram of the pointing control system in pitch or yaw during fine tracking. The pitch or yaw fine tracking signal (obtained from Fig. C.5-50) is fed through the tracking loop amplifier to the secondary mirror actuator system. The deflection of the secondary mirror is ideally proportional to the deflection command voltage  $E_m$ . Hence, the voltage  $E_m$  is used as an error signal to control the vehicle.

The parameters in the transfer functions of Fig. C.5-54 are defined as follows:

- $W_{cs}$  = gain crossover frequency of secondary mirror tracking loop
- $W_{cv}$  = gain crossover frequency of vehicle tracking loop
- $W_{is}$  = upper break frequency of secondary mirror loop integral network
- $\alpha_s$  = low-frequency amplification of secondary mirror loop integral network
- $W_{lv}$  = lower break frequency of vehicle loop lead network
- $B_v W_{lv}$  = upper break frequency of vehicle lead network
- $W_{iv}$  = upper break frequency of vehicle loop integral network
- $\alpha_v$  = low-frequency amplification of vehicle loop integral network
- $K_m$  =  $\theta_m/E_m$  = sensitivity of mirror actuation system (mirror angular deflection per volt)
- $K_{cmg}$  =  $T/E_t$  = sensitivity of control moment gyro package (torque per volt)
- $J_m$  = vehicle inertia
- $K_{Av}$  =  $W_{cv} W_{lv} J_v K_m / 2.5 K_{cmg}$

Note that the factor 2.5 is the ratio of secondary mirror angular deflection to the corresponding angular deflection of the line of sight.



$$K_{av} = \omega_{cv} \omega_{Jv} K_v / 2.5 K_{cmg}$$

Fig. C.5-54 — Fine tracking control system for LST

### C.5.d(3) Dynamic Performance of Fine Tracking\*

If the dynamic effects of structural resonance, the secondary mirror actuation system, and the control moment gyro system are ignored from Fig. C.5-54, it can be seen that the loop transfer functions of the secondary mirror control loop and the vehicle control loop are as follows:

#### Secondary Mirror Control Loop

$$G_s = \frac{W_{cs}}{s} \frac{(1 + W_{is}/S)}{1 + (W_{is}/\alpha_s)/S}$$

#### Vehicle Control Loop

$$G_v = \frac{K_{v1} (1 + S/W_{1v}) (1 + W_{iv}/S) K_{cmg} 2.5}{(1 + S/B_v W_{1v}) (1 + W_{iv}/\alpha_v S) J_v S^2 K_m}$$

where

$$K_{v1} = W_{cv} W_{1v} J_v K_m / 2.5 K_{cmg}$$

Substituting  $K_{v1}$  into  $G_v$  gives

$$G_v = \frac{W_{cv} (1 + W_{iv}/S) (1 + W_{1v}/S)}{S (1 + W_{iv}/\alpha_v S) (1 + S/B_v W_{1v})}$$

Bode plots of these loop transfer functions are shown in Fig. C.5-55.

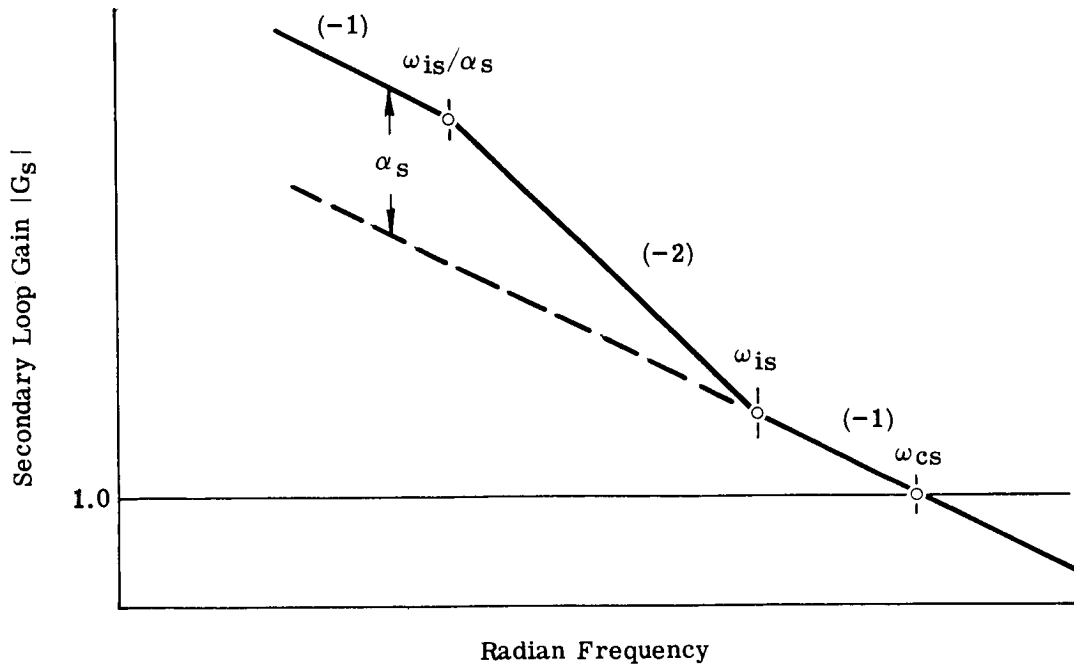
The loop transfer function of the complete fine tracking loop is equal to

$$G_t = G_s (1 + G_v)$$

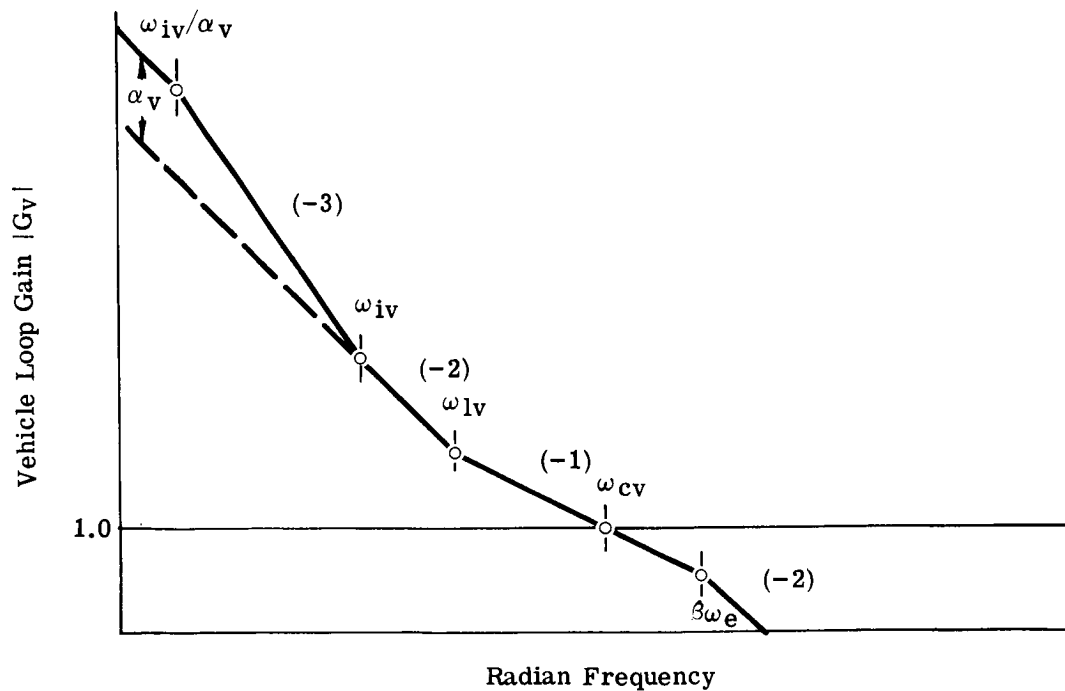
A Bode plot of this tracking loop transfer function is shown in Fig. C.5-56. The lower curve is the response of the secondary mirror loop gain ( $G_s$ ) and the upper curve is the plot of the fine tracking loop gain ( $G_t$ ). The crosshatched area shows the effect of the vehicle loop within the fine tracking loop.

Table C.5-7 lists the estimated parameters of the loop transfer functions of Figs. C.5-55 and C.5-56. These are based on the assumption that the gain crossover frequency of the secondary mirror control loop is 2 hz and that of the vehicle is 0.1 hz. Note that the maximum value of the gain crossover frequency of the vehicle is limited by the structural dynamics of the vehicle and that that of the secondary mirror control loop is limited both by guide star sensor noise and structural dynamics. With force isolation actuation for the secondary mirror, the gain crossover frequency of the secondary loop can probably be increased to 4 hz without any difficulty.

\*A detailed analysis of the dynamics of the LST tracking system has been given in Biernson, G., Approximate Analysis of Allowable LST Vehicle Pointing Errors, Memorandum LST 72-57, 14 Apr 1972. This subsection is a summary of the major results.



(a) Secondary mirror loop transfer function



(b) Vehicle loop transfer function

Fig. C.5-55 — Asymptotic plots of secondary and vehicle loop gains

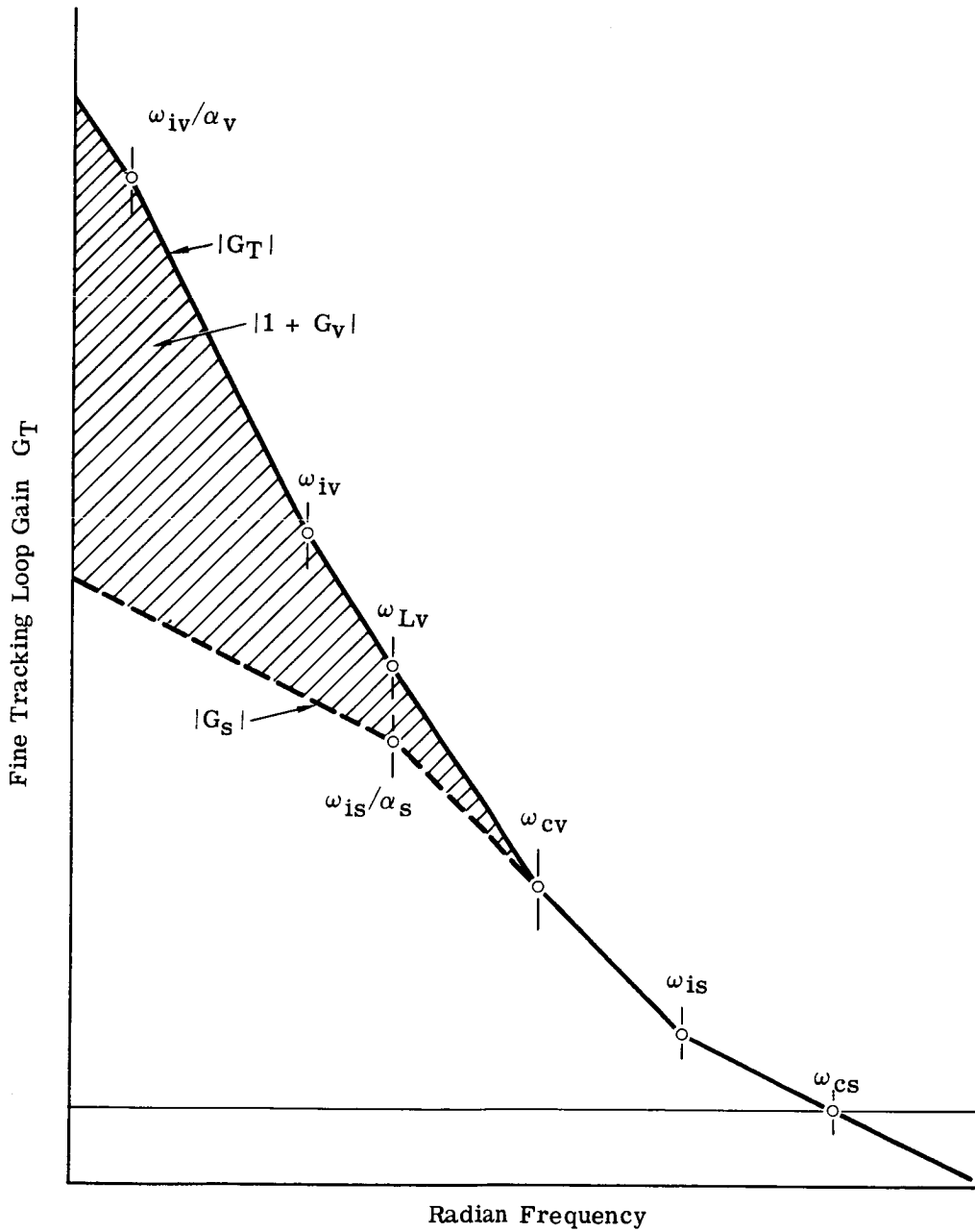


Fig. C.5-56 — Transfer function of fine tracking loop

The allowable rms pitch or yaw tracking error ( $\sigma$ ) due to torque disturbances has been budgeted at 0.00775 microradian (0.0016 arc-second). This is conservatively considered to be equivalent to peak tracking errors due to transient torques of  $\pm 2\sigma$ , which is  $\pm 0.01550$  microradian ( $\pm 0.0032$  arc-second). For this budgeted peak error, consider the allowable transient torque disturbances on the vehicle owing to control moment gyro perturbation torques and other effects.

Fig. C.5-57 shows a generalized transient torque disturbance, which is characterized by duration  $\tau_d$  and a rise time  $\tau_r$ . This disturbance may approximate either an impulse, step, or ramp to the tracking loop depending on the values of  $\tau_d$  and  $\tau_r$  relative to the time constants of the feedback loop.

The fine tracking loop transfer function can be approximated as follows:

$$G_t = (W_c/S) (1 + W_{ia}/S) (1 + W_{ib}/S)$$

Relating to this Fig. C.5-56, we have

$$W_c = W_{cs}, \quad W_{ia} = W_{is}, \quad W_{ib} = W_w$$

For this tracking loop transfer function, the torque disturbance of Fig. C.5-57 approximates an impulse if  $\tau_d < 1/W_{ia}$ , two consecutive steps  $\tau_d > 1/W_{ia}$  and  $\tau_r < 1/W_{ib}$ , and a series of ramps if  $\tau_r > 1/W_{ib}$ . The allowable limits on the torque disturbances for these three conditions are listed in Table. C.5-8.

For condition (a) (for which the pulse duration is less than  $1/W_{ia}$ ), the integral of the torque should not exceed  $\theta_e J W_c$ . For condition (b) (for which the pulse duration is greater than  $1/W_{ia}$  but the rise time is less than  $1/W_{ib}$ ), the amplitude of the torque disturbance should not exceed  $\theta_e J W_c W_{ia}$ . For condition (c) (for which the rise time is greater than  $1/W_{ib}$ ), the rate of change of torque should not exceed  $\theta_e J W_c W_{ia} W_{ib}$ .

It is assumed that  $W_c = 12$  radians/second, or about 2 hz. Reasonable values for  $W_{ia}$  and  $W_{ib}$  are then  $W_{ia} = W_c/3 = 4$  radians/second and  $W_{ib} = W_c/10 = 1.2$  radians/second. Assumed is a vehicle inertia in pitch or yaw of  $J_v = 10.85 \times 10^4$  meter-newton-second<sup>2</sup> ( $J = 80,000$  foot-pound-second<sup>2</sup>). The resultant limits on the integral of torque, amplitude of torque perturbation, and torque rate are shown in Fig. C.5-58 as a function of the rise time and duration of the torque perturbation. These plots indicate the regions where this torque perturbation approximates an impulse, step, or ramp.

These assumed frequency parameters would result in a value of 0.2 hz for the gain crossover frequency of the vehicle tracking loop (since, from Fig. C.5-54,  $W_{ib} = W_{cv}$ ). This may not be achievable because of the structural dynamics of the vehicle. However, the same effect can be achieved in the fine tracking loop by adding an integral network to the tracking loop amplifier having the transfer function  $(1 + W_{ib}/S)/(1 + W_{cv}/S)$ .

The most important conclusion to be drawn from Fig. C.5-58 is that the peak allowable step torque disturbance is 0.0815 meter-newton (0.06 foot-pound). This should be related to the cogging torques exerted by the

Table. C.5-7 – Parameters of Fine Tracking Control System

Parameter	Value
$f_{cs} = W_{cs}/2\pi$	2 hz
$f_{is} = W_{is}/2\pi$	0.67 hz
$\alpha_s$	10
$f_{cv} = W_{cv}/2\pi$	0.1 hz
$f_{1v} = W_{1v}/2\pi$	0.033 hz
$B_v$	10
$f_{iv} = W_{iv}/2\pi$	0.01
$\alpha_v$	5



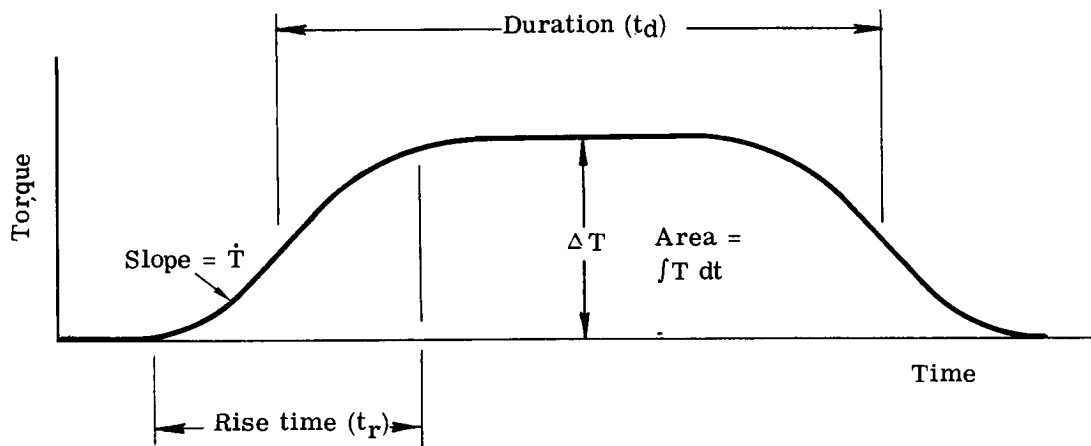


Fig. C.5-57 — General torque disturbance

Table C.5-8 – Limits on Allowable Torque Disturbances

Condition	Torque Limit
$\tau_d < 1/W_{ia}$	$\int T_d dt < \theta_e JW_c$
$\tau_d > 1/W_{ia}, \tau_r < 1/W_{ib}$	$\Delta T < \theta_e JW_c W_{ia}$
$\tau_r > 1/W_{ib}$	$\dot{T} < \theta_e JW_c W_{ia} W_{ib}$

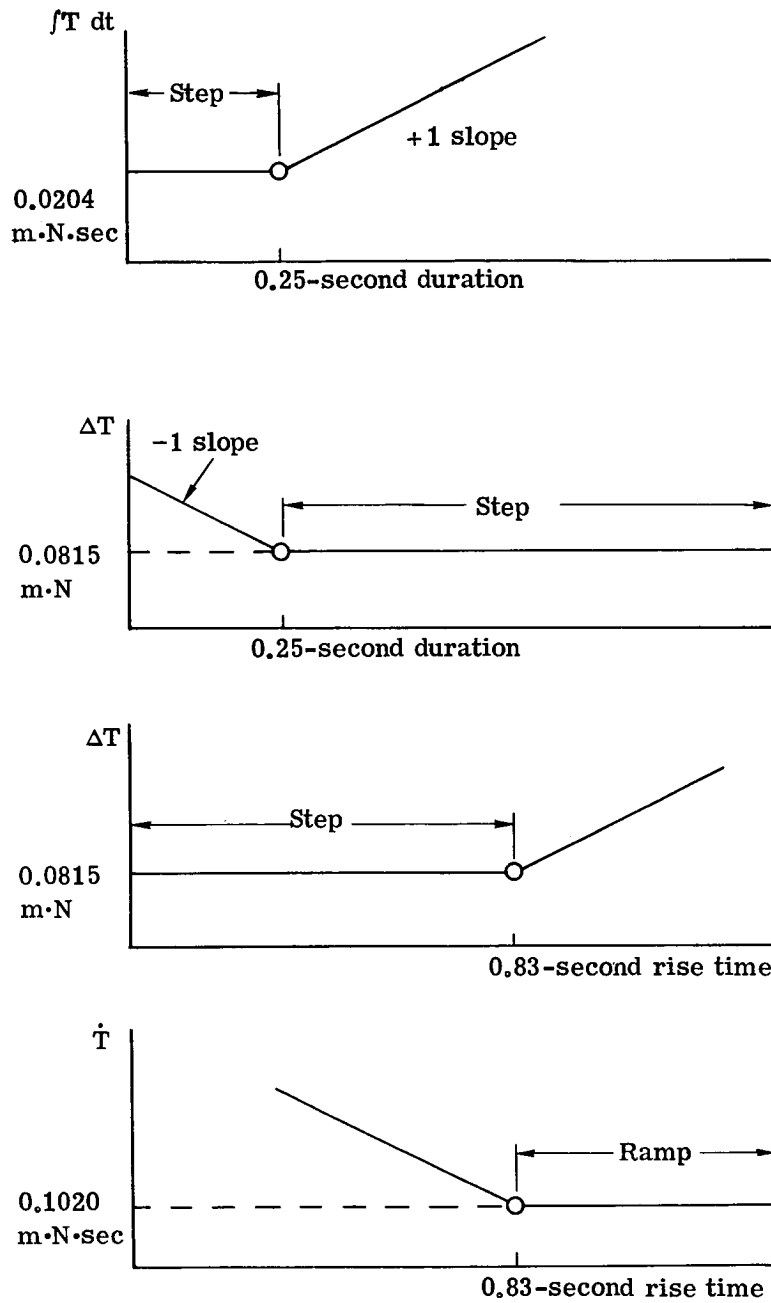


Fig. C.5-58 — Limits on allowable torque disturbances for  $J = 10.85 \times 10^4$  meter-newton second<sup>2</sup> ( $J = 80,000$  foot-pound second<sup>2</sup>) and peak tracking error of  $0.0155$  microradians ( $0.0032$  arc-second)

control moment gyros, which must be kept below this value. Information indicates that this requirement will probably be met with a comfortable margin.

The limits on allowable step torque disturbance can be expressed in terms of allowable motions of the vehicle as follows. Vehicle tracking must be controlled such that the maximum angular acceleration shall not exceed the value

$$0.776 \text{ microradian/second}^2 = 0.16 \text{ arc-second/second}^2$$

#### C.5.d(4) Computer Simulation of Stabilization of LST Line of Sight

##### Description of Simulation

Fig. C.5-59 is a block diagram of the LST line-of-sight stabilization simulation that was implemented for the condition of a simple piezoelectric actuation of the secondary mirror (no force isolation). To incorporate force isolation, the diagram was expanded by including the block diagram of Fig. C.5-60.

Three dynamic structural responses are included in this simulation:

- $\theta_{st}/T_s$  = Deflection of structure at the secondary mirror ( $\theta_{st}$ ) as a function of the reaction torque ( $T_s$ ) applied to the structure by secondary mirror
- $\theta_{ls}/T_s$  = Deflection of telescope line of sight ( $\theta_{ls}$ ) as a function of the reaction torque ( $T_s$ ) applied to the structure by the secondary mirror
- $\theta_{ls}/T_v$  = Deflection of telescope line of sight as a function of the torque applied to the vehicle by the control moment gyros.

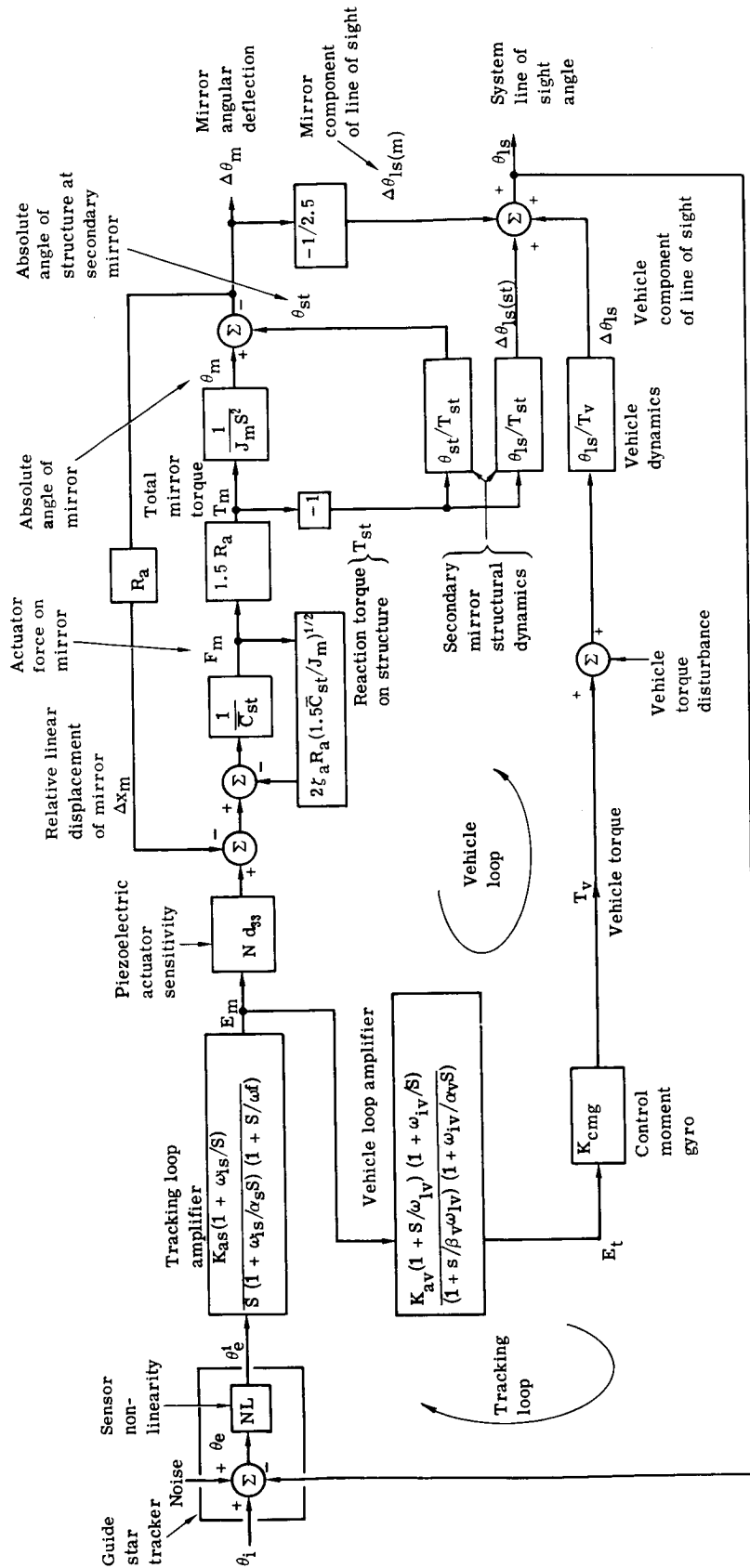
These transfer functions are of the form

$$\frac{\theta}{T} = \frac{1}{J_v S^2} + \sum \frac{K_q}{S^2 + 2\zeta_q \omega_{nq} S + \omega_{nq}^2}$$

The first term in this expansion ( $1/J_v S^2$ ) is the zero-frequency response, under which conditions the structure acts as a solid body. Hence,  $T = J_v S^2 \theta$ , where  $J_v$  is the vehicle inertia. The other terms represent the oscillatory modes of oscillation of the system. The first nine oscillatory modes have been simulated in order to provide a very good approximation of the structural dynamic response. Structural analysis yields each coefficient  $K_q$  and the natural frequency  $\omega_{nq}$ . The damping ratio  $\zeta_q$  has been set arbitrarily on the basis of experience with typical structures of this sort. These indicate a damping factor of  $\delta$  of 0.5 percent, which represents the relative amount of energy dissipated per cycle of the structural oscillation. The damping ratio  $\zeta$  is equal to  $\delta/2$  and so is assumed to be 0.0025.

To check the accuracy of the structural simulation of the modes, these various modes were excited with steps of torque to check that the incremental decay of the responses per cycle was equal to 0.5 percent.

The parameter  $R_a$  is the radial distance of the actuator from the axis of the mirror. The force  $F_m$  is the force delivered by a single actuator on the mirror as it rotates the mirror about an axis perpendicular to the radial vector to that actuation point. This actuator delivers the torque  $R_a F_m$  to the mirror. The other two actuators operating in synchronism, with this to provide an additional torque of  $0.5 R_a F_m$  to the mirror. Hence, the total torque  $T_m$  applied to the mirror by all three actuators is equal to  $1.5 R_a F_m$ , (Fig. C.5-59).



$$K_{as} = \omega_{cs}(2.5R_a/Nd_{33})$$

$$K_{av} = \omega_{cv}\omega_{cv}/(J_v N d_{33}/2.5 R_m K_{cmg})$$

Fig. C.5-59 — LST stabilization simulation without force actuation isolation system for secondary mirror

$$KD2 = 2\zeta_{st} R_{am} [1.5 \sqrt{C_{st}} (J_m + J_w)]^{1/2}$$

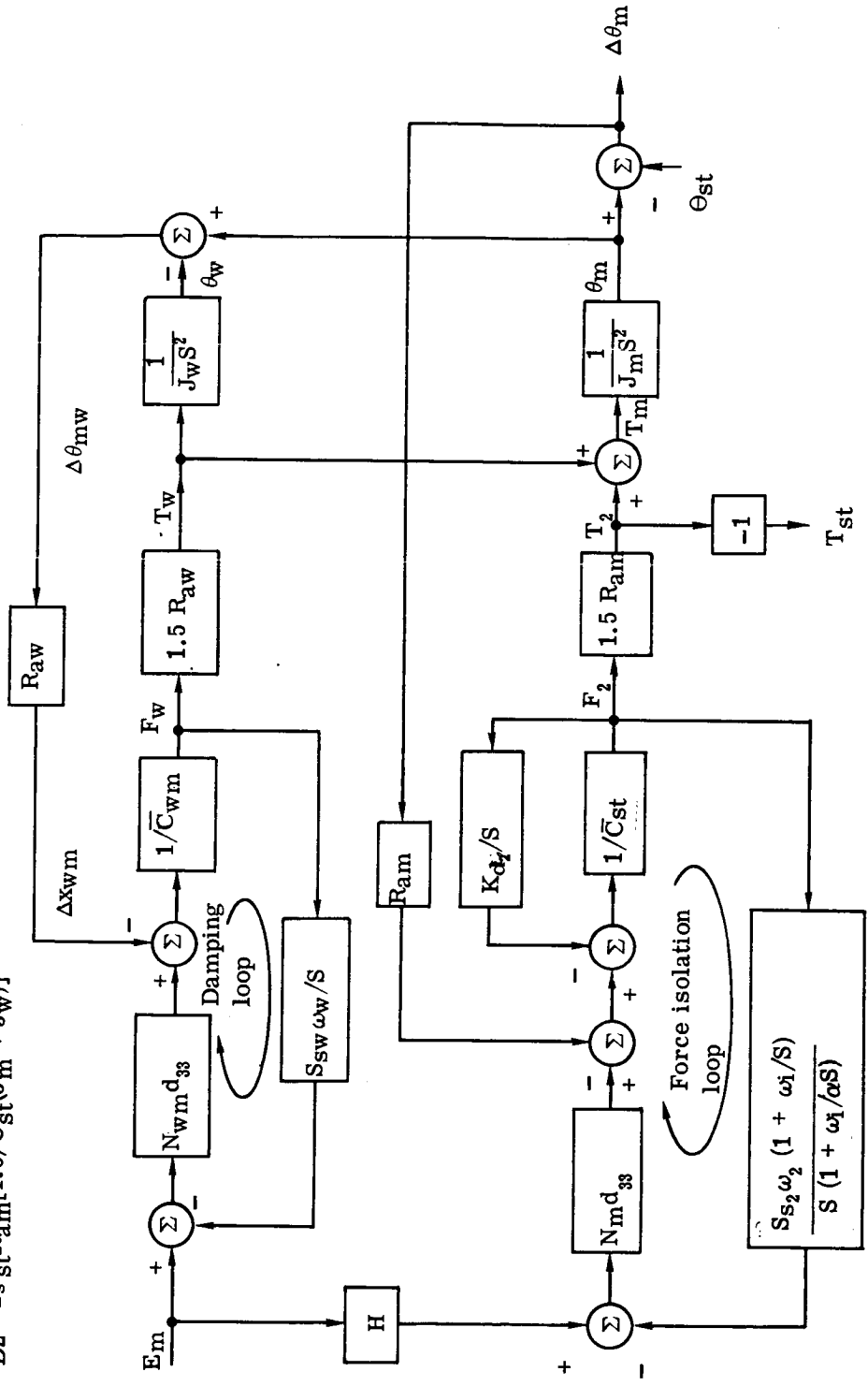


Fig. C.5-60 — Force isolation actuation system of secondary mirror control system

The parameter  $\bar{C}_{st}$  is the effective linear mechanical compliance of the telescope structure as seen from the actuation point. It includes the compliance of the actuators and related structure.  $\bar{C}_{st}$  has been chosen such that the resultant natural frequency of the mirror inertia resonating with this compliance is 35 hz. The damping ratio  $\zeta_a$  shown in Fig. C.5-59 represents the mechanical damping of this resonance, which is assumed equal to 0.0025, just as for the other structural resonances.

The parameter  $d_{33}$  is the sensitivity parameter of the piezoelectric material (PZT-4) and  $N$  is the number of elements in the actuator stack (40). The value for  $d_{33}$  is 12 nanometers/volt.

The control moment gyro package has been approximated as a simple constant  $K_{cmg}$  between applied voltage and resultant vehicle torque  $T_v$ . This is obviously a very severe approximation. Also it should be noted that the vehicle structural model does not include the effects of the solar panels, which can greatly affect the structural response of  $(\theta_{1s}/J_v)$ . Because of these approximations, the simulation of the vehicle loop dynamics is quite limited. However, this is not a serious problem for this case, because concern is primarily with the response of the fine tracking loop. The gain crossover frequency of the vehicle loop was arbitrarily set equal to 0.1 hz because studies performed elsewhere using a more detailed simulation of the dynamics of the control moment gyro package and vehicle structure have indicated that this value can be achieved reliably. Making this setting permits a reasonably good approximation of the vehicle for fine pointing studies.

The tracking loop amplifier contains a pure integration  $(1/S)$  and an integral network  $(1 + \omega_{is}/S)/[1 + (\omega_{is}/\alpha_s)/S]$ . The factor  $1/(1 + S/\omega_f)$  is a filter placed in the tracking loop to attenuate the effects of resonance peaks in the telescope structure.  $\omega_f$  was varied to allow the maximum gain crossover frequency of the fine tracking loop consistent with good stability, which results in setting  $\omega_f$  approximately equal to  $2\omega_{cs}$ .

The idealized frequency responses of the secondary mirror control loop and the vehicle control loop are shown in Figs. C.5-61 and C.5-62, respectively. These ignore the effects of structural dynamics. From these plots, it is seen that the dynamic loop parameters assumed for the simulation are as shown in Table. C.5-9.

The gain crossover frequency  $\omega_{cs}$  of the secondary mirror control loop (or the fine tracking loop) was a variable in the simulation studies. Table. C.5-10 lists the values of other parameters shown in the block diagrams of Figs. C.5-59 and C.5-60.

## Responses

### Summary

The results of the computer simulations of the stabilization system are presented in Figs. C.5-63 through C.5-66. Fig. C.5-67 shows the transfer characteristic of the guide-star sensor nonlinearity that was used in the responses of Fig. C.5-66. This is the approximate error characteristic of the reticle tracker and is represented by the block (NL) in Fig. C.5-59, between the actual tracking error  $\theta_e$  and the error signal  $\theta'_e$  from the guide star sensor. This nonlinear transfer characteristic is normalized such that its slope is unity in the region of zero error. It can be seen from Fig. C.5-67 that the output signal range is equivalent to  $\pm 0.18$  microradian ( $\pm 0.036$  arc-second). These limits gives us a simple quantitative measure of the dynamic range of the reticle tracking error detector.

Figs. C.5-63 through C.5-65 show the responses of the system to a 10-microradian step input (2 arc-seconds). Although such a large step would never be experienced in fine tracking, these responses are useful for providing a preliminary analysis of dynamic performance.

Figs. C.5-63 and C.5-64 show the responses with a simple piezoelectric actuation system on the secondary mirror. Fig. C.5-65 shows the responses with the dynamic force isolation actuation system that is actually being proposed for the secondary mirror. In Fig. C.5-63, the fine tracking loop has a gain crossover frequency of 1.0 hz. As

the curves show, the system has reasonably good stability. However, in Fig. C.5-64, the tracking loop gain crossover frequency was increased to 2 hz, which caused the system to become unstable. In Fig. C.5-65, the tracking loop gain crossover frequency was increased to 4 hz when the force isolation actuation system was used and good stability was still maintained. In this simulation, the conservative assumption was made that the sensitivities of the actuation systems driving the secondary mirror and counterweight were matched only to an accuracy of 10 percent.

The curves of Fig. C.5-64 give only the tracking loop responses because they were taken with the vehicle loop opened in order to simplify the curves. Since this response is unstable, and closing the vehicle loop tends to decrease stability, the responses for the vehicle loop closed would also oscillate.

These responses of Figs. C.5-63 to C.5-65 thus show that the design goal of 2-hz gain crossover frequency for the fine tracking loop cannot be achieved with a simple actuation system for the secondary mirror but can be satisfied with a good safety margin when the force isolation actuation system is used.

Fig. C.5-66 shows the operating tracking response of the force isolation actuation system with a 2-hz gain crossover frequency in the fine tracking loop. The nonlinearity of the reticle tracker is simulated (discussed earlier). A disturbing torque signal was applied to the vehicle, having the form of a square wave with a 2-second period and an amplitude of 0.0023 meter-newton ( $\pm 0.02$  inch-pound.) This simulates the effect of a stiction level in the control-moment gyro system of 0.0046 meter-newton (0.04 inch-pound) [which would produce step changes of torque of 0.0046 meter-newton (0.04 inch-pound)]. Tracking sensor noise was added to the system of such an amplitude that it produced an rms output noise of 0.005 microradian (0.001 arc-second) when the torque perturbation signal and the nonlinearity was removed.

Fig. C.5-66 shows that for these conditions the rms tracking error is 0.0085 microradian (0.0017 arc-second) and the peak-to-peak error is 0.0189 microradian (0.0039 arc-second). The static friction level of 0.0046 meter-newton (0.04 inch-pound) for the control moment gyro package is about twice what this static friction level was conservatively estimated to be, and the static friction level may actually be appreciably less than this. Since these tracking errors are quite acceptable, it is concluded that the stabilization performance of the system should be adequate.

#### Detailed Discussion

Table C.5-11 defines the response shown in Figs. C.5-63 through C.5-67. Curve A, which shows the residual line-of-sight perturbations, represents  $(\Delta\theta_{ls(st)} + \theta_{st}/2.5)$ , which is the total direct effect on the line of sight of the secondary mirror structural dynamic responses. Note that Figs. C.5-63 through C.5-65 show the actual line of sight error, which is curve E. In Fig. C.5-67, the rms value of the line of sight error is plotted instead as curve F.

The rise time  $t_r$  of the step response of a feedback control loop (i.e., the time for that response to reach 63 percent of its final value) is for conventional control loops equal approximately to  $1/\omega_c$  where  $1/\omega_c$  is the gain crossover frequency of the control loop. In Table C.5-12, the rise times of the step responses of the line of sight and vehicle angle are compared, respectively, with the gain crossover frequencies of the tracking and vehicle control loops. The theoretical gain crossover frequency values in hertz are defined as  $1/2\pi t_r$ . This is compared with the actual gain crossover frequency values of the tracking and vehicle control loops for the responses of Figs. C.5-63 and C.5-65. The reasonably good correspondence between these values provides an independent check on the adequacy of the simulation.



Table C.5-9 – Basic Dynamic Parameters for Control Loops

Parameter	Value
<b>Vehicle Loop</b>	
$\omega_{CV}$	$2\pi (0.1)$ radians/second
$\omega_{IV} = \omega_{CV}/4$	$2\pi (0.025)$ radians/second
$\beta_V$	20
$\omega_{iV} = \omega_{IV}$	$2\pi (0.025)$ radians/second
$\alpha_V$	10
<b>Secondary mirror loop</b>	
$\omega_f$	$2\omega_{CS}$
$\omega_{is}$	$\omega_{CS}/4$
$\alpha_s$	10

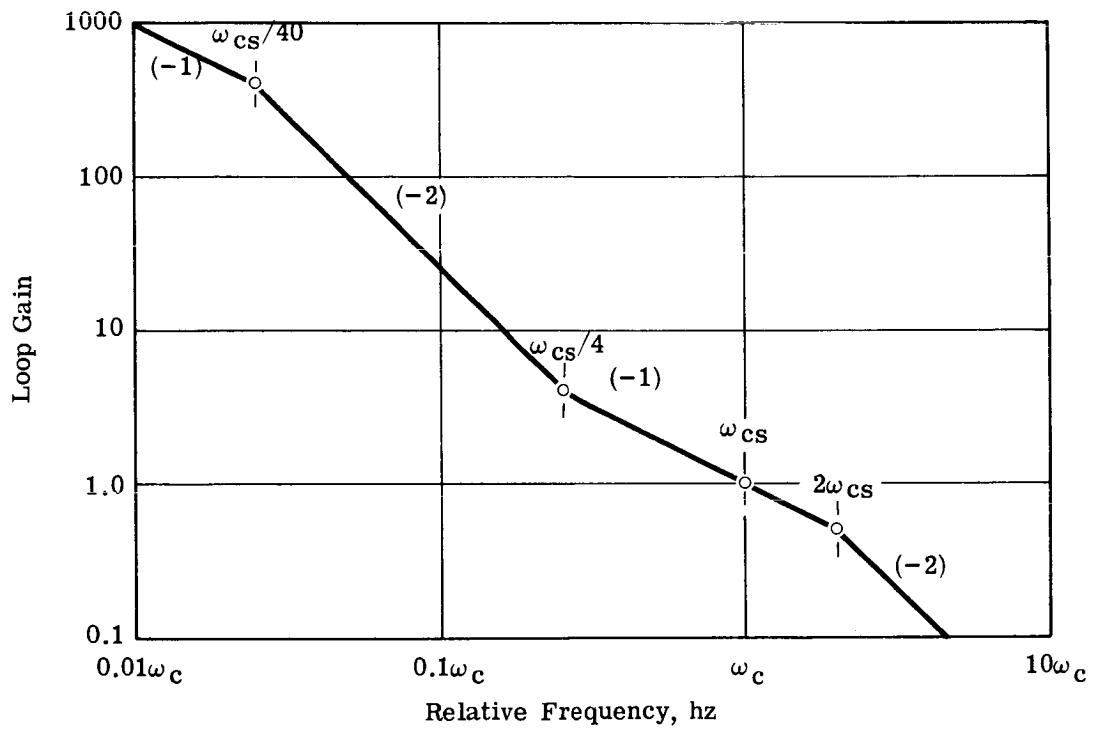


Fig. C.5-61 — Bode plot for secondary mirror control loop (structural dynamics ignored)

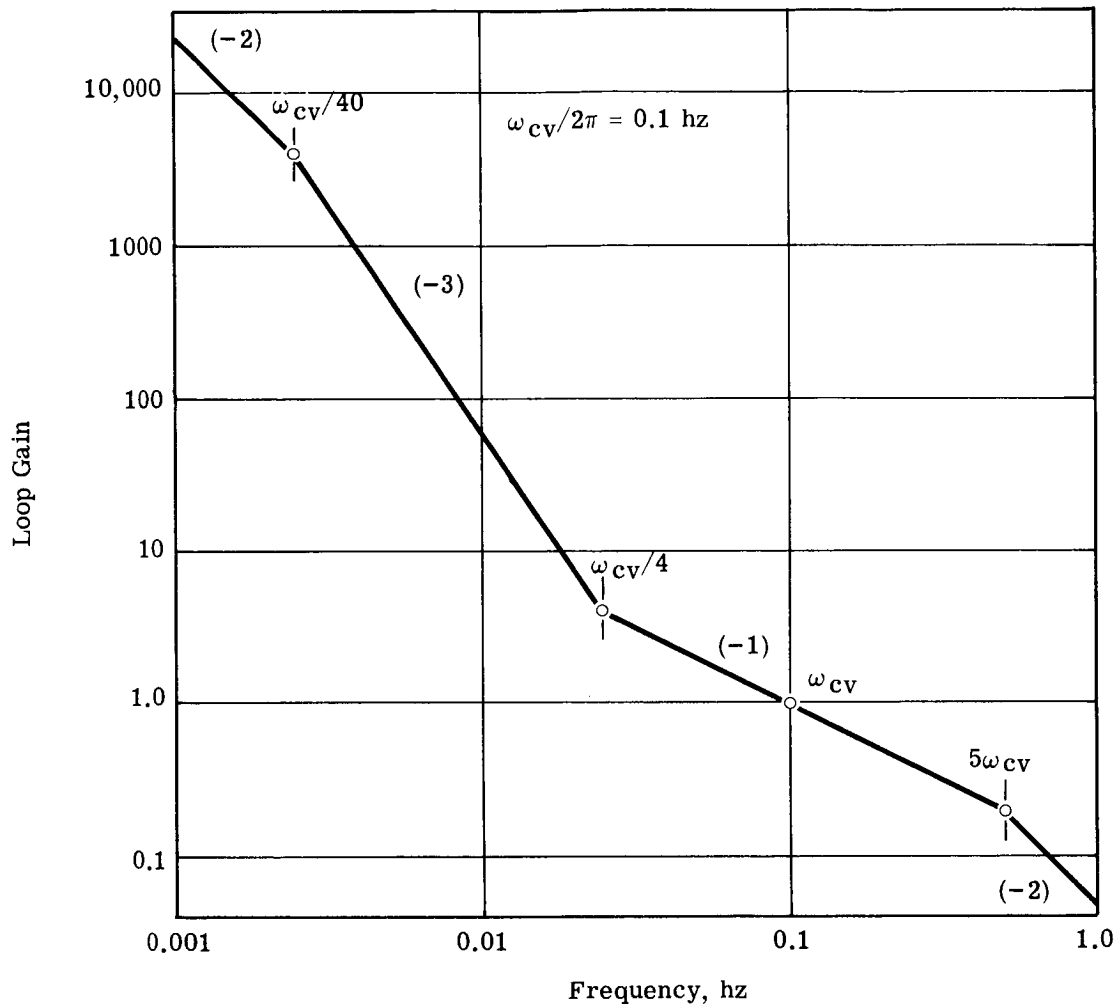


Fig. C.5-62 — Bode plot for vehicle control (structural dynamics ignored)

Table C.5-10 – Other Dynamic Parameters for Simulation

Parameter	Value
$N_{m d_{33}}$	$0.49 \times 10^{-6}$ inch/volt
$N_{w m d_{33}}$	$1.12 \times 10^{-6}$ inch/volt
$R_{am} = R_A$	10 inches
$R_{aw}$	7.6 inches
$J_M$	10 inches · pounds · seconds <sup>2</sup>
$J_w$	5 inches · pounds · seconds <sup>2</sup>
$1/\bar{C}_{wm}$	206,000 pounds/inch
$1/C_{st}$	1,620 pounds/inch
$\zeta_{st}$	0.0025
$S_{sm}$	5.7 volts/pound
$S_{sw}$	1.43 volts/pound
$\omega_m$	84,700 second <sup>-1</sup>
$\omega_w$	13,800 second <sup>-1</sup>
$\omega_i$	628 radians/second
$\alpha$	5

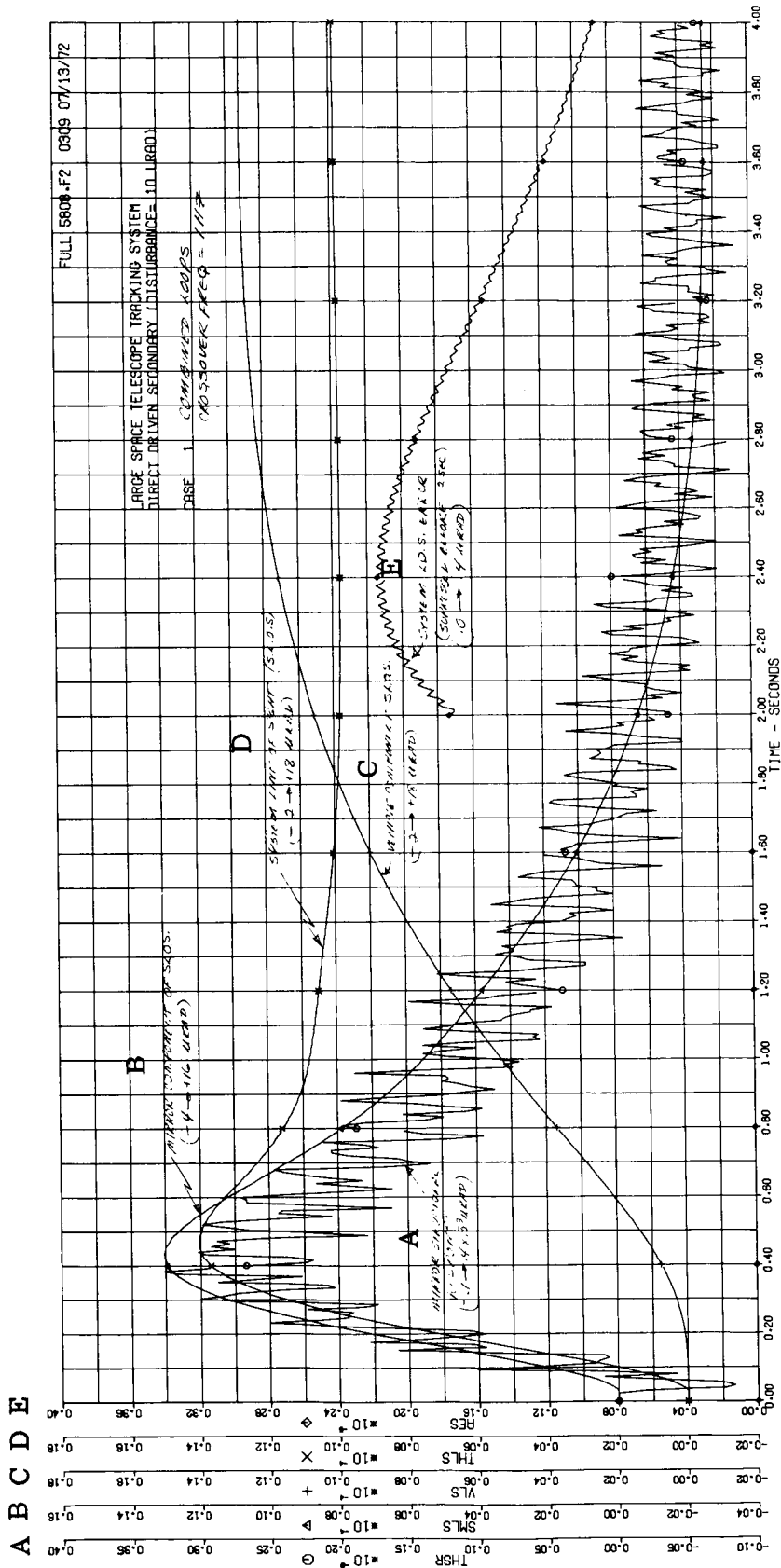


Fig. C.5-63 — LST tracking responses to line-of-sight step (direct driven secondary mirror crossover frequency of 1.0-hz, 10-microradian step tracking loop gain)

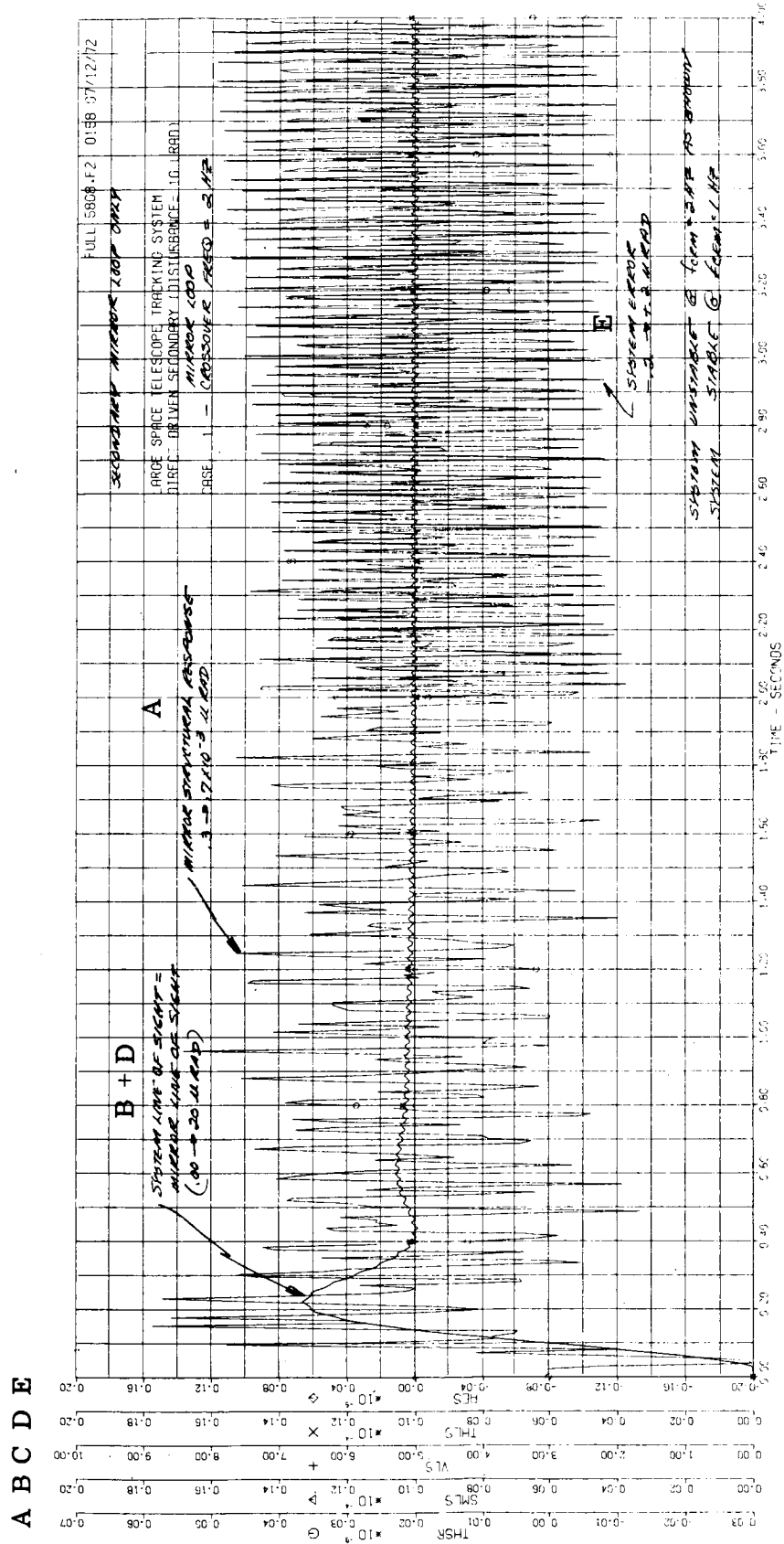


Fig. C.5-64 — LST tracking responses to line-of-sight step (direct driven secondary mirror crossover frequency of 2.0-hz, 10-microradian step tracking loop gain, vehicle loop open)

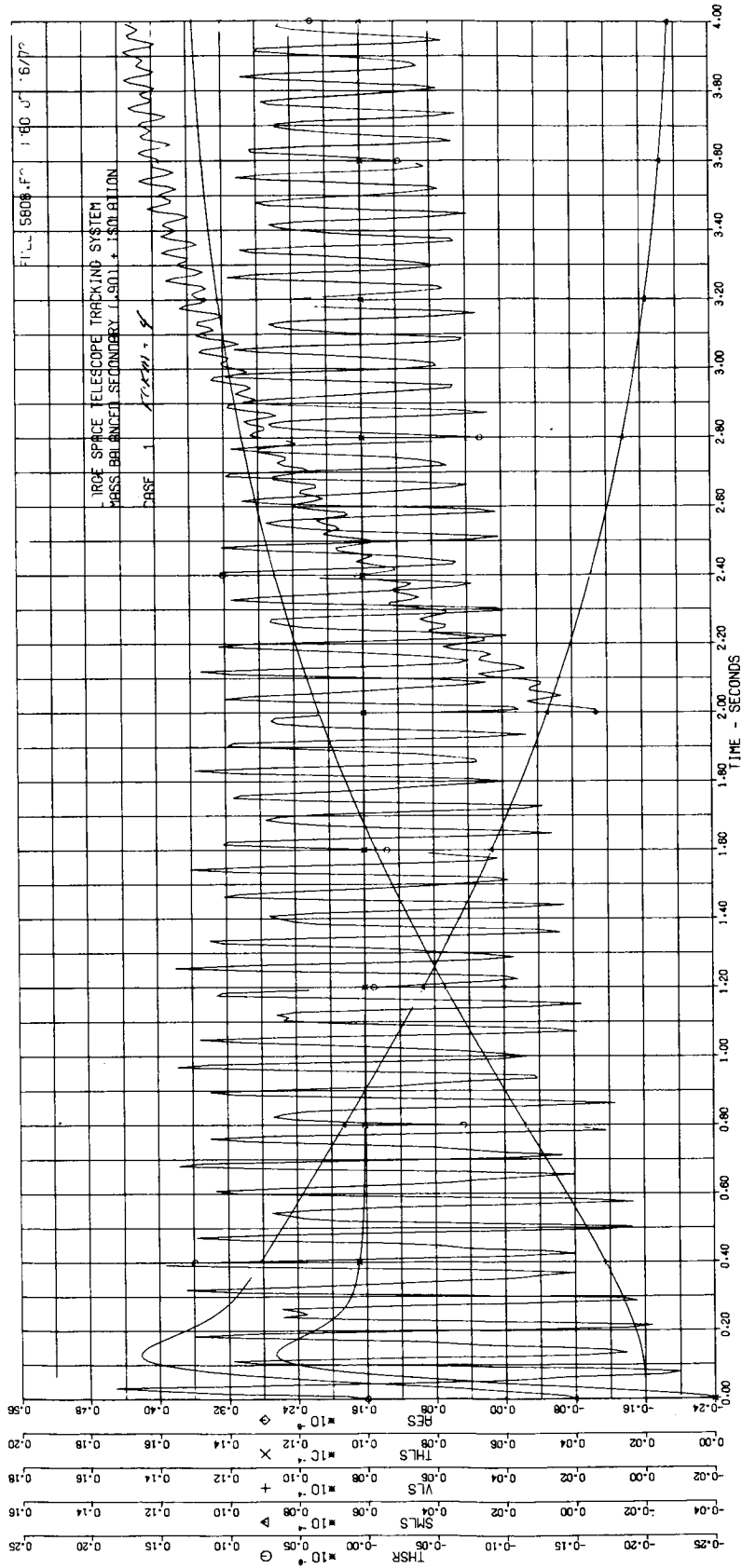


Fig. C.5-65 — LST tracking responses for line of sight step of 10 microradians  
 (force isolation secondary mirror actuation system with tracking loop gain  
 crossover frequency of 4.0 hz)

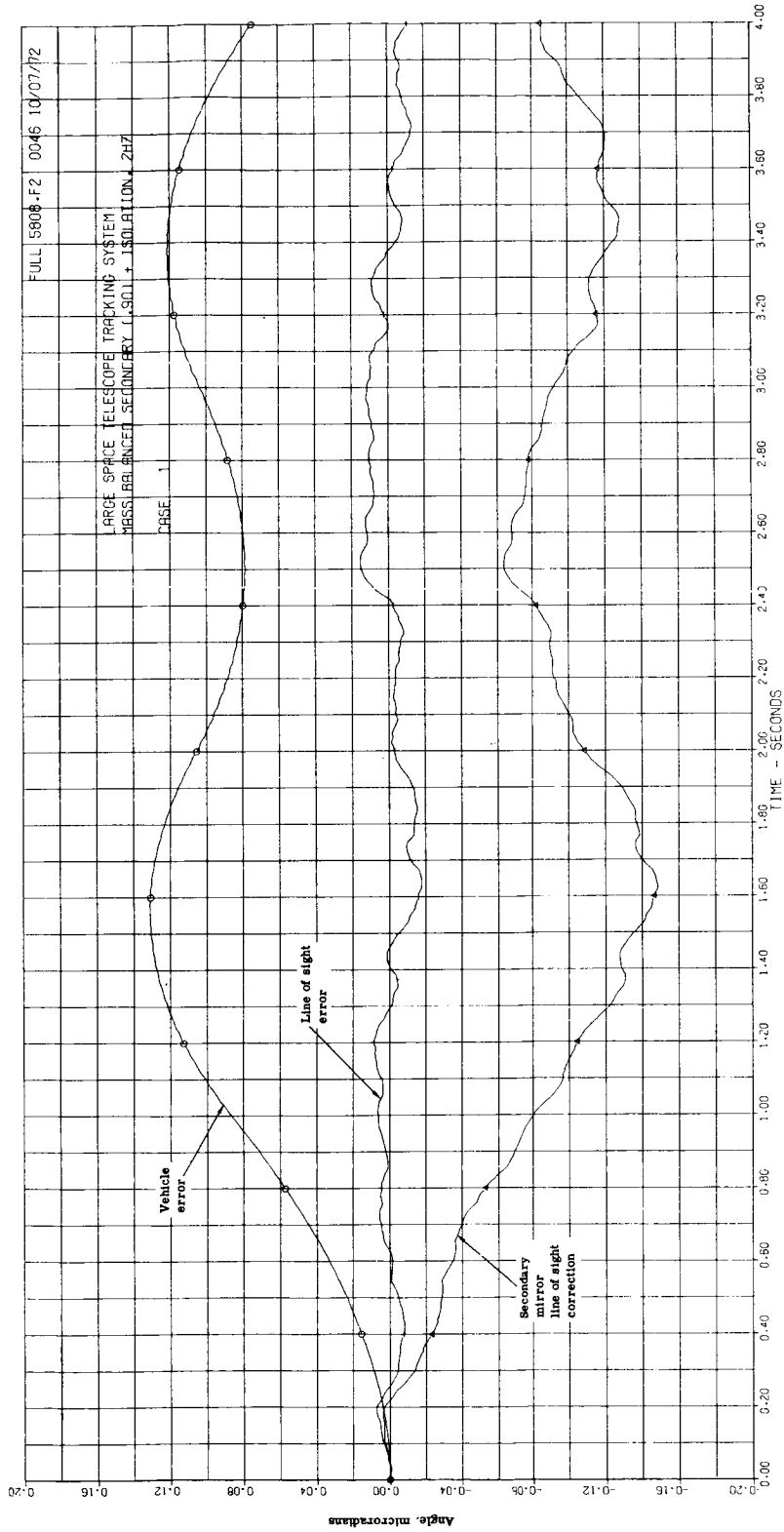


Fig. C.5-66 — LST tracking responses (force isolation secondary mirror actuation with tracking loop gain crossover frequency of 2.0 hz, includes tracking sensor nonlinearity, sensor noise of 0.005 microradian rms, torque disturbance of  $\pm 0.0023$  meter-newton square wave with 2-second period)



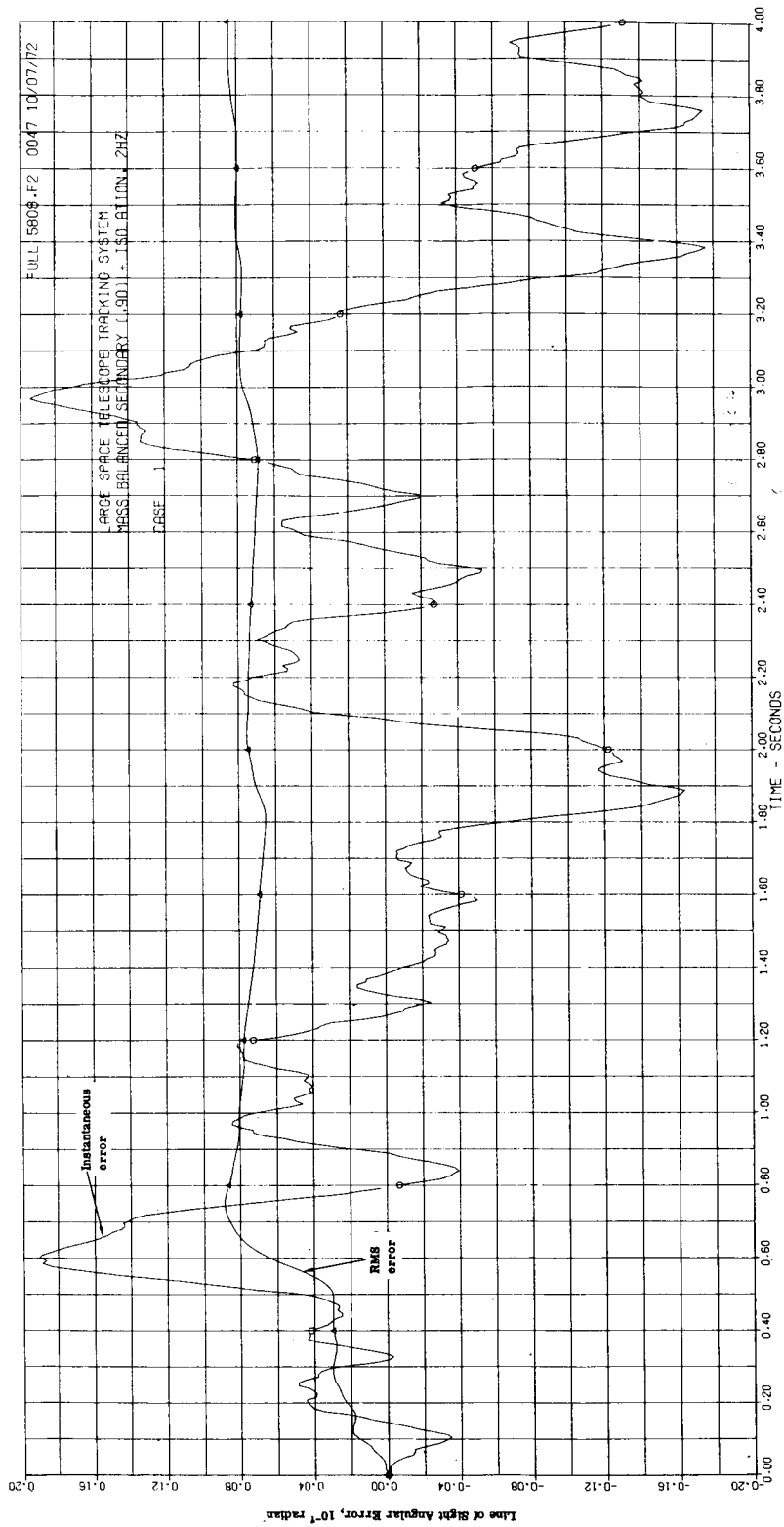


Fig. C.5-66 — LST tracking responses (force isolation secondary mirror actuation with tracking loop gain crossover frequency of 2.0 hz, includes tracking sensor nonlinearity, sensor noise of 0.005 microradians rms, torque disturbance of  $\pm 0.02$  inch-pounds square wave with 2-second period) (Cont.)

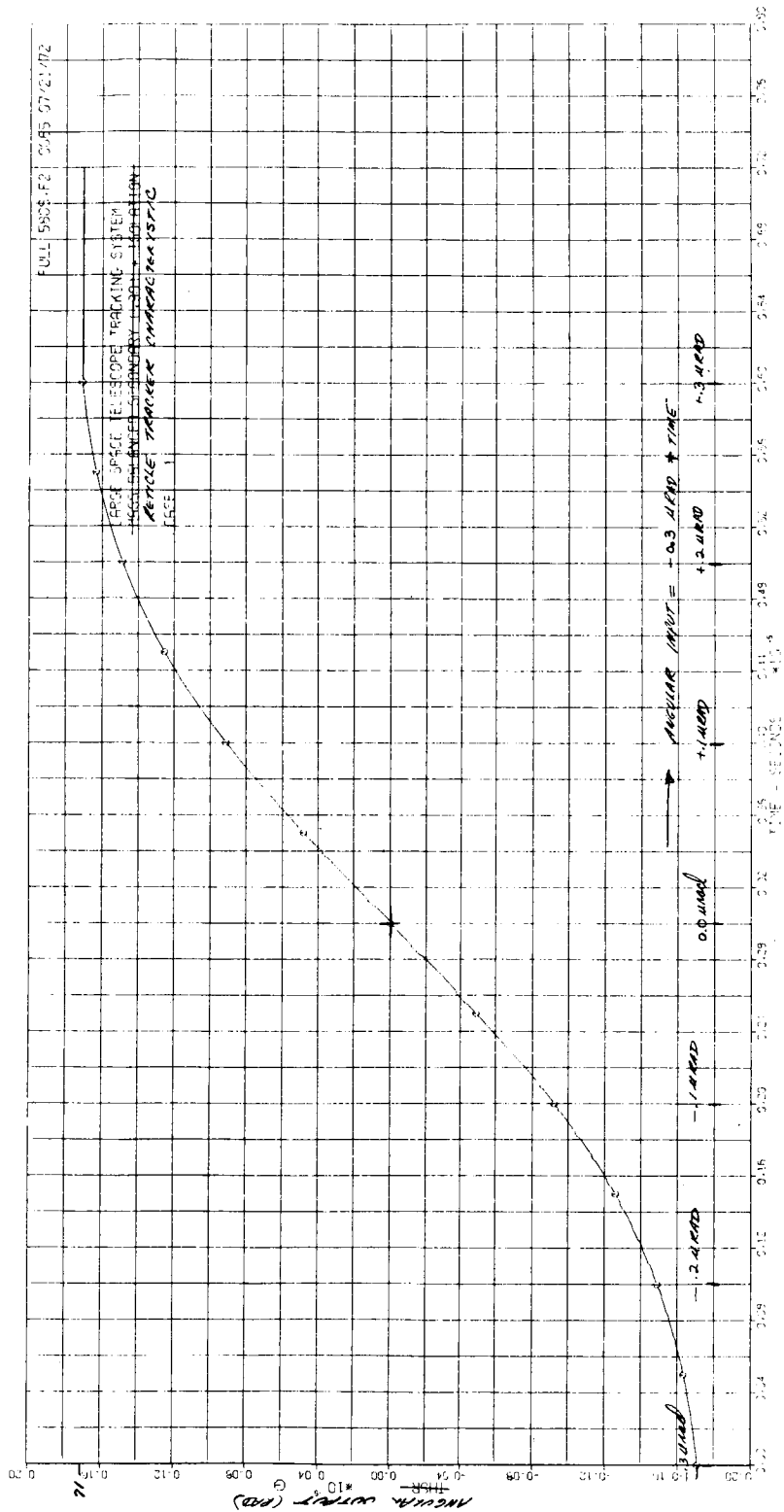


Fig. C.5-67 — Nonlinear transfer characteristic of guide star tracking error sensor

Table C.5-11 – Definition of Response Curves in Figs. C.5-63 Through C.5-66

Curve	Symbol	Definition
A	THSR	Residual line of sight perturbations due to dynamics of secondary mirror structure
B	SMLS	Mirror component of line of sight angle $\Delta\theta_{1s}(m)$
C	VLS	Vehicle component of line of sight angle $\Delta\theta_{1s}(v)$
D	THLS	System line of sight angle $\theta_{1s}$
E*	AES	System line of sight error $\theta_e$
F†	ERMS	RMS value of system line of sight error

\* Figs. C.5-63 through C.5-65

† Fig. C.5-66 only

Table C.5-12 – Comparison of Rise Time Values of Transient Responses

Figure	63-Percent Rise Time, Seconds		Gain Crossover Frequency ( $f_c$ ), hz			
	Line of Sight	Vehicle Angle	Tracking Loop		Vehicle Loop	
	D	C	Actual	Theoretical	Actual	Theoretical
C.5-63	0.19	1.14	1	0.85	0.1	0.14
C.5-65	0.04	1.3	4	4	0.1	0.12

Table C.5-13 summarizes some important values of the transient responses of Figs. C.5-63 and C.5-65, which can help to explain those responses. In Fig. C.5-63, curve D shows that the peak line-of-sight response caused by the 10-microradian step input is 14 microradians, which represents a 40 percent overshoot; whereas for Fig. C.5-65 the overshoot is 26 percent. Although a 26 percent overshoot (Fig. C.5-65) is quite reasonable, a 40-percent overshoot is excessive. This indicates that if the tracking loop gain crossover frequency were lowered to 1.0 hz, one would have to reduce the amount of integration in the fine tracking loop in order to reduce this overshoot. The problem is that the gain crossover frequencies of the vehicle and fine tracking loops are too close for the assumed ratios of dynamic parameters of the control loops.

Fig. C.5-59 showed that the system line-of-sight response  $\theta_{ls}$  (curve D) is equal to the mirror line-of-sight response  $\Delta\theta_{ls(m)}$  (curve B) plus the vehicle line-of-sight response  $\Delta\theta_{ls(v)}$  (curve C) plus the structural perturbation  $\Delta\theta_{lss(st)}$ , which is small when the system has reasonable stability. This small structural perturbation is ignored in the following discussion.

As shown in Table C.5-13, at  $t = 4$  seconds (the end of the curves), the system line of sight (curve D) is nearly equal to the 10-microradian input for Figs. C.5-63 and C.5-64 and the tracking error (curve E) is quite small. However, the mirror line of sight still has an appreciable deflection ( $-2.7, -2.8$  microradians) and the vehicle angle has a corresponding overshoot of (12.6, 12.8 microradians). Thus, there is a very long transient in the system response until the mirror deflection angle is reduced to zero.

The reason for this slow transient is that the open-loop response of the vehicle loop has a double zero, represented by the factors  $(S + \omega_{iv})(S + \omega_{1v})$ , where  $\omega_{iv} = \omega_{1v} = 0.157$  radian/second. These two factors produce transients having a time constant approximately equal to

$$\tau = (1/\omega_{iv}) + (1/\omega_{1v}) = 2/0.157 = 12 \text{ seconds}$$

Thus, we can expect transients in the system response having time constants of approximately 12 seconds. This accounts for the long transient effects observed in the responses of Figs. C.5-63 and C.5-65.

Fig. C.5-63 shows that, for a 1-hz gain crossover frequency in the tracking loop, the system without force isolation feedback has reasonably good stability. The high frequency jitter on curve B (the residual line-of-sight perturbations due to the secondary mirror dynamics) has a peak-to-peak value of 0.00012 microradian at the beginning and damps to 0.00004 microradian at the end. This damping of jitter is also shown in the system error shown in curve E.

Fig. C.5-64 shows that, for a 2-hz gain crossover frequency in the tracking loop, the system without force isolation feedback is unstable. The system error oscillates with an amplitude of 0.2 microradian peak to peak.

Fig. C.5-65 shows that, for a 4-hz gain crossover frequency, the tracking loop of a system with force feedback has reasonable good stability. The initial jitter in curve A (the residual line-of-sight perturbations due to secondary mirror dynamics) has an initial value of 0.00043 microradian peak to peak and damps to a final value of 0.00013 microradian peak to peak.

In the simulations, a variable time delay was placed in series with the tracking loop amplifier and was adjusted such as to maximize the oscillation. This simulated the effects of transport delay, dead space, and other unavoidable nonideal system characteristics.

Table C.5-13 – Parameters of Response Curves in Figs. C.5-63 and C.5-65

Response Curve	Angle, microradians						
	Peak	Fig. C.5-63			Fig. C.5-65		
		t = 4 seconds	Final		Peak	t = 4 seconds	Final
D. System line of sight	14.0	9.9	10.0	12.6	10.0	10.0	
E. System line of sight	–	0.09	0	–	0.0004	0	
B. Mirror line of sight	13.0	-2.7	0	12.5	-2.8	0	
C. Vehicle line of sight	12.7	12.6	10.0	13.0	12.8	10.0	

## C.5.e Error Budgets for the OTA Pointing Control System

### C.5.e(1) Fine Guidance System Error Budget

The overall stabilization budget allocates 0.012 microradian rms (0.0025 arc-second) to the fine guidance system of the OTA. This includes errors attributable to the fine guidance sensors, the optical micrometer, and the secondary mirror actuator system, although it does not include the following errors of a linearized secondary mirror system, since these errors are really residual errors of the spacecraft stabilization system and must be taken into account in the spacecraft stabilization error analysis. Table C.5-14 gives the fine guidance system error budget along with an explanation of each term used.

#### Guide Sensor Noise

The guide sensor noise for 90 percent of the targets at the galactic pole can be expected to be within 0.055 microradian (0.0011 arc-second).

#### Optical Micrometer Lateral Color

The optical micrometer introduces lateral color aberration in its tipped condition, as is explained in the optical micrometer discussion, and the presence of this aberration makes the calibration of the scale factor of the micrometer dependent upon the spectral characteristics of the guide star and the detector. For normal star observations in which the differential velocity aberration drift is less than 0.1 microradian (0.02 arc-second), the determination of the centroid of the color-smear star image could be off by even half the width of the color smear without introducing a significant error. In the case of tracking a planet through the full range of the optical micrometer, the motion of the centroid of the image in relationship to the motion of the plate must be calculated quite precisely, taking into consideration the actual guide star to be used.

#### Optical Micrometer Tracking

An assumption was made here of an error tolerance for the tracking drive sensor. In terms of the range of the optical micrometer, the assumed tolerance is 0.025 percent, which will be a factor in determining the type of sensor to be used.

#### Mirror Actuator Error

An assumption of 0.1 percent of the secondary mirror tracking range was made for noise and hysteresis sources.

#### Granularity in Control System.

The assumed tolerance here is merely an indication of the number of bits required in performing the control functions.

#### Roll Error Coordinate Transformation

The secondary mirror can compensate for only two angular motions of the spacecraft. So that the uncontrolled axis of rotation may appear to pass through the data star to minimize the effects of roll error, the two guide sensors must operate partly off null for part of the time. In this operation, the scale factor of the transfer function of the sensor must be known. It is assumed that this scale factor will be calibrated to within 10 percent. Means of calibration are movement of the secondary mirror or the optical micrometer prior to the observation, after the guide stars have been acquired.

### C.5.e(2) Dimensional Stability Error Budget

An important source of line-of-sight stabilization error is dimensional change in the telescope. In the overall stabilization budget, 0.012 microradian (0.0025 arc-second) has been allocated to this problem. The dimensional stability error budget is given in Table C.5-15. The following is an explanation of each item in the budget.

It should be noted that the use of the focal plane reticle plate and the artificial stars for stabilization of the high resolution imaging fields removes the first order effects of structural drift, leaving the second order axial drift effects to define the thermal tolerances.

#### Reticle Plate Dimensional Change

If the reticle plate of the guidance system expands or contracts during an observation, the result will be a stabilization error due to the change in the dimension between point at which the guide star is locked and the point at which the data star needs to be imaged. However, if the plate is made of a stable material such as fused silica, reticle plate dimensional changes will be negligible.

Table C.5-14 – Fine Guidance System Error Sources for Star Observation

Source	RMS Error	
	Microradians	Arc-Seconds
Guide sensor noise (90% of targets, maximum optical micrometer offset)	0.055	0.0011
Optical micrometer lateral color	0.0005	0.0002
Optical micrometer tracking for differential velocity aberration compensation and grid interpolation	0.005	0.001
Mirror actuator error, noise and hysteresis (0.1% of 5 microradians)	0.005	0.001
Granularity in control system (5 microradians divided into 11 bits)	0.0025	0.0005
Roll error coordinate transformation (10% calibration of loop gain)	0.00175	0.00035
	<hr/>	<hr/>
RSS	0.0095	0.0019
Allocation	0.012	0.0025

Table C.5-15 – Dimensional Stability Errors for f/96 Imagery

Source	RMS Error	
	Microradians	Arc-Seconds
Reticle plate dimensional change (fused silica, $\pm 1^\circ\text{C}$ )	0.002	0.0004
Primary-secondary spacing (2 micrometers)	0.0019	0.00038
Primary – SIP spacing (10 micrometers)	0.0039	0.00078
Primary mirror focal length (5 micrometers)	0.0046	0.00092
Secondary mirror focal length (2 micrometers)	0.0042	0.00085
Artificial star sensor noise and calibration to 1% of one star image diameter	0.005	0.001
	<hr/>	<hr/>
RSS	0.0095	0.0019
Allocation	0.012	0.0025



### Primary/Secondary Spacing

The changes in the spacing between the primary and secondary mirrors, as well as the spacing between other major optical components in the system, cause the scale at the focal plane to change, resulting in a stabilization error similar to that produced by a growth of the reticle plate. The sensitivities to changes in the component spacings are calculated in Image Scale Change From Dimensional Changes Within the OTA (LST-72-157). These sensitivities were used in the generation of the dimensional stability budget. The primary/secondary spacing change is restricted by the need to refocus out changes of greater than 2 micrometers. Hence, that is the number appearing in this budget.

### Primary/Instrument Package Spacing, Primary Mirror Focal Length, and Secondary Mirror Focal Length

Changes in these dimensions during the course of an observation will produce changes in the focus of the telescope, and so the primary/secondary spacing will be changed to refocus the telescope. It is under this condition that the sensitivities to changes in these dimensions were calculated. It is important to note that the tolerances for these dimensions given in the budget must be held during the entire course of an observation.

### Artificial Star Sensor

The artificial star sensor that provides the signal to compensate for dimensional changes within the  $f/96$  relay path can operate at a very low bandwidth because of the slow nature of the thermal drift of the structure. Therefore, it is reasonable to expect that with a very dim artificial star source, equivalent to a 15th magnitude star or dimmer, very low noise can be maintained because of the long integration time. Noise comparable to that of the guidance sensors should be achievable without a source so bright that a danger of scattered light is introduced. The amount of drift during an observation can be expected to be a fraction of the star image size. Calibration of the scale constant of the artificial star sensor to 1 percent should be sufficient.

## C.6 ALIGNMENT, FOCUS, AND FIGURE CONTROL DESIGN

### C.6.a Introduction

The system that monitors and maintains the optical geometry of the telescope is described very briefly in this section. The critical alignment problems of the LST are maintaining the position of the secondary relative to the primary in the lateral (decenter) and the axial (defocus) directions and, to a lesser degree, minimizing the secondary tilt. Housekeeping sensors are required for monitoring these alignments. A diagnostic sensor for monitoring the system wavefront error is also necessary to provide an absolute measure of optical performance, to check the calibration of the alignment sensors, and to measure changes in the mirror figures. Fig. C.6-1 is a schematic of the LST reference performance control system showing the mirrors, alignment devices, and geometric features.

The pages following discuss the optical geometry requirements and the approaches considered in maintaining it, the status of the LST reference design, details of the operation of the alignment and focus sensor system, and details of the sensors and the actuators used in the system.

#### C.6.a(1) Alignment and Focus Requirements

There are three major elements whose spatial relationships must be maintained within tight tolerances to maintain the designed telescope wavefront quality. They are the secondary mirror, the primary mirror, and the instrument group at the focal plane. Each one might be caused to move in three degrees of freedom of translation and three degrees of freedom of rotation. It is convenient to consider the primary mirror the reference and to consider motions of the secondary mirror and of the focal plane instruments as relative to the primary mirror.

Table C.6-1 shows the comparative sensitivities of the system to motions of the secondary mirror and the focal plane instruments. It shows the effects of element motion both upon the wavefront error and the image motion. Basically, the system wavefront quality is sensitive to the decenter, tip, and axial position change of the secondary mirror, is much less sensitive to defocus and tip of the focal plane, and is not sensitive at all to axial rotation of the secondary mirror or focal plane (because of the axial symmetry of the system) or to decenter of the focal plane. In terms of image motion, the system is orders of magnitude more sensitive to motions. The system can be stabilized only through closed loop control, using the focal plane guidance sensor. It is important to note here that whatever realignment is made to maintain the wavefront quality must not add image motion that is beyond the capability of accommodation by the fine guidance system.

Sources of misalignment are the gravity release, stresses, and thermal perturbations at launch, the cyclical thermal variations in orbit, the thermal perturbations from repointing the telescope to new targets, and slow structural creep during the life of the telescope.

#### C.6.a(2) Approaches to Design of the Alignment and Focus System

The alignment and focus system includes, in a sense, the optical design, the structure, the thermal control system, and the system of sensors and actuators that are used to monitor and correct the alignment. The subject of this section, however, is the sensor and actuator system alone.

The system would be less sensitive to misalignment if the primary mirror had a longer focal length, but system constraints on weight and length are the overriding factors in determining the actual optical configuration.

The approach in the structural and thermal design has been to make the system as stable as possible without active control. The structure's supporting and secondary mirror and the focal plane instruments are made with athermalized or minimum expansion coefficient construction and are structurally independent of the outer vehicle structure. They are thermally insulated to minimize temperature changes.

#### Sensors

Simple sensors for alignment and focus control have been developed in the past and prove adequate for the required alignment. The ideal sensor would operate at the focal plane and be accessible within the SSM compartment for replacement. An autocollimating focus sensor of this type, described in detail later, is available, but an alignment

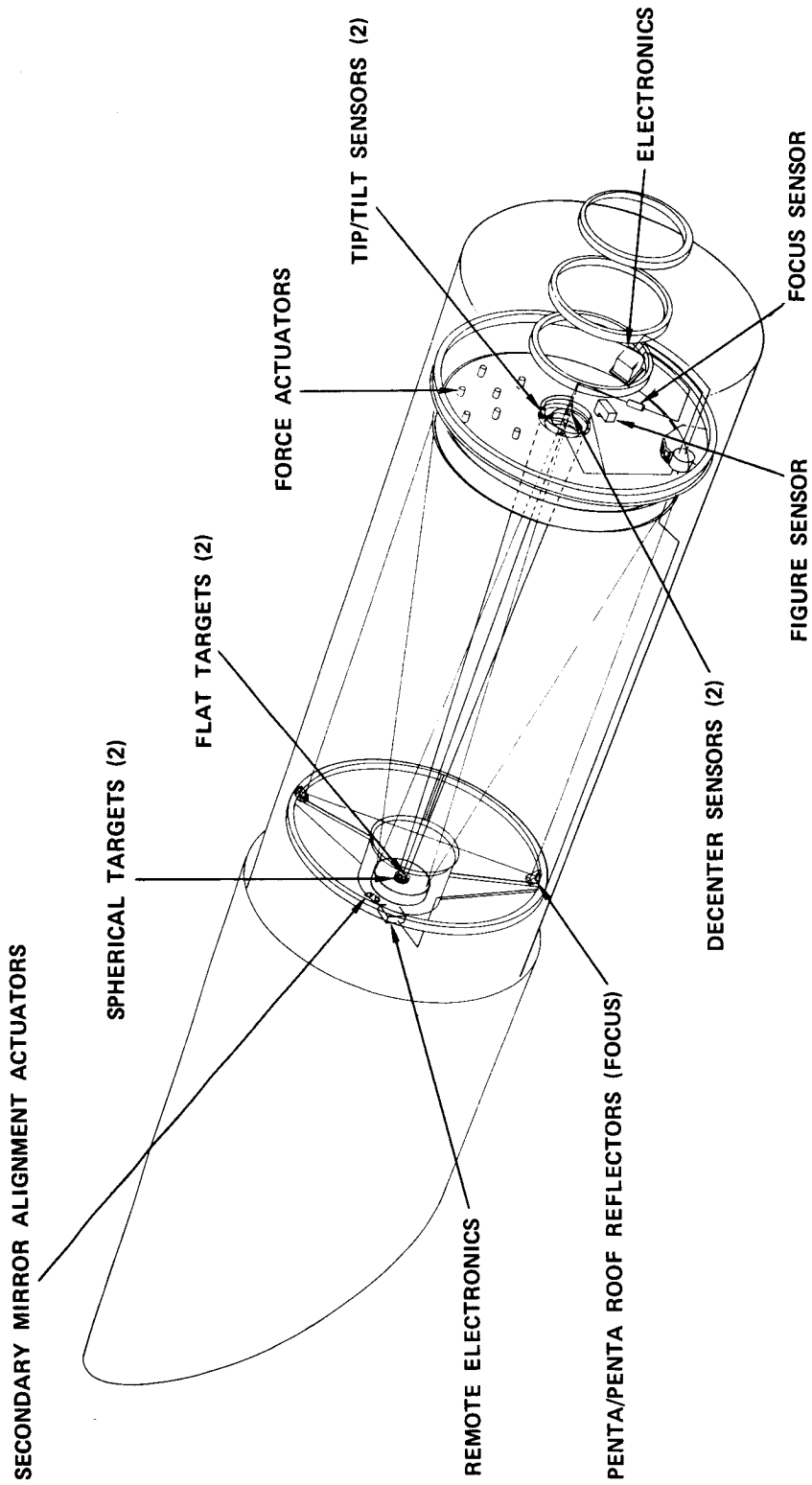


Fig. C.6-1 --- Performance control system components

Table C.6-1 – Comparative Sensitivities to Optical Element Motions\*  
 Errors = 1/5 Budget

	0.01 $\lambda$ rms Wavefront Error	0.005 microradian Image Motion
Secondary mirror decenter	18 micrometers	0.04 micrometer†
Secondary mirror axial spacing	1 micrometer	5 micrometers
Secondary mirror tip (about mirror vertex)	31 microradians	0.012 microradian†
Secondary mirror axial rotation	$\infty$	$\infty$
Focal plane decenter	12,000 micrometers	0.18 micrometer†
Focal plane axial spacing	28 micrometers	13 micrometers
Focal plane tip (for error 3.5 milliradians off axis)	220 microradians	102 microradians
Focal plane axial rotation (for error 3.5 milliradians off axis)	$\infty$	1.4 micrometers†

\*Relative to primary mirror.

†Compensated by fine guidance system.

sensor at the focal plane would require considerable development. The alignment sensors considered in this study are automatic alignment telescopes that attach to one mirror and detect motions of the other. They are described in detail later also.

#### Operation of Alignment and Focus System

The primary mirror has been considered as the fixed reference in the design study because of its size and its naturally close structural tie-in to the spacecraft. Optical and thermal analysis shows that all necessary alignment functions can be performed by motion of the secondary mirror. Thermal analysis has shown that intermittent operation of the alignment and focus system is adequate in keeping the alignment within acceptable tolerances. Intermittent operation in the reference system is considered desirable because of the extreme sensitivity of the optical system to vibrational image motion that might be introduced into an observation by continuous adjustment of the secondary mirror with wide-range actuators. This is indicated by the sensitivities of Table C.6-1. Another factor favoring intermittent use is the possibility of stray light from optical alignment sensors.

#### Secondary Mirror Actuation Systems

Requirements of a secondary mirror alignment actuation system are that it provide tip, decenter, and focus correction (5 degrees of freedom), that it be reliable and provide its service for the desired lifetime, and that it be dimensionally stable while inactive so that image motions are not introduced.

One approach to reliability is to choose a configuration that maximizes the redundancy obtainable from a given number of actuators. Such is the property of the modified A-frame mount shown schematically in Fig. C.6-2. The operation of this approach is explained more fully in Section C.6.d(4).

Extension of each linkage in turn influences or does not influence each of the mirror position coordinates, as is indicated in the influence matrix of Table C.6-2.

An opposite concept, considered and discarded, emphasizes the control simplicity of having the actuators behave orthogonally. An implementation of this concept utilizes a two-axis gimbal for tip control and separate stages for decenter control and focus control. The influence matrix for this system is given in Table C.6-3. Failure of any actuator results in loss of control in that coordinate, and hence redundancy must be achieved by some other means.

Digital control of the secondary actuator system provides the required flexibility. For an A-frame configuration with inherent redundancy, failure of up to three actuators can occur in 41 combinations, which makes the potential programmability of a digital system attractive.

#### Actuators

There are many kinds of actuators that might be suitable, but there is none that is perfect in terms of meeting all the requirements and being at the same time available off-the-shelf. Before an actuator can be selected, a detailed design tradeoff is necessary, which is beyond the scope of the present study.

An outline of desirable features is given in Table C.6-4. Mandatory features are starred. Some features are implied in others.

A partial listing has been made of mechanisms that might be used in actuators for the secondary mirror position control.

- Conventional mechanical-micrometer lead screw, self-locking
- Conventional mechanical – ball screw
- Mechanical – rolling nut lead screw
- USM Corporation linear actuator (harmonic drive)
- Thermal – metal, bimetal, restrained liquid or restrained rubber
- Stepping actuator – “inch worm”
- Peristaltic – Perkin Elmer Corporation developed for NASA

The USM harmonic drive actuator seems suitable from the point of view of meeting the requirements and its state of development, and has been carried through the reference system.

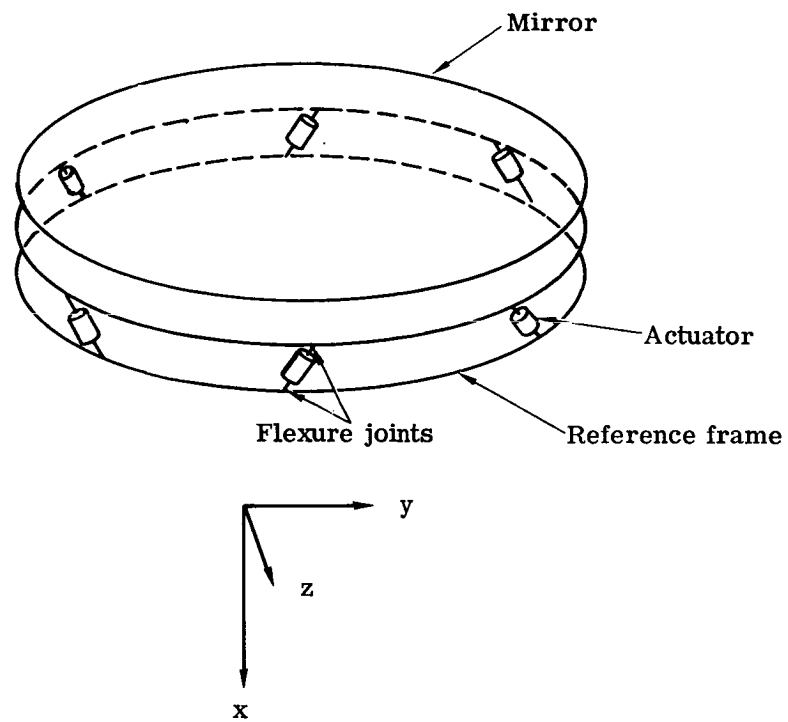


Fig. C.6-2 — A-frame secondary mirror actuation system

Table C.6-2 -- Modified A-Frame System Influence Matrix

Motion Coordinate	Transducer					
	1	2	3	4	5	6
y	X	X	X	X	X	X
z			X	X	X	X
x	X	X	X	X	X	X
$\phi_y$	X	X	X	X	X	X
$\phi_z$			X	X	X	X
$\phi_x$	X	X	X	X	X	X

Table C.6-3 -- Minimum Cross-Coupled System 5-Degree-of-Freedom Influence Matrix

Motion Coordinate	Transducer				
	1	2	3	4	5
y	X				
z		X			
x			X		
$\phi_y$				X	
$\phi_z$					X

Table C.6-4 -- Desirable Actuator Features

- |   |  |
|---|--|
| <ol style="list-style-type: none"> <li>1. *Reliability</li> <li>2. *Small size and weight</li> <li>3. *No play</li> <li>4. *No contamination danger to optics</li> <li>5. *High mechanical stiffness</li> <li>6. Rectilinear output motion</li> <li>7. Simplicity</li> <li>8. Self-locking basic mechanism</li> </ol> | <ol style="list-style-type: none"> <li>9. Stable when not energized</li> <li>10. Capable of carrying mirror through launch</li> <li>11. Lubricants and rubbing parts hermetically contained</li> <li>12. Minimum lubricants and moving parts</li> <li>13. Minimum commutators</li> <li>14. No deadband in actuator function</li> <li>15. Smooth operation which will not cause uncorrectable image motion</li> <li>16. Low development cost</li> </ol> |
|---|--|

\*Mandatory features.

### C.6.a(3) Figure Measurement and Control

To provide diagnostic information on the performance of the optical system, a real wavefront measurement sensor is desirable. The uses of this instrument include providing initial alignment information after launch, calibrating the alignment and focus sensors, and measuring overall wavefront quality at periodic intervals.

Initial alignment, including the setting of the alignment sensors, may be disturbed in launch, and so it is imperative to have a means of achieving the best alignment independently after launch. The alignment and focus sensors themselves measure only changes, and so the figure sensor must provide absolute calibration of these devices.

The mirror is designed to generate only low stress levels in ground handling and launch so that it should maintain its figure indefinitely. But, creep of the mirror material from unknown causes, a partial failure of the thermal control system, and errors in the design of the zero-gravity simulation manufacturing mount that would otherwise go undetected produce effects measurable by the figure sensor. The only figure sensor really suitable for such tasks is a focal plane shearing interferometer that uses a star as a source-collimated light source. A uniquely simple shearing interferometer developed and breadboarded at Itek in the course of other work is described later and has been assumed for the reference system.

Other studies have demonstrated the feasibility of correcting mirror figure errors by applying forces to the back of the mirror through a system of actuators. Such a system of actuators has been assumed for the reference system, although the mirror design is such that the actuators may never be needed.

### C.6.b Status of the Reference Design

Alignment, focus, and figure sensors tested at Itek in the past appear to be entirely adequate to provide information required to maintain the optical geometry. The sensor accuracy and the estimated actuator errors are easily accommodated in the optical wavefront error budget. The largest unknown is the real variations produced by thermal changes in the structure. A sizable portion of the wavefront error budget has been allocated to such dimensional changes. The structural and thermal analysis to date has indicated that the structural changes will remain within the budget tolerances for periods of 20 minutes and longer.

### C.6.c Performance Control System Description

The alignment problem consists of maintaining the secondary and primary mirrors in the correct spatial relationship to each other and maintaining the focus of the optical system at the detector plane.

A classical Cassegrain telescope consists of a paraboloid primary and a hyperboloid secondary. All rays entering parallel to the axis of the paraboloid are reflected toward its focus. One focus of the hyperboloid is made coincident with the focus of the paraboloid, and all rays directed toward that point are then intercepted and reflected to the other focus of the hyperboloid. This is true if the foci of the paraboloid and the hyperboloid are merely coincident, and tipping of either mirror about this focus point is harmless in terms of image quality for on-axis points. Axial displacement of the two foci produces defocus, and lateral displacement produces on-axis coma.

If either mirror is tipped about its own vertex, the wavefront suffers because the focus of one now becomes displaced with respect to the focus of the other. Thus, on-axis for a classical Cassegrain tip sensitivity is really just the displacement sensitivity multiplied by the appropriate distance. At points off-axis and for designs departing from the paraboloid-hyperboloid form (the Ritchey-Chretien LST design), there will be other components to the tip sensitivity, but at the small field angles encountered in the LST, the sensitivity to tip of the secondary about its own vertex consists primarily of decenter sensitivity. The point of secondary tip at which no on-axis degradation is introduced is displaced slightly inward in the Ritchey-Chretien design. It is referred to as the neutral point.

Consider now the overall focus of the telescope. If the primary mirror is imagined to be the reference point, defocus occurs if the secondary mirror or the detector moves axially relative to the primary. A combination of secondary and detector motions for which there is no defocus might occur. If a means of controlling the position of the detector is available, then the actual spacing between the primary and secondary mirrors is not so critical. As a practical matter, however, a given motion of the secondary would be corrected by 30 times that motion of the detector for the  $f/2.2$  primary/ $f/12$  system case (the square of the secondary magnification), and so slight changes in



the mirror spacing would require large positional changes at the detector to correct them. The same would hold true for thermal induced power changes in the primary mirror; a small amount of secondary mirror motion will correct the resulting defocus, whereas a large amount of detector motion would be required.

In summary, then, the most important criterion in alignment of the mirrors is maintaining the foci coincident (decenter and defocus), and of secondary importance is maintaining the mirror axes parallel (tip).

The degrees of freedom needed in a fully active alignment system are five: two lateral motions, two tip motions, and one axial motion. A rotational degree of freedom about the optical axis is not necessary because of the rotational symmetry of the mirrors.

#### C.6.c(1) Alignment

Because the tilt and decenter positioning of the secondary is critical relative to the primary mirror, the tilt and decenter sensors are mounted directly on the primary mirror, and their targets are mounted directly on the secondary mirror. Fig. C.6-1 indicates locations of the tilt and decenter sensors. These sensors are two-axis alignment telescopes that generate an error signal if the beam returned from a reflecting target on the secondary is offset from the beam as it originates at the alignment telescope. Stability of 1 microradian (0.2 arc-second) has been achieved for a space-hardened long life device with an aperture of approximately 40 millimeters. As a tilt sensor, the device is used as an autocollimator reflecting from a flat mirror at the secondary. This is shown in Fig. C.6-3.

As a decenter sensor, the device is focused at the neutral point of the system, and the beam is reflected back upon itself by a spherical mirror mounted on the secondary with its center of curvature at the neutral point. This is shown in Fig. C.6-4. Relative motion between the primary and secondary at the neutral point is measured directly with a positional accuracy equal to the alignment telescope angular accuracy (approximately  $1 \times 10^{-6}$  radian) times the distance from the alignment telescope to the neutral point (approximately 6.6 meters). Thus the centering accuracy of the alignment telescope can be expected to be 6.6 micrometers. When multiplied by the  $0.00055\lambda$  rms per micrometer decenter sensitivity of the optical system, this indicates a sensor-limited centering accuracy of  $0.0036\lambda$  rms.

The alignment sensors will be used to realign the secondary mirror a few times a day; the LST thermal design is such as to limit the thermal drift of the structure to acceptable values during the observation.

The sensors and targets can be directly mounted to the mirrors. Initial alignment and calibration is determined as a final step in the mirror manufacturing process. Two sensors of each type are included for redundancy.

#### C.6.c(2) Focus

The optical system is designed for certain spacing between the vertices on the primary and secondary mirrors. If this spacing changes, rotationally symmetric aberrations are introduced, but more important is the defocus. In the final figuring of the secondary (against the primary), the image is made aberration-free at the nominal image plane. After that time, if the spacing is changed, degradation due to defocus may be serious while the addition of rotationally symmetric aberration is negligible. Defocus caused by motion of the secondary relative to the primary is 30 times that caused by an equal motion of the instrument package, indicating that the critical focus problem is maintenance of the mirror spacing. Monitoring focus change at the focal plane, however, permits compensation of thermally induced power changes in the mirrors.

A lateral separation focus sensor in principle detects the absolute focus by autocollimation, but in practice is suitable only for sensing changes in focus in a system such as the LST. Current devices of this type measure focus changes of  $0.006\lambda$  rms at the wavelength of the focus sensor light source. Assuming a 900-nanometer light source, the focus sensor limit for the system at 632.8 nanometers is about  $0.009\lambda$  rms. A schematic of the configuration is shown in Fig. C.6-5.

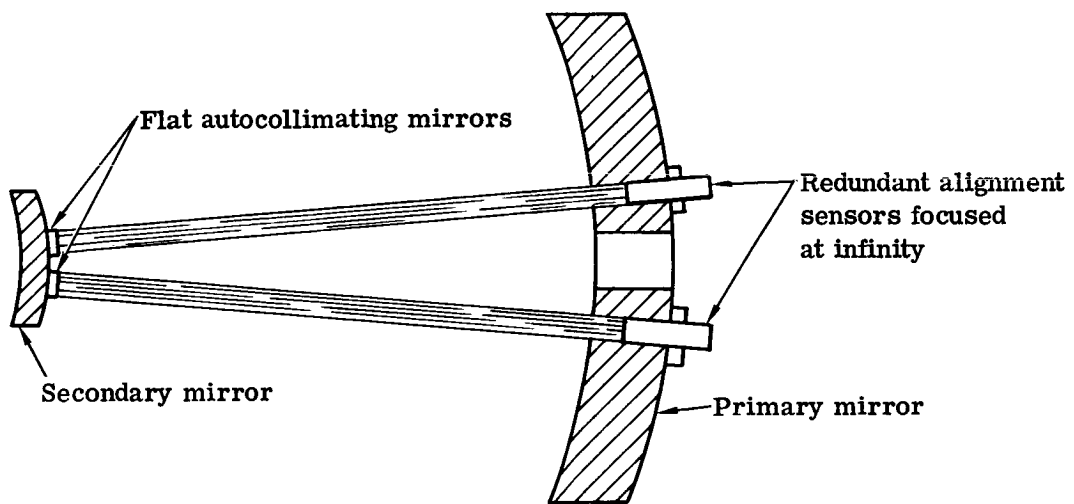


Fig. C.6-3 — Alignment sensors used to measure tip of secondary mirror

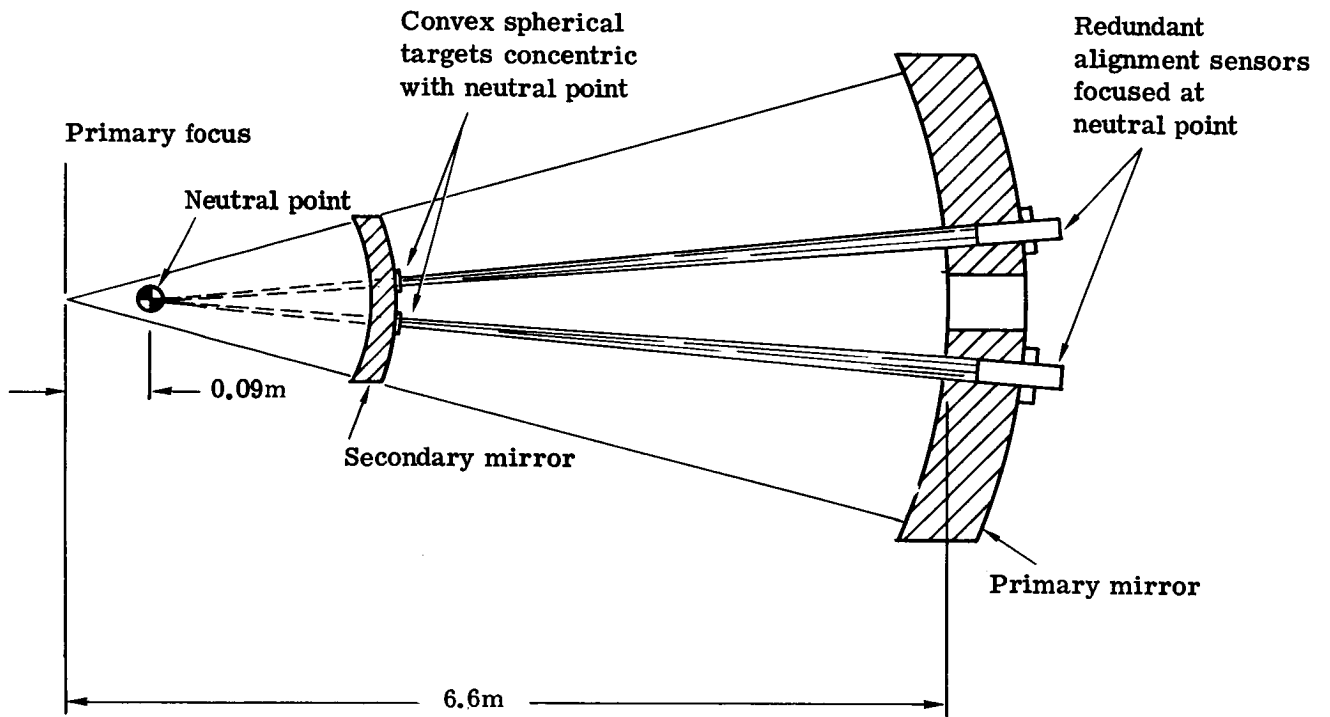


Fig. C.6-4 — Alignment sensors used to measure decenter at neutral point

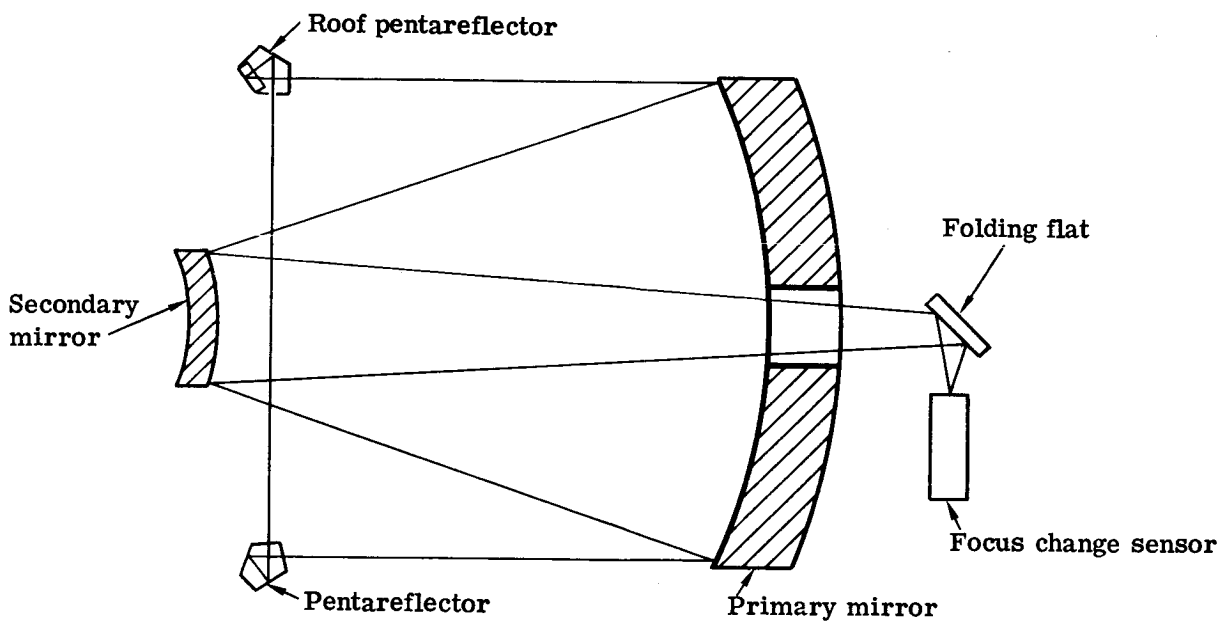


Fig. C.6-5 — Lateral separation focus sensor used in LST

As in the case of the alignment sensors, it is expected that the focus change sensor will be used a few times a day. Other factors that limit the accuracy of focus are primarily thermal drift of the structure during an observation and the initial absolute focus accuracy.

Absolute focus may be accomplished by through-focus runs of the focus-sensitive instruments. On-orbit determination of absolute focus is considered necessary because of the difficulty in determining the residual power of the large autocollimating flat that will be used in the ground alignment of the telescope. A through-focus run for the particular focus-sensitive instrument in question will not establish the best focus position as accurately as it can be determined interferometrically, but has the advantage of being directly related to the image plane of the data instrument.

#### C.6.c(3) Interferometer for Wavefront Measurement

The uses of a diagnostic interferometer include calibration of the focus change sensor, calibration of secondary alignment, and detection and evaluation of figure changes in the mirrors. It will be a lateral shearing interferometer operated with a bright star as a source.

The interferometer will be used to provide wavefront data for analysis on the ground. Should the wavefront quality deteriorate sufficiently, the interferometer data will be used to determine what corrections to centering, focus, and primary mirror figure will optimize performance again. It is expected that the use of the interferometer will limit the potential degradation of optical performance to very small values. The limit is that determined by the wavefront quality built into the system and the wavefront error of the interferometer. Analysis of the interferometer indicates that it will be comparable in accuracy to the Twyman-Green interferometer used in the manufacturing process.

#### C.6.c(4) Secondary Mirror Positioning Mechanism

The means by which the secondary mirror can be repositioned once an alignment error is detected is through a six-degree-of-freedom support for the secondary mirror consisting of six flexure linkages whose lengths can be controlled by mechanical actuators. Because of the rotational symmetry of the mirror, only five degrees of freedom are actually needed, but there is enough cross-coupling between the different actuators that, should one of them fail, the five desirable degrees of freedom can be retained at the expense of the sixth, unnecessary, degree of freedom.

#### C.6.c(5) Primary Mirror Figure Control

The primary mirror is designed to retain its optical figure in space without the use of the figure control actuators that bridge the space between the back of the mirror and the pressure bulkhead. Nevertheless, should there be some degree of unpredicted creep in the mirror, or should the thermal control system fail in a way such as to cause a significant figure error in the mirror, these actuators can be used to apply correcting forces to the back of the mirror. The commands to the actuators are derived from the figure sensor information.

#### C.6.c(6) Figure Control Under Ground Test Conditions

When the OTA is assembled and subject to the influence of gravity, the figures of the primary and secondary mirrors must be controlled to the extent of making ground tests of the system meaningful. The secondary mirror mount has nine points of axial support, so that the gravity sag is controlled to a large extent. The primary mirror mount is a three-point support which will require augmentation during ground test. One means of achieving such augmentation is through the use of the figure control actuators.

### C.6.d Performance Control System Components Design

#### C.6.d(1) Alignment Sensor for Decenter and Tip Measurement

The basic sensor used in each case is shown in Fig. C.6-6. The heart of the sensor is the small, truncated pyramid. The flat top of the pyramid forms a square aperture that is illuminated from behind by the lamp and

condenser. The four sloping sides of the pyramid are opaque and highly reflective, and light reflected from them is collected by four relay lenses and imaged onto detectors. The basic sensor is placed at the focus of the collimating objective (relay objective, for the decenter sensor), which projects an image of the square aperture toward the flat mirror (or retroreflector).

Consider the case of the tilt sensor. If the flat mirror is perfectly normal to the optical axis of the collimating objective, the light beam will be returned on itself and form an image of the square aperture that is coincident with the aperture. The only light seen by the four detectors in this case is the diffraction spillover, which should be identical in all four cases. If the flat mirror is tilted at a slight angle to the optical axis, the aperture image is displaced slightly, and the light reaching each detector will differ proportionally to the displacement toward or away from that detector. Opposite pairs of detectors are coupled to indicate the direction and magnitude of the displacement component along that axis. (See Fig. C.6-7.)

The decenter sensor works in a similar manner, differing only in that the square aperture is imaged onto a retroreflector. The returning light is imaged onto the square aperture, and any image displacements are a measure of the lateral displacement of the retroreflector. (See Fig. C.6-8.)

To control the alignment of the secondary mirror with respect to the primary mirror, the sensor packages are attached to the back of the primary mirror, and look at the secondary mirror through holes near the central aperture in the primary mirror. The targets for the sensors are cemented to the center of the secondary mirror within the unused spot that is in the shadow of the central obstruction. Geometric integrity for the entire system depends on absolute rigidity in the relationship between the sensors and the primary mirror reflecting surface, and between the alignment target mirrors and the secondary mirror reflecting surface.

Both these sensor devices involve an active light source. It is therefore undesirable to perform this type of alignment during an observation period if the data sensor will be affected by the light source. In all cases, it is assumed that this type of alignment will take place before the observation begins, the adjustable component is locked into position, and the sensor shut off, unless suitable filtration of the light is available. If the servos must be operated during exposure, there is the risk of introducing vibration and other problems of a dynamic system.

The alignment sensor is mounted on the primary mirror and utilizes a gallium arsenide infrared solid state lamp as its light source and an electronic circuit to modulate the light source. This two-axis system utilizes four silicon planer PIN photodiodes as detectors for the return beams from the target attached to the secondary mirror of the large optical system.

#### Engineering Model

In another study, an engineering model (see Fig. C.6-9) this alignment sensor was built. In the laboratory it easily met the following specifications:

Focal length	15.22 centimeters (6.0 inches)
Clear aperture	3.805 centimeters (1.5 inches)
f/number	4.0
Configuration	Air space doublet (possible single element aspheric)
Field of view	14.5 microradians (0.0833 degree) off axis
Sensor sensitivity	
Angular	0.97 microradian (0.2 arc-second)
Decenter (lateral)	$2.54 \times 10^6$ centimeters/centimeter

#### Optical System

The layout of the alignment sensor (see Fig. C.6-10) shows the two positions for the objectives lens, light baffles, slit prism, photodiode detectors, condenser lenses, and gallium arsenide light source. The optical system operates by modulation of the gallium arsenide light source at a frequency compatible with the detection circuit at a noncoherent radiation of  $9400 \text{ \AA}$  at  $25^\circ\text{C}$ . The radiated energy is focused at the 0.018- by 0.018-centimeter (0.007-

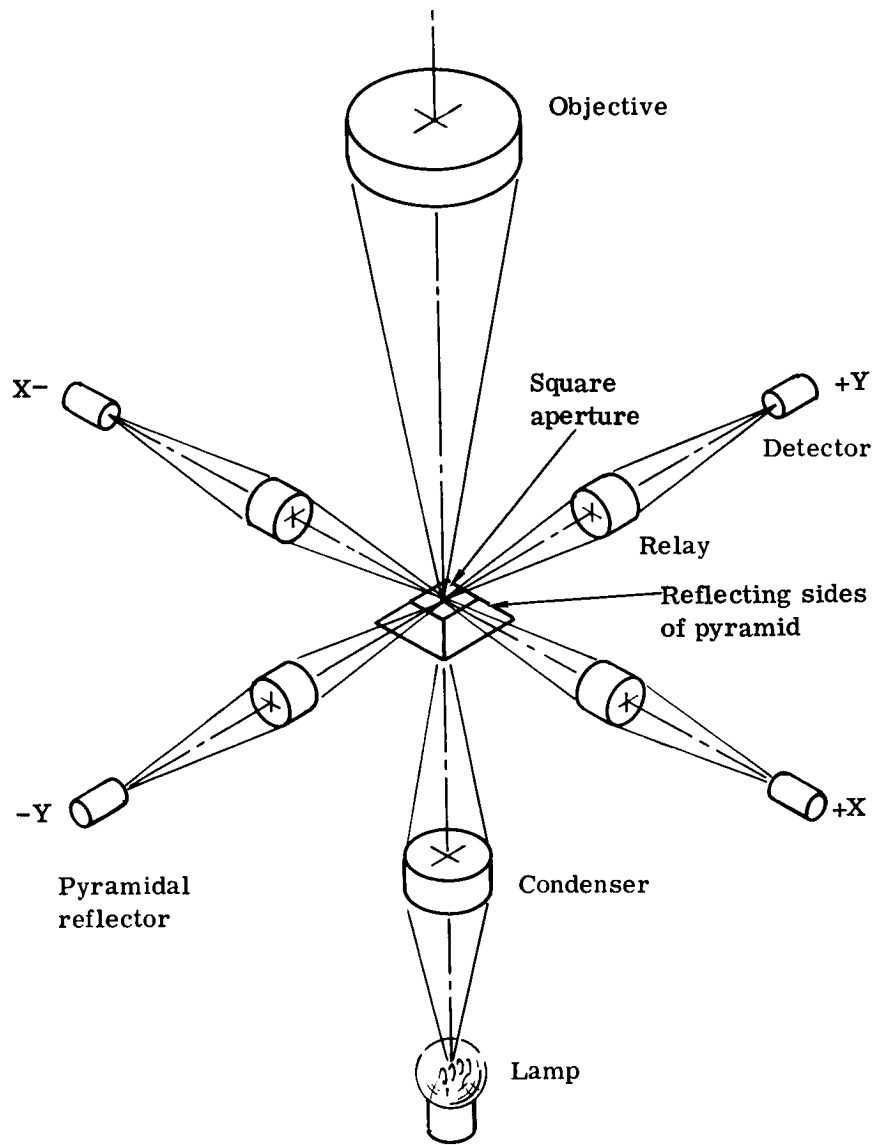


Fig. C.6-6 — Basic detector used in tilt and decenter sensors

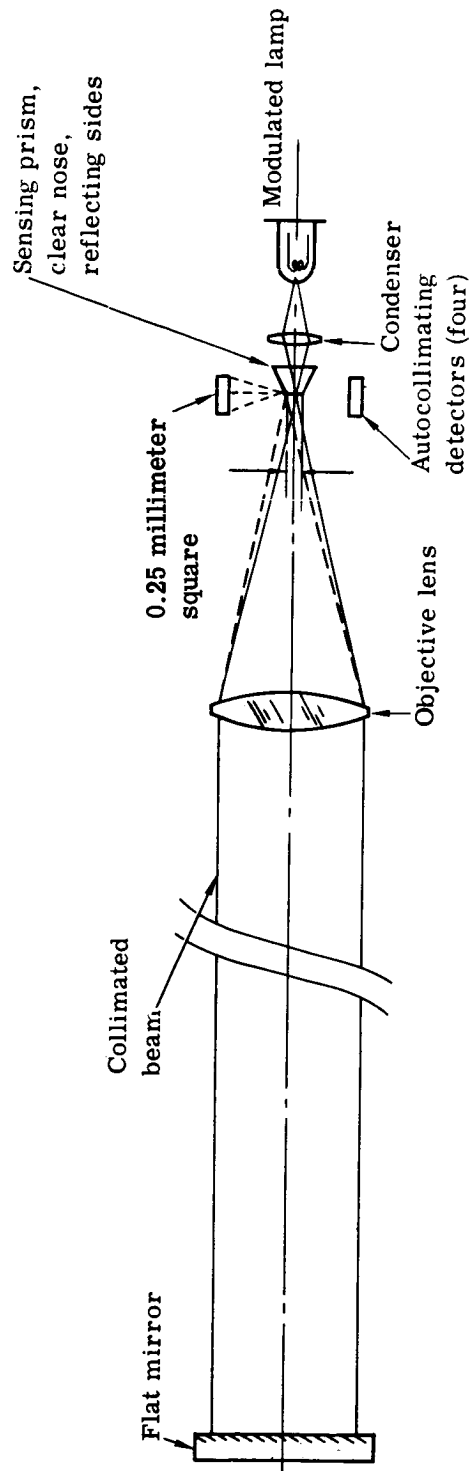


Fig. C.6-7 — Electro-optical schematic diagram of two-axis high stability, automatic tilt sensor



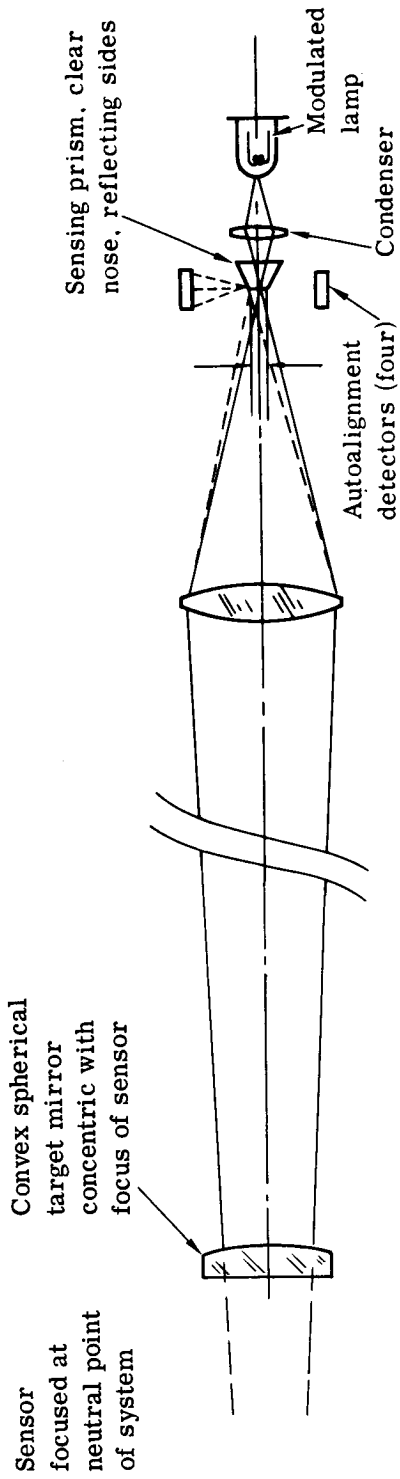


Fig. C.6-8 — Electro-optical schematic diagram of high stability, two-axis automatic decenter sensor

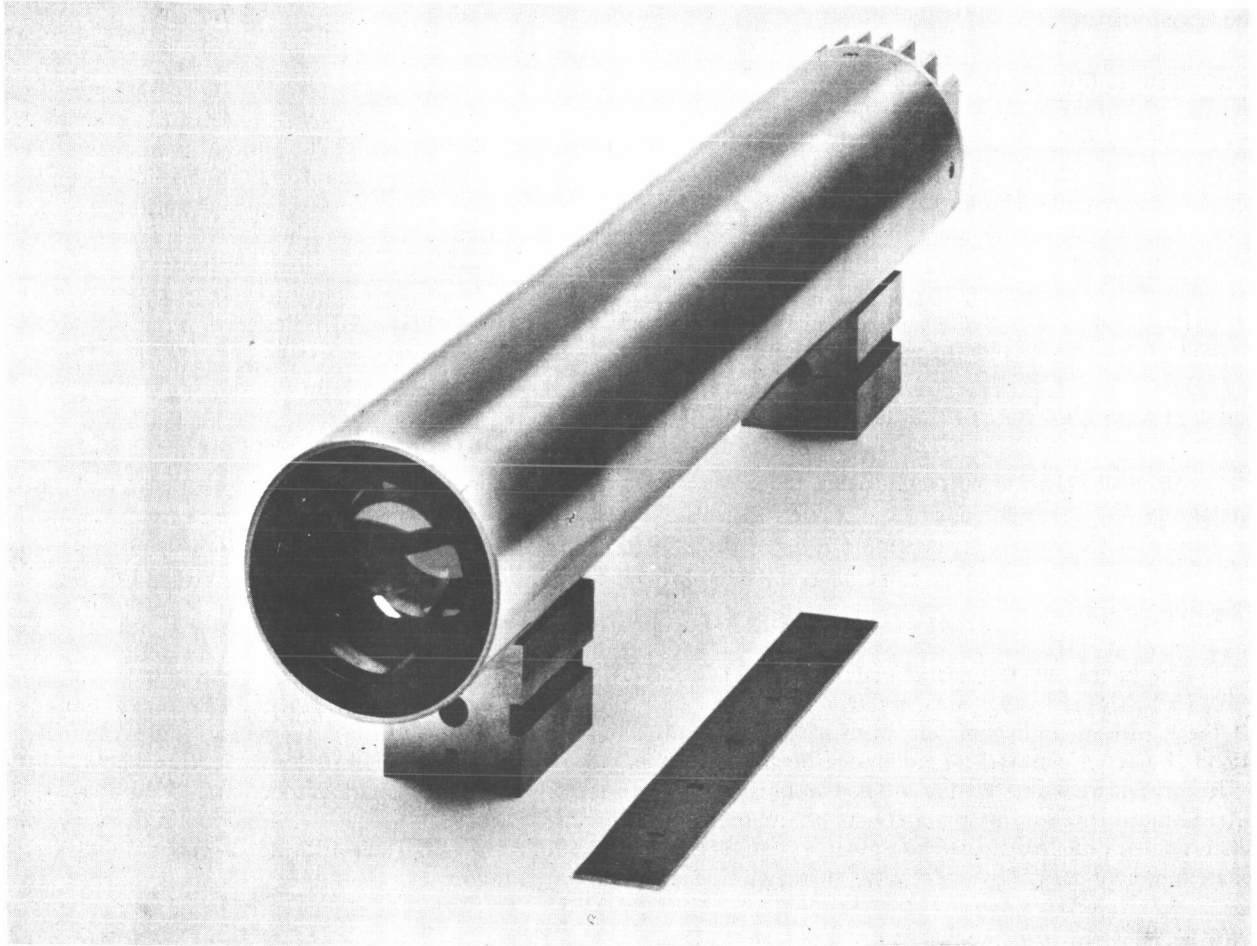


Fig. C.6-9 — Engineering model of alignment sensor

by 0.007-inch) opening of the truncated pyramidal prism by the condenser lens. The cone of light fills the objective lens, which is placed so that the outer beam is collimated and aligned to fill the target flat mirror mounted on the secondary mirror of the large optical system. The return will be reimaged on the truncated pyramidal prism when the system is nulled, and the four photodiode detectors will equally detect a uniform diffraction pattern created by the return beam and reflected from the mirrored surfaces of the prism. However, if an angular misalignment were present, the error signal on one or two of these detectors would be greater.

For the decenter sensor system, the operation is identical except for the substitution of a spherical mirror for the target mirror and the adjustment of the objective lens to focus the outgoing beam at the center of curvature of the target mirror.

### Mechanical Configuration

The layout of the sensor configuration (Fig. C.6-10) indicates the location of the various components. The body and the majority of the critical parts are fabricated from Invar, thereby minimizing thermal effects on the critical optical path. The sensor is mounted by a sensor mounting ring, which will interface into the primary mirror. This ring and a similar clamping ring are clamped around a spherical section of the sensor body, which allows for fine adjustment of the sensor at initial alignment.

The total weight of the sensor head is approximately 4.0 kilograms (9 pounds) as designed, but can probably be reduced to 1.8 kilograms (4 pounds) without affecting the overall operation of the sensor.

#### C.6.d(2) Autocollimating Focus Change Sensor

An electro-optical autocollimating focus sensor conceived and developed in 1964 has consistently exhibited the ability to resolve defocus of 0.2 Rayleigh depth of focus ( $1 \text{ Rayl} \approx \lambda F^2$ ) with optical systems varying widely in aperture and focal ratio. Its operation is based on detecting, as the sensor departs axially from the focal plane, the lateral departure from perfect coincidence of two autocollimated images of a common source formed by opposing system edge apertures.

The lateral separation focus sensor (LSFS) (see Fig. C.6-11) consists of a small sensor head in the focal plane outside the desired image area, a retroreflective set of two diametrically opposed small penta reflectors in the front of the telescope, and simple electronics. A light beam from a small illuminated slit in the sensor head is alternately directed at each pentaprism, collimated by the telescope, reflected across the aperture by the corresponding penta reflector, and reflected by the other pentaprism back into the telescope to form an autocollimated slit image. The alternating slit images are precisely superimposed on the slit when in focus but separate laterally with defocus. Two silicon detectors are arranged to detect light falling to either side of the slit. Their difference signal amplitude and phase uniquely indicate, respectively, the magnitude and direction of defocus.

The system previously designed utilized a tungsten filament lamp. However, the sensor to be used in the LST will be redesigned to utilize two gallium arsenide infrared solid state lamps modulated at the proper frequency and monitored by an AGC detector circuit to maintain the proper energy balance. This redesign is required for extended sensor life in space.

The LSFS is capable of operating outside the image area and spectral range of the primary system photosensor, and with its pentaprisms on a nondiametrical chord in the system aperture. Because of this flexibility, the LSFS is adaptable to the LST.

### Operation of LSFS

The basis of the LSFS is a means of providing suitably collimated light at the measuring apertures combined with a means of detecting image separation. Sensing the direction and magnitude of defocusing imposes two requirements: a need to identify the measuring aperture forming an image and a need to determine the amount of light falling on either side of the sensing axis.

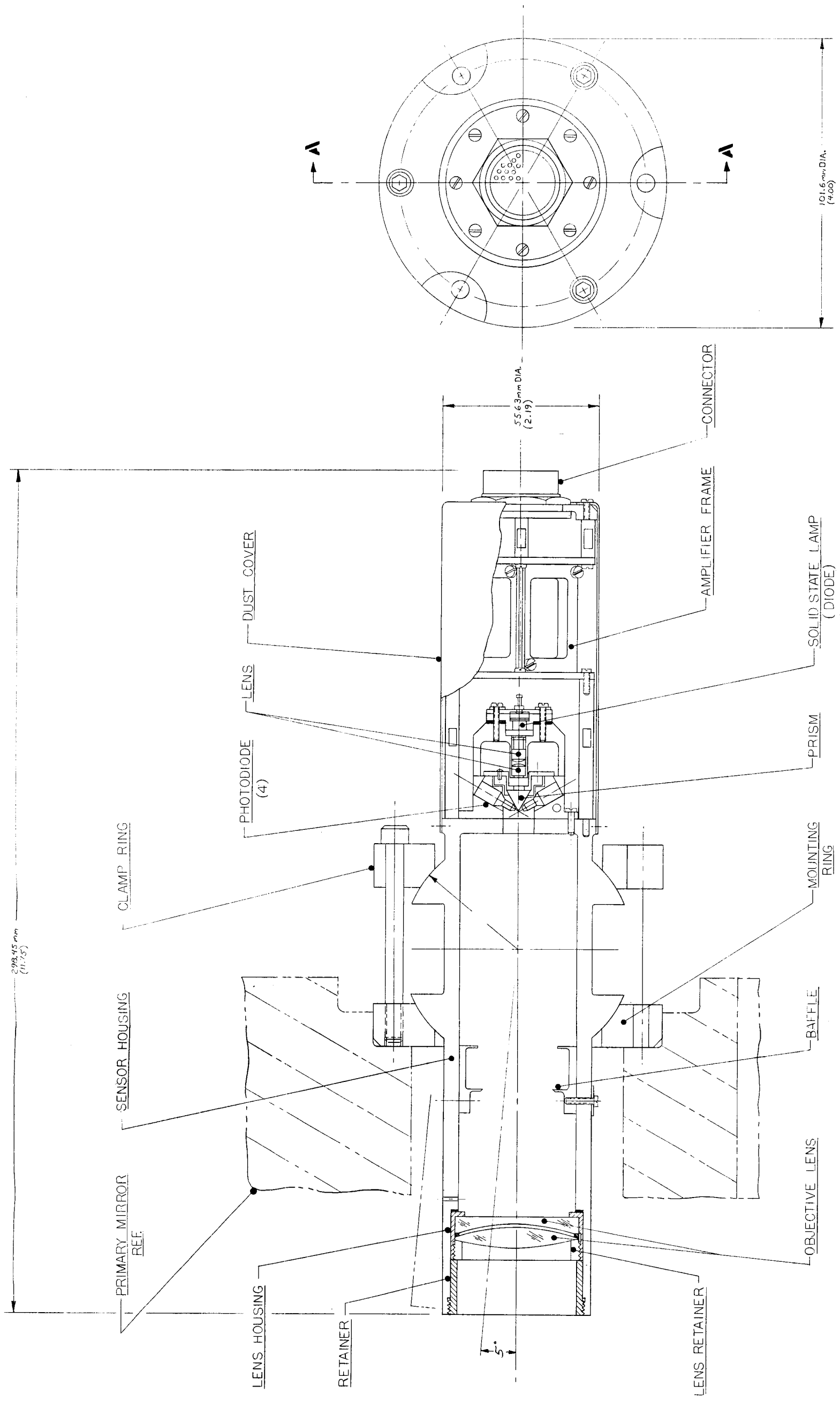
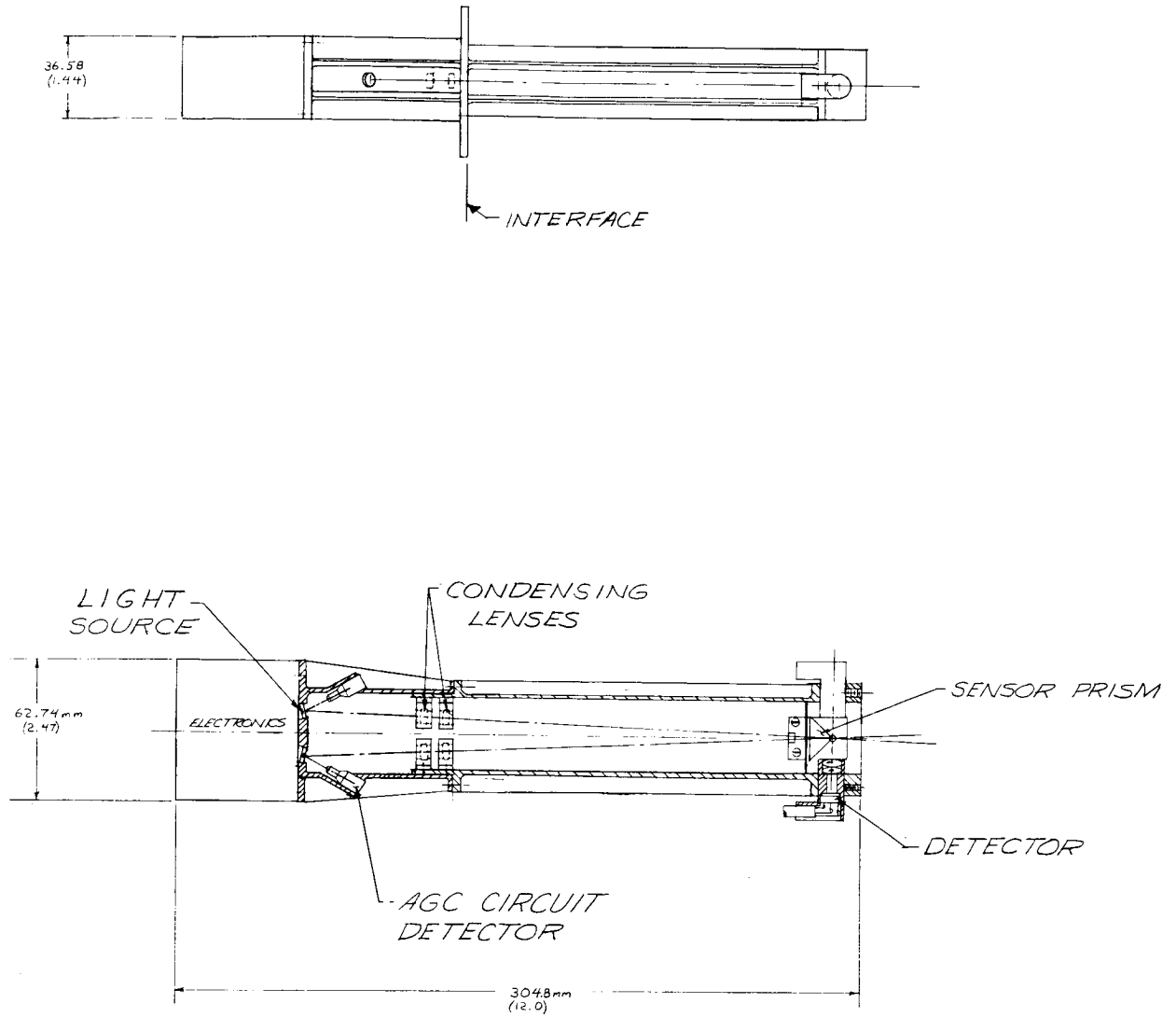


Fig. C.6-10 — Alignment sensor layout (dwg. no. 911385)



**Fig. C.6-11 — Focus sensor layout (dwg. no. 911389)**

One convenient implementation of these requirements is in the form of an autocollimator which utilizes an illuminated slit contiguous with two detectors of opposing polarity, and a chopper which sequentially transmits light through the slit to each of the measuring apertures (Fig. C.6-12a). A flat mirror can initially be assumed to be the autocollimating reflector external to the objective lens. In the autocollimator two lamps are imaged at the slit by a condenser lens obstructed by a stop plate and chopper which allows light alternately to reach each measuring aperture with the temporal pattern of Fig. C.6-12b.

When the slit is in the focal plane, its autocollimated image through either path is perfectly superimposed on the slit. The only light reaching the detectors is spillover due to diffraction, which may be approximated as shown in Fig. C.6-13. If we assume precise balance in the slit illumination system, the spillover has the same magnitude at both slit edges and for both optical paths. If the two detectors are connected with opposing polarity, their output is zero, as shown for the focused condition in Fig. C.6-12b. Thus, a properly configured focus sensor of this type has a null output when in the true focal plane.

When defocused, the illuminated slit and its autocollimated image are equidistant in opposite directions from the focal plane (magnification change is negligible.) With the slit ahead of the focal plane as in Fig. C.6-12c, lateral image separation causes an increase in light from the R aperture falling on  $D^+$ , and a similar increase in light from the L aperture falling on  $D^-$ . When the slit is behind the focal plane as in Fig. C.6-12d, there is a reversal in the distribution of light on the detectors from each of the apertures.

The net detector output when defocused is therefore a signal at the fundamental frequency whose magnitude is proportional to the extent of defocusing and whose phase is uniquely related to the direction of defocusing. This signal can be used directly as the error signal in a focus correcting servo.

### Autocollimating Optics

If the mirror is replaced by penta reflectors at the measuring apertures, several important advantages ensue. The pentas reflectors' primary contribution is their constant deviation characteristics in the direction of image separation. This provides autocollimating performance similar to a flat mirror without having to maintain a high level of stability, of the order of 0.5 microradian in a 1-meter-diameter system, over the dimension of the lens aperture. In addition, the pentas allow all light to circulate through the same elements, ensuring equality of all external factors affecting the two slit images.

A set of two standard pentas, however, is not a constant deviator in the direction normal to the plane of the diagram, and in this direction their alignment with the LSFS must be held within a few milliradians to avoid focus sensor null shift. A number of alternative external prism systems were therefore considered for this application, and one consisting of a regular penta and a roof penta proved to be optimum (Fig. C.6-14). This combination provides true retroreflection (transmitted rays are returned parallel to their entering direction) and greatly reduces the need for precise alignment of these elements.

The retroreflecting characteristics of the standard roof penta set, in addition to its other benefits, ensure that the slit image is returned precisely onto itself regardless of the slit location in the focal plane, exhibiting what might be called retrocollimation. Thus, misalignment of the slit and its image, caused by transverse shift of the slit prism with respect to the lens in conventional flat mirror autocollimation, is completely obviated in this system. A particularly important benefit of retrocollimation and symmetrical circulation of light is that they permit LSFS operation at large off-axis angles and in the presence of image motion compensation movement without performance degradation. It is this capability that transforms the LSFS from a laboratory device to a practical operational unit, readily integrable with real optical systems.

### Operational Form of LSFS

The operational schematic of the LSFS (Fig. C.6-15) follows almost exactly the schematic diagrams used to explain its operating principles (see Fig. C.6-12). The only significant difference lies in the use of a slit prism to

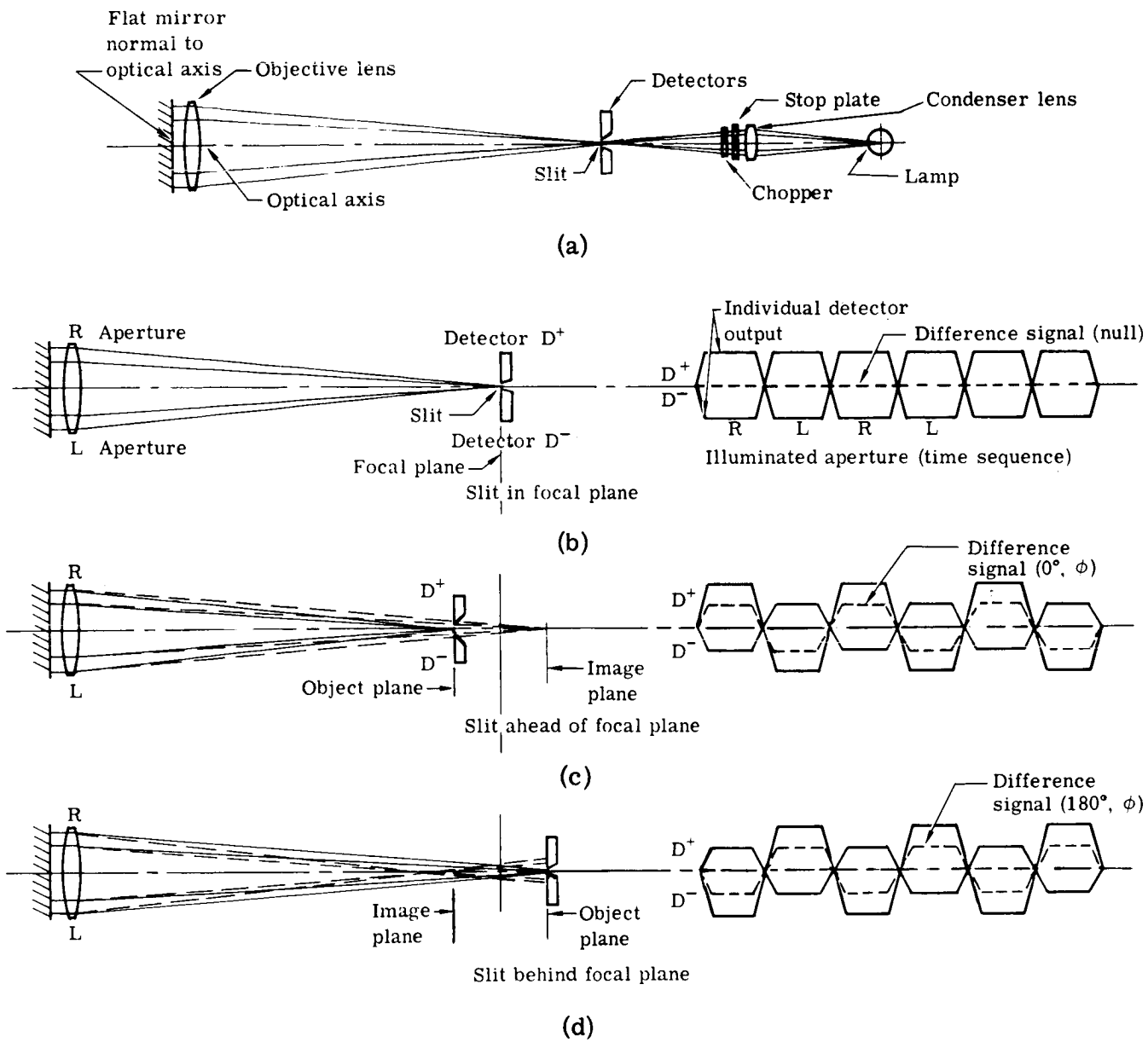
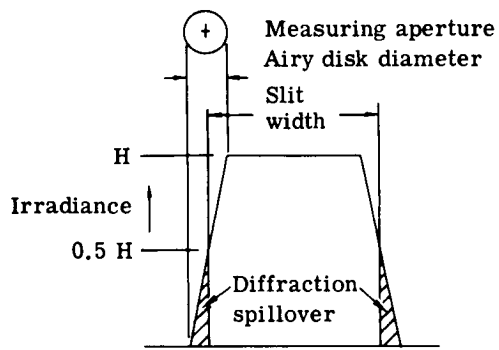
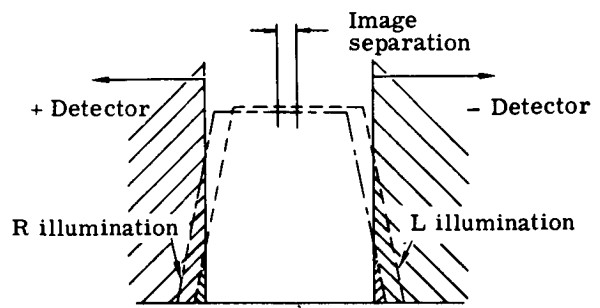


Fig. C.6-12 — Optical arrangement and signal characteristics



(a) Slit image irradiance distribution



(b) Irradiance unbalance with image separation

Fig. C.6-13 — Slit image diffraction characteristics



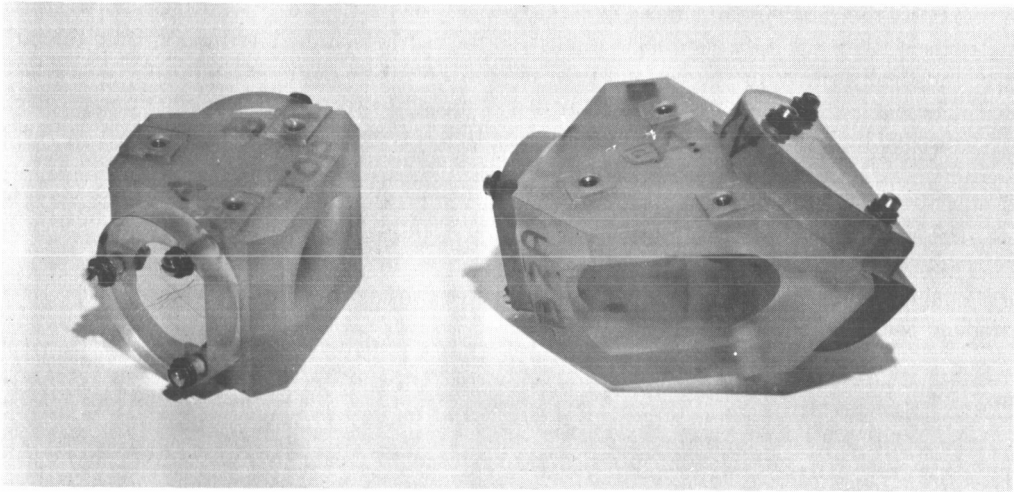


Fig. C.6-14 — Cer-Vit air path retroreflective penta set

obtain precise optical contiguity of the slit and the detectors. It is impractical to use the detectors to outline the slit because of the large signal that would be generated by the light at the slit edges. Instead, a slit prism with a clear slit area and reflecting sides separates the detectors from the exiting light but reflects to the detectors any autocollimated light falling outside the slit area. The slit is a few times as wide as the measuring aperture Airy disk (see Fig. C.6-13), and its illuminated height may be as large as required to achieve a given level of sensitivity.

All other basic elements are familiar, including the lamps, the condenser, the pentas, and the detectors. Maximizing defocus sensitivity and noise rejection requires amplification and synchronous demodulation of the detector signals. As shown in Fig. C.6-15, the ac error detector difference signal is amplified in an ac amplifier and then demodulated relative to the chopper phase reference signal. The final dc output signal has an amplitude proportional to the magnitude of defocus and a polarity determined by its direction.

### C.6.d(3) Focal Plane Figure Sensor

The proposed focal plane figure sensor is a novel form of shearing interferometer which, when used with a new data analysis approach, provides an unusually sensitive yet stable device. In this section we first describe the interferometer itself, then the data handling and analysis through which the information from the interferometer is made usable, and finally the error sources and their effects. For many of the components, a variety of approaches can be taken. These alternatives are described and the reasons for the recommended selections are given. The design and analysis described here were taken from a proposal by Itek for the LST figure sensor.

The proposed device is illustrated in Fig. C.6-16. An engineering model of a device very similar to that proposed for the LST is shown in Fig. C.6-17.

In understanding the interferometer it is worthwhile to consider three essential parts: (1) interference optics, (2) pupil scanner, and (3) modulator.

#### Interference Optics

In any type of interferometer, an optical system is used to create two wavefronts that can be interfered, converting unobservable phase variations into measurable intensity changes. It is in this area, the interference optics, combined with the data analysis procedure that our proposed interferometer is unique. Briefly (see Fig. C.6-16) superimposed diffraction gratings are used to produce two wavefronts slightly displaced from one another, and a second grating achromatizes the system so that operation in white light is possible. A field lens images the telescope primary mirror onto the interference plane, where wavefront errors are then measured as desired over the pupil.

A number of important advantages are gained with this approach. Most important, shear takes place at the front surface of the first diffraction grating. From that point on, both interfering wavefronts traverse a common path. Thus the interference pattern is not affected by the quality of the optics in the interferometer. The common path feature also minimizes the degrading effects of vibration and eliminates the need for close tolerances in the mechanical design. It is an ideal arrangement to provide the needed stability during launch. The actual instrument accuracy can then approach the pattern phase measurement accuracy. The combination of gratings and a field lens also eliminates the need for telescope pointing accuracy or stability. It is only necessary for the star image to remain in the interferometer field of view, which is limited only by the restrictions on focal plane space in the LST. The effective transmittance of the optics is also very high since unfiltered white light can be used. Furthermore, the gratings themselves, when properly made, provide nearly as much transmittance as a system of beam splitters in a Twyman-Green type interferometer.

The basic principles of the interferometer can be seen in Fig. C.6-18. Two diffraction gratings having slightly different line spacings are placed near the focal plane of the telescope. For any given wavelength of light, this produces two diffracted cones of rays at two slightly different angles. The diffraction angle is chosen large enough to keep the zero-order undiffracted rays separate. The amount of shear is determined by the angular difference between the two diffracted beams.

In practice, the two grating frequencies are produced holographically on a single plate. A photograph of a breadboard arrangement using this technique is shown in Fig. C.6-19. A second grating having a line spacing midway between the two frequencies on the initial grating is then introduced into the beam. The rays are then nearly parallel to the initial optical axis. This is true regardless of the wavelength of the light. The field lens then produces two white images on the telescope entrance pupil. The result of this is that the interferometer works in white light. The amount of shear is proportional to the wavelength, and the optical path difference for a defocused beam is proportional to the amount of shear. Since the fringe spacing is inversely proportional to wavelength for a given path difference, it follows that the fringe spacing is the same for all wavelengths. Sharp black and white fringes can be obtained even with a very large amounts of defocus. For other wavefront errors, the fringes will become only slightly blurred with color, and since the blurring decreases as the measured wavefront error decreases, this in no way sets a limit to measuring accuracy.

Astigmatism cannot be measured with a single fixed shearing pattern. Thus two sets of gratings and two field lenses are used, producing interference patterns sheared at right angles. This is shown in Fig. C.6-16.

In practice, all four gratings are placed on a single bleached hologram: two sets of lines in two orthogonal directions. The gratings have been made with lines at about 300 and 320 lines per millimeter. By proper exposure, development, and bleaching, 10 percent of the incident light in one shearing pattern and 15 percent in the other was obtained. That means that approximately 25 percent of the incident light was used. This ratio compares favorably to effective transmittances usually obtained with beam splitting arrangements. The second grating can be a blazed grating such that over 70 percent of the incident energy is transmitted. Allowing for minor improvements in the ability to make gratings, it can be expected that 8 to 10 percent of the total incident energy over all wavelengths will reach each of the two pupil images, for a total effective light utilization of 16 to 20 percent. Thus not only can white light be used, but also a reasonably efficient shearing arrangement is obtained.

### Pupil Scanner

Any focal plane figure sensor must produce an image of the system being tested so that the wavefront errors, now converted to intensity changes, can be measured at desired points over the system pupil. Three possible means for obtaining information over the pupil with a starlight source are:

1. Mechanical scanning with an appropriate aperture, using a photomultiplier as the detector
2. Use of an image dissector to achieve electronic scanning while retaining photomultiplier sensitivity
3. Use of an array of solid state channel-type photomultipliers.

The mechanical scan and the image dissector result in a series of measurements, while the multiplier array offers the possibility of parallel processing. However, it is felt that the state of the art in channel multipliers is such that either of the first two options appears preferable at this time; image dissector scan is recommended for the proposed unit. For long range development, however, the channel array may be the most compact and the most appropriate choice.

### Modulator

The interference optics produce a pattern in which the intensity is a simple function of the wavefront error. Although this intensity pattern could be scanned and sensed directly, greater accuracy can be obtained by modulating the pattern. The wavefront phase error is then measured directly by the phase differences in the modulated intensity pattern. In real-time interferometers of the Twyman-Green type that have been constructed, the modulation is obtained by translating a corner cube that acts as the reference flat. In the proposed grating interferometer, the procedure is even simpler. It is necessary only for the image and the grating to have a relative motion. For laboratory use a motor can be used to translate the grating. Almost any source of motion is usable; an electromagnetic loudspeaker-type linear motor on flexure mounts has been selected. In flight, scanning could also be obtained by allowing the telescope to cycle back and forth across the desired star or by scanning with the secondary mirror. This provides a unique failsafe backup capability.

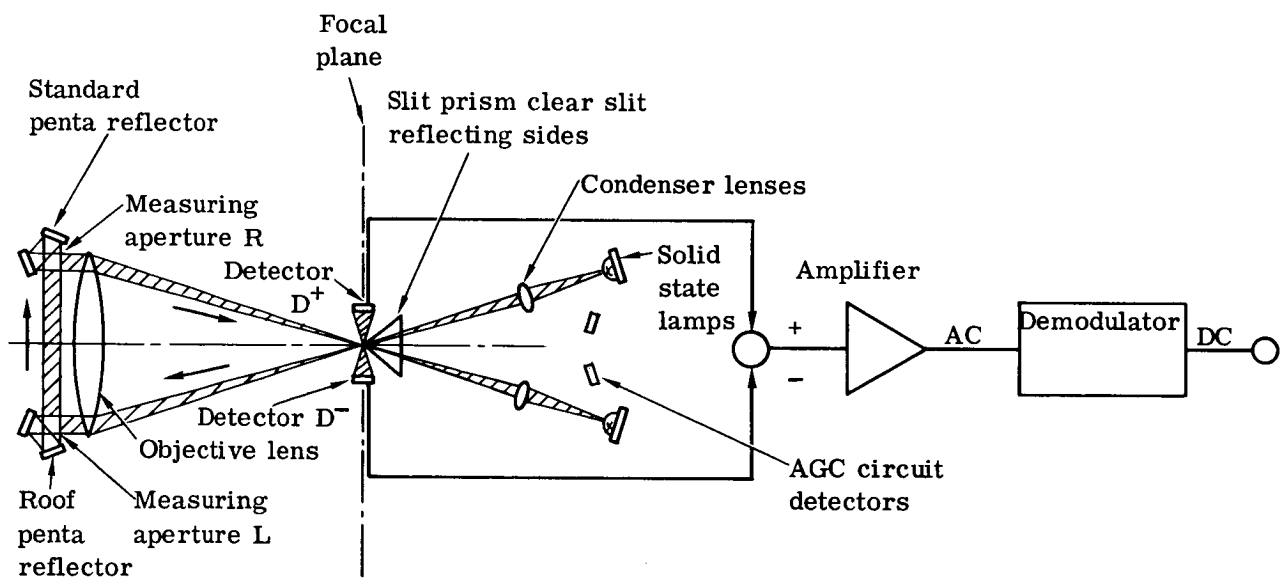


Fig. C.6-15 — LSF functional diagram

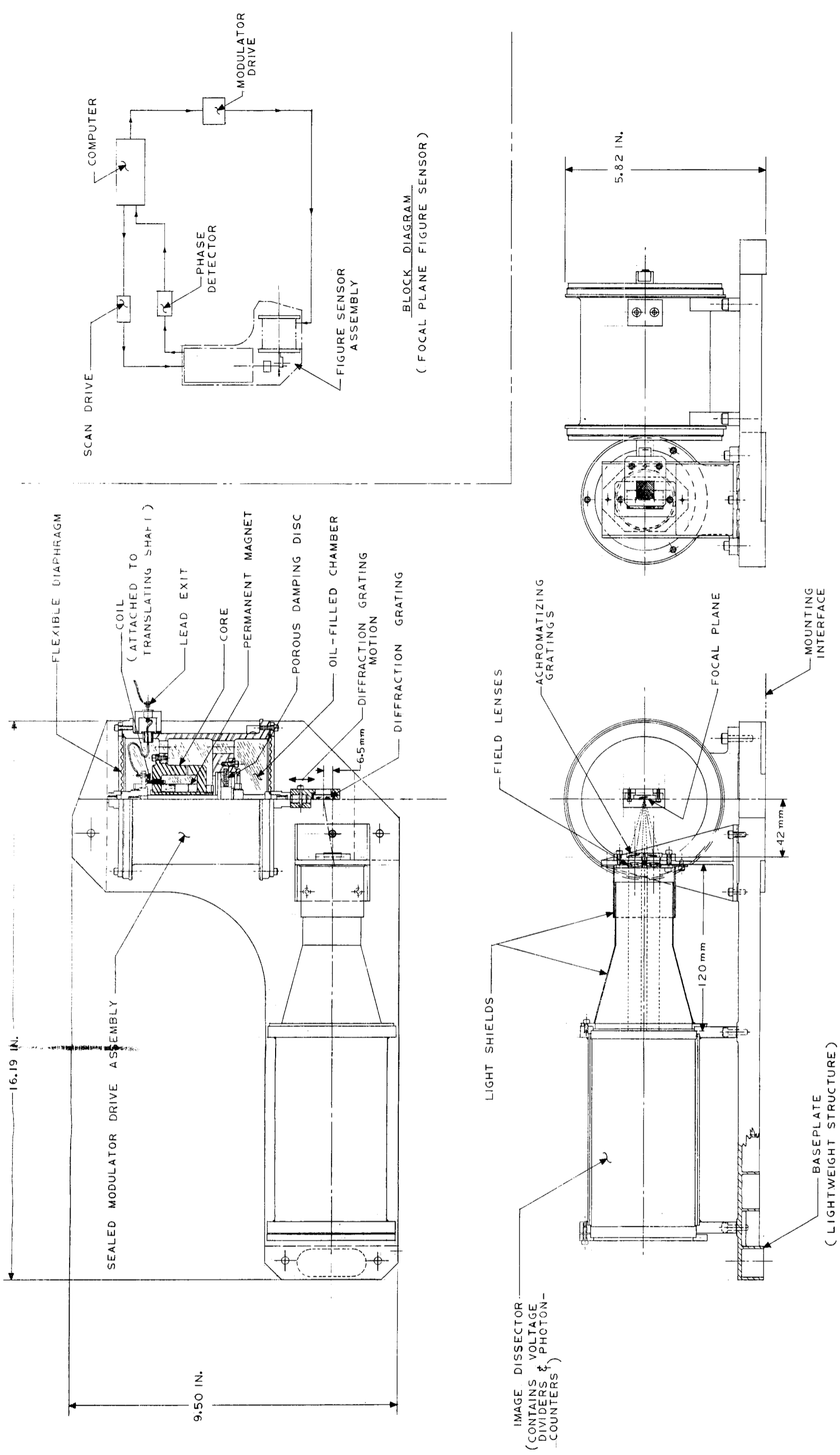


Fig. C.6-16 — Focal plane figure sensor using image dissector (dwg. no. 915927)

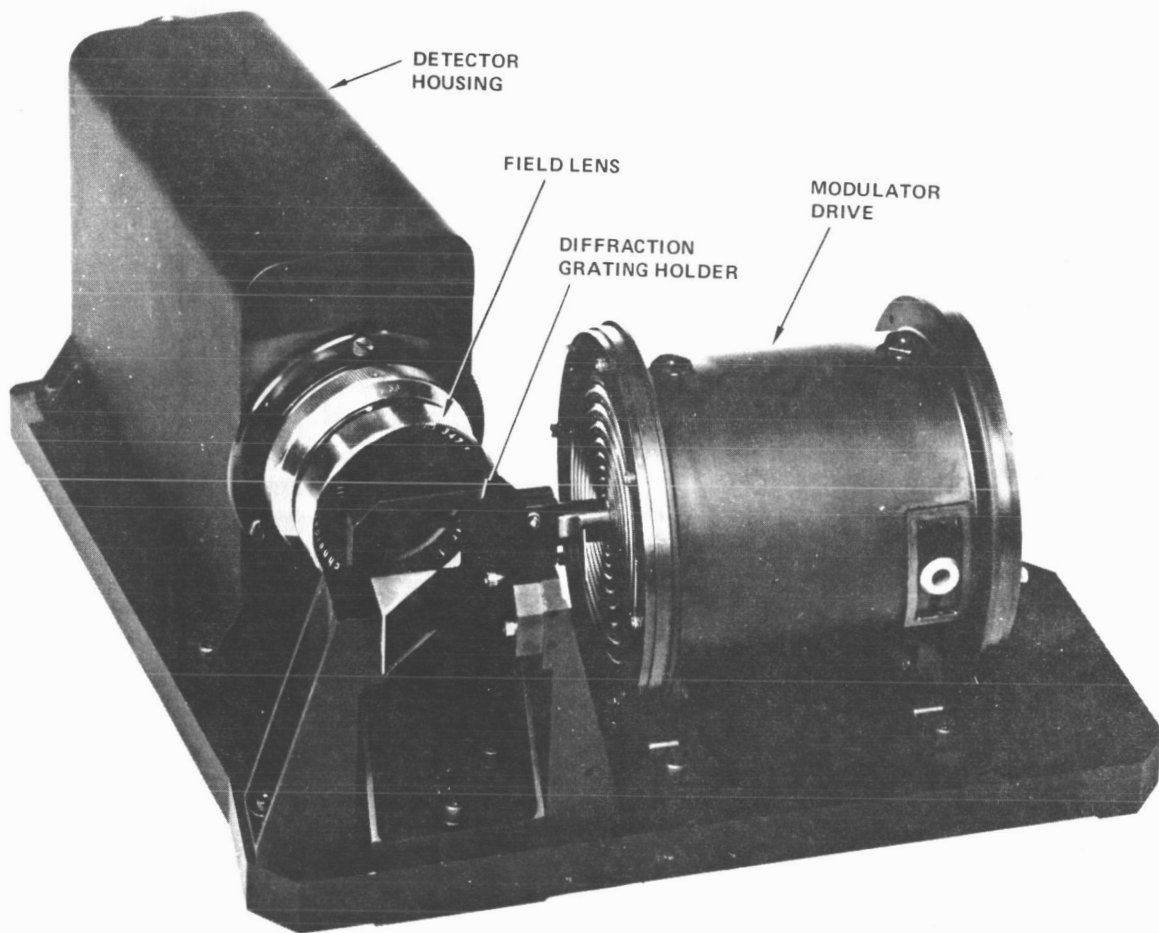


Fig. C.6-17 — Diffraction grating shearing interferometer

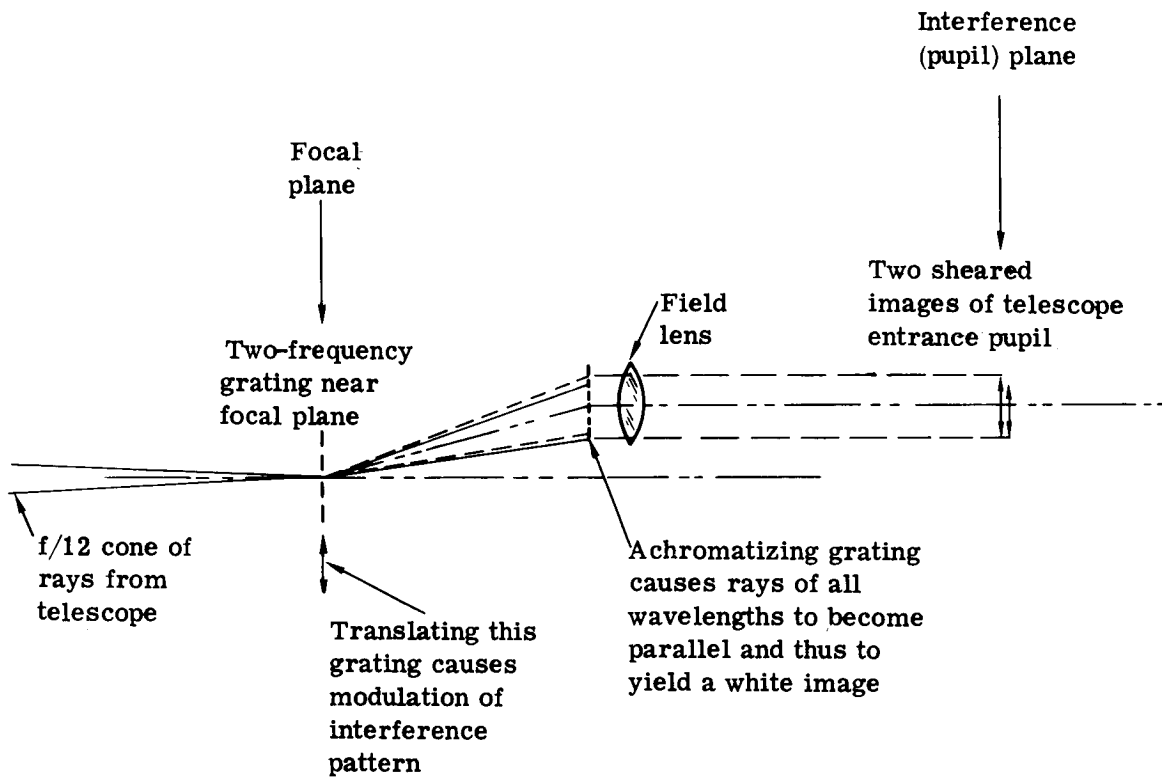


Fig. C.6-18 — Principles of white light grating shearing interferometer

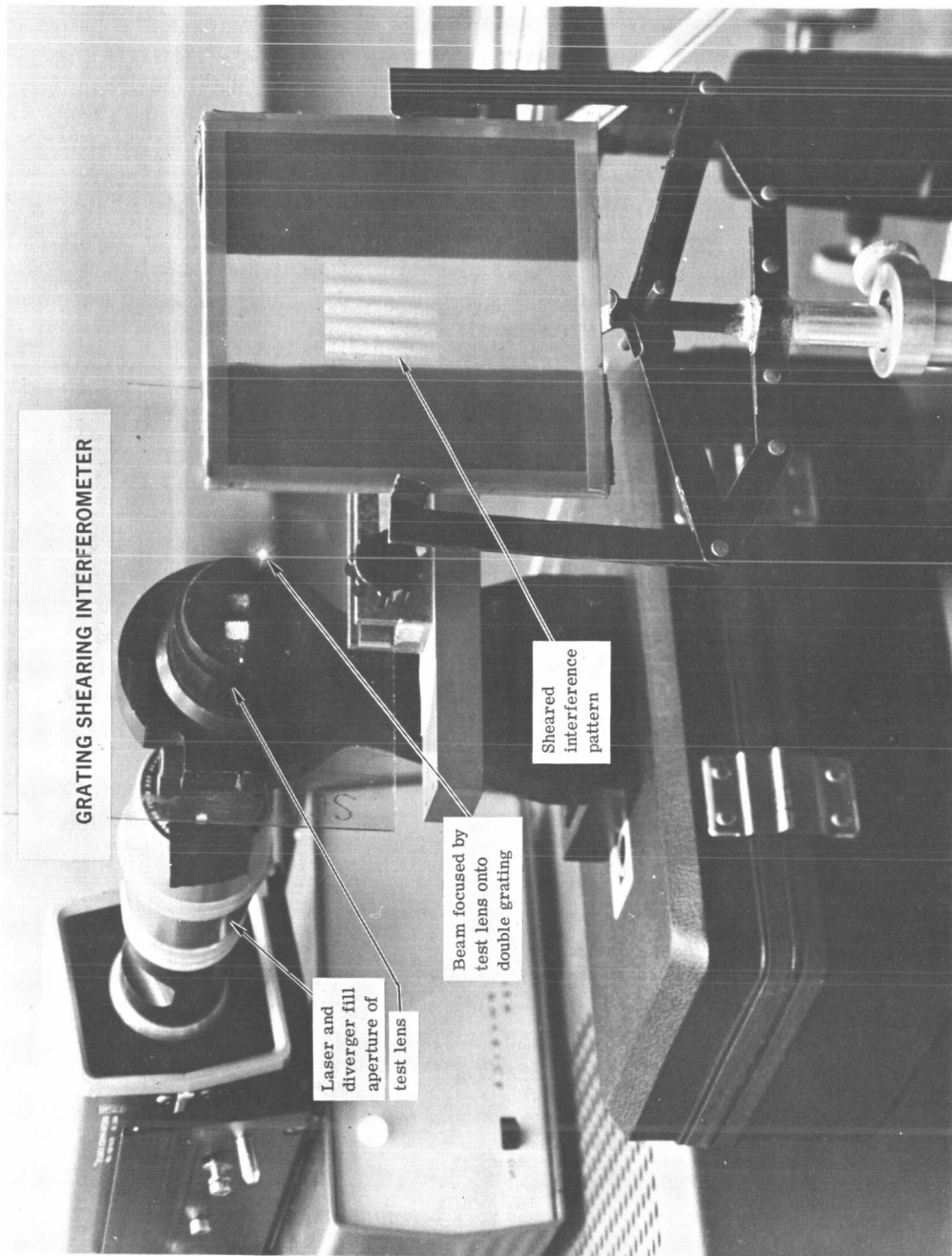


Fig. C.6-19—Breadboard grating shearing interferometer



## Data Handling

The basic detector to be used is an image dissector, which will be operated in a photon-counting mode. This allows for operation at the lowest possible light level, provides a reasonable dynamic range, and is ideally suited to computer-controlled operation. The modulation will be servo-controlled to operate at approximately 25 hz. Each cycle will then be divided into four equal parts, and the photon count in each segment will be recorded. Counting will be continued for as many cycles as necessary to obtain a large enough total count. This will be under computer control. The next area of the pupil image to be measured will then be addressed by the computer and counts again recorded. When all desired areas of the pupil have been sampled, the computer will determine phase from the relative value of the four count totals at each point, and then will convert this to an array of wavefront errors.

The figure sensor will operate under computer control, with most logic operations performed in the flight computer and analysis operations performed in the ground computer. This approach will provide great flexibility in analysis and control, and will minimize the need for special processing electronics. It is shown later that the operations needed to describe the surface in terms of focus, astigmatism, coma, and other aberrations, or to determine actuator forces needed to correct a mirror, are nearly identical to the basic data analysis routines.

It is also intended that the image dissector be operated in the photon-counting mode. Photon counts will then be supplied directly to the computer.

The operating logic is illustrated in Fig. C.6-20. All operations are under computer control. A signal is sent to the pupil scanner, indicating the appropriate xy address for the image dissector. No feedback from the devices is required. The servo then begins the modulation drive with feedback from the reference detector. When the proper velocity has been reached and stable motion is obtained, an enable signal is sent to the photon counter. This counts photons for one-fourth of a modulation cycle, and supplies the count to the computer after each quarter cycle. Since each quarter cycle is 0.01 second, there is no problem with access to the computer. It is also possible to provide four counters for the quarter cycle counts and to sum over several cycles in these counters. The quarter-cycle signals may come from either a 100-hz clock, which also provides 25 hz for the modulator, or from reference detectors that measure the actual modulation rate.

The counts for corresponding quarter cycles will be summed either in the counters or in the computer until an adequate number of counts has been obtained and a satisfactory signal to noise ratio, based on photon-counting statistics, has been obtained. The computer will then address the next area to be sampled by the pupil image scanner, and repeat the process until all desired areas have been sampled.

The sheared wavefront values are then computed for each point from the four photon-count sums that have been stored. Four intervals have been chosen because that is the minimum that will provide information on phase error over a full cycle, and because there are no apparent advantages to be gained from more samples.

If  $\psi$  is the phase error in the sheared interference pattern, and if A, B, C, and D are the summed photon counts in the quarter cycles, then the general form of the equations is

$$\sin \psi = \left(\frac{\pi}{2}\right) \left(\frac{A + B}{A_0 + B_0}\right) - 1$$

## Data Analysis

After the sheared phase values are computed from the photon counts, they can be sent to ground for the data analysis to put the information into useful form.

First, the phase measurements in the sheared interference pattern must be converted to wavefront values for the unshaded incident wave. Second, the wavefront information must be analyzed to determine secondary mirror misalignment and defocus, and possibly to determine other quantities such as actuator forces to correct the figure of the primary mirror.

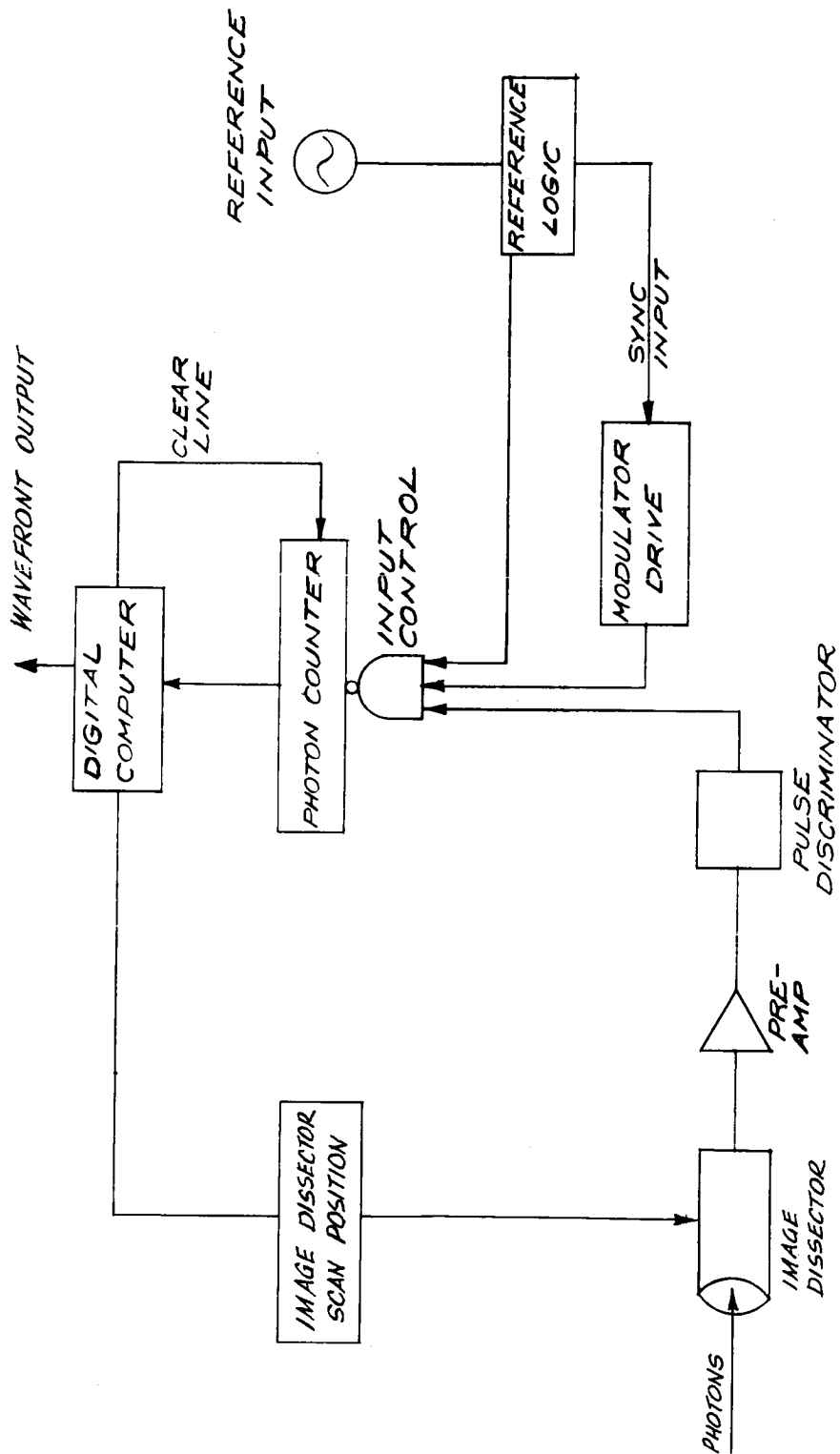


Fig. C.6-20 — Focal plane figure sensor block diagram

### Wavefront Calculation From Shearing Data

The use of shearing interferometry for precision measurement is made possible by proper analysis of the data. It is shown here that the resulting data is at least as accurate as that obtained by a conventional Twyman-Green type interferometer. In fact, the common path characteristic of the shearing interferometer will permit more accurate use in real environments by decreasing the sensitivity of the instrument to ambient vibrations.

Phase values are determined in the interference plane. These represent the optical path difference between points on the wavefront and other points on the same wavefront separated by the shear distance. Each measurement is then a wavefront difference. The problem is to derive the incident wavefront shape from the measurements of wavefront difference from point to point.

For this approach to data reduction, the measured points are separated by a space equal to the shear distance.\* This is illustrated in Fig. C.6-21. The mirror is shown with a grid representing a shear distance of  $5/16$  the mirror radius. The grid intersections represent points at which the wavefront is to be evaluated. Allowing for a central obscuration, this results in a set of 36 points. A smaller shear value would give a finer grid and thus a greater number of points; a larger shear would give fewer points. Both x-shear and y-shear patterns are used. Each measurement in the interferometer gives a difference in wavefront between two points separated by the shear distance. Thus the measurements are represented by arrows connecting adjacent points. It is not necessary to make all connections, but each point to be determined must have at least one connection. For the 36-point grid, as shown, there are a total of 56 possible connections.

Given the grid and the measured shear values, the wavefront values are reconstructed by a least squares minimization approach. In this approach we find a value for each of the points on the reconstructed wavefront. Let  $W_{i,j}$  describe the points on the wavefront, where  $i$  and  $j$  are the row and column number of the wavefront points. The measured values will then correspond to  $W_{i,j} - W_{i+1,j}$  and other combinations where  $i$  or  $j$  differ by one. It is then possible to write all the shear measurements (56 in this case) in terms of the 36 values of  $W_{i,j}$ . The equations, of course, are linear, so that a least squares solution can be written for the  $W_{i,j}$  values. The analysis operates so as to minimize the mean square error between the shear measurements and the values that would be calculated by the differences between adjacent  $W_{i,j}$  values. The effects of measurement error were examined by using analysis. Assuming an input surface, random errors were introduced to give simulated real measured data. The wavefront was then reconstructed as it would be in the signal processing section of the real interferometer. The reconstructed surface was then evaluated in terms of its rms error from the original input surface.

One thousand sets of random data were taken, and the results were evaluated. The results are very favorable. One case considered was the 36-point grid shown, using 56 measured shear values. For an rms measurement error of  $0.01\lambda$  for each measured shear value, the resulting rms surface error will be less than  $0.008\lambda$  for 90 percent of the measurements. In 1,000 simulated random surface measurements, the maximum rms surface error was only  $0.01\lambda$ . The significance of this is that errors are not cumulative as in usual procedures for analyzing shearing interferograms.

Other grids were investigated with comparable results, as shown in Table C.6-5, for different values of shear. The shear is expressed as a fraction of a unit radius. The table gives the resulting rms surface errors determined in the 1,000 random error runs for each case. The first column gives the rms surface error that includes 90 percent of the runs; the second column indicates the worst-case rms value.

---

\*This is not necessary, but it simplifies the analysis and greatly aids understanding. There seems to be no practical reason not to hold to this restriction.

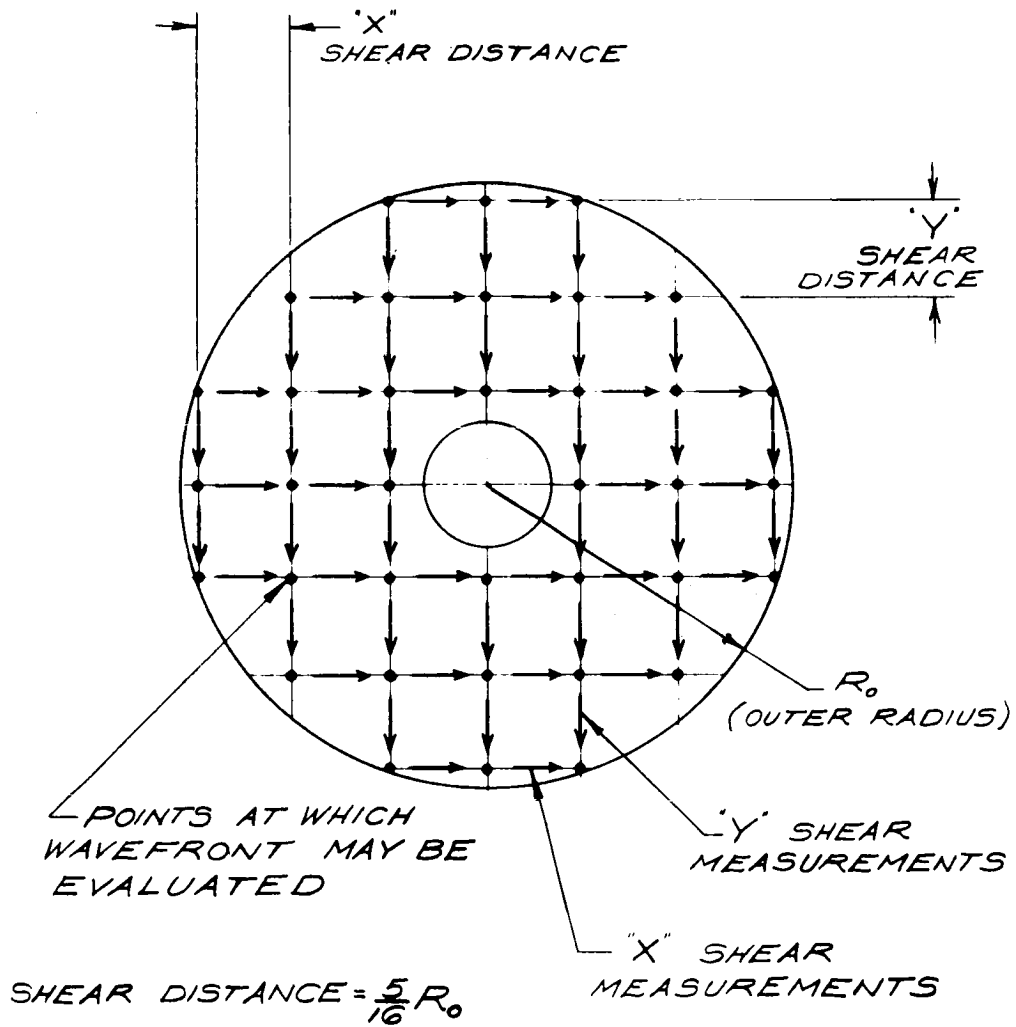


Fig. C.6-21 — Shearing interferometer measuring grid (36 points, 56 measurements)

Table C.6-5 -- Reconstructed Wavefront Errors for  $0.01\lambda$  RMS  
Shear Measurement Error

Shear	Number of Wavefront Points Determined	Number of Shear Values Measured	Reconstructed Wave	
			90% RMS Error	Peak RMS Error in 1,000 Runs
0.375	20	28	0.008	0.011
0.375	24	36	0.008	0.012
0.3125	36	56	0.008	0.010
0.300	37	60	0.008	0.010
0.250	48	76	0.008	0.011

The wavefront error sensitivity is a function of the noise in the measurement, which in turn is a function of the number of photons collected and counted. The measurement time is a function of the photon arrival rate, the system transmission, and the collecting aperture. Table C.6-6 gives the calculated photoelectron noise and measurement time in starlight.

As shown previously, an overall transmittance of 8 to 10 percent can be expected. Table C.6-6 gives the sampling time required to make measurements. It is based on 5 percent and thus represents a conservative estimate. Based on previous work, we would expect to use a grid of up to 36 sampled points, with each sampled area covering a square about 1/13 the aperture diameter on a side.

The errors indicated here are values for the rms error for each measurement point. For a 5th magnitude star, the measurement times are 27 to 680 milliseconds per sampled point. Even with 36 sampled points, the total time is between 1 and 25 seconds, and in many cases fewer points will be needed. However, there seems to be no problem with these times. So long as the measuring time is longer than the system vibrational periods and shorter than the system thermal time constants, the measurement time is not critical from a figure-sensing standpoint. Very short times (short as compared to vibrational periods) may be desirable, but these are not likely to be obtained with any technique other than parallel processing.

### Measurement Accuracy

Instrumental factors, other than detector signal-to-noise ratio, were considered that may limit the accuracy obtained by the figure sensor. The analyses presented here are necessarily brief and approximate. It is seen that there are no important sources of errors other than the signal-to-noise ratio. All identifiable sources, e.g., grating nonuniformity or modulator velocity errors, affect accuracy only indirectly, through second-order effects. As a result, it is difficult to estimate the real measurement accuracy. It appears likely that the actual limit may be set by external factors such as vibrations during the measurement time.

Specific error sources that were analyzed include:

1. Velocity errors in the modulator drive
2. Nonuniformity and uncertainty in knowledge of grating spacing
3. Imperfect optics in the interferometer
4. Misalignments in the interferometer
5. Operation with the star image not on the axis of the interferometer
6. Effects of white light operation.

No instrumental error sources were found that, under reasonable conditions, result in errors larger than  $\lambda/500$  rms. Furthermore, the figure sensor does not need calibration when used to reach a system wavefront error null.

### C.6.d(4) Secondary Mirror Alignment System

#### Summary

Requirements of a secondary mirror alignment actuation system are that it provide tip, decenter, and focus correction (five degrees of freedom); that it be reliable and provide its service for the desired lifetime; and that it be dimensionally stable while inactive so that image motions are not introduced. Further requirements as to what ranges of motion it must provide and whether or not it must operate during an observation have not yet been established.

One approach to reliability is to choose a configuration that maximizes the redundancy obtainable from a given number of actuators. Such is the property of the modified A-frame mount shown schematically in Fig. C.6-22. A model of such an actuator system is pictured in Fig. C.6-23.

Table C.6-6 – Interferometer Measurement Time in Starlight

Visual Magnitude	Photon Counts Per Second	Measurement Time/Sampled Point for Photoelectron Noise Equivalent to			
		$\lambda/100$	$\lambda/300$	$\lambda/500$	
1	2,340,000	0.7	6.1	17	} milliseconds
2	933,000	1.7	15	43	
3	364,000	4.4	39	110	
4	146,000	11	98	270	
5	58,300	27	240	680	
6	23,400	68	610	1.7	} seconds
7	9,330	170	1.5	4.3	
8	3,640	440	3.9	11	
9	1,460	1.09	9.8	27	
Needed photon counts ( $N_T$ )		1,590	14,300	39,800	

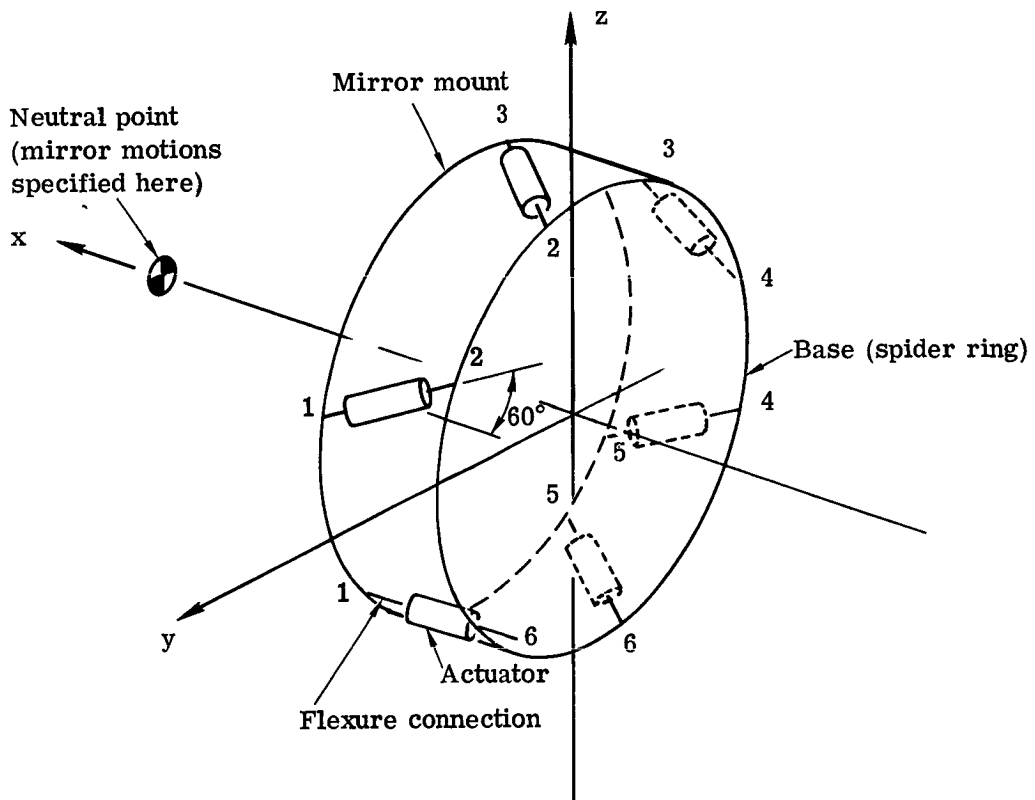
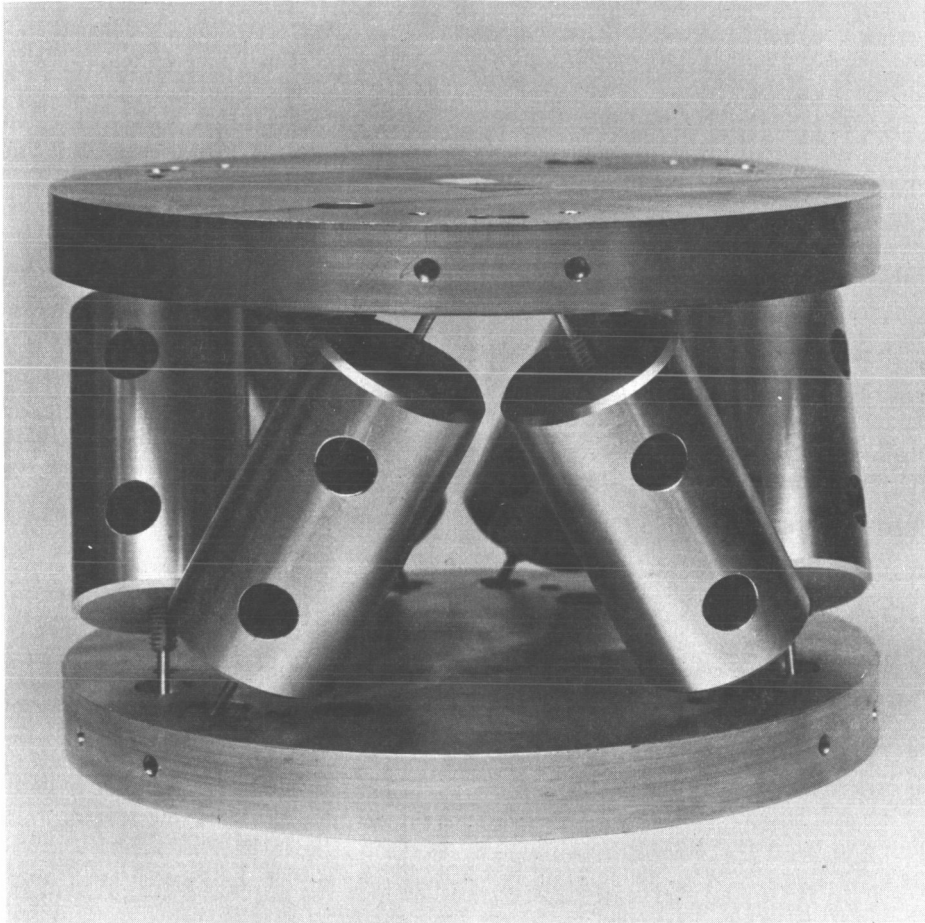


Fig. C.6-22 — A-frame secondary mirror actuation concept





20,081

Fig. C.6-23 — Secondary mirror actuator system

Six linkages define the position of the mirror relative to the reference frame, and if each linkage is extendible at will, then six-degree-of-freedom control of the mirror position is obtained.

If any one of the actuators fails, becoming a rigid linkage, there are sufficient influence coefficients in the matrix to retain control of the mirror position in any five coordinates, provided that control of the sixth coordinate is relinquished. Of course, the unnecessary degree of freedom is rotation about the axis, in the notation of Fig. C.6-22

If any two other actuators fail, control is still maintained over any three of the remaining degrees of freedom. In this case, the control to be retained would be that of the focusing and centering adjustment.

Certain aspects of the secondary mirror alignment and focus actuator system have been analyzed in some detail (see LST Secondary Mirror Actuator System, LST-72-130) and the results are given here. The actuator design proposed is a linear harmonic drive of the USM Corporation, with a stepping motor drive and a stepping increment of 0.5 micrometer. In operation, the error signal derived from the alignment sensors would be used to compute the correction required of each actuator; then the actuators would all be stepped to their new positions simultaneously, after which a new reading would be taken from the sensors.

The system as designed would accommodate structural deflections of about  $\pm 1.25$  millimeters. Should larger deflections be expected, the design could be modified to accommodate them.

The actuators can be expected to contribute 3.5 micrometers of decenter, 0.5 micrometers of mirror spacing errors, and 3 microradians tilt of the secondary mirror to the system alignment errors.

The lowest natural frequency for the proposed system is estimated to be about 38 hz in the lateral mode of vibration of the mirror.

### Design

The mirror actuation system design is shown in Fig. C.6-24. The flexures that form the joints of the linkages are designed for a lateral deflection of 2.5 millimeters and an axial loading of 230 kilograms (500 pounds), which corresponds to the loading of each of the six flexures of a 90-kilogram (200-pound) mirror under 5 g lateral acceleration. The expected twist of each flexure is less than 0.01 radian. A heat-treated steel flexure with a diameter of about 2 millimeters and a length of 12.5 millimeters would be adequate.

What appears to be a suitable actuator is shown in Fig. C.6-25 which was proposed for the LST secondary mirror system by the USM Corporation. It is described here as one example of a workable actuator.

The following comments are applicable to the design concept as shown per USM sketch SK3423-1 (reference: USM File No. 3423).

1. Response Time – At an input pulse rate of 8.4 pulses per second, the response time for 1/2-micrometer motion is in the order of 0.12 second.

2. Types of Failure Possible – The device functions at essentially no load; therefore, the only two principal considerations are the bellows and harmonic drive flexspline fatigue life, since they are flexing elements.

Failure of the bellows would result in eventual loss of controlled atmosphere and lubricant.

A flexspline crack would normally cause a functional failure under rated load. In this case, however, the harmonic drive will continue to function due to the no-load condition but with a probable increase in the output positional error.

3. Accuracy or Sensitivity – Essentially all of the backlash will be in the motor gear head and under worst case conditions will be 8.7 milliradians (30 arc-minutes). This reflected to the output represents a positional error of 0.5+ micrometer.

4. Reliability – Would approach 1.0, predicated on the harmonic drive wave generator bearing B10 life. Assuming continuous adjust, 12 hours per day for 10 years, R would be 0.9995+.

5. Power Requirements – The concept envisions the use of a size 8 Kearfott-type PM stepper motor, which requires 2.1 watts input. No power will be required to maintain actuator position.

6. Lubrication – - The relatively low operating speed can be satisfied with a light film of silicone type oil such as the GE F50 and an impregnated sponge type reservoir.

7. Weight – Estimated weight of the actuators is < 0.23 kilogram (8 ounces), excluding the connecting struts.

This system is designed for a lateral positioning of the mirror of about  $\pm 2.5$  millimeters, which corresponds to a lengthening of the actuator of  $\pm 1.25$  millimeters and a flexure deflection of  $\pm 2.2$  millimeters. Some of this range of motion must be retained for use in case one actuator fails in an extended position, so the tolerance for structural deflection should be about  $\pm 1.25$  millimeters.

The influence matrix and the specifications given for the actuator can be combined to predict the decenter, defocus, and tilt errors of the secondary mirror due to the adjustment mechanism. The actuators have a step error tolerance of 1.0 micrometer. Table C.6-7 is the influence matrix for the baseline system in which the mirror motions are described at the neutral point 1.37 meters behind the mirror. The coefficients in Table C.6-7 can be used to determine the error contribution from each actuator. The worst-case and rss errors for the system are computed from these individual contributions and are given in Table C.6-8.

In calculating the stiffness of the proposed configuration, it is assumed that the mirror inertia is that of a disk ( $J = \pi r^2/4$ ) in which r is about 0.33 meter. For steel flexures of the type discussed, the axial stiffness is about  $26.3 \times 10^4$  newtons/cm ( $15 \times 10^4$  lb/in). Assuming, then, a composite stiffness of  $1.75 \times 10^5$  newtons/cm ( $10 \times 10^4$  lb/in) and a mirror mass of 90 kilograms (200 pounds), the lowest natural frequency is estimated to be about 38 hz.

#### C.6.d(5) Primary Mirror Figure Control

##### Number of Actuators

The overall design of the telescope is based on a concept of maintaining the performance of the system without active control of the primary mirror figure. Thus it is unknown factors or system failures that could cause a deformation of the mirror figure. Because of the unknown nature of what might cause defiguring of the mirror, it is not possible at this time to devise an optimum figure control system in terms of the number of actuators required and the weight of the actuator system. Nevertheless, studies to date indicate that without a doubt, actuators augmenting a thick mirror in conjunction with a suitable figure sensing system and actuator control law can produce marked improvements in the mirror's figure should deformation of the mirror occur. It would appear that approximately 25 actuators would provide significant improvement in most cases.

Work along several lines in following phases of the program would aid in the judicious selection of an actuator system:

1. Analysis of expected mirror figure errors, based on assumed electrical, mechanical, or thermal control failures caused by assumed design, manufacture, or operational problems
2. Consideration of mirror material stability data as it becomes available
3. Optimization of actuator location for various numbers of actuators, considering the mirror deformations most likely to occur

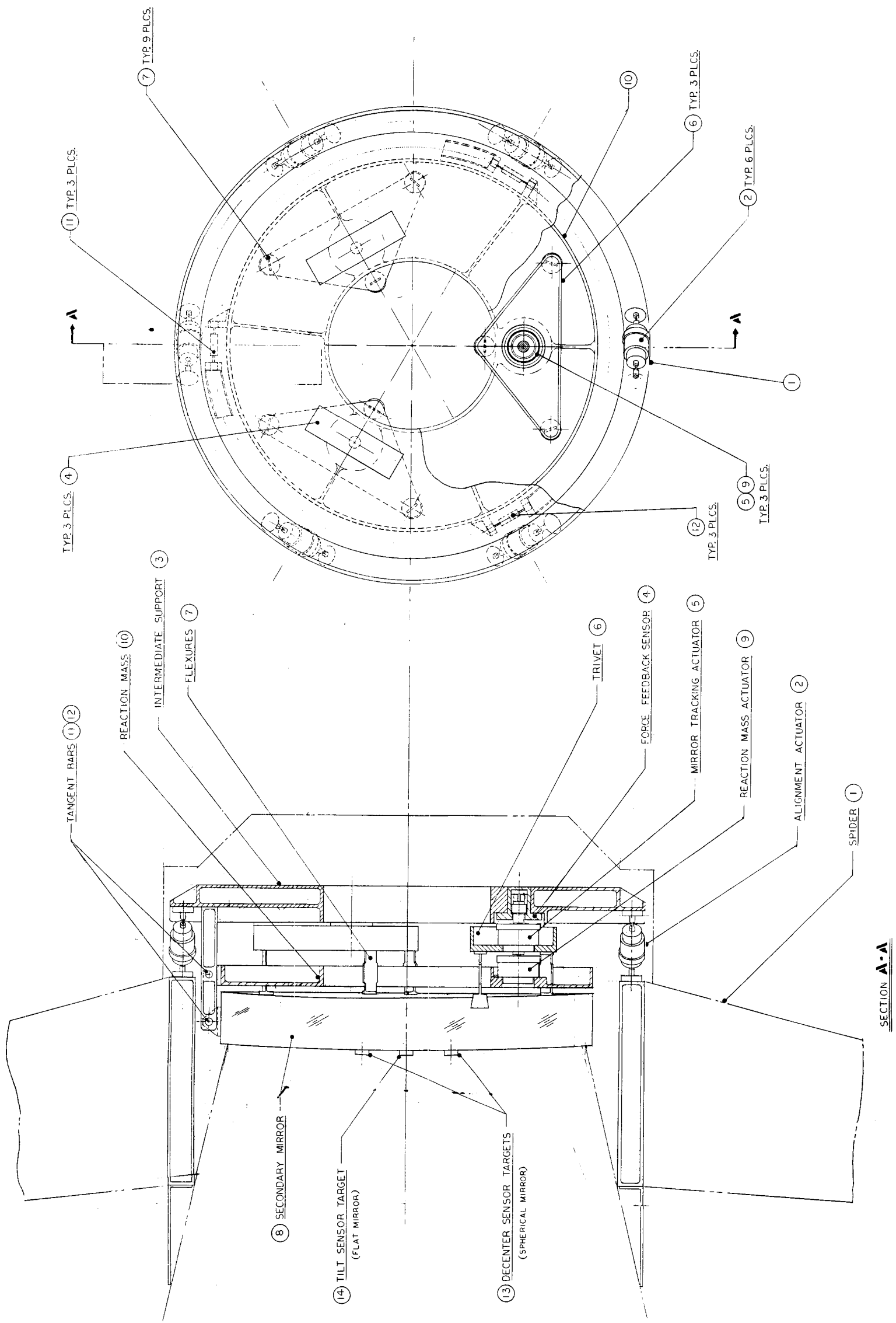


Fig. C.6-24 — Secondary mirror alignment actuator system design (dwg. no. 911329)

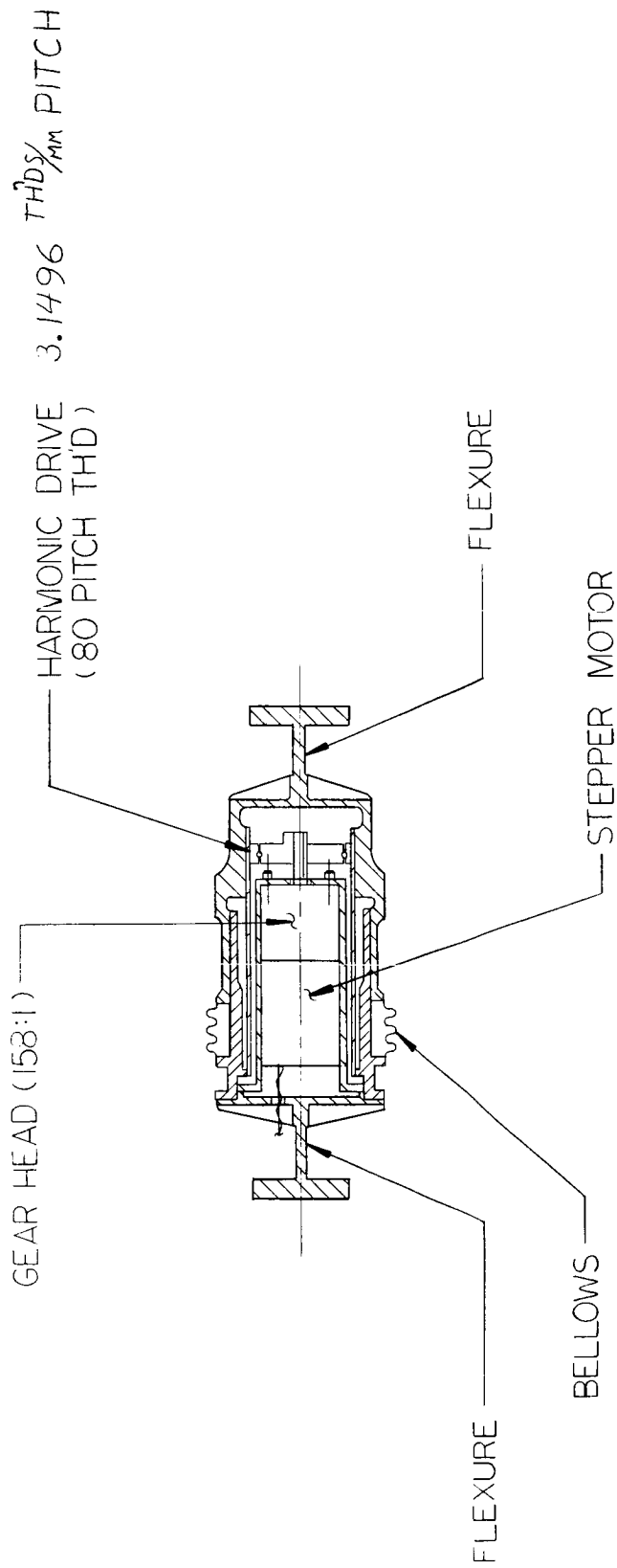


Fig. C.6-25 — Secondary mirror alignment actuator layout (dwg. no. 911388)

Table C.6-7 -  $|\Delta \Gamma^1$  for Baseline System at Neutral Point

	$\delta_{16}$	$\delta_{12}$	$\delta_{32}$	$\delta_{34}$	$\delta_{54}$	$\delta_{56}$
$\delta_y$	-1.44	-1.44	+0.667	+0.77	+0.77	+0.667
$\delta_z$	+0.06	-0.06	-1.27	-1.21	+1.21	+1.27
$\delta_x$	-0.192	-0.192	-0.192	-0.192	-0.192	-0.192
$\delta_z$	+0.608/m	-0.608/m	-1.22/m	-6.08/m	+0.608/m	+1.22/m
$\phi_z$	+1.05/m	+1.05/m	0	-1.05/m	-1.05/m	0
$\phi_x$	-1.05	+1.05/m	-1.05/m	-1.05/m	-1.05/m	+1.05/m

Table C.6-8. — Alignment Errors From Actuator Error

	Decenter, micrometers		Defocus, micrometers		Tip, microradians		
	$\delta_y$	$\delta_z$	$\delta_x$	$(\delta_y^2 + \delta_z^2)^{1/2}$	$\theta_y$	$\theta_z$	$(\theta_y^2 + \theta_z^2)^{1/2}$
Worst-case error	5.8	5.1	1.15	7.7	4.9	4.2	6.5
RSS error	2.5	2.5	.47	3.5	2.1	2.1	3.0

#### 4. Evaluation of the weight versus performance tradeoffs.

To indicate the effectiveness of a few actuators in correcting astigmatism produced by simple warping in a thick, lightweight, monolithic mirror, a recent study (Controlling Astigmatism With 10 or Fewer Actuators, LST-72-171) considered actuator configurations as shown in Fig. C.6-26. The three-actuator system corrected the astigmatism to a residual of 12 to 14 percent, whereas the six-actuator system left a residual of 7 to 8 percent.

Further analysis yielded the data in Fig. C.6-27 for different classes of mirror figure errors. The lowest curve shows the effect of the number of actuators in controlling astigmatism, which might be the most likely type of figure error to occur, since it represents a simple warping. The next curve represents the effectiveness of correcting third-order spherical aberration.

Spherical aberration might be the predominant nonrefocusable effect of a design error in the zero-gravity simulation mount used in fabrication. Together, astigmatism and spherical aberration probably represent the bulk of the nonrefocusable error resulting from a failure in the thermal control system, with the exception of the effect of a soak temperature change in conjunction with randomly distributed variations in the thermal coefficient of expansion of the mirror material. This latter effect is represented by the third curve from the bottom in Fig. C.6-27. The effect of random thermal coefficient variation appears to be considerably more difficult to compensate. There is some reason to believe that in a Cer-Vit mirror, the thermal coefficient variations would have a systematic distribution because the coefficient is a function of the temperature in the annealing process, and the temperature during the annealing process would have a systematic, axially symmetric distribution through the mirror blank.

The top curve in Fig. C.6-27 represents the effects of large tangential torques introduced through the mirror mounts. This curve indicates that a moderate number of force actuators distributed across the mirror is not very effective in correcting figure errors introduced at the mounts. Thus it is important that a proper mount be designed. Should later failure mode analysis indicate that under some conditions, large disturbances can be introduced through the mounts, the problem would be solved most directly by placing force and torque actuators directly on the mounts so that the mirror could be brought back to an unstressed condition.

To summarize the data that indicate the effectiveness of various numbers of actuators, let us assume a minimum criterion that an effective actuator system will attenuate a figure error to within 20 percent of its initial value. Then we have the situation in which, if analysis indicates

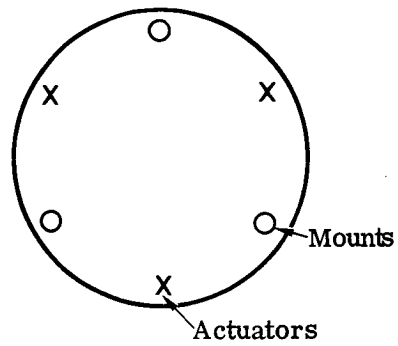
That the predominant figure error is	Then the number of actuators for attenuation to 20 percent is
Astigmatism	3
Spherical aberration	25
Random	75
Mount disturbances	Mount actuators

It is felt that most causes of figure error will be of a somewhat systematic nature, giving an error akin to the spherical aberration case above, and so it seems that 25 actuators would represent a minimum number that would yield significant improvement for most situations that might occur. If it is necessary that the force actuators also serve as a zero-gravity simulation in the OTA during ground test, then up to 75 actuators might be required.

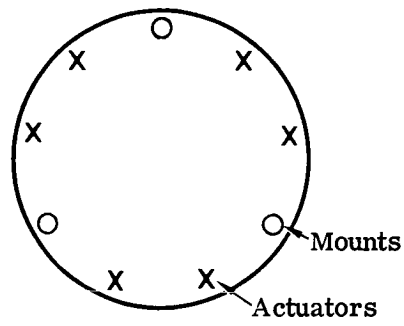
#### Actuators

The figure control actuators proposed are similar to the secondary mirror alignment actuators except that the linear motion output of the actuator mechanism pushes against a spring, which in turn pushes against the back of the primary mirror, making the actuator, in effect, a force-producing actuator. The heart of the actuator is a USM Corporation linear harmonic drive with a stepper motor control. The springs against which this drive pushes are set





(a) Three-actuator system



(b) Six-actuator system

Fig. C.6-26 — Minimum actuator configurations for controlling astigmatism

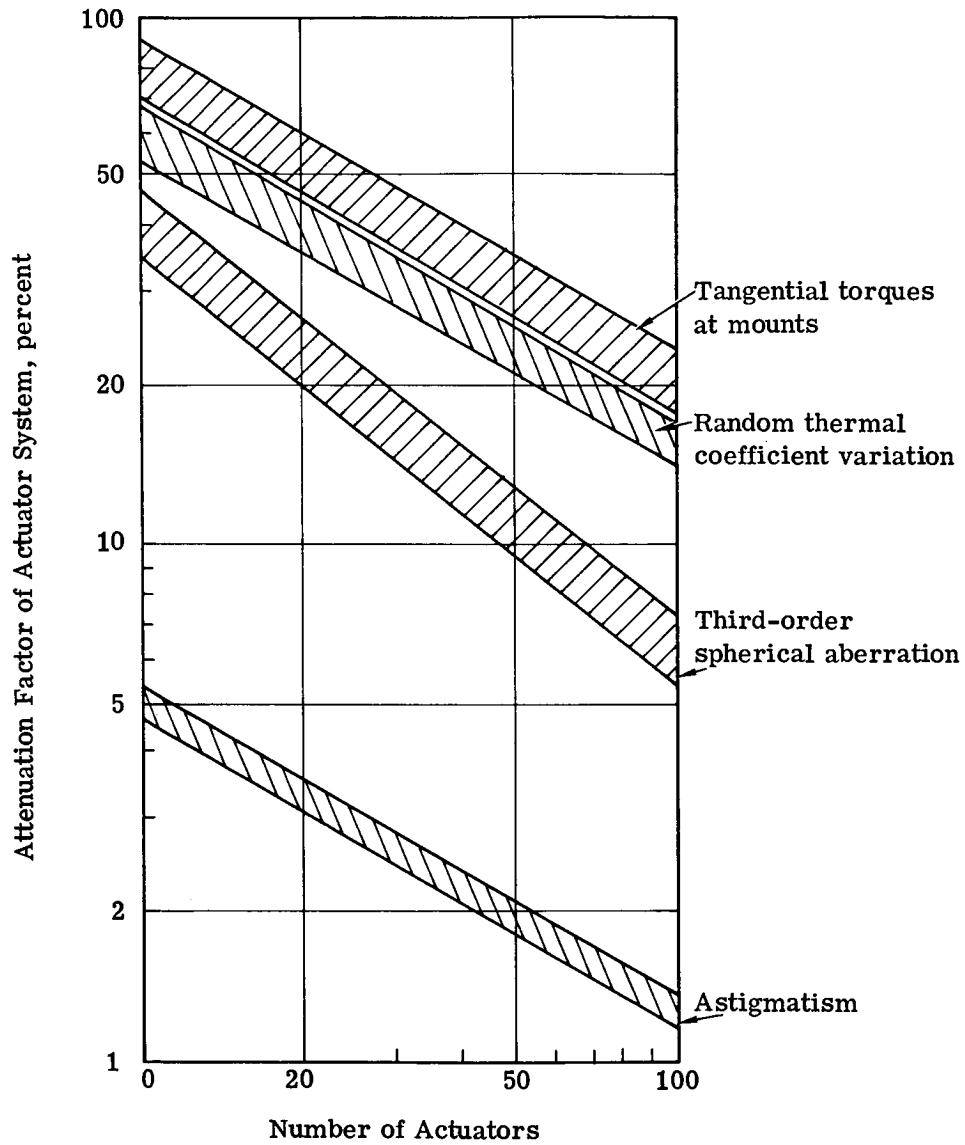


Fig. C.6-27 — Figure correction in a thick, lightweight, monolithic mirror

with a small neutral zone so that about the initial position of each drive, there is a small clearance for motion which will produce no force. In the expected normal operation of the LST, the actuators will never be used, and this small neutral zone will allow for normal deflection of the pressure bulkhead without causing forces to develop against the back of the primary mirror. The actuator is pictured in Fig. C.6-28.

#### Use of Figure Sensor Data

Processed data from the figure sensor describe the mirror figure and, should it appear necessary to make corrections to the figure, the actuators will then be set to correct for the surface error represented by the processed data. It will be an iterative, open loop solution: the wavefront measurement will be made, the required number of actuator steps will be computed, the actuator motors will be driven the required number of steps, and then the measurement and correction process will be repeated until the number of actuator drive steps for the next correction is less than some threshold number. This process avoids dynamic instability problems of real-time continuous sensing yet does not impose a requirement for accurate calibration of the force actuators or the incorporation of force sensors. It does not guarantee convergence of the process to the desired figure, however. That is a function of the control algorithm used.

The operation to determine the required number of actuator steps can be accomplished by simple multiplication of a vector by representing the measured figure errors by an invariable matrix:

$$\begin{array}{|c} F_i \\ \text{array size} \\ N_A \times 1 \end{array} = \begin{array}{|c} P_{i,n} \\ \text{array size} \\ N_A \times N_S \end{array} \times \begin{array}{|c} Z_n \\ \text{array size} \\ N_S \times 1 \end{array}$$

in which

$F_i$  = number of actuator steps

$N_A$  = number of actuators

$Z_n$  = wavefront error at each sampled point

$N_S$  = number of sampled points

$P_{i,n}$  = invariable array describing the geometry of the measured points, the geometry of the actuators, the force characteristics of the actuators, and the flexibility characteristics of the primary mirror.

This latter matrix can be changed to account for unusual conditions, failure of some of the actuators, etc.

#### C.6.e Performance Control Subsystem Interface Summary

Table C.6-9 gives a summary of interface characteristics of the components of the performance control subsystem.

#### C.6.f Alignment Error Budgets

The sensitivities of the OTA to misalignment of the components are given in Table C.6-10. A lateral positioning error of the secondary mirror with respect to the primary mirror (secondary decenter) and changes in the axial spacing of the components result in wavefront errors that are approximately constant over the field of view. Tip of the secondary mirror about an arbitrary point on the optical axis can be considered geometrically to be a combination of pure decenter plus tip about the specific point, and if the specific point is defined as the neutral point, the wavefront error attributable to tip about that point becomes a field-dependent function which has a zero value on the optical axis and is approximately linear with field angle. Sensitivity to tip about the mirror surface given in Table C.6-10 is determined by dividing the decenter sensitivity by the distance of the mirror from the neutral point. Tip of the focal plane also results in a field-dependent error with about 1/10th the sensitivity of tip of the secondary mirror. Since the data for the scientific instruments are taken near the center of the field, tip of the secondary and of the focal plane affect mainly the guide field.

HARMONIC DRIVE 3.1496 THDS/mm PITCH (80 PITCH TH'D)  
REF. SK 3423-1 USM CORP  
GEAR SYSTEMS DIV. WAKEFIELD, MASS.

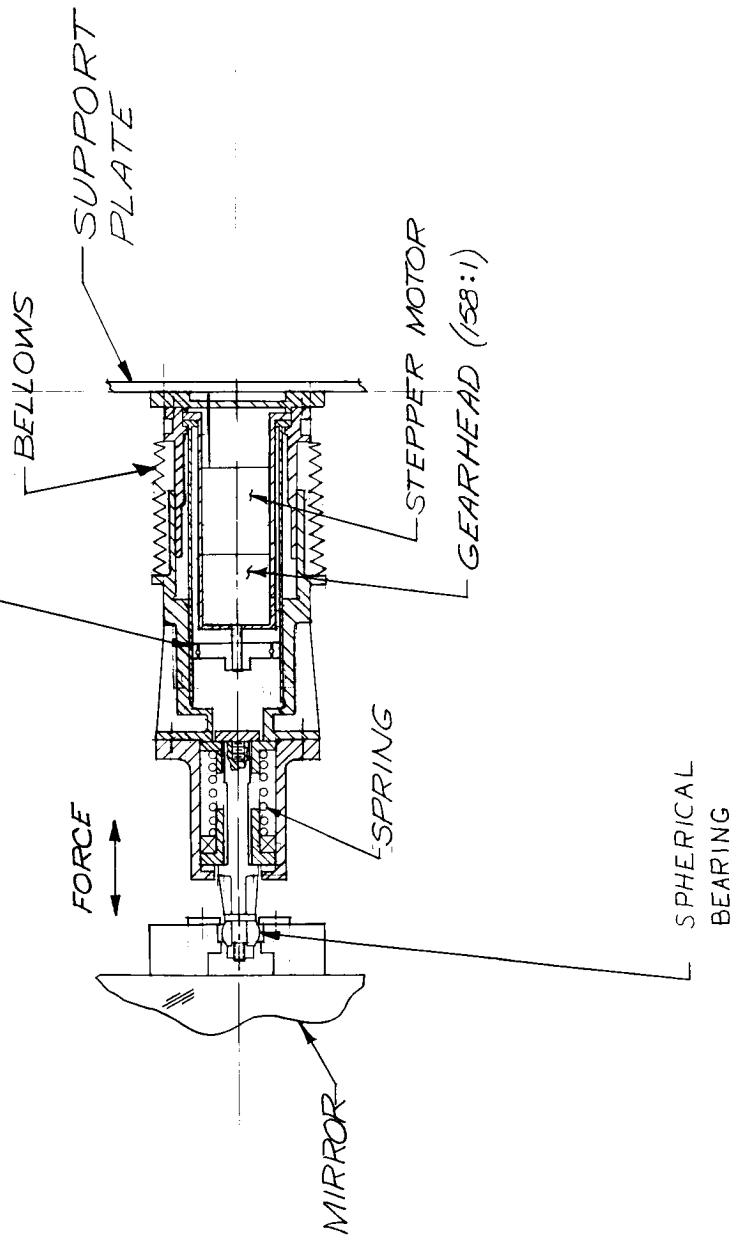


Fig. C.6-28 -- Primary mirror force actuator layout (dwg. no. 911375)

Table C.6-9 – Performance Control Subsystem Interface Summary

	Range	Replacement	Calibration
Secondary mirror alignment actuator system		Replace on ground	Alignment sensors
Lateral displacement	±1.25 mm		
Tip	±1 mrad		
Axial displacement	±1.25 mm		
Alignment sensors			
Decenter	±48 mm	Replace on ground, interferometrically	Figure sensor
Tip	±0.7 mrad		
Focus change sensor	±25 mm	Within SSM to stop	Figure sensor
Figure sensor	1λ p-p	Within SSM to stop	—
Primary mirror actuators	± 220 newtons (±50 pounds)	Replace on ground	Figure sensor

Table C.6-10 – Alignment Sensitivities for f/2.2-f/12 System

	Error at 633 Nanometers, wavelengths rms
Field-independent errors	
Secondary decenter	0.00054/μm
Secondary tip about secondary surface	0.00032/μrad
Secondary-primary spacing	0.01 μm
Focal Plane defocus (f/12)	0.00036/μm
Field-dependent errors	
Secondary tilt about neutral point	0.00013/μrad tip/mrad field angle
Focal plane tilt	0.000013/μrad tip/mrad field angle

### C.6.f(1) Secondary Mirror Decenter and Tip Error

The budget for decentering and tipping errors is given in Table C.6-11. The following is an explanation of each item in the budget:

#### Initial Alignment

When the OTA is assembled in the optical shop, it can be aligned interferometrically to the state of final figuring of the secondary against the primary. At this time, the alignment sensors will be adjusted, and the limitation of this adjustment will be the sensitivity of the alignment sensors.

#### Alignment Maintenance

In the course of operation, the sensor again will limit the accuracy of alignment by its sensitivity level. Between adjustments, the support structure for the secondary mirror may shift laterally or tip. Ten micrometers have been allocated to decenter from this source and 5 microradians to tip about the mirror center. When adjustment is made, limitations in the resolution of the six alignment actuators combine to give an rss centering adjustment error of 3.5 micrometers.

When the secondary is used for stabilization of the line of sight, it is tipped via the image stabilization actuators about its own center by an amount that must be  $2\frac{1}{2}$  times the desired line of sight correction angle, at most 12 microradians.

### C.6.f(2) Focus Maintenance Budget.

The best focus of the system with a particular instrument in use may best be found by means of a through-focus run with that instrument. At that time, the focus change sensor is calibrated, and the performance control system must maintain that best focus during the subsequent observations. The focus maintenance budget is given in Table C.6-12 and the individual items in the budget are explained below.

#### Calibration of Relative Focus Sensor

The proposed focus sensor has been found to have a focus resolving ability of about  $0.2\lambda F^2$  which at  $f/12$  with a 0.9-micrometer gallium arsenide diode light source is about 26 micrometers. The sensitivity to defocus at the focal plane is  $0.00036\lambda$  rms per micrometer, so that 26 micrometers defocus corresponds to  $0.009\lambda$  rms. The focus sensor cannot be calibrated with an accuracy exceeding its resolution without a great deal of effort, so this limit to calibration is placed in the budget.

The focus sensor must, in general, return the telescope to a condition of focus which is different slightly from the true null of the focus sensor, and thus the focus sensor is not used under ideal conditions. If the focus sensor location is held close to the plane of best focus within a fraction of its resolution and can have its scale factor calibrated from time to time by known focus changes introduced at the secondary mirror, then there should be no significant error introduced by operating the focus sensor slightly off null.

#### Internal Dimension Knowledge

Once the position of best focus is determined, changes in the dimension between the focus sensor and the plane of best focus will cause the focus sensor to return the telescope to other than best focus. It has been assumed in the error budget that this dimension can be held to within 5 micrometers. The chief problem is that of holding the components of the  $f/96$  relay in constant focal relationship to the  $f/12$  image plane, but the structural integrity of the system is such that a 5-micrometer tolerance should be achievable.

#### Relative Focus Sensor Threshold

Once the system is calibrated, the focus sensor is again limited by its resolution in returning the system to focus.

Table C.6-11 - Alignment Error Budget (Decenter and Tip)

	Wavefront Error, wavelengths rms
Initial alignment	
Sensor, 1 microradian at 6.6 meters	0.0036
Alignment maintenance	
Sensor, 1 microradian at 6.6 meters	0.0036
Thermal drift during observation, 10 micrometers (decenter)	0.0055
Tilt of secondary for 5-microradian (1-arc-second) line of sight correction (tip)	0.0016
Adjustment mechanism, 3.5 micrometers	<u>0.0019</u>
RSS error	0.0088

Table C.6-12 – Focus Maintenance Budget

	Wavefront Error, wavelengths rms
Calibration of relative focus sensor	0.009
Internal dimension knowledge, 5 micrometers	0.0018
Relative focus sensor threshold	0.009
Mechanism error, 0.47 micrometer	0.005
Thermal drift, 2 micrometers	<u>0.021</u>
RSS error	0.025

### Mechanism Error

Because of the magnifying effect of the secondary mirror, the system is 29 times more sensitive to focal motions of the secondary mirror as it is to focal motions of the instruments at the f/12 focal plane. The positional errors of the six secondary mirror actuators combine to an rss error of 0.47 micrometer, which corresponds to  $0.005\lambda$  rms error from this source.

### Thermal Drift

Since it is not desirable to operate the focus adjustment during an observation period more times than is necessary, a generous portion of the focus budget was allocated to thermal drift of the metering structure between the primary and secondary mirrors.

#### C.6.f(3) Field-Dependent Errors

The field-dependent errors resulting from tip of the secondary mirror and of the focal plane affect mainly the guide field, and although no overall optical error budget has been devised for the guide field, the probable magnitudes of these field-dependent errors are examined here. At the maximum field radius of 3.5 milliradians (12 arc-minutes), tip of the secondary attributed to a 1-microradian sensitivity limitation in the tip sensor results in a wavefront error of only  $0.00045\lambda$  rms. The expected tip adjustment error of the secondary mirror is 3 microradians, which yields a wavefront error at the edge of the field of only  $0.0014\lambda$  rms. Tip of the focal plane resulting in 30 micrometers defocus at the edge of the field would result in  $0.011\lambda$  of error, which is small compared to the  $0.1\lambda$  rms error assumed in the guide sensor sensitivity analysis. This corresponds to a focal plane tip of 0.24 milliradian or 0.8 arc-minute.



## C.7 ELECTRONIC SYSTEMS DESIGN

There are six basic electronic subsystems for the optical telescope assembly (OTA) (Fig. C.7-1): thermal control, pointing control, performance control, telescope protective, data management, and power distribution. The performance control system includes the alignment sensors, matrix translator, alignment actuators, figure sensor, and primary force actuators. The telescope protective system contains the sun shield, aperture doors, pressurized bulkhead door, and diagnostics.

All subsystems are powered and controlled through the system support module (SSM) interface. Wiring is simple and is minimized by interfacing through the electrical distribution units, command decoders, and data acquisition units (DAU's). The command decoders, data acquisition units, and electrical distribution units are considered to be SSM responsibility although they are integrated with the OTA electronic subsystems. As a consequence, the data management system for the OTA consists simply of a listing of command and data requirements and interfacing units. The SSM computer/data processor controls both the OTA and the scientific instrument package (SIP). Since there is no electronic interface with the scientific instruments, inhibit signals are made available to the SSM through the DAU's.

Numbers in the top right-hand corner of a block designate the quantity associated with a subsystem, including redundancy. The blocks with the top left-hand corners clipped indicate the assemblies to be designed and furnished by the SSM.

Most of the electronic subsystems are located in four packages within the SSM. Each is made accessible for maintenance or replacement. When sensors cannot be easily replaced, owing to remote location in the OTA, they are made redundant. Preamplifiers are included with the sensors to avoid low signal level paths. Wires requiring high currents are kept short to minimize electromagnetic interference, and high voltage power supplies are located close to the units that use them.

The peak power for each subsystem is listed in the OTA summary weight statement. The total average power per orbit is about 400 watts. The probable peak power is about 550 watts. A power profile for a typical orbit is shown in Fig. C.7-2.

### C.7.a Thermal Control System

A thermal controller consists of a thermistor sensor connected in bridge in a heater loop. When a sensor is below a required temperature, it unbalances the bridge, calling for more heat. The sensor and heater are mounted close together on the equipment to be thermally controlled.

There are throughout the OTA 38 such sensors and heaters capable of supplying heat energy either in 10- or 20-watt blocks. A diagram of the overall power controls for the 38 units is shown in Fig. C.7-3. The power conditioner supplies the required voltages to operate the analog and digital circuits in all thermal controllers, but the power to the heater is supplied unregulated. Each thermal controller is provided with a command-operated gate that controls each heater circuit individually.

A typical thermal controller is diagrammed in Fig. C.7-4. It consists of a Wheatstone bridge, temperature adjustment control, amplifier, switching circuit, heater element, and monitoring.

The thermistor sensor is connected to the bridge with a Siemens three-wire connection to permit operation with long lead lengths (Fig. C.7-5). As shown in the equivalent circuit, power is carried to the sensor by wire  $r_1$ . Wires  $r_2$  and  $r_3$  are effectively in series with different bridge arms. Thus, changes in lead wire resistance due to temperature drifts tend to cancel one another if the wires are of equal length and kept together.

The temperature control is varied by changing the resistance of one of the arms of the bridge. This is provided by the temperature adjust logic driver which switches in shunt resistors. It consists of solid state switches controlled by commands from the decoder. The temperature adjustments will be small so that the bridge essentially will be an equal arm bridge.

The thermal controller will be operated as an off/on control. The power transistor switch operates most efficiently in two modes: deep saturation and cutoff. The rate limiter/driver contains logic to sense bridge imbalance and drivers to switch the power transistors in the two modes. In addition, it limits the rate at which the power transistor is turned on or off to reduce transients which cause electromagnetic interference. The driver will provide adjustments to control a specific temperature to within a  $\pm 0.5^\circ\text{C}$  differential.

In series with each power switch, there will be a heating element and a thermal cutout. The heating element will be installed in a flexible silicone rubber mat cemented to the equipment. It will have a power density to be determined. The thermal cutout is a safety device that disconnects the heater in the event of a runaway controller.

The on-time counter is a solid state device that monitors the time duration that the heater is energized. It provides a measurement of the amount of heat energy delivered. The information is stored in digital form and periodically clocked down the data bus.

Each controller has a signal conditioner to process a temperature monitor and other diagnostic data.

#### C.7.b Pointing Control System

The pointing control system (Fig. C.7-6) consists of theta servos, guide star sensors, a signal processor/loop amplifier, and a tracking servo. There are three sets of subsystems, any two of which may be used to point the LST. Only the theta servo subsystem is discussed in this section. The remaining subsystems are covered in other portions of the report.

Three guide star sensors are arranged to operate within a tracking field (Fig. C.7-7a), each serving a third of the ring and each requiring two servos to move it to a designated position. A guide star position such as G is defined in polar coordinates with respect to a target and a telescope reference. The sensor, however, is limited to motion in a circle of constant radius so that a pair of planetary rotating fold mirrors is required for radial positioning. To place a sensor at position G, one servo rotated to angle  $\theta_{1A}$  and a second servo rotates to angle  $\theta_{1B}$  (Fig. C.7-7b).

The servos are high accuracy types, using high resolution optical encoders to control position. A typical theta servo is diagrammed in Fig. C.7-8. A digital theta angle is stored in the shift register to provide a reference. The servo drives the sensor and encoder until a null is produced.

#### C.7.c Performance Control System

This group of electrical subsystems is responsible for the optical alignment of the OTA, wavefront measurements, and wavefront corrections.

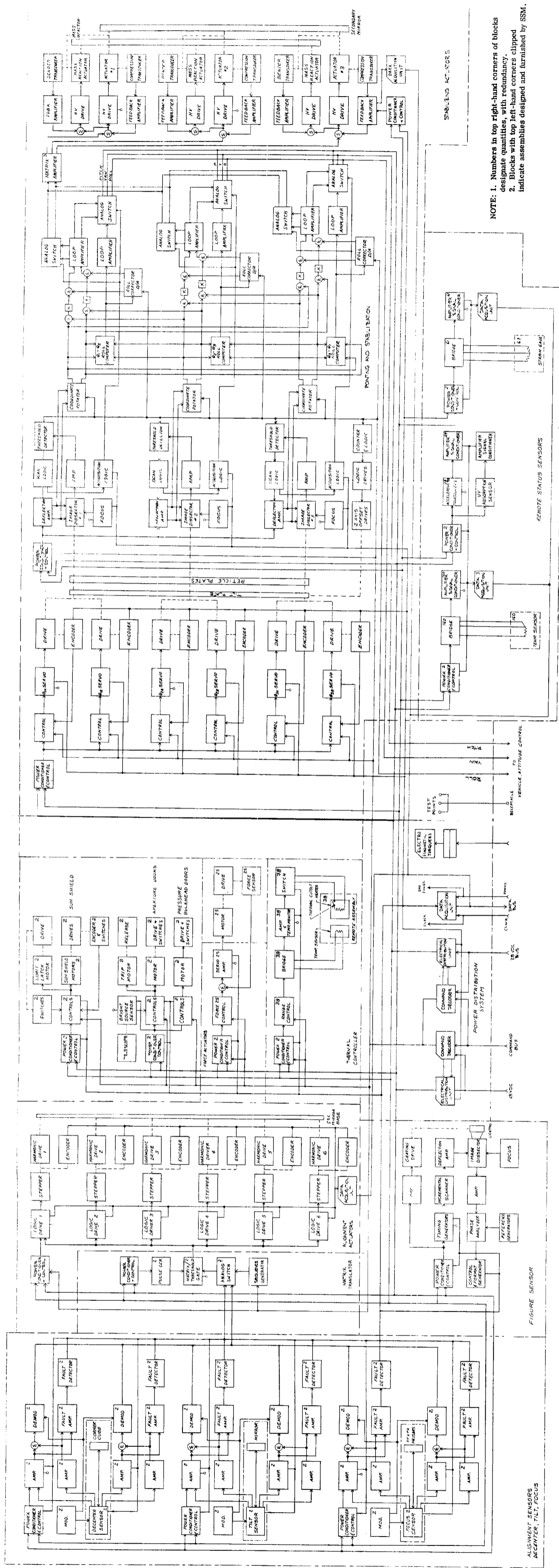
The optical alignment group consists of decenter, tilt, and focus sensors, a matrix translator, and alignment actuators. It is essentially an open loop system in which a sequencer operates a sensor to measure alignment error, inserts the error into a matrix, translates the error to actuator positions, and then moves the actuators. This is reiterated until the error is negligible. The procedure is repeated with each sensor sequentially until the optics are aligned.

Only the matrix translator and alignment actuators are discussed in this section. The decenter, tilt, and focus sensors and electronics are covered in Section C.6.

A figure sensor provides an interferogram of the optical system wavefront that is down-linked to be analyzed. Wavefront error is computed and those corrections attributable to the primary mirror are up-linked and put into the primary mirror force actuator subsystem. Only the force actuator subsystem is discussed in this section. The figure sensor is covered in Section C.6.

##### C.7.c(1) Matrix Translator Electronics

This subsystem consists of a linear circuit matrix, sequencer, analog switches, threshold gate, and pulse generator, as shown in Fig. C.7-9.



NOTE: 1. Numbers in top right-hand corners of blocks designate quantities, with redundancy.  
 2. Blocks with top left-hand corners clipped indicate assemblies designed and furnished by SSM.

Fig. C.7-1 — LSI/OTA block diagram (drg. no. 185506)

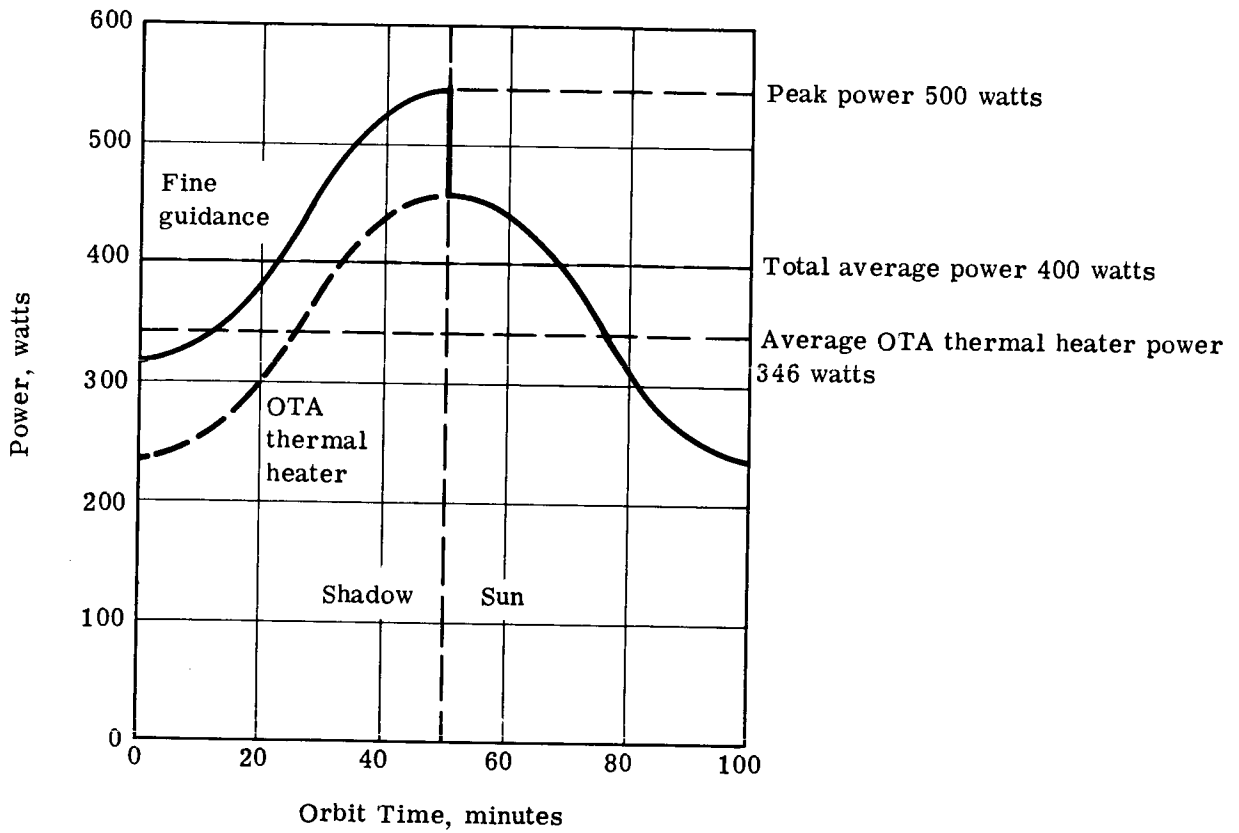


Fig. C.7-2 — Maximum sustained power expected versus orbit time

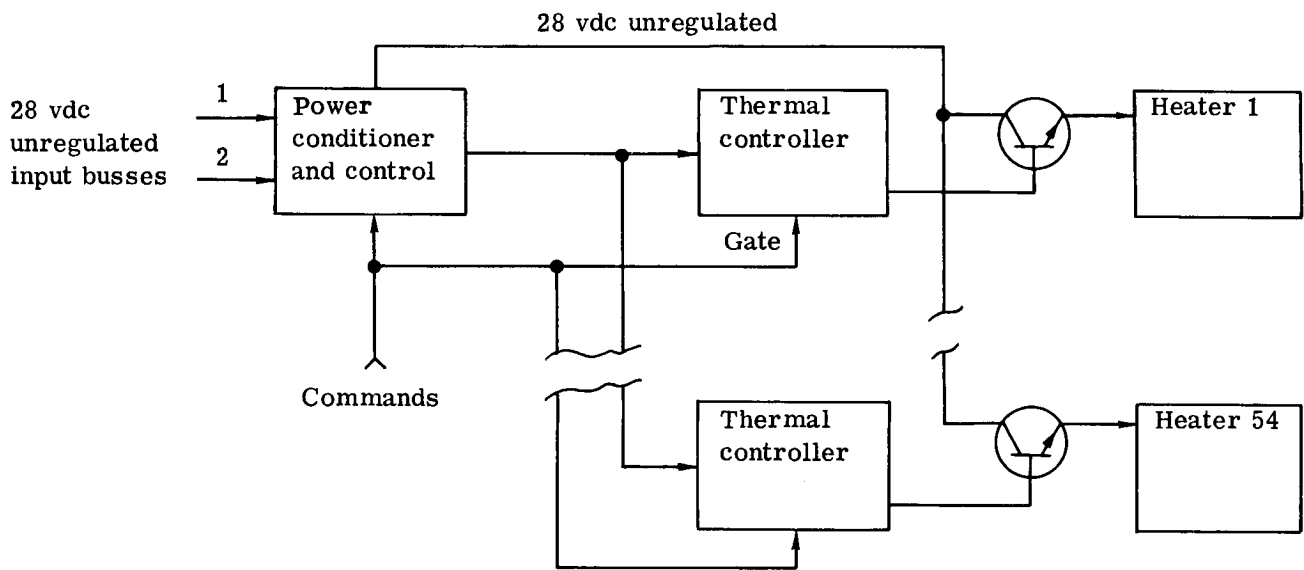


Fig. C.7-3 — Thermal control system—overall power control

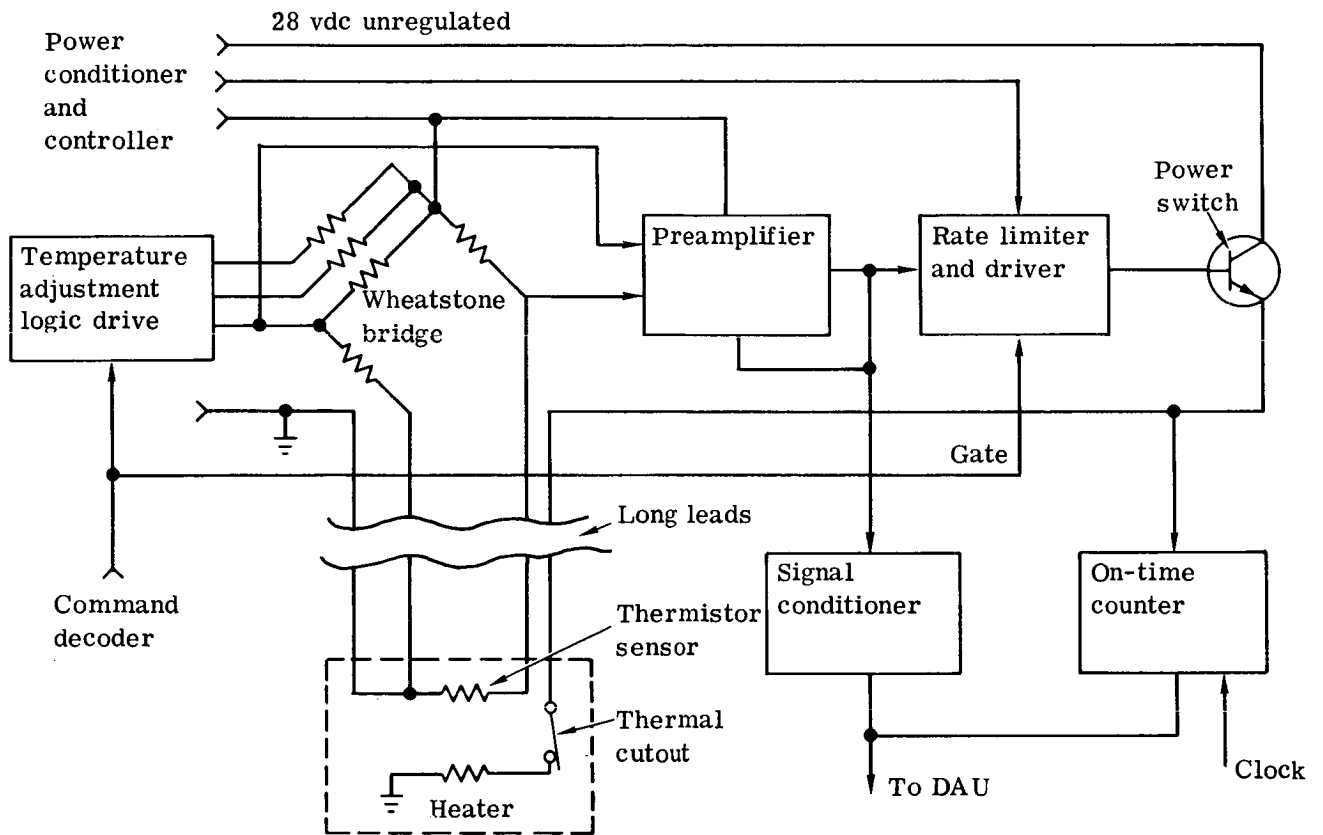


Fig. C.7-4 — Typical thermal controller

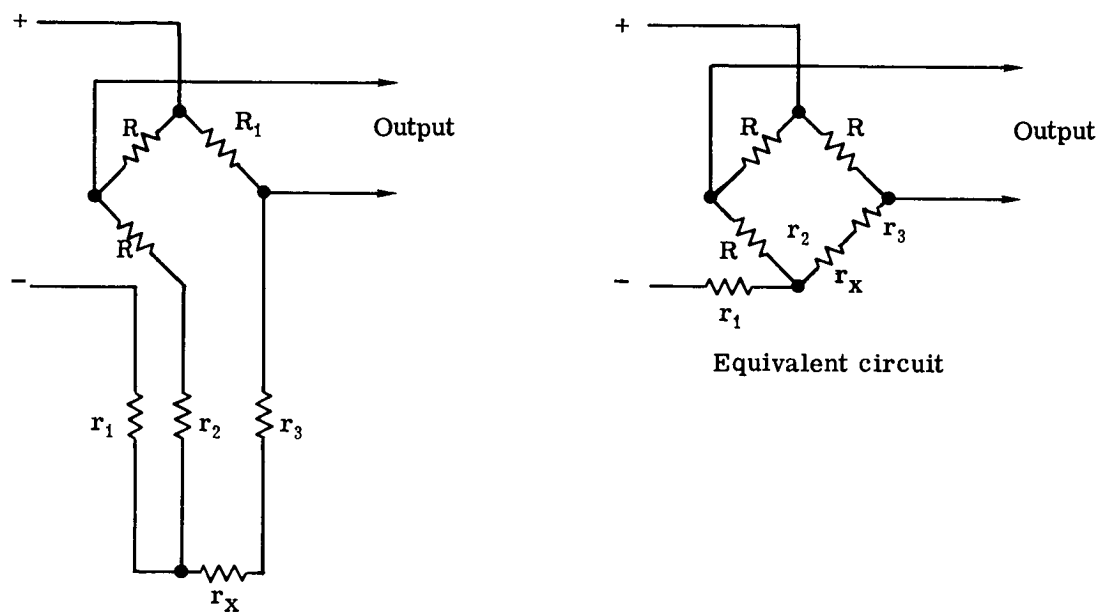


Fig. C.7-5 — Siemens three-wire connection

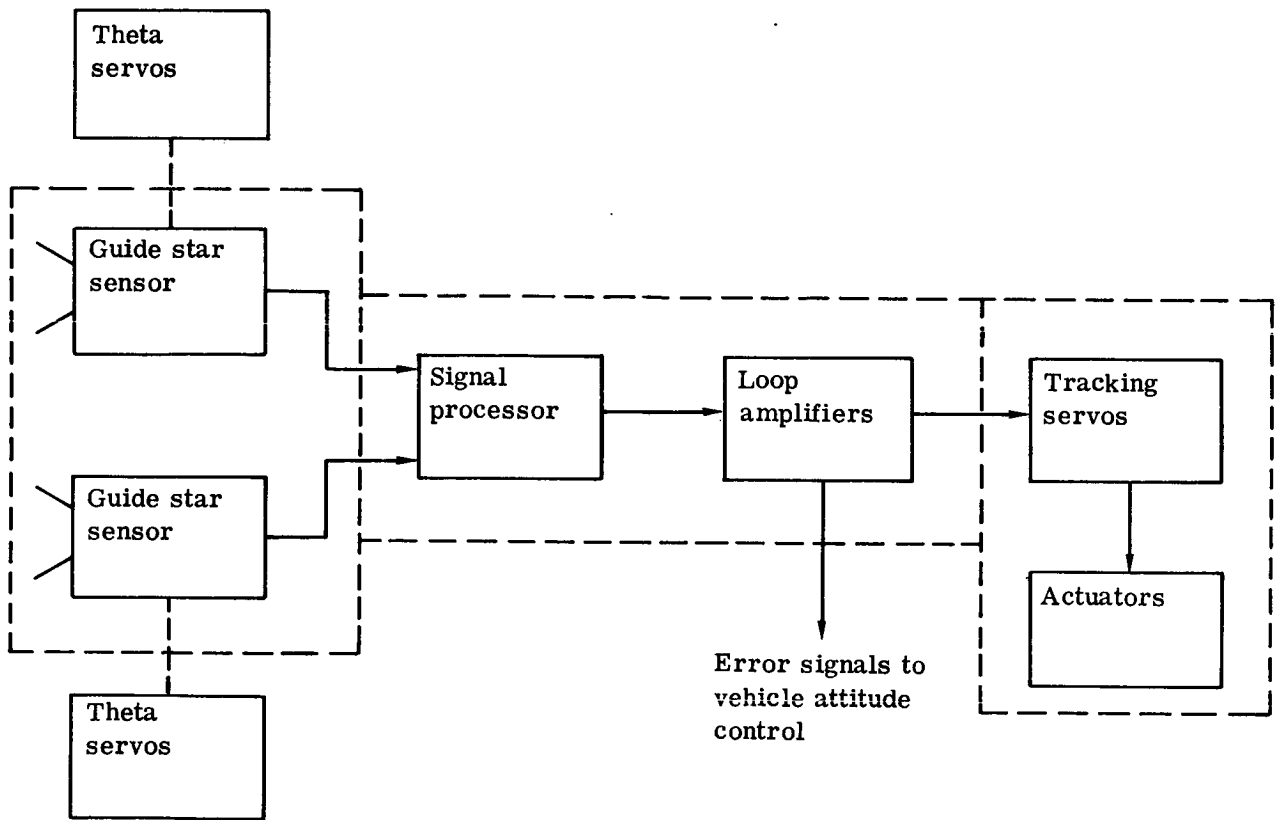
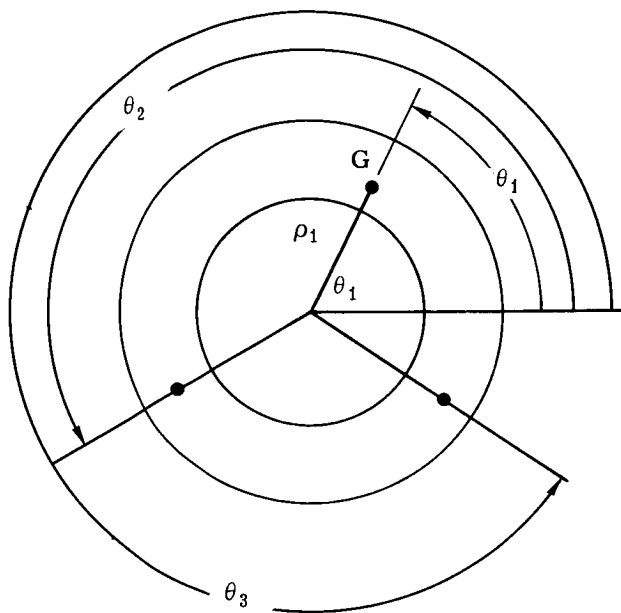
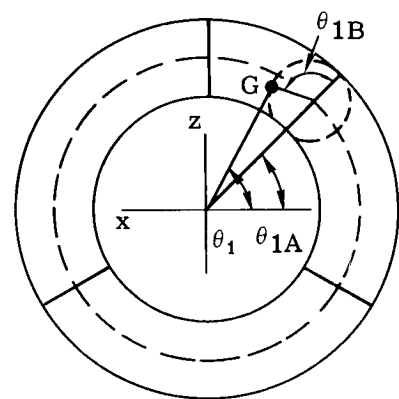


Fig. C.7-6 — Pointing control system





(a)



(b)

Fig. C.7-7 — Guide star coordinates

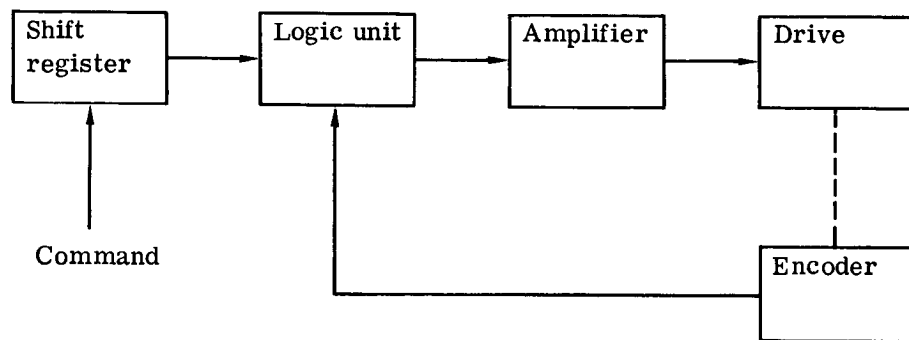


Fig. C.7-8 — Typical theta servo

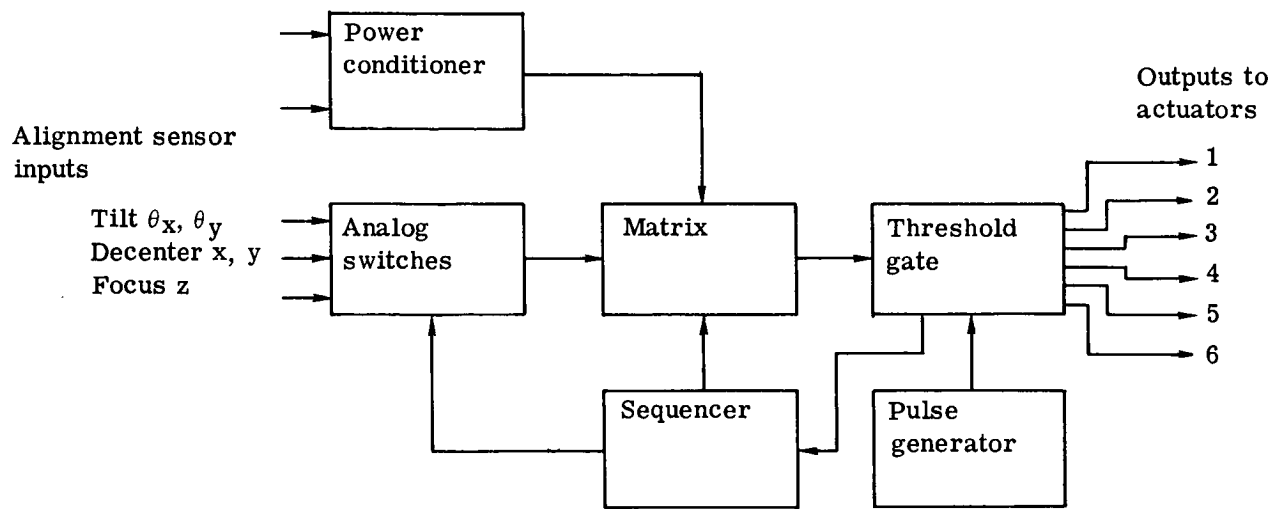


Fig. C.7-9 — Alignment matrix electronics

Analog alignment inputs (tilt, decenter, and focus) are switched sequentially into the matrix electronics that translate alignment signals into appropriate actuator signals. The matrix threshold gate converts actuator signals from a sensor into a number of pulses that are fed to the logic drivers of each alignment actuator. When the alignment error is minimized, the sequencer switches to the next set alignment sensor until the optics are fully aligned.

The matrix circuits consist of summing amplifiers and inverters arranged to translate misalignments into actuator input as shown in Fig. C.7-10. Scale factors are adjustable at the summing junctions. The matrix circuit is determined by the configurations of the alignment actuators, shown in Fig. C.7-11. Since actuators are shown point up, their movement is taken with respect to the reference at the center. Table C.7-1 shows the relative direction of the actuators for a positive misalignment direction for five degrees of freedom. Should an actuator fail, it is removed from the matrix and proper scale factor adjustments are made for the remaining actuators. The translator may be either analog or digital. This can be decided when detail design is considered.

#### C.7.c(2) Alignment Actuator Electronics

Each actuator is driven by a logic driver/stepper motor and harmonic drive, as shown in Fig. C.7-12. The power conditioner and control is a dual unit supplying power to each actuator. It also controls them individually so that malfunctioning units can be disabled.

The logic driver accepts clockwise and counterclockwise input pulses generated by the matrix electronics and translates them to outputs controlling the stepper motor. It operates in the switching mode to minimize internal power dissipation. Pulse rates can vary from 500 to 1,000 pulses per second. The stepper motor is a two-phase variable reluctance type requiring least power for rated operation.

The alignment actuator electronics will be mounted close to the actuators on the secondary mirror to avoid long leads carrying high current pulses. Five-microsecond signal pulses from the matrix electronics unit in the electronics package will feed the logic drivers.

#### C.7.c(3) Primary Mirror Force Actuators

Twenty-five servo drives operate double acting actuators that apply either tension or compression forces to 25 different points on the primary mirror. The servos are energized only when a force is to be applied. Once applied, the force will remain until it is changed.

The force actuator system consists of a servo amplifier, motor drive, feedback potentiometer, digital to analog (D/A) converter, shift register buffer, and a power conditioner (Fig. C.7-13).

The power conditioner is a dual unit that provides power to each individual actuator. The servo is a simple position type. It operates a low power motor that moves the actuator slowly until the force-sensing feedback potentiometer provides a voltage to null the input signal.

The analog input is provided by a shift register buffer and a D/A converter. The shift register is a serial-parallel buffer that stores a single 8-bit digital signal from the command decoder. The D/A converter is a bipolar parallel type that supplies a bipolar direct current signal to the servo.

#### C.7.d Telescope Protective System

##### C.7.d(1) Sun Shield Control

The sun shield will be extended and retracted with three linear actuators: one master driving two slaves using an off/on servo loop. When fully extended, a latching device will operate to hold the shield rigidly in place. It will require 50 watts for 10 minutes to either extend or retract the shield fully.

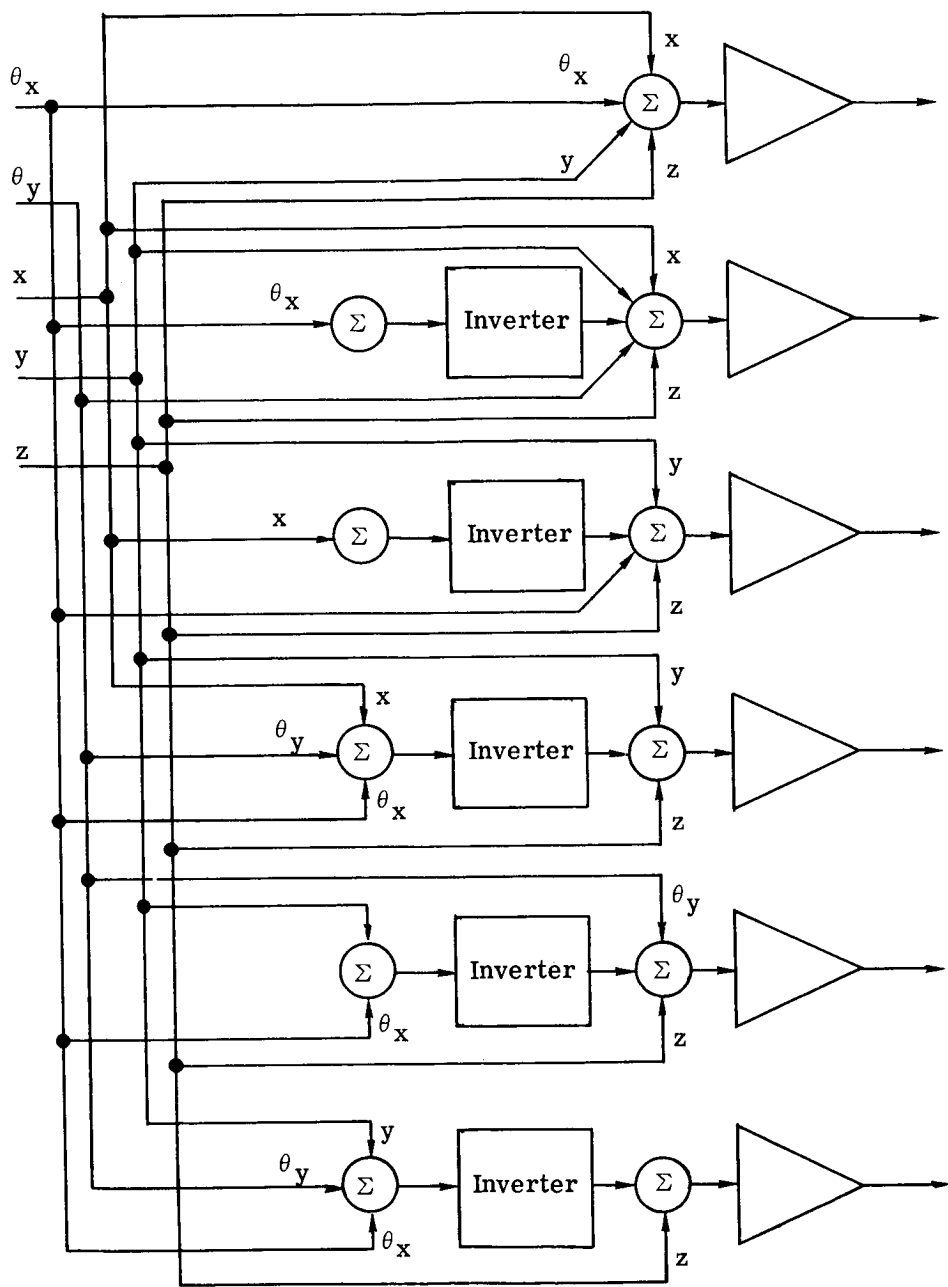


Fig. C.7-10 — Matrix electronics

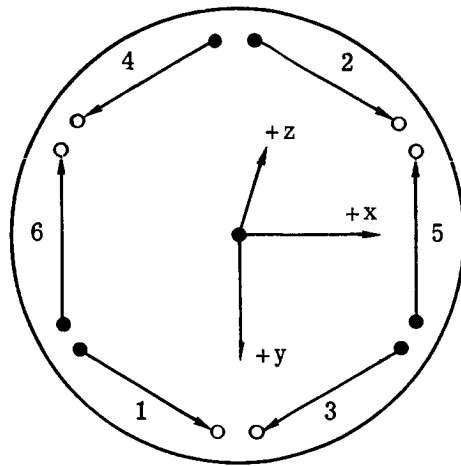


Fig. C.7-11 — Secondary alignment actuators

Table C.7-1 – Relative Direction of Actuators for Positive Misalignment Direction,  
Five Degrees of Freedom

	Alignment Motions					
	1	2	3	4	5	6
$+\theta_x$	+	-	+	-	-	-
$+\theta_y$		+		-	+	-
+X	+	+	-	-		
+Y	+	+	+	+	-	-
+Z	+	+	+	+	+	+

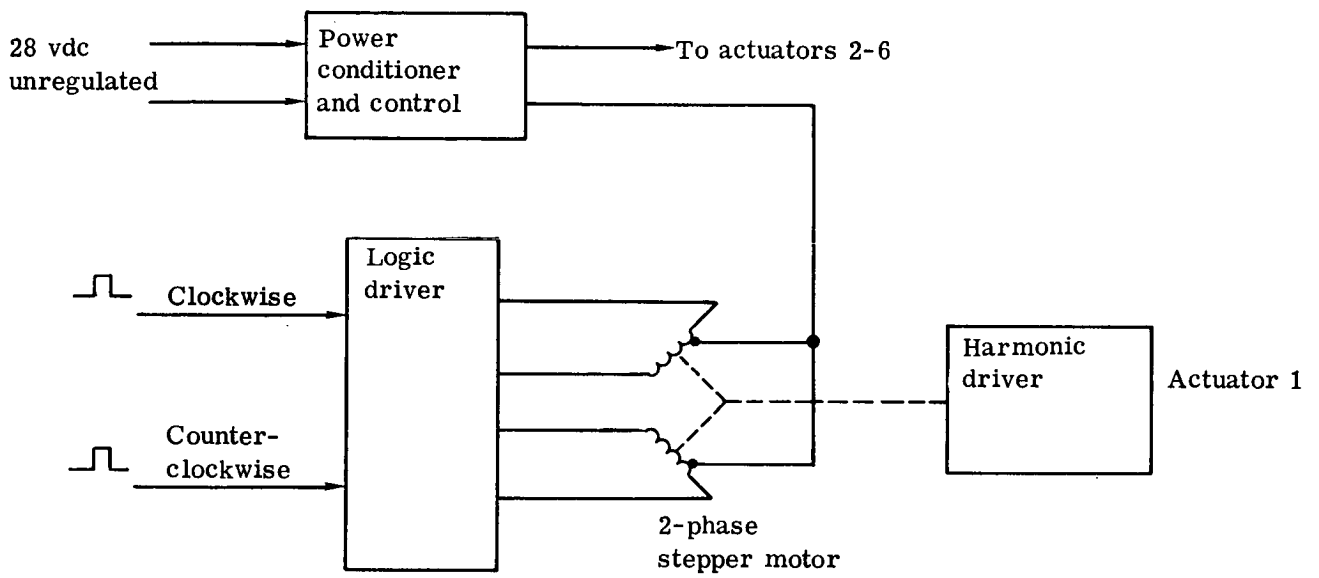


Fig. C.7-12 — Alignment actuator electronics



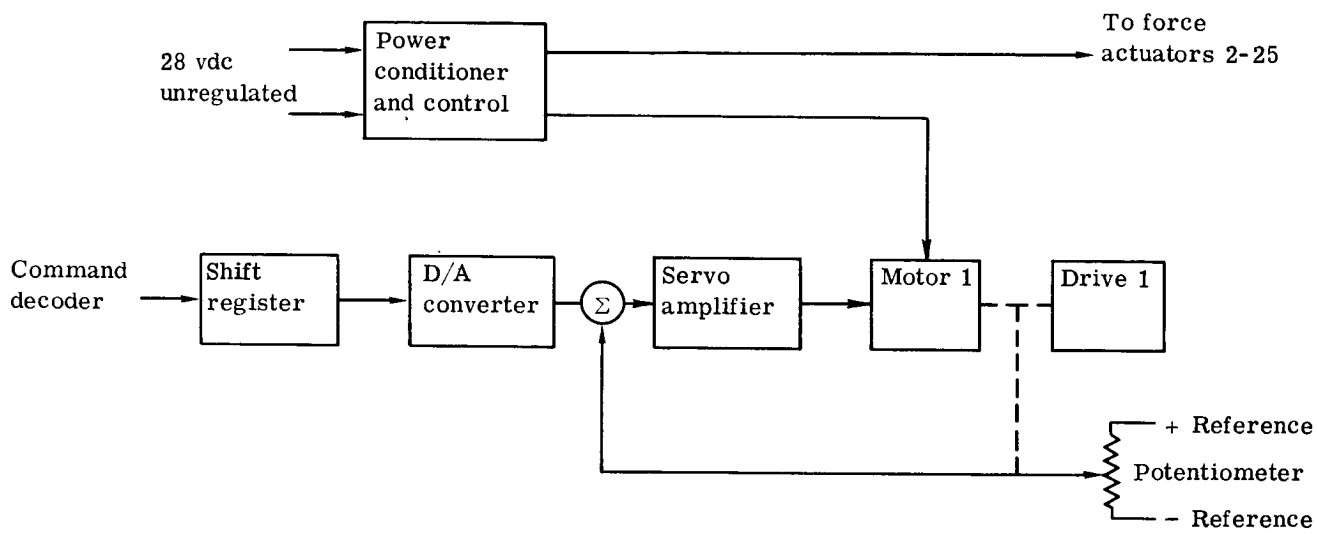


Fig. C.7-13 — Typical force actuator—servo subsystem

The sun shield control circuit for a single actuator is shown in Fig. C.7-14. Dual winding motors operating on 28 vdc unregulated are used to provide bidirectional movements. The power conditioner supplies the required voltages for the analog and digital circuits in the signal conditioner and the logic driver. A command to the logic driver switches power on to extend the shield. When fully extended, the limit switch operates the latch motor until the latch limit functions. A command to retract reverses the procedure by first unlatching and then operating the retract motor. Inhibit circuits in the logic driver will ensure that only one switch operates at a time. Monitors to the DAU are processed by the signal conditioner. They include the four limit switch positions, extend and retract signals, as well as the power conditioner and logic driver monitors. An encoder on the driver mechanism provides data on the shield motion and position and a means for sharing the other two actuators with an off/on servo.

#### C.7.d(2) Aperture Door Control

The aperture doors are required to protect the optics and instruments from contamination and high illumination levels. They will normally be operated to open and close with a two-winding motor. A bright source sensor and quick release mechanism will close the doors rapidly.

The aperture door control diagram is shown in Fig. C.7-15. An appropriate command to the logic driver will open or close the aperture doors at a to be determined time. If, at any time while the doors are partially or fully open, the bright source sensor is exposed to a high level of radiation, the quick release mechanism will activate until the trip functions to close the doors. When the radiation level drops, the quick release will reset itself and the aperture doors may be reopened. This system will be on standby for the entire mission, necessitating a complete redundant set of controls. The remaining features of the controls are similar to those on the sun shield controls.

#### C.7.d(3) Pressure Bulkhead Door Controls

The pressure bulkhead door controls (Fig. C.7-16) are similar to but simpler than the aperture door controls. To increase reliability, this system will also have a complete redundant set of controls.

#### C.7.d(4) Diagnostics

This portion of the protective system is concerned with sensors that provide data on the health and status of the OTA, according to the following basic categories: structural monitors – vibration and strain; thermal monitors – temperature; optical monitors – ultraviolet absorption; and electronic monitors – functional and status. The last category deals with the functioning and the positional status of the electronics. These monitors are integral with the electronic assemblies and are mentioned in the discussion of each electronic subsystem.

##### Thermal Monitors

At least 160 temperature sensors will be distributed throughout the OTA structure and optics and electronic assemblies. The electronics will be located in the OTA electronics package and all sensor circuits will fan out from there.

To avoid catastrophic failure of all 160 temperature sensors, they are divided among eight blocks of 20 sensors each, as shown in Fig. C.7-17. The blocks can be operated individually or simultaneously. Should a block fail such that the power conditioner is threatened, the block is automatically disconnected by a switch.

The temperature sensor consists simply of a bridge, preamplifier, and signal conditioner, as shown in Fig. C.7-18. The Siemens three-wire connection is used with the thermistor sensor to secure accurate temperatures though using long lead lengths.

Analog signals from the signal conditioner are connected to the DAU to provide temperature data.

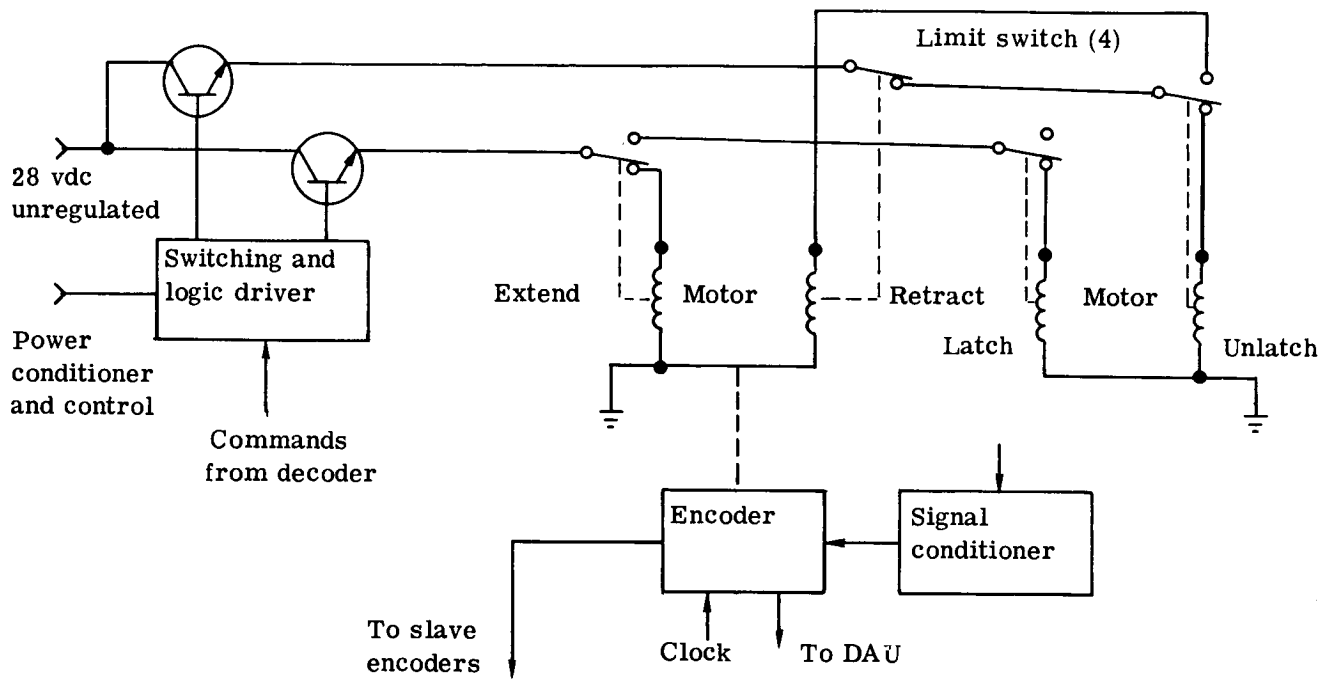


Fig. C.7-14 — Sun shield master control

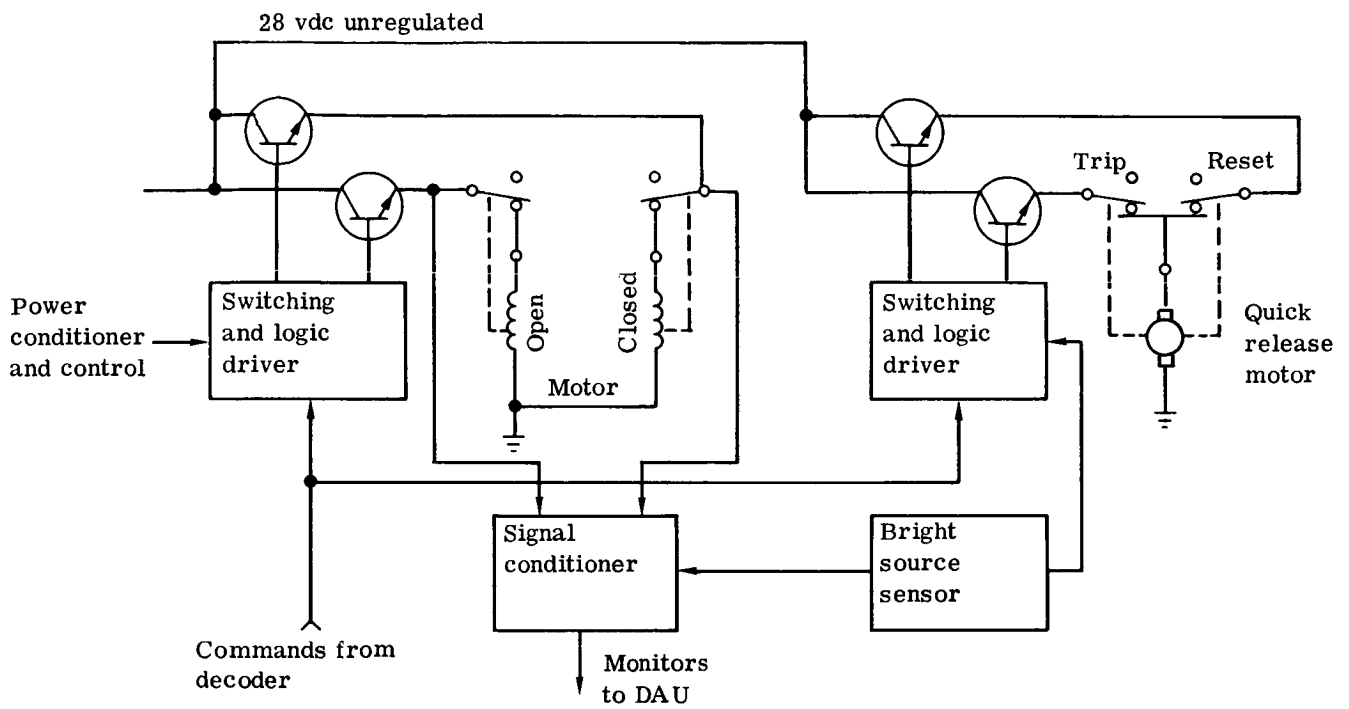


Fig. C.7-15 — Aperture door control

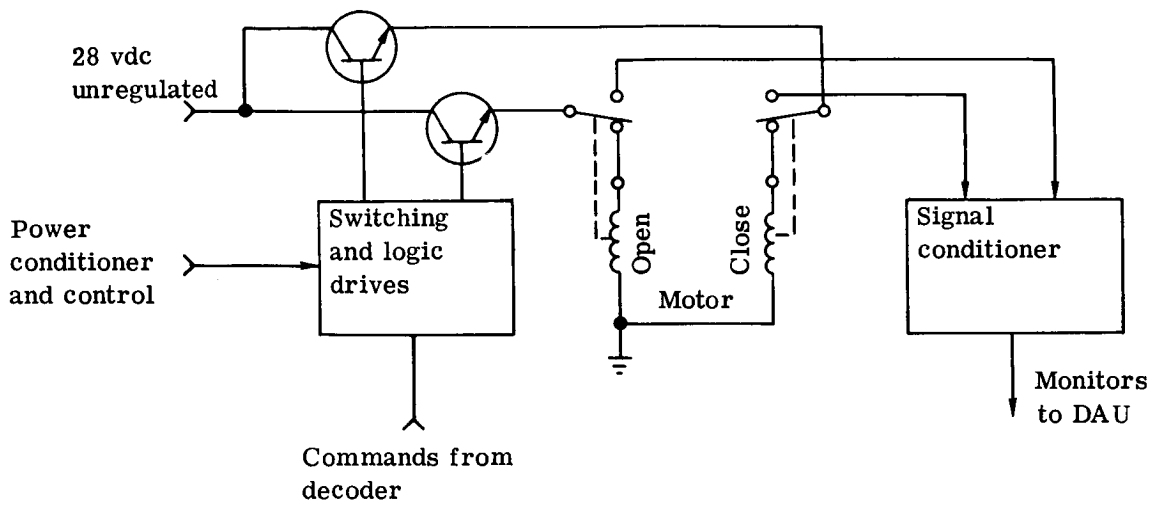


Fig. C.7-16 — Pressure bulkhead door controls

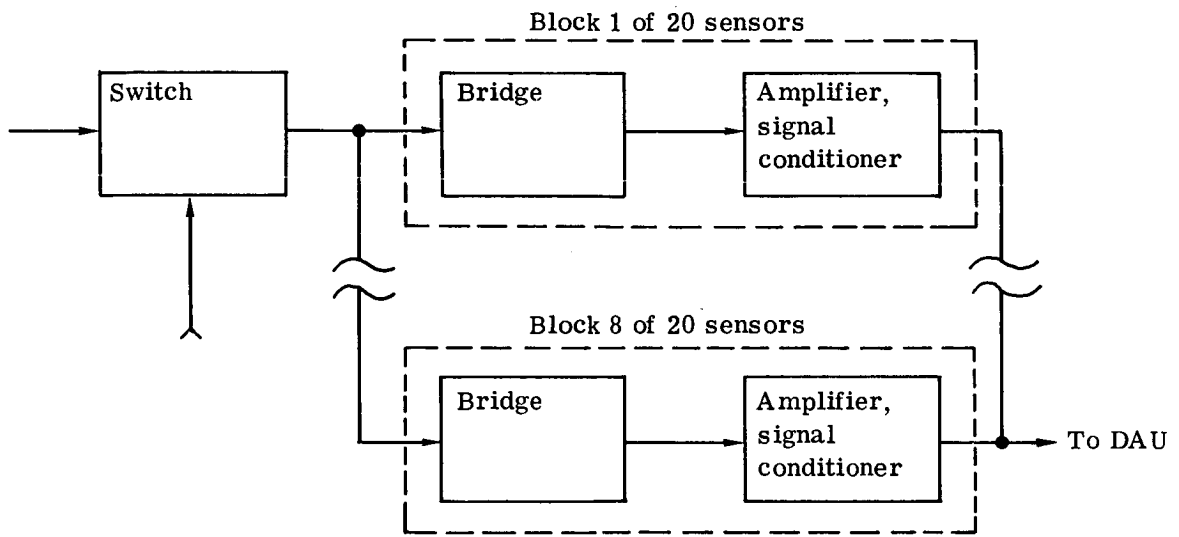


Fig. C.7-17 — Temperature sensor controls

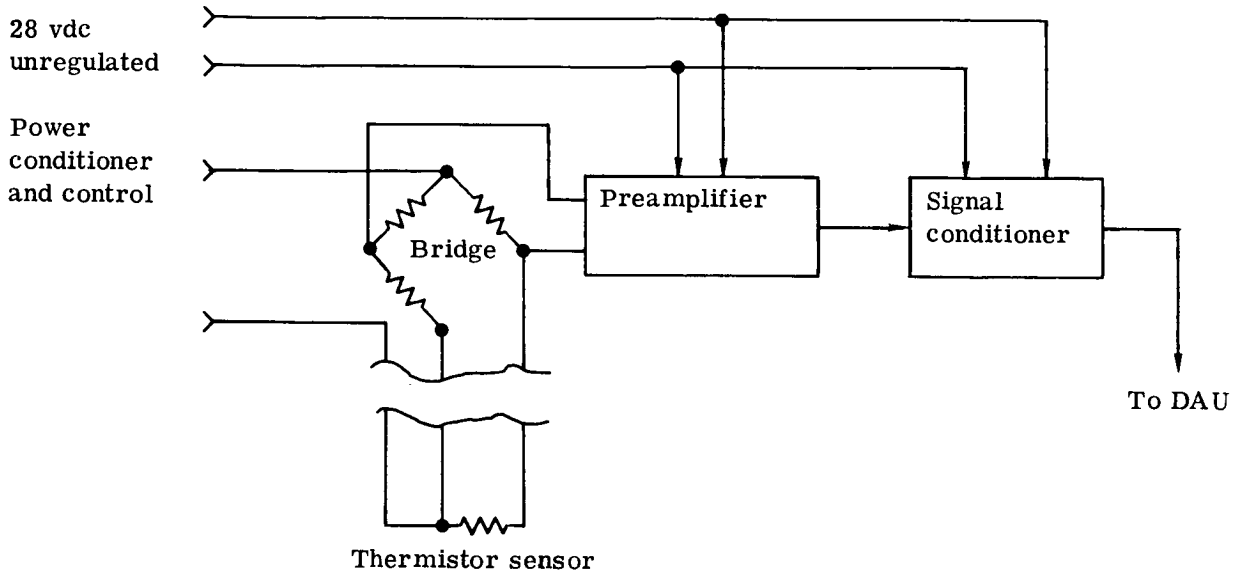


Fig. C.7-18 — Typical temperature sensor

## Structural Monitors

Strain monitors will be installed in the following locations:

Primary mirror flexures	6
Secondary mirror flexures	6
Primary mirror	4
Secondary mirror	4
Metering truss	12
SIP	12
Pressure bulkhead ring	9
Spider structure	8
	<hr/>
	61

They will be connected in six blocks of 10 sensors each, so that a catastrophic failure will not cause a loss of all sensors. They will have a minimum threshold sensitivity of 10 micrometers per micrometer (4 microinches per inch).

A typical strain sensor circuit (Fig. C.7-19) consists of a resistance bridge, preamplifier, and a signal conditioner. The resistance bridge is split, with the reference half in the electronics assembly and the sensor half remotely located throughout the structure. The sensor half-bridge also uses a three-wire Siemens connection, which provides accurate strain measurements while permitting the use of long leads. Only one element of the sensor half-bridge is attached to the structure. The other element, which is physically close, provides temperature compensation.

The signal conditioner that is located within the electronics assembly provides analog strain input to the DAU.

Vibration monitors will be installed in the following locations:

Primary mirror	3
Secondary mirror	3
Pressure bulkhead ring	3
Spider structure	3
SIP structure	12
	<hr/>
	24

As shown in Fig. C.7-20, two types of accelerometers will be used. A high level transducer operating between 0.5 and 20 g provides information on structural loading such as may occur during the launch phase. A seismic transducer monitoring low levels of vibration provides information on telescope stability during the data gathering phase. These transducers will be individually controlled. They will be used sparingly except at the beginning of the mission.

### Optical Monitor

This monitoring device consists of an ultraviolet radiation source and sensor located close to the primary mirror. It will be operated periodically to check the effect of contamination on the ultraviolet performance of the optical system.

### C.7.e Data Management System

This system (considered as part of the SSM equipment) consists of command decoders and DAU's. They will be integrated with the OTA electronic subsystems. They are indicated on figures by clipped-corner rectangles to distinguish them from the OTA subsystems that are Itek's responsibility. Power and control to each unit will be directly from the SSM. It is Itek's responsibility only to interface with them properly and to specify the channel requirements.



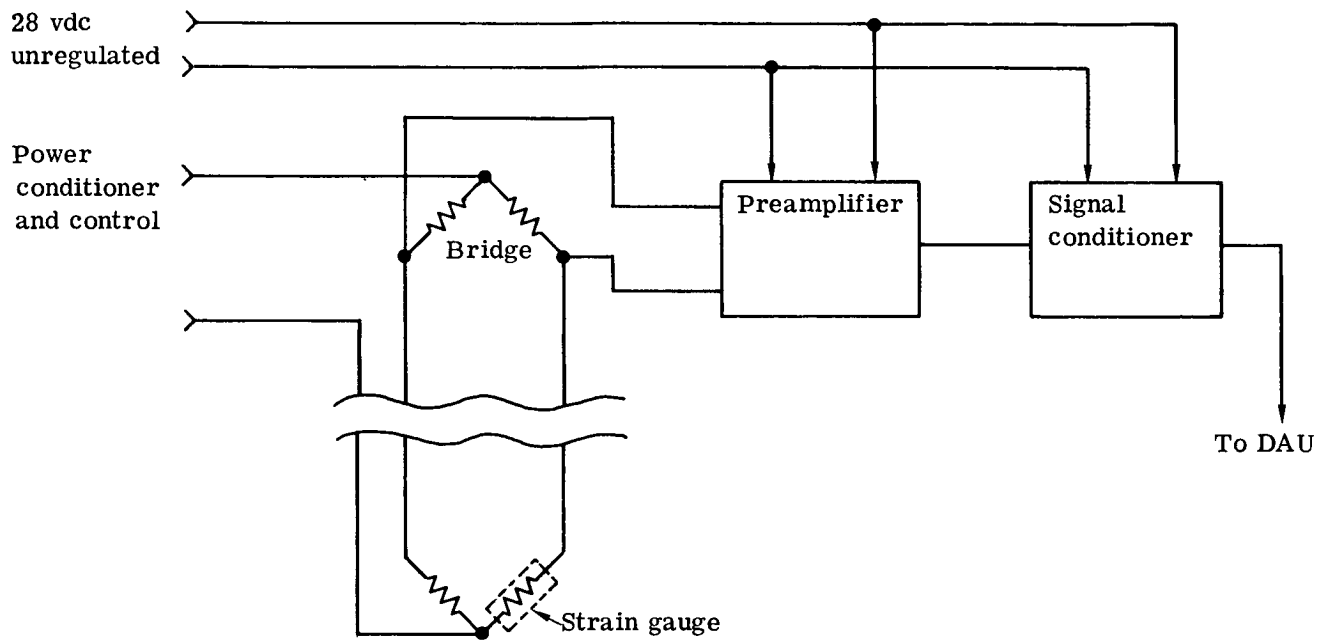


Fig. C.7-19 — Typical strain sensor

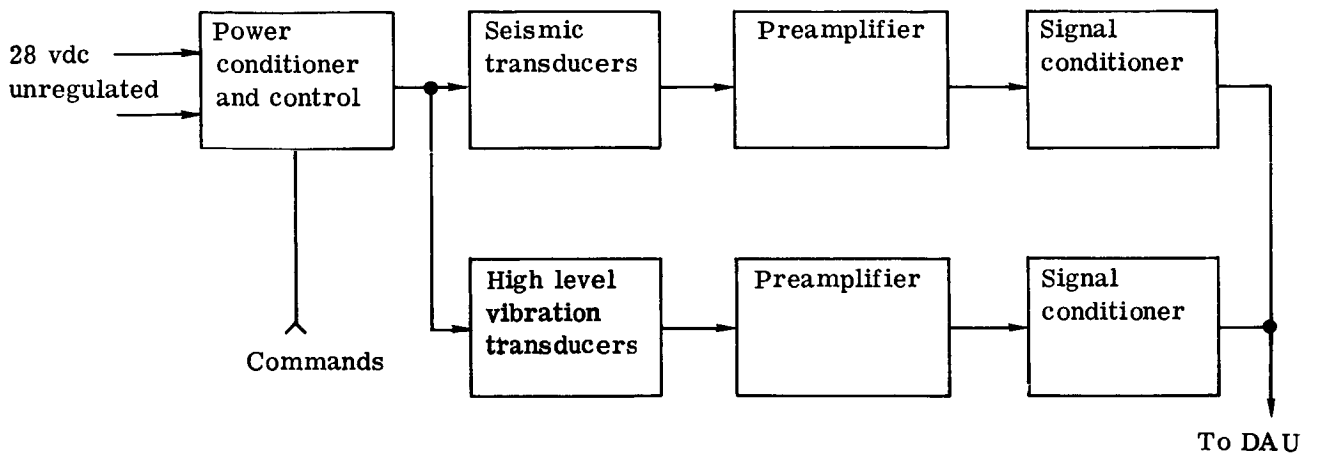


Fig. C.7-20 — Vibration sensor controls

#### C.7.f Power Distribution System

Power is distributed and controlled through an EDU and PCCU's, as shown in Fig. C.7-22.

The EDU provides power switching, circuit protection, electromagnetic interference isolation, and voltage and current monitoring, and the output is under direct control of a command decoder.

The PCCU provides the necessary regulated voltages to operate the electronic subsystems. It also provides short circuit protection, current limiting, electromagnetic interference isolation, voltage monitoring, and control switching for individual OTA subsystem loads.

There are two EDU's, each with their own input and output busses to provide redundancy. Either unit is capable of distributing power to all power conditioners and each unit has its individual command decoder.

The EDU provides electromagnetic interference isolation on the input bus to protect the OTA from interference by the SSM. Protection on the output busses not only prevents interference from the OTA subsystems but also prevents interference between OTA subsystems.

Individual output circuits may be controlled by solid state power switches if the load is below 500 milliamperes. Latching relays are used for higher power loads. Logic and drivers are provided for all output switching under the command decoder control. Current sensors and threshold detectors provided for each circuit protect the busses and other circuits. Input switching and isolation are under the control of the SSM main distribution. Voltage, current, and status signals are furnished for telemetry through interfaces with DAU's. Circuit reset can be arranged to be automatic or by remote command.

Power conditioners and controls are dual devices, with only one operating at any time. One-half of a typical unit is shown in Fig. C.7-24. It consists of power supply modules, circuit switching units, and signal conditioners. The power supply modules provide the necessary regulated voltages to operate each electronic subsystem. They are regulated and filtered and have overvoltage protection and current limiting. The circuit switching units will be similar to the solid state controllers in the EDU but of lower capacity. They will be controlled either by the command decoder or a sequencing unit. Analog monitors will be processed by signal conditioners to provide diagnostic data to the DAU.

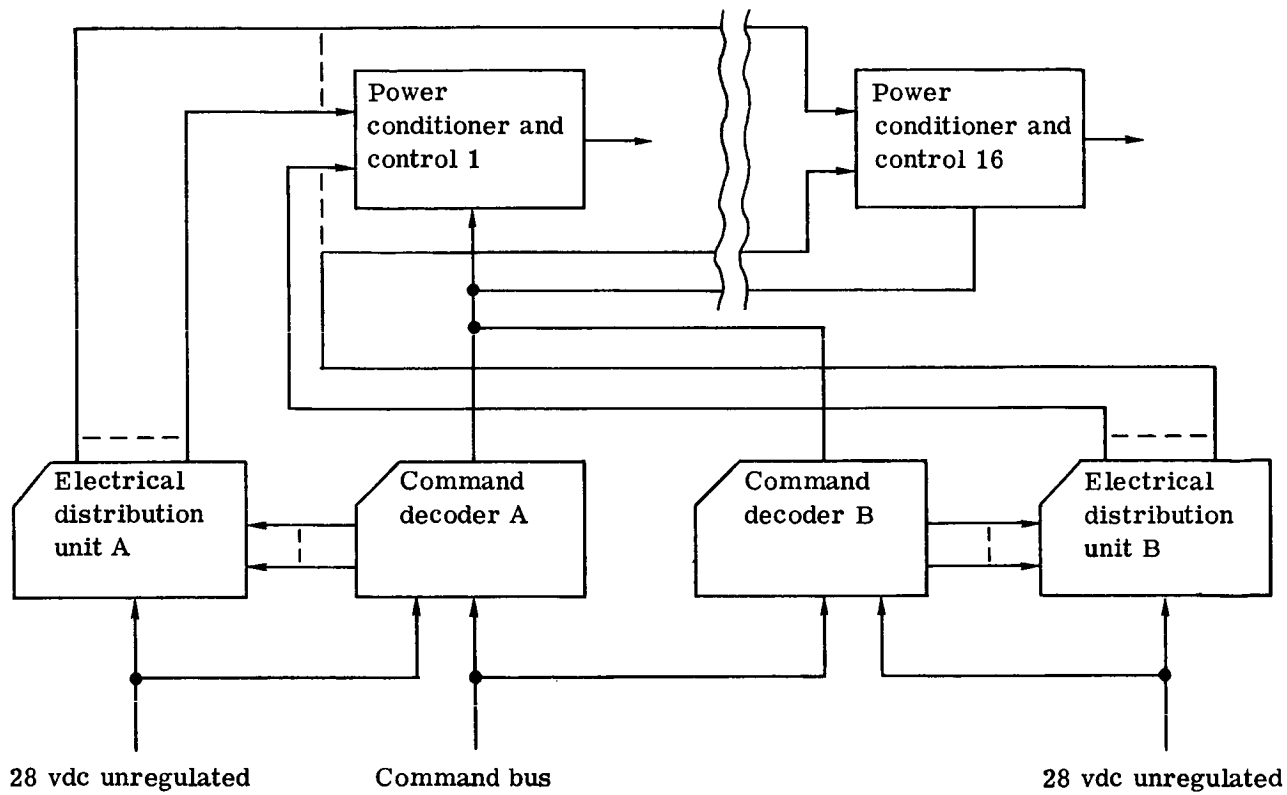


Fig. C.7-21 — Power distribution system

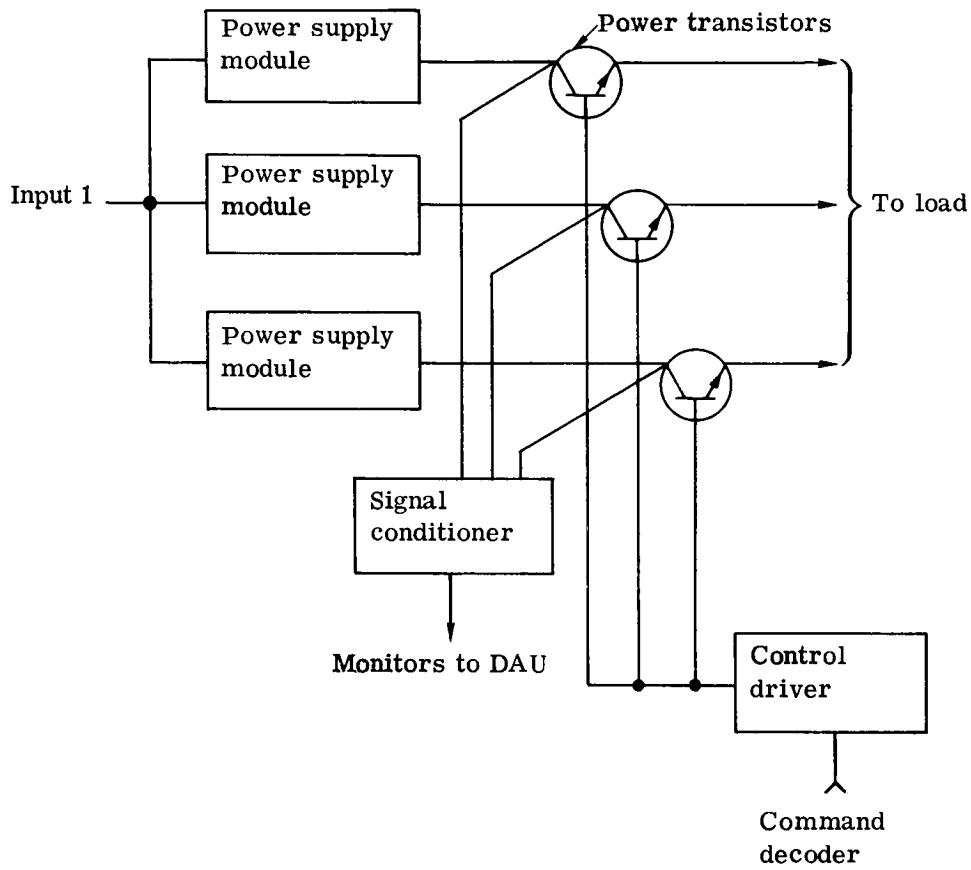


Fig. C.7-22 — Typical power conditioner and control unit

## C.8 SCIENTIFIC INSTRUMENT DESIGN

Work on scientific instruments was performed by both Itek and Kollsman Instruments Corporation under interrelated contracts from both Marshall and Goddard Centers. The principal work was on the scientific instrument package (SIP) design. The work described in this report was accomplished by Kollsman under subcontract to Itek, in support of MSFC tasks. The following review of focal plane arrangements will serve to place in order the historical events that led to the current baseline SIP concept. This area of design is under intensive review from the astronomical scientific community and by Itek and Kollsman, and we fully expect this to result in different and possibly simplified concepts that will be generated on later contract phases of the LST definition task.

### C.8.a Focal Plane Arrangements

The layout of the focal plane has undergone continuous analysis and change to provide maximum scientific output and flexibility in the most reliable manner possible. It must contain both astronomical instruments (field cameras, spectrographs, photometers, and polarimeters) and housekeeping devices (guiders, focus and wavefront error sensors). The alignment sensors for tilt and decenter of the secondary mirror are mounted on the primary, and are not considered here.

The phase A study started with the focal plane layout drawing (Fig. C.8-1) shown in NASA GSFC X-670-70-480. This drawing shows the focal plane arrangement in conceptual form. The design has good flexibility since it can accommodate many scientific instruments. It also has the feature of all instruments being used on the optical axis, so they all receive the best possible image from the telescope. The most serious drawback is in the fold mirror. This must rotate and slide depending on which instrument is used. If the mirror freezes, then at most only one instrument can be used. Another serious problem is the long optical and mechanical paths between the guide system and the f/96 camera; these two should be well coupled to prevent image motion.

This focal plane layout shown in Figs. C.8-2 and C.8-3 has evolved after several interim designs. The rotating-sliding fold mirror of the initial design has been replaced by several stationary mirrors; the data star is imaged on the desired scientific instrument by offset pointing. Each optical path has been tailored to the requirements of its instrument. For highest resolution, the on-axis f/12 field is relayed through an all-reflecting 8x magnifier to give an f/96 image of 174-microradian (0.6 arc-minute) diameter. This magnification is necessary to ensure that the electronic image tube does not degrade resolution. The f/12 field camera is provided when a large field of 1.39 milliradians (4.8 arc-minutes) is more important than resolution. Though it is centered 1.60 milliradians (5.5 arc-minutes) from the optical axis, the telescope image at f/12 is still better than the image tube capabilities.

There are several instruments which are relatively small and which have negligible fields of view; these include the visual and infrared spectrographs and radiometers, and the focus and wavefront error sensors. These receive light via small fold mirrors 1.02 milliradians (3.5 arc-minutes) from the optical axis. By making the mirrors spherical in shape it is possible to correct the astigmatism that would normally be observed this far off axis.

The large ultraviolet spectrographs operate from a slit assembly located 0.725 milliradian (2.5 arc-minutes) off axis. The choice of instrument is made by appropriate rotation of the collimator mirror (not shown).

The optical and structural coupling between the guide system and the f/96 camera has been maximized by introducing a two-stage guider. The first stage operates at the f/12 image and stabilizes the spacecraft by observing two guide stars. Its fold mirror and the f/96 camera fold mirror are mounted together to give closest coupling. The three f/12 guiders operate with a reticle plate made of low expansion glass to ensure stability. The second guide stage consists of an artificial star placed at the f/12 focal plane, so that any changes in the 8x relay or its fold mirror will be detected with the fine sensor, which introduces corrective deflections in the f/96 image tube. This star is mounted on the reticle plate, again ensuring highest stability.

This focal plane layout, then, has highest reliability and stability. It is flexible in accommodating many instruments, and is serviceable by astronauts. We have used it as the basis for the various analyses in this phase A report, as has Kollsman Instruments in its report on the instrument section (Volume IV).

### C.8.b SIP Optical and Pointing Requirements

The SIP performance prediction is based on the optical interface with the OTA, the  $f/12$  focal plane. The telescope aperture of 3 meters with 30 percent obscuration is used, and has been modified by the optical efficiency of the mirror coatings shown in Fig. C.8-4 for the far-ultraviolet range.

The image encircled energy distribution given in Fig. C.8-5 applies to each instrument's field angle. Pointing accuracy and stability requirements are given in Table C.8-1 for each scientific instrument. The slit-jaw camera, which detects the image and the selected spectrograph slit, determines the initial pointing accuracy required. The spectrograph spectral range and selected slit width determine the final image pointing accuracy and stability.

Further, to protect the sensitive devices in the SIP, the incoming energy must be prevented from entering the SIP whenever it would produce a density exceeding  $100 \text{ nW/mm}^2$  at the  $f/12$  focal plane.

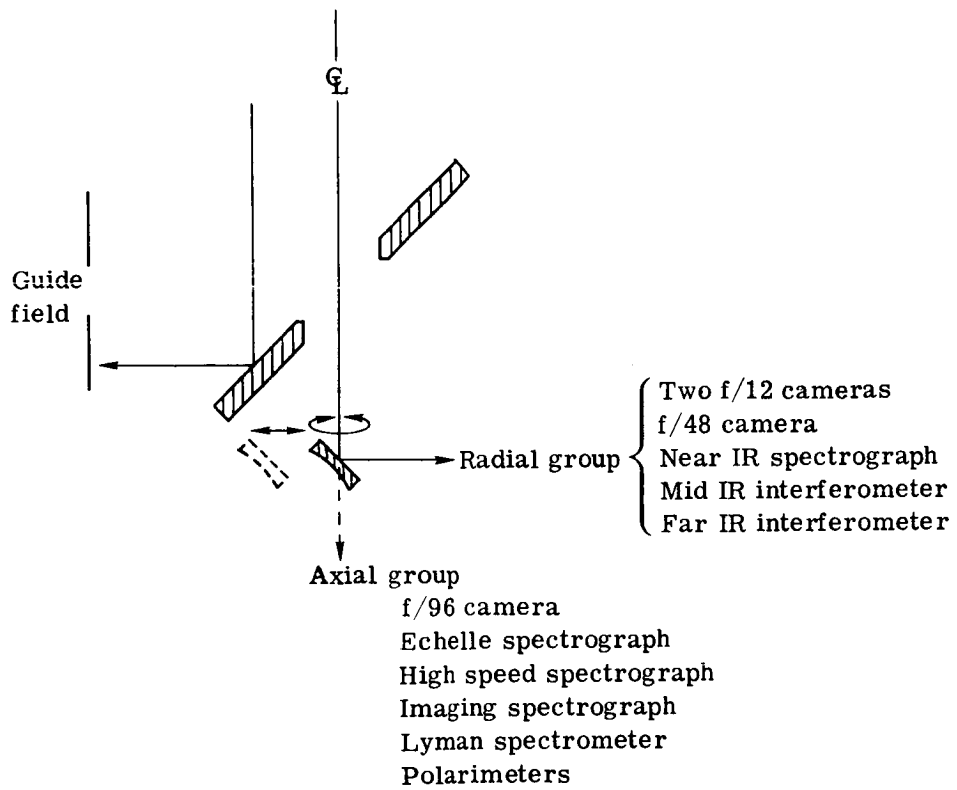


Fig. C.8-1 — Former focal plane layout from NASA GSFC X-670-70-480



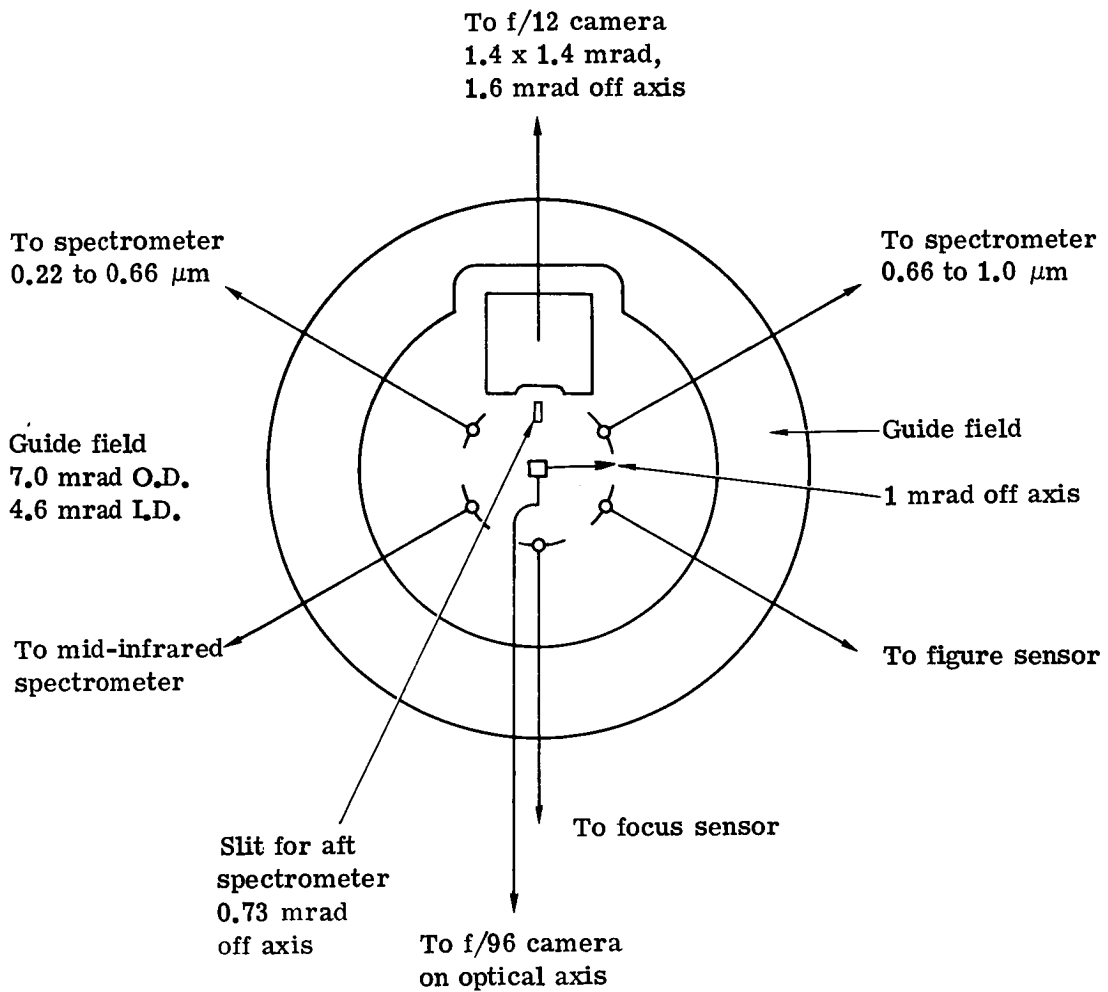
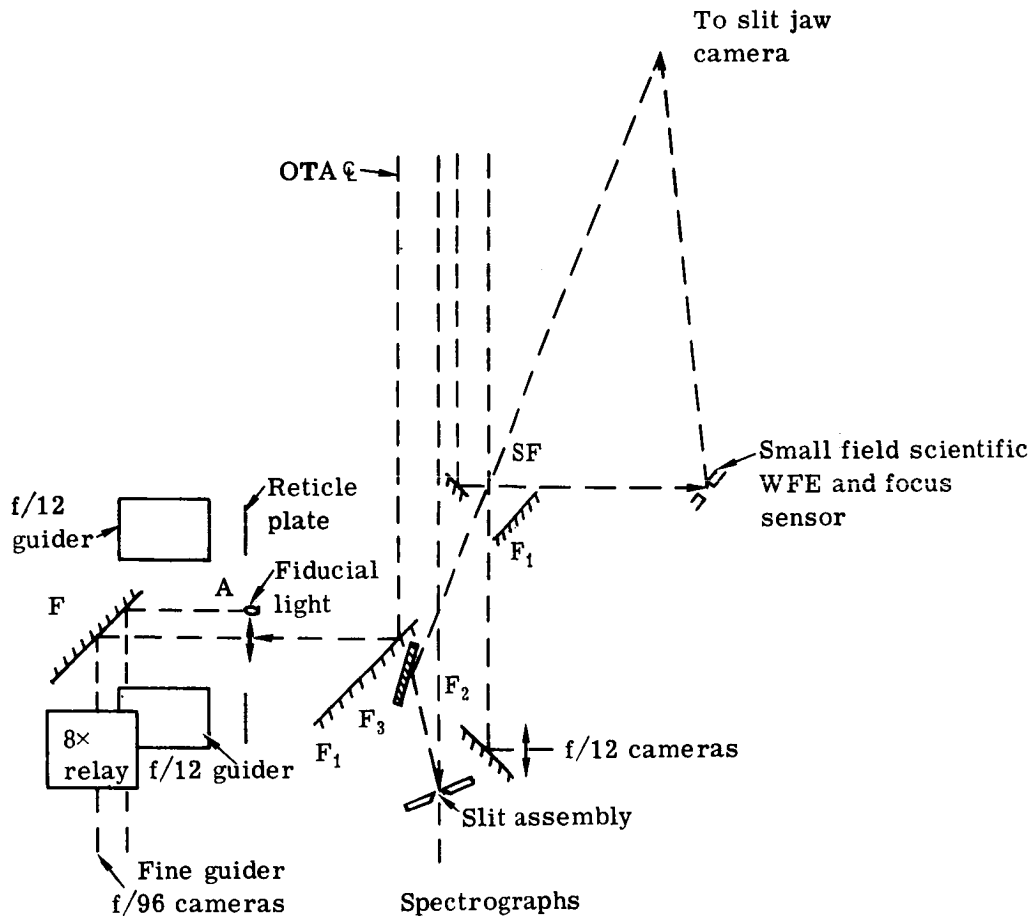


Fig. C.8-2 — f/12 image plane format



F—fold mirror  
 SF—spherical fold mirror  
 A—artificial star

Fig. C.8-3 — Reference focal plane layout

Reflectance of Haas Coating  
Normal Incidence Angle,  
Two Surfaces

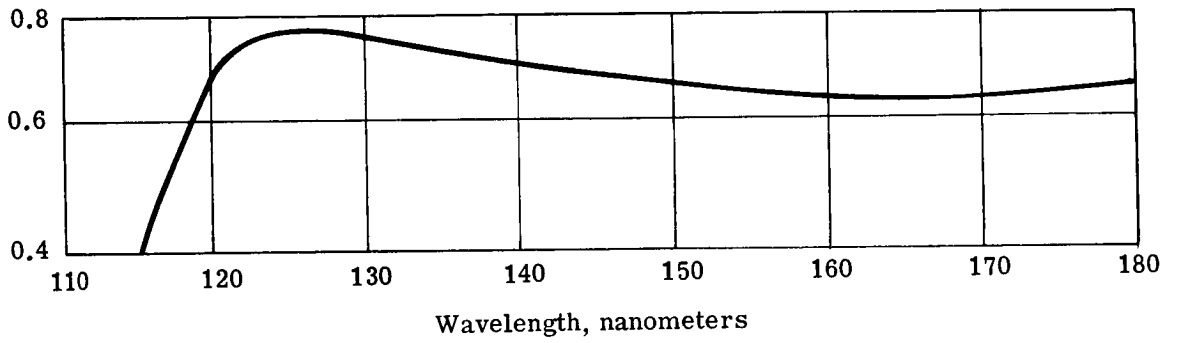


Fig. C.8-4 — LST/OTA reflectance in far-ultraviolet

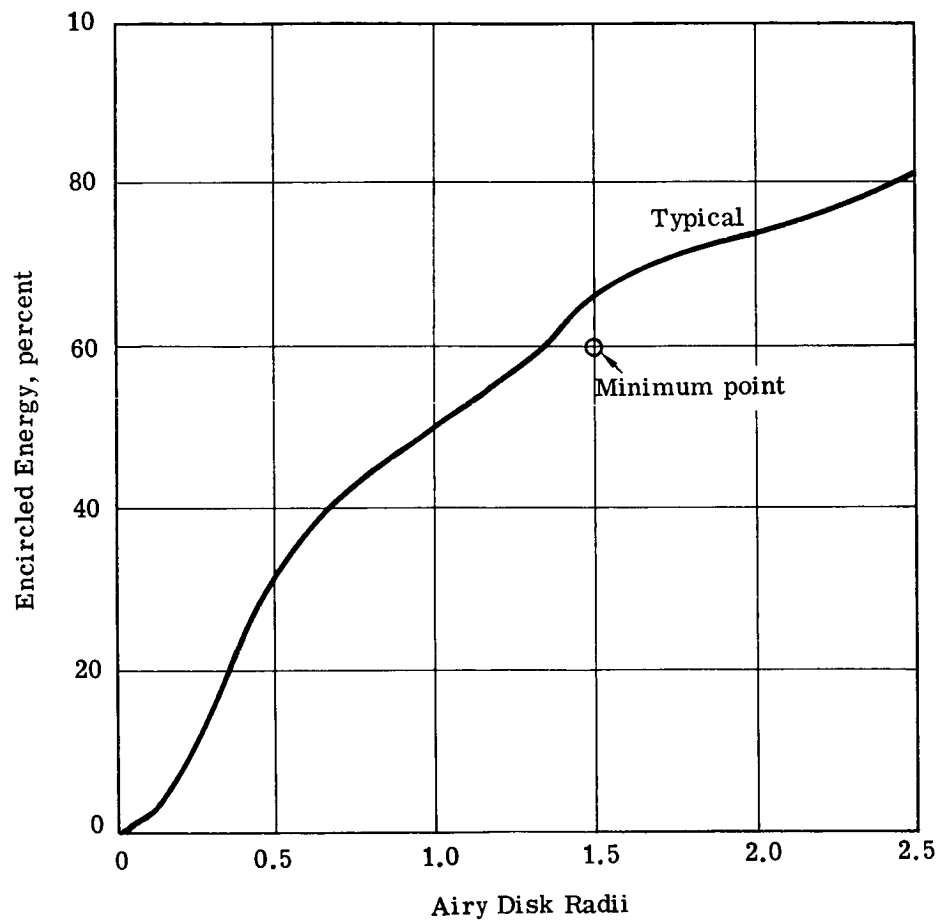


Fig. C.8-5 — LST/OTA encircled energy at 300 nanometers (including pointing error)

Table C.8-1 – LST/OTA Pointing Requirements Based on Telescope WFE =  $0.05\lambda$   
 at  $\lambda = 633$  Nanometers

SIP Instrument	Target Pointing Error, microradians		1 $\sigma$ Stability Pitch, Yaw, Roll	
	Initial	Final	Nanoradians	Microradians
f/96 camera				
Range I at 150 nm	10	10	25	5
Range II at 300 nm	10	10	25	5
Range III at 500 nm	10	10	25	5
Faint object spectrograph				
110 to 220 nm	10	0.05	25	5
220 to 660 nm	10	0.05	25	5
660 to 1,000 nm	10	0.10	50	10
High resolution spectrograph				
110 to 180 nm	10	0.05	25	5
180 to 350 nm	10	0.05	25	5
f/12 camera at 300 nm	10	10	100	30

## C.9 INTERFACE AND SUPPORT REQUIREMENTS\*

The LST as defined in the statement of work includes the optical telescope assembly (OTA) and the scientific instrument package (SIP). These two elements will be assembled with a system support module (SSM) to complete a free-flying LST spacecraft. Separate requirements for support needed by the SSM have not been included in this document since they will be identified during the SSM study.

The specific interfaces covered in this section include:

1. OTA/SIP
2. OTA/SSM
3. LST/mission launch operations
4. LST/mission control operations
5. LST/mission support operations.

### C.9.a OTA/SIP Interfaces

A 2.9-milliradian (10-arc-minute) field of view has been established as a design goal for the telescope to provide to the scientific instrumentation. This field size will cover most of the identified scientific objectives and can be achieved without the use of corrective refractive elements in the optical system.

The telescope field of view outside this central 2.9-milliradian 10-arc-minute field shall be used for fine pointing the telescope by means of guide stars near the target position. Detectors used for tracking guide stars should not infringe on the space near the focus needed by the scientific instruments.

#### C.9.a(1) Optical Beam Interfaces

The OTA will contain a main optics system which will deliver to a principal focus plane a near-diffraction-limited image over a 1.46-milliradian (5-arc-minute) total field of view. The principal focus plane will be located 1.93 meters (76 inches) behind the vertex of the primary mirror (see Fig. C.9-1). The plane will be flat to TBD millimeters and perpendicular to the telescope longitudinal axis to TBD milliradians.

The OTA will utilize the telescope field of view from 4.6 to 7.0 milliradians (16 to 24 arc-minutes) diameter centered around the central 2.9 milliradians (10-arc-minute) scientific data field for the fine guidance system.

The OTA will position a reflector to fold the guide field to a side area of the instrument compartment. The reflector will be centered 23.9 centimeters (9.4 inches) forward of the focal plane. The area behind the reflector will be available for SIP instruments.

The OTA will position small fold mirrors within the convergent data beam to route the beam to scientific instruments located within the forward section of the instrument compartment. The arrangement of these mirrors in the image plane will be as shown in Fig. C.9-2. The data beam for each instrument will be located as follows:

		Axial Position <sup>†</sup>		Radial Position <sup>‡</sup>	
		Meters	Inches	Radians	Degrees
Spectrograph, 0.22 to 0.66 $\mu$ m	Station	1.43	56.4	3.93	225
Spectrograph, 0.66 to 1 $\mu$ m	Station	1.43	56.4	2.36	135
Spectrograph, 1 to 5 $\mu$ m	Station	1.43	56.4	5.50	315
f/96 camera assembly	Station	1.69	66.6	0	0
f/12 camera assembly	Station	1.82	71.5	3.14	180

\*This report section was abstracted and revised to reflect the interfaces of the OTA only, taken from a report by Martin Marietta Corporation, Denver Div., MMC-LST-13, LST Interfaces Study Final Report, Sept 1972, performed under subcontract to Itek Corporation. See this report for fuller details.

<sup>†</sup>Relative to primary mirror vertex at Station 0.0.

<sup>‡</sup>As viewed looking forward with guidance package at 0 degree.

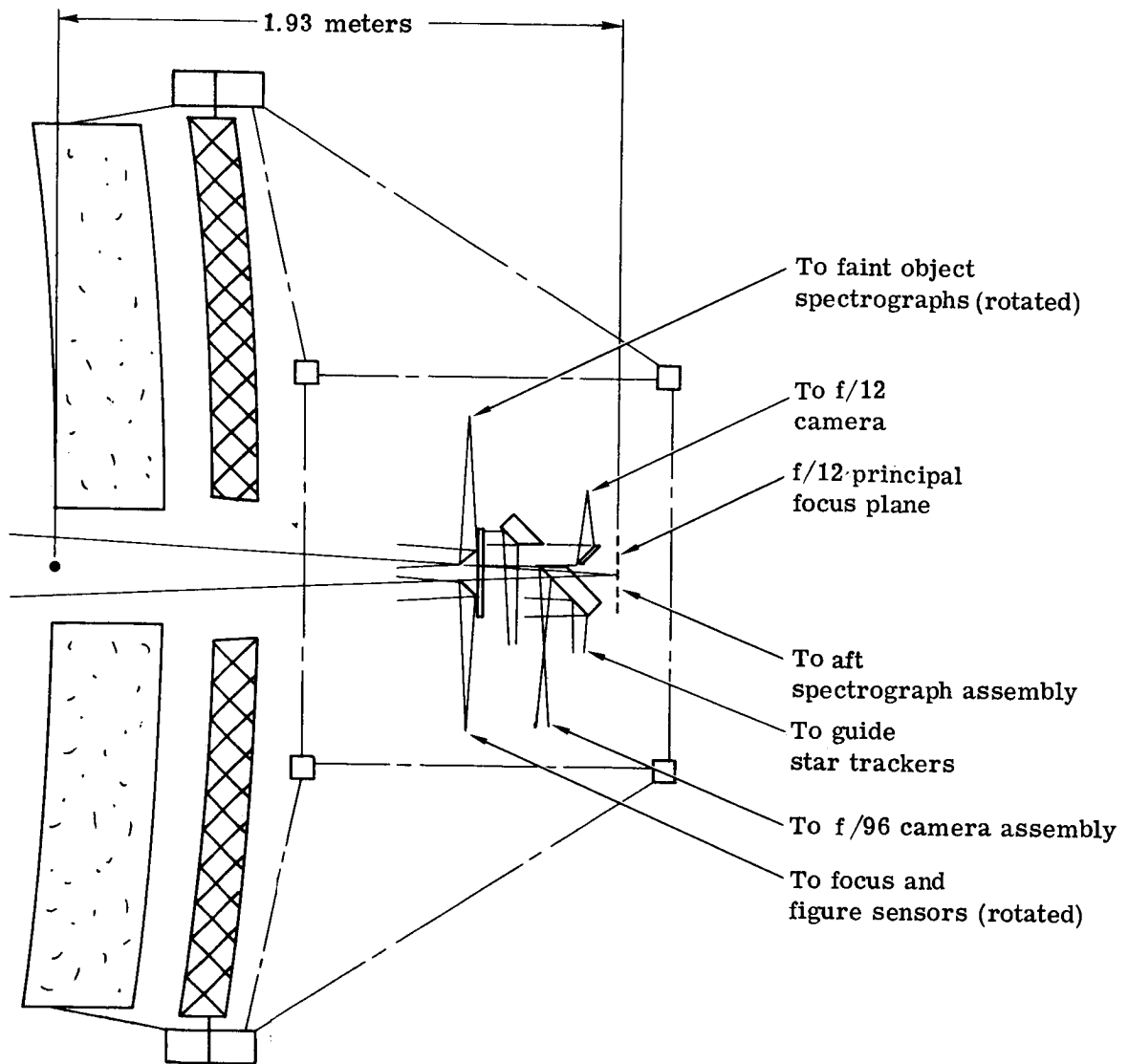


Fig. C.9-1 — Location of f/12 image plane

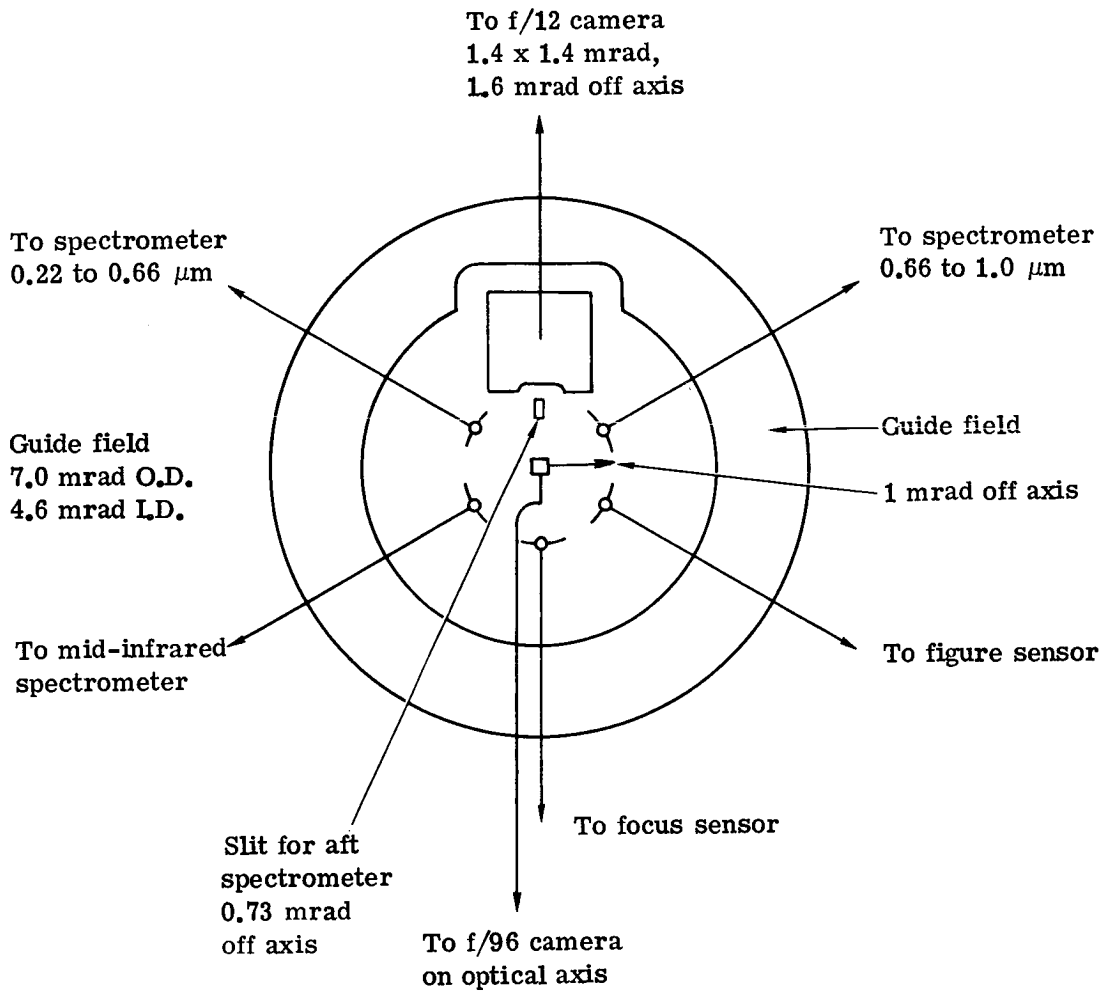


Fig. C.9-2 — f/12 image plane (in object space coordinates)



The optical characteristics of each of these fold mirrors will be specified by the SIP to match the requirements of the associated instrument.

The OTA will also position fold mirrors for a focus sensor and a figure sensor in the convergent data beam, as indicated in Fig. C.9-2. The data beam for these instruments will be located as follows:

		Axial Position*		Radial Position†	
		Meters	Inches	Radians	Degrees
Focus sensor	Station	1.43	56.4	0	0
Figure sensor	Station	1.43	56.4	0.78	45

The SIP will mount an ultraviolet spectograph assembly behind the principal focus plane, with the entrance slit mechanism centered 0.73 milliradian (2.5 arc-minutes) off axis at radial position 180 degrees.

The SIP will include a slit-jaw camera assembly on the OTA instrument truss. This assembly will view mirrors on the three spectograph entrance slits.

The reticle plate of the OTA fine guidance assembly will contain lighted fiducial marks. The f/96 camera assembly of the SIP will utilize these marks to maintain alignment of the cameras with respect to the stellar target.

Each SIP instrument will contain all field stops, shutters, filters, and other modifications to the data beam needed by the instruments.

The OTA will include a protective device to prevent incoming light energy in excess of  $10^{-7}$  watt/mm<sup>2</sup> at the principal focus from reaching the SIP.

The SIP will be designed to scatter a minimum of light energy back into the fine guidance system or OTA.

#### C.9.a(2) Structural Interfaces

The OTA will contain a structural assembly for the instrument compartment which will support OTA subsystem equipment and provide a mounting surface for installation of SIP instruments. This OTA instrument structure will be tied to the telescope primary ring for orientation reference. The position of the mounting surface of each instrument of the SIP will be controlled relative to the primary ring. The OTA instrument structure will include a mounting surface within the radial bay for each of the following instruments:

- |  |   |
|--|---|
| 1. f/12 camera                                       | 4. Faint object spectograph, 0.66 to 1 micrometer |
| 2. f/96 camera assembly                              | 5. Mid-infrared spectograph, 1 to 5 micrometers   |
| 3. Faint object spectograph, 0.22 to 0.66 micrometer | 6. Slit-jaw camera assembly.                      |

These mounting provisions will support each instrument centered over the folded optical axis for that instrument within ±0.4 millimeter and the mounting surface plane will be perpendicular to the optical axis within 0.03 milliradian (0.1 arc-minute) when the instruments are installed on the structure. The location of the optical axes are described in Section C.9.a(1).

The OTA instrument structures will include a mounting surface for an ultraviolet spectograph assembly containing two Echelle spectographs and a faint object spectograph, 0.115 to 0.22 micrometer. This surface will be

\*Relative to primary mirror vertex at station 0.0.

†As viewed looking forward with guidance package at 0 degree.

located 1.97 meters (77.6 inches) aft of the primary mirror vertex and perpendicular to the telescope data beam axis within 1 arc-minute. The surface will not decenter more than 0.4 millimeter when the spectograph assembly is installed with the instrument structure in a horizontal position.

The baseline location of each instrument in the truss is shown in Fig. C.9-3.

The instruments of the SIP will not exceed the weight and center of gravity locations listed below:

	Weight		CG Distance from Mounting Plane	
	Kilograms	Pounds	Centimeters	Inches
f/12 Camera	67.1	148	10.2	4.0
f/96 camera assembly	240	530	11.4	4.5
Faint object spectograph, 0.22 to 0.66 $\mu$ m	45.4	100	10.2	4.0
Faint object spectograph, 0.66 to 1 $\mu$ m	44.5	98	10.2	4.0
Mid-infrared spectograph, 1 to 5 $\mu$ m	18.1	40	7.6	3.0
Slit-jaw camera	42.2	93	10.2	4.0
Ultraviolet spectograph assembly	173	381	63.5	25

The mounting provisions for the f/96 camera assembly will be located on the fine guidance assembly. The mounting plane will be centered to 0.10 millimeter and perpendicular to the f/12 data beam routed through the fine guidance assembly to 2.9 milliradians (10 arc-minutes).

The coordinate system for the combined OTA/SIP instrument assembly is shown in Fig. C.9-4.

### C.9.a(3) Thermal Interfaces

The design goal of the thermal interface is to have a minimum interchange of sensible heat between the OTA and SIP.

Each instrument of the SIP will be insulated or thermally controlled. Additional heat needed will be supplied as electrical energy and surplus heat from the instrument and/or camera will be removed by a controlled path to a suitable heat sink of the SSM.

Each component of the OTA will be thermally insulated or temperature-controlled. Additional heat needed will be provided as electrical energy and surplus heat will be removed by a controlled path to a suitable heat sink of the SSM.

### C.9.a(4) Pointing Control Interfaces

The SIP has no direct interfaces with the OTA image stabilization system that maintains the accuracy and stability of the f/12 image.

The SIP f/96 camera assembly will include a separate image correlation mechanism to maintain the position of a stellar target on the image tube relative to the positions of the guide stars being used for the f/12 image stabilization. This system will utilize fiducial marks on the guide head reticle plate.

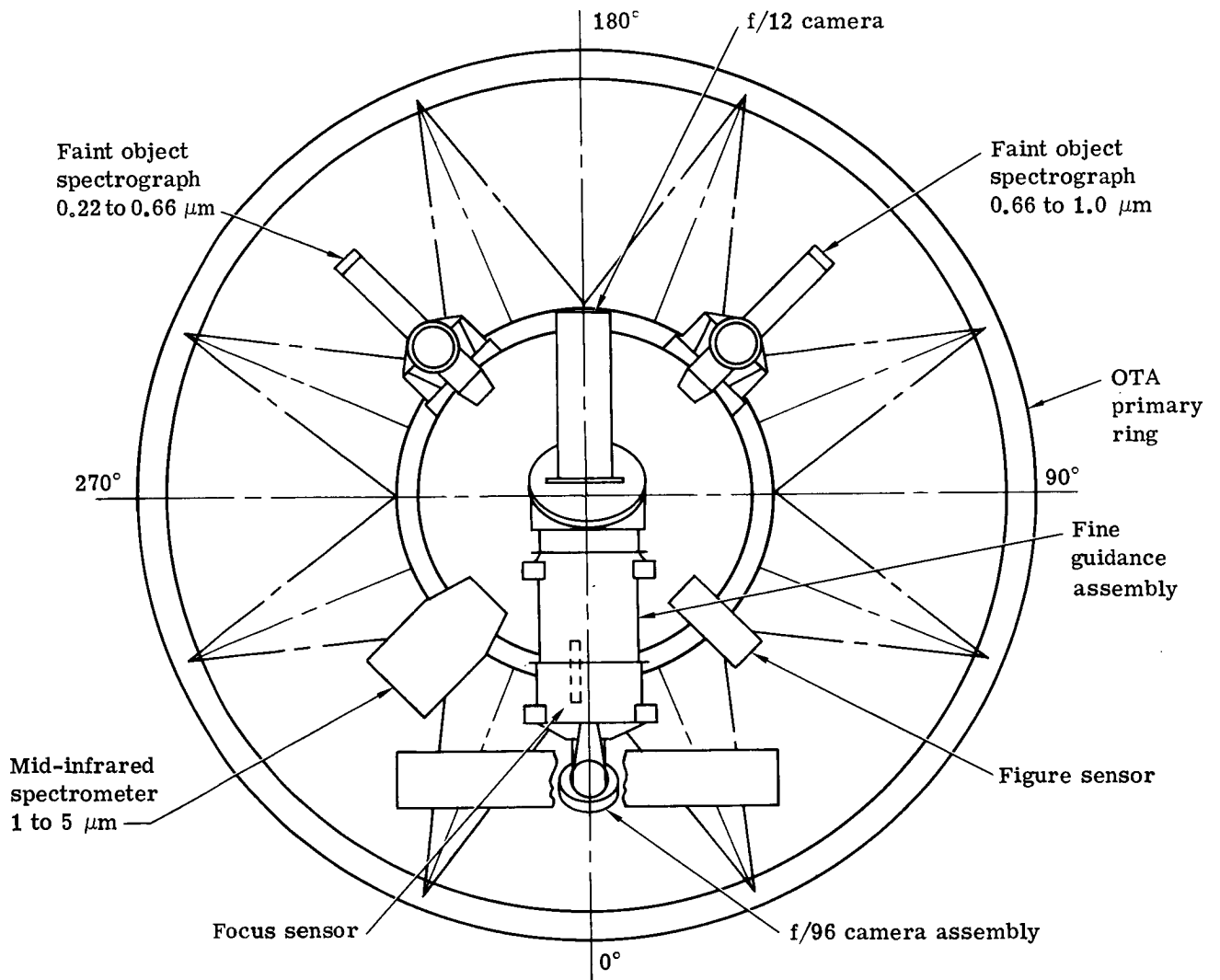


Fig. C.9-3 — Instrument locations in SIP forward truss

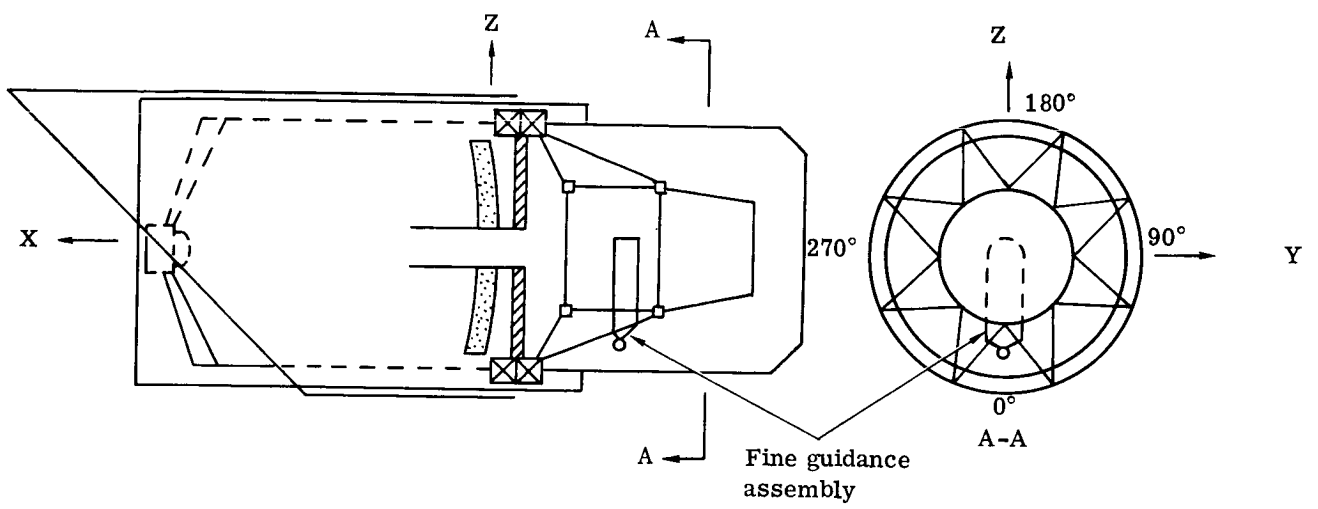


Fig. C.9-4 — OTA/SIP coordinate system

#### C.9.a(5) Data Management Interfaces

There are no direct data interfaces between the OTA and SIP identified to date. Each assembly will have a data interface directly to the SSM.

#### C.9.a(6) Electrical Interfaces

There are no identified direct electrical connections required between the OTA and the SIP. Each assembly will interface directly with the SSM, which will have supervisory control of the electrical power and data handling circuits.

#### C.9.a(7) Environmental Interfaces

Both OTA and SIP equipment in the instrument compartment may be sources and recipients of contaminants of optical surfaces. All subsystems will exert design efforts to eliminate sources of contaminant substances.

#### C.9.a(8) Compatibility Tests

The OTA contractor will perform an optical beam quality test to verify that a collimated light source is focused the specified distance from the SIP mounting surface to  $\pm$  TBD meters, centered on the optical axis to  $\pm$  TBD meters and a centration instability of not more than 0.254 nanometer ( $1 \times 10^{-6}$  inch) rms during 10 hours of simulated closed loop operation (including focus sensor and fine pointing) in a temperature range from +19 to +23°C, with a total wavefront error of not more than  $0.05\lambda$  rms as measured at 633 nanometers.

The OTA contractor will install witness plates on the primary and secondary mirror assemblies to serve as contamination monitors. Tests will be performed on these plates when optical contamination is suspected.

A final OTA/SIP interface test will be performed after assembly of the LST spacecraft in the Spacecraft Integration Facility to verify quality of throughput.

#### C.9.b OTA/SSM Interfaces

This section lists the design requirement controlling the interfaces between the OTA element of the LST and the SSM that will complete the spacecraft. The requirements evolved from a study guideline that the OTA subsystems should be restricted to those functions vital to performance of the telescope, while the SSM should provide all the support services and commodities required by the telescope.

#### C.9.b(1) Structural Interfaces

The overall spacecraft configuration design goal is to develop the OTA and the SSM as separate physical assemblies which will be mated when the spacecraft is integrated.

Both OTA and SSM interface surfaces will include a clocking key to ensure specified angular relationship when integrated. Mounting provisions are required on the OTA meteoroid shield to install six desaturation magnets of the SSM ASCS system.

#### C.9.b(2) Thermal Interfaces

The system design goal is to have the OTA provide passive thermal control as much as feasible, and the SSM will provide electrical power for supplementary heat needed. The SSM will also remove and eject excess heat from OTA components if required. A second thermal design goal is to minimize transfer of heat between the SSM and OTA. The design of the SSM section from plane 1 to a plane 2 shall require the concurrence of the telescope contractor to provide adequate thermal control of the OTA truss and instruments. OTA and SSM surfaces and components facing each other will use low emissivity finishes and insulation as appropriate.

The OTA requires an average of 346 watts of 28-vdc power from the SSM for heater power. This load will be cycled and controlled by demand thermostats in the OTA and may reach a peak demand of 500 watts.

#### C.9.b(3) Pointing Control Interfaces

The system design goal is to have the SSM responsible for coarse pointing the telescope line of sight to commanded celestial coordinates to  $\pm 4.9$ -microradian ( $\pm 1$ -arc-second) accuracy, while the OTA will perform the final pointing and image stabilization.

The SSM will maneuver the spacecraft line of sight to coordinates commanded by ground control to  $\pm 145.5$ -microradian ( $\pm 30$ -arc-second) accuracy without utilizing data from the OTA.

When the telescope line of sight is within  $\pm 145.5$  microradians ( $\pm 30$  arc-seconds) of the target, the OTA by means of guide star trackers will generate and deliver to the SSM proportional error signals in pitch, yaw, and roll, referred to spacecraft coordinate systems. The SSM will utilize these error signals to reduce the pointing error to  $\pm 4.85$  microradians ( $\pm 1$  arc-second).

The OTA will then stabilize the image for the SIP instruments to 0.49-microradian (0.1-arc-second) accuracy and 0.024-microradian (0.005-arc-second) stability, using error signals from guide star trackers fed to transducers producing corrective motions of the secondary mirror.

The OTA will send to the SSM roll error signals and secondary mirror pitch/yaw signals. The SSM will generate torques to reduce these error signals and maintain spacecraft pointing accuracy to  $\pm 4.9$  microradians ( $\pm 1$  arc-second).

The pitch, yaw, and roll error signals generated by the OTA will be in analog format for transmission to the SSM.

The pointing control system interfaces are shown in schematic concept in Fig. C.9-5.

The SSM will forward to the OTA pointing control system commands to position star trackers and insert velocity aberration corrections over the data management interface, described in Section C.9.b(4).

An electrical circuit is required from the SSM attitude control system to the OTA structure for connection to an electromagnetic assembly used for desaturating CMG's.

#### C.9.b(4) Data Management Interfaces

The spacecraft system design goal is for the SSM to maintain supervisory control over the receipt and distribution of ground commands to the OTA, and the receipt, storage, and transmission of the diagnostic data generated by the OTA subsystems to the ground data network.

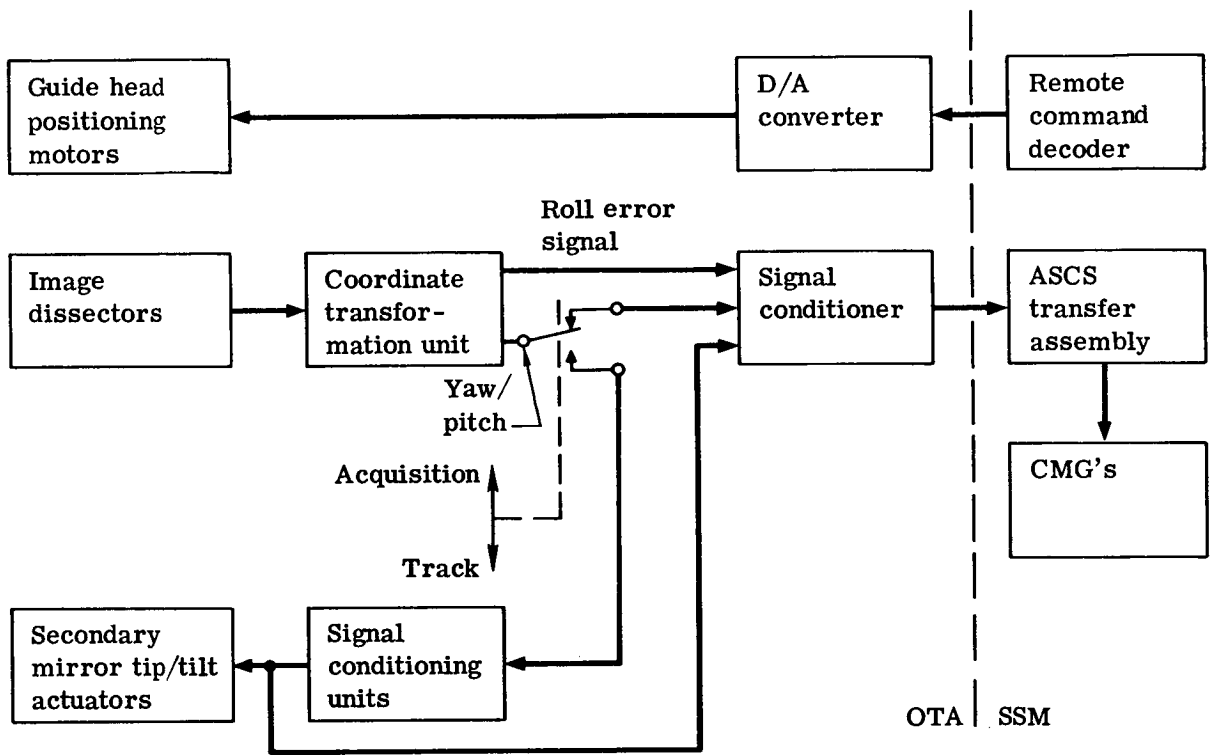


Fig. C.9-5 — OTA/SSM pointing control interfaces

The SSM will route to the OTA all operating commands, whether initiated by ground control or by a stored program. These commands will be issued in digital format from an SSM remote command decoder at a 1,600-bit-per-second transmission rate. Up to 256 commands may be sent to the OTA through one command decoder.

The OTA will receive the decoded commands and will convert to analog form and route to the appropriate OTA subsystem for implementation.

The OTA will generate diagnostic data concerning the status of subsystems and the execution of commands, will precondition the data to 0- to 5-vdc analog format, convert to digital format, and route the data to a data acquisition unit (DAU) of the SSM. Each DAU can accept 64 analog or bilevel signals, and as many DAU's as required will be assigned to the OTA interface. The SSM will provide all data synchronizing signals required. Sampling will be 200 times per second for real-time transmission and four times per second for stored data.

The SSM will provide all on-board data storage capacity required.

The data management interfaces are illustrated in Fig. C.9-6.

The OTA will include a selected list of diagnostic measurements which will be routed through the SSM and to the boost vehicle for monitoring during the launch phase.

#### C.9.b(5) Electrical Power Interfaces

The spacecraft system guideline is for the SSM to furnish all basic electrical power needs of the OTA in the form of nominal 28 to 30 vdc. The SSM will provide electrical power to the OTA via redundant electrical distribution units (EDU) located near the OTA, but under switching control of the SSM. The voltage will be within 28 to 30 vdc, regulated to 2 percent. Each EDU can supply up to 500 watts average power. Each EDU will automatically isolate an overload fault on its input.

The OTA will route the dc power received from the EDU's to the OTA subsystems and will provide internal regulation and overload isolation circuits via five power distribution units. The OTA will also generate any special voltage or frequencies required by their subsystems.

#### C.9.b(6) Environmental Interfaces

Both the OTA and the SSM equipment are potential sources and recipients of electromagnetic interference. The design of all subsystems will utilize techniques to minimize EMI susceptibility by proper cable routing, shielding, bonding, and grounding techniques.

The SSM equipment will generate electromagnetic fields in the vicinity of OTA equipment.

Both the OTA and SSM equipment in the instrument compartment are potential sources and recipients of contamination material. The design of all subsystems will avoid use of nonapproved materials and will provide protection against introduction of contaminating substances.

The SSM will control pressurization of the OTA instrument compartment for man-maintenance activities. This atmosphere will consist of the following characteristics:

Pressure	101.5 x 10 <sup>3</sup> newtons/m <sup>2</sup> (14.7 psia)
Composition	20 percent oxygen, 80 percent nitrogen
Humidity	<50 percent



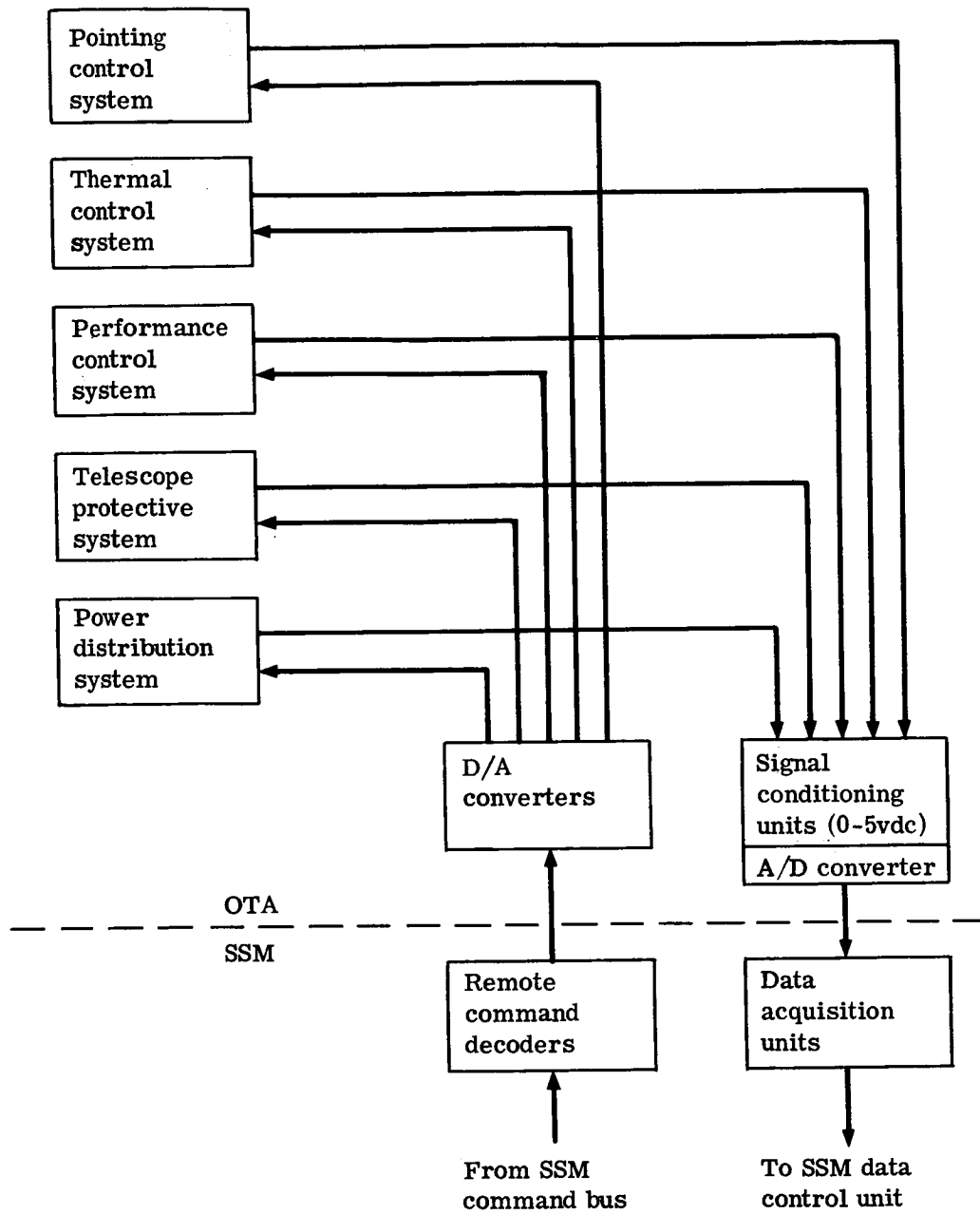


Fig. C.9-6 — OTA/SSM data management interface

### C.9.c LST/Mission Launch Operations Interfaces

This section identifies the requirements for support needed by the LST during the mission launch operations portion of a mission. They are listed as interfaces with the facility that will be responsible for providing the support.

#### C.9.c(1) LST/Spacecraft Integration Facility Interface

The spacecraft integration facility (SIF) will provide a "clean room" for post-transportation inspection and assembly of the OTA and SIP with the SSM. The environment will include air of 10,000 class quality, temperature controlled to  $21 \pm 2^\circ\text{C}$  and humidity controlled to 35 to 50 percent.

SIF personnel will move the OTA and SIP with contractor-furnished handling equipment and low acceleration hoists.

If extended storage of the LST is required, the SIF will provide an enclosure with nitrogen atmosphere to MIL-P-27401, Type I.

The OTA and SIP will be designed with adequate handling points for horizontal assembly with the SSM.

The LST contractors will furnish all test equipment needed for final systems testing of the assembled LST in the SIF.

#### C.9.c(2) LST/Booster Launch Complex Interfaces

The booster launch complex (BLC) will provide a low acceleration hoist to load the LST/SSM spacecraft into the booster.

The LST contractor will furnish suitable handling slings and structural strong points on the LST for vertical installation of the spacecraft.

The BLC will furnish conditioned air of class 10,000 quality to the spacecraft launch shroud after installation over the spacecraft. This air supply will be maintained at a temperature of  $21 \pm 2^\circ\text{C}$  until launch.

The BLC will furnish circuitry and monitoring facilities to display critical status signals from the LST during launch countdown operations.

The LST will furnish status monitoring signals through the SSM to BLC umbilical cables. The signals will be in a format specified by the BLC.

A launch readiness test will be performed on the OTA and SIP via umbilical cables through the BLC and SSM.

#### C.9.c(3) LST/Space Shuttle Boost Vehicle Interfaces

The principal LST interfaces with the shuttle are through the SSM. There will be one structural interface between the telescope primary ring and a shuttle payload support cradle. The maximum expected longitudinal, lateral, and torsional loads through this interface during boost are yet to be determined.

The LST will be subjected to the following maximum environmental conditions during a shuttle boost phase:

Vibration	TBD
Shock	TBD
Acoustic pressure	145 db overall
Pressure change	$1.73 \times 10^3$ newtons/m <sup>2</sup> /sec (0.25 psi/sec)
Temperature	65.5°C (+150°F)

### C.9.c(4) LST/Titan III Boost Vehicle Interfaces

The LST will withstand without damage the boost environment maximum conditions listed below:

Local factor	
Longitudinal	+6.0 = 2.5 g
Lateral	±1.5 g
Vibration	4 g rms
Shock	2,400 g at 4,000 hz
Acoustic pressure	145 db
Pressure change	1.73 x 10 <sup>3</sup> newtons/m <sup>2</sup> /sec (0.25 psi/sec)
Temperature	57.3°C (135°F)
Heating rate	346.5 watts/m <sup>2</sup> (110 Btu/ft <sup>2</sup> hr)

The LST will not undergo transient excursions outside the boost dynamic envelope of 3.8 meters (150 inches) diameter imposed by shroud separation. (See Sections C.1-2 and C.2-20 for load factors used in this study, MSFG.)

### C.9.d LST/Mission Control Operations Interfaces.

This section identifies the requirements for support needed by the LST during the mission control operations phase of an LST mission. They do not include separate support requirements needed by the SSM vehicle.

These interfaces are principally with a Mission Control Center (MCC) which will have control of the LST through a ground data network (GDN) and the SSM, which transmits data without alteration. Thus, the LST can be viewed as having direct interfaces with the MCC.

The MCC will transmit to the LST commands for setup and operation of all instruments and components to conduct a stellar observation program. The format will be suitable for digital transmission and storage and conversion to analog as needed within the LST.

The MCC will receive from the LST diagnostic data concerning status of the LST system. The MCC will process the data and display it for review by mission support personnel.

The LST will generate sufficient diagnostic data of systems performance to permit mission support personnel to monitor the health of the LST systems. The data will be in a format suitable for display and rapid interpretation.

The GDN will record the diagnostic data received from the spacecraft and transmit via land line to MCC with minimum delay.

### C.9.e LST/Mission Support Operations Interfaces

This section identifies the requirements for support needed by the LST during the mission support or maintenance phase of an LST mission. The requirements have been compiled under three major facets of support operations:

1. Operations monitoring program
2. Telescope maintenance program
3. Shuttle logistics vehicle.

The requirements listed are those areas where the needs of one element have an impact on the design of the other element and must be considered during Phase B of the development program.

#### C.9.e(1) LST Operations Monitoring Program (OMP) Interfaces

The OMP will establish a list of engineering data needed to adequately monitor operations of the LST in orbit and isolate causes of malfunctions and/or degradation of performance.

The OMP will establish a data handling system to process diagnostic data received from the spacecraft and display and store in the MCC as required by the monitoring program.

Each subsystem of the OTA and the SIP will include sensors and circuitry to route to the OMP via the SSM and MCC the items of essential engineering data defining the performance status of the subsystems.

Each subsystem will include alternate arrangements of hardware and circuitry as feasible to provide the OMP methods for establishing alternate operations in event of malfunction or degradation of subsystem performance.

#### C.9.e(2) LST/Telescope Maintenance Program (TMP) Interfaces

The LST program will perform a reliability analysis of each of the subsystems which will identify those components that require replacement or refurbishment in orbit at each servicing visit by the logistics shuttle.

The configuration of each OTA and SIP subsystem design will include modular arrangements which will permit those components identified to be readily replaced or refurbished in orbit by maintenance personnel in a "shirtsleeve" mode.

The OTA and SIP subsystems will be configured so that replacement of components or instruments will not necessitate a complex alignment or calibration procedure by maintenance personnel.

The TMP will prepare criteria for the configuration of in-orbit replacement modules or components as an impact to LST subsystems design.

The TMP will procure and store replacement components and refurbishment materials and maintenance tasks identified so that execution of the planned servicing program in-orbit will restore the LST to essentially "as new" operating condition.

The LST/SSM spacecraft will be outfitted with restraints and handrails needed within the instrument compartment for maintenance personnel maneuvering.

Astronaut maintenance personnel will be required to train in the LST servicing program in an LST simulator prior to performing a logistics mission.

#### C.9.e(3) LST/Shuttle Logistics Vehicle (SLV) Interfaces

The LST will be configured for insertion into the shuttle logistics vehicle (SLV) and restraint for return to earth. The restraints may include a "cradle" support under the LST to withstand a portion of the lateral loads of the LST.

The SLV will provide a cradle type support at the primary mirror support section of the LST to absorb transverse loads during reentry of the SLV.

The LST will contain protective devices to withstand contaminating effluents from the SLV while the two vehicles are in close proximity in orbit.

The LST will withstand without damage the environment induced by return to earth by the SLV.

## C.10 RELIABILITY

The following subparagraphs of this report present a Reliability Prediction and a Failure Mode Effects Analysis of the Optical Telescope Assembly. These have been jointly prepared by the Martin-Marietta Corporation, Denver, Colorado, and the Itek Corporation. The work takes full advantage of the Martin-Marietta Corporation's earlier analysis experience for space missions similar to those anticipated for the OTA and it embodies the Itek concept of redundancy to achieve "Mission Success" probabilities.

The effort was undertaken in conjunction with the conceptual design effort in order to incorporate into the design practical and realistic levels of subassembly redundancy. This, in turn, permitted an early assessment of attainable OTA reliability and a realistic review of preliminary maintenance concepts based on failure expectancies and the system effects of various potential subassembly failures.

The reliability analyses will be used in subsequent program phases to minimize critical single failure points and to serve as the basis for tradeoff studies to select optimum subassembly designs. The considerations to be used in these studies will include modifications in the redundancy levels, and introduction of alternate (backup) operational modes with various levels of permissible degradation, and the effects of various in-flight maintenance approaches on overall mission success.

### C.10.a Preliminary Critical Path Analysis

This analysis is based on the operation of the OTA and the scientific instrument package (SIP) in the two basic modes of a typical LST mission. These are defined as the acquisition mode and the tracking mode which starts after target acquisition and the coarse pointing performed by the system support module (SSM).

The acquisition mode includes the fine pointing function from 145.4 to 4.8 microradians (30 to 1-arc-seconds) and is accomplished by using the OTA fine guidance to provide error signals to the SSM attitude control subsystem that does the pointing.

The tracking mode includes the fine pointing function from 4.8 to 0.5 microradians (1 to 0.1 arc-seconds) and is accomplished by using the OTA pointing and stabilization subsystem. Also included in the tracking mode are the stabilization, data acquisition, and data handling functions, accomplished by using the OTA and SIP subsystems.

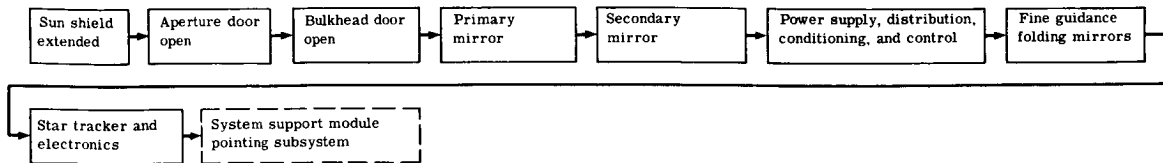
Fig. C.10-1, a critical path diagram of acquisition and tracking modes of operation, shows the major assemblies that must operate to perform the functions successfully. The preliminary critical path analysis formed the basis for the preliminary failure mode and effects analysis, described in Section C.10.b(1).

The critical areas identified in the OTA that are required for successful operation in the acquisition mode are the aperture door, the primary and secondary mirrors, the power supply, and the guide star tracker loops.

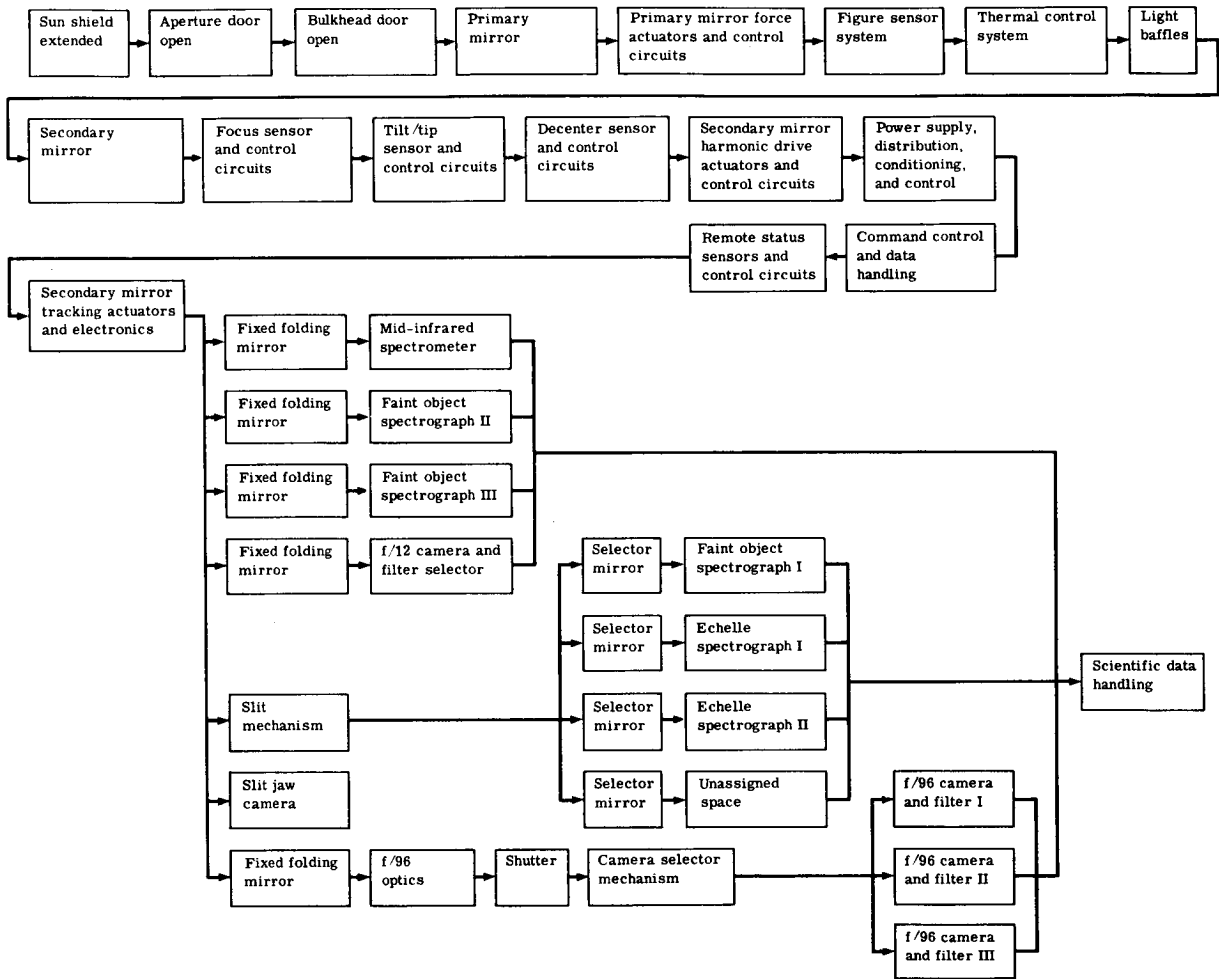
The critical areas identified in the OTA that are required for successful operation in the tracking mode are the aperture door, the primary and secondary mirrors, the alignment sensors and control circuits, the secondary mirror harmonic drives and control circuits, the power supply, the command control and data handling subsystem, and the secondary mirror tracking actuator loops. The incorporation of redundancy in the areas identified as critical permits some failures to be tolerated without significant degradation to the system. Failures can be tolerated in most of the other areas, with only part of the scientific data being lost.

The OTA subsystems in which redundancy has been incorporated are:

1. Thermal Control Subsystem -- 23 separate zones with a redundant sensor and heater for each zone.
2. Electrical Power Distribution -- 15 separate power conditioning and control units with redundant units for each of the 15.



(a) Acquisition mode



(b) Tracking mode

Fig. C.10-1 — OTA/SIP critical paths

3. Pointing and Stabilization – 2 loops of an available 3 are normally required, leaving the third loop as available redundancy. Additional redundancy can be considered available in that degraded-mode operation is possible using 1 loop and using the vehicle system “Roll-Control” stabilization.

4. Harmonic Drive Actuators and Control – 5 arms required for system success, with one redundant arm available if needed.

5. Sun Shield – 1 motor could accomplish extension and retraction of the sun shield. Separate motors have been provided for the extension and the retraction, and each has a redundant motor for improved success probability.

6. Aperture Door – 1 drive motor required for door operation, 3 redundant motors provided, 1 latch motor required, 1 additional motor provided as redundancy to improve the probability of success.

7. Pressure Bulkhead Door – 1 motor is required, 1 additional motor is provided as redundancy. Provision for manual operation may also be provided.

During subsequent design phases, the critical path analysis can be expanded to lower levels and the critical areas identified to component or lower level. This will in turn support a failure mode and effects analysis to a lower hardware level.

#### C.10b Reliability and Maintainability Analysis

##### C.10.b(1) Preliminary Failure Mode and Effects Analysis

The OTA conceptual design was analyzed to identify single failure points critical to the LST mission. Fig. C.10-2 shows the LST system elements considered in the analysis. Although the specific hardware to be used for each of the system elements has not been selected in all cases, the failure modes identified were considered typical for the particular function and would generally apply to such hardware.

The potential critical failure modes identified for each of the OTA system elements are summarized in Table C.10-1. For each identified failure mode, the following were determined: prime cause of failure, method of failure, prevention or reduction of effects, method of detection, failure effect, and corrective action that could be taken prior to the first maintenance visit.

##### C.10.b(2) Preliminary Maintainability Analysis

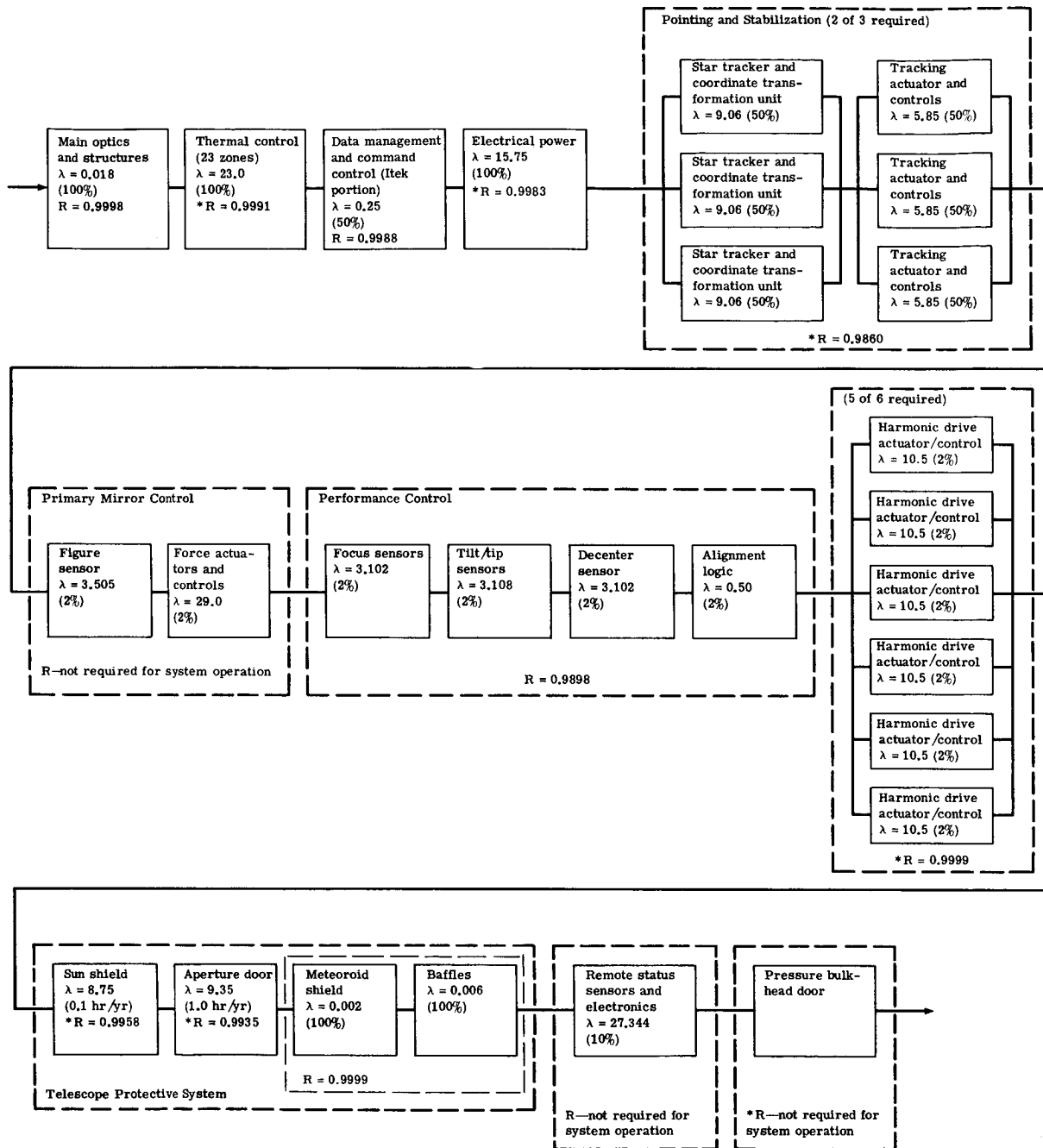
A preliminary maintainability analysis (Table C.10-1) was conducted and the following requirements identified: corrective action that can be performed at the first visit, special tools or test equipment required, and spares required.

The resultant remarks or recommendations based on the preliminary reliability and maintainability analysis are also given in the table.

#### C.10.c Subsystem Summary – Failure Modes

##### C.10.c(1) Structures

The failure modes identified for the structures elements are those typical for most structures items and are generally caused by the vibration and shock environments during launch, the release of structural loads in the zero-gravity condition, and the space thermal environment. Since it is not feasible to utilize redundant structure, the effects of these environmental conditions are minimized by selecting materials properly, designing to the microyield strength, and providing adequate thermal protection. The most critical structural items are the elements that



$\lambda$  = failure rate in parts per  $10^6$  hours  
 ( ) = duty cycle  
 R = 1-year success probability  
 \* = indicates redundancy incorporated to achieve stated success probability

Fig. C.10-2 — OTA reliability prediction



Table C.10-1 – Preliminary Reliability and Maintainability Analysis Summary

Subsystem	Failure Mode	Prime Cause of Failure	Methods of Failure Prevention or Reduction of Effects	Method of Failure Detection	Failure Effect	Corrective Action Prior to First Visit	Corrective In-Flight Maintenance	Other	Special Tools or Test Equipment Required	Spares Required	Remarks/Recommendations
Structural elements, struts, rings, mounts, bulkheads	<ul style="list-style-type: none"> <li>Cracks</li> <li>Misalignment</li> <li>Structural creep when loads are released in zero-gravity</li> </ul>	<ul style="list-style-type: none"> <li>Launch environment</li> <li>Thermal environment</li> <li>Structural yielding</li> <li>Defective material</li> </ul>	<ul style="list-style-type: none"> <li>Design to microyield strength</li> <li>Select material least sensitive to thermal changes</li> <li>Adequate thermal protection</li> <li>Material inspection and testing</li> <li>Provide adequate design safety margins and thermal protection</li> <li>Open door during pre-launch operations and verify door is open prior to launch</li> </ul>	<ul style="list-style-type: none"> <li>Strain gauge measurement</li> <li>Focus tilt &amp; decenter sensors</li> </ul>	<ul style="list-style-type: none"> <li>Misalignment of secondary mirror affecting focus, tilt, and centering</li> </ul>	<ul style="list-style-type: none"> <li>Adjust focus decenter or tilt to compensate</li> </ul>	<ul style="list-style-type: none"> <li>Replace seals</li> </ul>	<ul style="list-style-type: none"> <li>If failure effect cannot be compensated for, return to earth for repair</li> </ul>	<ul style="list-style-type: none"> <li>None in flight</li> </ul>	<ul style="list-style-type: none"> <li>None in flight</li> </ul>	
Mirrors	<ul style="list-style-type: none"> <li>Contamination</li> <li>Distortion</li> <li>Surface deterioration/damage</li> </ul>	<ul style="list-style-type: none"> <li>Materials outgassing</li> <li>External source such as spacecraft propulsion</li> <li>Warping due to thermal environment or supporting structure</li> <li>Meteoroid damage</li> </ul>	<ul style="list-style-type: none"> <li>Material selection and testing</li> <li>Provide isolation from external source</li> <li>Thermal blanket and heaters to maintain constant temperature</li> </ul>	<ul style="list-style-type: none"> <li>Figure sensor</li> <li>Data quality</li> <li>Tilt, focus, or decenter sensor</li> <li>Temperature sensors</li> <li>Strain gauges</li> </ul>	<ul style="list-style-type: none"> <li>Degradation of or loss of data</li> </ul>	<ul style="list-style-type: none"> <li>Adjust force actuators, primary mirror</li> <li>Adjust thermal blanket temperatures</li> <li>Adjust focus decenter or tilt to compensate</li> </ul>	<ul style="list-style-type: none"> <li>None</li> </ul>	<ul style="list-style-type: none"> <li>If mirror surface badly damaged or deteriorated, return to earth for repair</li> </ul>	<ul style="list-style-type: none"> <li>None</li> </ul>	<ul style="list-style-type: none"> <li>None</li> </ul>	<ul style="list-style-type: none"> <li>Cleaning or repair of mirrors not considered feasible on orbit</li> </ul>
Thermal Control	<ul style="list-style-type: none"> <li>Heaters/blanks fail on or off</li> <li>Deterioration</li> </ul>	<ul style="list-style-type: none"> <li>Parts failure in amplifiers or control circuits</li> <li>Switch or thermostat failure</li> </ul>	<ul style="list-style-type: none"> <li>Material inspection/testing</li> <li>Redundant thermostats, controls, and heaters</li> </ul>	<ul style="list-style-type: none"> <li>Strain gauge detectors on structure</li> <li>Change in data quality</li> </ul>	<ul style="list-style-type: none"> <li>Degradation or loss of data</li> </ul>	<ul style="list-style-type: none"> <li>Possible adjustment to adjacent heaters to compensate</li> </ul>	<ul style="list-style-type: none"> <li>Possible replacement of failed items</li> </ul>	<ul style="list-style-type: none"> <li>If degradation sufficiently bad, return to earth for repair</li> </ul>	<ul style="list-style-type: none"> <li>None</li> </ul>	<ul style="list-style-type: none"> <li>Thermal blankets</li> <li>Heaters</li> <li>Thermostats</li> </ul>	<ul style="list-style-type: none"> <li>In-flight replacement of blankets, thermostats, and heaters considered feasible</li> </ul>

Table C.10-1 - Preliminary Reliability and Maintainability Analysis Summary (cont.)

Subsystem	Failure Mode	Prime Cause of Failure	Methods of Failure Prevention or Reduction of Effects	Method of Failure Detection	Failure Effect	Corrective Action Prior to First Visit	Corrective Action at Visit	Special Tools or Test Equipment Required	Spares Required	Remarks/Recommendations
Data handling and command control	<ul style="list-style-type: none"> <li>Loss of one or more channels</li> </ul>	<ul style="list-style-type: none"> <li>Provide environment</li> <li>Parts failure</li> </ul>	<ul style="list-style-type: none"> <li>Provide environmental protection</li> <li>Use Hi-Rel screened parts</li> <li>Provide internal redundancy</li> </ul>	<ul style="list-style-type: none"> <li>Data loss</li> </ul>	<ul style="list-style-type: none"> <li>Loss of one or more measurements</li> </ul>	<ul style="list-style-type: none"> <li>None</li> </ul>	<ul style="list-style-type: none"> <li>Replace component</li> </ul>	<ul style="list-style-type: none"> <li>None</li> </ul>	<ul style="list-style-type: none"> <li>Multi-plexer</li> <li>Converters</li> <li>Decoder</li> <li>Encoder</li> </ul>	<ul style="list-style-type: none"> <li>Provide accessibility for ease of replacement in a suited condition</li> </ul>
Electric power distribution and control (PDU)	<ul style="list-style-type: none"> <li>Open circuit</li> <li>Short circuit</li> </ul>	<ul style="list-style-type: none"> <li>Launch or thermal environment</li> </ul>	<ul style="list-style-type: none"> <li>Redundant buses</li> <li>Provide adequate thermal protection and vibration/shock isolation</li> </ul>	<ul style="list-style-type: none"> <li>Voltage/current measurements monitored on ground</li> </ul>	<ul style="list-style-type: none"> <li>Loss of one or more functions, depending where failure occurred</li> </ul>	<ul style="list-style-type: none"> <li>Isolate failed bus</li> </ul>	<ul style="list-style-type: none"> <li>Repair as required</li> </ul>	<ul style="list-style-type: none"> <li>None identified</li> </ul>	<ul style="list-style-type: none"> <li>None identified</li> </ul>	<ul style="list-style-type: none"> <li>Provide ability to isolate failed bus or PDU in event of short circuit</li> <li>Provide ability to switch to redundant circuits</li> </ul>
Pointing and stabilization	<ul style="list-style-type: none"> <li>Loss of error signals</li> <li>Inability to move actuator</li> </ul>	<ul style="list-style-type: none"> <li>Mechanical failure of fold mirror or drives</li> <li>Electrical parts failure</li> </ul>	<ul style="list-style-type: none"> <li>Provide environmental protection</li> <li>Specify compatible lubricants</li> <li>Materials inspections</li> <li>Use Hi-Rel screened parts</li> <li>Redundant tracker is provided</li> </ul>	<ul style="list-style-type: none"> <li>Inability to locate target or to stabilize image</li> </ul>	<ul style="list-style-type: none"> <li>Loss of one star tracker loop</li> </ul>	<ul style="list-style-type: none"> <li>Switch out failed loop</li> </ul>	<ul style="list-style-type: none"> <li>Replace guide star tracker</li> </ul>	<ul style="list-style-type: none"> <li>None</li> </ul>	<ul style="list-style-type: none"> <li>Guide star tracker</li> </ul>	<ul style="list-style-type: none"> <li>Only two tracker loops required to perform functions.</li> <li>One loop can serve with degraded performance if vehicle roll control system relied on for roll stabilization</li> </ul>
Primary mirror control	<ul style="list-style-type: none"> <li>Distorted image sent to ground</li> </ul>	<ul style="list-style-type: none"> <li>Parts failure in video circuits or control circuits</li> <li>Failure of force actuators</li> </ul>	<ul style="list-style-type: none"> <li>Provide environmental protection</li> <li>Use Hi-Rel screened parts</li> <li>Provide adequate structural design safety margins</li> </ul>	<ul style="list-style-type: none"> <li>Observe data quality</li> </ul>	<ul style="list-style-type: none"> <li>Degradation of data</li> </ul>	<ul style="list-style-type: none"> <li>Adjust figure by observing actual data and error adjustment if sensor system failed</li> </ul>	<ul style="list-style-type: none"> <li>Replace sensor package</li> <li>Replace control package</li> </ul>	<ul style="list-style-type: none"> <li>None</li> </ul>	<ul style="list-style-type: none"> <li>Figure sensor package</li> <li>Control circuit package</li> </ul>	

Table C.10-1 – Preliminary Reliability and Maintainability Analysis Summary (cont.)

Subsystem	Failure Mode	Prime Cause of Failure	Methods of Failure Prevention or Reduction of Effects	Method of Failure Detection	Failure Effect	Corrective Action Prior to First Visit	Corrective Action at Visit Other	Special Tools or Test Equipment Required	Spares Required	Remarks/Recommendations
Performance control	<ul style="list-style-type: none"> <li>Telescope will not focus automatically</li> <li>Secondary mirror cannot be aligned in pitch and yaw automatically</li> <li>Secondary mirror cannot be centered automatically</li> </ul>	<ul style="list-style-type: none"> <li>Misalignment of prism sensor</li> <li>Failure of mechanical fold mirror</li> <li>Parts failure in electric circuits</li> <li>Failure of light source</li> <li>Failure of harmonic drive actuators</li> </ul>	<ul style="list-style-type: none"> <li>Provide environmental protection</li> <li>Use Hi-Rel screened parts</li> <li>Provide adequate structural design safety margins</li> <li>Provide redundant light sources</li> <li>Design permits degraded operation with up to 3 out of 6 actuators operable</li> </ul>	<ul style="list-style-type: none"> <li>Observe data quality</li> </ul>	<ul style="list-style-type: none"> <li>Degradation of data</li> </ul>	<ul style="list-style-type: none"> <li>Adjust by trial and error from data observation</li> </ul>	<ul style="list-style-type: none"> <li>None</li> </ul>	<ul style="list-style-type: none"> <li>None</li> </ul>	<ul style="list-style-type: none"> <li>Sensor packages</li> <li>Harmonic drive actuators</li> <li>Electronic control modules</li> </ul>	<ul style="list-style-type: none"> <li>Sensor or actuator replacement will probably be performed in unpressurized area in suited condition</li> </ul>
Sun shield	<ul style="list-style-type: none"> <li>Failure to extend</li> <li>Failure to retract</li> <li>Binding or sticking on tracks</li> </ul>	<ul style="list-style-type: none"> <li>Launch or thermal environment causes structural misalignment</li> <li>Motor failure</li> <li>Mechanism failure</li> <li>Control circuit failure</li> </ul>	<ul style="list-style-type: none"> <li>Adequate design safety margin and thermal protection</li> <li>Redundant motors and drives</li> <li>Selection of proper lubricant</li> <li>Prelaunch inspections and tests</li> <li>Use Hi-Rel screened parts</li> </ul>	<ul style="list-style-type: none"> <li>Observe position indicators</li> <li>Observe data quality</li> <li>Observe bright source detector</li> </ul>	<ul style="list-style-type: none"> <li>Loss of data quality during bright side observation</li> <li>Failure to retract would have no effects until return to earth</li> <li>Loss of gyro unload capability</li> </ul>	<ul style="list-style-type: none"> <li>Maintain pointing away from bright sources</li> </ul>	<ul style="list-style-type: none"> <li>If failure cannot be repaired in flight, return to earth</li> </ul>	<ul style="list-style-type: none"> <li>None identified</li> </ul>	<ul style="list-style-type: none"> <li>Motor mechanism</li> <li>Control electronics</li> </ul>	<ul style="list-style-type: none"> <li>Data can be acquired on dark side and away from bright sources</li> </ul>
Aperture door	<ul style="list-style-type: none"> <li>Binds or sticks during opening or closing</li> <li>Failure to open</li> <li>Failure to close</li> <li>Closes inadvertently</li> </ul>	<ul style="list-style-type: none"> <li>Misalignment or warping due to launch or thermal environment</li> <li>Motor failure</li> <li>Mechanism failure</li> <li>Bright source sensor failure</li> </ul>	<ul style="list-style-type: none"> <li>Adequate design safety margin</li> <li>Redundant motors and actuators</li> </ul>	<ul style="list-style-type: none"> <li>Bright source detector</li> <li>Position indicators</li> </ul>	<ul style="list-style-type: none"> <li>Inability to collect data (closed mode)</li> <li>Loss of mirror protection if sun viewed (open mode)</li> </ul>	<ul style="list-style-type: none"> <li>None (closed mode)</li> <li>Program maneuvers to avoid direct sun viewing (open mode)</li> </ul>	<ul style="list-style-type: none"> <li>If closed mode, attempt EVA repair</li> <li>Return to earth if EVA cannot accomplish repair</li> </ul>	<ul style="list-style-type: none"> <li>None identified</li> </ul>	<ul style="list-style-type: none"> <li>Motors</li> <li>Mechanism</li> </ul>	<ul style="list-style-type: none"> <li>In-flight replacement of motors and mechanisms considered feasible with EVA</li> </ul>

Table C.10-1 - Preliminary Reliability and Maintainability Analysis Summary (cont.)

Subsystem	Failure Mode	Prime Cause of Failure	Methods of Failure Prevention or Reduction of Effects	Method of Failure Detection	Failure Effect	Corrective Action Prior to First Visit	Corrective Action at Visit	Special Tools or Test Equipment Required	Spares Required	Remarks/Recommendations	
Meteoroid shield and baffles	<ul style="list-style-type: none"> <li>Cracks</li> <li>Deterioration</li> <li>Structural failure</li> <li>Finish deterioration</li> </ul>	<ul style="list-style-type: none"> <li>Launch environment</li> <li>Thermal environment</li> <li>Defective materials</li> <li>Meteoroid punctures</li> </ul>	<ul style="list-style-type: none"> <li>Adequate design safety margins</li> <li>Materials selection and testing</li> </ul>	<ul style="list-style-type: none"> <li>Scattered light sensors</li> <li>Data</li> </ul>	<ul style="list-style-type: none"> <li>Degradation or loss of data if damage severe</li> </ul>	<ul style="list-style-type: none"> <li>None</li> </ul>	<ul style="list-style-type: none"> <li>If damage significant, return to earth for repair</li> </ul>	<ul style="list-style-type: none"> <li>None</li> </ul>	<ul style="list-style-type: none"> <li>None</li> </ul>	<ul style="list-style-type: none"> <li>This type of failure considered unlikely</li> </ul>	
Remote status sensors and electronics	<ul style="list-style-type: none"> <li>Failure of a remote sensor</li> <li>Failure of an electronic sensor</li> <li>Loss of a status measurement</li> </ul>	<ul style="list-style-type: none"> <li>Launch and thermal environment</li> <li>Parts failure</li> </ul>	<ul style="list-style-type: none"> <li>Parts selection, inspections, and testing</li> </ul>	<ul style="list-style-type: none"> <li>Loss of a specific measurement</li> </ul>	<ul style="list-style-type: none"> <li>None if only a few measurements lost</li> </ul>	<ul style="list-style-type: none"> <li>None</li> </ul>	<ul style="list-style-type: none"> <li>Replace defective part or module</li> </ul>	<ul style="list-style-type: none"> <li>None</li> </ul>	<ul style="list-style-type: none"> <li>Various sensors</li> <li>Status electronics package</li> </ul>	<ul style="list-style-type: none"> <li>Loss of only a few measurements would probably not be detrimental to interpretation of telemetry.</li> </ul>	
Pressure bulkhead door	<ul style="list-style-type: none"> <li>Cracks</li> <li>Warping</li> <li>Seal failure</li> <li>Failure to open prior to initial LST operation</li> <li>Failure to close for in-flight maintenance</li> </ul>	<ul style="list-style-type: none"> <li>Structural failure</li> <li>Motor or drive mechanism failure</li> </ul>	<ul style="list-style-type: none"> <li>Open door during prelaunch operations and verify door open prior to launch</li> </ul>	<ul style="list-style-type: none"> <li>Door position indicators</li> </ul>	<ul style="list-style-type: none"> <li>Inability to point telescope or acquire data or to pressurize SIP and perform shirt sleeve maintenance</li> </ul>	<ul style="list-style-type: none"> <li>None required</li> </ul>	<ul style="list-style-type: none"> <li>Replace seals or motors</li> </ul>	<ul style="list-style-type: none"> <li>If in-flight maintenance not feasible return to earth for repair</li> <li>None</li> </ul>	<ul style="list-style-type: none"> <li>None</li> </ul>	<ul style="list-style-type: none"> <li>Seals</li> <li>Drive motor and mechanism</li> <li>None</li> </ul>	<ul style="list-style-type: none"> <li>Determine feasibility of dual seals</li> <li>Ensure procedures require door open prior to launch</li> <li>Consider manual backup for door closure</li> </ul>

maintain the proper primary mirror, secondary mirror, and instrument alignments. The ability to compensate for some misalignment of these structures is provided by the focus, decenter, and tilt sensor systems. However, major structural failures cannot be compensated for and would result in mission failure.

The chance of a major structural failure occurring is considered very low if the above described methods of failure prevention and controls are used.

The preliminary maintainability analysis indicates that little or no in-flight maintenance is feasible for the structural elements because it would necessitate extravehicular activity (EVA). The alignments are of such a critical nature that they probably could not be satisfactorily achieved in flight.

#### C.10.c(2) Main Optics

The failure modes identified for the mirrors are contamination of the surface, distortion, and surface deterioration/damage. The contamination, caused by materials outgassing and external sources such as spacecraft propulsion, can be prevented or minimized by proper materials selection and isolation of the mirrors from external sources. The distortion, caused by the thermal environment and misalignment of the supporting structure, can be compensated for by the force actuators and thermal blanket/heaters on the primary mirror and by the focus, centering, and tilt adjustments on the secondary mirror. In general, most of the failure modes identified for the optics would result in degradation of the data. Complete loss of all data would be very unlikely.

In-flight maintenance and mirror replacement are considered impractical since it would necessitate EVA.

#### C.10.c(3) Thermal Control

The failure modes identified in this subsystem are primarily the failures of heaters or thermostats in remote assemblies and electronics parts in the thermal controller. These failures generally result in data degradation owing to mirror distortion or misalignment. Redundancy will be incorporated. Also, Hi-Rel screened electronic parts will be specified.

The preliminary maintainability analysis indicates that in-flight maintenance should be considered for the electronics control package and for the remote heater assemblies.

#### C.10.c(4) Data Handling and Command Control

The failure modes identified in this subsystem are primarily parts failures. They would result in loss of only one or a few channels. The effects of these failures can be minimized by providing internal redundancy and/or more than one channel for critical data, particularly command functions. Failure prevention methods include use of Hi-Rel screened electronics parts and provision of adequate environmental protection for sensitive parts and components.

#### C.10.c(5) Electrical Distribution

The failure modes identified in this subsystem are open and short circuits caused by the environments or parts failures. All of these failure modes will be protected against by redundancy incorporation and the ability to cross switch and isolate power distribution units and controllers to operate circuits and components of failed units. Also, Hi-Rel screened parts will be used and adequate environmental protection provided.

There is no corrective action that can be taken prior to the first maintenance visit other than cross-switching units and isolating failed units. At the first visit, the corrective action could consist of replacement of the power distribution units and power controllers.

#### C.10.c(6) Pointing and Stabilization

The failure modes identified in this subsystem consist of parts failures in the star trackers, encoders, computer, and electronics and of electrical or mechanical failures in the resolvers, drive motors, actuators, and folding mirrors.

Redundancy will be used to reduce the effects of failures in this subsystem, resulting in the elimination of critical effects of any single failure. Three complete tracking loops including actuators are provided, with two required to perform the function.

A backup mode will permit operation with only one loop operation, with rotational tracking and stability provided by the vehicle rotational control system.

In this subsystem, the corrective action that can be performed prior to the first maintenance visit consists of switching out a failed star tracker loop or using different combinations of the three tracking actuators in the event of a failure. The corrective action performed at the first maintenance visit will be to replace all failed components in the pressurizable area.

#### C.10.c(7) Performance Control

The failure modes identified for the components of this subsystem are primarily failure of one of the components such as the sensor, actuator, target, light source, or control circuit. The effect of these failures generally is degradation of the experiment data in varying degrees. The design allows degraded operation with as many as three harmonic drive actuator failures. Redundancy is provided to reduce the effects of these failures and most of the adjustments can be performed without the sensor by trial and error, using the returned data. None of these failure modes are considered as mission-critical.

The corrective action at the first maintenance visit is limited to replacement of control packages, sensor packages, and light sources.

#### C.10.c(8) Primary Mirror Control

The ability to detect and correct slight degradation in primary mirror geometry is treated separately from the elements of performance control since the degradations are expected to be very minor. Acceptable performance should be experienced without need for correction. The correction capability is an added system refinement to achieve maximum resolution. Failures in this capability should not be of serious concern. Its design will be fail-safe such that a failure will not cause an actuator to exert a dangerous, damaging, or seriously degrading force on system performance.

Maintenance of the primary mirror figure control circuits should be limited to replacement of a faulty control module during a maintenance visit. Replacement of force actuators is considered neither necessary nor practical.

#### C.10.c(9) Telescope Protective System

The elements of the protective system are the sun shield, aperture door, meteoroid shield, pressure bulkhead door, and telemetry elements. Of these, the sun shield and aperture door are possible single failure point sources. Failure of either could be caused by parts failure or by structural misalignment.

Structural warping can be held to an acceptable level by providing adequate tolerances and clearances, structural safety margins, and thermal protection. The other failure modes identified in this system have much less effect on mission success and are much less likely to occur. Therefore, these are considered neither critical nor a significant risk to the mission.

The bulkhead door will be in the open position during launch and system operation and, therefore, is not considered a possible operational failure source. However, because the door is needed for shirtsleeve maintenance activity in the instrument area, it is provided with redundant drives. Repairs to the door should consist of possible gasket or drive motor replacement.

#### C.10.d Reliability Prediction

A reliability prediction has been performed on the OTA conceptual design to provide a basis for evaluation of the selected design approach and to permit incorporation of optimum combinations of redundancy to satisfy overall OTA mission requirements. This prediction, when expanded to lower levels in the subsequent design phases, will provide the basis for determining the frequency of maintenance visits and the spares requirements.

Since this analysis was performed on the conceptual design, the failure rates used in most cases are those from hardware proposed for similar functions on other programs. For example, the primary failure rate data source was the ATM follow-on study\* performed by Martin-Marietta Corporation for MSFC.

OTA reliability prediction is diagrammed in Fig. C.10-2, which shows that redundancy is utilized in the case of the tracking loops where two of three loops are required and in the case of the harmonic drive actuators where five of six are required. Redundancy is also included (not depicted) for the thermal control, the electrical power distribution and control, the sun shield, the aperture door, and the bulkhead door. In the case of the remote status sensors, it was reasoned that some sensors and controls could be lost without serious effect since their functions could be superseded by analysis of data from other sensors and from the outputs of the instrument packages.

OTA success probability values have been calculated and are presented in Table C.10-2. The total predicted OTA reliability for 1 year is quite excellent at 0.961. This is achieved by incorporating redundancy where necessary and by deleting nonessential assemblies from the reliability calculation.

The reliability effort during subsequent design phases will involve primarily selection of designs that eliminate or reduce the effects of critical single failure points. This will necessitate the incorporation of a certain amount of redundancy and may result in some additional reliability improvement to most if not all of the subsystems of the OTA.

---

\*ED-2002-795, Vol. IV, Contract NAS8-24000 (Apr 1969).

Table C.10-2 – OTA Failure Rate Tabulation and Reliability Prediction

	Subsystem Failure Rate ( $\lambda$ ) (note 1)	1-Year Success Probability	2-Year Success Probability
Main optics and structures	0.018	0.9998	0.9996
Thermal control (note 2)	23.00	0.9991	0.9982
Data handling and command control (note 3)	0.25	0.9988	0.9976
Electrical power (note 2)	16.75	0.9983	0.9966
Pointing and stabilization (note 2)	44.73	0.9860	0.9722
Figure sensor (note 4)	3.505	—	—
Primary force actuators and control (note 4)	29.0	—	—
Alignment sensors and logic	9.812	0.9898	0.9798
Harmonic drive actuators and control (note 2)	10.50	0.9999	0.9999
Sun shield (note 2)	8.75	0.9958	0.9916
Aperture door (note 2)	9.35	0.9935	0.9871
Meteoroid shield and baffles (note 5)	0.008	—	—
Remote status sensors and electronics (note 4)	—	—	—
Pressure bulkhead door (notes 2 and 6)	—	—	—
Overall		0.9615	0.9248

- Notes:
- 1 Failure rates include those of any incorporated redundant elements.  $\lambda$  = failures per  $10^6$  hours.
  - 2 Subassemblies include redundancy.
  - 3 OTA responsibility for data handling includes only one D/A converter. Other elements are considered system responsibility.
  - 4 Subassemblies provide refined performance or capability but are not essential and, hence, not included in the reliability prediction.
  - 5 The meteoroid shield and baffles can suffer damage without affecting system performance and are not included in the reliability calculation.
  - 6 The bulkhead door is a maintenance aid to permit shirtsleeve module replacement and is not considered an operational failure contributor.



## C.11 MASS PROPERTIES

This section presents the final mass properties data for the optical telescope assembly (OTA), phase A. The final mass properties mathematical model is based on the configuration detailed in Figs. A.1-1 and C.11-1. The mass properties coordinate system (Fig. C.11-2) has been modeled per Figure 1 of specification MIL-M-38310, Mass Properties Control Requirements for Missile and Space Vehicles, with the following exception. As indicated in Fig. C.11-2, the +z direction of the z axis in the LST coordinates is upward; the -z direction is downward. This is the opposite of the direction given in specification MIL-M-38310.

The drawings, part numbers, and dates given in the following list comprise the basis for the weights expressed in this section:

185510	LST/SIP Configuration
185522	LST Structural Baseline Design
213226	Cer-Vit 101 Lightweight Mirror
911329	LST Secondary Mirror Actuator Configuration as Modified by Sketch Dated 7/6/72
185505	OTA Structural Configuration No. 3 Dated 6/8/72
911386	SIP Structure Instrument Layout Dated 9/1/32, as Modified
185512	Tracker Assy L/O W/Scan Head
911379	Optical Micrometer Tilting Plate
914549	Alignment Sensor

The following items have been designed by the coordinated efforts of Itek and Martin Marietta:

1. Bulkhead pressure door assembly
2. Main baffle assembly
3. Meteoroid shield and DMM assembly
4. Sun shield assembly
5. Aperture door assembly

The primary mirror mass properties are reflective of the Itek design P/N 213226 with a face and back plate final thickness of 1.00 and 1.19 inches, respectively, as opposed to the blank thickness delineated on the drawing.

The system configuration, station number, butt lines, and water lines are delineated on Fig. C.11-2.

The electronics weight reflects redundancy for increased reliability as follows:

Alignment actuators electronics	100%
Alignment sensor electronics	Built in by design
Sun shield electronics	100%
Aperture door electronics	100%
Pressure bulkhead electronics	100%
Temperature control electronics	100%
Power distribution electronics	100%
Pointing and control electronics	100%
Stabilization actuator electronics	50%

The totals of the OTA mass properties analysis are as follows:

	Design Goal Mass kilograms	Present Mass Without Contingency, kilograms	Present Mass With Contingency, kilograms
OTA without instrument support thermal control system	4,468.48	4,554.95	5,076.40
OTA with instrument support thermal control system	4,642.18	4,720.58	5,268.79

The present mass without contingency for the OTA with thermal control system (i.e., 4,720.58 kilograms) is further subdivided into the following categories:

	Mass Kilograms	Weight Pounds
Structural	1,831.56	4,038.58
Mechanical	469.55	1,035.35
Electrical	48.34	106.59
Optical	2,059.22	4,540.58
Harness (cable), external	31.75	70.00
Thermal	94.44	208.24
Hardware	23.82	52.52
Electronics	161.90	356.99
Total	4,720.58	10,408.85

The following pages reflect the summary weight statements, contingency factors, and maximum condition mass properties summary of the OTA.

LARGE OPTICAL TELESCOPE ASSEMBLY  
SUMMARY WEIGHT STATEMENT (Maximum)  
Ref. Dwg. 185510  
(Pounds) and Kilograms

DESCRIPTION	(WEIGHT) MASS WITH-OUT CONTING.	4720.14	(WEIGHT) MASS WITH CONTING.	UNIT POWER-W
Optical Telescope Assembly			(11617.70)	5268.79
Structural Support Assembly		(10408.85)		
Metering Truss	(3387.59)	1535.99	(3895.23)	
Telescope Inst. Supt. Stru.	(888.16)	402.79	(1021.38)	
Meteoroid Shell	(330.66)	149.96	(380.26)	
(Desaturation Magnets)*	(1481.60)	671.93	(1703.84)	
Baffles	(310.40)	(140.77)	(772.72)	
Electronics Structure	(643.55)	291.56	(356.96)	
Main Optics Assembly	(43.62)	19.75	(739.59)	
Primary Mirror Assembly	(4589.12)	2081.23	(335.41)	
Secondary Mirror Assembly	(4412.65)	2001.20	(4798.23)	2176.07
Focal Plane and Fold Optics	(88.27)	40.03	(2084.03)	
	(88.20)	40.00	(46.06)	
			(101.51)	
			(101.42)	
Thermal Control System				
Primary Mirror Thermal Syst.	(591.01)	268.04	(685.93)	452
Secondary Mirror Thermal Syst.	(31.02)	14.07	(36.67)	
Passive Thermal Syst.	(20.68)	9.38	(24.79)	
SIP Thermal Cont. Syst.	(174.12)	78.97	(200.24)	
	(365.19)	165.62	(424.23)	
Pointing Control System				
Fine Guidance Sensor	(321.98)	145.92	(401.50)	110
Tracking Actuators	(256.83)	116.48	(326.58)	
	(65.15)	29.44	(74.92)	
Performance Control System				
Focus Sensor	(304.34)	138.05	(360.71)	163.58
Angle Sensor	(27.92)	12.66	(34.11)	40
Decenter Sensor	(19.50)	8.84	(22.83)	21
Figure Sensor	(35.50)	16.10	(42.83)	21
Secondary Mir. Align Actuators	(38.29)	17.36	(45.18)	40
Primary Mirror Force Transducers	(145.13)	65.86	(168.36)	75
	(38.00)	17.23	(47.40)	100

\* Desaturation magnets are part of attitude control system and this mass value appears in the SSM Section of the Master Equipment List.

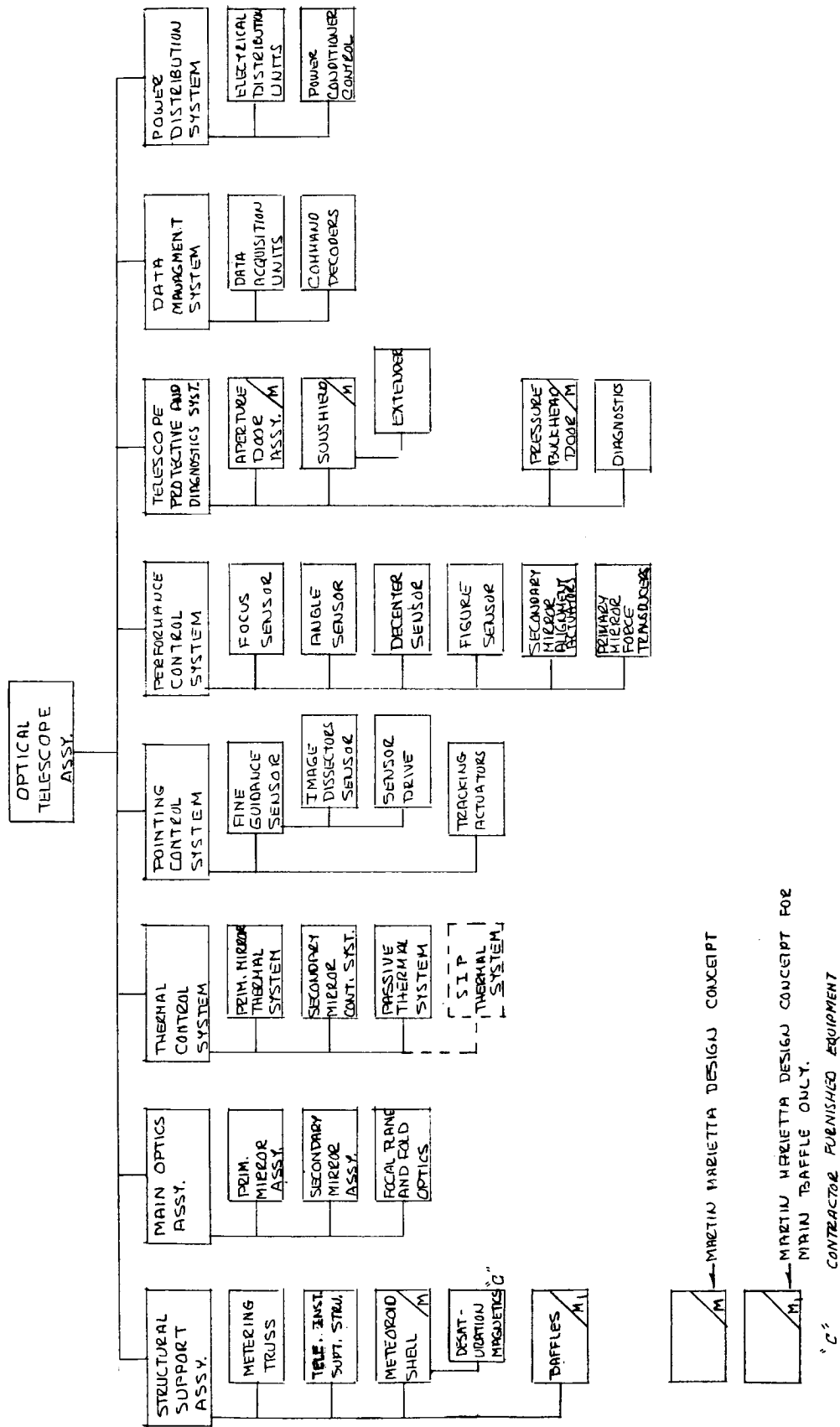
LARGE OPTICAL TELESCOPE ASSEMBLY  
SUMMARY WEIGHT STATEMENT (Maximum)  
(continued)

DESCRIPTION	(WEIGHT) MASS WITH-OUT CONTING.	(WEIGHT) MASS WITH CONTING.	UNIT POWER-W
Telescope Protective Diag. System	(1132.80)	(1320.41)	598.87
Aperture Door Assembly	(217.30)	(250.57)	30
Sunshield	(757.60)	(880.73)	60
Pressure Bulkhead Door	(105.90)	(123.96)	40
Diagnostics	(52.00)	(65.25)	115
Data Management System	(7.00)	(9.10)	4.13
Data Acquisition	(4.70)	(6.11)	
Command Decoders	(2.30)	(2.99)	
Power Distribution System	(75.00)	(146.50)	66.44
Electrical Distribution	2.27	2.95	
Power Conditioner Control Cabling	(70.00)	(140.00)	63.49

( ) = Pounds Wt.  
= Kilograms Mass

CONTINGENCY FACTORS

<u>ITEM</u>	<u>DESCRIPTION</u>	<u>ESTIMATED MASS</u>	<u>CALC. MASS PRE-QUAL.</u>	<u>CALC. MASS POST-QUAL.</u>	<u>ACTUAL MASS</u>
1	Structural, Mechanical, Optical, Thermal and Hardware	15%	5%	3%	0
2	Electro-Mechanical	30%	20%	10%	0
	0 to 4 kg	20%	15%	5%	0
	4 to 80 kg	15%	10%	5%	0
	80 + kg				
3	Wiring	100%	25%	5%	0
4	Electronics	25%	15%	5%	0



M → MARTIN HARIETTA DESIGN CONCEPT  
 M1 → MARTIN HARIETTA DESIGN CONCEPT FOR MAIN BAFFLE ONLY.  
 'C' → CONTRACTOR FURNISHED EQUIPMENT

Fig. C.11-1 — Mass properties system configuration and math model

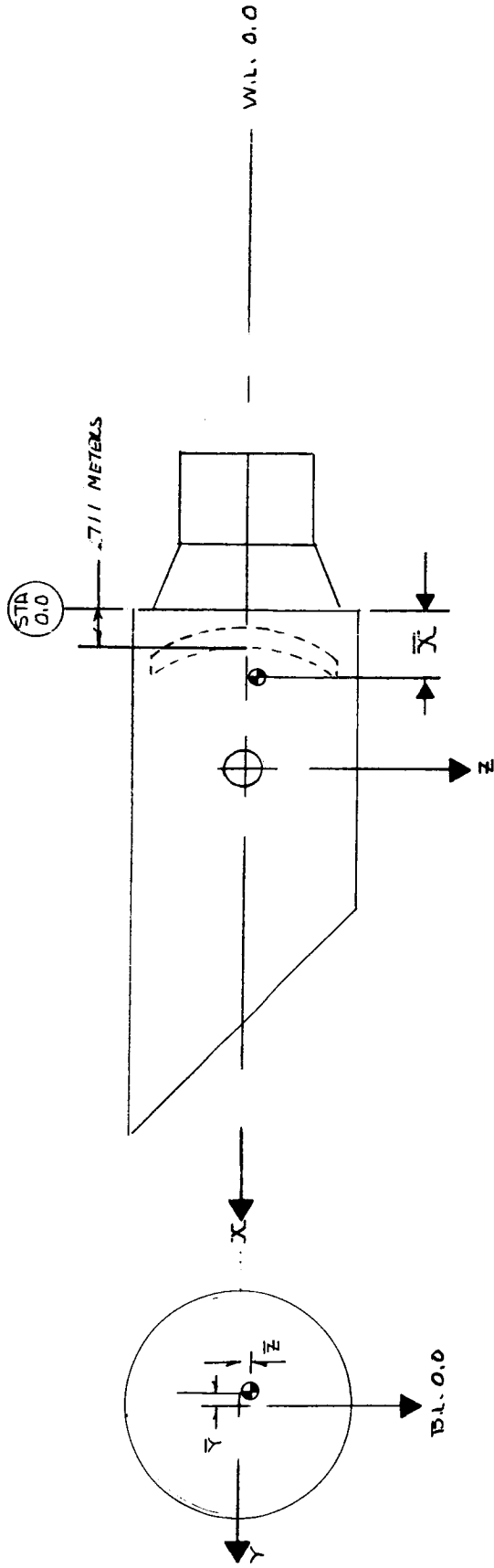


Fig. C.11-2 — System coordinates and reference data

APPROVAL

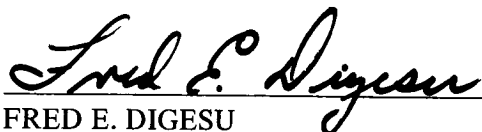
LARGE SPACE TELESCOPE  
PHASE A FINAL REPORT

Volume III – Optical Telescope Assembly

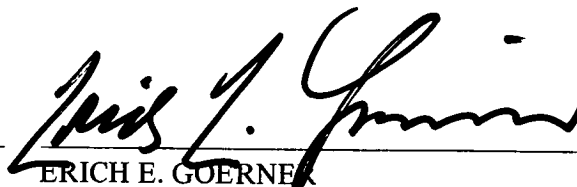
By Program Development  
(This volume prepared by Itek Corporation)

The information in this report has been reviewed for security classification. Review of any information concerning department of Defense or Atomic Energy Commission programs has been made by the MSFC Security Classification Officer. This report, in its entirety, has been determined to be unclassified.

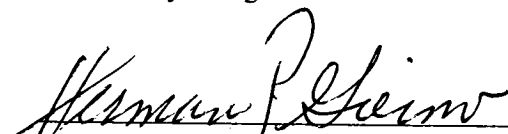
This document has also been reviewed and approved for technical accuracy.



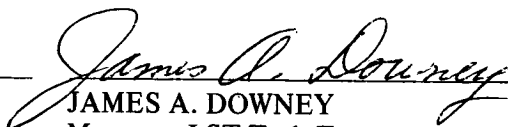
FRED E. DIGESU  
Chief, Electronics and Control Division  
Preliminary Design Office



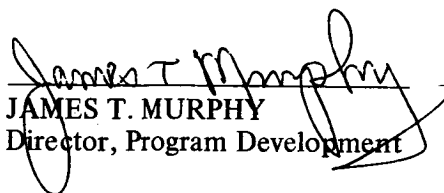
ERICH E. GOERNE  
Director, Preliminary Design Office



HERMAN P. GIEROW  
Director, Mission and Payload  
Planning Office



JAMES A. DOWNEY  
Manager, LST Task Team



JAMES T. MURPHY  
Director, Program Development



DISTRIBUTION

INTERNAL

DIR  
Dr. Petrone

DEP-T  
Dr. Lucas

AD-S  
Dr. Stuhlinger

PD-DIR  
Mr. Murphy  
Mr. Jean  
Dr. Mrazek

PD-LST  
Mr. Downey  
Dr. O'Dell  
Mr. McCulloch  
Mr. Olivier (8)  
Mr. Heyer (8)  
Mr. Hamilton  
Mr. Perry  
Mr. Nelson (6)  
Mr. Ealy  
Mr. Conway  
Mr. Teuber

PD-PL  
Mr. Huff

PD-MP  
Mr. Gierow (3)  
Mr. Emanuel  
Mr. Bradford

PD-PP  
Mr. Sneed (3)

PD-SL  
Mr. Trott

PD-DO  
Mr. Goerner  
Mr. Marshall  
Mr. Laue  
Mrs. Kozub  
Mr. Darwin  
Mr. Butler  
Mr. Blumrich  
Mr. Colley  
Mr. Love  
Mr. Nixon  
Mr. Fritz  
Mr. Mordan  
Mr. Goldsby  
Mr. Burton  
Mr. French  
Mr. Fults  
Mr. Kromis  
Mr. Digesu (10)  
Mr. Fikes  
Mr. Schultz  
Mr. Davis  
Mr. Green  
Dr. Steincamp  
Mr. Sanders  
Mr. W. Price  
Mr. Boehme

PD-DO (Cont'd)  
Mr. Rood  
Mr. Arsement  
Mr. Reed

SS-H  
Dr. Speer  
Mr. Fichtner  
Mr. Dailey  
Mr. Shields  
Mr. Wiesenmaier  
Mr. Carlile

SP-EM  
Mr. Harden  
Dr. Thomason

MO  
Mr. Kurtz (2)

S&E-DIR  
Dr. Weidner  
Mr. Richard

S&E-S&P  
Mr. Vreuls (2)

S&E-R  
Dr. Johnson

S&E-AERO  
Dr. Geissler  
Mr. Horn  
Mr. Dahm (2)  
Mr. Baker (3)  
Mr. Lindberg (3)  
Dr. Lovingood (5)

S&E-ASTR  
Mr. Moore  
Mr. Horton  
Mr. Powell  
Mr. Mack (3)  
Mr. Barr (8)  
Mr. Hosenthien (3)  
Mr. Wojtalik (3)  
Mr. Swearingen (3)  
Mr. Taylor (3)  
Mr. Boehm (3)  
Mr. Aden (3)  
Mr. Dugan (3)  
Mr. Justice  
Mr. Counter  
Mr. Zurasky  
Mr. Shearer  
Dr. Clarke  
Mr. Tutt  
Mr. Golley

S&E-ASTN  
Mr. Heimburg  
Mr. Kingsbury  
Mr. Kroll (2)  
Mr. Isbell (2)  
Mr. Sterett (2)  
Mr. Paul (2)  
Mr. Connor (2)  
Mr. Swinghamer (2)

S&E-SSL  
Dr. Haeussermann  
Dr. Naumann (2)  
Dr. Decher  
Dr. Sieber (2)  
Mr. Snoddy (2)

A&PS-MS-D  
Mr. Garrett

A&PS-MS-I  
Mr. Ziak

A&PS-MS-IP  
Mr. Ledbetter (2)

A&PS-MS-IL  
Miss Robertson (8)

A&PS-MS-H  
Mr. Akens

A&PS-PAT  
Mr. Wofford

A&PS-TU (6)

EXTERNAL

NASA Headquarters  
MH/Mr. Donlan (Vol I only)  
MK/Mr. Culbertson (Vol I only)  
MTL/Mr. Armstrong (Vol I only)  
SG/Dr. Nancy Roman (Vol I only)  
SG/Mr. Aucremanne (3 complete sets plus 10 of Vol I)  
WX/Mr. Krueger (3 complete sets plus 6 of Vol I)

Goddard Space Flight Center  
Code 604/Mr. Meese (80)

Johnson Space Center  
LP/Mr. Heberlig  
LP/Mr. Battey  
ER-4/Mr. Davis  
ER-4/Mr. Hirasaki  
ER-4/Mr. Casey

Kennedy Space Center  
FP-B/Mr. McCoy  
LL-OPN-2/Mr. Sheppard  
FP-B/Mr. Engle  
FP-B/Mr. Bailey

Dr. Herbert Flicker  
L-DOT TA-35  
Los Alamos Scientific Lab  
Los Alamos, N. W. 87544

Dr. Robert E. Danielson  
Princeton University Observatory  
Peyton Hall  
Princeton, N. J. 08540

Scientific and Technical  
Information Facility  
College Park, Maryland 20740  
Attn: NASA Representative (S-AK/RKT) (25)